DISSERTATION

Multi-Use Operation of Battery Energy Storage Systems

Ausgeführt zum Zwecke der Erlangung des akademischen Grades eines
Doktors der technischen Wissenschaften
unter der Leitung von

Univ.-Prof. Dr.-Ing. Wolfgang Gawlik

Institut für Energiesysteme und Elektrische Antriebe

eingereicht an der

Technischen Universität Wien
Fakultät für Elektrotechnik und Informationstechnik

von

Dipl.-Ing. Jürgen Marchgraber

Wien, im Juli 2021

Forschungsbereich Energiesysteme und Netze
A-1040 Wien, Gusshausstr. 25, Internet: http://www.ea.tuwien.ac.at

Eidesstattliche Erklärung

Hiermit erkläre ich, dass die vorliegende Arbeit ohne unzulässige Hilfe Dritter und ohne Benutzung anderer als der angegebenen Hilfsmittel angefertigt wurde. Die aus anderen Quellen oder indirekt übernommenen Daten und Konzepte sind unter Angabe der Quelle gekennzeichnet. Die Arbeit wurde bisher weder im In- noch im Ausland in gleicher oder in ähnlicher Form in anderen Prüfungsverfahren vorgelegt.

Wien, 9. Juli 2021

Danksagung

Die vorliegende Arbeit entstand während meiner Tätigkeit als wissenschaftlicher Mitarbeiter am Institut für Energiesysteme und Elektrische Antriebe der Technischen Universität Wien.

Mein besonderer Dank gilt meinem Betreuer Univ.-Prof. Dr.-Ing. Wolfgang Gawlik, der mir die Möglichkeit einer Anstellung verschaffte und durch zahlreiche bereichernde Gespräche das Entstehen dieser Arbeit unterstützte. Inbesondere für seinen stets wertschätzenden Umgang und seinen leitenden Rat während außergewöhnlicher Umstände möchte ich mich sehr herzlich bedanken.

Ebenfalls bedanke ich mich bei allen heutigen und ehemaligen Mitarbeiten des Forschungsbereichs Energiesysteme und Netze für die fachlichen Diskussionen und vor allem für das angenehme und kollegiale Arbeitsumfeld.

Ein weiterer Dank gilt den teilnehmenden Mitarbeitern der EVN AG und Netz Niederösterreich GmbH, welche die Durchführung eines gemeinsamen Forschungsprojekts ermöglichten. Insbesondere danke ich Herrn Dipl.-Ing. Dr. Manfred Wurm für seinen fachlichen Rat und bedauere zutiefst sein allzu frühes Ableben.

Mein herzlichster Dank gilt meiner Familie und insbesondere meinen Eltern Monika und Walter für deren bedingungslose und aufopfernde Fürsorge, deren finanzielle Unterstützung während meines Bildungswegs und deren unentwegte moralische Unterstützung.

Zu guter Letzt danke ich meiner Lebensgefährtin Eva für ihre liebevolle Unterstützung und ihre Geduld während der Erstellung dieser Arbeit. Insbesondere ihre zahlreichen ermutigenden Worte, gerade in diesen so zermürbenden Zeiten der Covid-19-Pandemie, gaben mir die nötige Kraft, diese Arbeit fertigzustellen.

Kurzfassung

Batterie-Energiespeichersysteme (BESS) auf Basis von Li-Ionen-Technologie gelten als mögliche Anbieter von Diensten im zukünftigen Stromversorgungssystem. Obwohl die Preise für Li-Ionen-Akkus kontinuierlich sinken, ist es heute immer noch schwierig, mit der Ausübung eines einzigen Dienstes Rentabilität zu erzielen. Der Mehrzweckbetrieb von BESS, um ein sogenanntes "value-stacking" von Diensten zu erreichen, ist daher ein stark diskutiertes Thema in der aktuellen Forschung und Fachliteratur. Mehrfach wurde bereits nachgewiesen, dass ein solcher Mehrzweckbetrieb das Potential birgt, die Rentabilität von BESS enorm zu steigern. Die vorliegende Arbeit untersucht einen solchen Mehrzweckbetrieb und konzentriert sich dabei auf drei Aspekte. Der erste Aspekt betrifft die Charakterisierung von BESS anhand von Messungen, die an einem realen BESS durchgeführt werden, dessen Konstruktion wissenschaftlich begleitet wurde. Der zweite Aspekt betrifft die Identifizierung von Diensten, für die BESS geeignet sind, und eine detaillierte Untersuchung ausgewählter Dienste. Diese detaillierten Untersuchungen basieren auf der Betrachtung der entsprechenden rechtlichen und technischen Anforderungen, Simulationen in MATLAB/SIMULINK und DIGSILENT POWERFACTORY sowie auf Feldtests, welche für jeden der ausgewählten Dienste am BESS-Teststandort durchgeführt wurden. Der dritte Aspekt betrifft die Untersuchung und mögliche Implementierung eines Mehrzweckbetriebs. Der Mehrzweckbetrieb eines BESS kann in zwei Teile unterteilt werden: die operative Planungsphase und der Echtzeitbetrieb. Während die operative Planungsphase bereits in einigen Studien untersucht wurde, ist die Überführung in einen Echtzeitbetrieb ein selten behandeltes Thema. Aus diesem Grund werden in der vorliegenden Arbeit Konzepte zur Implementierung eines Echtzeit-Mehrzweckbetriebs diskutiert und die Methode der dynamischen Priorisierung vorgeschlagen, die Zielkonflikte während eines Mehrzweckbetriebs löst. Darüber hinaus wird ein Mehrzweckbetrieb für vier ausgewählte Dienste durch Simulation in MATLAB/SIMULINK untersucht und der vorteilhafte Einfluss eines Mehrzweckbetriebs auf die erzielbaren Erlöse nachgewiesen.

Zur Charakterisierung von BESS werden mehrere entscheidende Indikatoren zusammengefasst, die zur Erstellung und Parametrierung von Simulationsmodellen benötigt werden. Es wird ein geeignetes Testverfahren vorgeschlagen, mit dem Indikatoren wie die Spannungskurve, der Wirkungsgrad des Umrichters, der tatsächliche Energiegehalt, die tatsächliche Kapazität oder Verluste mithilfe eines einzelnen Tests gemessen werden können. Dieses Testverfahren eignet sich zur Überwachung dieser Indikatoren, indem es nach bestimmten Zeiträumen erneut ausgeführt wird, und liefert dadurch vergleichbare Messergebnisse über die gesamte Lebensdauer des BESS.

Aus allen für BESS geeigneten Diensten werden die Dienste Primärregelreserve/Frequency Containment Reserve (FCR), Energiearbitrage, synthetische Schwungmasse, dynamische Netzstützung und Schwarzstart/Inselbildung ausgewählt, um diese detailliert zu betrachten. Insbesondere für FCR werden weiterführende Untersuchungen durchgeführt, die nicht nur das Verhalten bei der Erbringung von FCR analysieren, sondern auch das Verhalten des SoC-Managements, das erforderlich ist, um eine kontinuierliche Bereitstellung von FCR sicherzustellen. Durch die Untersuchung der sogenannten "Freiheitsgrade" für FCR als Methode zur Beeinflussung des SoC ohne die Notwendigkeit von Markttransaktionen wird gezeigt, dass ihre Verwendung den für das SoC-Management erforderlichen Energiebedarf erheblich reduziert. Darüber hinaus wird ein Algorithmus vorgeschlagen, der eine wesentliche Reduktion der Verluste ermöglicht, die während der Bereitstellung von FCR auftreten. Mehrere Messergebnisse von Feldtests illustrieren den erfolgreichen Betrieb zur Bereitstellung von FCR, eines entsprechenden SoC-Managements und des vorgeschlagenen Verfahrens zur Reduktion von Verlusten, welche alle mit dem untersuchten realen BESS implemen-

tiert wurden. Für die synthetische Schwungmasse liegt ein Schwerpunkt auf der Untersuchung des Verhaltens möglicher Implementierungen auf der Grundlage von netzfolgenden und netzbildenden Umrichterdesigns. Mithilfe von Electromagnetic Transient (EMT)-Simulationen werden zwei Ansätze unter Verwendung dieser Umrichterdesigns untersucht und verglichen. Auf Basis des netzfolgenden Ansatzes wurde der Dienst einer synthetischen Schwungmasse am realen BESS implementiert. Da die Netzfrequenz als Steuergröße für einen netzfolgenden Ansatz einer synthetischen Schwungmasse dient, ist die Qualität der Frequenzmessung von entscheidender Bedeutung dafür, wie genau das Verhalten einer realen Schwungmasse imitiert werden kann. Entsprechende Feldtests konzentrieren sich auf die Messung des Verhaltens der synthetischen Schwungmasse mit dem Ziel, ein mögliches Testverfahren zum Nachweis der Funktionsfähigkeit einer synthetischen Schwungmasse im Rahmen einer Präqualifikation zu beleuchten. Zur Untersuchung der dynamischen Netzstützung werden EMT- und Root Mean Square (RMS)-Simulationsmodelle erstellt, die einen geeigneten Strombegrenzungsalgorithmus berücksichtigen. Während das in MATLAB/SIMULINK erstellte EMT-Simulationsmodell das genaue Zeitverhalten eines Umrichters bei Fehlern gemäß den aktuellen Gridcodes reproduzieren kann, stellt das in DIGSILENT POWERFACTORY erstellte RMS-Simulationsmodell eine Vereinfachung der EMT-Version dar, welches in das Modell eines Netzabschnitts integriert ist und für Berechnungen zur Planung entsprechender Feldtests verwendet wird. Die Messergebnisse dieser Feldtests werden verwendet, um das Gridcode-konforme Verhalten des BESS hinsichtlich der dynamischen Netzstützung basierend auf erzwungenen symmetrischen sowie unsymmetrischen Kurzschlüssen zu validieren. Zudem werden diese Messergebnisse verwendet, um das Gridcode-konforme Verhalten hinsichtlich der Anforderungen an die Fault-Ride-Through-Fähigkeit zu validieren. Die Durchführung eines Schwarzstarts und der Betrieb eines Inselnetzabschnitts, eines sogenannten Microgrids, werden ebenfalls mithilfe eines Feldtests am realen BESS demonstriert. Die entsprechende Vorbereitung dieses Feldtests erfolgt mit Hilfe von EMT-Simulationen. In den Feldtests werden ein erfolgreicher Schwarzstart eines Microgrids demonstriert und die dynamischen Fähigkeiten des nachfolgenden Betriebs des Microgrids über Wirk- und Blindleistungssprünge untersucht. Darüber hinaus werden Windkraftanlagen während der Feldtests mit dem Insel-Microgrid synchronisiert, um die Möglichkeiten eines Inselbetriebs mit Unterstützung von regenerativen Einspeiseanlagen zu studieren, welcher eine länger andauernde Versorgung eines Microgrids während einer Störung des überlagerten Netzes ermöglichen könnte. Eine frequenzbasierte Steuerkurve wird vorgeschlagen und getestet, um die Leistung der Windkraftanlagen zu begrenzen und damit eine Überlastung bzw. Überladung des BESS zu verhindern.

In Bezug auf den Mehrzweckbetrieb von BESS wird ein neuartiges mathematisches Gerüst vorgeschlagen, in dem mehrere Dienste und ihre Interaktion unter Berücksichtigung des Konzepts der dynamischen Priorisierung zur Behandlung von Konflikten beschrieben werden. Es werden verschiedene Anwendungen vorgestellt, um das Verhalten des Konzepts unter normalen und außergewöhnlichen Netzbedingungen zu demonstrieren. Der Mehrzweckbetrieb von BESS wird mittels Langzeitsimulation in MATLAB/SIMULINK für die Dienste FCR, Energiearbitrage, Blindleistungsbereitstellung und SoC-Management untersucht. Die entsprechenden Ergebnisse belegen die Steigerung der erzielbaren Einnahmen durch die gleichzeitige Erbringung dieser Dienste im Vergleich zu ihrer alleinigen Bereitstellung. Da die gleichzeitige Bereitstellung auch mit einer erhöhten Belastung des BESS verbunden ist, wird berücksichtigt, dass ein Kompromiss zwischen steigenden Einnahmen und der Begrenzung der Auswirkungen auf die zyklische Alterung getroffen werden muss, um durch einen Mehrzweckbetrieb eine entsprechende Rentabilität zu erzielen.

Abstract

Battery Energy Storage System (BESS) based on Li-Ion technology are considered to be one of the possible providers of services in the future power system. Although prices for Li-Ion batteries are declining continuously, it is still difficult to achieve profitability from a single service today. Multi-use operation of BESS to reach a so-called "value-stacking" of services is therefore a hotly debated topic in literature since such an operation holds the potential to increase profitability dramatically. This thesis investigates such a multi-use operation and focuses on three aspects. The first aspect relates to the characterization of BESS based on measurements that are carried out at a real BESS, the construction of which was scientifically accompanied. The second aspect relates to identifying services BESS are suitable to provide and a detailed examination of a selection of these services. This detailed examination is done based on investigations of corresponding legal and technical requirements, simulations in MATLAB/SIMULINK and DIGSILENT POWERFACTORY, as well as field tests carried out at a real BESS for each of these selected services. The third aspect relates to the investigation and possible implementation of a multi-use operation. The multi-use operation of a BESS can be divided into two parts: the operational planning phase and the real-time operation. While the operational planning phase has been examined in many studies, there seems to be a lack of discussion for the real-time operation. For this reason, concepts for implementing a real-time multi-use operation are discussed and a procedure called dynamic prioritization is proposed, which resolves conflicts of functions during multi-use operation. Furthermore, a multi-use operation for a selection of four services is investigated by simulation in MATLAB/SIMULINK and proves the beneficial influence of stacking services regarding achievable revenues.

To characterize BESS, several decisive indicators are summarized that are useful for the creation and parameterization of simulation models. A suitable test procedure that allows measurement of indicators such as the voltage curve, the converter efficiency, actual energy content, actual capacity or losses within a single test is proposed. This test procedure is suitable to monitor these indicators throughout the lifetime of the BESS by rerunning it after certain time periods and delivers comparable measurement results.

From all identified services for which BESS are assumed to be suitable, the services Frequency Containment Reserve (FCR), energy arbitrage, synthetic inertia, dynamic voltage support and black-starting/islanding are selected to be examined in more detail. For FCR in particular, advanced investigations are carried out that not only examine the behavior of the provision of FCR, but also the behavior of the State of Charge (SoC)-management required to ensure continuous provision of FCR. By examining the so-called "degrees of freedom" for FCR, as a method of influencing the SoC without the need for market transactions, it is shown that their use significantly reduces the energy required for SoC-management. Furthermore, an algorithm is proposed which allows a substantial reduction of the losses that occur during the provision of FCR. Several measurement results from field tests illustrate the successful operation for the provision of FCR, a corresponding SoC-management and the proposed method for reducing losses, all of which were implemented at the real BESS. For the service synthetic inertia, an emphasis is placed on studying the behavior of possible implementations using grid-following and grid-forming converter designs that are investigated and compared using Electromagnetic Transient (EMT) simulations. A grid-following approach for realizing synthetic inertia was implemented in the real BESS. A strong dependence on the quality of the frequency measurement used as input for this service of this grid-following approach is identified as the most relevant issue that prevents ideal imitation of the behavior of

real inertia. Corresponding field tests focus on the measurement of the behavior of synthetic inertia based on the actual grid frequency with the foresight of how tests can be carried out in the future to prequalify the service synthetic inertia. For the investigation of the service dynamic voltage support EMT and Root Mean Square (RMS) simulation models are created that take into account an appropriate current limitation algorithm. While the EMT simulation model created in MATLAB/SIMULINK is able to reproduce the exact time behavior of a converter during faults according to the latest grid codes, the RMS simulation model created in DIGSILENT POWERFACTORY represents a simplification of the EMT version that is integrated in the model of a grid section, which is used for calculations to plan corresponding field tests. The measurement results of these field tests are used to validate the grid code conform behavior of the BESS regarding dynamic voltage support based on forced symmetrical as well as asymmetrical short-circuits at different locations. At the same time these measurement results are used to validate the grid code conform behavior regarding fault ride through requirements. The services of black-starting and operating an islanded grid section, a so-called Microgrid, are also demonstrated in the field. The corresponding preparation of this field test is carried out with the help of EMT simulations. A successful black-start of a Microgrid is demonstrated in the field tests. The dynamic capabilities of the subsequent operation of the Microgrid are investigated via active and reactive load-steps. Furthermore, wind-turbines are synchronized to the islanded Microgrid during the field tests in order to demonstrate the possibility of operating an islanded Microgrid for a longer duration. A frequency-based control curve is proposed and tested in order to limit the power output of the wind-turbines to prevent the BESS from being overloaded.

Regarding multi-use operation of BESS, a novel mathematical framework is proposed to describe several services and their interaction, considering the concept of dynamic prioritization capable of resolving conflicts of services. Several applications are presented in order to demonstrate the behavior of the concept during normal and abnormal grid conditions. The multi-use operation of BESS is investigated via long-time simulation in MATLAB/SIMULINK for the services FCR, energy arbitrage, reactive power provision and SoC-management. The corresponding results prove the increase of achievable revenues by stacking any of these services compared to their sole provision. Since the stacked provision is also coupled with an increased stress of the BESS, it is taken into account that there is a trade-off between increasing revenues and limiting the effects on cyclic aging in order to reach optimal profitability by a multi-use operation.

Contents

1 Introduction

This chapter gives an overview of the global trends for renewable energy systems and the role that Battery Energy Storage System (BESS) play in them today and in the future. In addition, this chapter defines the motivation for this thesis, formulates three research questions that are dealt with in this thesis, and lists all conference and journal articles published in the context of this thesis.

1.1 Global Trends for Renewable Energy Systems

The greenhouse gas levels in the atmosphere, in particular CO_2, which have increased since the beginning of industrialization, have already led to higher temperatures worldwide. The environmental effects of this climate change are far-reaching and include effects on the oceans, ice and weather. All of these effects may cause secondary effects such as droughts, heat waves and other extreme weather phenomena that all affect humanity, for example through associated crop failures and the associated malnutrition. Based on the scientific consensus that global warming is occurring and it is extremely likely that human-made CO_2 emissions have predominantly caused it, the United Nations Conference on the Environment and Development was held in Rio de Janeiro in 1992 and resulted in the United Nations Framework Convention on Climate Change (UNFCCC). In 1997 the members of the UNFCCC concluded the "Kyoto Protocol", which was the first international treaty that commits state parties to reduce greenhouse gas emissions. To strengthen the global response to these threats of climate change, the majority of all members of the UNFCCC ratified the so-called "Paris Agreement" in 2015, whose objective is to keep the global temperature rise well below 2 °C above pre-industrial levels this century and to pursue efforts to limit the temperature increase even further to 1.5 °C. These temperature levels mark sensitive limits, the exceeding of which is associated with an even higher risk of more serious environmental effects. In order to achieve the goal of the Paris Agreement, the Intergovernmental Panel on Climate Change (IPCC) assumes that greenhouse gas emissions will have to drop to zero by 2060 at the latest.

Following the Kyoto Protocol the European Parliament issued the "Renewable Energy Directive" (2009/28/EC), whose objective is to promote the use of energy from renewable sources. Based on this directive, all member states of the European Union were committed to defining targets for the development of renewable energy by 2020. These targets were described in National Renewable Energy Action Plans (NREAP). The entirety of these NREAP led to the European Union's "20-20-20"-goal of increasing the share of renewable energy of the total gross final energy consumption, of reducing the greenhouse gas emission and of increasing the energy efficiency in the European Union by 20 %, each compared to 1990. These goals were expanded in 2018 in the "Renewable Energy Directive II", which describes corresponding goals until 2030 as part of the "Clean energy for all Europeans package". These goals comprise an expected increase of the share of renewable energy to 32 % in gross final energy consumption, a reduction of the greenhouse gas emissions by 55 % and an increase of energy efficiency by 32.5 % by 2030, where the relative change of the last two goals is related to corresponding values in 1990. These goals go back on the "REmap"-study of the International Renewable Energy Agency (IRENA) [91], which identifies cost-effective renewable energy options for all member states of the European Union. One of the key findings is that the European Union could double the renewable share in its energy mix cost-effectively up to 34 % until 2030. This share refers to the whole energy demand in the European Union, including the

heating and cooling sector, the transport sector and the power sector. The share of renewable energy in the power sector alone is estimated to rise from 29 % in 2015 [58] up to 50 % in 2030.

In general, the "Clean Energy for all Europeans Package (CEP)" describes an energy policy framework of the European Union, which was completed in 2019 and facilitates the transition away from fossil fuels towards cleaner energy in order to deliver on European Union's Paris Agreement commitments. Besides the "Renewable Energy Directive II" mentioned above, this CEP includes seven other legislative acts, such as the "Electricity Market Directive", the "Electricity Regulation", the "ACER Regulation", the "Regulation on Risk Preparedness in the Electricity Sector", the "Regulation on the Governance of the Energy Union", the "Energy Efficiency Directive" and the "Energy Performance of Buildings Directive". All members of the European Union have 1-2 years to transpose these new directives of the CEP into national law.

Considering only the power sector, the REmap study of IRENA [91] assumes a massive integration of wind power and solar photovoltaic generation in the power system, which will represent the majority of the 50 % share of renewable energy in the power sector in 2030, while in 2010 the share of renewable energy was only 20 % (with 11 % hydro, 4 % wind, 4 % biomass and 1 % solar photovoltaic). The potential identified in the REmap case would result in 327 GW of installed capacity for wind and 270 GW for solar photovoltaic, while other technologies, including biomass, hydropower, geothermal and concentrated solar power would contribute further 217 GW. Compared to 2010 this would represent a 4-fold growth of wind power and a 9-fold growth of solar photovoltaic. Considering the full-load hours of the corresponding technology, this results in an energy share of renewable energy of 50 % in 2030, where 29 % are based on variable generation, namely wind power and solar photovoltaic generation.

In Austria the "Erneuerbaren-Ausbau-Gesetz (EAG)" has the objective to ensure the expansion and integration of renewable energy and implements the requirements according to the European Renewable Energy Directive II. The EAG is planned to come in force in 2021 and describes a goal of 100 % coverage of the total electricity consumption (meaning only the power sector) in Austria by renewable energy in 2030. Taking into account an increase of the annual electricity consumption from 72 TWh in 2018 to 76 TWh – 85 TWh in 2030 [136], an additional integration of renewable energy amounting up to 27 TWh/yr is necessary, when assuming a share of renewable energy of 80 % in 2018. This additional amount of 27 TWh/yr is planned to be achieved using 11 TWh/yr of additional solar photovoltaic, 10 TWh/yr of additional wind power plants, 1 TWh/yr of additional hydro power plants and 1 TWh/yr of additional power plants based on biomass. Assuming realistic full-load hours of the corresponding technologies, Fig. 1.1 illustrates a predicted electricity demand and generation in Austria in 2030 compared to their counterpart in 2018. The prediction uses the time characteristics of 2018 and scales them up with the planned increase of demand and generation, with the amounts as described above.

Although Fig. 1.1(b) only shows a rough prediction of the electricity demand and renewable generation in 2030, it illustrates the expected behavior of a 100 % renewable supply well enough. Fig. 1.1(a) shows the electricity demand and renewable generation in 2018 and demonstrates that the power difference between demand and renewable generation has to be covered by conventional (fossil) power plants or imports, which can be operated or marketed in a flexible manner. Assuming an increase of renewable energy with an amount of 27 TWh/yr, Fig. 1.1(b), on the other hand, demonstrates that for much of the time the demand can be fully covered by renewable energy. Considering only the total annual energy, a 100 % renewable supply is possible, because the surplus of power during moments of renewable peak power keeps up with the low power during moments of renewable troughs power. However, the price for this 100 % renewable supply are increased power fluctuations as shown in Fig. 1.1(b), which have to be compensated by flexibilities in the energy system, for example, conventional power plants that can react very quickly. Since it is planned to reduce the share of conventional power plants, other forms of flexibility may be indispensable in the future.

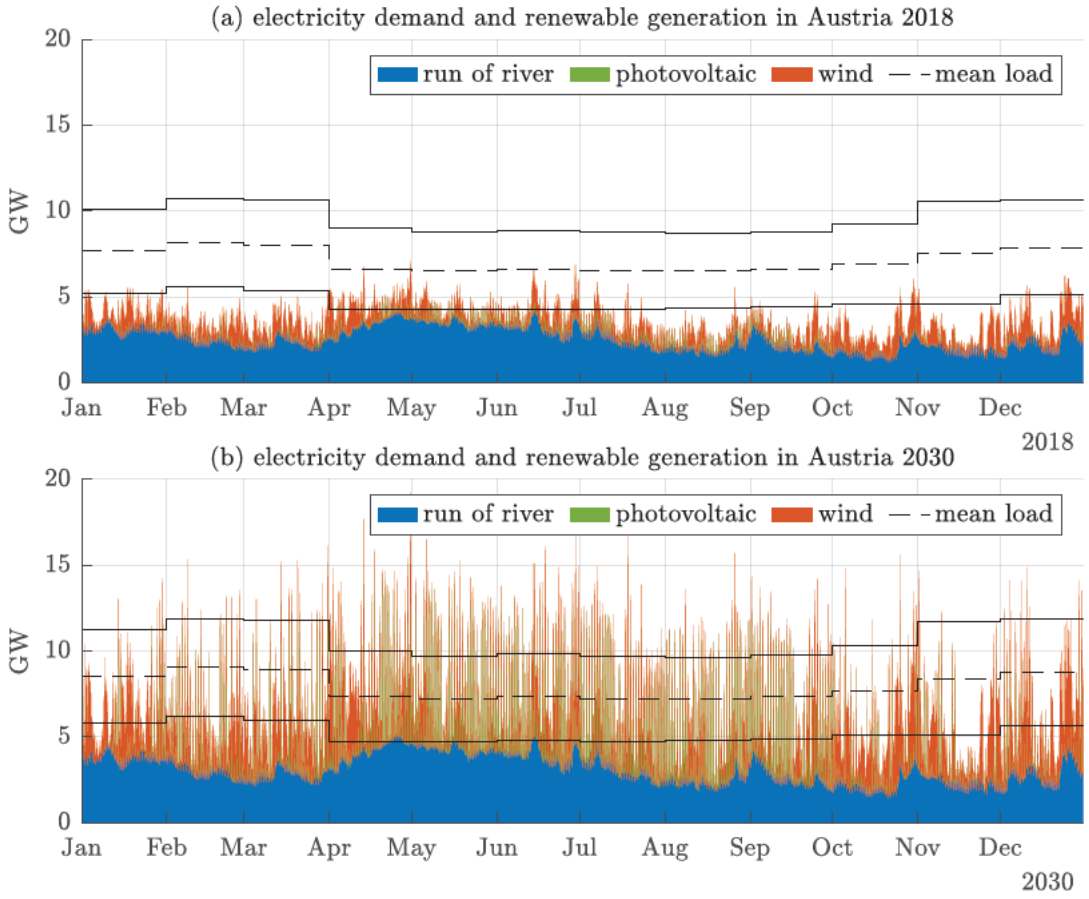

Figure 1.1: Comparison of electricity demand and generation in Austria in 2018 and predicted for 2030, calculated based on the planned integration of additional renewable energy of 27 TWh/yr. The solid black lines represent the monthly minima and maximuma of the load. The raw data for this figure is based on data of [39] and [61].

According to IRENA [91] the massive amount of variable renewable generation in the future poses new challenges for the operation of the power system. Fig. 1.1(b) illustrates one of these challenges in the form of increased power fluctuations. According to Sterner and Stadler [168] such power fluctuations in the range of several gigawatts will become the norm. The need for flexibilities is therefore undisputed. Such flexibilities include

(a) electricity transmission, by expanding the electric power grid with new interconnection lines in the distribution and transmission grid,
(b) flexibilization of remaining conventional (fossil) power plants,
(c) additional storage, including short-term storage (e.g. battery storage systems) and long-term storage (e.g. pumped hydro storage systems),
(d) demand side management, which allows influencing the actual load behavior and
(e) curtailment of variable renewable energy.

The latter flexibility, curtailment of renewable energy, however, should be minimized whenever possible, since any amount of renewable energy that is "thrown away" leads the energy transition to renewable energy ad absurdum. In general, any of the flexibilities mentioned above are considered to be necessary to cope with power fluctuations induced by variable renewable generation. According to Fraunhofer Institute [69], for example, performing a grid expansion by increasing transfer

capacities of interconnection lines between countries, on the one hand, leads to requirements on curtailment which are ten times lower than a hypothetical national autarchy, but on the other hand, avoiding curtailment would be difficult to achieve just by increasing transfer capacities, as highly correlated feed-in situations might occur. Therefore, also a more flexible use of conventional power plants, storage usage, demand side management and even curtailment will be necessary as additional flexibilities in the future power system.

Long-term and short-term storage technologies are therefore expected to be increasingly integrated in the power system [168]. According to IRENA [90], about 176 GW of totally installed power capacity was deployed worldwide in 2017, dominated by pumped hydro storage systems (96 %). This value goes back on the "DOE Global Energy Storage Database" [82], which collects and lists storage systems, categorized into "Electro-Chemical", "Electro-Mechanical", "Chemical", "Pumped Hydro Storage" and "Thermal Storage" systems worldwide. In the power sector, an amount of 4.67 TWh of electricity storage was estimated in 2017, where the major part (97 %) is being provided by Pumped Hydro Storage Systems (PHSS) [90]. It is worth noting that storage used in electromobility is not covered in this value. It is expected that the amount of electricity storage will increase to a value of 7.82 GWh up to 15.27 GWh in 2030 [90]. Besides PHSS, which is predicted to make out a major part of the total storage capability also in the future, the share of other storage technologies increases and includes technologies such as Compressed Air Energy Storages, flywheels, storage capacity of electromobility, as well as stationary BESS. Although BESS were estimated to provide only a small share of 11 GWh of the total storage capacity, with a total installed power capacity of 10 GW in 2017, also the storage capacity provided by BESS is expected to increase to a value of 100 GWh up to 421 GWh until 2030 [92]. This storage capacity can be assigned to home use BESS, also referred to as behind-the-meter BESS and utility-scale BESS, which are also referred to as large-scale, grid-scale or front-of-the-meter BESS. Utility-scale BESS are usually connected to the distribution, the transmission grid or in connection with a generation asset. They provide services required by system operators, such as ancillary services or grid stress relief. Behind-the-meter BESS are usually connected behind the utility meter of commercial, industrial or residential customers. They are primarily aiming at electricity bill savings through demand-side management. Several case studies for utility-scale BESS are listed in [92]. Unlike PHSS, BESS have the advantage of geographical and sizing flexibility and can therefore be installed closer to the location where additional flexibility is needed and can be easily scaled. The installation of PHSS, on the other hand, requires specific geological conditions. Furthermore, by 2030 the costs for BESS could fall by 50 % – 60 %, pushing forward their integration [90].

BESS therefore are expected to cover a part of the short-term storage demand for durations between minutes, hours or days, especially due to their unique capability to quickly absorb, hold and then reinject electricity. According to IRENA [92] it is estimated that front-of-the-meter (utility-scale) BESS and behind-the-meter BESS will make out an even share of 50 % of the total storage capacity in 2030. There are several services which are using the BESS's flexibility and contribute to handling power fluctuations in the future. Besides the prevention of curtailment of variable renewable energy, for example, by performing "peak-shaving", which may aim to cache the energy surplus in times of high stress of the grid and release it in times of low stress of the grid, other services such as frequency control or voltage support are the main services currently provided by BESS [92]. Due to the moderate feed-in tariff for photovoltaic systems, the self-consumption optimization today is the most frequently used service for behind-the-meter BESS, which also contributes to de-stress the grid and to prevent curtailment. A description of possible services, which are provided by BESS, is discussed in Chp. 3.3.

1.2 Trends of the Integration and the Use of BESS

Chp. 1.1 mentions the estimation of IRENA [92] of a total installed storage capacity of 11 GWh of BESS with a total power capacity of 10 GW in 2017. The International Energy Agency (IEA)

published values of the annual energy storage deployment from 2013 – 2019 in their Tracking Report on Energy Storage 2020 [89], which are shown in Fig. 1.2.

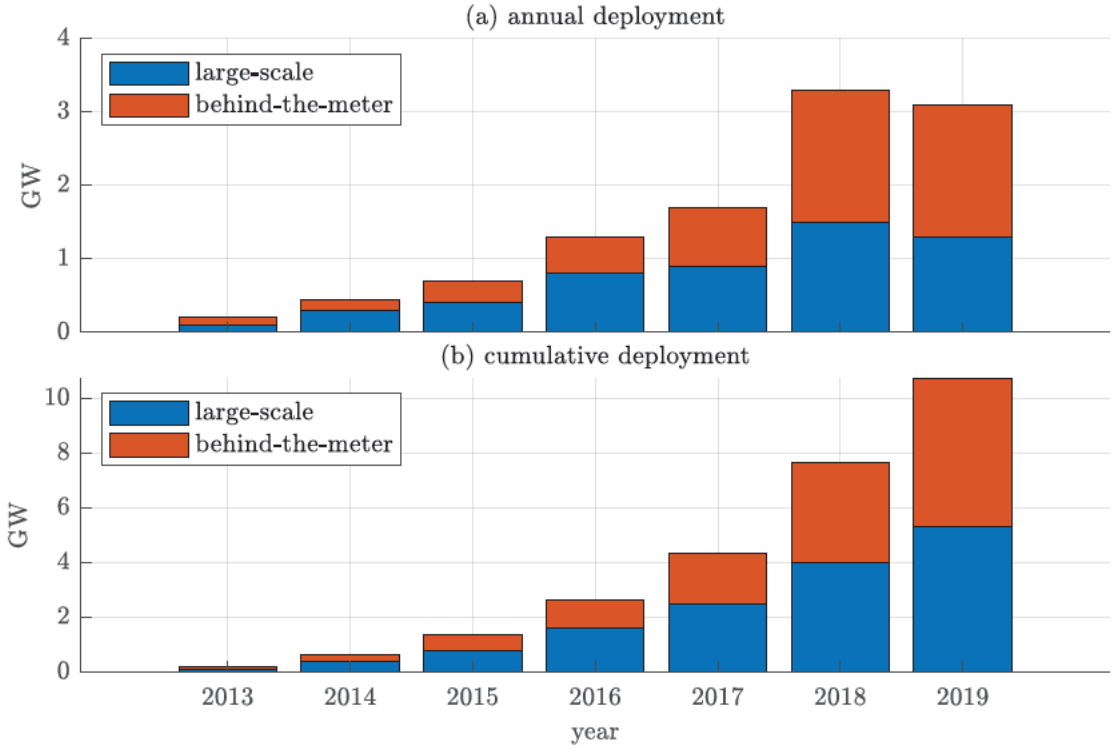

Figure 1.2: Annual and cumulative energy storage deployment according to IEA [89].

Fig. 1.2(b) shows the cumulative trend of the total power capacity from 2013 – 2019, which leads to a value of about 10.5 GW in 2019, but does not take into account the already deployed capacities before 2013. BESS based on Lithium ion (Li-Ion) technology are the most widely used, making up the majority of all new capacity installed. Considering that the market of Li-Ion batteries for electromobility is currently ten times larger than the market for stationary batteries, the indirect effects of innovation and cost reductions could be a significant boost for front-of-the-meter and behind-the-meter BESS. This is also reflected in the IRENA's projections on the deployment of BESS, expected to grow from 11 GWh in 2017 to a value of 100 GWh to 421 GWh until 2030 [92], as already mentioned in Chp. 1.1.

The "DOE Global Energy Storage Database" [82] has already been mentioned in Chp. 1.1 as database, which collects and lists utlity-scale storage systems worldwide. It also lists BESS in the category "Electro-chemical" systems. Filtered by this category, this database lists a total power capacity of 3.3 GW of BESS in 2020, which are currently in operation (1.7 GW) or already decommissioned and sum up to a total storage capacity of 7.8 GWh (3.8 GWh). Compared to PHSS, the size of BESS is rather small, which explains the difference to the amount of BESS of 10 GW in 2017, estimated by IRENA [92], due to the difficulties to gather all information on projects integrating BESS into the grid. However, IRENA [90] uses the information in this database to give an overview for which services BESS are mainly being used for. Fig. 1.3 illustrates the result of this investigation, showing the share of the power capacity of the mainly provided service of utility-scale BESS in relation to the total power capacity.

Fig. 1.3 shows that 50 % of all BESS currently integrated in the power system are providing services for conventional frequency control and additional 9 % are providing spinning reserves.

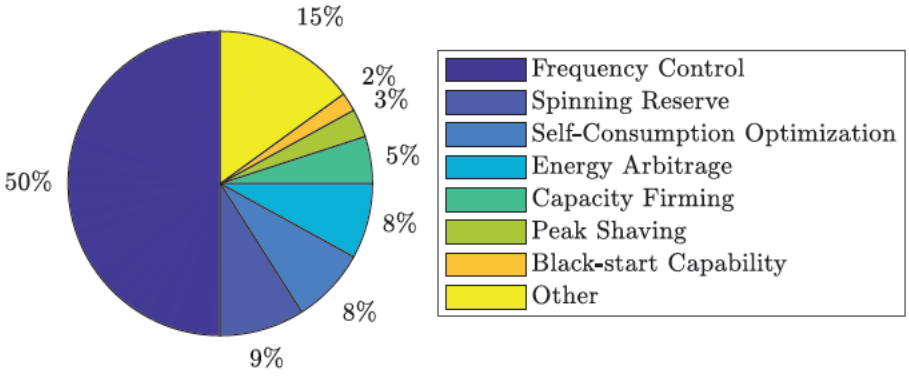

Figure 1.3: Share of the power capacity of the mainly provided service of utility-scale BESS in relation to the total power capacity, based on [92].

Besides services for frequency control, BESS are providing services for Energy Shifting, including Self-Consumption Optimization with 8 %, Capacity Firming with 5 % and Peak Shaving with 3 %, services for performing Bill Management/Energy Arbitrage with 8 % and services to provide backup supply, for example, by providing Black-Start Capability. The remaining 15 % are assigned to other services, for example firm supply capacity provision.

According to IRENA [90], the main use case for BESS until 2030 is likely to be influenced by the economic opportunities to provide services for energy shifting in order to increase self-consumption or avoid peak demand charges in the residential and commercial sectors. Besides these service for energy shifting, which are probably most interesting for behind-the-meter BESS, providing renewable capacity firming at the utility scale is estimated to effectively contribute to 11 % – 14 % of the total storage capacity of BESS in 2030. Services for frequency control also represent a market where utility-scale BESS are likely to become increasingly competitive as costs fall, mainly due to the rapid response characteristic of BESS. The use case of frequency control is estimated to account for 10 % – 15 % of the total storage capacity of BESS in 2030.

The report of IRENA [90] also summarizes experiences in the USA, Europe and Australia, which show that remuneration based on how quickly or how often systems react as well as the removal of regulatory barriers for BESS could help developers to monetize the value of BESS. At the moment the value of storage systems is often poorly accounted for in electricity market, resulting in so-called "missing money", where revenues for investors are insufficient to realize projects [93]. IRENA's Electricity Storage Valuation Framework [93] tries to support the development of policies in order to push monetization of the benefits of storage systems based on their system value and fair allocation of such benefits among stakeholders. Deployment of storage systems can bring a number of indirect cost savings to the system and society in general. These could relate to system reliability (e.g. when storage provides spinning reserve), reliability (e.g. black-start capability and islanding) or system security (e.g. when storage supports penetration of renewables). These might be difficult to quantify. For example, a cost benefit analysis for a BESS can result in a situation where the estimated system benefits of a BESS are exceeding the project costs, whereas the gainable project revenues are estimated to be below these project costs. Without policy intervention this leads to a situation where less BESS are integrated in the system than projected to be beneficial for it.

IRENA's Electricity Storage Valuation Framework [93] lists several policy incentives to support cost-effective storage deployment. These are divided into options to compensate investors for the economic viability gap or options to improve existing market mechanisms. The first category includes options such as feed-in-tariffs, capacity payments or grants for storage systems. For the second category, it can be a policy incentive option to design a new product where storage could participate to provide its full value. The creation of new markets for services for which BESS are

particularly suitable, e.g. fast frequency reserves, therefore can be a way of monetizing the system benefits of BESS. Regarding the existing markets, changes of the market structure and regulations in order to lower barriers for BESS are policy incentives. An example for barriers could be the reserve duration requirement to participate in the balancing markets, which could be too long for many storage systems, or the minimum capacity to participate in the balancing markets, which could be too large for some storage systems. Furthermore, a promising approach for behind-the-meter systems can be to have access to utility-scale markets by aggregation in order to maximize the potential for BESS. The Electricity Market Directive [62], as part of the Clean Energy Package of the European Union, mandates non-discriminatory and competitive procurement of balancing services and fair rules in relation to network access and charging in order to reduce barriers to storage systems. IEA [89] describes the barriers of BESS integration as issue of the ownership. In many markets, distribution and transmission system operators are not allowed to own storage systems. Especially for distribution and transmission grid expansion deferral this is a significant barrier. Fig. 1.2(a) shows a slower annual deployment of energy storages in 2019, mainly driven by the slow progress on this issue of establishing corresponding rules for ownership. The "Electricity Market Directive" [62] of the "Clean Energy Package" of the European Union addresses this issue in Article 36 and Article 54 allowing distribution and transmission system operators to own and operate storage systems under exceptional circumstances and requires the approval by the national regulatory authority.

1.3 Motivation for This Thesis

With decreasing number of conventional power plants, system services need to be provided by new suppliers. The need for system services, such as conventional and faster frequency reserves, voltage support, and capacity reserve, will grow in significance as the penetration of variable renewable energy increases. Some services require high power for short durations (e.g. instantaneous reserve), while others call for power over longer periods (e.g. capacity firming). BESS are considered to contribute to covering a part of such system services in the future, some of which are not remunerated today because it is difficult to quantify the remuneration. Until new markets (e.g. for faster frequency reserves) are established, where BESS are technically superior to other technologies to provide them and as long as compensation for integrating BESS into the grid are economically absent, the "value-stacking" of services by BESS is considered a crucial issue in order to reach profitability.

By "stacking" benefits, that means by bundling together a range of services provided by one system, the economics of a BESS [89] is improved. Such a provision of multiple services and user benefits can unlock multiple revenue streams for BESS. IRENA [90, 93] describes such a stacked provision of services as a capability, which can be a critical issue for BESS in order to achieve or increase profitability, since it allows capturing higher revenue streams. Especially in the short-term and medium-term, when the costs of BESS continue to fall, such an operation can be important in order to compete in a challenging environment. Numerous studies have used data from electricity markets confirming that investing in storage systems providing a single service only, e.g. energy arbitrage, often does not pay off. However, when storage systems provide additional services, for example a variety of system services in parallel, and these services are monetized, then profits are notably improved [134, 33, 163, 153, 202].

The following Chp. 1.3.1 tries to discuss in more detail the current problem of reaching profitability of BESS when offering a single service only, using the example of Frequency Containment Reserve, which is the most used service BESS are used for today. The following Chp. 1.3.2 discusses future services for faster frequency reserves in more detail, for which BESS are considered as one of the few options to provide them in a future power system.

1.3.1 Analysis of the Profitability of BESS by Providing a Single Service Using the Example of Frequency Containment Reserve

To demonstrate the difficulties of reaching profitability of BESS by offering a single service as mentioned above, the service of FCR is discussed in more detail in the following. Especially since FCR is the most commonly used service for BESS, as shown in Fig. 1.3, the following investigation shall demonstrate a starting point to show the necessity of a multi-use operation of BESS in order to reach profitability.

For this reason, Fig. 1.4 shows the settlement prices for FCR [145] from 2014 to 2020, which are identical to the revenues that can be generated for a BESS providing FCR.

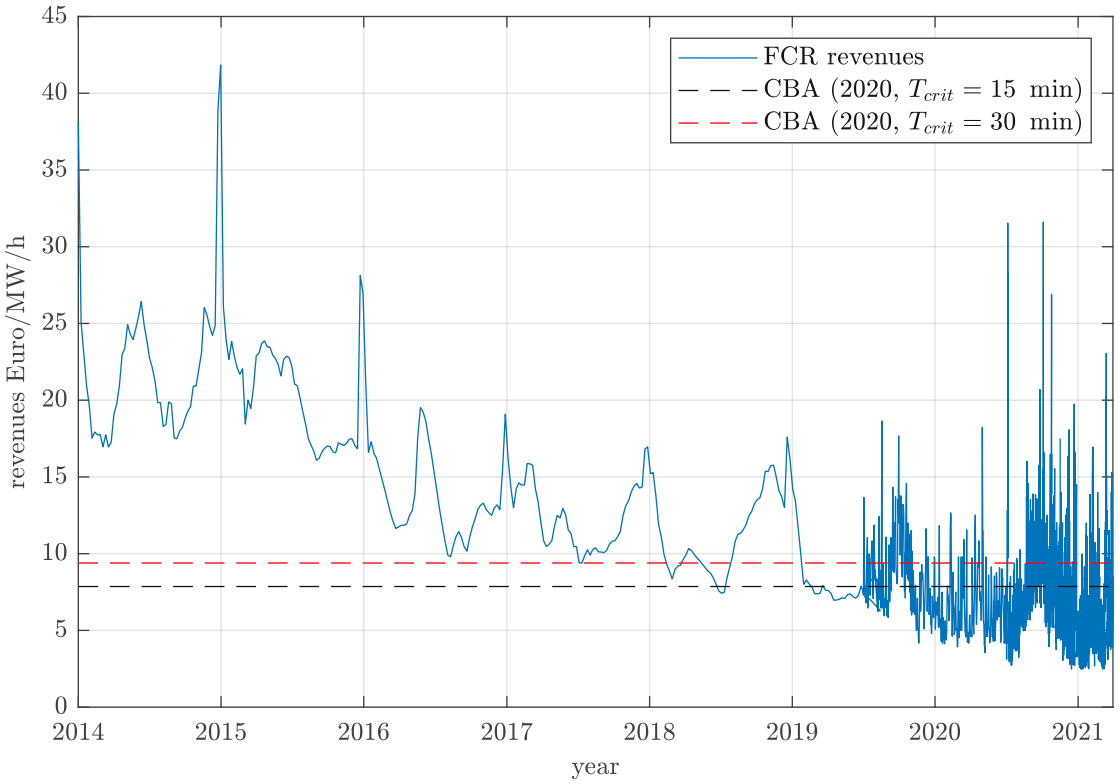

Figure 1.4: Trend of the price on FCR market normalized to the achievable, hourly revenues. Based on data from [10] (until 01.09.2019) and [4] (from 01.09.2019 ongoing). The two additional lines show the costs that derive from a cost-benefit analysis (CBA) of ENTSO-E, which investigated the costs of FCR-units with limited energy reservoir (LER) (Capital Expenditure (CAPEX) and Operational Expenditure (OPEX)) on the basis of a Monte-Carlo simulation [95]. The two curves differ regarding the necessary minimum energy reservoir/energy duration requirement of FCR, which will be discussed in detail in Chp. 4.1.1

The downward trend in Figure 1.4 shows the difficulties of operating a BESS that only offers FCR today. To further illustrate the profitability of a BESS offering FCR, a short example is being investigated for a BESS with a rated power of 1 MW and an energy-to-power ratio of 1.25 h, which is planned to be used for 10 a in Austria. According to Mongrid et al. [130], a realistic price range for today's capital costs of such a BESS is 704 $/kW – 1131 $/kW. Assuming a capital rent of 10 % and operational costs of 2 % of the capital costs per year, and further assuming the BESS offering FCR continuously, this leads to a yearly cost range of 117 €/(kW a) – 188 €/(kW a), assuming an

exchange rate of 0.91 €/$, while the yearly range of revenues is 61 €/(kW a) – 219 €/(kW a) for a settlement price of FCR between 7 €/(MW h) – 25 €/(MW h). In this example, profitability is reached at a settlement price of FCR of 13 €/MWh.

A more detailed analysis of such a profitability analysis of BESS is carried out by ENTSO-E in the frame of a cost-benefit-analysis (CBA) [95]. Based on the reserve duration requirement on the FCR balancing market, which can take values between 15 min – 30 min, the outcome of this analysis comes to a result of about 7.9 €/(MW h) (15 min) to 9.4 €/(MW h) (30 min) to reach profitability of a BESS providing FCR. As shown in Fig. 1.4, the latest settlement prices in Austria tend to be below this limit, which underpins the statement that a BESS offering a single service alone is economically infeasible today.

The investigation above shows one motivation for ongoing research activities related to the multi-use operation of BESS.

1.3.2 Future Services for Frequency Control

As an example of a system service whose need will grow as the penetration of variable renewable energy increases, Chp. 1.3 mentions frequency reserves (also termed as operating reserves or balancing reserves). Sterner and Stadler [168] assume the need for such frequency reserves to have an essential influence on storage demand until 2030. Although different simulations show the demand for frequency reserves not to increase tremendously, the amount of conventionally provided frequency reserves that is replaced by renewable energy has to be compensated for. As already mentioned in Chp. 3.3.1, utility-scale BESS are well-suited to take over part of this compensation. Aggregated behind-the-meter BESS may also be a possibility to fill the gap of declining conventionally provided frequency reserves. Barriers such as minimum capacity or reserve duration requirements in order to pre-qualify for participation in the corresponding markets for frequency reserves are an issue that makes the market entrance of BESS on a large scale difficult today. But foreseeable changes of the pre-qualification requirements and the decreasing costs for BESS pave the way for using BESS to provide frequency reserves on a larger scale.

The more severe influence of the decreasing amount of conventional power plants on frequency stability is the coupled decrease of available system inertia. A reduced system inertia leads to a more pronounced influence on the frequency during the occurrence of power imbalances between load and generation. In the worst case a lack of system inertia brings the risk of blackouts due to massive frequency deviations. While conventional power plants provide inertia inherently due to their coupling to the grid with synchronous machines, converter-based systems do not contribute to system inertia inherently. The amount of inertia that is available in the system is depending on the actual composition of conventional and converter-based infeed. Therefore, the amount of system inertia is also depending on the time of the day, considering solar photovoltaics, for example, to reach their maximum power infeed during mid day. Especially during such periods, the risk of reduced system inertia is highest. The Ten Year Development Plan (TYNDP) of ENTSO-E [52] considers several scenarios in order to estimate the available system inertia in the future. These scenarios describe possible European energy futures up to 2040, each taking into account different targets and focusing on different areas. The scenarios include “Sustainable Transition (ST)”, “Distributed Generation (DG)”, “Global Climate Action (GCA)” and an external scenario of the European Commission (EUCO). Excluding the last scenario, each scenario describes results for the years 2030 and 2040. The results include predictions of the available system inertia in 2030 and 2040, which are presented in the form of yearly duration curves. Fig. 1.5 shows these duration curves of the starting time constant T_A, which is a measure for the inertia in the system, for the different scenarios for 2030 and 2040, and an estimation for 2020. This trend of decreasing system inertia is also documented by frequency measurement data of ENTSO-E in the report [54]. The measurement data shows a development of the mean value of the frequency gradient from 2 mHz/s – 3 mHz/s in 2010 to 3 mHz/s – 4 mHz/s in 2019, each calculated over a period of 30 s.

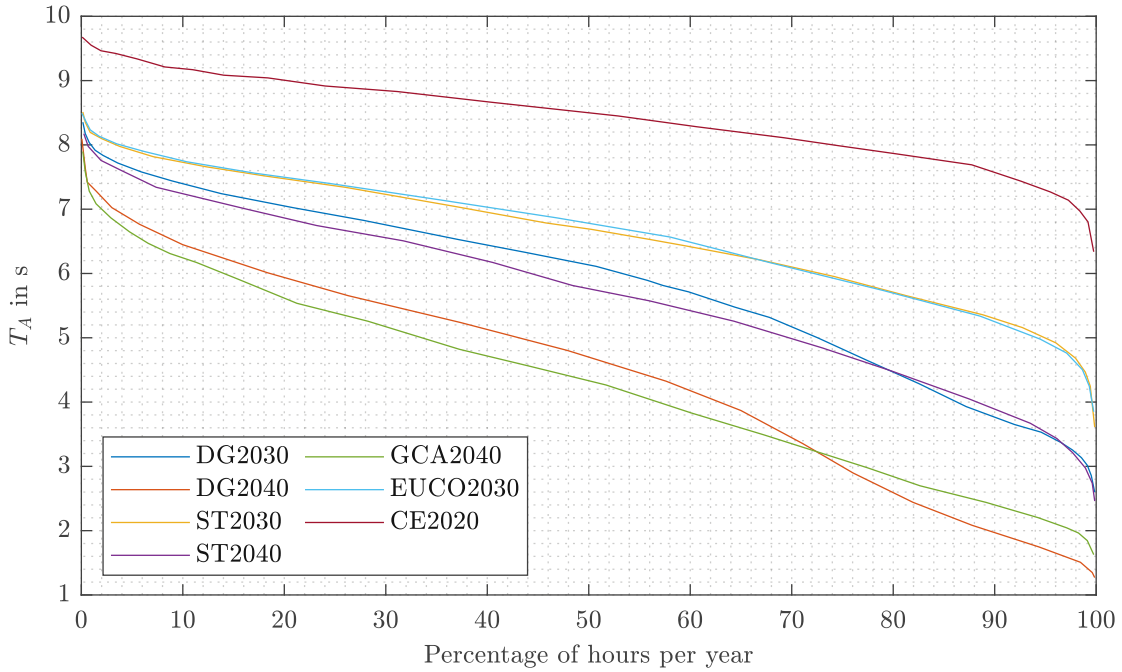

Figure 1.5: Yearly duration curves of the starting time constant in 2030 and 2040 in the Regional Group Continental Europe for the different scenarios used in the TYNDP 2018 of ENTSO-E [52] and the yearly duration curve of the starting time constant in 2020.

Especially the prediction for 2040 in Fig. 1.5 shows that there are periods when the starting time constant T_A reaches values near 2 s. To demonstrate the influence of such a reduced starting time constant, Fig. 1.6 shows the course of the frequency during a so-called "reference-incident", which corresponds to a major outage of a power plant with a power capacity of 3 GW in the Regional Group Continental Europe.

Fig. 1.6 shows that the shorter the starting time constant T_A, the lower the so-called "frequency nadir", which indicates the lowest value of the frequency during such a frequency event. The value of 49 Hz represents a limit, the crossing of which is associated with a number of relief measures, such as "load-shedding", which describes the procedure of disconnecting a certain amount of loads in a stepwise approach in order to stabilize the frequency. A starting-time constant of $T_A = 6\,\mathrm{s}$ corresponds to a frequency nadir that may trigger load-shedding actions during a reference incident. Fig. 1.5 demonstrates that in some scenarios there are periods in which the risk of endangering the frequency stability could be increased.

By equipping BESS with the functionality of providing instantaneous reserve in the form of "Synthetic Inertia (SI)", as described in Chp. 3.3.1, they are able to compensate the reduced inertia shown in Fig. 1.5. It is considered very likely that BESS will offer such a service in the future [93].

According to Fig. 1.5, the minimum starting time constant in the Regional Group Continental Europe in 2020 can be considered to be larger than 6 s. According to Fig. 1.6 this starting time constant represents a sensitive limit from which the frequency stability can be endangered. The duration curves in Fig. 1.6 do not give any information when the corresponding starting time constant occurs. Therefore, Fig. 1.7 shows a comparison of duration curves of the frequency deviation for the years 2014 – 2018 for three different times of the day, which are night (00:00 – 08:00), day (08:00 – 16:00) and evening (16:00 – 24:00). Fig. 1.7 is divided into four sub figures,

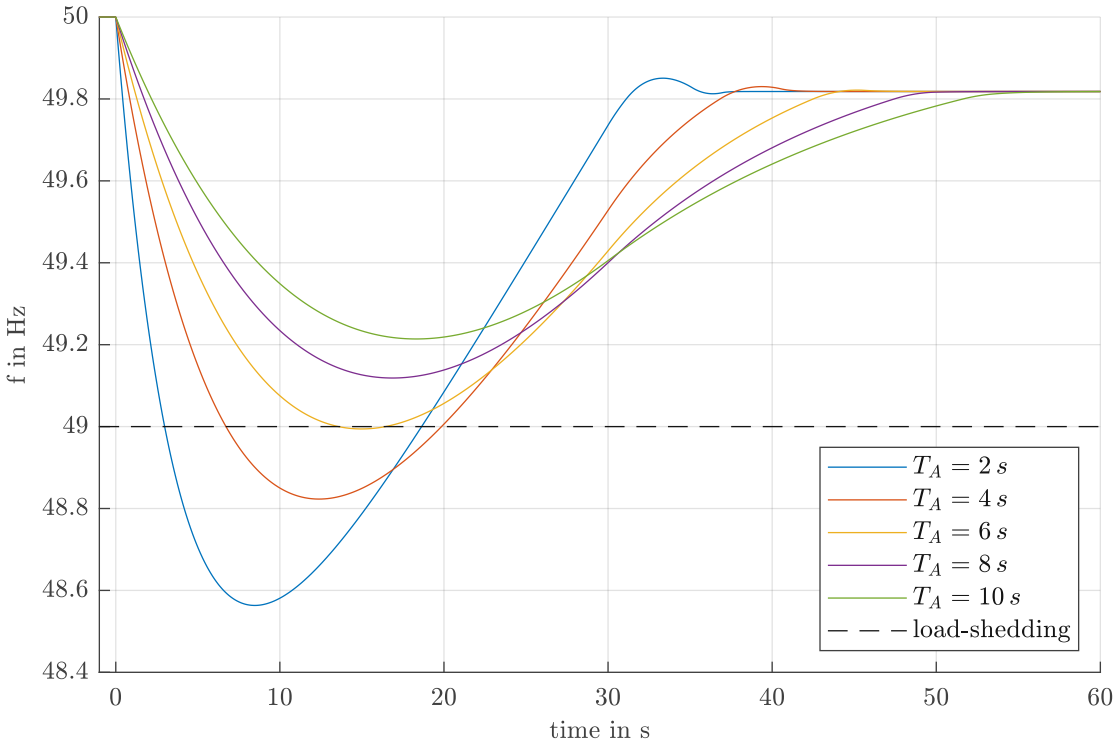

Figure 1.6: Frequency course during a reference incident in the Regional Group Continental Europe based on the design hypothesis.

which represent four different values for frequency deviation limits, which are −25 mHz, −50 mHz, −75 mHz and −100 mHz. Each of the four sub figures shows the duration curves of the frequency deviations that occurred in the corresponding year, which were larger than the corresponding frequency deviation limit and were above this limit for a certain duration. This duration is plotted on the x-axis of the figures. With increasing value of the frequency deviation limit the number of occurrences and durations decreases, as there are less frequency events, which are coupled with a large and long frequency deviation. By comparing Fig. 1.7(a)-(d), it is also visible that the largest and longest frequency deviations occur during the evening. The first reason is due to the traditional load peak in the evening during which the massive load changes are coupled with larger frequency deviations. But a second reason is the low system inertia during evening time when many plants used to meet intermediate and peak load are turned off. The increasing amount of wind power between 2014 – 2018 and the coupled power fluctuations due to changes in the wind speed may contribute to the increasing trend of larger and longer frequency deviations in Fig. 1.7 in the evening. By comparing the different years, especially Fig. 1.7(d) shows a trend of larger frequency deviations with longer durations in younger years. Although Fig. 1.7 shows the least number of frequency deviations during the day (time of day "2"), a trend of larger and longer frequency deviations in younger years is visible as well. During the day, besides the increasing amount of wind power systems, also the increasing amount of solar photovoltaic systems may contribute to this trend.

Fig. 1.7 demonstrates that the consequences of reduced system inertia and power fluctuations due to an increasing amount of variable renewable energy are already visible today.

Besides the provision of instantaneous reserve, the provision of faster reserves can also be a way to counteract the issues of reduced system inertia. By establishing a service for frequency control, which acts faster than Frequency Containment Reserve, the system is better suited for handling

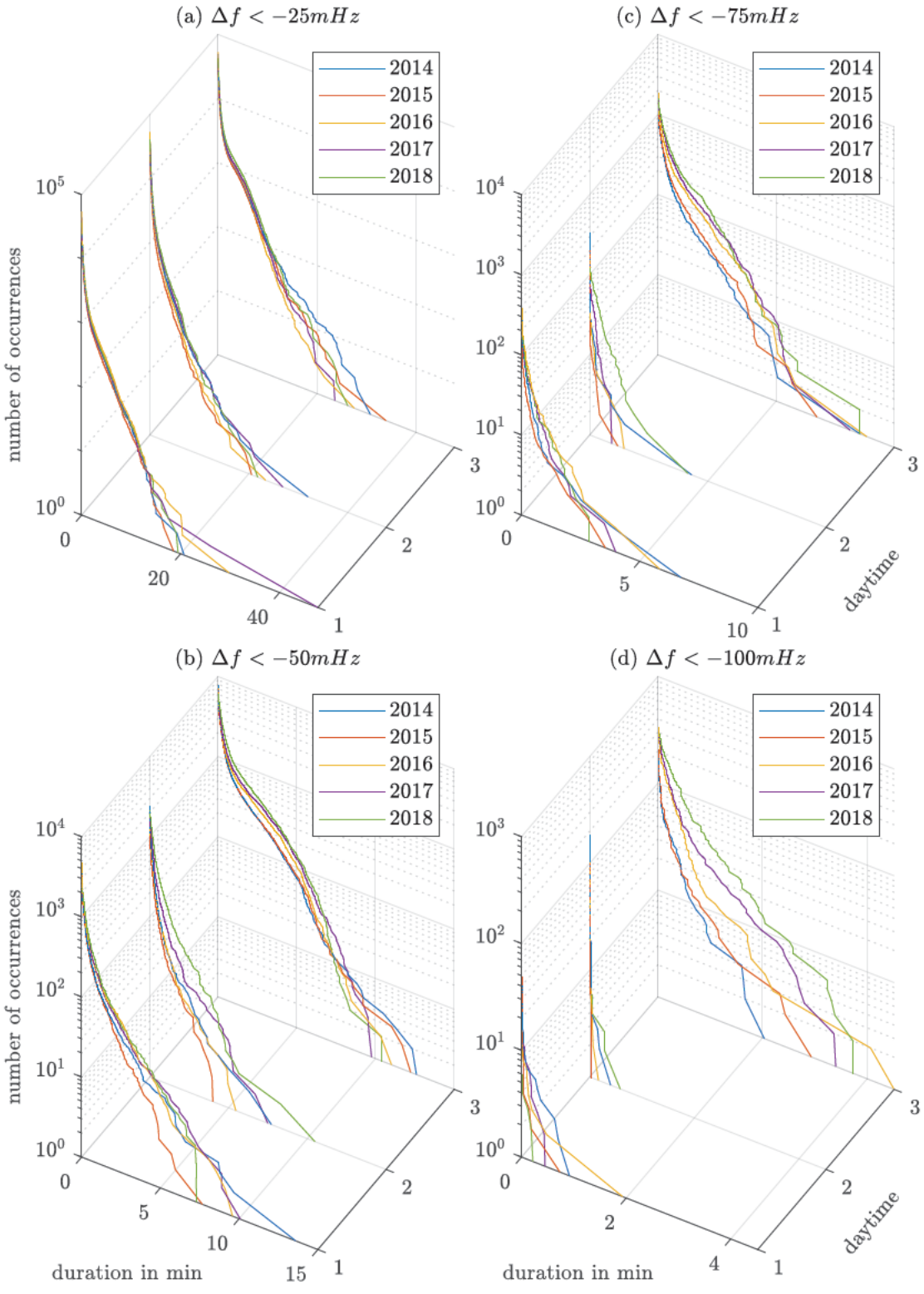

Figure 1.7: Comparison of duration curves of frequency deviations during the last five years, with $\Delta f = f - f_n$ as the frequency deviation, f as the frequency measurement and $f_n = 50\,\mathrm{Hz}$ as the nominal frequency for three different times of the day ("1": 00:00–08:00, "2": 08:00–16:00, "3": 16:00–24:00). The duration curves are calculated based on frequency measurement data of [1].

power imbalances in case of a reduced system inertia. IRENA, therefore, recommends the introduction of such "innovative ancillary services" in its report on innovation landscape [92] and lists several examples of recent developments in countries where corresponding products were already investigated in pilot stages. Some of the products and examples for such faster reserves are discussed in Chp. 3.3.

1.4 State of the Art Regarding Multi-Use Operation of BESS

As already mentioned, providing multiple services simultaneously holds the potential for a more cost-effective operation of BESS and is a hotly debated topic in literature [83]. However, there are several issues to be taken into account regarding the compatibility of services. These constraints can be location-related, time-related or related to the prioritization among services. Some services are only accessible at certain locations. For example, self-consumption optimization requires a location behind-the-meter, either on residential or community scale. Time-related constraints refer to the feasibility of providing concurrent services. For example, that a service that requires discharging does not conflict with a service that requires charging, or that providing one service now does not preclude the provision of another service in the future (e.g. an acceptable range of State of Charge (SoC) for future applications). Constraints regarding prioritization of services refer to the circumstance that certain services may have priority over other service. For example, the service of congestion management may provide power reserves during periods of peak infeed at a congestion point in order to store surplus power to prevent congestion or curtailment. Such a service demands power reserves regardless of wholesale market prices. Assuming congestion management to be valuable for system stability, it may have priority over services that are aiming on gaining revenues on the energy market, such as energy arbitrage or self-consumption optimization. During periods when a conflict of interest arises for such services, priorities are an option to handle their behavior.

These global location-related, time-related and priority-related constraints are leading to the local constraints of power capability, power constraints, power reservations, energy constraints and energy reservations. BESS have limited power capability, which may not be exceeded at any time. Certain services require power constraints, demanding the total power of all services to be kept below a corresponding limit for specific times, for example, at periods of high risk of congestion. Power reservations refer to the necessity of certain services to reserve power capabilities at any time. For example, frequency reserves are such services that require the pre-qualified power to be available at any time. Energy constraints refer to the limited energy reservoir of BESS, which require services to be limited when critical limits of the state of charge are reached. Energy reservations, on the other hand, refer to the requirement of certain services to have a certain value of energy reserve available at any time. For example, the provision of backup supply requires a BESS to have a certain amount of energy reserves available when the backup supply is requested.

There are two states in which the above constraints must be considered. The first state is the operational planning, in which it is planned which service is active with which power and for what duration in advance to the online operation. The second state is the online operation, during which the actual power demands of services may differ from the result of operation planning. Especially the behavior of services such as frequency and voltage control are hardly predictable for the operational planning and may lead to a situation where the planned operation strongly differs from the actual operation. Unexpected events such as short-circuits or blackouts are also situations which cannot be handled via operational planning, but only during online operation. The main task of the operational planning is to achieve an optimization goal, which may be optimizing profitability, while also taking into account constraints such as power reservations for services, e.g. frequency control. Assuming perfect foresight, all services can be dispatched via operational planning in order to achieve optimal profitability, while ensuring that constraints such

as performance are met at all times. Since there may be strong differences from the assumed forecasts during online operation, the main task of the online operation is to ensure that all constraints are met in real-time.

Several studies investigate the operational planning of the multi-use operation of BESS [9, 42]. The Electric Power Research Institute (EPRI), for example, provides the storage valuation estimation tool "StorageVET" [42], which calculates the optimal dispatch of energy storage projects and provides economic results and power time-series for the dispatch of services. These results represent the best case scenario of storage operation while still following the technical limitations imposed by the user. The tool incorporates time-series data on customer and system electric loads and energy and ancillary service prices in different resolution. Fig. 1.8 shows an example of a result of this tool.

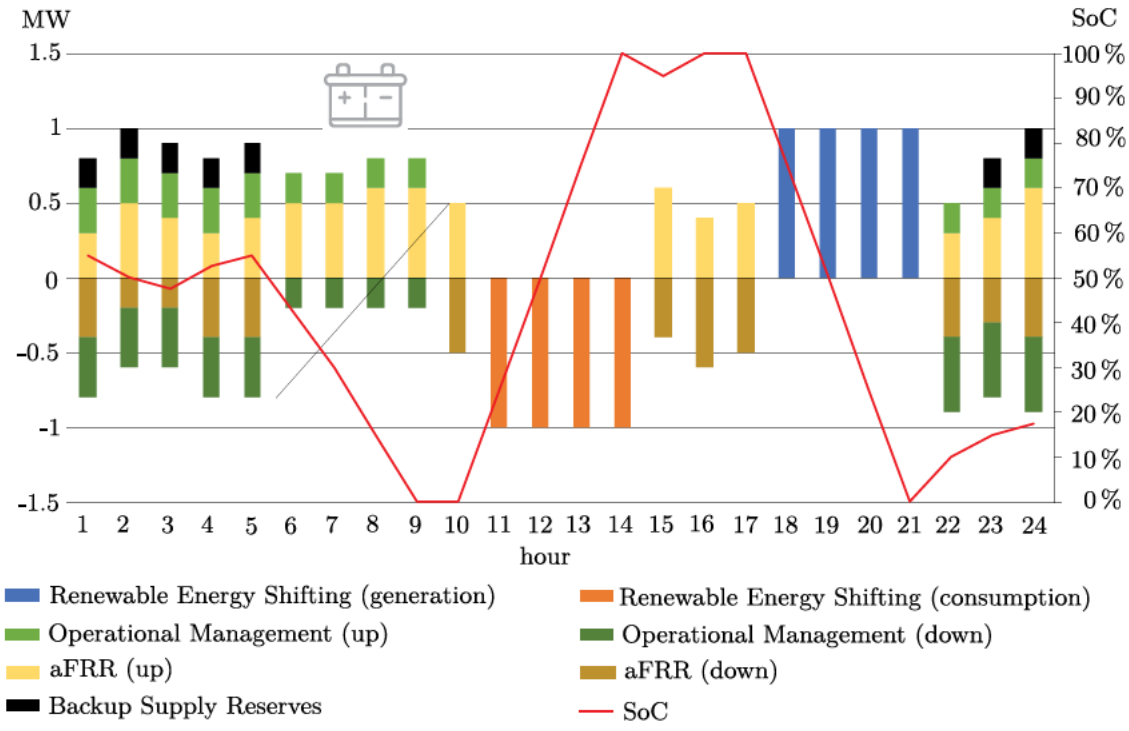

Figure 1.8: BESS dispatch including provision of services [93, 42].

The BESS of the example shown in Fig. 1.8 provides several services, such as Renewable Energy Shifting, Operational Management, automatic Frequency Restoration Reserve (aFRR) and Backup Supply. A detailed discussion of these services can be found in Chp. 3.3. These services are provided by a BESS with a storage capacity of 6 MWh, which is fully used in order to shift variable renewable energy from hours 11–14 to hours 18–21. In the remaining hours the services are dispatched in a way to maximize revenue streams. For each hour positive as well as negative activation of services is considered. For the dispatch of Operational Management, the user input of generation curves is used in order to identify periods when ramping or congestion management is necessary. Based on the user input of reserve prices on the secondary control reserve market, the dispatch of aFRR is decided. For the service of Backup Supply the tool ensures a minimum state of charge during normal operation, which can be used during blackouts to supply critical loads. Since a power capacity provided for such a service leads to a higher minimum state of charge that has to be ensured during normal operation, the potential use of energy reserves for other services is diminished. Therefore, only a small value of power capacity is dispatched for this service. The dispatch of services between hours 1–10, hours 14–18 and hours 21–24 takes into account that the

BESS is able to shift energy with its full amount of storage capacity between hours 11–14 and hours 18–21. Based on the prices for the different services the dispatch of services maximizes the revenue streams.

Operational planning assumes perfect foresight in order to calculate the service dispatch. Online operation, on the other hand, has to deal with unforeseen events, but has to ensure that all constraints are met in real-time. Assuming services for voltage control to be provided by a BESS, the occurrence of a short-circuit, for example, demands high reactive power outputs, which cannot be reserved during operational planning in advance. During a short-circuit, the original dispatch plan of the operational planning, therefore, differs from the actual operation. Another example for such a situation is the occurrence of unforeseen peak power of variable renewable energy that may exceed the planned dispatch of power capacity that is assigned to the service peak shaving. Such a situation may arise due to bad forecasts of variable renewable energy or due to the occurrence of unforeseen load events, such as a power outage of a whole feeder the variable renewable energy is connected to. A similar situation arises due to the unforeseen congestion of the grid. Although it is possible to reserve only a limited amount of power capacity for such a service, grid security may require higher power capacity in order to prevent congestion of the grid. Due to the limited power capacity of a BESS such events require a proper strategy to cope with possible power requests of services, which add up to a total power that exceeds the power capacity of the BESS.

A report from Sandia National Laboratory [63] from 2010 deals with the topic of aggregating benefits from different services of BESS in order to increase profitability. This report distinguishes the compatibility of services by technical and operational compatibility. Whereas technical compatibility of several services is already given when the same BESS is capable of providing them, operational compatibility is determined based on operational conflicts. These operational conflicts are argued for different combinations of services throughout the report and are summarized in a "synergies matrix", which evaluates the compatibility of couples of services based on the following categories: excellent, good, fair, poor and incompatible. This synergies matrix can be considered as a basis for the conceptional phase of a BESS project, which allows an identification of which services are basically compatible with each other at a certain location.

Stephan et al. [167] developed a techno-economic model, which is based on designing a BESS for "primary" services and using the same BESS for "secondary" services in times when the primary services do not fully utilize the resources of a BESS. For different combinations of primary and secondary services, such as arbitrage, self-consumption optimization, grid deferral, frequency control and reserve capacity, they show the substantial increase of the investment attractiveness of BESS. But especially for the secondary services, actual regulatory requirements are deliberately ignored since the resources are entirely reserved for the primary service when required.

Namor et al. [132] present a mathematical framework for the simultaneous provision of services. They distinguish between the two phases day-ahead and real-time, but focus on the first phase, where they solve an optimization problem that allocates the BESS power and energy budgets to the different services in the form of virtual BESS. The first phase therefore corresponds to the phase of operational planning as referred to in this thesis. With respect to existing literature the focus lies on a technical- rather than a revenue-driven control objective.

Such investigations of the phase of operational planning are examined also in other papers, such as in [45, 104], where the tool "SIMSES", which is capable of simulating a BESS that serves multiple services simultaneously, is presented and is used in order to investigate the techno-economic impact of a multi-use operation. For example, in [46] this tool is used to techno-economically compare the three types of multi-use operation sequential, parallel and dynamic, based on the combined provision of the services self-consumption optimization, peak shaving, FCR and energy arbitrage. The comparison is undertaken based on key performance indicators such as annual profit, full cycles, state of health and aging of the BESS. The results show an increasing annual profit with an increasing number of stacked services and with the type of multi-use operation, which is lowest with the type sequential and highest with the type dynamic. The authors divide the resources of

a BESS of the size 1.25 MW/1.34 MWh into virtual partitions which are assigned to each service. They emphasize the distinction between front-of-the-meter and behind-the-meter services in order to respect regulatory affairs. Due to the size of the BESS an aggregated provision of FCR is assumed.

A similar tool named "StorageVET" is used by EPRI [42] in order to calculate the optimal operation of BESS and provide economic results and power time-series for the dispatch of services. These results represent the best case scenario of storage operation while still following the technical limitations imposed by the user. The tool incorporates time-series data on customer and system electric loads and energy and ancillary service prices in different resolution.

Truong et al. [181] describe an abstract definition of a multi-use operation and discuss possible issues during real-time operation. They describe several conflicts of services during real-time operation and introduce the concept of priorities of services which solves a conflict of services that leads to a total power exceeding the limits of the BESS. However, these descriptions only take into account active power and are only described on an abstract level.

Arteaga et al. [9] propose an optimization model that calculates the scheduling of several services of a BESS in a day-ahead phase, which is later refined closer to real-time. They consider services for frequency control (up regulation and down regulation), spinning reserves and arbitrage. Since the frequency can be considered as a random variable and the uncertainty of the behavior of services for frequency control is therefore very high in the day-ahead optimization, their real-time optimization uses the information of the actual behavior of the services for frequency control and the corresponding actual state of charge, for optimizing the rest of the day.

Although there are several papers that deal with the operational planning phase of a multi-use operation via optimization models, there is a lack of discussion for an actual implementation of a real-time multi-use operation in real systems. There is a common opinion in literature regarding several services, e.g. services for frequency control, to be unpredictable for optimization models. However, the question of how to deal with the unpredictable behavior of services in the control system of BESS in real-time seems to be an open question. Therefore, this thesis tries to discuss this problem and proposes the method of dynamic prioritization in order to deal with such situations. Applications of such a dynamic prioritization are investigated by describing several common services for BESS in a basic mathematical framework and investigating their interaction in selected situations. Besides the analysis of such interaction between services, a second focus of this thesis lies on the detailed analysis of existing and possible future services provided by BESS. Especially the implementation of such services in a real BESS, the investigation of their behavior in the scope of field tests and proposals for algorithms to optimize their functionality are major contributions of this thesis.

1.5 Research Questions and Research Activities

The explanations in the previous chapters lead to the following research questions that are investigated in this thesis.

1. What are characteristic values of BESS related to the provision of services, especially regarding modeling of BESS, and what are the requirements regarding measuring these values?
2. Which existing or possible future services BESS are capable of providing, what are BESS particularly suitable for and how can these services be implemented as functions in BESS which comply with legal and technical requirements and constraints? Since BESS are particularly suitable for the provision of frequency control reserves, a sub-objective of this research question is to optimize the operation of the provision of such frequency control reserves, including the reduction of losses and operating costs.

3. How do different services interact with each other during simultaneous provision and how to ensure appropriate behavior of a BESS when conflicts of services due to limitations arise? How does this kind of value stacking influence the profitability of BESS?

The work published in the context of this thesis is listed below.

Journal Papers:

1. J. Marchgraber and W. Gawlik, "Dynamic prioritization of functions during real-time multi-use operation of battery energy storage systems," *Energies*, vol. 14, no. 3, p. 655, 2021.
2. W. Gawlik, C. Alacs, J. Marchgraber, Y. Guo, A. Anta, J. Kathan, B. Weiss, K. Oberhauser, M. Lenz, M. Froschauer *et al.*, "Improving synthetic inertia provision by power electronic interfaced power sources to support future system stability," *Elektrotech. Inftech.*, vol. 137, no. 8, pp. 460–469, 2020.
3. J. Marchgraber and W. Gawlik, "Investigation of Black-Starting and Islanding Capabilities of a Battery Energy Storage System Supplying a Microgrid Consisting of Wind Turbines, Impedance- and Motor-Loads," *Energies*, vol. 13, no. 19, p. 5170, 2020.
4. J. Marchgraber, C. Alács, Y. Guo, W. Gawlik, A. Anta, A. Stimmer, M. Lenz, M. Froschauer, and M. Leonhardt, "Comparison of control strategies to realize synthetic inertia in converters," *Energies*, vol. 13, no. 13, p. 3491, 2020.
5. J. Marchgraber and W. Gawlik, "Dynamic Voltage Support of Converters during Grid Faults in Accordance with National Grid Code Requirements," *Energies*, vol. 13, no. 10, p. 2484, 2020.
6. J. Marchgraber, W. Gawlik, and G. Wailzer, "Reducing SoC-management and losses of battery energy storage systems during provision of frequency containment reserve," *Journal of Energy Storage*, vol. 27, p. 101107, 2020.
7. M. Wurm, P. Jonke, J. Marchgraber, W. Gawlik, and W. Vitovec, "Ortsnetz- Inselbetriebsversuch mit einem 2,5-MVA/2,2-MWh-Batteriespeicher: Messergebnisse und Vergleich mit einem Controller Hardware-in-the-loop Setup," *Elektrotech. Inftech.*, vol. 136, no. 8, pp. 368–376, 2019.
8. J. Marchgraber, W. Gawlik, and C. Alács, "Modellierung und Simulation von Batteriespeichern bei der Erbringung von Primärregelleistung," *Elektrotech. Inftech.*, vol. 136, no. 1, pp. 3–11, 2019.
9. J. Marchgraber, W. Gawlik, and M. Wurm, "Modellierung der dynamischen Netzstützung von über Umrichter angebundenen Erzeugungsanlagen und Speichern," *Elektrotechn. Inftech.*, vol. 136, no. 1, pp. 31–38, Feb 2019.
10. H.-P. Vetö and J. Marchgraber, "Betrachtung von Kurzschlüssen in dieselgeneratorversorgten Inselnetzen–Vergleich transienter Rechnung mit Rechnung gemäß IEC 60909-0: 2016," *Elektrotech. Inftech.*, vol. 133, no. 8, pp. 407–415, 2016.

Conference Papers:

1. A. Stimmer, M. Lenz, M. Forschauer, M. Leonhardt, W. Gawlik, C. Alacs, C. Corinaldesi, G. Lettner, Y. Guo, J. Marchgraber, A. Anta, and K. Oberhauser, "Options for the implementation of fast control reserves in the continental european power system," in *Proc. of the 4th Grid Service Markets Symposium*, Luzern, Switzerland, Oct. 19 – 20, 2020, pp. 54–65.
2. J. Marchgraber, C. Alacs, G. Lettner, W. Gawlik, P. Jonke, M. Wurm, R. Lechner, R. Igelspacher, G. Wailzer, and W. Vitovec, "Erkenntnisse aus dem Forschungsprojekt BatterieSTABIL," in *Proc. of the 16th Symposium Energieinnovation (EnInnov 2020)*, Graz, Austria, Feb. 12 – 14, 2020, pp. 1–13.

3. C. Alacs, J. Marchgraber, Y. Guo, W. Gawlik, A. Anta, J. Kathan, B. Weiss, K. Oberhauser, M. Lenz, A. Stimmer, and M. Leonhardt, "Mögliche Umsetzung von schnellen Regelreserven im kontinentaleuropäischen Verbundystem," in *Proc. of the 16th Symposium Energieinnovation (EnInnov 2020)*, Graz, Austria, Feb. 12 – 14, 2020, pp. 1–2.

4. W. Gawlik, C. Alács, J. Marchgraber, Y. Guo, A. Anta, J. Kathan, B. Weiss, K. Oberhauser, M. Lenz, M. Forschauer, A. Stimmer, and M. Leonhard, "Improving synthetic inertia provision by power electronic interfaced power sources to support future system stability," in *Proc. of the CIGRE Session 2020*, Paris, France, Aug. 23 –Sep. 4 2020, pp. 1–10.

5. J. Marchgraber, C. Alács, S. Nemec-Begluk, W. Gawlik, P. Jonke, M. Wurm, G. Wailzer, and W. Vitovec, "Schwarzstart und Inselbetrieb eines Netzabschnitts mit Windenergieeinspeisung mithilfe eines Batteriespeichers," in *Proc. of the 11th Internationale Energiewirtschaftstagung (IEWT 2019)*, Vienna, Austria, Feb. 13 – 15, 2019, pp. 1–17.

6. J. Marchgraber, C. Alacs, W. Gawlik, J. Kathan, M. Wurm, G. Wailzer, and W. Vitovec, "Netzdienstleistungen und Netzstabilisierung - Erste Erkenntnisse aus dem Forschungsprojekt BatterieSTABIL," in *Proc. of the 15th Symposium Energieinnovation (EnInnov 2018)*, Graz, Austria, Feb. 14 – 16, 2018, pp. 1–13.

7. J. Marchgraber, E. Xypolytou, I. Lupandina, W. Gawlik, and M. Stifter, "Measurement-based determination of static load models in a low voltage grid," in *Proc. of the IEEE PES Innovative Smart Grid Technologies Conference Europe (ISGT-Europe 2016)*, Ljubljana, Slovenia, Oct. 9 – 16, 2016, pp. 1–6.

8. J. Marchgraber, D. Fasthuber, , M. Litzlbauer, and W. Gawlik, "Entwicklung von Regel-und Betriebsführungsstrategien für Microgrids im Zuge des SORGLOS-Projekts," in *Proc. of the D-A-CH Energieinformatik 2014*, Zürich, Switzerland, Nov. 13 – 14, 2014, pp. 1–7.

1.6 Structure of This Thesis

This thesis includes five further chapters, which follow on from the introduction dealt with in this chapter.

Chp. 2 describes fundamentals of power systems and batteries, which are relevant for this thesis. Chp. 2.1 describes symmetrical components, space vectors and corresponding transformations based on the nomenclature that is used throughout this thesis. Chp. 2.4 describes basics of converters which are relevant for the simulations in Chp. 4. Chp. 2.2 describes the basics of the calculation of short-circuits and includes an exemplary calculation of short-circuits in a grid part according to IEC 60909, whose results are used in Chp. 4.3. Chp. 2.3 describes the load-frequency control in the power system and summarizes the characteristics of established products for the load-frequency control in detail. Chp. 2.5 summarizes characteristic values of batteries. Chp. 2.6.1 describes the construction, the components and the cost structure of BESS. Additional fundamentals of power systems and batteries that are also relevant for this thesis are described in the appendix A. Especially Chp. A.1 may be relevant to understand the nomenclature used in this thesis.

Chp. 3.1 describes an exemplary BESS on which various tests and investigations were carried out that are presented and discussed in this chapter. Chp. 3.2 deals with the first research question described in Chp. 1.5 and summarizes measurement results from the exemplary BESS which are relevant to characterize a BESS and necessary to create simulation models of a BESS. Based on existing literature and BESS projects the last Chp. 3.3 lists and discusses services for which BESS are suited to provide.

Chp. 4 deals with the second research question described in Chp. 1.5. The chapter describes in detail the legal and technical requirements and constraints of selected services, such as FCR, arbitrage, SI, dynamic voltage support and island operation. Each of these services is dealt with in a separate sub-chapter that includes a general description, results on simulating these services and corresponding measurement results taken at the exemplary BESS. A focus of Chp. 4 lies on the service FCR, which is the most intended use for BESS today. For this reason, Chp. 4 also includes investigations on the management of the state of charge during provision of FCR, possibilities to reduce the required energy for this management of the state of charge, as well as a procedure to reduce losses during the provision of FCR.

Chp. 5 includes a mathematical framework to describe a multi-use operation of a BESS. Depending on the behavior of each service during such a multi-use operation, situations may arise, when the current capability of the BESS is exceeded by the requested overall output of all services. The handling of such "conflicts" is crucial for a successful multi-use operation of a BESS. Chp. 5 presents the concept of "dynamic prioritization of functions" to deal with these conflicts based on priorities assigned to each service. The mathematical framework which is presented allows the description of this concept, including a proper current limitation algorithm. Within this mathematical framework, services are described via functions. Based on these functions, several applications are presented in which a part of the entire set of services is provided in a multi-use operation. Each of these applications demonstrates the behavior of the concept of dynamic prioritization of functions based on simulations in MATLAB/SIMULINK and proves a better utilization of the power reserves compared to other concepts for the realization of a multi-purpose operation. Chp. 5.8 compares the achievable revenues by value stacking various services and proves the beneficial use of a multi-use operation of BESS regarding increased profitability.

Finally, Chp. 6 concludes this thesis and describes an outlook of suitable future research work.

1.7 Nomenclature

Uppercase and lowercase letters are used to distinguish between unit-based and normalized values. Uppercase letters are used for unit-based values, while lowercase letters are used for normalized values. The unit of the normalized values is described with "pu". To distinguish between phasors and instantaneous values, the index "t" is used for instantaneous values. Symbols in bold indicate a vector or a matrix. Nominal values are described with the index "n".

2 Fundamentals of Power Systems and Batteries

This chapter describes fundamentals of power systems and batteries, which are relevant for this thesis.

2.1 Transformations in Three-Phase Systems

In the following chapters, the fundamentals of symmetrical components, the space vector transformation, the Clarke transformation, and the Park transformation are summarized.

2.1.1 Symmetrical Components

In electrical engineering, the method of symmetrical components simplifies the analysis of unbalanced three-phase power systems under both normal and abnormal conditions. The basic idea is that an asymmetrical set of N phasors can be expressed as a linear combination of N symmetrical sets of phasors by means of a complex linear transformation [78]. Fortescue [68] demonstrated that any set of N unbalanced phasors could be expressed as the sum of N symmetrical sets of balanced phasors, for values of N that are prime. In a three-phase system, this set of balanced phasors are called "positive-sequence system"

$$\underline{\mathbf{U}}_{\mathbf{1}+} = \underline{U}_{1+} \cdot \begin{pmatrix} 1 \\ \underline{a}^2 \\ \underline{a} \end{pmatrix}, \tag{2.1}$$

"negative-sequence system"

$$\underline{\mathbf{U}}_{\mathbf{1}-} = \underline{U}_{1-} \cdot \begin{pmatrix} 1 \\ \underline{a} \\ \underline{a}^2 \end{pmatrix} \tag{2.2}$$

and "zero-sequence system"[1]

$$\underline{\mathbf{U}}_{\mathbf{10}} = \underline{U}_{10} \cdot \begin{pmatrix} 1 \\ 1 \\ 1 \end{pmatrix}. \tag{2.3}$$

The Root Mean Square (RMS)-vectors of the three symmetrical components are calculated with the help of the "Fortescue-Matrix" $\mathbf{A}$:

$$\underline{\mathbf{U}}_{\mathbf{1\pm0,N}} = \begin{pmatrix} \underline{U}_{10,N} \\ \underline{U}_{1+,N} \\ \underline{U}_{1-,N} \end{pmatrix} = \mathbf{A} \cdot \begin{pmatrix} \underline{U}_{1N} \\ \underline{U}_{2N} \\ \underline{U}_{3N} \end{pmatrix} = \frac{1}{3} \cdot \begin{pmatrix} 1 & 1 & 1 \\ 1 & \underline{a} & \underline{a}^2 \\ 1 & \underline{a}^2 & \underline{a} \end{pmatrix} \cdot \begin{pmatrix} \underline{U}_{1N} \\ \underline{U}_{2N} \\ \underline{U}_{3N} \end{pmatrix} \tag{2.4}$$

[1] The index "1" gives information of only considering the fundamental of the waveforms.

where index "N" refers to the phase-to-neutral voltage in each phase.

The inverse transformation from symmetrical components to the phase voltages is calculated as follows:

$$\underline{\mathbf{U}}_{\mathbf{N}} = \begin{pmatrix} \underline{U}_{1N} \\ \underline{U}_{2N} \\ \underline{U}_{3N} \end{pmatrix} = \mathbf{A}^{-1} \cdot \begin{pmatrix} \underline{U}_{10,N} \\ \underline{U}_{1+,N} \\ \underline{U}_{1-,N} \end{pmatrix} = \begin{pmatrix} 1 & 1 & 1 \\ 1 & \underline{a}^2 & \underline{a} \\ 1 & \underline{a} & \underline{a}^2 \end{pmatrix} \cdot \begin{pmatrix} \underline{U}_{10,N} \\ \underline{U}_{1+,N} \\ \underline{U}_{1-,N} \end{pmatrix}. \tag{2.5}$$

The symmetrical components of the voltage based on the phase-to-phase voltages are calculated by

$$\mathbf{U}_{\mathbf{1\pm0}} = \begin{pmatrix} U_{10} \\ U_{1+} \\ U_{1-} \end{pmatrix} = \sqrt{3} \cdot \begin{pmatrix} U_{10,N} \\ U_{1+,N} \\ U_{1-,N} \end{pmatrix}. \tag{2.6}$$

The same method can be applied to the current:

$$\underline{\mathbf{I}}_{\mathbf{1\pm0}} = \begin{pmatrix} \underline{I}_{10} \\ \underline{I}_{1+} \\ \underline{I}_{1-} \end{pmatrix} = \mathbf{A} \cdot \begin{pmatrix} \underline{I}_{L1} \\ \underline{I}_{L2} \\ \underline{I}_{L3} \end{pmatrix} = \frac{1}{3} \cdot \begin{pmatrix} 1 & 1 & 1 \\ 1 & \underline{a} & \underline{a}^2 \\ 1 & \underline{a}^2 & \underline{a} \end{pmatrix} \cdot \begin{pmatrix} \underline{I}_{L1} \\ \underline{I}_{L2} \\ \underline{I}_{L3} \end{pmatrix}. \tag{2.7}$$

The apparent power based on symmetrical components can be calculated according to Oswald [137] with Eq. (2.8). The backwards transformation of voltage and current vectors can be used in Eq. (A.19) to calculate the apparent power as follows:

$$\begin{aligned} \underline{S} &= \underline{\mathbf{U}}_N^{\top} \cdot \underline{\mathbf{I}}^* = \left(\mathbf{A}^{-1} \cdot \underline{\mathbf{U}}_{\mathbf{1\pm0,N}}\right)^{\top} \cdot \left(\mathbf{A}^{-1} \cdot \underline{\mathbf{I}}_{\mathbf{1\pm0,N}}\right)^* = \\ &= \underline{\mathbf{U}}_{\mathbf{1\pm0,N}}{}^{\top} \cdot \left(\mathbf{A}^{-1}\right)^{\top} \cdot \left(\mathbf{A}^{-1}\right)^* \cdot \underline{\mathbf{I}}^*_{\mathbf{1\pm0,N}} = \\ &= \underline{\mathbf{U}}_{\mathbf{1\pm0,N}}{}^{\top} \cdot \begin{pmatrix} 3 & 0 & 0 \\ 0 & 3 & 0 \\ 0 & 0 & 3 \end{pmatrix} \cdot \underline{\mathbf{I}}^*_{\mathbf{1\pm0,N}} = \\ &= 3 \cdot \underline{\mathbf{U}}_{\mathbf{1\pm0,N}}{}^{\top} \cdot \underline{\mathbf{I}}^*_{\mathbf{1\pm0}} = \\ &= 3 \cdot \left(\underline{U}_{10,N} \cdot \underline{I}^*_{10} + \underline{U}_{1+,N} \cdot \underline{I}^*_{1+} + \underline{U}_{1-,N} \cdot \underline{I}^*_{1-}\right). \end{aligned} \tag{2.8}$$

The positive-sequence, negative-sequence and zero-sequence systems are symmetrical three-phase systems. Therefore, the apparent power based on phase-to-phase voltages can be calculated as follows:

$$\begin{aligned} \underline{S} &= 3 \cdot \left(\underline{U}_{10,N} \cdot \underline{I}^*_{10} + \underline{U}_{1+,N} \cdot \underline{I}^*_{1+} + \underline{U}_{1-,N} \cdot \underline{I}^*_{1-}\right) = \\ &= 3 \cdot \left(\frac{\underline{U}_{10}}{\sqrt{3}} \cdot \underline{I}^*_{10} + \frac{\underline{U}_{1+}}{\sqrt{3}} \cdot \underline{I}_{1+}{}^* + \frac{\underline{U}_{1-}}{\sqrt{3}} \cdot \underline{I}_{1-}{}^*\right) = \\ &= \sqrt{3} \cdot \left(\underline{U}_{10} \cdot \underline{I}^*_{10} + \underline{U}_{1+} \cdot \underline{I}^*_{1+} + \underline{U}_{1-} \cdot \underline{I}^*_{1-}\right). \end{aligned} \tag{2.9}$$

2.1.2 Space Vector Transformation

Considering induction machines, there are three windings arranged at an angle of 120°, as shown in Fig. 2.1. In each of these windings, a separate magnetic field is generated when current flows in the machine. If the machine is now connected to a three-phase system, a different magnetization of the windings results for each instantaneous value. As the three magnetic fields overlap, a non-uniform magnetic flux density distribution results in the air gap between stator and rotor. The distribution of the flux density along the circumference of the air gap has a maximum at a certain

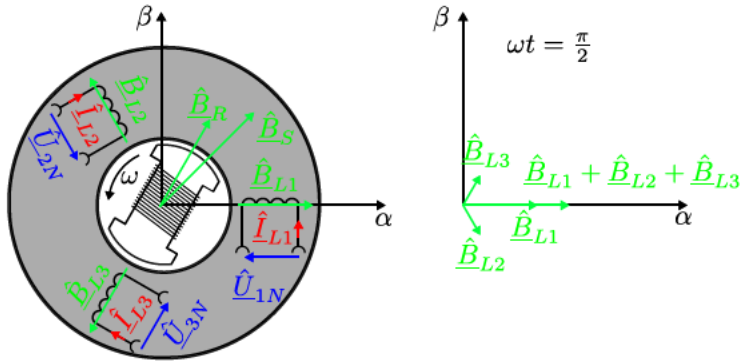

Figure 2.1: Rotating field.

point. For each instantaneous value of the phase currents, the magnetic flux density thus has a certain orientation in the machine. This geometric orientation can now be represented by a space vector.

The flux density in the stator $\underline{B}_S$ is a space vector that can be calculated according to Eq. (2.10):

$$\underline{B}_S = \frac{2}{3}\left(\hat{\underline{B}}_{L1} + \hat{\underline{B}}_{L2} + \hat{\underline{B}}_{L3}\right) = \frac{2}{3}\left(B_{L1,t} + \underline{a}\cdot B_{L2,t} + \underline{a}^2\cdot B_{L3,t}\right). \tag{2.10}$$

Assuming the generator is connected to a symmetrical three-phase system, the resulting flux densities in the phases are calculated as follows:

$$\hat{\underline{B}}_{L1} = B_{L1,t} = \hat{B}_{L1}\cdot\sin(\omega t) \tag{2.11}$$

$$\hat{\underline{B}}_{L2} = \underline{a}\cdot B_{L2,t} = \underline{a}\cdot\hat{B}_{L2}\cdot\sin\left(\omega t + \frac{4\pi}{3}\right) \tag{2.12}$$

$$\hat{\underline{B}}_{L3} = \underline{a}^2\cdot B_{L3,t} = \underline{a}^2\cdot\hat{B}_{L3}\cdot\sin\left(\omega t + \frac{2\pi}{3}\right). \tag{2.13}$$

The space vector $\underline{B}_S$ represents the maximum flux density in the air gap between stator and rotor. Assuming $\omega t = \frac{\pi}{2}$ and $\hat{B}_{L1} = \hat{B}_{L2} = \hat{B}_{L3}$, the space vector becomes

$$\begin{aligned}\underline{B}_S\left(\omega t = \frac{\pi}{2}\right) &= \frac{2}{3}\left(\hat{B}_{L1}\cdot\sin\left(\frac{\pi}{2}\right) + \underline{a}\cdot\hat{B}_{L2}\cdot\sin\left(\frac{\pi}{2}+\frac{4\pi}{3}\right) + \underline{a}^2\cdot\hat{B}_{L3}\cdot\sin\left(\frac{\pi}{2}+\frac{2\pi}{3}\right)\right) = \\ &= \frac{2}{3}\left(\hat{B}_{L1} - \underline{a}\cdot\frac{\hat{B}_{L2}}{2} - \underline{a}^2\cdot\frac{\hat{B}_{L3}}{2}\right) = \\ &= \hat{B}_{L1}\cdot\frac{2}{3}\left(1 + 0.5\cdot e^{-j\cdot 60^\circ} + 0.5\cdot e^{j\cdot 60^\circ}\right) = \hat{B}_{L1}\cdot\frac{2}{3}\cdot\frac{3}{2} = \hat{B}_{L1}\end{aligned} \tag{2.14}$$

and assuming $\omega t = \pi$ and $\hat{B}_{L1} = \hat{B}_{L2} = \hat{B}_{L3}$, the space vector becomes

$$\begin{aligned}\underline{B}_S(\omega t = \pi) &= \frac{2}{3}\left(\hat{B}_{L1}\cdot\sin(\pi) + \underline{a}\cdot\hat{B}_{L2}\cdot\sin\left(\pi+\frac{4\pi}{3}\right) + \underline{a}^2\cdot\hat{B}_{L3}\cdot\sin\left(\pi+\frac{2\pi}{3}\right)\right) = \\ &= \frac{2}{3}\left(0\cdot\hat{B}_{L1} + \underline{a}\cdot\hat{B}_{L2}\cdot\frac{\sqrt{3}}{2} - \underline{a}^2\cdot\hat{B}_{L3}\cdot\frac{\sqrt{3}}{2}\right) = \\ &= \hat{B}_{L1}\cdot\frac{2}{3}\left(\frac{\sqrt{3}}{2}\cdot e^{j\cdot 120^\circ} - \frac{\sqrt{3}}{2}\cdot e^{-j\cdot 120^\circ}\right) = j\hat{B}_{L1}\cdot\frac{2}{3}\cdot\frac{3}{2} = j\hat{B}_{L1}.\end{aligned} \tag{2.15}$$

These two examples show that the space vector $\underline{B}_S$ changes its angle with time, but its absolute value remains constant. Based on the arrangement of the windings in Fig. 2.1, the space vector rotates counterclockwise with time, which equals a mathematically positive direction. It is worth mentioning that the definition of the space vector according to Eq. (2.10) is based on this convention of counterclockwise rotation. Changing the positions of the windings in the phases L2 and L3 in Fig. 2.1 would lead to a space vector that rotates clockwise. In electrical engineering such a positioning of windings is standardized for electrical machines, such as asynchronous motors, in order to ensure a clockwise rotation of the rotor. Since the direction of rotation is crucial for applications such as pumps or fans, this convention has an influence on the mechanical construction of the corresponding electrical machines. This convention of clockwise rotation is also used in Fig. A.2 and Fig. A.1. Therefore, the space vector according to Eq. (2.10) may only be interpreted as mathematical construct. When using a space vector in order to describe the magnetic field in an electrical machine it has to be kept in mind that the rotation direction of the actual magnetic field may be opposite to the rotation direction of the space vector.

A space vector can be calculated also for voltages and currents. The general space vector is defined by

$$\underline{W}_S = \frac{2}{3}\left(W_{L1,t} + \underline{a}\cdot W_{L2,t} + \underline{a}^2\cdot W_{L3,t}\right). \tag{2.16}$$

In case of a harmonic, symmetrical three-phase system, the space vector $\underline{W}_S$ becomes the RMS-vector $\underline{W}$:

$$\begin{aligned}\underline{W}_S &\overset{symm}{=} \frac{2}{3}\hat{W}\left(\frac{e^{j\omega t}+e^{-j\omega t}}{2} + e^{j\frac{2\pi}{3}}\frac{e^{j\left(\omega t+\frac{4\pi}{3}\right)}+e^{-(j\omega t+\frac{4\pi}{3})}}{2} + e^{j\frac{4\pi}{3}}\frac{e^{j\left(\omega t+\frac{2\pi}{3}\right)}+e^{-(j\omega t+\frac{2\pi}{3})}}{2}\right) = \\ &= \frac{2}{3}\hat{W}\left(\frac{3e^{j\omega t}}{2} + \frac{3e^{-j\omega t}}{2}\cdot\left(1+e^{j\frac{4\pi}{3}}+e^{j\frac{8\pi}{3}}\right)\right) = \hat{W}e^{j\omega t} = \underline{\hat{W}}\end{aligned} \tag{2.17}$$

Using the space vectors $\underline{U}_S$ and $\underline{I}_S$ of voltage and current, the power can be calculated and derived according to Binder [20] by

$$\begin{aligned}P_t &= \frac{3}{2}\cdot\mathfrak{Re}\left(\underline{U}_S\cdot\underline{I}_S^*\right) = \\ &= \frac{3}{2}\mathfrak{Re}\left[\frac{2}{3}\left(U_{1N,t}+\underline{a}\cdot U_{2N,t}+\underline{a}^2\cdot U_{3N,t}\right)\cdot\frac{2}{3}\left(I_{L1,t}+\underline{a}\cdot I_{L2,t}+\underline{a}^2\cdot I_{L3,t}\right)\right] = \\ &= \frac{2}{3}\left[U_{1N,t}I_{L1,t} - \frac{U_{1N,t}I_{L2,t}+U_{1N,t}I_{L3,t}+U_{2N,t}I_{L2,t}}{2} + U_{2N,t}I_{L2,t}\right] + \\ &+ \frac{2}{3}\left[-\frac{U_{2N,t}I_{L3,t}+U_{3N,t}I_{L1,t}+U_{3N,t}I_{L1,t}}{2} + U_{3N,t}I_{L3,t}\right] = \\ &= \frac{2}{3}\left[U_{1N,t}I_{L1,t} - \frac{U_{1N,t}(I_{L1,t}+I_{L3,t})}{2} + U_{2N,t}I_{L2,t} - \frac{U_{2N,t}(I_{L1,t}+I_{L3,t})}{2}\right] + \\ &+ \frac{2}{3}\left[U_{3N,t}I_{L3,t} - \frac{U_{3N,t}(I_{L1,t}+I_{L2,t})}{2}\right] = \\ &= \frac{2}{3}\left[U_{1N,t}I_{L1,t} + \frac{U_{1N,t}I_{L1,t}}{2} + U_{2N,t}I_{L2,t} + \frac{U_{2N,t}I_{L2,t}}{2} + U_{3N,t}I_{L3,t} + \frac{U_{3N,t}I_{L3,t}}{2}\right] = \\ &= U_{1N,t}I_{L1,t} + U_{2N,t}I_{L2,t} + U_{3N,t}I_{L3,t}\end{aligned} \tag{2.18}$$

where the factor $\frac{3}{2}$ is explained by the derivation as shown above.

2.1.3 Clarke-Transformation

Fig. 2.1 shows that the space vector of a symmetrical three-phase system rotates with the angular frequency ω in a $\alpha\beta$-coordinate system. The Clarke-transformation is defined by

$$\begin{pmatrix} \hat{W}_{S,\alpha} \\ \hat{W}_{S,\beta} \end{pmatrix} = \begin{pmatrix} \frac{2}{3} & -\frac{1}{3} & -\frac{1}{3} \\ 0 & \frac{\sqrt{3}}{3} & -\frac{\sqrt{3}}{3} \end{pmatrix} \cdot \begin{pmatrix} W_{L1,t} \\ W_{L2,t} \\ W_{L3,t} \end{pmatrix} \tag{2.19}$$

and allows the direct calculation of the components of the space vector $\underline{W}_S$. The relation of the space vector and the two components of the Clarke-transformation is

$$\underline{W}_S = \begin{pmatrix} W_{S,\alpha} \\ W_{S,\beta} \end{pmatrix} = \begin{pmatrix} \mathfrak{Re}(\underline{W}_S) \\ \mathfrak{Im}(\underline{W}_S) \end{pmatrix} = \frac{2}{3} \left(W_{L1,t} + \underline{a} \cdot W_{L2,t} + a^2 \cdot W_{L3,t} \right). \tag{2.20}$$

When $W_{L1,t} + W_{L2,t} + W_{L3,t} \neq 0$, then the Clarke-transformation receives a third component, which results in

$$\mathbf{W}_S = \begin{pmatrix} W_{S,\alpha} \\ W_{S,\beta} \\ W_{S,0} \end{pmatrix} = \begin{pmatrix} \frac{2}{3} & -\frac{1}{3} & -\frac{1}{3} \\ 0 & \frac{\sqrt{3}}{3} & -\frac{\sqrt{3}}{3} \\ \frac{1}{3} & \frac{1}{3} & \frac{1}{3} \end{pmatrix} \cdot \begin{pmatrix} W_{L1,t} \\ W_{L2,t} \\ W_{L3,t} \end{pmatrix}. \tag{2.21}$$

The inverse Clarke-transformation is defined by

$$\begin{pmatrix} W_{L1,t} \\ W_{L2,t} \\ W_{L3,t} \end{pmatrix} = \begin{pmatrix} 1 & 0 & 1 \\ -\frac{1}{2} & \frac{\sqrt{3}}{2} & 1 \\ -\frac{1}{2} & -\frac{\sqrt{3}}{2} & 1 \end{pmatrix} \cdot \begin{pmatrix} W_{S,\alpha} \\ W_{S,\beta} \\ W_{S,0} \end{pmatrix}. \tag{2.22}$$

2.1.4 Park-Transformation

In case of a symmetrical three-phase system, the space vector rotates with a constant angular frequency ω. The space vector is therefore independent of time in the case of a rotating coordinate system. A space vector $\underline{W}_S$ in such a rotating coordinate system $dq0$ is calculated by the Park-transformation:

$$\mathbf{W}_{S,dq} = \begin{pmatrix} W_{S,d} \\ W_{S,q} \\ W_{S,0} \end{pmatrix} = \sqrt{\frac{2}{3}} \begin{pmatrix} \cos(\omega t) & \cos\left(\omega t - \frac{2\pi}{3}\right) & \cos\left(\omega t + \frac{2\pi}{3}\right) \\ -\sin(\omega t) & -\sin\left(\omega t - \frac{2\pi}{3}\right) & -\sin\left(\omega t + \frac{2\pi}{3}\right) \\ \frac{\sqrt{2}}{2} & \frac{\sqrt{2}}{2} & \frac{\sqrt{2}}{2} \end{pmatrix} \cdot \begin{pmatrix} W_{L1,t} \\ W_{L2,t} \\ W_{L3,t} \end{pmatrix}. \tag{2.23}$$

The inverse Park-transformation is defined by

$$\begin{pmatrix} W_{L1,t} \\ W_{L2,t} \\ W_{L3,t} \end{pmatrix} = \sqrt{\frac{2}{3}} \begin{pmatrix} \cos(\omega t) & -\sin(\omega t) & \frac{\sqrt{2}}{2} \\ \cos\left(\omega t - \frac{2\pi}{3}\right) & -\sin\left(\omega t - \frac{2\pi}{3}\right) & \frac{\sqrt{2}}{2} \\ \cos\left(\omega t + \frac{2\pi}{3}\right) & -\sin\left(\omega + -\frac{2\pi}{3}\right) & \frac{\sqrt{2}}{2} \end{pmatrix} \cdot \begin{pmatrix} W_{S,d} \\ W_{S,q} \\ W_{S,0} \end{pmatrix}. \tag{2.24}$$

When there is no zero system, the space vector in the $dq0$-coordinate system can simply be calculated with

$$\underline{W}_{S,dq} = \underline{W}_{S,\alpha\beta} \cdot e^{-j\omega t}. \tag{2.25}$$

Since at $t = 0$ the angle of $\underline{W}_{L1}$ may be different from zero, usually an angle $\theta = \omega t + \theta_0$ is used, which leads to

$$\underline{W}_{S,dq} = \underline{W}_{S,\alpha\beta} \cdot e^{-\theta}. \tag{2.26}$$

2.1.5 Calculation of Active and Reactive Power Based on Park-Components

The instantaneous apparent power S_t is defined by

$$S_t = \frac{3}{2} \left|\underline{U}_{S,dq}\right| \left|\underline{I}_{S,dq}\right| = \sqrt{P_t^2 + Q_t^2} \tag{2.27}$$

where P_t is the instantaneous active power

$$P_t = \frac{3}{2} \underline{U}_{S,dq}^{\top} \cdot \underline{I}_{S,dq} = \frac{3}{2} \left(U_{S,d} I_{S,d} + U_{S,q} I_{S,q}\right) \tag{2.28}$$

and Q_t is the instantaneous reactive power

$$Q_t = \frac{3}{2} \underline{U}_{S,dq} \times \underline{I}_{S,dq} = \frac{3}{2} \left(U_{S,d} I_{S,q} - U_{S,q} I_{S,d}\right). \tag{2.29}$$

Because the normalized current space vector is calculated by

$$\underline{i}_{S,dq} = \frac{1}{\sqrt{2} I_n} \frac{3}{2} \left(I_{L1,t} + \underline{a} I_{L2,t} + \underline{a}^2 I_{L3,t}\right) \tag{2.30}$$

with $\underline{a} = e^{j\frac{2\pi}{3}}$, $I_{L1,t}$, $I_{L2,t}$, $I_{L3,t}$ as the instantaneous phase currents and I_n as the nominal current and the normalized voltage space vector is calculated by

$$\underline{u}_{S,dq} = \frac{\sqrt{3}}{\sqrt{2} U_n} \frac{3}{2} \left(U_{1N,t} + \underline{a} U_{2N,t} + \underline{a}^2 U_{3N,t}\right) \tag{2.31}$$

with $U_{1N,t}$, $I_{2N,t}$, $U_{3N,t}$ as the instantaneous phase-to-neutral voltages and U_n as the nominal phase-to-phase voltage, the normalized instantaneous power can be calculated by

$$s_t = \left|\underline{u}_{S,dq}\right| \left|\underline{i}_{S,dq}\right| \tag{2.32}$$

$$p_t = u_{S,d} i_{S,d} + u_{S,q} i_{S,q} \tag{2.33}$$

$$q_t = u_{S,d} i_{S,q} - u_{S,q} i_{S,d} \tag{2.34}$$

where the relation between S_t, P_t, Q_t and s_t, p_t, q_t is defined by the factor $\frac{1}{S_n}$, where S_n is the nominal apparent power.

Considering positive-sequence and negative-sequence components, any normalized space vector in the dq-plane can be described according to Eq. (5.27) in Chp. 5.5.1. Therefore, a normalized current space vector is defined by

$$\underline{i}_{S,dq} = \underline{i}_{S,dq_{1+}} + \underline{i}_{S,dq_{1-}} e^{-j2\theta} e^{j\varphi_{\pm}} = \left(i_{S,d_{1+}} + j \cdot i_{S,q_{1+}}\right) + \left(i_{S,d_{1-}} + j \cdot i_{S,q_{1-}}\right) e^{-j2\theta} e^{j\varphi_{\pm}} \tag{2.35}$$

and a normalized voltage space vector is defined by

$$\begin{aligned} \underline{u}_{S,dq} &= \underline{u}_{S,dq_{1+}} + \underline{u}_{S,dq_{1-}} e^{-j2\theta} e^{j\varphi_{\pm}} = \\ &= \left(u_{S,d_{1+}} + j \cdot u_{S,q_{1+}}\right) + \left(u_{S,d_{1-}} + j \cdot u_{S,q_{1-}}\right) e^{-j2\theta} e^{j\varphi_{\pm}} = \\ &= u_{S,d_{1+}} + u_{S,d_{1-}} e^{-j2\theta} e^{j\varphi_{\pm}} = \\ &= u_{1+} + u_{1-} e^{-j2\theta} e^{j\varphi_{\pm}} \end{aligned} \tag{2.36}$$

where the components $u_{S,q_{1+}}$ and $u_{S,q_{1-}}$ can be considered to be zero, assuming the positive-sequence and negative-sequence system to be aligned with the direct-axis. In this case, the direct components are identical to the normalized positive-sequence and negative-sequence voltage u_{1+} and u_{1-}. By defining an angle

$$\vartheta = 2\theta - \varphi_{\pm} \tag{2.37}$$

the voltage space vector becomes

$$\underline{u}_{S,dq} = u_{1+} + u_{1-}e^{-j\vartheta} \tag{2.38}$$

with the corresponding Park-components

$$u_{S,d} = u_{1+} + u_{1-}\cos\vartheta \tag{2.39}$$
$$u_{S,q} = -u_{1-}\sin\vartheta. \tag{2.40}$$

The normalized instantaneous powers according to Eq. (2.33) and Eq. (2.34) can be calculated under different assumptions for the current components. For three different assumptions, the following chapters describe the calculation of the corresponding instantaneous powers.

2.1.5.1 Quadrature/Reactive Current Components in the Positive-Sequence and Negative-Sequence System

Assuming only reactive current components, the current space vector becomes

$$\underline{i}_{S,dq} = j \cdot i_{S,q_{1+}} + j \cdot i_{S,q_{1-}}e^{-j\vartheta} \tag{2.41}$$

which leads to the following Park-components

$$i_{S,d} = i_{S,q_{1-}}\sin\vartheta \tag{2.42}$$
$$i_{S,q} = i_{S,q_{1+}} + i_{S,q_{1-}}\cos\vartheta. \tag{2.43}$$

By using the voltage space vector of Eq. (2.38), the corresponding normalized instantaneous active power according to Eq. (2.33) becomes

$$\begin{aligned} p_t &= u_{S,d}i_{S,d} + u_{S,q}i_{S,q} = (u_{1+} + u_{1-}\cos\vartheta)(i_{S,q_{1-}}\sin\vartheta) + (-u_{1-}\sin\vartheta)(i_{S,q_{1+}} + i_{S,q_{1-}}\cos\vartheta) = \\ &= u_{1+}i_{S,q_{1-}}\sin\vartheta + u_{1-}\sin\vartheta\cos\vartheta - u_{1-}i_{S,q_{1+}}\sin\vartheta - u_{1-}i_{S,q_{1+}}\sin\vartheta\cos\vartheta \end{aligned} \tag{2.44}$$

and the corresponding normalized instantaneous reactive power according to Eq. (2.34) becomes

$$\begin{aligned} q_t &= u_{S,d}i_{S,q} - u_{S,q}i_{S,d} = (u_{1+} + u_{1-}\cos\vartheta)(i_{S,q_{1+}} + i_{S,q_{1-}}\cos\vartheta) - (-u_{1-}\sin\vartheta)(i_{S,q_{1-}}\sin\vartheta) \\ &= u_{1+}i_{S,q_{1+}} + u_{1-}i_{S,q_{1+}}\cos\vartheta + u_{1+}i_{S,q_{1-}}\cos\vartheta + \\ &+ \frac{1}{2}u_{1-}i_{S,q_{1-}}(1+\cos 2\vartheta) + \frac{1}{2}u_{1-}i_{S,q_{1-}}(1-\cos 2\vartheta). \end{aligned} \tag{2.45}$$

The corresponding normalized powers p and q are defined by the time mean value of the corresponding instantaneous power. Because the time mean values of $\sin\vartheta$, $\cos\vartheta$ and $\sin\vartheta\cos\vartheta = \frac{1}{2}\sin 2\vartheta$ are zero, the corresponding powers can be calculated by

$$p = \overline{p_t} = 0 \tag{2.46}$$
$$q = \overline{q_t} = u_{1+}i_{S,q_{1+}} + u_{1-}i_{S,q_{1-}}. \tag{2.47}$$

2.1.5.2 Direct/Active Current Component in the Positive-Sequence System

Assuming only an active current component in the positive-sequence system, the current space vector becomes

$$\underline{i}_{S,dq} = i_{S,d_{1+}} \tag{2.48}$$

which leads to the following Park-components

$$i_{S,d} = i_{S,d_{1+}} \tag{2.49}$$
$$i_{S,q} = 0. \tag{2.50}$$

By using the voltage space vector of Eq. (2.38) the corresponding normalized instantaneous active power according to Eq. (2.33) becomes

$$\begin{aligned} p_t &= u_{S,d}i_{S,d} + u_{S,q}i_{S,q} = (u_{1+} + u_{1-}\cos\vartheta)(i_{S,d_{1+}}) + (-u_{1-}\sin\vartheta)(0) = \\ &= u_{1+}i_{S,d_{1+}} + u_{1-}i_{S,d_{1+}}\cos\vartheta \end{aligned} \tag{2.51}$$

and the corresponding normalized instantaneous reactive power according to Eq. (2.34) becomes

$$\begin{aligned} q_t &= u_{S,d}i_{S,q} - u_{S,q}i_{S,d} = (u_{1+} + u_{1-}\cos\vartheta)(0) - (-u_{1-}\sin\vartheta)(i_{S,d_{1+}}) = \\ &= u_{1-}i_{S,d_{1+}}\sin\vartheta. \end{aligned} \tag{2.52}$$

The corresponding normalized powers p and q are defined by the time mean value of the corresponding instantaneous power. Because the time mean values of $\sin\vartheta$ and $\cos\vartheta$ are zero, the corresponding powers can be calculated by

$$p = \overline{p_t} = u_{1+}i_{S,d_{1+}} \tag{2.53}$$
$$q = \overline{q_t} = 0. \tag{2.54}$$

2.1.5.3 Quadrature/Reactive Current Component in the Positive-Sequence System

Assuming only a reactive current component in the positive-sequence system, the current space vector becomes

$$\underline{i}_{S,dq} = ji_{S,q_{1+}} \tag{2.55}$$

which leads to the following Park-components

$$i_{S,d} = 0 \tag{2.56}$$
$$i_{S,q} = i_{S,q_{1+}}. \tag{2.57}$$

By using the voltage space vector of Eq. (2.38) the corresponding normalized instantaneous active power according to Eq. (2.33) becomes

$$\begin{aligned} p_t &= u_{S,d}i_{S,d} + u_{S,q}i_{S,q} = (u_{1+} + u_{1-}\cos\vartheta)(0) + (-u_{1-}\sin\vartheta)(i_{S,q_{1+}}) = \\ &= -u_{1-}i_{S,q_{1+}}\sin\vartheta \end{aligned} \tag{2.58}$$

and the corresponding normalized instantaneous reactive power according to Eq. (2.34) becomes

$$\begin{aligned} q_t &= u_{S,d}i_{S,q} - u_{S,q}i_{S,d} = (u_{1+} + u_{1-}\cos\vartheta)(i_{S,q_{1+}}) - (-u_{1-}\sin\vartheta)(0) = \\ &= u_{1+}i_{S,q_{1+}} + u_{1-}i_{S,q_{1+}}\cos\vartheta. \end{aligned} \tag{2.59}$$

The corresponding normalized powers p and q are defined by the time mean value of the corresponding instantaneous power. Because the time mean values of $\sin\vartheta$ and $\cos\vartheta$ are zero, the corresponding powers can be calculated by

$$p = \overline{p_t} = 0 \tag{2.60}$$
$$q = \overline{q_t} = u_{1+}i_{S,q_{1+}}. \tag{2.61}$$

2.1.5.4 Direct/Active and Quadrature/Reactive Current Component in the Positive-Sequence System

Assuming only active and reactive current components in the positive-sequence system, the current space vector becomes

$$\underline{i}_{S,dq} = i_{S,d_{1+}} + j i_{S,q_{1+}} \tag{2.62}$$

which leads to the following Park-components

$$i_{S,d} = i_{S,d_{1+}} \tag{2.63}$$
$$i_{S,q} = i_{S,q_{1+}}. \tag{2.64}$$

By using the voltage space vector of Eq. (2.38) the corresponding normalized instantaneous active power according to Eq. (2.33) becomes

$$\begin{aligned} p_t &= u_{S,d} i_{S,d} + u_{S,q} i_{S,q} = (u_{1+} + u_{1-}\cos\vartheta)(i_{S,d_{1+}}) + (-u_{1-}\sin\vartheta)(i_{S,q_{1+}}) = \\ &= u_{1+} i_{S,d_{1+}} + u_{1-} i_{S,q_{1+}}\cos\vartheta - u_{1-} i_{S,q_{1+}}\sin\vartheta \end{aligned} \tag{2.65}$$

and the corresponding normalized instantaneous reactive power according to Eq. (2.34) becomes

$$\begin{aligned} q_t &= u_{S,d} i_{S,q} - u_{S,q} i_{S,d} = (u_{1+} + u_{1-}\cos\vartheta)(i_{S,q_{1+}}) - (-u_{1-}\sin\vartheta)(i_{S,d_{1+}}) = \\ &= u_{1+} i_{S,q_{1+}} + u_{1-} i_{S,q_{1+}}\cos\vartheta + u_{1-} i_{S,d_{1+}}\sin\vartheta. \end{aligned} \tag{2.66}$$

The corresponding normalized powers p and q are defined by the time mean value of the corresponding instantaneous power. Because the time mean values of $\sin\vartheta$ and $\cos\vartheta$ are zero, the corresponding powers can be calculated by

$$p = \overline{p_t} = u_{1+} i_{S,d_{1+}} \tag{2.67}$$
$$q = \overline{q_t} = u_{1+} i_{S,q_{1+}}. \tag{2.68}$$

2.2 Calculation of Short-Circuits

A complete calculation of short-circuit currents should give the currents as a function of time, as it is shown in Fig. A.9 for a generator short-circuit. However, in most practical cases a determination of the short-circuit current as a function of time is not necessary. The calculation of the occurring short-circuit currents in the event of a fault is based on a worst-case calculation. The procedure is described in the standard IEC 60909 [87]. The method used for calculation is based on the introduction of an equivalent voltage source at the short-circuit location. The equivalent voltage source is the only active voltage of the system. All network feeders, synchronous and asynchronous machines are replaced by their internal impedances. Based on a voltage factor c the extreme cases of the voltage conditions during the short-circuit are included in the calculation. The maximum short-circuit current is responsible for the rating of equipment regarding the mechanical and thermal stresses, the minimum short-circuit current has to be calculated for the selection of the system protection. In the calculation of the short-circuit currents in systems supplied by generators, power-stations and motors, it is of interest to know not only the initial symmetrical shortcircuit current I_k'' and the peak short-circuit current $\hat{I}_p$, but also the steady-state short-circuit current I_k. In Fig. A.9 the short-circuit current is shown as a function of time in case of a near-to-generator short-circuit. In such a case, the AC component of the short-circuit current normally decays with time. In case of a far-from-generator short-circuit the AC component stays constant and only a DC component can be observed.

The procedure for calculating a three-phase short-circuit, a two-phase short-circuit, and an earth fault is explained using a grid section which contains the grid section where the real BESS according to Chp. 3.1 is integrated. The results of the following calculations are used in Chp. 4.3 to plan a corresponding field test to investigate the service "dynamic voltage support". A larger number of calculation examples can be found in [98]. Fig. 2.2 shows the single line diagram of the example grid which spreads over the Network Layers 1 to 5. The relevant data of the equipment is given with

- the short-circuit power S_k'' of the equivalent circuit of the feeding grid,
- the vector group, the transformation ratio, the rated voltages U_{r1} and U_{r2}, the nominal apparent power S_n, the short-circuit voltage u_k in the positive-sequence system, the short-circuit voltage u_{k0} in the negative-sequence system and the copper losses of the transformers P_k,
- the length-related resistance R'_+ and reactance X'_+ in the positive-sequence system, the length-related resistance R'_0 and reactance X'_0 in the zero-sequence system, the zero-capacitance C'_0 and the length of lines.

The impedances are assumed to be identical in the positive-sequence and negative-sequence system. In three-phase AC systems the calculation of the current values resulting from balanced and unbalanced short-circuits is simplified by the use of symmetrical components. In IEC 60909-0:2016 [87], the basis for further calculations is the initial short-circuit current I_k''. Several simplifications of the equipment are assumed to allow a simple calculation but at the same time to achieve a sufficient accuracy of I_k''. The feeding grid is assumed to have a behavior identical to that of a synchronous machine. According to Chp. A.3.1.2, the initial short-circuit current of a synchronous generator is defined by the subtransient reactance X_d''. The relation between the short-circuit power S_k'' and the subtransient reactance X_d'' is defined by

$$S_k'' = c \cdot \frac{U_n^2}{X_d''}. \tag{2.69}$$

For the transformers in the short-circuit calculation, the reactance X_h and the resistance R_{Fe} of the equivalent circuit shown in Fig. A.10 can be neglected, so that only the leakage reactances and the copper resistances are effective. The relations between the short-circuit voltage u_k and the copper losses P_k are defined by

$$u_k = (X_{1\sigma} + X'_{2\sigma}) \cdot \frac{1}{\frac{U_{r1}^2}{S_n}}, \tag{2.70}$$

$$P_k = (R_1 + R'_2) \cdot \frac{S_n}{\frac{U_{r1}^2}{S_n}}. \tag{2.71}$$

With these assumptions, the equivalent circuit of the example grid is shown in the symmetrical components in Fig. 2.2. The feeding grid and the transformers in the positive-sequence and negative-sequence system are represented as described above. The lines in the positive-sequence and negative-sequence system are described with their corresponding impedances. In the negative-sequence system the transformers and lines are represented with their corresponding zero-sequence impedances. The vector groups of the transformer only have an influence in the zero-sequence system. Wye-windings are forwarding the zero-sequence current, while delta-windings are short-circuiting the zero-sequence current. The influence of the vector groups can be described as shown in Fig. 2.2.

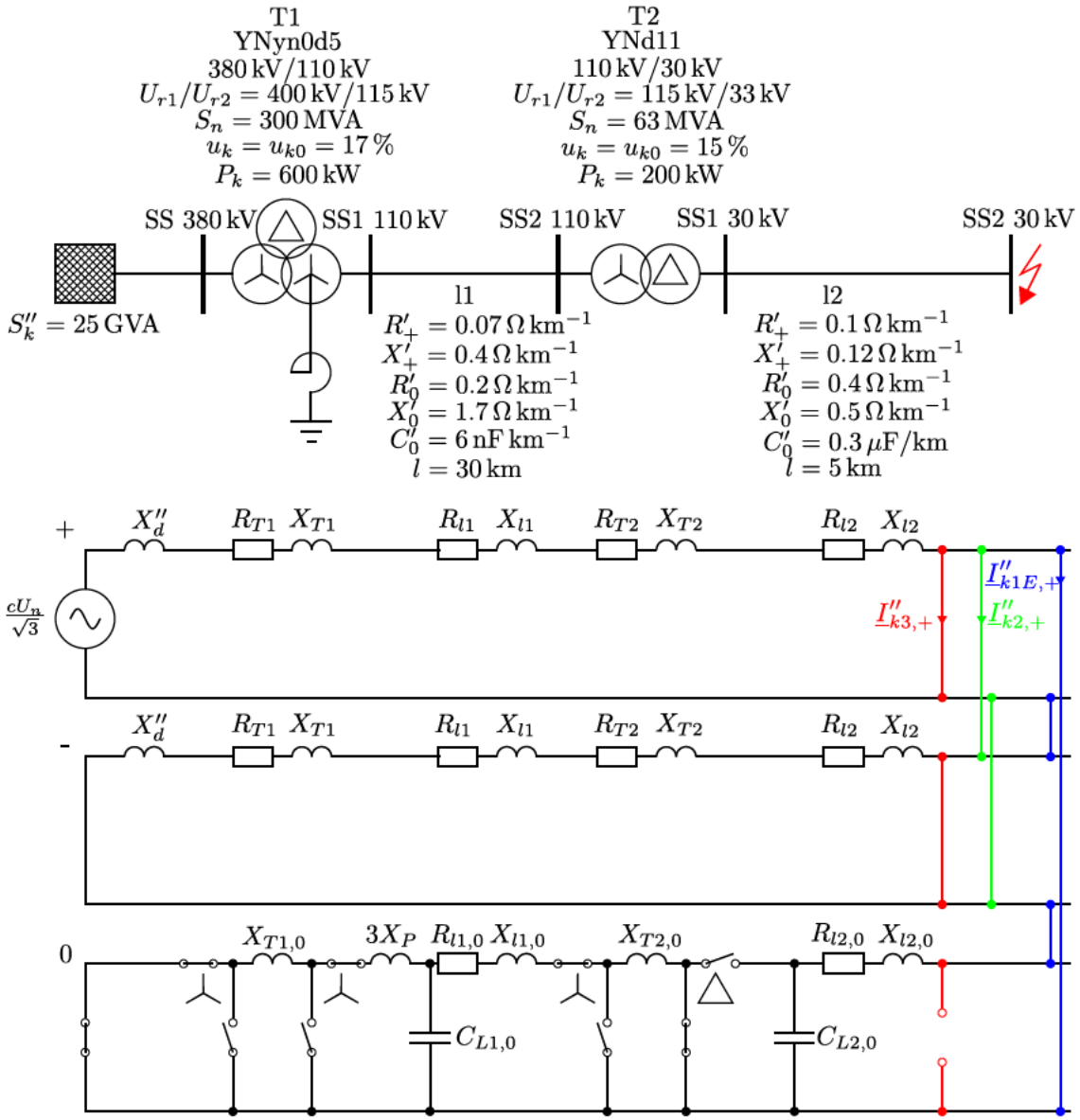

Figure 2.2: Example for calculation of three different types of short-circuits; three-phase short-circuit in red, two-phase short-circuit in green and earth-fault in blue.

Based on the data in Fig. 2.2, the impedances of the equipment at the point of the short-circuit can be calculated as follows. The subtransient reactance of the feeding grid can be calculated by

$$X''_d = c \cdot \frac{U_n^2}{S''_k} \left(\frac{U_{T1,n2}}{U_{T1,n2}}\right)^2 \left(\frac{U_{T2,n2}}{U_{T2,n2}}\right)^2 = 1.05 \cdot \frac{(30\,\text{kV})^2}{25\,\text{GVA}} \left(\frac{115\,\text{kV}}{400\,\text{kV}}\right)^2 \left(\frac{33\,\text{kV}}{115\,\text{kV}}\right)^2 = 41\,\text{m}\Omega \quad (2.72)$$

where the last two terms represent the transformation of the impedance at the fault location due to the transformation ratios of the transformers T1 and T2. For the calculation of the impedance, reactance and resistance of transformer T1, IEC 60909-0:2016 requires the use of a correction

factor

$$K_{T1} = \frac{0.95 \cdot c_{max}}{1 + 0.6\sqrt{u_{T1,k}^2 - \left(\frac{P_{T1,k}}{S_{T1,n}}\right)^2}} = \frac{0.95 \cdot 1.1}{1 + 0.6\sqrt{0.17 + 0.6\sqrt{0.17^2 - \left(\frac{600\,\text{kVA}}{300\,\text{MVA}}\right)^2}}} = 0.9483 \quad (2.73)$$

with which these values can be calculated by

$$Z_{T1} = K_{T1} u_{T1,k} \frac{U_{T1,r2}^2}{S_{T1,n}} \left(\frac{U_{T2,r2}}{U_{T2,r1}}\right)^2 = 0.948 \cdot 17\,\% \cdot \frac{(115\,\text{kV})^2}{300\,\text{MVA}} \left(\frac{33\,\text{kV}}{115\,\text{kV}}\right)^2 = 0.58\,\Omega \quad (2.74)$$

$$R_{T1} = K_{T1} P_{T1,k} \frac{U_{T1,r2}^2}{(S_{T1,n})^2} \left(\frac{U_{T2,r2}}{U_{T2,r1}}\right)^2 = 0.948 \cdot 600\,\text{kW} \cdot \frac{(115\,\text{kV} \cdot 33\,\text{kV})^2}{(300\,\text{MVA} \cdot 115\,\text{kV})^2} = 6.9\,\text{m}\Omega \quad (2.75)$$

$$X_{T1} = X_{T1,0} = \sqrt{Z_{T1}^2 - R_{T1}^2} = \sqrt{(0.58\,\Omega)^2 - (6.9\,\text{m}\Omega)^2} \approx 0.58\,\Omega \quad (2.76)$$

and where the factor $\left(\frac{U_{T2,r2}}{U_{T2,r1}}\right)^2$ is used to get the effective values of the impedance, reactance and resistance at the fault location.

The reactance and resistance of the line l1 can be calculated by

$$R_{l1} = R'_{l1,+} \cdot l_{l1} \cdot \left(\frac{U_{T2,r2}}{U_{T2,r1}}\right)^2 = 0.07\,\Omega/\text{km} \cdot 30\,\text{km} \cdot \left(\frac{33\,\text{kV}}{115\,\text{kV}}\right)^2 = 0.17\,\Omega \quad (2.77)$$

$$X_{l1} = X'_{l1,+} \cdot l_{l1} \cdot \left(\frac{U_{T2,r2}}{U_{T2,r1}}\right)^2 = 0.4\,\Omega/\text{km} \cdot 30\,\text{km} \cdot \left(\frac{33\,\text{kV}}{115\,\text{kV}}\right)^2 = 0.99\,\Omega \quad (2.78)$$

$$R_{l1,0} = R'_{l1,0} \cdot l_{l1} \cdot \left(\frac{U_{T2,r2}}{U_{T2,r2}}\right)^2 = 0.2\,\Omega/\text{km} \cdot 30\,\text{km} \cdot \left(\frac{33\,\text{kV}}{115\,\text{kV}}\right)^2 = 0.49\,\Omega \quad (2.79)$$

$$X_{l1,0} = X'_{l1,0} \cdot l_{l1} \cdot \left(\frac{U_{T2,r2}}{U_{T2,r2}}\right)^2 = 1.7\,\Omega/\text{km} \cdot 30\,\text{km} \cdot \left(\frac{33\,\text{kV}}{115\,\text{kV}}\right)^2 = 4.19\,\Omega \quad (2.80)$$

where the factor $\left(\frac{U_{T2,r2}}{U_{T1,r2}}\right)^2$ is used to get the effective values of the reactance and resistance on the side of the fault location.

The correction factor of the transformer T2 is

$$K_{T2} = \frac{0.95 \cdot c_{max}}{1 + 0.6\sqrt{u_{T2,k}^2 - \left(\frac{P_{T2,k}}{S_{T2,n}}\right)^2}} = \frac{0.95 \cdot 1.1}{1 + 0.6\sqrt{0.15 + 0.6\sqrt{0.15^2 - \left(\frac{200\,\text{kVA}}{63\,\text{MVA}}\right)^2}}} = 0.9587 \quad (2.81)$$

with which the impedance, reactance and resistance of transformer T2 can be calculated by

$$Z_{T2} = K_{T2} u_{T2,k} \cdot \frac{U_{T2,r2}^2}{S_{T2,n}} = 15\,\% \cdot \frac{(33\,\text{kV})^2}{63\,\text{MVA}} = 2.49\,\Omega \quad (2.82)$$

$$R_{T2} = K_{T2} P_{T2,k} \cdot \frac{U_{T2,r2}^2}{(S_{T2,n})^2} = 200\,\text{kW} \cdot \frac{(33\,\text{kV})^2}{(63\,\text{MVA})^2} = 55\,\text{m}\Omega \quad (2.83)$$

$$X_{T2} = X_{T2,0} = \sqrt{Z_{T2}^2 - R_{T2}^2} = \sqrt{(2.49\,\Omega)^2 - (55\,\text{m}\Omega)^2} \approx 2.48\,\Omega \quad (2.84)$$

which are the effective values at the fault location.

The reactance and resistance of the line l2 can be calculated by

$$R_{l2} = R'_{l2,+} \cdot l_{l2} = 0.1\,\Omega/\mathrm{km} \cdot 5\,\mathrm{km} = 0.5\,\Omega \tag{2.85}$$
$$X_{l2} = X'_{l2,+} \cdot l_{l2} = 0.12\,\Omega/\mathrm{km} \cdot 5\,\mathrm{km} = 0.6\,\Omega \tag{2.86}$$
$$R_{l2,0} = R'_{l2,0} \cdot l_{l2} = 0.4\,\Omega/\mathrm{km} \cdot 5\,\mathrm{km} = 2\,\Omega \tag{2.87}$$
$$X_{l2,0} = X'_{l2,0} \cdot l_{l2} = 0.5\,\Omega/\mathrm{km} \cdot 5\,\mathrm{km} = 2.5\,\Omega \tag{2.88}$$
$$X_{Cl2,0} = \frac{1}{\omega C'_{l2,0} \cdot l_{l2}} = \frac{1}{2\pi \cdot 50\,\mathrm{Hz} \cdot 0.3\,\mu\mathrm{F/km} \cdot 5\,\mathrm{km}} = 2.12\,\mathrm{k}\Omega. \tag{2.89}$$

Based on the fault conditions described in Chp. 2.2, for the three different types of short-circuits, the result is an interconnection of symmetrical components as shown in Fig. 2.2. The calculation of I''_k for the three types of short-circuits is done in the following chapters. The usage of the safety factor "c" is described in [87] and [98]. In the following the factor $c_{max} = 1.1$ for Medium Voltage (MV) grids is used to calculate the maximum initial short-circuit current. This maximum value is not further indicated.

2.2.1 Three-Phase Short-Circuit

According to Fig. 2.2 the positive-sequence current $\underline{I}''_{k3,+}$ in case of a three-phase short-circuit can be calculated by

$$\underline{I}''_{k3,+} = \frac{c_{max} \cdot U_n}{\sqrt{3} \cdot \underline{Z}_+} = \frac{1.1 \cdot 30\,\mathrm{kV}}{\sqrt{3}\,(0.73 + j4.7)\,\Omega} = (0.62 + j3.9)\mathrm{kA} \tag{2.90}$$

with

$$\begin{aligned} \underline{Z}_+ &= (R_{T1} + R_{l1} + R_{T2} + R_{l2}) + j \cdot (X''_d + X_{T1} + X_{l1} + X_{T2} + X_{l2}) = \\ &= ((0.0069 + 0.1729 + 0.055 + 0.5) + j(0.0413 + 0.58 + 0.99 + 2.48 + 0.6))\,\Omega = \\ &= (0.73 + j4.7)\Omega. \end{aligned} \tag{2.91}$$

The currents in the negative-sequence and zero-sequence system are $\underline{I}''_{k3,-} = \underline{I}''_{k3,0} = 0$. Therefore, the initial short-circuit current in the three phases is calculated with

$$\begin{pmatrix} \underline{I}''_{k3,L1} \\ \underline{I}''_{k3,L2} \\ \underline{I}''_{k3,L3} \end{pmatrix} = \mathbf{A}^{-1} \cdot \begin{pmatrix} \underline{I}''_{k3,0} \\ \underline{I}''_{k3,+} \\ \underline{I}''_{k3,-} \end{pmatrix} = \mathbf{A}^{-1} \cdot \begin{pmatrix} 0 \\ \underline{I}''_{k3,+} \\ 0 \end{pmatrix} = \underline{I}''_{k3,+} \cdot \begin{pmatrix} 1 \\ \underline{a}^2 \\ \underline{a} \end{pmatrix} \tag{2.92}$$

while I''_{k3} is normally referred to $|\underline{I}''_{k3,L1}|$. Therefore, the result for the initial short-circuit current I''_{k3} is

$$I''_{k3} = 4.005\,\mathrm{kA}. \tag{2.93}$$

2.2.2 Two-Phase Short-Circuit

According to Fig. 2.2 the positive-sequence current $\underline{I}''_{k2,+}$ in case of a two-phase short-circuit can be calculated by

$$\underline{I}''_{k2,+} = \frac{c_{max} \cdot U_n}{\sqrt{3} \cdot \left(\underline{Z}_+ + \underline{Z}_-\right)} = \frac{1.1 \cdot 30\,\mathrm{kV}}{\sqrt{3} \cdot 2 \cdot (0.73 + j4.7)\,\Omega} = (0.31 + j1.9)\mathrm{kA} \tag{2.94}$$

with $\underline{Z}_+ = \underline{Z}_-$ which is identical to $\underline{Z}_+$ of the three-phase short-circuit. The currents in the zero-sequence system and the negative-sequence system are $\underline{I}''_{k2,0} = 0$ and $\underline{I}''_{k2,-} = -\underline{I}''_{k2,+}$. Therefore, the initial short-circuit current in the three phases is calculated with

$$\begin{aligned}\begin{pmatrix}\underline{I}''_{k2,L1}\\ \underline{I}''_{k2,L2}\\ \underline{I}''_{k2,L3}\end{pmatrix} &= \mathbf{A}^{-1}\cdot\begin{pmatrix}\underline{I}''_{k2,0}\\ \underline{I}''_{k2,+}\\ \underline{I}''_{k2,-}\end{pmatrix} = \mathbf{A}^{-1}\cdot\begin{pmatrix}0\\ \underline{I}_{k2,+}\\ -\underline{I}_{k2,+}\end{pmatrix} = \underline{I}_{k2,+}\cdot\begin{pmatrix}0\\ \underline{a}^2-\underline{a}\\ \underline{a}-\underline{a}^2\end{pmatrix} = \\ &= j\sqrt{3}\underline{I}''_{k2,+}\cdot\begin{pmatrix}0\\ -1\\ 1\end{pmatrix}\end{aligned} \tag{2.95}$$

while I''_{k2} is normally referred to $|\underline{I}''_{k2,L2}|$. Therefore, the result for the initial short-circuit current I''_{k2} is

$$I''_{k2} = 3.46\,\mathrm{kA}. \tag{2.96}$$

2.2.3 Earth Fault

According to Fig. 2.2 the positive-sequence current $\underline{I}''_{k1E,+}$ in case of an earth fault can be calculated by

$$\underline{I}''_{k1E,+} = \frac{c_{max}\cdot U_n}{\sqrt{3}\cdot\left(\underline{Z}_+ + \underline{Z}_- + \underline{Z}_0\right)} = \frac{1.1\cdot 30\,\mathrm{kV}}{\sqrt{3}\cdot\left(2\cdot(0.73+j4.7)\,\Omega + (-j2.12\mathrm{k}\Omega)\right)} \approx j9.03\,\mathrm{A} \tag{2.97}$$

with $\underline{Z}_+ = \underline{Z}_-$ which is identical to $\underline{Z}_+$ of the three-phase short-circuit and with

$$\underline{Z}_0 = R_{l2,0} + j(X_{l2,0} - X_{Cl2,0}) = 2\,\Omega + j(2.5 - 2.12\cdot 10^3)\Omega \approx -j2.12\mathrm{k}\Omega. \tag{2.98}$$

The currents in the zero-sequence system and the negative-sequence system are $\underline{I}''_{k1E,0} = \underline{I}''_{k1E,-} = \underline{I}''_{k1E,+}$. Therefore, the initial short-circuit current in the three phases is calculated with

$$\begin{pmatrix}\underline{I}''_{k1E,L1}\\ \underline{I}''_{k1E,L2}\\ \underline{I}''_{k1E,L3}\end{pmatrix} = \mathbf{A}^{-1}\cdot\begin{pmatrix}\underline{I}''_{k1E,0}\\ \underline{I}''_{k1E,+}\\ \underline{I}''_{k1E,-}\end{pmatrix} = \mathbf{A}^{-1}\cdot\begin{pmatrix}\underline{I}''_{k1E,+}\\ \underline{I}''_{k1E,+}\\ \underline{I}''_{k1E,+}\end{pmatrix} = 3\cdot\underline{I}_{k1E,+}\cdot\begin{pmatrix}1\\ 0\\ 0\end{pmatrix} \tag{2.99}$$

while I''_{k1E} is normally referred to $|\underline{I}''_{k1E,L1}|$. Therefore, the result for the inital short-circuit current I''_{k1E} is

$$I''_{k1E} = 27\,\mathrm{A}. \tag{2.100}$$

2.2.4 Short-Circuits in Island Grids

Island grids sometimes are not sufficiently modeled by the methods used in the standard IEC 60909-0. This is especially the case if the minimum short-circuit current needs to be calculated. Checking the compliance with fault clearing times and testing of selectivity of protection depends on this kind of short-circuit current. In [185] the short-circuit currents calculated according to standard IEC 60909-0 are compared to those calculated by a transient simulation for a real-world example.

2.3 Load-Frequency Control

In the electric power system, the active power has to be generated at the same time as it is consumed. Disturbances in this balance are causing the system frequency to change and deviate from its set-point values. The system frequency is a measure for the rotation speed of the synchronized generators. If total demand surpasses the generation, the frequency decreases, while a surplus in generation increases the frequency. In order to restore the nominal value of the frequency a phased load-frequency control is used. Frequency deviations will be offset initially by the kinetic energy of the rotating generators and motors connected, which is called the "instantaneous reserve". Regulating units will then provide the first phase of the load-frequency control, the "Frequency Containment Reserve (FCR)", which is a P-control action and leads to a permanent control offset. In the second phase of the load-frequency control regulating units provide aFRR, which is a PI-control action and diminishes this control offset. In order to release full stroke of aFRR for the next frequency deviation, the third phase then comes into force, which is "manual Frequency Restoration Reserve (mFRR)". Within a control area there are several balance groups. One hour after a frequency deviation the reserves to replace mFRR are managed by the Balance Group Representative (BGR).

The three different phases of the load-frequency control FCR, aFRR and mFRR are also known as "Primary Control Reserve", "Secondary Control Reserve" and "Tertiary Control Reserve". The three phases, the foregoing instantaneous reserve and subsequent provision of reserve by the BGR are shown in Fig. 2.3. The given time in the figure is related to a frequency deviation at the moment 0 s.

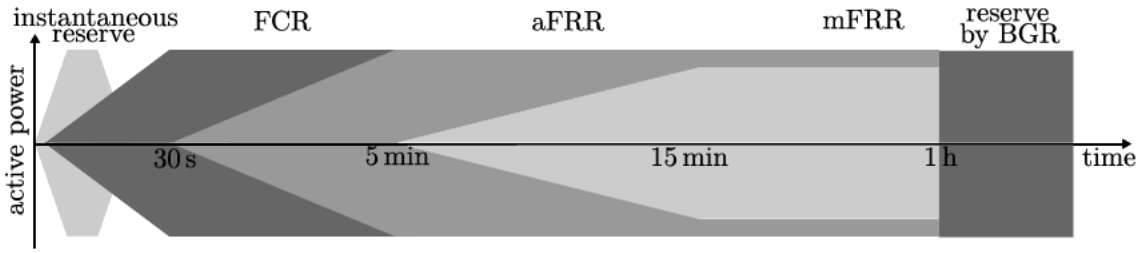

Figure 2.3: Phases of the load-frequency control.

The three different phases of load-frequency control are related to the three different products FCR, aFRR and mFRR. Regulating units that provide such products have to fulfill certain characteristics for each product e.g. related to the shape of the product. The shape of the products can be divided into several parts:

(a) preparation period,

(b) ramping period,

(c) full activation time,

(d) delivery period,

which are different for each product and described in Fig. 2.4. Other characteristics of the products are

- full activation frequency deviation (=maximum steady state frequency deviation),
- intentional frequency response deadband.

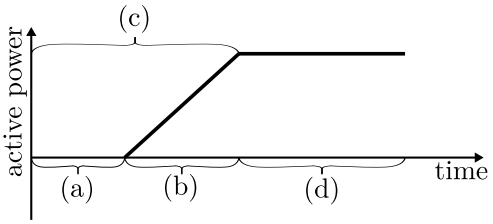

Figure 2.4: Parts of the shape of products for load-frequency control. The times are related to the moment of the occurence of a frequency deviation.

The participation on load-frequency control is handled via a market-based tendering platform, which is called "balancing market". Units that pass a prequalification process can participate on this market. The procurement of balancing power works with auctions. The characteristics of these auctions differ for the different products of the load-frequency control and can be divided into

- auction frequency (identical to product duration),
- asymmetry (symmetrical products can only be provided in a single bid, while asymmetrical products can be provided separately),
- minimum bid size,
- bid granularity.

The values of these characteristics and other necessary requirements of the products of load-frequency control are defined in the System Operation Guideline (SOGL) [60], which is an European regulation. According to article 154 of the SOGL, for the synchronous area Continental Europe (CE) additional properties are defined in [50]. The SOGL and the additional properties are transposed into national regulations. At the moment these national regulations in Austria are defined in [11].

2.3.1 Instantaneous Reserve (Inertia)

Before the three phases of the load-frequency control react to a frequency deviation, initially the deviation will be offset by the kinetic energy of the rotating generators and motors connected. This kinetic energy is the instantaneous reserve or inertia of the power system. The behavior of the system in this phase can be described by the swing equation, which is introduced in detail in Eq. (A.76):

$$P_{M,t} - P_{E,t} = T_A \frac{S_n}{\omega_n^2} \omega \frac{d\omega}{dt}. \tag{2.101}$$

In contrast to Eq. (A.76), which describes the behavior of only one synchronous generator, on a system level $P_{M,t}$ can be interpreted as the actual mechanical power that is provided by all connected rotating machines and $P_{E,t}$ can be interpreted as the actual electrical power demand of all loads. Therefore, with N as the number of connected rotating machines, the equation can be rewritten to

$$\sum_{k=1}^{N} P_{M,t,k} - P_{E,t} = \sum_{k=1}^{N} T_{A,k} S_{n,k} \cdot \frac{1}{\omega_n^2} \omega \frac{d\omega}{dt}. \tag{2.102}$$

By defining the "network starting time constant"

$$T_{A,\Sigma} = \frac{\sum_{k=1}^{N} T_{A,k} S_{n,k}}{P_\Sigma} \tag{2.103}$$

the equation becomes

$$\sum_{k=1}^{N} P_{M,t,k} - P_{E,t} = T_{A,\Sigma} P_\Sigma \cdot \frac{1}{\omega_n^2} \omega \frac{d\omega}{dt} \tag{2.104}$$

where P_Σ usually is the peak load demand in the network.

2.3.2 Frequency Containment Reserve (FCR)

As the first phase of the load-frequency control, FCR works as described by Fig. 2.5 by the static behavior of FCR. The FCR-regulating units provide regulating power P_{FCR} as a reaction of a frequency deviation Δf according to their parameterized droop $\sigma = \frac{\Delta f / f_n}{P_{FCR}/S_n}$, with $P_{FCR} = \frac{\Delta f / f_n}{S_n / \sigma}$ and $\Delta f = f - f_n$ when using the load reference system[2]. The bid size of the regulating unit is defined by X_{FCR}, which is $|P_{FCR}|$ at $|\Delta f| = 200\,\text{mHz}$. Therefore, the bid size which is offered at the balancing market is only retrieved at a maximum steady-state frequency deviation of 200 mHz. At frequency deviations above, the regulating units do not have to follow their parameterized droop characteristic. At very small frequency deviations a frequency-deadband of ±10 mHz is defined in which the regulating units also do not have to follow their droop characteristic. This value stems from the required accuracy of at least 10 mHz for the local frequency measurement of FCR-regulating units [3].

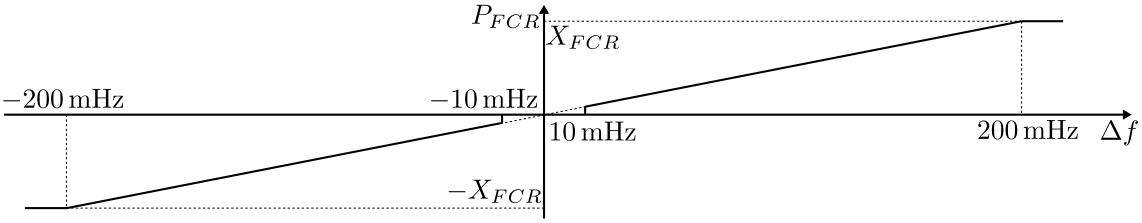

Figure 2.5: Static behavior of FCR.

The dynamic behavior of the FCR-regulating units is defined by the shape of the product as shown in Fig. 2.6. The full activation of FCR has to be established at the latest 30 s after a frequency deviation of ±200 mHz. Therefore, the full activation time of FCR according to Fig. 2.4 is 30 s. For smaller frequency deviations the required time to reach the setpoint P_{FCR} is accordingly smaller as shown in Fig. 2.6. The first 15 s of Fig. 2.6 are defined as the preparation time of FCR according to Fig. 2.4. Slow regulating units are allowed to have this preparation time, but every regulating unit has to react as fast as technically possible. According to the German Transmission System Operator(s) (TSO) [3] an artificial delay is not allowed.

FCR is jointly provided by every control area within a synchronous area. Every control area is operated by a corresponding TSO. Austria is part of the regional group CE and has one active TSO only, which is the Austrian Power Grid (APG). Since in general, the behavior of generation and load is the basis for the needed amount of FCR, the distribution key for the individual TSO should reflect generation and demand connected in the area of a TSO. The result is the FCR obligation. Besides, the fair distribution of obligations, the calculation method for the FCR obligation implicitly results

[2] In the load reference system the power is greater than zero when consuming power and the power is smaller than zero when providing power.

in an even geographic distribution of FCR [49]. The FCR obligation of every control area is calculated based on the yearly energy consumption within this control area. In Austria the FCR obligation is approximately ±70 MW. All characteristics of the FCR are summarized in Tab. 2.1.

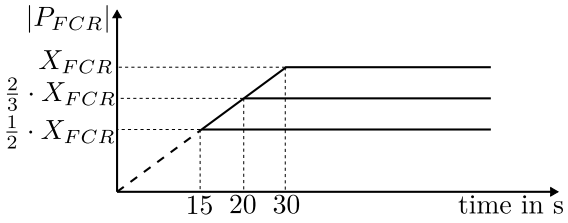

Figure 2.6: Dynamic behavior of FCR (shape).

Table 2.1: Characteristics of FCR in Austria.

characteristic	**value**
full activation time (FAT)	30 s
preparation time	maximum 2 s
delivery period	minimum 15 min
full activation frequency deviation	200 mHz
intentional frequency response deadband	10 mHz
capacity requirement for Limited Energy Reservoir (LER)-units	30 min full activated FCR-power
auction frequency (=tendering period)	daily
tendered products	4 h [5]
bid symmetry	symmetrical
minimum bid size	1 MW
bid granularity	1 MW
total FCR obligation in the control area AT in 2019	±70 MW

2.3.3 Reference Incident and Design Hypothesis

The basic criterion used for FCR dimensioning is to withstand the "reference incident". The reference incident is defined as the maximum expected instantaneous power deviation between generation and demand in the synchronous area for which the dynamic behavior of the system is designed. This expected instantaneous power deviation includes the losses of the largest power generation units or loads, loss of a line sector or a bus bar. According to the SOGL [60] (article 153), the reference incident for the regional group CE is determined with ±3 GW (corresponds to an outage of the two biggest nuclear power units of 1.5 GW each). For this reference incident a design hypothesis is set up, which assumes the synchronous area to behave as described by Eq. (2.104). The power demand of the loads is dependent on the actual system frequency. This behavior is called "self-regulating-effect" of the loads and its quantity is described with k_L (in $\frac{\%}{\text{Hz}}$). The contribution of the self-regulating effect can be considered in the term $P_{E,t}$ of Eq. (2.104). The behavior of all regulating units providing FCR is dependent on the network power frequency characteristic K_{SA}, which is $K_{SA} = \frac{f_n}{S_n \cdot \sigma}$ in relation to the droop σ of the units. Based on Fig. 2.6 the full activation of FCR has to be established within 30 s. This behavior can be described by

the following equation, with $\epsilon(t)$ as the unit step function:

$$\Lambda(f,t) = \begin{cases} \frac{t \cdot \epsilon(t)}{30\,\mathrm{s}}, & \Lambda(t) < 1 \wedge \Delta f \leq 0.2\,\mathrm{Hz}, \\ 1, & \Delta f \leq 0.2\,\mathrm{Hz}, \\ 0.2\,\mathrm{Hz} \cdot \frac{1}{f}, & else. \end{cases} \tag{2.105}$$

The FCR regulation of the regulating units can be considered in the term $\sum_{k=1}^{N} P_{M,t,k}$ of Eq. (2.104). Considering this, the Eq. (2.104) can be rewritten as

$$\underbrace{\left(\sum_{k=1}^{N} P_{M,f_n,t,k} + P_{FCR}\right)}_{\sum_{k=1}^{N} P_{M,t,k}} - \underbrace{(P_{E,f_n,t} - P_{E,SR})}_{P_{E,t}} = T_{A,\Sigma} P_\Sigma \frac{1}{\omega_n^2} \omega \frac{d\omega}{dt} \tag{2.106}$$

with $\sum_{k=1}^{N} P_{M,f_n,t,k}$ as the total mechanical power of the rotating machines at nominal frequency, $P_{E,f_n,t}$ as the total load consumption of all loads in the system, P_{FCR} as the total regulating power of all FCR-regulating units and $P_{E,SR}$ as the power deviation of all loads due to the self-regulation effect. Describing P_{FCR} and $P_{E,SR}$ in more detail considering the definitions above, this leads to

$$\underbrace{\left(\sum_{k=1}^{N} P_{M,f_n,t,k} + \Lambda\left(f,t\right) K_{SA} \frac{\Delta\omega}{2\pi}\right)}_{\sum_{k=1}^{N} P_{M,t,k}} - \underbrace{(P_{E,f_n,t} - k_L \Delta f P_\Sigma)}_{P_{E,t}} = T_{A,\Sigma} P_\Sigma \frac{1}{f_n^2} f \frac{df}{dt} \tag{2.107}$$

where the difference $\sum_{k=1}^{N} P_{M,f_n,t,k} - P_{E,f_n,t}$ can be rewritten as ΔP, which is the power difference of the total mechanical power of the rotating machines and the total load at $f = f_n$, which finally leads to

$$\begin{aligned} \Delta P &= T_{A,\Sigma} P_\Sigma \frac{1}{f_n^2} f \frac{df}{dt} - k_L \Delta f P_\Sigma - \Lambda(f,t) K_{SA} \Delta f = \\ &= P_I - P_{E,SR} - P_{FCR} \end{aligned} \tag{2.108}$$

where P_I represents the inertial response of the inertia in the system, $P_{E,SR}$ represents the self-regulating-effect of the loads and P_{FCR} represents the frequency containment reserve.

According to ENTSO-E [182] the following assumptions are made for the design hypothesis:

- $\Delta P = -3\,\mathrm{GW}$
- $k_L = 1\,\%/\mathrm{Hz}$
- $P_\Sigma = 150\,\mathrm{GW}$
- $T_{A,\Sigma} = 10\,\mathrm{s}$
- $K_{SA} = 15\,000\,\mathrm{MW/Hz}$

With these assumptions, the frequency response to the reference incident of $\Delta P = -3\,\mathrm{GW}$ according to Eq. (2.108) looks like shown in Fig. 2.7(c). Fig. 2.7(b) shows the behavior of the three components of Eq.(2.108). The inertial response P_I instantly provides balances the imbalance between load and generation ΔP, but leads to a decreasing frequency since the corresponding energy is provided by all rotating masses, which are slowed down during this process. With decreasing frequency the loads demand less power due to the self-regulating-effect and the frequency containment reserve is activated gradually. The so-called frequency nadir is reached after about 18 s, from where the frequency increases again until it stabilizes at a value of 49.8 Hz.

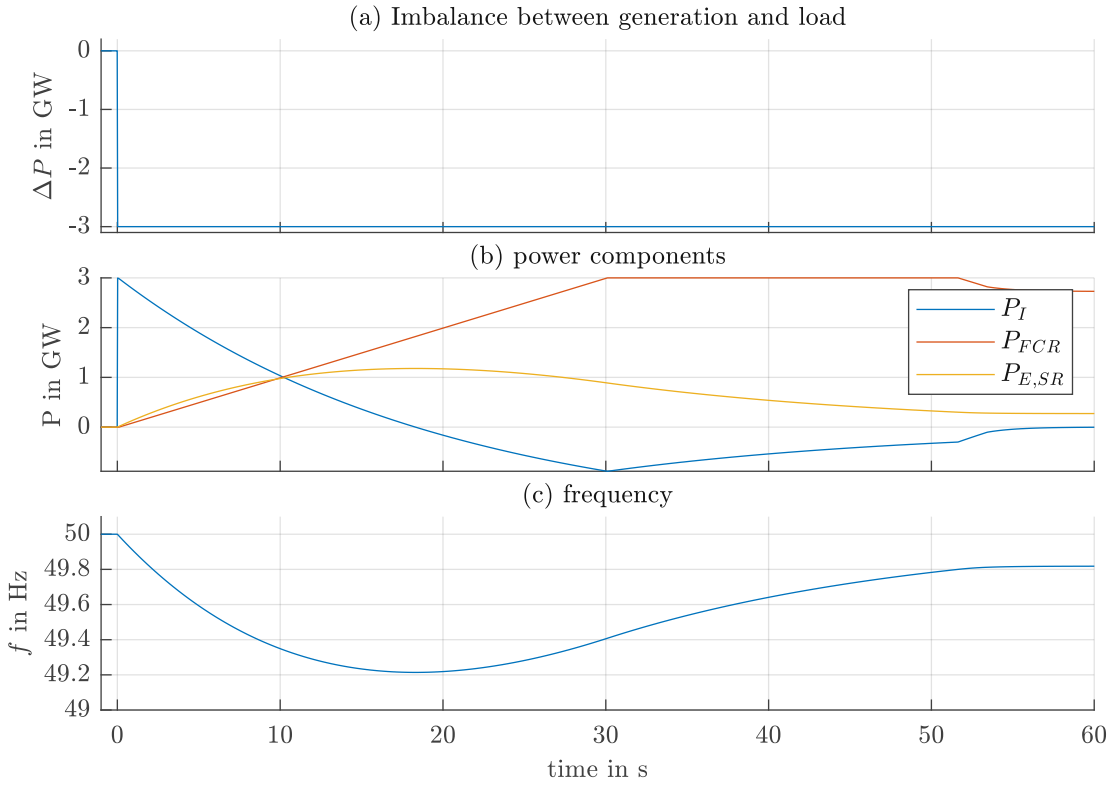

Figure 2.7: Frequency response to the reference incident for the design hypothesis. (a) shows the power imbalance, (b) shows the three power components according to Eq. (2.108) and (c) shows the course of the frequency during the reference incident. Simulated with MATLAB/SIMULINK.

In Austria, the Technische und Organisatorische Regeln (TOR) part E [37] regulates the handling of major disturbances in the network. It describes a step-by-step procedure for frequency-dependent load shedding. The first stage of load shedding starts at a frequency lower than 49 Hz. The design hypothesis is designed in a way that in case of a reference incident this step-by-step plan for frequency-dependent load shedding should not enter into force. Fig. 2.7 shows that a reserve margin of about 200 mHz remains to the first stage of load shedding at 49 Hz. Therefore, the maximum instantaneous frequency deviation is about 800 mHz, whereas the maximum steady-state frequency deviation is 200 mHz.

2.3.4 Automatic Frequency Restoration Reserve (aFRR)

As Fig. 2.7 exemplarily shows, any change in the power balance of load and generation ΔP in a synchronous area leads to a permanent control offset after all regulating units have fully activated their share of FCR. Neglecting the self-regulation effect of the loads, this permanent control offset is given by Eq. (2.108) with $\frac{df}{dt} = 0$, which leads to

$$\Delta f = -\frac{\Delta P}{K_{SA}}. \tag{2.109}$$

FCR is designed in a way of solitary contribution of all regulating units in a synchronous area. Therefore, all control areas are contributing to stabilize the frequency, which affects the power flows

between control areas. aFRR aims to restore these scheduled power flows between the control areas in a synchronous area. Taking the design hypothesis as an example, the frequency deviation is caused by the outage of two power plants. These two power plants are part of one control area. Because this control area is responsible for the power imbalance in the whole synchronous area, aFRR guarantees that the corresponding ΔP will be compensated by other power plants within the responsible control area. After full activation of aFRR, the scheduled power flows between control areas is restored.

The network power frequency characteristic K_{SA} of the synchronous area is composed by the power frequency characteristics of the control areas $K_{CA,i}$ in the synchronous area. Assuming a number of N control areas in the synchronous area, the network power frequency characteristic can be calculated by

$$K_{SA} = \sum_{i=1}^{N} K_{CA,i}. \tag{2.110}$$

The area control error G_i is calculated according to the "network characteristic method" [47], and described by

$$G_i = P_{meas,i} - P_{set,i} + K_{CA,i}\Delta f. \tag{2.111}$$

with $P_{meas,i}$ as the measured total inter-control area power flow and $P_{set,i}$ as the scheduled total inter-control area power flow. In case of a power imbalance, the area control error $|G_i| > 0$ is only different to zero for the responsible control area. The required aFRR-activation ΔP_i of a control area is activated according to the following equation in the stationary case:

$$\Delta P_i = -\beta_i \cdot G_i - \frac{1}{T_{r,i}} \int G_i \, dt \tag{2.112}$$

with β_i as a control area specific proportional factor and $T_{r,i}$ as the integration time constant of the control area. The integration term in the equation guarantees that the frequency deviation becomes zero after full activation of aFRR. A $|\Delta P_i| > 0$ of a control area is disitributed to participating power plants within the control area by the corresponding TSO. Mostly this is done fully automatic.

The aFRR obligation of every control area typically depends on the size of typical load variations, schedule changes and generating units and is basically calculated based on the empirical equation $\sqrt{a \cdot L_{max} + b^2} - b$ [48], with $a = 10\,\text{MW}$, $b = 150\,\text{MW}$ and L_{max} as the maximum load. In Austria this equation leads to a aFRR obligation of about 170 MW, considering $L_{max} = 8\,\text{GW}$. However, the sizing of the required reserve is also done based on the assumption and expectation of the largest possible generation incident or load demand due to special situations such as events of public interest.

Just as for FCR, certain characteristics are also defined for aFRR, which are summarized in Tab. 2.2.

2.3.5 Manual Frequency Restoration Reserve (mFRR)

Typically, the operation of mFRR (in succession to aFRR) is bound to the time-frame of scheduling, but has on principle the same impact on interconnected operation as aFRR. mFRR is a manual or automatic change of the working points of generators or loads in order to distribute the aFRR to various generators in the best possible way, in terms of economic considerations. Ways of providing mFRR include:

Table 2.2: Characteristics of aFRR in Austria.

characteristic	value
full activation time (FAT)	5 min
preparation time	30 s
delivery period	15 min
capacity requirement for LER-units	1 h full activated aFRR-power
auction frequency (=tendering period)	daily
tendered products	4 h
asymmetry	asymmetrical
minimum bid size	5 MW (will possibly be reduced to 1 MW in near future [51])
bid granularity	1 MW
total aFRR obligation in the control area AT	±200 MW (in 2019)

- connection and tripping of power,
- redistributing the output from generators participating in aFRR,
- changing the power interchange programme between interconnected undertakings,
- load control (e.g. controlled load shedding).

mFRR is primarily used to free up the aFRR in a balanced system situation, but it is also activated as a supplement to aFRR after larger incidents to restore the system frequency and consequently free the system wide activated FCR.

Just as for FCR and aFRR, certain characteristics are also defined for mFRR, which are summarized in Tab. 2.3.

Table 2.3: Characteristics of mFRR in Austria.

characteristic	value
full activation time (FAT)	15 min
preparation time	5 min
delivery period	15 min
auction frequency (=tendering period)	weekly and daily
tendered products	4 h
bid symmetry	asymmetrical
minimum bid size	1 MW
bid granularity	1 MW
total aFRR obligation in the control area AT	+280 MW and -195 MW (in 2019)

2.4 Converters

The following chapters summarize the fundamentals of converters relevant to this thesis.

2.4.1 Overview

Photovoltaic panels as well as batteries provide a DC-voltage as output voltage. To connect them to the power grid, it is necessary to convert the DC-voltage into a synchronous three-phase AC-voltage. This task is performed by a “converter”. The actual task of converting DC-voltage to AC-voltage

is fulfilled by an "inverter". Therefore, the inverter is a part of a converter. To connect Distributed Energy Resources (DER) to the grid "DC-link inverters" are used. The DC-link decouples the AC-voltage from the DC-side and, therefore, simplifies the controls on the AC and DC-side. There are two types of DC-link-inverters: "Voltage Source Inverter (VSI)" and "Current Source Inverter (CSI)", which differ in the usage of the used energy storage element. VSI use parallel capacitors and CSI use series inductors as energy storage elements. An inverter uses switches to generate an AC-voltage. A "half-bridge" is a basic structure of an inverter and consists of two switching elements in series which are switched complementary during operation. The simplest version of a single-phase inverter uses one half-bridge. According to the two switching states such inverters can have, they are called "two-level inverters". Two-level three-phase inverters consist of three half-bridges for each phase. The "space-vector modulation" technique in the switching control is used to generate an appropriate three-phase voltage system at the output. "Multi-level inverter" use more than one half-bridge per phase and are used to reach a lower switching frequency or decrease switching losses. The primary objective is the use of a higher number of switches to perform the power conversion in small voltage steps.

The switching actions generate harmonics in the output voltage. Thus, filters are used to smooth the output voltage.

The direct connection of a DC-generator (e.g. a battery) and an inverter is termed "single-stage converter". The direct connection of the DC-link of an inverter with the DC-generator brings the disadvantage of having a floating voltage in the inverter's DC-link. Especially the range of the output voltage of batteries is very high. To guarantee a certain AC-voltage at the output of the converter when the DC-voltage of the connected battery is smallest (as it is the case at very low state of charge), the rated voltage of the battery has to be chosen rather high. According to Chp. 2.4.3 the minimum rated voltage of a battery in such a case would have to be a factor of the nominal phase-to-phase voltage $U_B(SoC = 0) > \frac{U_n}{1.155}$ (see Chp. 2.4.3) at the output of the converter. To decouple the DC-link voltage from the voltage of the DC-generator an intermediary DC-DC-converter can be used. This combination of DC-DC-converter and an inverter is called "two-stage converter".

Fig. 2.8 shows the basic structure of a typical battery-converter, with a CSI used as inverter. A DC-link-center (N) is provided by a capacitive voltage divider and serves as a reference point for the output voltages. Because the value of the DC-output-voltage of the battery varies dependent on the output current and on the SoC, a buck-boost-converter is used to decouple the DC-battery-voltage from the DC-link-voltage. Therefore, this converter is a two-stage converter.

Fig. 2.8 shows the different hardware parts of the converter and its control structure. The grid synchronization provides the grid angle θ, based on the voltages $\mathbf{u}_{N,t}$ and currents $\mathbf{i}_t$ measured at the output of the LCL-filter of the converter. The voltages $\mathbf{u}_{N,t}$ are also used to calculate the voltage in the positive-sequence system u_{1+} and in the negative-sequence system u_{1-}. The grid angle θ and these two voltages u_{1+} and u_{1-} are used in the active and reactive power control to calculate corresponding reference currents, based on reference values for the active power p_{ref} and the reactive power q_{ref}. The active reference current in the positive-sequence system $i'_{S,d_{1+},ref}$ for the inverter current control is provided by the DC-link control, which is fed by the measured DC-link-voltage u_{DCL} and the reference DC-link-voltage $u_{DCL,ref}$. The DC-link-voltage u_{DCL} results from the output of the buck-boost converter, which is controlled by the battery current control, that uses a reference current of the active power control and the measured DC-voltage u_B and DC-current i_B of the battery to provide a reference voltage $u_{BB,ref}$ for the switching control of the buck-boost converter. The remaining reference currents for the inverter current control are provided by the reactive power control. Based on these reference currents, the inverter current control provides reference voltages $\underline{u}_{N,t,ref}$ for the switching control of the inverter. In case of unbalanced grid faults, the inverter control also has to inject current in the negative sequence system. A detailed description of the behavior of converter during unbalanced grid faults as well as a detailed description of the control structure shown in Fig. 2.8 is described in Chp. 4.3.

The different hardware parts of the converter and selected parts of the control structure are described in more detail below.

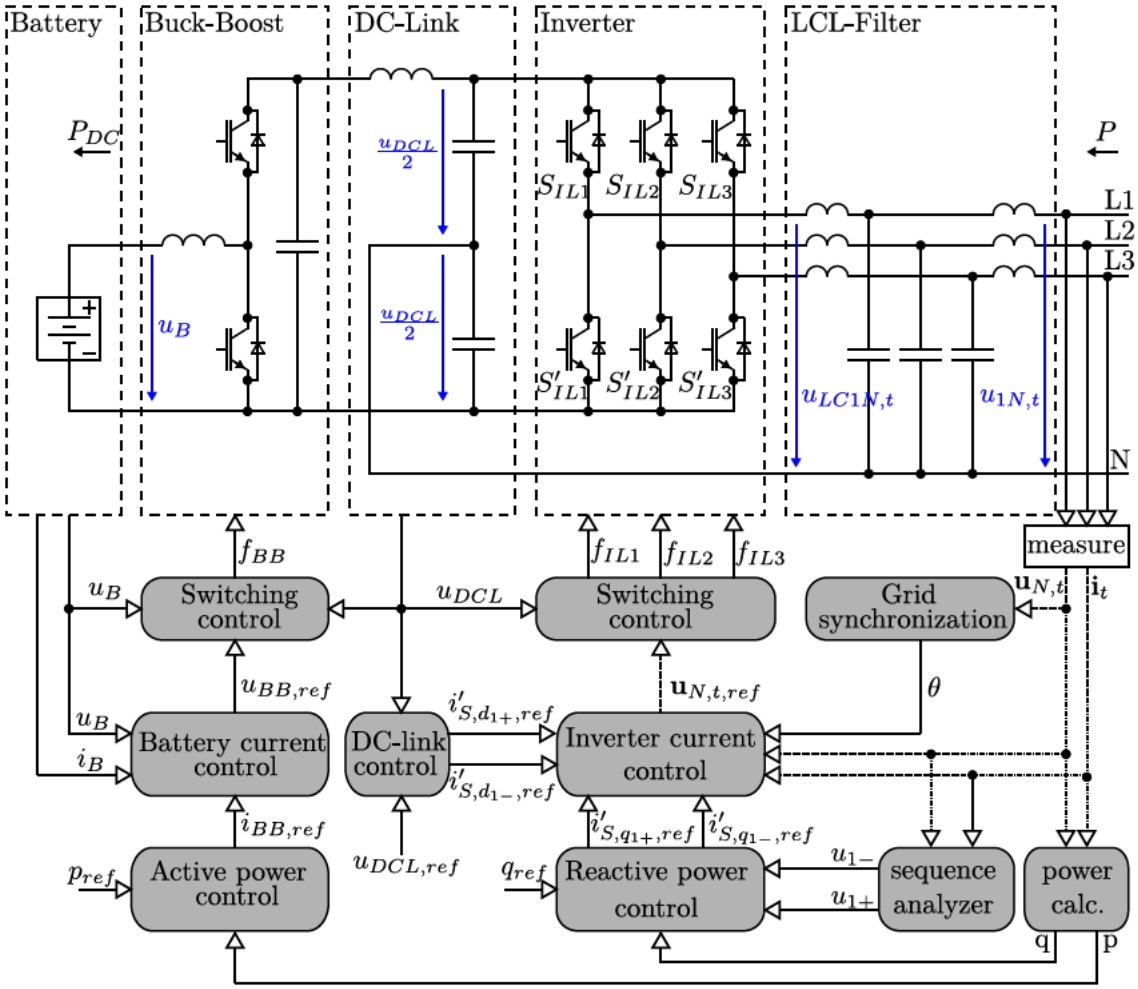

Figure 2.8: Basic structure of a battery-converter and its control.

2.4.2 Grid Synchronization

One of the most important aspects to consider in the control of power converters connected to electrical grids is the proper synchronization with the three-phase utility voltages. As already shown in Fig. A.6, under ideal operating conditions , the voltage space vector describes a circular locus in the $\alpha\beta 0$ coordinate system. In practice, however, there are multiple nonidealities in power systems that originate disturbances on the three-phase voltage space vector. A grid-connected power converter is particularly sensitive to voltage disturbances since its control system might lose controllability on the power signals under such distorted operating conditions. Therefore, the disturbances should be properly detected by the grid synchronization system [177].

Power converters generally inject positive-sequence currents at the fundamental frequency into the grid and only intentionally inject negative-sequence and harmonic currents in unusual cases, i.e. injecting unbalanced reactive currents to compensate the unbalanced grid voltage at the Point of Common Coupling (PCC). Therefore, the correct detection of the positive-sequence component

at the fundamental frequency of the three-phase grid voltage can be considered as the main task of the synchronization system of a grid-connected three-phase power converter. One technique to detect the positive-sequence component at the fundamental frequency is the Phase Locked Loop (PLL) based on the Synchronous Reference Frame (SRF). A Park-transformation is performed on the measured waveforms of the grid voltage and the angular position of the $dq0$-reference frame is controlled by a feedback loop that regulates the q-component to zero via PID-control. The basic structure of a SRF-PLL is shown in Fig. 2.9. To filter the signals under distorted operating conditions, low-pass filters are used.

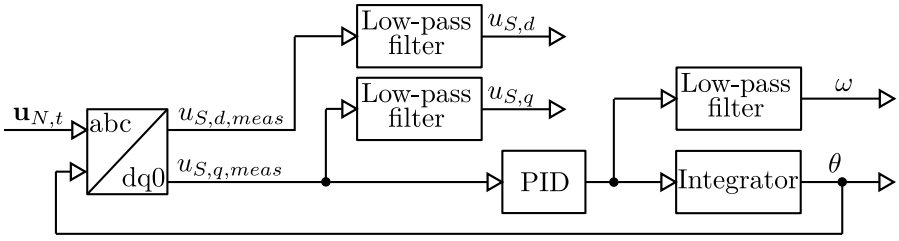

Figure 2.9: Basic structure of a SRF-PLL for grid synchronization.

Based on the test cases of Fig. A.6, the behavior of the SRF-PLL of Fig. 2.9 is shown in Fig. 2.10.

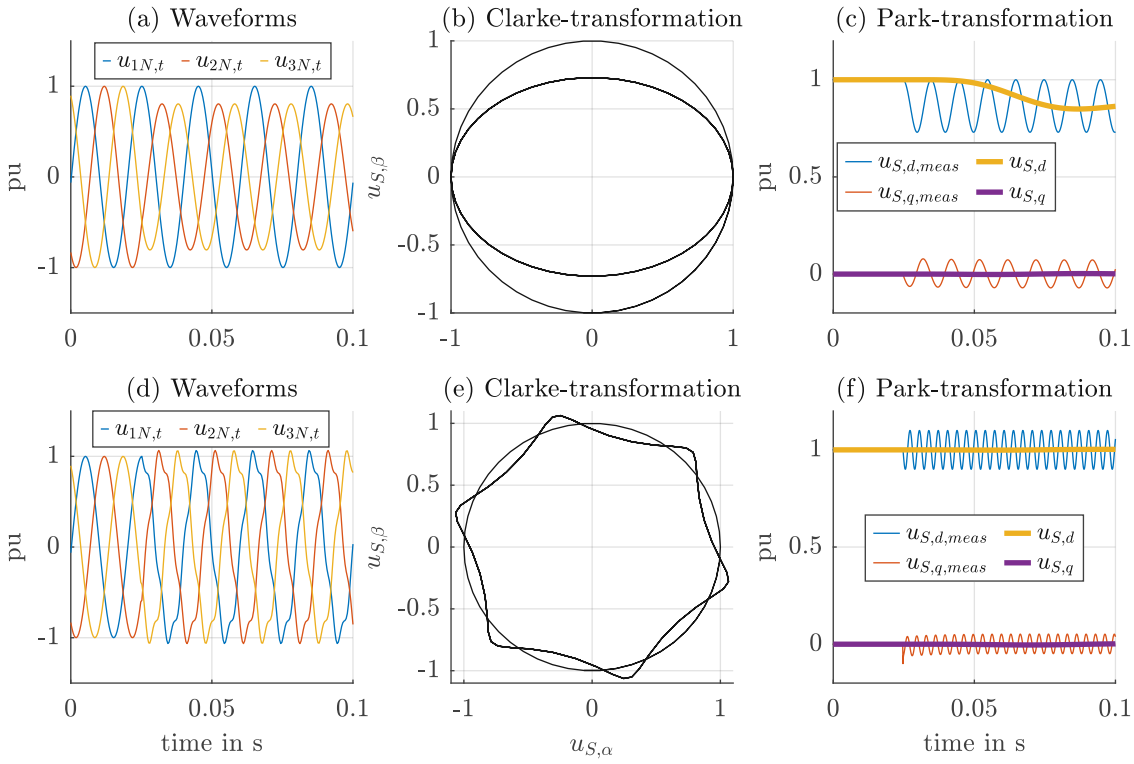

Figure 2.10: Behavior of the SRF-PLL of Fig. 2.9 in case of unsymmetry [(a),(b) and(c)] and harmonic distortion [(d),(e) and (f)] simulated with MATLAB/SIMULINK.

In contrary to Fig. A.6, the test cases start with a harmonic, symmetrical three-phase system. The unsymmetry and the harmonic distortion begins after 25 ms. The space vector in the $\alpha\beta 0$-plane,

as well as the space vector in the $dq0$-plane show the behavior before and after the distortion. The ripple that can be observed is filtered using low-pass filters, as shown in Fig. 2.9. For this example, a sixth order Butterworth filter with a cut-off frequency of 18 Hz is used. The PID-controller is tuned with $\{K_P, K_I, K_D\} = \{180, 3200, 1\}$.

More sophisticated techniques for grid synchronization can be found in [177].

2.4.3 Inverter Switching Control

There are two types of inverters: "self-commutated inverters" and "grid-commutated inverters". In the first type the valves can be switched on and off with a clock generated by the inverter itself, no reference from the grid is necessary. Self-commutated inverters can thus serve to generate an AC-voltage independently of the power grid and build an island grid. Therefore, they are also called "island-inverters". As valves, transistors as well as Insulated-Gate Biploar Transistor (IGBT) are used. Grid-commutated inverters usually also use IGBT, but also thyristors or triacs. They require an AC-voltage in the grid for operation and consume so-called commutation reactive power.

The functional principle of self-commutated inverters is described based on Fig. 2.8 as follows. The output voltage of the inverter $\mathbf{U}_{LCN,t}$ can be described as

$$\mathbf{U}_{LCN,t} = \begin{pmatrix} m_{L1,t} \cdot \frac{U_{DCL}}{2} \\ m_{L2,t} \cdot \frac{U_{DCL}}{2} \\ m_{L3,t} \cdot \frac{U_{DCL}}{2} \end{pmatrix} \tag{2.113}$$

with $m_{L1,t}$, $m_{L2,t}$ and $m_{L3,t}$ as the "modulation-functions" of the three phases. These modulation-functions can be calculated based on the reference voltage $\mathbf{u}_{N,t,ref}$, which is delivered by the inverter current control:

$$\mathbf{m_t} = \begin{pmatrix} m_{L1,t} \\ m_{L2,t} \\ m_{L3,t} \end{pmatrix} = \frac{1}{\frac{U_{DCL}}{2}} \cdot \hat{\mathbf{U}}_{N,t,ref} = \frac{1}{\frac{U_{DCL}}{2}} \frac{\sqrt{2} \cdot U_n}{\sqrt{3}} \cdot \mathbf{u}_{N,t,ref} = \begin{pmatrix} \hat{m}_{L1} \\ \hat{m}_{L2} \\ \hat{m}_{L3} \end{pmatrix} \cdot \mathbf{u}_{N,t,ref} \tag{2.114}$$

where $\hat{m}_{L1}$, $\hat{m}_{L2}$ and $\hat{m}_{L3}$ are the "modulation depths" of the three phases, which vary in the range of $\hat{m}_{Li} \in (0, 1)$ in case of using a Pulse Width Modulation (PWM) switching signal[3].

In case of a modulation depth $\hat{m}_{Li} > 1$, the inverter is "overmodulated". In this case it would not be possible to generate a continuous modulation function as shown in Fig. 2.11. Therefore, the peak value $\hat{U}_{1N}$ of the output voltage to prevent overmodulation is limited to $\frac{\hat{U}_{1N}}{U_{DCL}}\Big|_{\max} = \frac{2}{\sqrt{3}} \approx 1.155$. The relationship between the switching functions $\{f_{IL1}, f_{IL2}, f_{IL3}\}$ and the modulation functions is defined by

$$\begin{pmatrix} \overline{f}_{IL1} \\ \overline{f}_{IL2} \\ \overline{f}_{IL3} \end{pmatrix} = \begin{pmatrix} m_{L1,t} \\ m_{L2,t} \\ m_{L3,t} \end{pmatrix}. \tag{2.115}$$

Therefore, the mean values of the switching functions are equal to the modulation functions. This relationship is realized by a PWM and the LCL-filter. The switching signals are generated based on triangular carrier signals with a defined modulation frequency f_{IC}, called "switching frequency of the inverter", and the modulation functions, as shown exemplarily for L1 in Fig. 2.11. Based on the switching signal f_{IL1} the valve S_{IL1} is closed if $f_{IL1} = 1$ and opened if $f_{IL1} = 0$. The switching

[3] In case the switching signal is generated based on a static fundamental frequency signal, the modulation depth can vary in the range of $\hat{m}_{Li} \in \left(0, \frac{4}{\pi}\right)$. The factor $\frac{4}{\pi} \approx 1.273$ is the Fourier coefficient of the fundamental oscillation of a rectangular signal with the amplitude 1.

signal f'_{IL1} for the complementary valve S'_{IL1} is generated by $f'_{IL1} = 1 - f_{IL1}$. Therefore, the valves S_{IL1} and S'_{IL1} are not closed at the same time. This prevents the occurrence of a short-circuit. The switching signal for the other two phases are generated in the same way with the corresponding modulation signals. More details on inverters and modulation can be found in [165].

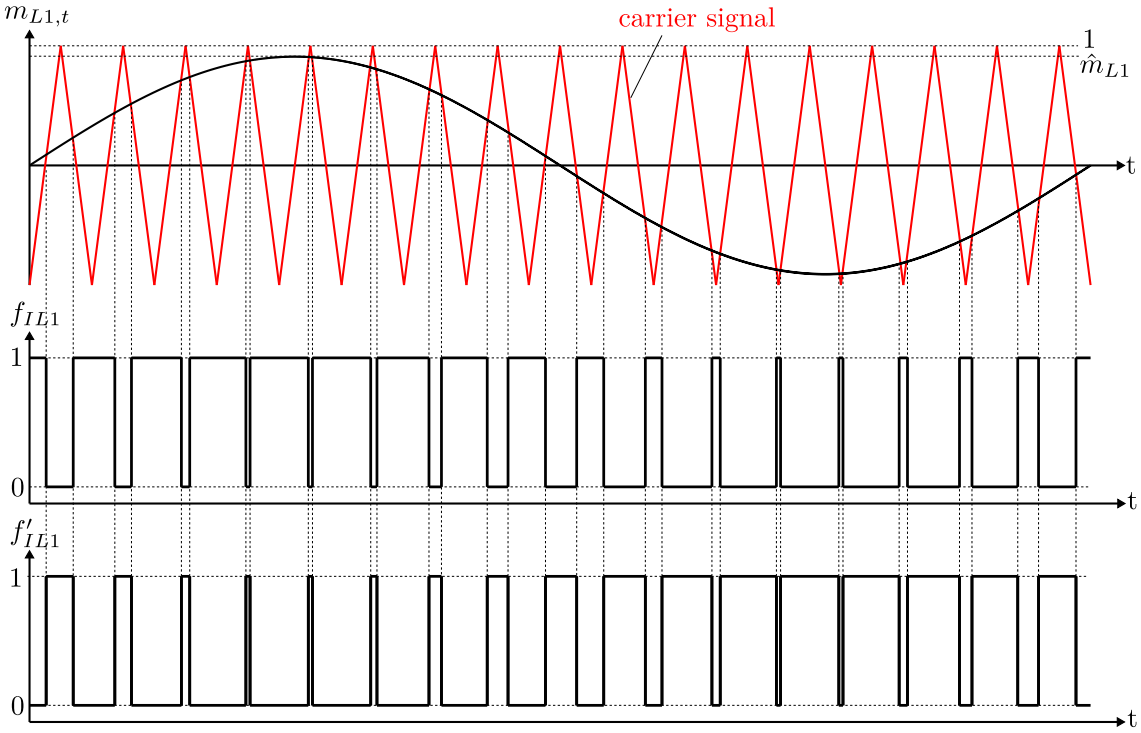

Figure 2.11: Generation of switching signals.

2.4.4 LCL-Filter

Due to the fast-switching inverter, an output filter is necessary to smooth the AC output currents. A series inductance accomplishes this task. Its value is determined as the maximum AC current ripple ΔI_{rip} that is allowed at the converter output. According to [177] a rough approximation of the value of this inductance can be calculated by

$$L = \frac{U_{DCL}}{2 \cdot \Delta I_{rip} \cdot f_{IC}} \tag{2.116}$$

for two-level PWM converters, where f_{IC} is the switching frequency of the carrier signal. The use of the capacitors is justified by the necessity to filter the switching frequency harmonics. In case the capacitor voltage is sensed, a part of the reactive power of the inductances will be compensated by the capacitors with a consequent decrement of the power factor seen at the PCC. According to [16] the value of the capacitors can be determined based on

$$C = 0.05 \cdot \frac{1}{\omega_n \frac{U_n^2}{S_n}} \tag{2.117}$$

where S_n is the nominal apparent power of the converter.

At the input of the LCL-filter in the phase L1 the following voltage signal $U_{LC1N,t}$ is superposed by the switching actions of the valves S_{IL1} and S'_{IL1}:

$$U_{LC1N,t} = f_{IL1} \cdot \hat{m}_{L1} \cdot \frac{u_{DCL}}{2} + f'_{IL1} \cdot \hat{m}_{L1} \cdot \frac{-u_{DCL}}{2}. \tag{2.118}$$

Since $f'_{IL1} = 1 - f_{IL1}$, the voltage signal becomes

$$U_{LC1N,t} = \hat{m}_{L1} \cdot u_{DCL} \cdot \left(f_{IL1} - \frac{1}{2} \right). \tag{2.119}$$

Based on a simulation model of Fig. 2.8 realized in MATLAB/SIMULINK, the influence of the LCL-filter is investigated. The DC-Link is modeled with two ideal DC-voltage sources in series. Therefore, the battery and the buck-boost converter are neglected. A DC-link voltage of $U_{DCL} = 900\,\mathrm{V}$ is used. The modulation frequency of the carrier signal is varied between $f_{IC} \in \{2, 6\}\,\mathrm{kHz}$. The values for the capacitor and the inductor of the LCL-filter are $600\,\mu\mathrm{F}$ and $260\,\mu\mathrm{H}$. To get a RMS-voltage of $U_n = 550\,\mathrm{V}$ at the output of the converter, a modulation depth of $\hat{m}_{L1} = \hat{m}_{L2} = \hat{m}_{L3} = 0.98$ is chosen. Therefore, the amplitude of the phase-to-neutral voltages becomes $U_{1N} \approx \frac{\sqrt{2}}{\sqrt{3}} \cdot 550\,\mathrm{V} \approx 450\,\mathrm{V}$. No load is connected to the output of the converter.

The simulation results show that with suitable design of the LCL-filter and a sufficiently high frequency of the carrier signal f_{IC}, the rectangular shaped voltage output of the inverter $U_{LC1N,t}$ is converted into a sinusoidal form $U_{1N,t}$.

2.4.5 Buck-Boost Converter

A buck-boost converter is a DC-to-DC power converter, as are the boost-converter and the buck-converter. A buck-converter steps down voltage (while stepping up current) from its input (supply) to its output (load). In contrast, a boost-converter steps up voltage from its input to its output. Therefore, as the name says, a buck-boost converter is a composition of buck and boost converter. A synchronous buck-boost converter, as shown in Fig. 2.8 is a modified version of the basic buck-boost converter that uses two switches instead of a switch and a diode and therefore is bi-directional. In case of an energy flow from the battery to the DC-link the buck-boost converter acts as a boost converter; the input voltage is smaller than the output voltage. In case of a reversed energy flow from the DC-link to the battery, the buck-boost converter acts as a buck converter; the input voltage is larger than the output voltage.

As with any DC-DC converter, the output voltage is determined by the on-time and the off-time of the switches. In a buck converter or boost converter it is sufficient to control the one actively switchable semiconductor switch. The second switch, the diode, switches independently, depending on which direction the current has through it. Since the synchronous converter is made up of two switchable semiconductor switches, the second must be actuated in push-pull to the first one. If the first switch becomes conductive, the second opens, and vice versa. It is therefore at any time - apart from a small dead time to safely avoid short-circuits due to finite switching times - a switch conductive.

The multiphase buck-boost converter is a circuit topology where basic buck-boost converter circuits are placed in parallel between the input and load. Each of the n “phases” is turned on at equally spaced intervals over the switching period. This circuit is typically used with the synchronous buck topology, described above. This type of converter can respond to load changes as quickly as if it switched n-times faster, without the increase of switching losses.

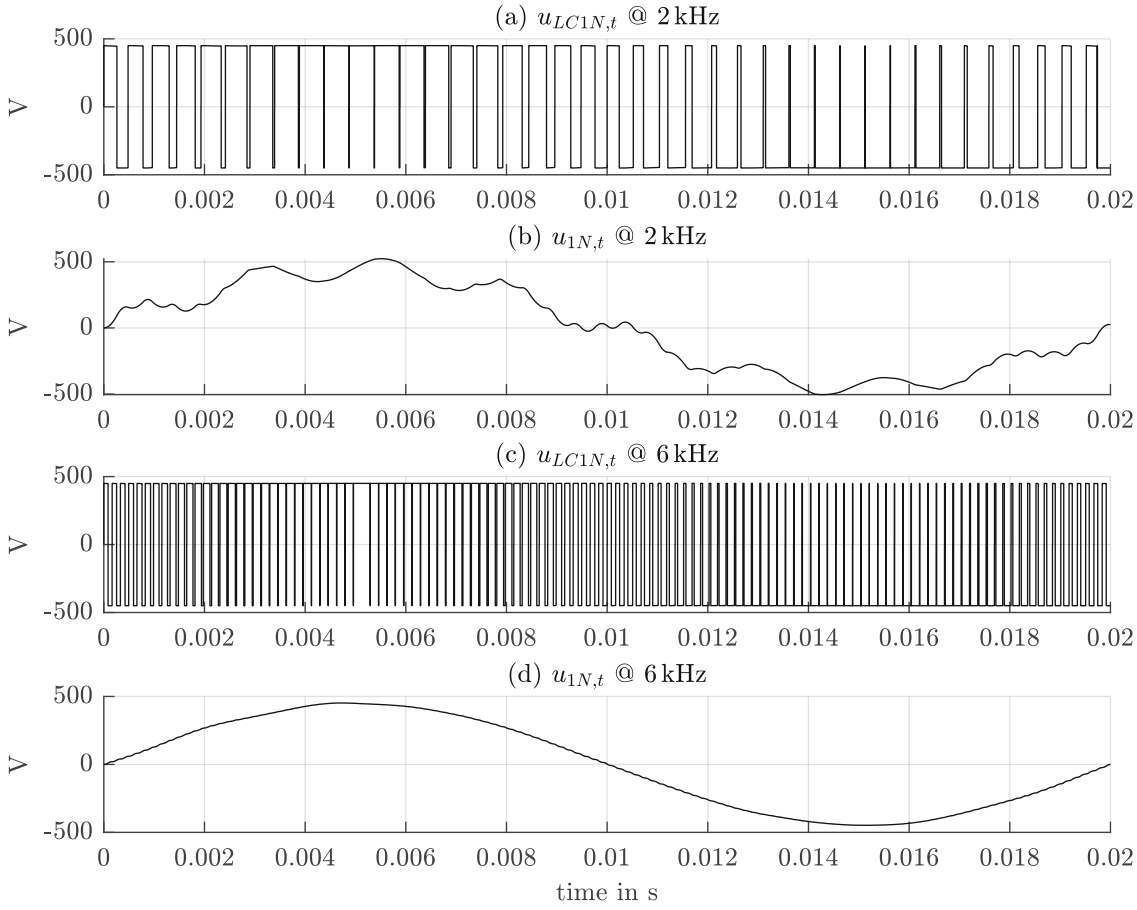

Figure 2.12: LCL Filter output simulated with MATLAB/SIMULINK.

2.4.6 Power Control and Current Control

There are several approaches to realize the active and reactive power control. Fig. 2.8 shows a closed-loop power control. The "power calculation" calculates the power output of the converter, based on the measured voltage $\mathbf{u}_{N,t}$ and the measured current $\mathbf{i}_t$, for example, by using Eq. (A.26) and Eq. (A.28) with an appropriate filtering (e.g. mean value over a time period of 20 ms) of the calculated values. These measured values p and q are used in the "active power control" and in the "reactive power control", together with reference values p_{ref} and q_{ref} as input of PI-controllers. In case of reactive power control, the output directly provides the reference current $i'_{S,q_{1+}}$. Assuming there is no current injection in the negative-sequence system during normal operation, the second reference current $i'_{S,q_{1-}} = 0$ is zero. This second reference current is only being used during grid faults, as it will be discussed in Chp. 4.3.2.2.

In case of active power control, also the buck-boost converter and DC-link have to be taken into account. Basically, the active power control also uses the measured value p, together with a reference power p_{ref} as input of a PI-controller. But to track the reference power p_{ref}, the control alters the storage reference current $i_{BB,ref}$ through the buck-boost converter. The resulting power flow is followed by the inverter since its active current component $i_{S,d_{1+}}$ is used to control the DC-link voltage.

Both the active power control as well as the reactive power control are followed by corresponding current controls. The "battery current control" uses the reference current $i_{BB,ref}$ of the active power control, together with the measured battery voltage u_B and battery current i_B, to provide a voltage signal $u_{BB,ref}$ for the "switching control". The "inverter current control" uses the reference currents of the reactive current control and the DC-link control to provide a voltage signal $\mathbf{u}_{N,t,ref}$ for the "inverter switching control". A detailed description of the inverter current control will be discussed in Chp. 4.3.2.2.

Since there are two control loops to control active power, as well as to control reactive power, the corresponding PI controllers must be tuned so that the two control loops do not influence each other. The power control loop is called "outer control loop" and the current control loop "inner control loop". The inner control loop has to be tuned very fast, whereas the outer control loop has to be tuned slower. Besides the closed-loop power control, the more straightforward power control is the open-loop power control. Due to the complex tuning of the outer and inner control loop, the open-loop power control is less complex than the closed-loop power control. Therefore, the open-loop control approach is used in Chp. 4.3.2.2 to model the behavior of a converter during grid faults. The inverter current control for both control approaches is identical.

2.4.7 Short-Circuit Behavior of Converters

The valves of an inverter are limited to a maximum current $\hat{I}_{max}$. In the event of a short-circuit, a voltage dip occurs and the inverter control increases the output current to compensate for the reduction in active power output. The maximum current of inverters is typically about 10 % higher than the nominal current $\hat{I}_{max} = 1.1 \cdot \sqrt{2} I_n$. The contribution of the inverter to a short-circuit current in the grid is also limited to $\hat{I}_{max}$. Therefore, the initial short-circuit current of an inverter is defined as $I''_k = \hat{I}_{max}$.

Occurrences of grid faults usually give rise to the appearance of unbalanced grid voltages at the point of connection of the power converter. Grid codes, which are defining the requirements of converter-based systems, often list specific requirements regarding the injection of active and reactive power during grid faults. A detailed description of the behavior of converters during grid faults is described in Chp. 4.3.

2.5 Batteries

A battery is a device that converts the chemical energy contained in its active materials directly into electric energy by means of an electrochemical oxidation-reduction (redox) reaction. In the case of a rechargeable system, the battery is recharged by a reversal of the process. This type of reaction involves the transfer of electrons from one material to another through an electric circuit [108]. This chapter summarizes the basics of chemical reactions inside batteries and other fundamentals of batteries, like characteristic values and construction details of battery cells.

2.5.1 Characteristic Values

The most important parameters for battery cells are the voltage curve $U_B(SoC)$, the capacity and the energy content. A description of the voltage curve is given in Chp. A.4.1.1.

2.5.1.1 Cell Capacity

The capacity C of a cell is determined by the amount of active materials in the cell. It is expressed as the total quantity of electricity involved in the electrochemical reaction and is defined in terms of coulombs or ampere-hours. Faradays law of electrolysis says "The amount of material produced at an electrode (or liberated from it) during an electrochemical reaction is directly proportional to the total conducted charge or, equivalently, the average current multiplied by the total time". Therefore, the theoretical capacity per molar mass can be calculated by

$$\left(\frac{C}{n}\right)_{\mathrm{Ah/mol}} = \frac{z \cdot e \cdot N_A}{3600\frac{s}{h}} \overset{z=1}{=} 26.8\,\mathrm{A\,h/mol} \tag{2.120}$$

with z as the number of electrons involved in stoichiometric reaction and n as the amount of substance (mol). For the Daniell cell (see Chp. A.4.1), the theoretical gravimetric capacity $\frac{C}{m}$ can be calculated with the molar mass of the involved active material based on the reaction in Eq. (A.93):

$$\left(\frac{C}{m}\right)_{\mathrm{Ah/kg}} = \frac{z \cdot e \cdot N_A}{3600\frac{s}{h} \cdot M} = \frac{2 \cdot e \cdot N_A}{3600\frac{s}{h} \cdot (M_{Zn} + M_{Cu} + M_S + 4M_O)} = 238.2\,\mathrm{A\,h/kg}. \tag{2.121}$$

2.5.1.2 C-Rate

To indicate the charge and the discharge current of a cell, the c-rate is used. The c-rate expresses the value of the current as a multiple of the rated capacity C_r:

$$I_B = \text{C-rate} \cdot C_r. \tag{2.122}$$

For example, a current of 200 mA used to charge a cell with a rated capacity of $C_r = 1\,\mathrm{A\,h}$ would be expressed as C/5 or 0.2C. Fig. 2.13 shows the cell voltage during discharging of fully charged cells at different C-rates.

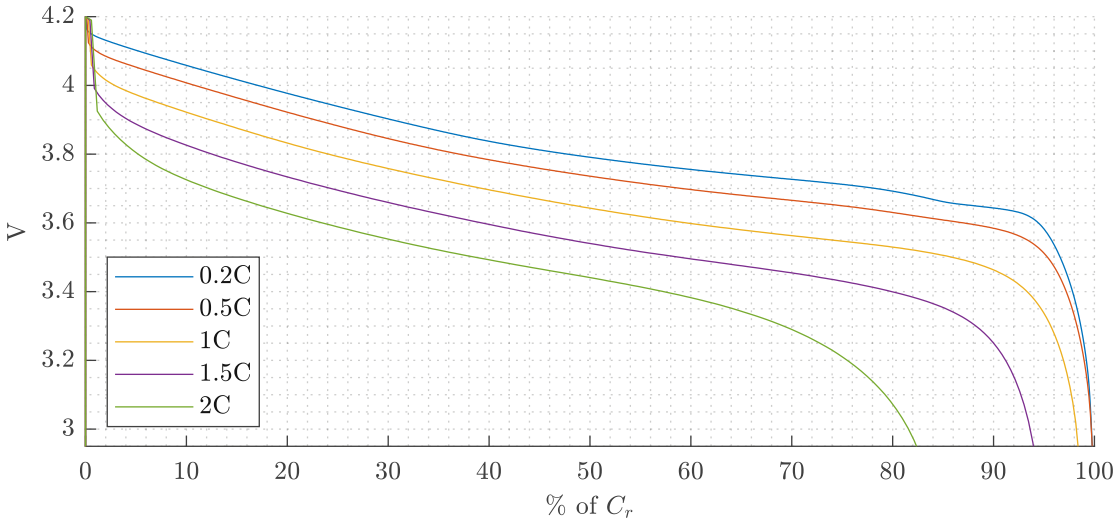

Figure 2.13: Cell voltage curve of a graphite/$LiCoO_2$ prismatic cell during discharging with different (constant) c-rates (based on measurement data of [193]).

2.5.1.3 State of Charge (SoC) and Depth of Discharge (DoD)

Generally the SoC is defined with $SoC : \mathbb{R}^+ \to (0,1)$ by Eq. (2.123), where T_1 is the starting time of consideration, $C(t)$ is the usable capacity of the battery and I_B is the DC-current consumption of the battery:

$$SoC(t) = SoC(T_1) + \frac{1}{C(t)} \int_{T_1}^{t} I_B(\tilde{t})\, d\tilde{t}. \tag{2.123}$$

The usable capacity at the beginning of life of the battery is $C(0) = C_r$. The influence of degradation on the usable capacity is discussed in Chp. 2.5.1.8 and results in $C(t) = SoH(t) \cdot C_r$, by using the so-called State of Health (SoH). The DoD, on the other hand, is defined as the complement of the SoC with $DoD : \mathbb{R}^+ \to (0,1)$ by Eq. (2.124):

$$DoD(t) = DoD(T_1) - \frac{1}{C(t)} \int_{T_1}^{t} I_B(\tilde{t})\, d\tilde{t} = 1 - SoC(t). \tag{2.124}$$

2.5.1.4 Energy Content and Energy Density

The cell's energy content is defined by the quantity of material used and the voltage curve during discharging. The energy content can be calculated as follows:

$$E = \int U_B \left[SoC(t), T\right] \cdot I_B(t)\, dt. \tag{2.125}$$

The voltage curve is a complex function of the SoC and the temperature. Therefore, the energy content is specified as nominal value with the help of the rated cell voltage $U_{B,r}$ and the cell capacity:

$$E_r = U_{B,r} \cdot C_r. \tag{2.126}$$

The gravimetric energy density of a cell is calculated with the help of Eq. (2.121) and the nominal cell voltage:

$$\left(\frac{E}{m}\right)_{\mathrm{Wh/kg}} = U_{B,r} \cdot \left(\frac{C}{m}\right)_{\mathrm{Ah/kg}}. \tag{2.127}$$

The volumetric energy density is calculated analogous with the corresponding value of the volumetric capacity. The theoretical energy content of a battery is based on the types of active materials that are used (this determines the voltage) and on the amount of the active materials that are used (this determines the capacity). In practice, only a part of the theoretical energy content of the battery can be used, because the battery does not discharge at the nominal voltage, nor is it discharged completely to zero volts.

2.5.1.5 Self-Discharge

The self-discharge rate of a battery cell is defined as the loss of charged capacity under open-circuit conditions. The main cause of self-discharge are side reactions between the active material and the electrolyte. These side reactions include chemical changes that result from the component's limited stability (for example electrolyte decomposition, reactions with additional components, corrosion, etc.) [168].

2.5.1.6 Cycle Life

The cycle life is defined as the number of complete charge - discharge cycles (full cycles) a battery can perform before its nominal capacity falls below a defined value, which is often defined as 80 % of its initial rated capacity. Fig. 2.14 shows the discharge behavior of an exemplary battery cell until the cycle life of 1000 full cycles is reached. Cycle depth and SoC-range are known to have a strong impact on the cycle life of Li-ion batteries [83]. Especially at low temperatures and high charge rates "lithium plating" can be observed, which describes the irreversible deposition of metallic lithium. "Woehler curve" models have been proposed to Li-ion battery degradation which take into account these effects. Also increased aging can be observed at high temperatures and high SoC. This may affect the growth of the solid electrolyte interface (see Chp. A.4.3.3) and loss of available lithium [83]. The capacity fade of Li-ion batteries due to cycle aging can be summarized in the following equation according to [83]:

$$C_{cycle} = f_{Woehler}(DoD); f_{Li-plating}(T, I), f_{SEI-growth}(T, SoC), \text{etc.} \tag{2.128}$$

The Woehler curve models use statistical data of different effects influencing cycle degradation, such as growth of the solid electrolyte interface and lithium-plating on the example of lithium-ion batteries, whose degradation is described in more detail in Chp. A.4.3.4.

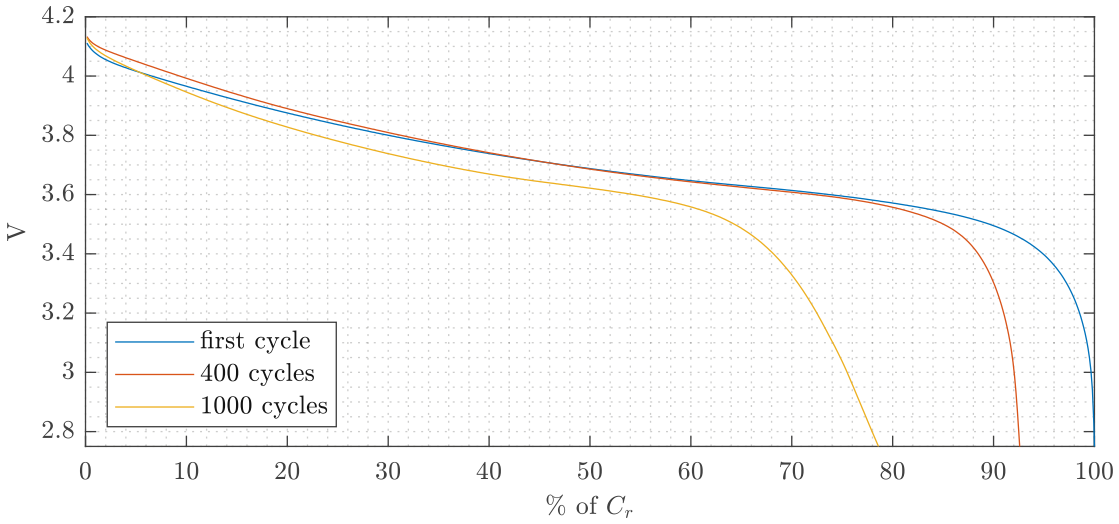

Figure 2.14: Discharge behavior of a graphite/$LiCoO_2$ pouch cell during constant current charge/discharge cycles with 0.5C (based on measurement data of [154]).

2.5.1.7 Calendar Aging/Capacity Fading

Calendar aging comprises all aging processes that lead to a degradation of a battery cell independent of charge-discharge cycling. The predominant mechanism of calendar aging is the evolution of passivation layers at the electrode–electrolyte interfaces [102]. The battery cell temperature is known to have a strong effect on calendar aging. According to [156] the thermally activated undesired side reactions in Li-ion batteries can be modeled by the following equation

$$C_{calendar} = k_{cal}(T, SoC) \cdot \sqrt{t} \tag{2.129}$$

by using a stress factor k_{cal}, whose temperature dependency is modeled by using the "Arrhenius law", which is an exponential function.

2.5.1.8 State of Health (SoH)

The SoH represents a measure of the cell's ability to store and deliver electrical energy, compared to its ideal (rated) conditions. Due to cycle and calendar aging the capacity of the cell decreases. As shown in Fig. 2.14 the capacity degrading has the consequence that the minimal voltage of the cell is reached earlier during discharging. To prevent damage due to low cell voltage, the decreased capacity of the cell has to be considered in the battery management system in BESS (see Chp. 2.6.1.2). Therefore, the Battery Management System (BMS) has to consider the actual SoH of each cell. The formal definition of the SoH relies on the aging effects described above and can be defined as follows:

$$SoH(t) = \frac{C(t)}{C_r} = \frac{C_r - C_{cycle} - C_{calendar}}{C_r} \tag{2.130}$$

with $C(t)$ as the usable (actual, degraded) capacity of the cell that is dependent on the cycle aging and the calendar aging and C_r as the rated capacity. Based on the SoH the aging effects can be considered in the SoC as defined in Eq. (2.123) as follows:

$$SoC(t) = SoC(T_1) + \frac{1}{SoH(t) \cdot C_r} \int_{T_1}^{t} I_B(\tilde{t})\, d\tilde{t}. \tag{2.131}$$

2.5.1.9 Cell Polarization

As described in Chp. A.4.1.1, in case of an electric current I_B through the cell, the actual cell voltage U_B differs from the Open Circuit Voltage (OCV) (e.g. illustrated in Fig. A.14) due to cell polarization. The cell polarization inevitably causes the cell system to deviate from the equilibrium state and the actual cell voltage shifts away from the equilibrium value. Due to the cell polarization, losses occur when a current I_B passes through the electrodes, accompanying the electrochemical reactions. The cell polarization can be divided into three parts:

- activation polarization: chemical reaction at the electrode surface (e.g. surface conversions preceding the electron transfer),
- concentration polarization: arises when the rate of mass transport to or from the electrode hinders current production [105],
- ohmic polarization (sometimes termed "IR-drop"): total internal resistance of the cell, which is the sum of the resistance of the electrolyte, the resistances of the active material, the current collectors and electrical tabs of both electrodes, and the contact resistance between the active material and the current collector.

Fig. 2.15 illustrates the effects of polarization in the "polarization curve", which shows the cell voltage U_B over the c-rate of the cell. At very low currents the activation polarization is dominant. This area is not visible in Fig. 2.15. At moderate currents the ohmic polarization is dominant, which leads to the linear behavior shown in Fig. 2.15. At high currents the concentration polarization becomes dominant due to limited mass transfer through diffusion to the electrode surface [105]. This area of high current is also not visible in Fig. 2.15 but leads to a rapid drop of the cell voltage.

2.5.1.10 Efficiency

Since a part of the electrons during charging/discharging is typically consumed by chemical side-reactions, the efficiency is less than one. These side-reactions appear as heat and/or chemical

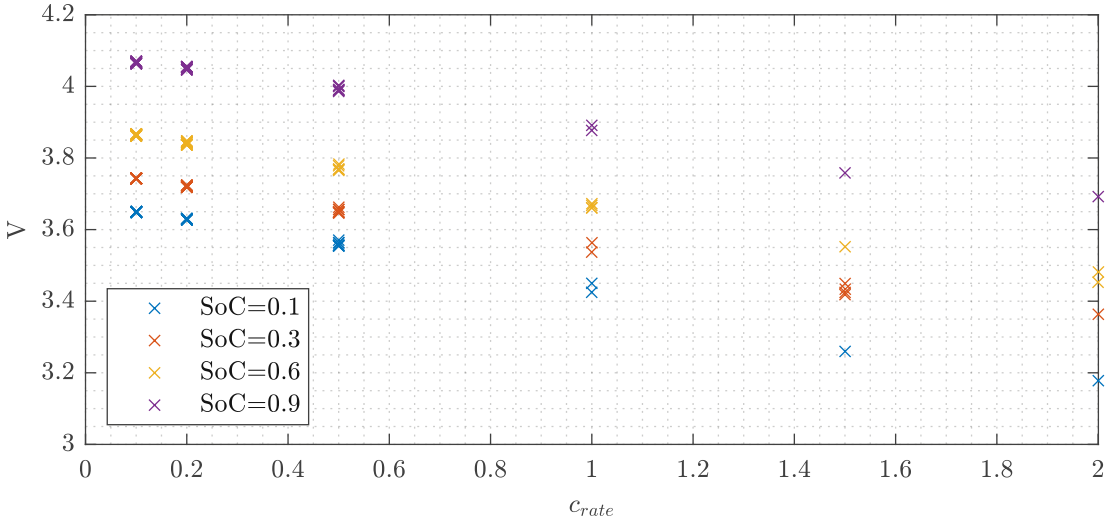

Figure 2.15: Polarization of a graphite/$LiCoO_2$ prismatic cell during discharging with different c-rates at different SoC-levels (based on measurement data of [193]).

byproducts. The efficiency of batteries can be divided into the "coulombic efficiency"

$$\eta_C = \frac{\int_{t(SoC=1)}^{t(SoC=0)} I_B(\tilde{t})\, d\tilde{t}, \quad I_B < 0}{\int_{t(SoC=0)}^{t(SoC=1)} I_B(\tilde{t})\, d\tilde{t}, \quad I_B > 0} \tag{2.132}$$

which defines the factor of dischargeable capacity to the chargeable capacity, and the "energy efficiency"

$$\eta_E = \frac{\int_{t(SoC=1)}^{t(SoC=0)} U_B(\tilde{t}) I_B(\tilde{t})\, d\tilde{t}, \quad I_B < 0}{\int_{t(SoC=0)}^{t(SoC=1)} U_B(\tilde{t}) I_B(\tilde{t})\, d\tilde{t}, \quad I_B > 0} \tag{2.133}$$

which defines the factor of dischargeable energy to the chargeable energy of a battery. In Li-ion batteries theoretically η_C is one, because side-reactions are excluded (as lithium is the only active material). Practically the coulombic efficiency $\eta_C \approx 1$, because for example the formation and repair of the Solid Electrolyte Interface (SEI) consumes Li^+ and e^- at the negative electrode, which is described in more detail in Chp. A.4.3.

The energy efficiency also takes into account the cell voltage during charging/discharging. Ohmic polarization, for example, leads to a voltage variation compared to the OCV. As a result of this voltage variation the cell voltage during charging is greater than the cell voltage during discharging, which leads to an energy efficiency $\eta_E < 1$.

2.5.1.11 Power Density

The power density describes the maximum power per mass that can be extracted from the battery. As a high power density requires a low internal resistance the corresponding value of power density depends on the cell design. For example a low internal resistance in Li-ion batteries can be achieved by thin electrodes. As a result a tradeoff between power density and energy density can arise [106]. On the one hand for low-power-applications, the energy density can be improved by enlarging the electrode thickness and reducing the porosity. On the other hand for high power applications, thin and highly porous electrodes are favorable [84].

The relationship between power density and energy density is often presented in a chart called "Ragone chart" on a log-log scale. In a Ragone chart different storage technologies can be compared. Most of the storage technologies only cover a wider range of either power density or energy density. For example, lead-acid cells cover a wide range of power density up to 1100 W/kg, but only at relatively low energy density of 35 W h/kg [126]. Compared to other technologies Li-ion batteries cover a relatively wide range of power and energy densities. Dependent on the actual requirement a corresponding cell design can be used.

2.5.1.12 Comparison of Characteristic Values for Different Cell Chemistries

Tab. 2.4 shows a comparison for different cell chemistries of the characteristic values described above. These values given are examples of commercially available battery cells. Especially the gravimetric energy density listed in the table is strongly dependent on the cell construction (e.g. cell shape).

Table 2.4: Comparison of characteristic values of different cell types [166][108][135][71]. The different types of lithium-batteries will be described in Chp. A.4.3. The column "capacity density" shows the theoretical capacity density and the column "energy density" shows the energy density of battery cells commercially available.

cell type	cathode material	capacity density	energy density	cell voltage $U_{B,r}$	self-discharge	cycle life
Lead-acid		83.4 Ah/kg	35 W h/kg	2.1 V	8 %/month	200-1500
NiCd		180 Ah/kg	50 Wh/kg	1.35 V	20 %/month	500-2000
NiMh		289 Ah/kg	75 Wh/kg	1.35 V	25 %/month	300-600
Lithium-ion	LCO	274 Ah/kg	190Wh/kg	3.65 V	2 %/month	1000
	LMO	285 Ah/kg	120Wh/kg	3.8 V	2 %/month	700
	LFP	170 Ah/kg	115Wh/kg	3.2 V	2 %/month	>3000
	NCA	279 Ah/kg	150Wh/kg	3.65 V	2 %/month	>2000
	NMC	280 Ah/kg	170Wh/kg	3.7 V	2 %/month	>2000

2.5.2 Charging and Discharging

Battery cells can only be operated safely within certain voltage limits specified by the manufacturer. Whatever cell chemistry is used, these voltage limits must be followed. Deep-discharge (resulting in voltages lower than the minimum voltage specified by the manufacturer) of a cell results in electrode damage (for example copper dissolution in Li-ion cells) and electrolyte decomposition. Cell overcharging (resulting in voltages higher than the maximum voltage specified by the manufacturer) also results in irreparable damage, as for example decomposition of electrode material or electrolyte.

As described in Chp. 2.5.1.9, polarization effects shift the voltage curve during charging/discharging higher/lower compared to the OCV curve. Depending on the c-rate that is used for charging/discharging a cell, the voltage limits of the manufacturer are exceeded before the rated capacity of the cell is fully reached/exhausted. Fig. 2.13 illustrates this effect in case of discharging a battery cell. To be able to fully charge/discharge a battery cell a method termed "Constant Current Constant Voltage (CCCV)" is used. This method is also used to determine the rated cell capacity. CCCV is divided into two phases. A Constant Current (CC) phase and a Constant Voltage (CV) phase. In the CC phase, a higher current leads to higher/lower cell voltages during charging/discharging compared to the OCV-curve. The CC-phase continues until a voltage limit is reached. The higher the current that is used, the faster the voltage limits are reached. At this

point the CV phase begins. In order to comply with the voltage limits, the current in this phase is gradually reduced with the course of the SoC.

Fig. 2.16 illustrates the behavior of the cell voltage during charging/discharging at different c-rates. During charging at a c-rate of 1C the CV phase begins at a value of about 95 % of SoC to fully charge the cell, as shown in Fig. 2.16(a). The corresponding cell voltage is shown in Fig. 2.16(b). During the CV phase the cell voltage remains constant, whereas the current, shown in 2.16(c), gradually decreases. The charging/discharging in the CV phase is usually stopped when a certain lower limit of the c-rate (e.g. C/20) is reached.

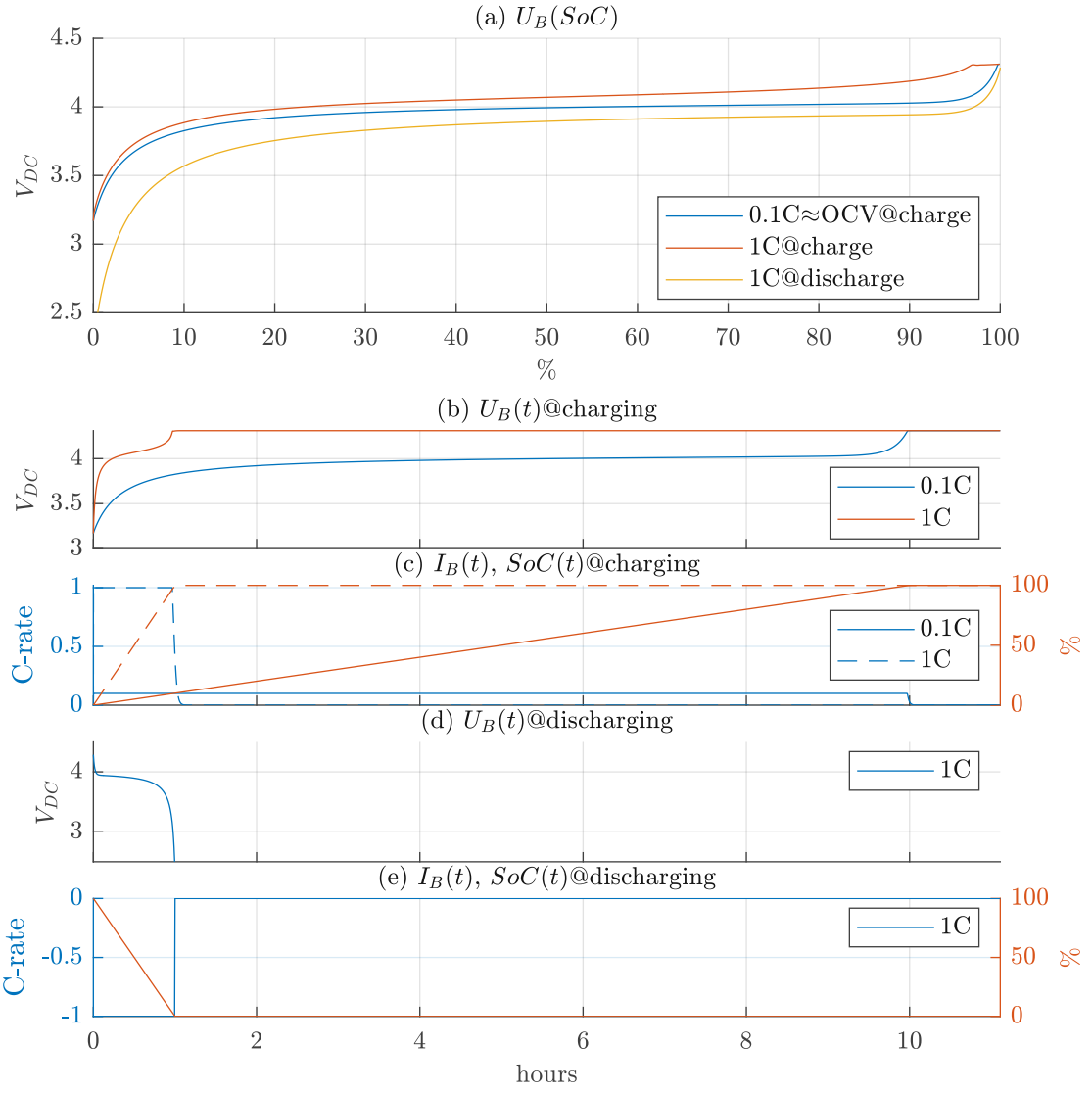

Figure 2.16: Charging and discharging of a battery cell simulated with MATLAB/SIMULINK based on the Li-ion `generic battery model` (representing an experimental/stochastical model according to Chp. A.4.4) with $U_{B,r} = 3.7\,\mathrm{V}$ and the `CCCV battery charger` with a float voltage of 4.34 V.

The power consumed/delivered during charging/discharging in Fig. 2.16 varies over time, because in the CC phase the voltage varies and in the CV phase the current varies as well. Especially

in stationary BESS for many applications a constant power output is necessary. As power is the product of cell voltage and cell current, the limiting values for the maximum power are the maximum current and the maximum cell voltage. A constant power output P over the full SoC-range is not possible. In the low SoC-range the corresponding low cell voltage requires a rather high current to guarantee P, which is limited by the maximum current the cell is capable of. A second limitation in this area is caused by the CV phase, in case the lower voltage limited is reached. Depending on the value P, the maximum current or the CV phase is responsible for limitation. In the high SoC-range the corresponding high cell voltage requires a limitation of the current - due to the necessary beginning of the CV phase, as described above. The higher the desirable constant power output P, the larger the low and high SoC-ranges. The actual spread of the low and high SoC-ranges depends on the cell chemistry regarding maximum cell current (affecting aging) and polarization/resistance. In the middle SoC-range a constant power P can be guaranteed by controlling the current in dependence of the varying cell voltage.

2.6 Battery Energy Storage System (BESS)

BESS usually consist of several components besides the actual battery that stores the energy. There are generally two types of BESS:

- grid-scale/utility-scale/front-of-the-meter BESS and
- behind-the-meter BESS (home storage BESS).

Although both types share the same construction principles, behind-the-meter BESS have a more simple and cheaper design. The focus in the following descriptions lies on grid-scale BESS. To reach a certain amount of capacity and energy content, several battery cells are connected. Their connection requires an appropriate BMS to control the voltage and temperature of each cell. As battery cells provide a DC-voltage, converters are necessary to provide AC-voltage at the output of the BESS. The converters are also called Power Conversion System (PCS). Transformers are necessary to transform the AC-voltage of the PCS to the required voltage level at the PCC. An appropriate switchgear connects and disconnects the BESS to/from the power grid. Its circuit breakers are also controlled by its corresponding protection devices, that guarantee safety of people and equipment. The network form and corresponding neutral point treatment of the transformers according to Chp. A.5.2 has a major impact on the parameterization of these protection devices. To ensure the safety of the battery cells and converters and to limit their degradation, Heating, Ventilation and Air Conditioning (HVAC) systems are required in the building structure, in which the individual components are housed. Finally, the control system performs certain functions that implement BESS services, for example ancillary services such as FCR, and controls the components of the BESS according to the inputs of a human-machine interface (HMI). A detailed description of BESS, their components and typical applications can be found in [195]. In [180] an exemplary BESS and its components are described. The following chapters summarize the most relevant details about the construction of BESS, including its components, the costs of BESS, an exemplary BESS field plant and measurements of characteristic values of this exemplary field plant. Furthermore, all services BESS are capable of providing are summarized and discussed in the last section.

2.6.1 Construction and Components

The term Battery Energy Storage System (BESS) is used for the whole equipment necessary to maintain a power exchange with the electrical power grid or an electrical machine in case of electric vehicles. A BESS usually consists of the following main components:

- battery,

- BMS,
- converters,
- transformers,
- switchgear,
- Heating, Ventilation and Air Conditioning (HVAC),
- control system,
- building structure,

which are described in detail in the following chapters.

2.6.1.1 Battery

Depending on the cell type and cell chemistry, the cell voltage of a single cell is in the range of 0.5 V to 5 V. Many battery cells are connected in a BESS in order to obtain a certain total voltage and total capacity. To obtain higher voltages, several cells are connected in series. To obtain higher capacities cells are connected in parallel. The connection of battery cells is usually done in a modular manner. The following terms are used for different degrees of modularity.

- battery cell: basic unit of a battery consisting of two electrodes, an electrolyte and a separator as described in Chp. A.4.1.
- battery module/pack: A "battery module/pack" consists of a combination of series and parallel connections of battery cells that are put into a frame to protect them better from external shocks such as heat or vibration. To describe the connection of several battery cells inside a battery module a convention is used which is described with the help of the following example. A connection of 14 cells in series and two in parallel is called "14s2p".
- battery rack/string: A rack is a standardized frame or enclosure for mounting multiple equipment modules. In case of a battery rack it serves as mounting platform for several battery modules and its cabling.

2.6.1.2 Battery Management System (BMS)

Voltage monitoring is the most important function of the BMS. As already mentioned in Chp. 2.5.2 overcharging and deep-discharging leads to damage of the cells. Each battery cell has its own safe voltage range and capacity, which makes it necessary to monitor each cell. Overloading is particularly safety-critical as it causes the temperature to rise and the cells to vent, which can both cause the cell to catch fire.

The BMS monitors the actual cell voltage of each cell. To prevent the cell voltage to exceed the limits, the BMS will request a change in power flow in/out of the cell to hold or bring the voltage back within limits. In case this doesn't work the BMS opens the contacts of the corresponding cell. The management of power flow is termed "cell balancing". Usually cell balancing becomes active if at least one cell of a BESS has reached its voltage limits. Either passive or active cell balancing methods are possible. The simpler passive methods bypass relevant cells for example by a parallel transistor that is switched on in case of violation of voltage limits. By active methods energy from cells with a higher charge is transferred to cells with a lower charge. In principle, the charge control represents several switching regulators specially optimized for the application, which work per cell and actively transmit energy.

For larger BESS consisting of several battery racks, the BMS often is designed in a modular way. Every module is controlled by a Module Battery Management System (MBMS), which is located

within the module. All the MBMS in a battery rack are controlled by a Rack Battery Management System (RBMS), which is usually one of the MBMS that acts as the "master BMS" of the rack. In case of a BESS with several battery racks, a Battery Section Controller (BSC), which is usually an external device, controls the corresponding RBMS.

2.6.1.3 Converters

As already described in Chp. 2.4, converters are used to transform the DC-output of the battery into an AC-output that can be fed into the public grid. In order to connect a BESS to the public grid, different converter topologies are available. The classification can be done into single and two-stage converters. The latter one brings benefits to batteries as they decouple the batteries from the DC-AC-conversion. On the other hand, the DC-DC-converter of a two-stage converter decreases the overall efficiency of the converter compared to single-stage converters. For Low Voltage (LV) storage applications, two-level converters are the most used technology [141]. But its usage comes with several drawbacks such as high switching frequency and large output filters in order to comply with harmonic standards. For MV storage applications, multi-level converters are the key technology. In BESS the converter and all its components, including its control, is often termed as PCS.

2.6.1.4 Transformers

Commercial IGBT switches for BESS converters have a maximum breakdown voltage of up to 1200 V – 1500 V. This value also represents the limit of the maximum DC-link voltage. As described in Chp. 2.4, the maximum AC-output voltage is also limited by the maximum DC-link voltage. A trend to higher DC-link voltages in the future, e.g. by using high voltage IGBTs based on Silicon Carbide, is expected to reduce the necessary diameter of DC-cabling between battery and converter. Due to the limited DC-link voltage, the connection of BESS with high power ratings to the public grid requires transformers to be able to connect the BESS to the MV/HV grid. As a rule of thumb, for 1 MW peak power, a connection to the MV-grid may become competitive compared to an appropriate LV cable connection at lengths below 100 m [83]. Essential for the choice of the transformer vector group is the network form of the BESS site. The possibility to feed in asymmetrical currents into the grid requires a network form with solid earthing. A vector group Dyn often is chosen for the corresponding transformer.

2.6.1.5 Switchgear

The quantized power ratings of commercially available converters as well as the housing of batteries and converters in standardized containers makes it necessary to build up a BESS in a modular way. The battery is divided into several Battery Group (BG) which are connected to a converter each. The connection of these battery groups requires a proper switchgear consisting of circuit breakers and disconnectors. The power ratings of commercial transformers are also quantized. This requires another level of modularity when combining several BGs. Also the necessity of redundancy (failure of a transformer) requires the use of several transformers. The connection of several transformers on the high-voltage side requires an appropriate switchgear.

2.6.1.6 Superordinate Control System

To perform a certain application (frequency containment reserve, peak-shaving, etc.) with a BESS and to control the components of the BESS to work in unity, a Supervisory Control and Data Acquisition (SCADA) is necessary. The SCADA usually runs on industrial PCs that gather all

measurement data of the components of the BESS and distributes corresponding control signals to them. Fig. 2.17 shows a typical control structure of a BESS. The BSC of the batteries, the converter control, as well as the thermal managements systems are connected to a programmable logic controller (PLC), which is then connected to the system control SCADA. Protection devices and measurement devices are connected directly to the SCADA. All auxiliary components (fire protection, etc.) are also connected to the SCADA. The network connection between the SCADA and the BESS components is usually done via Modbus or Ethernet.

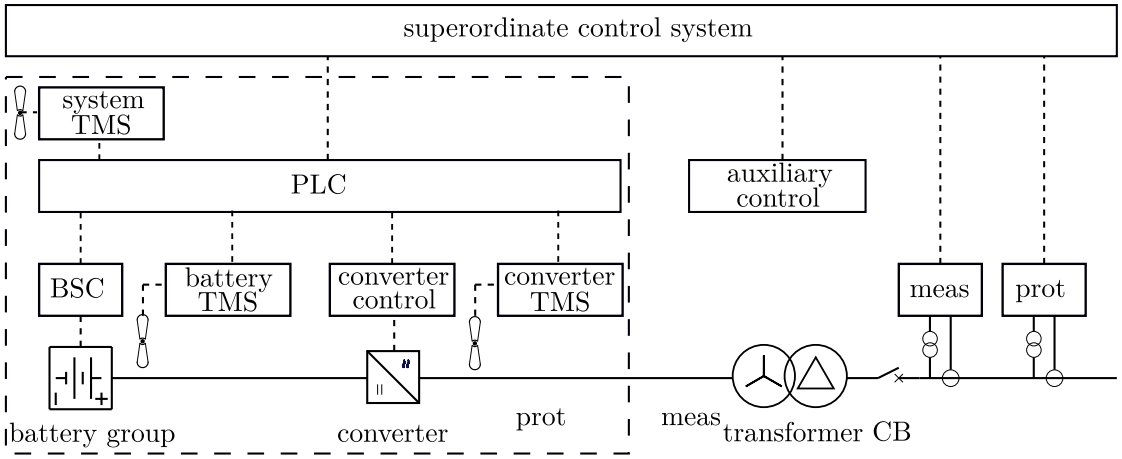

Figure 2.17: Typical BESS control structure.

2.6.1.7 Heating, Ventilation and Air Conditioning (HVAC)

When batteries charge and discharge, they release enormous amounts of heat that must be dissipated to keep the system operational and maintain the service life of the batteries. The usable capacity of a Li-ion cell is strongly dependent on the temperature. Compared to a rated capacity at 25 °C, the usable discharge capacity is reduced by 30 % at a temperature of −25 °C [188]. Heating batteries at cool ambient temperatures, therefore, is necessary to guarantee a certain capacity of the battery. At high ambient temperatures battery degradation will increase. Also the ohmic losses of the battery during operation lead to a temperature increase that increases battery degradation. Therefore, an appropriate HVAC system is necessary.

The HVAC system is mostly constructed in a modular way and controlled by a Thermal Management System (TMS) which may be located inside the system control. The modularity begins with an appropriate ventilation/cooling system of the battery modules in combination with a battery TMS to control all ventilation/cooling devices of the modules. Besides that, a converter TMS controls an appropriate ventilation/cooling system of the converter. Grid-scale BESS also feature an additional system TMS, which acts as a thermal barrier against the direct impact of environmental conditions to the battery modules and controls the HVAC system of the building structure, such as a container.

2.6.1.8 Building Structure

BESS can be placed in a building or within containers. Using containers will be cheaper as well as more modular in most cases, which simplifies planning. For example, each battery group of a BESS could be placed inside one container together with its corresponding converter and HVAC,

while another container could accommodate the switchgear and the SCADA system. In some cases it can be beneficial to use buildings, for instance in very cold environments.

A very important issue regarding building structure is fire protection. Especially BESS with Li-ion batteries, which are very sensitive to thermal run-away, have to be well designed regarding fire protection. Burning Li-ion batteries cannot be extinguished because they provide their own oxygen for the fire. Besides extensive monitoring of the battery states and an appropriate HVAC system, the BESS site is often constructed with separate fire protection sections to minimize risks.

2.6.2 Costs and Return of Investment

In [130] cost and performance parameters for BESS are defined and evaluated. Basically, the CAPEX of BESS can be divided into several parts:

- costs for the battery and its BMS (typically expressed in $/kWh),
- costs for the PCS (typically expressed in $/kW),
- costs for balance of plant (BOP) including components such as site wiring, interconnecting transformers and other additional ancillary equipment (typically expressed in $/kW) and
- costs for construction and commissioning (C&C) consisting of site design costs, costs related to equipment procurement/transportation and the costs of labor/parts of installation (typically expressed in $/kWh).

Tab. 2.5 gives an overview of corresponding cost ranges for the different parts listed above.

Table 2.5: Costs of BESS based on Li-ion technology (based on data of [130]).

type of costs	**cost range** 2018	**expected cost range 2025**
battery module[4]	190 $/kWh – 300 $/kWh	-
battery[5]	223 $/kWh-323 $/kWh	156 $/kWh – 203 $/kWh
PCS	230 $/kW – 470 $/kW	184 $/kW – 392 $/kW
Balance of BESS (BOP)	80 $/kW – 120 $/kW	75 $/kW – 115 $/kW
Construction and Commissioning	92 $/kWh – 110 $/kWh	87 $/kWh – 105 $/kWh
Total project cost $/kW	$\frac{E}{P}\cdot$(315 $/kWh–433 $/kWh)+(310 $/kW–590 $/kW)	$\frac{E}{P}\cdot$(243 $/kWh–308 $/kWh)+(259 $/kW–444 $/kW)
Total project cost $/kWh	(315 $/kWh–433 $/kWh)+$\frac{1}{\frac{E}{P}}\cdot$(310 $/kW–590 $/kW)	(243 $/kWh–308 $/kWh)+$\frac{1}{\frac{E}{P}}\cdot$(259 $/kW–444 $/kW)
Total project cost $/kW for $\frac{E}{P}$=4 h	1570 $/kW – 2322 $/kW	1231 $/kW – 1676 $/kW
Total project cost $/kWh for $\frac{E}{P}$=4 h	392 $/kWh – 580 $/kWh	308 $/kWh – 419 $/kWh

To name an explicit example, the total project costs to install a TESLA powerpack are 172 707 $[6]. The size of a TESLA powerpack is 232 kWh/130 kW[7], which leads to a price per kWh of 744 $/kWh. According to Tab. 2.5 the total project cost for this size of BESS can be calculated to 764 $/kWh

[4]Data according to Tab. 4.10 in [130]
[5]Data according to Tab. 4.3 in [130]
[6]https://teslamag.de/news/preis-tesla-grossspeicher-powerpack-bekannt-172-707-dollar-232-kwh-27800
[7]https://www.tesla.com/de_AT/powerpack

by using the maximum of the given price ranges. Therefore, the price of the TESLA powerpack can be specified as rather high.

The costs of the battery module depends on the cell chemistry that is used. The relation between the costs c of different cathode types can be ranked as follows: $c_{NCA} < c_{NMC/LMO} < c_{LFP} < c_{LTO}$. LTO cells are not sensitive to thermal run-away but do have a very low cell voltage. In relation to the costs of cell types based on graphite anodes the costs are about three times higher.

The OPEX of BESS consist of the personal costs to operate and maintain the BESS, e.g. they include the replacement of damaged battery modules.

In order to calculate the Return of Invest (ROI) of BESS, it is necessary to estimate the profit made from the services it provides. An analysis of the annualized revenues of BESS categorized for different system services can be found in [66]. Especially for system services where no market is available today (e.g. providing instantaneous reserve) it is difficult to estimate a profit. Also for system services like black-start and islanding, the profit is dependent on individual contracts between the operator of a BESS and local network operators or industries. As an example, the profit generated by providing FCR can be estimated according to Fig. 1.4 in Chp. 1.3.1. Today, the market price for providing FCR lies around 10 Euro/MW/h, which leads to an annualized profit of 87 600 Euro/MW/yr. According to ENTSO-E [95] the costs for providing FCR with a BESS are in the range of 7 Euro/MW/h – 9 Euro/MW/h, assuming a project lifetime of 15 yr. This leads to a ROI in the range of 10 yr – 14 yr.

3 Characterization of BESS Used in Field Tests

This thesis has been done as a part of a related research project funded by the Austrian Climate and Energy Fonds. While it was a significant task of the research project to participate in the design and implementation of a BESS, this chapter focuses on how to retrieve essential model data for the investigations of this thesis from an implemented arbitrary BESS. In addition, this chapter lists and describes services BESS are suitable to provide.

3.1 Exemplary BESS Field Plant

The paper [114] describes a BESS designed and built for research activities on the functionality of BESS in multi-use operation. A summary of the characteristics of this BESS is given in the following. Fig. 3.1 shows the single line diagram of the BESS. It consists of four battery groups, each connected to a converter/PCS. Two BGs and corresponding PCSs are connected in parallel to a Storage Unit (SU). The two SUs are connected via transformer to the MV grid. More details of the BESS components are summarized in the following chapters.

3.1.1 Battery

Each BG in a SU consists of nine Battery Strings (BS) connected in parallel, wherein each BS consists of 14 Battery Module (BM) which are connected in series. A BM consists of battery cells of Li-ion NMC cells with a total rated capacity of 63 Ah, a rated cell voltage of 3.7 V, a cell voltage window of 3 V – 4.2 V and a maximum c-rate of 1 for charging/discharging. The cell connection inside a BM is of the type 14s2p. Therefore, a BM has a rated module capacity of 126 Ah and a rated module voltage of 51.8 V. The serial connection of 14 battery module inside a battery string leads to a rated string voltage of 725 V. The parallel connection of nine battery strings in a battery group leads to a rated string capacity of 1134 Ah. The parallel connection of two battery groups in a storage unit leads to a rated storage unit capacity of 2268 Ah and with a rated storage unit voltage of 725 V this leads to a rated storage unit energy content of 1.644 MWh. The parallel connection of two storage units leads to a rated capacity of 4536 Ah and a rated energy content of 3.286 MWh of the whole BESS. As a consequence of aging of the battery cells, the usable energy content of the BESS is controlled by a scalable SoC-window. Dependent on the actual SoH of the cells, the scalable window is adapted to guarantee a certain minimum capacity in the future. At the time of installation, this window is set to 6 % – 96 %. Therefore, the usable energy content of the BESS is 2.96 MWh. As described in Chp. 2.5.2, the charging/discharging process of the battery cells has to respect the minimum/maximum cell voltage, as well as the maximum c-rate. The nominal power of 2.5 MW of the BESS can be provided in a SoC window of 2.3 % – 95 %. Due to the internal resistance of the battery cells, the provision of the rated power outside of this SoC-window would exceed the minimum/maximum voltage limits. Tab. 3.1 summarizes the rated values of the BESS according to [114].

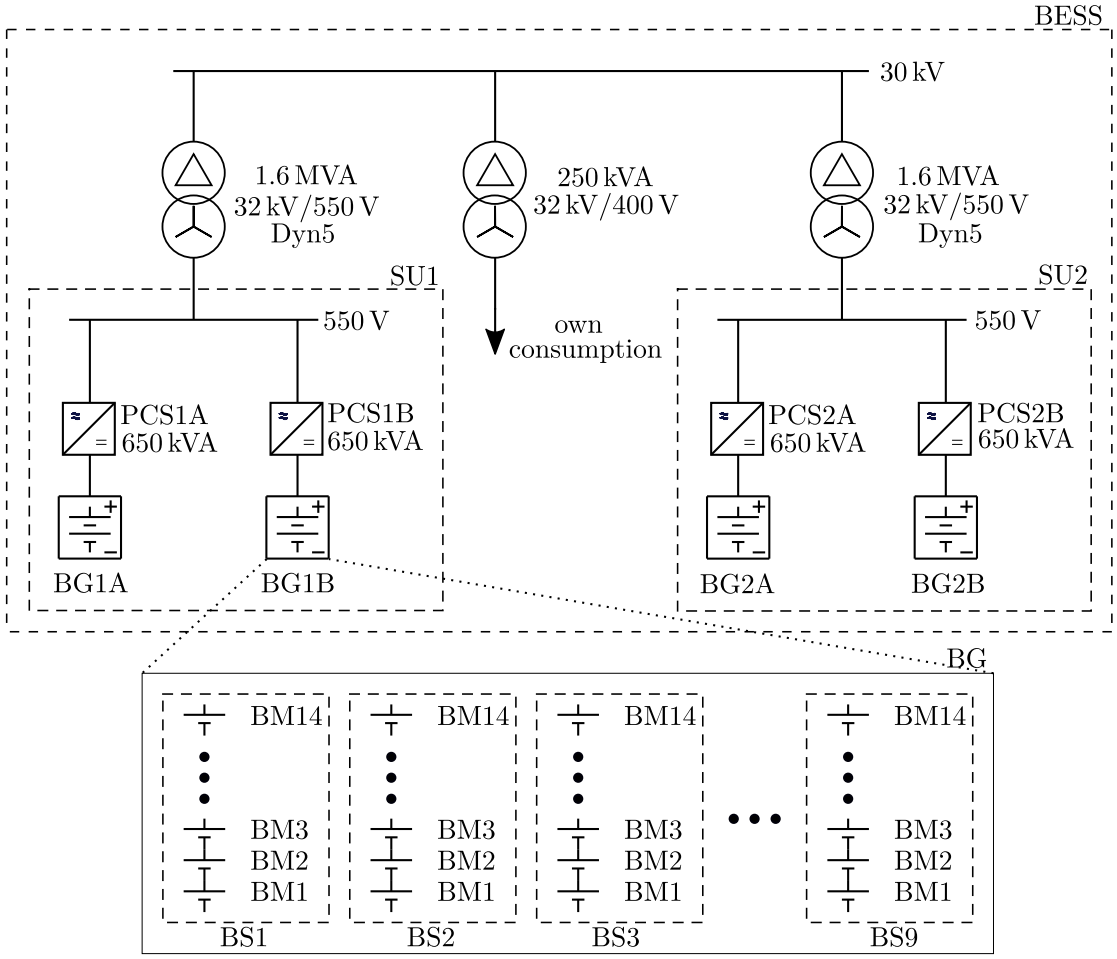

Figure 3.1: Single line diagram of an exemplary BESS field plant [114].

Table 3.1: Rated values of BESS characteristic values [114].

characteristic	**value**
rated cell capacity	63 Ah
rated cell voltage	3.7 V
cell voltage range	3 V – 4.2 V
module cell connection type	14s2p
rated module capacity	128 Ah
rated storage unit voltage	725 V
rated storage unit capacity	2268 Ah
rated storage unit energy content	1.644 MWh
rated BESS capacity	4536 Ah
rated BESS energy content	3.286 MWh
BESS voltage range	588 V – 823 V
nominal power S_n	2.5 MW
usable SoC-window@SoH=100 % (managed by the supplier)	6 % – 98 %
maximum usable SoC-window@nominal power (respecting voltage range)	2.3 % – 95.25 %

3.1.2 Converter/PCS

Each converter/PCS in Fig. 3.1 is a two-stage, two-level converter and has a rated power of 650 kVA. The structure of the converters is shown in Fig. 2.8.

3.1.3 Transformers

Each transformer in Fig. 3.1 has a rated power of 1.6 MVA, a vector group of Dyn5 and their star point is grounded on the low-voltage side.

3.1.4 Building Structure

Each storage unit and its converters is located in a 20 ' ISO container each. The switchgear and the SCADA system is located in a separate 20 ' ISO container. The two transformers are located inside a separate transformer station building.

3.1.5 Measurement Setup

The BESS field plant was equipped with measurement devices which allow a remote access to measurement values in real-time. This measurement setup allowed scientific accompanying the construction and commissioning of the BESS and represents an appropriate solution as measurement setup for the field tests described in Chp. 4. Fig. 3.2 shows an overview of the measurement setup which was installed to perform scientific measurements in the BESS field plant.

Four measurement devices of the type "KoCoS EPPE-CX" were installed to measure the behavior of each battery group on the 550 V-level. Another measurement device of the same type was installed to measure the behavior of the whole BESS at the 30 kV-level. Each measurement device measures voltage and current at the corresponding feeder where the four measurement devices of the battery groups additionally measure the DC-values of voltage and current of the corresponding converter. Furthermore, each of the measurement devices is able to retrieve real-time measurement values from the SCADA of the BESS in order to store values such as the actual SoC synchronized with other values. The five measuring devices were connected to the Internet, via which the measurement data was transmitted to a data center located at TU Wien and via which each device could be parameterized. A synchronized measurement of measurement values was done continuously with a sample rate of 1 s throughout the test phase. For the field tests described in Chp. 4, several trigger conditions were parameterized in order to perform synchronized high-resolution measurements each device is capable of.

An additional measurement device which is termed as energy meter in Fig. 3.2 was installed to measure the energy consumption of the auxiliary systems such as the HVAC, the BMS or the BESS SCADA. The corresponding measurement data was stored locally.

3.2 Measurements of Characteristic Values at a BESS Field Plant

This chapter summarizes relevant characteristics of BESS and corresponding measurements procedures and results, which are necessary to accurately model the BESS in the following parts of the thesis.

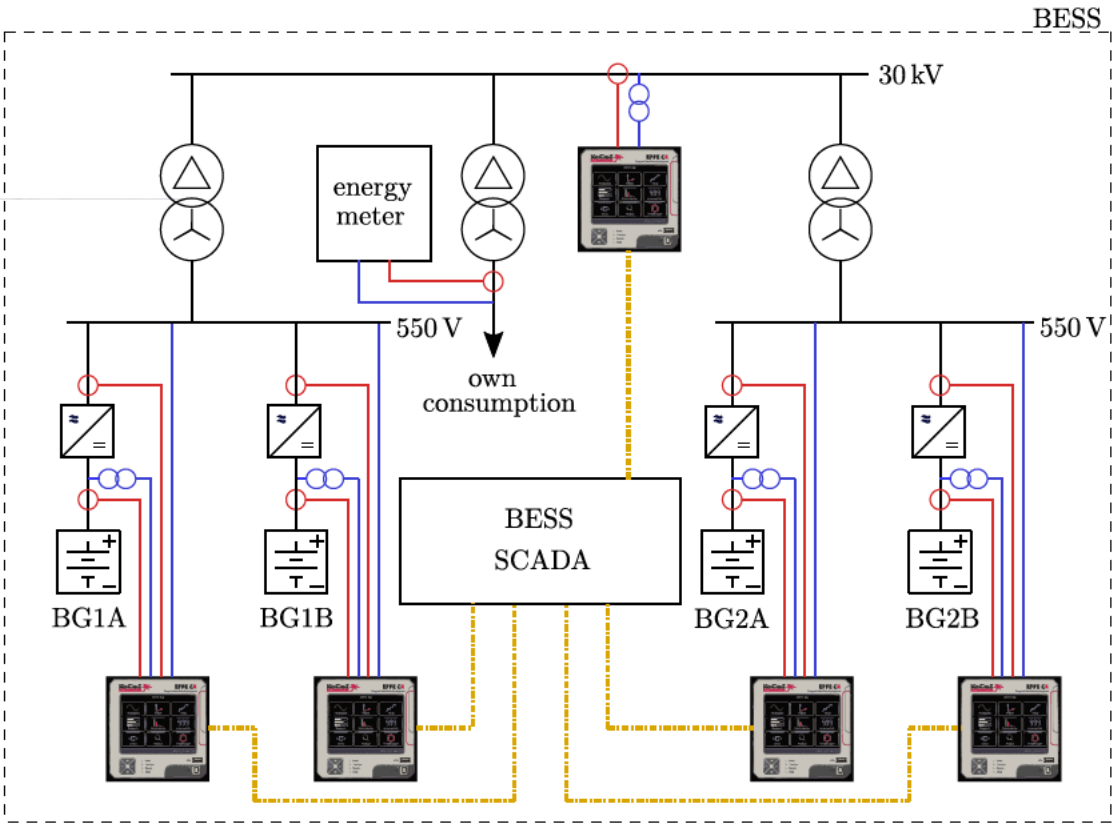

Figure 3.2: Overview of fixed installed measurement devices inside the BESS field plant. Red lines indicate current measurement, blue line indicate voltage measurements and yellow lines indicate signal paths of other measurement values provided by the BESS SCADA.

3.2.1 BESS Voltage Curve

In Chp. A.4.1.1 the voltage curves of several battery cells are discussed and shown in Fig. A.14. Based on the current that is provided by a battery cell, the voltage curve changes as shown in Fig. 2.13. As a BESS consists of many battery cells, the voltage curve of the BESS basically shows the same behavior as the single battery cells it is composed of.

Fig. 3.3 shows the voltage curve of the BESS described in Chp. 3.1 during two charging/discharging cycles at two different constant power values with the rated power 2.5 MW and a quarter of the rated power of 0.625 MW, in relation to the Point of Common Coupling (PCC) at the 30 kV-bus. During the charging/discharging process of the BESS, the values according to Tab. 3.1 have to be respected. The most critical value to be respected is the maximum usable SoC-window, that corresponds to the minimum/maximum voltage range of the BESS at rated power. Therefore, the cycle at rated power respects the maximum SoC of 95.25 % with the corresponding maximum voltage of 823 V. During the cycle at a quarter of the rated power a SoC of 98 % can be reached during the charging process, which is the higher value of the scalable SoC-window according to Tab. 3.1. In both cycles, the charging process would only be possible to be continued by reducing the charging current (therefore charging power) according to the CCCV method according to Chp. 2.5.2. The discharging process in both cycles stops at a SoC of 6 % respecting the lower value of the usable SoC-window@SoH=100 %.

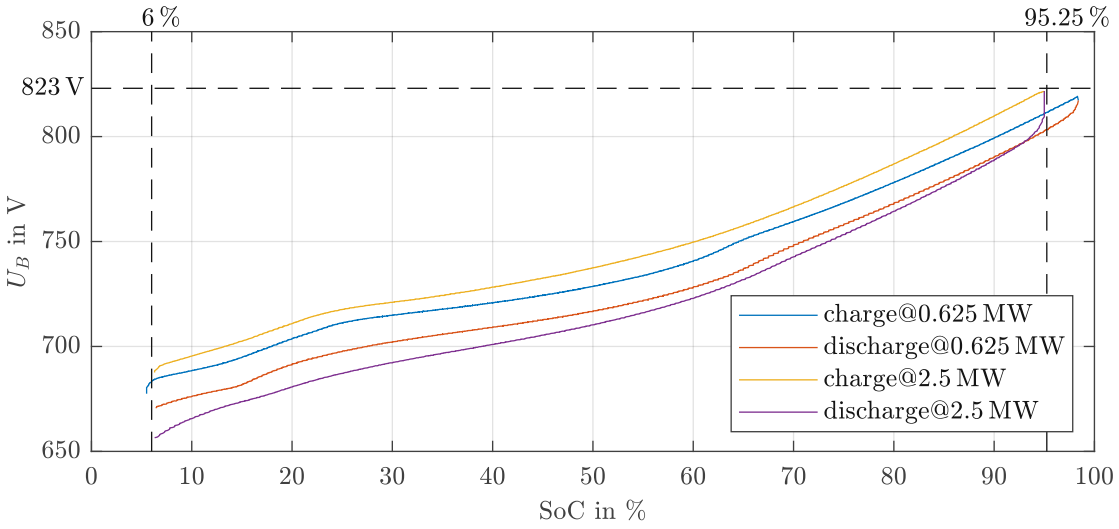

Figure 3.3: Measured battery voltage curve of the BESS described in Chp. 3.1. For the limits the last two entries of Tab. 3.1 take effect. The lower limit is defined by the lower limit of the usable SoC-window of Tab. 3.1, while the upper limit is defined by the upper limit of the maximum usable SoC-window@nominal power. Therefore, the limits are defined by the unlocked SoC-window from the supplier and the possible maximum SoC at nominal power.

3.2.2 Converter Efficiency

A power converter's efficiency η is determined by comparing its input power to its output power. In case of a battery-converter the reference point of the input and output power is dependent on the direction of the power flow. Considering the battery-converter shown in Fig. 2.8, in case of charging the battery the input power is P and the output power is P_{DC}, whereas in case of discharging the input power is P_{DC} and the output power is P. Therefore, the converter's efficiency results to

$$\eta_{chg} = \frac{P}{P_{DC}}, \tag{3.1}$$

$$\eta_{dchg} = \frac{P_{DC}}{P}. \tag{3.2}$$

The efficiency results from the losses that occur in the converter. Independent from the design of the actual converter, all converters include switching elements (nowadays often IGBTs) and inductances (with corresponding DC-resistances). The losses of the converter P_{loss} can be classified into

- inductor conduction losses,
- IGBT conduction losses and
- IGBT switching losses.

The conduction losses increase with the square of the current the converter carries, due to the DC-resistance of the inductor and the on-resistance $R_{DS(ON)}$ of the IGBT. The switching losses are dependent on the switching frequency, the DC-link-voltage and the current the converter carries. A detailed description and model of converter losses are described by Schimpe et al. [155]. At small operating points of the power output P of the converter, the factor $\frac{P_{loss}}{P}$ is relatively high,

whereas with increasing values of P, the factor $\frac{P_{loss}}{P}$ decreases. Assuming a constant output power of a converter, the reduction of the DC-input-voltage leads to a higher current compared to a given DC-input-voltage U_B. Therefore, higher losses occur and the efficiency decreases. An example of efficiency curves for different setpoints of P, different input voltages U_B and dependent on the direction of power flow is shown in Fig. 3.4.

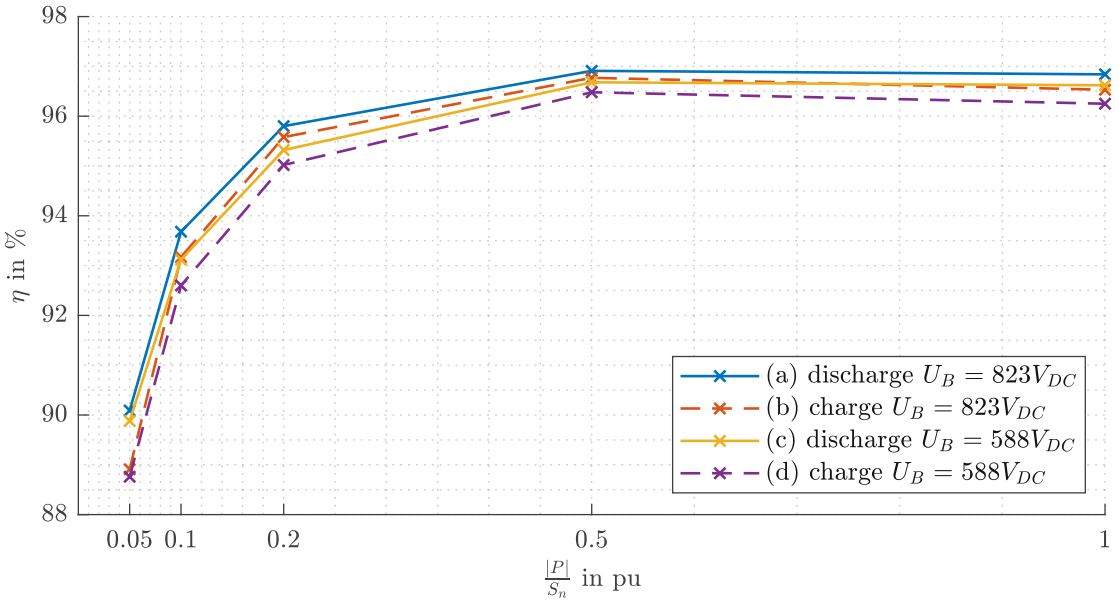

Figure 3.4: Measurement of converter efficiency values for different operating points P, which are plotted as normalized values with the maximum power capability S_n as a reference value. The different efficiency curves (a)-(d) show efficiency values dependent on the input voltage U_B on the DC-side of the BESS described in Chp. 3.1 and which is shown in detail in Fig. 2.8.

Fig. 3.5 shows measurement values of the efficiencies of one converter of the BESS described in Chp. 3.1 for different operating points of the power output P. For every operating point a full cycle of charging and discharging the battery was measured. Therefore, the influence of the battery voltage U_B according to Fig. 3.3 is shown. In case of a fully charged battery, the efficiencies η_{chg} and η_{dchg} are highest. They decrease with a decreasing SoC of the battery.

A future trend to reduce converter losses may be the use of multilevel converter that can address challenges of BESS more specifically, such as low efficiency at low operating points [83]. In addition there is a trend to higher DC-voltages up to 1500 V, which also reduces converter losses. However, a drawback of higher DC-voltages may be a reduced reliability as a single cell fault can potentially deactivate the entire string [83].

3.2.3 Own Consumption of HVAC, BMS and Auxiliary Equipment

The HVAC, the BMS and other auxiliary equipment drain power during charging/discharging of the battery which is also dependent on the operating point of the BESS. Tab. 3.2 summarizes the corresponding power own consumption of the BESS during charging/discharging.

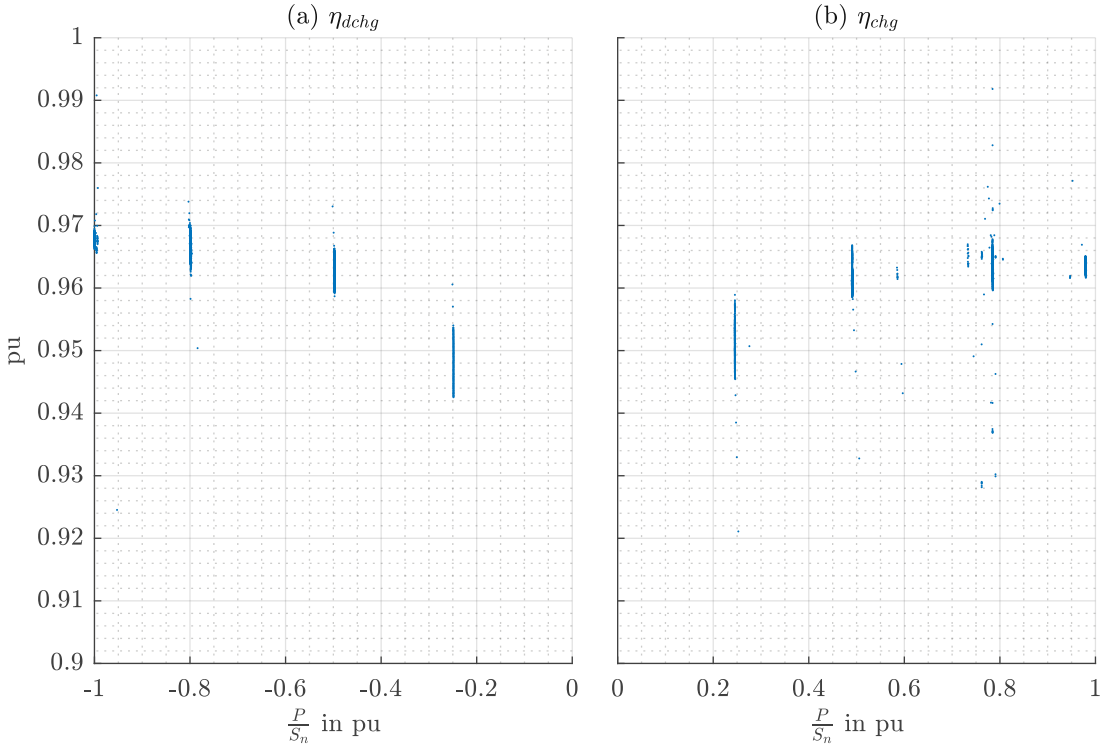

Figure 3.5: Converter efficiency curves based on measurements of the BESS described in Chp. 3.1, where full cycles were run through at different operating points.

Table 3.2: Measurement of own consumption during cycling of the BESS described in Chp. 3.1 according to Fig. 3.6.

cycle	HVAC	BMS
charging@S_n	38 kW	1 kW
discharging@S_n	37 kW	1 kW
charging@0.8S_n	28 kW	1 kW
discharging@0.8S_n	28 kW	1 kW
charging@0.5S_n	18 kW	1 kW
discharging@0.5S_n	20 kW	1 kW
charging@0.25S_n	13 kW	1 kW
discharging@0.25S_n	14 kW	1 kW

3.2.4 BESS Capacity and Energy Content

In Chp. 2.5.1.10 the coulombic efficiency was introduced as the ratio of dischargeable capacity and chargeable capacity of a battery. As the current of the BESS and the battery is identical, this value is not only valid for the battery but also valid for the BESS. The chargeable capacity is basically defined by the rated capacity of the BESS. As shown in Fig. 2.13 the chargeable capacity reduces with increasing current. The rated capacity of the BESS described in Chp. 3.1 is 4.5 kAh. Considering the scalable SoC-window of 6 % – 98 % given in Tab. 3.1, the usable capacity reduces to 4.2 kAh. In order to measure the usable capacity and the energy content, several charging and discharging cycles were performed, whose measurement results are illustrated in Fig. 3.6.

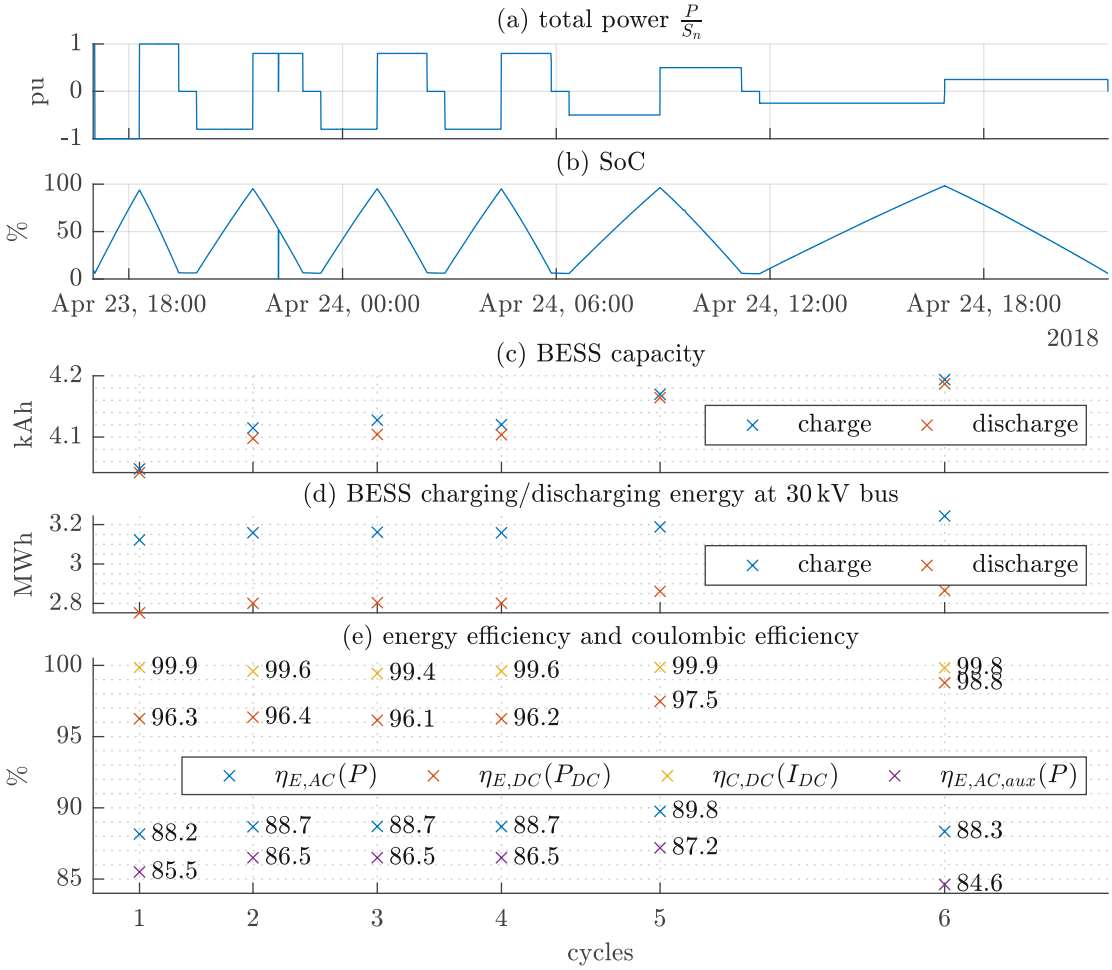

Figure 3.6: Measurement of roundtrip efficiency for 6 full cycles of the BESS while charging and discharging with rated power (first cycle), 80 % of the rated power (second – fourth cycle), 50 % of the rated power (fifth cycle) and 25 % of the rated power (sixth cycle). (a) shows the total power output of the BESS, (b) shows the total SoC of the BESS, (c) shows the capacity that is stored/provided in/from the BESS, (d) shows the energy that is stored/provided in/from the BESS at the 30 kV (including all losses) and (e) shows the corresponding energy efficiencies of each cycle $\eta_{E,AC}(P)$ and $\eta_{E,AC,aux}(P)$ at the 30 kV-bus, respectively on the DC-side of a converter $\eta_{E,DC}(P_{DC})$ and the coulombic efficiency $\eta_{C,DC}(I_{DC})$ of the batteries.

Fig. 3.6(a) shows six full cycles within the usable SoC-window according to Fig. 3.3 at four operating points, which are $\{S_n, 0.8S_n, \frac{S_n}{2}, \frac{S_n}{4}\}$. Fig. 3.6(c) shows the chargeable capacity, with a maximum value of about 4.2 kAh for an operating point of $\frac{S_n}{4}$, which matches with the value as calculated in Tab. 3.1. With increasing power the capacity decreases to a minimum value of 4.05 kAh at an operating point of S_n. By comparing the charge capacity with the discharge capacity in Fig. 3.6(c) a slightly lower value can be noticed. Therefore, the coulombic efficiency near to one becomes visible, which is familiar for Li-Ion batteries.

Compared to the capacity, the chargeable and dischargeable energy of the BESS is also dependent on the voltage and on the losses that occur in the path of energy flow. The corresponding value, therefore, is depending on the location where the energy measurement takes place. Depending on

the location, the losses due to cables, transformers, the converter and/or the internal resistance of the battery has an influence on the measured energy. Fig. 3.6(d) shows the corresponding measured charged and discharged energy at the PCC, which is the 30 kV-bus according to Fig. 3.1, and, therefore, includes all losses mentioned above. The usable energy content according to Tab. 3.1 is about 3 MWh, considering the usable SoC-window at a SoH=100 %. The maximum charged energy in Fig. 3.6(d) has a value of about 3.2 MWh for a operating point of $\frac{S_n}{4}$. The corresponding losses as mentioned above, however, reduce the amount of energy that is finally stored inside the batteries. During discharging, on the other hand, these losses have to be covered by the batteries, but are not available at the PCC of the BESS. Therefore, the discharged energy decreases to a value of about 2.8 MWh, compared to the charged energy of 3.2 MWh. This leads to total energy losses of about 200 kWh during charging/discharging at a cycling power of $\frac{S_n}{4}$. With increasing cycling power, the chargeable and dischargeable energy decrease, and the losses increase, as shown in Fig. 3.6(d).

3.2.5 BESS Efficiencies and Losses

From the point of view of the PCC of the BESS, several proportions of losses can be distinguished, which are losses due to lines and transformers, losses due to converter efficiency, losses due to the battery itself and losses that arise from the energy consumption of all auxiliary systems. However, the losses due to energy consumption of all auxiliary systems may not occur in the same path of energy flow as the other proportions of losses. For example, Fig. 3.1 shows that the auxiliary systems are supplied by an additional transformer connected to the 30 kV-substation. Depending on the location of measurement devices, the energy consumption of auxiliary systems, therefore, may have to be measured separately. For this reason, a corresponding standard [86] defines the energy efficiency (also called round-trip efficiency) as a measure for losses in the BESS with separate values for the measured energy of the BESS and the auxiliary systems. This results in an energy efficiency of the BESS that is defined by

$$\eta_{E,AC,aux} = \frac{E_{dchg,AC} - E_{aux,dchg}}{E_{chg,AC} + E_{aux,chg}} \tag{3.3}$$

where the index "AC" indicates the measurement at the AC-side of the BESS. The energy efficiency without consideration of auxiliary systems is defined by

$$\eta_{E,AC} = \frac{E_{dchg,AC}}{E_{chg,AC}}. \tag{3.4}$$

A third energy efficiency can be found for the energy efficiency of the battery itself, which is defined by

$$\eta_{E,DC} = \frac{E_{dchg,DC}}{E_{chg,DC}} \tag{3.5}$$

where energy values measured at the DC-side of the BESS are considered.

The so-called coulombic efficiency (or current efficiency) is another measure for the efficiency of the BESS. It is an indicator for the reversibility of batteries. Due to parasitical chemical reactions during charging and discharging, a certain amount of electric charge becomes unusable. The coulombic efficiency can be defined by

$$\eta_{C,DC} = \frac{\int_{t_0}^{t_1} I_{DC,dchg}(t)\,dt}{\int_{t_0}^{t_1} I_{DC,chg}(t)\,dt} \tag{3.6}$$

where t_0 and t_1 define the beginning and ending of the corresponding charging or discharging cycle.

Fig. 3.6(e) shows the coulombic efficiency, the energy efficiency of the BESS at the PCC at the 30 kV-bus and the energy efficiency of the battery at the DC-side of the converter.

As already described above and shown in Fig. 3.6(c), the coulombic efficiency $\eta_{C,DC}(I_{DC})$ is nearly 100 %. For a cycling power of $\frac{S_n}{4}$ the total losses were described above and have a value of about 200 kWh during charging/discharging. Fig. 3.6(e) shows the corresponding energy efficiency $\eta_{E,AC}(P)$ of the BESS with $\frac{2.8\,\mathrm{MWh}}{3.2\,\mathrm{MWh}} = 88.3\,\%$. For the other cycling powers this energy efficiency lies in the range 88 % – 90 %. The corresponding percentage of the total losses during charging/discharging lies in the range of 5 %–6 %. Considering the energy consumption of auxiliary systems, additional 1 % – 2 % of losses arise. The corresponding energy efficiency $\eta_{E,AC,aux}$ lies in the range of 85 % – 87 %.

Fig. 3.6(e) also shows the energy roundtrip efficiency of the battery $\eta_{E,DC}(P_{DC})$ in the range 96 % – 99 %. The corresponding losses only occur at the internal resistance of the battery. The difference between $\eta_{E,AC}(P)$ and $\eta_{E,DC}(P_{DC})$ corresponds to the losses at the converter, the cables and the transformers that lie in the range of 4 % – 5 % during charging/discharging, which rises to values in the range of 5 % – 6 % when also considering the energy consumption of auxiliary systems.

3.3 Services Provided by BESS

Sterner and Stadler [168] list services for which different storage technologies are suited. These services are divided into several categories and for each storage technology its suitability for the corresponding service is assessed based on the four options “very well-suited”, “well-suited”, “basically suited” and “not suited”. The result is a suitability matrix for each storage technology, also including BESS. Based on this entry for BESS in the matrix, this chapter describes all services that are assessed as at least “basically suited” for BESS. Although the categorization of Sterner and Stadler [168] is used as basis for further considerations, also alternative categorizations, for example based on [83, 92, 93, 63], are taken into account. Hesse et al. [83], for example, categorize the various services into four application families, which are “ancillary service”, “behind-the-meter”, “energy trade” and “grid support and investment deferral”. IRENA [92] uses the categories “system operation”, “investment deferral”, “solar photovoltaics and wind generation” and “mini-grids”. In IRENA’s Electricity Storage Valuation Framework [93] another categorization is used, distinguishing between “Bulk Energy Services”, “Ancillary Services”, “Transmission Infrastructure Services”, “Distribution Infrastructure Services” and “Customer Energy Management Services”. The report [63] uses the categorization “electric supply applications”, “ancillary services applications”, “grid system applications”, “customer applications”, “renewables integration applications” and “distributed energy storage applications”. However, all studies get to a similar result of services BESS are suitable to provide. Based on the services identified in the different studies [168, 83, 92, 93, 63], Fig. 3.7 presents an overview of possible services provided by BESS, which are categorized mainly based on the categorization of Sterner and Stadler [168]. It is worth mentioning, that further categorizations may be done based on the sector of implementation (commercial, industrial, residential), or on the voltage-level of integration.

According to Fig. 3.7, services can be divided into system services and trading services. Compared to system services, trading services do not contribute to stabilizing and securing the operation of the power system, but are used to trade energy on the energy market, for example, to recharge the energy reservoir of the BESS on the intra-day market, or to generate additional revenues by using the energy reservoir of the BESS to perform energy arbitrage transactions on the energy market. In general, some of the possible services in each category may generate revenues for the owner of the BESS, while others cannot, because they have prescribed regulatory requirements, for

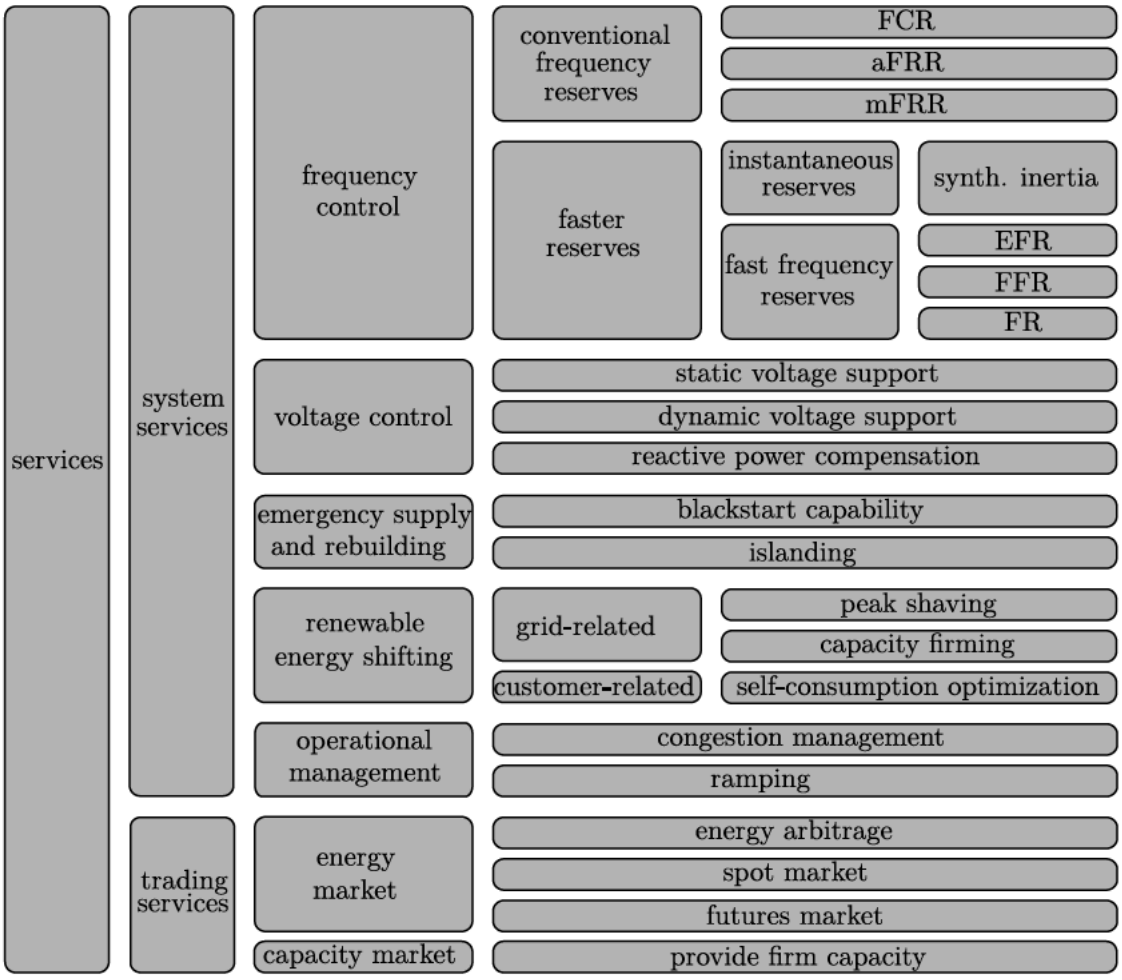

Figure 3.7: Categorization of services for which BESS are suited.

example. Energy arbitrage is an example for trading services which can be used to generate such revenues. Managing the state of charge of the BESS, on the other hand, is necessary for the BESS to ensure a sufficient energy reservoir at any time, and may lead to additional costs by trading energy on the energy market. For the system services, the conventional frequency reserves, as for example FCR, are tendered on a market-based tendering platform, which generates revenues for the owner of the BESS. Voltage control, on the other hand, is also a part of the system services and is coupled with rather strict regulatory requirements, which are prescribed by grid codes and therefore are not associated with any revenues. Each of the categories and their individual sets of services of Fig. 3.7 are discussed in the following chapters in more detail.

3.3.1 Frequency Control

Traditionally, conventional power plants such as thermal and hydro power plants have provided frequency control services. However, the amount of conventional power plants is expected to decrease in the coming years. Furthermore, the traditional role of thermal power plants as base-load power plants is expected to change to a more flexible operation with more starts and stops [69]. Since the provision of frequency control services requires the thermal power plants either to be on standby or to be forced to run at capacity levels that do not use fuel efficiently, such

operation may be both technically and economically inefficient. Especially utility-scale BESS are well-suited to provide services for frequency control and to compensate for the decreasing amount of thermal power plants in the future [8].

System services for frequency control are the well established services for load-frequency control, consisting of three stages, which are Frequency Containment Reserve (FCR), automatic Frequency Restoration Reserve (aFRR) and manual Frequency Restoration Reserve (mFRR), as well as "faster reserves" for frequency stabilization. Such "faster reserves" are currently subject of intensive research activities [74]. There is a huge variety of possible implementations for such "faster control reserves", which can be divided into implementations of instantaneous reserves and implementations of fast frequency reserves.

Instantaneous reserve is inherently provided by conventional synchronous generators in the form of mechanical inertia, but may also be provided by inverter-based generation units in the form of SI by adapting their control accordingly [115]. Instantaneous reserve is provided instantly after a load disturbance in the electric power grid in order to balance the difference between load and generation. Since instantaneous reserve is activated based on the mechanical inertia and or SI of the corresponding technical entity, the amount of activation depends on the actual frequency gradient.

Fast frequency reserves, on the other hand, are mostly activated identically to FCR, namely based on the frequency deviation according to droop curves. The difference between fast frequency reserves and FCR is the much shorter "full activation time", which defines the period between the occurrence of a frequency deviation and an actual activation of the frequency reserve according to the corresponding value of its droop curve. Furthermore, the droop curves of fast frequency reserves may differ from the droop curve that is applied for FCR. There are various implementations, which are summarized under the term "fast frequency reserves". Examples for actual products of such fast frequency reserves are the product "Enhanced Frequency Response (EFR)", which has already been established in the United Kingdom [133], the product "Fast Frequency Response (FFR)", which has already been established in Scandinavia [44], or the product "Fast Reserve (FR)", which will be established in Italy [178] shortly.

As already mentioned above, there are market-based tendering platforms for conventional frequency reserves such as FCR, aFRR and mFRR. For faster reserves, on the other hand, currently there are only a few examples where such services have actually been tendered. EFR in the United Kingdom [133] is one such example. Especially for instantaneous reserves, currently there are only concepts on how to realize a tendering platform [76].

3.3.2 Voltage Control

Fig. 3.7 shows three representatives of the category voltage control. Static and dynamic voltage support can be considered as services, which are often prescribed by national grid codes. In Austria the corresponding requirements are described in the TOR [41]. The basic idea is to also require converter-based systems to contribute to voltage regulation. BESS are connected to the grid via converters and are therefore also required to contribute to voltage regulation according to TOR.

The static voltage support is active during normal operation, while the dynamic voltage support is active during fault conditions such as short-circuits. Both services rely on injecting or absorbing reactive power into/from the grid in order to influence the voltage. Currently, the connection of BESS to the grid requires such a provision of reactive power according to the corresponding grid code without the possibility of receiving a corresponding remuneration. As third representative of the category voltage control Fig. 3.7 lists the reactive power compensation. It describes the service of compensating the reactive power demand of commercial or industrial loads. Compared to private customers, commercial or industrial customers often have to measure their reactive power demand, which then has to be paid for accordingly. By offering a service such as reactive

power compensation a BESS is capable of compensating or reducing these reactive power demands. By contractual agreements on remuneration between commercial or industrial customers and the owner of the BESS, this service may generate additional revenues for the owner of the BESS.

3.3.3 Emergency Supply and Restoration

The increasing amount of variable renewable energy in the future power system leads to massive power fluctuations in the power grid. This brings the risk of blackouts to become more likely in the future. In Fig. 3.7 and many studies [168, 83, 92], black-starting and islanding capabilities are therefore listed as services that BESS will most likely also offer in the future. By building local Microgrids and perform an island operation during such blackouts, the reliability of supply can be increased. According to Marney et al. [125] Microgrids comprise low voltage distribution systems with distributed energy sources, storage devices, and controllable loads, operated connected to the main power grid or islanded, in a controlled, coordinated way. During a blackout of the main grid, such Microgrids may also be de-energized. By performing a black-start, which describes the process of restoring a Microgrid after a shutdown without any external voltage support, the supply within a Microgrid can be restored. Such a black-start is followed by the island operation, which ensures a continuous and stable operation of the Microgrid.

The capability of a BESS to perform a black-start may also be used in conventional power plants in order to perform corresponding start-up procedures for restoring the grid after a blackout.

3.3.4 Renewable Energy Shifting

All services listed under the category “renewable energy shifting” in Fig. 3.7 can be considered as the services that are directly related to cope with power fluctuations of variable renewable energy today and in the future. The services are divided into grid-related services, which includes peak shaving and capacity firming and customer-related services, where Fig. 3.7 only lists self-consumption optimization. The basic idea of peak shaving is to prevent peak power infeed by storing all the energy above a certain power level. This stored power can then be used during peak demand when most needed. Capacity firming, on the other hand, is used to smoothen the power output of variable renewable energy. Power fluctuations of variable renewable energy are mainly caused by cloud movements and variability of wind speed. Local coupling of variable renewable energy with BESS opens up the possibility of achieving such a smoothing. By limiting the ramp rate, rapid voltage and power fluctuations can therefore be prevented. The third service comprised in the sub category energy shifting listed in Fig. 3.7 is self-consumption optimization, sometimes also termed as bill management. This service is mainly offered by behind-the-meter BESS in connection with photovoltaics in private households in order to achieve savings in retail tariffs by maximizing the energy demand for own consumption based on the energy infeed of photovoltaics in combination with the BESS. Another emerging trend is the use of centralized BESS in a district to store the surplus energy generated by local renewable energy, such as rooftop photovoltaics. This service can also be referred to as self-consumption optimization, not of a household but of the whole district. Although the different services of energy shifting seem very similar, it has to be stated that the major difference are the corresponding goals. Peak shaving, for example, has the goal to prevent the occurrence of certain power infeed levels in order to prevent curtailment of renewable energy and congestion of the grid. The goal of self-consumption, on the other hand, is to maximize the amount of energy in a household or district, regardless of the stress level of the grid. However, self-consumption optimization can also indirectly help to relieve the grid, for example since it leads rooftop photovoltaic energy to be stored during mid day, when a total peak power infeed of variable renewable energy is likely to occur.

3.3.5 Operational Management

Massive power fluctuations of variable renewable energy are coupled with two extreme situations, which are surplus and shortage of power. A surplus of power brings the risk of congestion of the grid. Traditionally, system operators have addressed this issue by increasing the carrying capacity of the distribution and transmission grid. However, when such situations occur only for very limited time periods, investments in reinforcing the entire grid might not be the optimal solution. In order to prevent a curtailment of renewable energy, which can be considered as the last resort to solve such a problem, BESS can be used instead of grid reinforcement to balance the actual power demand and power infeed by storing the corresponding surplus of power. A shortage of power, on the other hand, traditionally is covered by peak power plants, which are usually thermal power plants. Considering the decreasing amount of thermal power plants, BESS are an option of deferring further investment in peak power plants.

Renewable energy shifting may contribute to prevent congestion of the grid, as all services comprised in this category are leading to a smoothening of the infeed curve. However, BESS which are used to provide such services will be integrated nearby to the location where the renewable power infeed takes place. Therefore, the corresponding services can be considered as local services. The category of operational management, on the other hand, includes services that are related to centrally controlled grid services. According to IRENA [92], instead of overbuilding the transmission- and distribution grid, BESS located at congestion points can be used as "virtual power lines" to enhance the performance and reliability of the system. Such kind of service is referred to as congestion management, where BESS can be considered as part of the infrastructure, centrally controlled by system operators. These BESS providing the service of congestion management are used to store energy from renewable energy generation to address peak demand exceeding the carrying capacity of the grid. For the few hours each year when the existing substations and lines may be overloaded, system operators can control BESS directly to provide an instantaneous response. Besides congestion management the category operational management in Fig. 3.7 lists the service ramping, which is related to flatten the so-called "load duck curve". Especially for a high share of photovoltaic penetration, the shape of the traditional load curve starts to change. Instead of having a peak demand during midday, the load duck curve requires the system to ramp downward in the morning when solar generation increases and to ramp upwards in the evening when solar generation decreases and demand increases. This leads to a corresponding nadir of the load duck curve during midday. The ramping service aims to smooth the load duck curve and to raise its nadir. For example, IRENA [93] describes the "flexible ramping product" (FRP), recently implemented by some independent system operators in the United States, which allows the system operator to procure enough ramping capability in the system and avoid any power imbalance that the high ramping requirements of variable renewable energy could cause.

Both the services of the category renewable energy shifting and operational management may contribute to transmission and distribution grid expansion deferral. But the services of the category operational management may be used directly to achieve such a goal, whereas services of the category renewable energy shifting are only indirectly contributing to this goal. For example, a BESS can be integrated as "virtual power line" instead of a corresponding grid expansion. A corresponding design of such a system is rather easy to accomplish, compared to an estimation of how services for renewable energy shifting have to be coordinated in order to prevent congestion of the grid.

3.3.6 Trading Services

Besides system services, Fig. 3.7 lists trading service as second sub category of services provided by BESS. Energy arbitrage has already been mentioned as possibility to generate revenues for the owner of a BESS. A common way of performing energy arbitrage in energy markets is by

buying or selling electricity in day-ahead markets and then taking an offset position in intra-day and real-time markets. Another possibility is to use the price spread during the day to perform energy arbitrage by charging when the price is low and discharging when the price is high. The goal of performing energy arbitrage is to gain revenues. However, such an operation automatically counteracts the peaks and valley of variable renewable energy, since high prices are coupled with low generation, leading BESS performing energy arbitrage to discharge, and low prices are coupled with high generation, leading BESS performing energy arbitrage to charge, storing the surplus power of variable renewable energy. A high amount of BESS performing energy arbitrage automatically contributes to a better price stability, but also leads to a lower price spread, making the business case of performing energy arbitrage less attractive.

Trading services are also essential to the restoration of the energy reservoir of the BESS, while it provides system services. It is not possible to coordinate the provision of system services in a way that an ideal exploitation of the energy reservoir of the BESS is possible. Therefore, sometimes it is necessary to restore the energy reservoir by corresponding transactions on the energy market.

Traditionally, regulators have been using security of supply mechanisms to procure sufficient capacity in order to maintain a certain level of reliability. However, these mechanisms include only thermal and hydro power plants. With increasing amount of variable renewable energy however, these mechanisms should be redesigned to allow the participation of new technologies that could contribute to system reliability more efficiently and avoid investment in unnecessary peaking plants. Fig. 3.7, therefore lists the provision of firm capacity on a capacity market as further trading service of BESS. IRENA [93] gives the United Kingdom as an example, where storage systems are allowed to participate on a capacity market, that, however, is currently not in operation.

3.3.7 Other Services

There are other services from the literature that are not shown in Fig. 3.7. In the following list several of such examples are listed:

- Services to improve power quality, which include the compensation of short-term voltage spikes of dips or the reduction of harmonics in current and voltage. For example, mentioned in [63].
- Services for damping oscillations, for example, sub-synchronous resonances. For example, mentioned in [63] and investigated in [191].
- Services for reducing deterministic frequency deviation. For example, mentioned in [14].

Furthermore, other services that can be found in the literature are often related to a more application-specific topic. For example, the service “Transmission and Distribution Upgrade Deferral” mentioned in [66] seeks the goal to prevent the grid from being expanded. However, the corresponding service the BESS provides in order to fulfill this goal can be found in Fig. 3.7 as congestion management. A similar example can be found for the charging management of electric cars, whose goal is also to prevent the grid from being overloaded, but which is also fulfilled by the service congestion management. As third such example a service “load shifting” can be mentioned. Therefore, for several services in Fig. 3.7 a more detailed distinction may be possible to be created for which explicit application they are used.

4 Investigation of Selected Functions That Implement Services Provided by BESS

Chp. 3.3 lists all services that BESS can provide in general. This chapter focuses on selected services out of this list, which are investigated in more detail. For each service the explicit implementation in BESS is described and investigated. Such an explicit implementation of a service in a BESS is referred to as "function". A service is considered to have an abstract definition, whereas a function has a detailed definition of its implementation in a system. The implementation of a service as a function may differ between systems. For example, the service FCR can be implemented as a function with or without the use of a frequency deadband. Functions therefore describe in detail how a service is executed. Besides such functions that are executing services, there may be additional functions that are necessary to operate a BESS or to guarantee the continuous execution of services. For example, the management of the SoC is one such function.

For each of the selected services investigated in this chapter, a general description of its implementation as a function in a BESS is given in addition to the requirements that may arise, e.g. by regulatory prescriptions. Based on simulations and field measurements each of the selected functions is investigated.

4.1 Frequency Containment Reserve

BESS providing FCR count among the FCR providing units with limited energy reservoir (LER-units). In the following chapters the special requirements on LER-units are summarized, the prequalification process is explained, the possibilities for SoC-management are discussed and simulation results as well as field measurements are presented.

This chapter incorporates investigations and analyses published in paper [122] and in paper [121].

4.1.1 Requirements for LER-Units

In addition to the general requirements of FCR, which are defined in Chp. 2.3.2, there are a number of other requirements that BESS must meet in order to provide FCR. Article 154 of the SOGL allows the definition of additional requirements for FCR providing groups. For the regional group CE, these additional requirements are defined in article 3 in [50]. Those specific requirements for FCR providing units with limited energy reservoir are listed below.

(a) To have enough power capabilities for the SOC management, LER-units in stand-alone operation shall have a ratio of rated power to prequalified FCR-power of at least 125 % and a sufficient energy reservoir dimensioning of at least 1 MW h[1] per 1 MW prequalified FCR-power to be sufficient to cover a $\Delta f = \pm 200\,\text{mHz}$ for at least $T_{crit} = 30\,\text{min}$[2] in positive and negative direction.

[1] The value depends on the outcome of a cost-benefit analysis which has to be carried out by every TSO according to article 156 (9,10,11) of the SOGL. Values in a range of $(0.5, 1)$MW h can be expected.

[2] The value depends on the outcome of a cost-benefit analysis which has to be carried out by every TSO according to article 156 (9,10,11) of the SOGL. Values in a range of $(0.25, 0.5)$h can be expected.

(b) Any lead time for the charging process needs to be considered for the energy management.

(c) The energy management of FCR providing units shall not rely on overfulfillment of activation.

(d) Converter-based units shall ensure that close to the limit of their usable SoC, the remaining capacity is sufficient for keeping its reactivity on short-term frequency deviations. To do so, these units shall switch from "normal mode" to "reserve mode" 15 min before exhaustion of the energy reservoir due to maximum FCR provision in one direction. In reserve mode the units shall only react on the short-term frequency deviation $\overline{\Delta f}_{0-mean}$, which is defined by

$$\overline{\Delta f}_{0-mean}(t) = \Delta f(t) - \frac{1}{n(t-15\,\mathrm{min})} \sum_{i=0}^{n(t-15\,\mathrm{min})} \Delta f(t-t_i) \tag{4.1}$$

with n as the number of discrete measurement points of the frequency deviation Δf during a period of 15 min.

4.1.1.1 Minimum Energy Reservoir and Allowable Working Area of LER-Units

By defining the energy reservoir with E and the prequalfified FCR-power with X_{FCR}, the first requirement (a) listed above leads to $\frac{E}{X_{FCR}} > 1\,\mathrm{h}$ (assuming a delivery period of 30 min) respectively $\frac{E}{X_{FCR}} > 0.5\,\mathrm{h}$ (assuming a delivery period of 15 min). The requirement of a delivery period of 30 min is called "30 min-criterion" and the requirement of a delivery period of 15 min is called "15 min-criterion". Any of these two criteria leads to a permissible Working Area (WA) of the SoC, which is shown in Fig. 4.1. The figure also shows the SoC-limits to switch from normal mode to reserve mode according to point (d) above. The SoC-borders to switch to reserve mode are identical to the SoC-borders of the 15 min-criterion.

4.1.1.2 Dimensioning the Energy Reservoir in the Working Area

The point (a) of the list above indirectly defines the defines the allowable working area of LER-units based on the maximum steady state frequency deviation of $\Delta f = \pm 200\,\mathrm{mHz}$ and the energy reservoir. In order to establish exact conditions when the work area can be left, a distinction is made between the states "normal state", "alert state" and "emergency state", which are defined as follows according to [60]:

- normal state: means a situation in which the system is within operational security limits in the N-situation[3] and after the occurrence of any contingency from the contingency list, taking into account the effect of the available remedial actions
- alert state: means the system state in which the system is within operational security limits, but a contingency from the contingency list has been detected and in case of its occurrence the available remedial actions are not sufficient to keep the normal state
- emergency state: means the system state in which one or more operational security limits are violated

In normal state, the SoC must be kept in the working area. When the alert state or emergency state is reached, the work area can be left. This is the case if Δf meets one of the following conditions

- $|\Delta f| > 200\,\mathrm{mHz}$

[3] "N-situation" means the situation where no transmission system element is unavailable due to occurrence of a contingency.

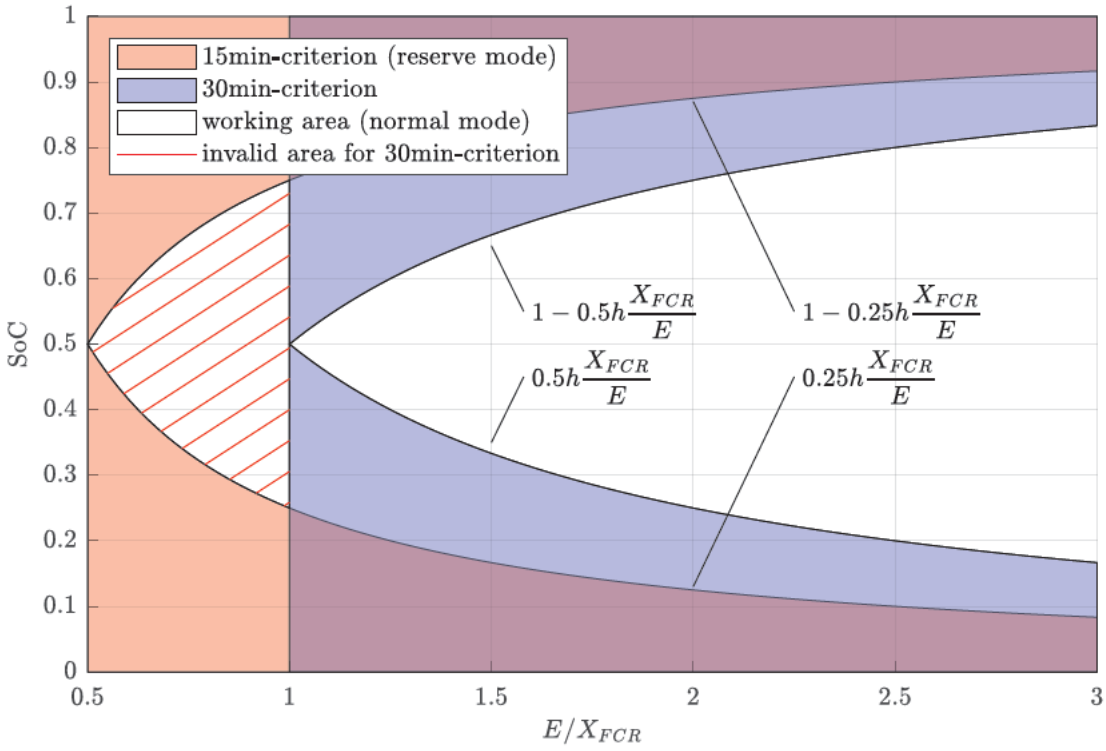

Figure 4.1: Minimum energy reservoir and allowable working area of LER-units. Related to BESS, the relevant limits are actually based on the State of Energy (SoE), since the SoC is based on the capacity, which differs from the energy content of a BESS. However, since the descriptions relate to LER-units in general, the SoC is used as general indicator of the actual energy state.

- $|\Delta f| > 100\,\text{mHz}$ for 5 min
- $|\Delta f| > 50\,\text{mHz}$ for 15 min

which are shown graphically in Fig. 4.2.

To guarantee the "30 min-criterion" (or the "15 min-criterion") the SoC-management has to keep the SoC inside the working area during normal state. Based on Fig. 4.2, worst case scenarios for a "previous FCR-call" in normal state can be identified, which can happen during a "pre-alert state phase". To enable the SoC-management to be able to handle such worst case scenarios, a minimum energy reservoir of the working area is necessary. In [3] a worst case frequency deviation of $\Delta f = 100\,\text{mHz}$ for 15 min is assumed. In this case the minimum energy reservoir in the working area has to be at least $2 \cdot X_{FCR} \cdot \frac{100\,\text{mHz}}{200\,\text{mHz}} \cdot 0.25\,\text{h}$. According to Fig. 4.2 a more strict worst case scenario would be a frequency deviation of $\Delta f = 200\,\text{mHz}$ for 5 min followed by a frequency deviation of $\Delta f = 100\,\text{mHz}$ for 10 min. Every TSO has the freedom to define such scenarios, which are relevant for dimensioning the working area. Because of point (a) in the list above, the rated power of a LER-unit has to be at least 125 % of the prequalified FCR-power. Therefore, worst case scenarios with frequency deviations below the standard frequency deviation of $\Delta f = \pm 50\,\text{mHz}$ do not affect the necessary minimum energy reservoir in the working area, because the SoC-management is capable of handling such situations by shifting the operating point correspondingly. Considering other regulatory requirements, a rated power larger than 125 % could be necessary for LER-units. For example, requirements on static voltage support may require the rated power to be larger.

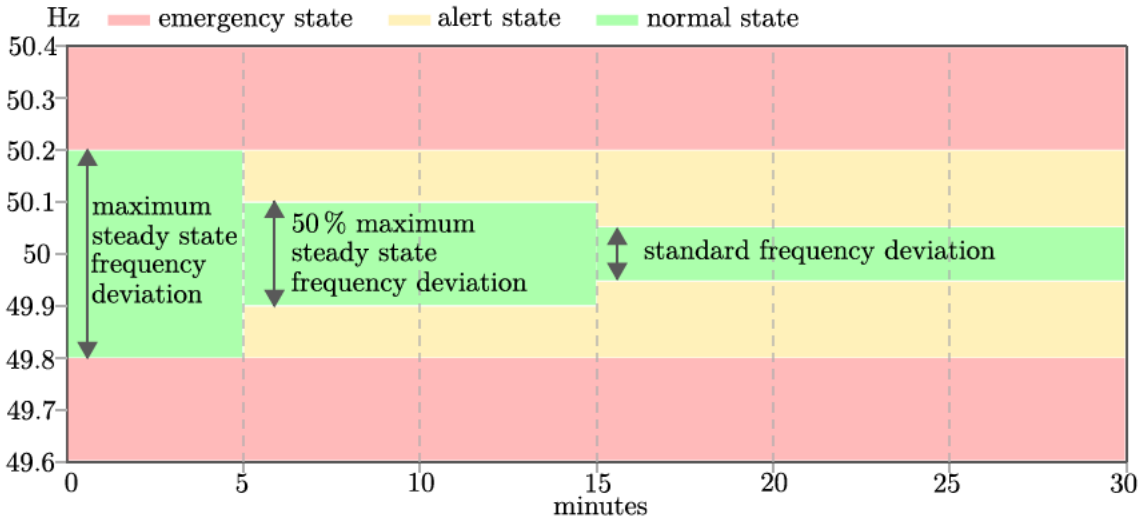

Figure 4.2: Definitions of frequency states in the regional group CE.

According to point (b) in the list above, a lead time for the charging process has to be considered. Similar to the worst case definition as described above, a lead time for activation of the SoC-management also affects the necessary minimum energy reservoir of the working area. A lead time T_{Lead} for the execution of an SoC-management operation to handle the standard frequency deviation of $\Delta f = \pm 50\,\text{mHz}$ contributes to the necessary minimum energy reservoir in the working area with an additional energy of $2 \cdot X_{FCR} \cdot \frac{50\,\text{mHz}}{200\,\text{mHz}} \cdot T_{Lead}$.

4.1.1.3 Dimensioning the Total Energy Reservoir of LER-units

Considering all aspects mentioned above, the necessary energy reservoir E of LER-units can be specified based on three points:

- the minimum energy reservoir according to the "30 min-criterion" (or "15 min-criterion"),
- the worst case scenario of a previous FCR-call,
- and any lead time to execute the SoC-management.

Based on these three points [3] calculates E according to Eq. (4.2):

$$E = X_{FCR} \cdot 2 \cdot \left[T_{crit} + max\left(\frac{100\,\text{mHz}}{200\,\text{mHz}} \cdot 0.25\,\text{h}, \frac{50\,\text{mHz}}{200\,\text{mHz}} \cdot T_{Lead} \right) \right]. \tag{4.2}$$

The necessary total energy reservoir under several assumptions for T_{crit} and T_{Lead} is shown in Fig. 4.3.

The dimensioning of the minimum energy reservoir according to Eq. (4.2) is based on the assumption of worst-case scenarios that are based on the definition of an alert state as defined in Chp. 4.1.1.2. However, there may be situations where the working area is exceeded without an alarm state occurring. An SoC-management which is executed with a power of $\frac{X_{FCR}}{4}$, as described in (a) in the list in Chp. 4.1.1, is capable of compensating a continuous frequency deviation whose mean value over a certain time has an absolute value of 50 mHz. Values above 50 mHz lead to an on-holding change of the SoC. Since an alert state is defined as the continuous exceedance of certain frequency deviation values, oscillations around the smallest value of 50 mHz may not count

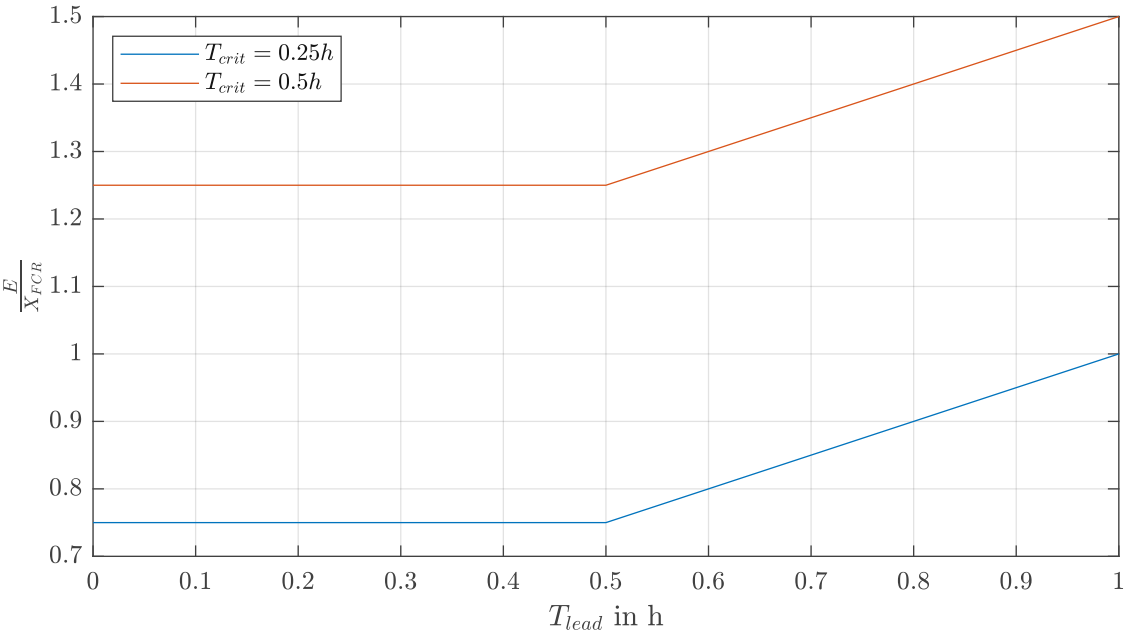

Figure 4.3: Necessary total energy reservoir of LER-units.

as alert state. Therefore, such oscillations may lead to situations where the working area if left without the requirements of an alert state to be fulfilled.

4.1.2 Prequalification Process for LER-Units

Besides the contractual prequalification process which includes the documentation of basic information about the FCR-providing unit (e.g. its affiliation to balance groups or its data connection to the TSO), the technical prequalification process includes the documentation on the integration of the FCR-providing unit in the network and its concept of operation.

The technical prequalification process also requires a certain accuracy of the frequency measurement system and the proof of correct dynamic behavior, proof of compliance with the deadband and proof of correct application of the parameterized droop via measurement protocols. For LER-units a proof for the total energy reservoir is necessary. While in Austria [11] only an indication of the total energy reservoir is to be made, in Germany [3], a measurement protocol is required which proves the available energy reservoir of the unit. For this measurement a (quasi-)standardized test named “Doppelhöckerkurve” is defined in [3]. Examples for the different measurement protocols are described in the following chapters and were generated based on the BESS described in Chp. 3.1 for a prequalified FCR-power of $X_{FCR} = 2\,\text{MW}$.

4.1.2.1 Measurement Protocol of the Dynamic Behavior and Droop

Fig. 4.4 shows the reaction of the BESS described in Chp. 3.1 to intentional shifts of the nominal frequency $f_n = \{49.8\,\text{Hz}, 50.2\,\text{Hz}\}$. According to Fig. 2.4 the preparation period has to be smaller than 2 s and the full activation time has to be smaller than 30 s. Assuming a tolerance band of 5 %, the full activation time to a frequency shift is 2 s and the preparation time is 0.5 s. Therefore, the requirements on the dynamic behavior are respected. The power steepness of the system can be calculated to 2 MW/s. The droop can be calculated to $\sigma = \frac{\Delta f/f_n}{\Delta P/S_n} = \frac{0.4\,\text{Hz}/50\,\text{Hz}}{4\,\text{MW}/2.5\,\text{MVA}} = 0.5\,\%/\%$.

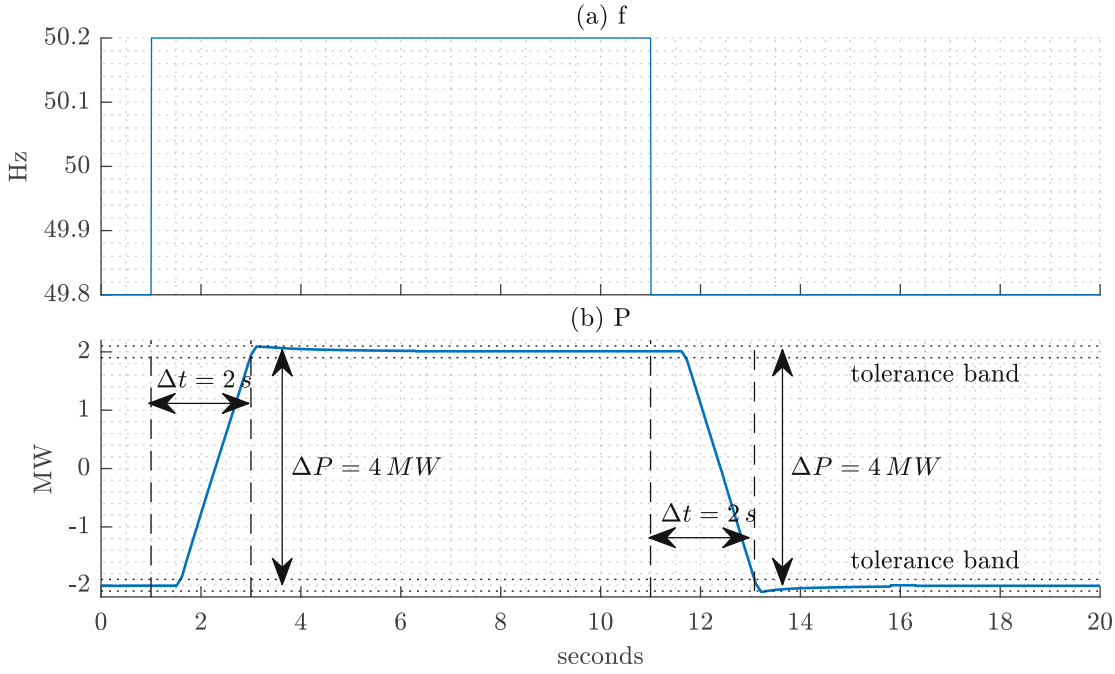

Figure 4.4: Measurement protocol of the dynamic behavior of the system described in Chp. 3.1. (a) shows the effective frequency signal which is generated by shifting the nominal frequency f_n. (b) shows the power output of the system.

4.1.2.2 Measurement Protocol To Prove the Compliance with the Frequency Deadband

Fig. 4.5 shows the measurement protocol of the system described in Chp. 3.1 to proof the reaction to frequency deviations inside the frequency deadband. According to Fig. 2.5 the frequency deadband is defined with $\Delta f = \pm 10\,\text{mHz}$. Fig. 4.5 shows that the system only reacts with a power output to frequency deviations outside the frequency deadband. Therefore, the requirements on the frequency deadband are respected.

4.1.2.3 Measurement Protocol of the "Doppelhöckerkurve"

The "Doppelhöckerkurve" is a (quasi-)standardized test that has been established among the TSO's to proof the droop, the dynamic behavior and the available energy reservoir of LER-units. It consists of two activations of the full prequalified FCR-power in 15 min-timeslots with a 15 min-pause between them. For LER-units, the test is followed by a third call of the full prequalified FCR-power until the maximum/minimum SoC of the BESS is reached. Fig. 4.6 shows the measurement protocol of the "Doppelhöckerkurve" of the BESS described in Chp. 3.1. The call of the full prequalified FCR-power is generated by shifting the nominal frequency f_n. Fig. 4.6(b) shows that the system reacts according to a droop of $\sigma = 0.5\,\%/\%$. Because the full activation of FCR-power is reached much faster than within 30 s the requirements on the dynamic behavior are met. According to Fig. 4.3 the necessary minimum energy reservoir of a LER-unit with a prequalified FCR-power of $X_{FCR} = 2\,\text{MW}$ is $E_{min} = X_{FCR} \cdot 1.25\,\text{h} = 2.5\,\text{MW h}$ under the assumption of $T_{crit} = 0.5\,\text{h}$ and $T_{Lead} = 0.5\,\text{h}$. Fig. 4.6(c) shows the energy exchanged with the grid during the "Doppelhöckertest". At the beginning of the test the system has the maximum SoC. The energy exchanged with the grid while discharging is lower than while charging, because losses on the lines and transformer between the BESS and the PCC arise. Therefore, to proof the system to have a

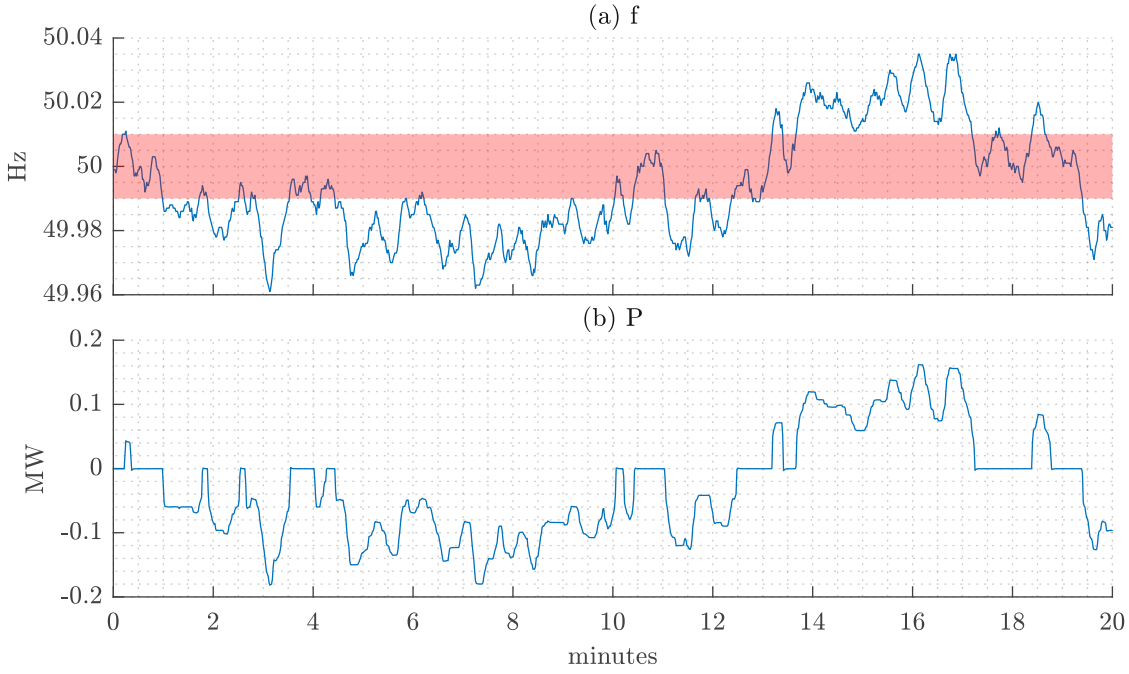

Figure 4.5: Measurement protocol to proof the compliance with the frequency deadband of the system described in Chp. 3.1.

larger energy reservoir than E_{min}, the energy while discharging the system has to be investigated. Fig. 4.6(c) shows that this requirement is met.

4.1.3 SoC-Management of LER-Units

In Chp. 4.1.1 the requirements on SoC-management were already summarized and discussed. The implementation of the SoC-management is discussed in the following.

Two different implementations of SoC-management are possible:

(a) SoC-management within balance groups,

(b) and SoC-management across balance groups.

The difference between the two implementations is the need to respect market rules. The SoC-management generates compensation energy, which can be compensated by other generators inside the balance group or can be announced on the energy market as the change of the balance group's schedule. In the second case the corresponding market rules have to be respected. In Austria, these market rules are summarized in [40]. The frequency deviations are not predictable, therefore, the charging or discharging actions of the SoC-management to keep the SoC-level inside the allowable working area are also not predictable. As a consequence of this, schedules of the SoC-management can only be tendered via intra-day-market. These intra-day-transactions have to be announced a specified lead time before execution, which is the first market rule that has an influence on the implementation of the SoC-management. A second market rule that has such an influence is the form of the schedules, which are based on a quarter-hourly basis. These two market rules result in a worst case delay of a necessary SoC-management which composes of the lead time for announcement of a new schedule T_{ann} and the maximum delay that results from the quarter-hourly

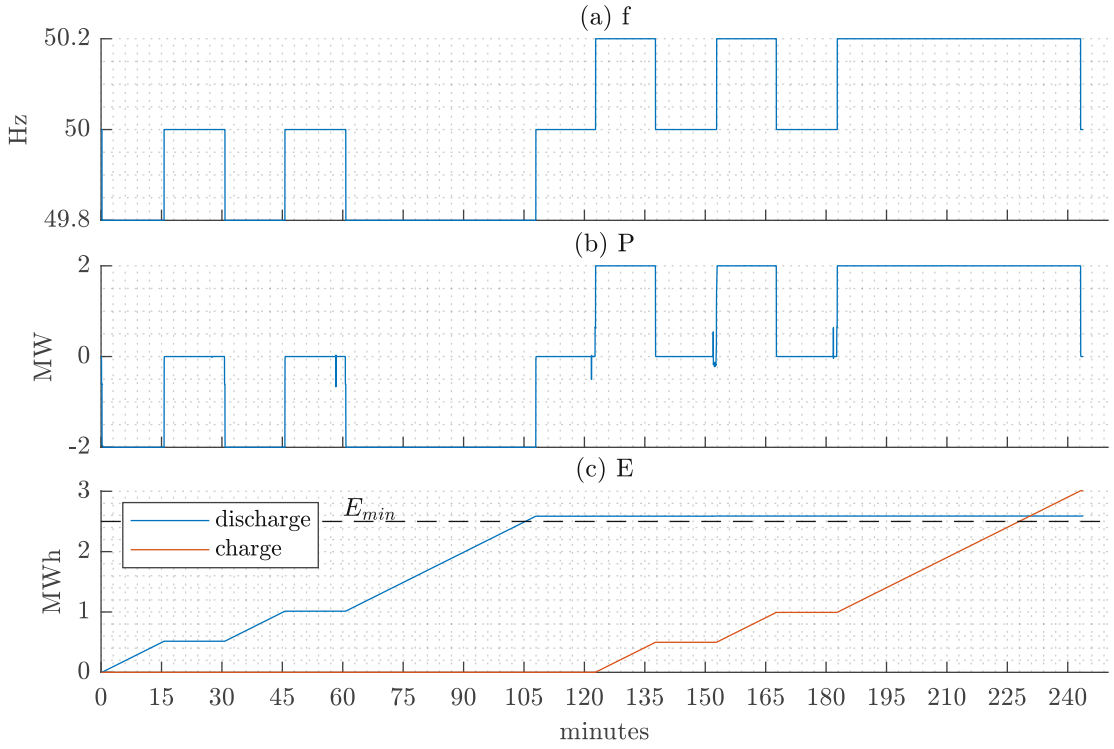

Figure 4.6: Measurement protocol of the "Doppelhöckerkurve" of the system described in Chp. 3.1 to verify the energy reservoir necessary to fulfill the 30-minutes-criterion, which is extended by a third hump in order to measure the total energy reservoir, additionally to the requirements based on the 30-minutes-criterion. (a) shows the frequency signal which is generated by shifting the nominal frequency f_n. (b) shows the power output of the system. (c) shows the energy that is exchanged with the grid and E_{min} indicates the minimum necessary energy reservoir according to Fig. 4.3 with $T_{crit} = 0.5\,\text{h}$ and $T_{Lead} = 0.5\,\text{h}$.

basis. This maximum delay is 15 min. Therefore, the total lead time is $T_{Lead} = T_{ann} + 0.25\,\text{h}$. A similar approach is described by Henninger et al. [81].

An indicator of how much energy is required for SoC-management while providing FCR is the cumulative frequency deviation. Fig. 4.7 shows the cumulative frequency deviation for the years 2014 – 2018. Fig. 4.7 shows the positive and negative cumulative frequency deviation as well as the addition of these two. While the positive frequency deviation requires a LER-unit to discharge in order to restore the SoC, the negative frequency deviation requires a LER-unit to charge in order to restore the SoC. Fig. 4.7 therefore shows a tendency of LER-units to charge, since the frequency deviation tends to be negative.

Assuming a LER-unit with an energy-to-power ratio of 1 and the "30 min-criterion" to be prescribed, the cumulative frequency deviations in Fig. 4.7, multiplied by $\frac{X_{FCR}}{0.2\,\text{Hz}}$ results in the required energy for the SoC-management per year. For higher energy-to-power ratios, the required energy may be diminished since the working area according to Fig. 4.1 enables the possibility of positive and negative cumulative frequency deviations to cancel each other out while the SoC stays within the working area.

For the sake of simplicity the state of energy (SoE) is treated as equivalent to the SoC for the following investigations. For this reason the battery voltage U_B is assumed to be constant, which

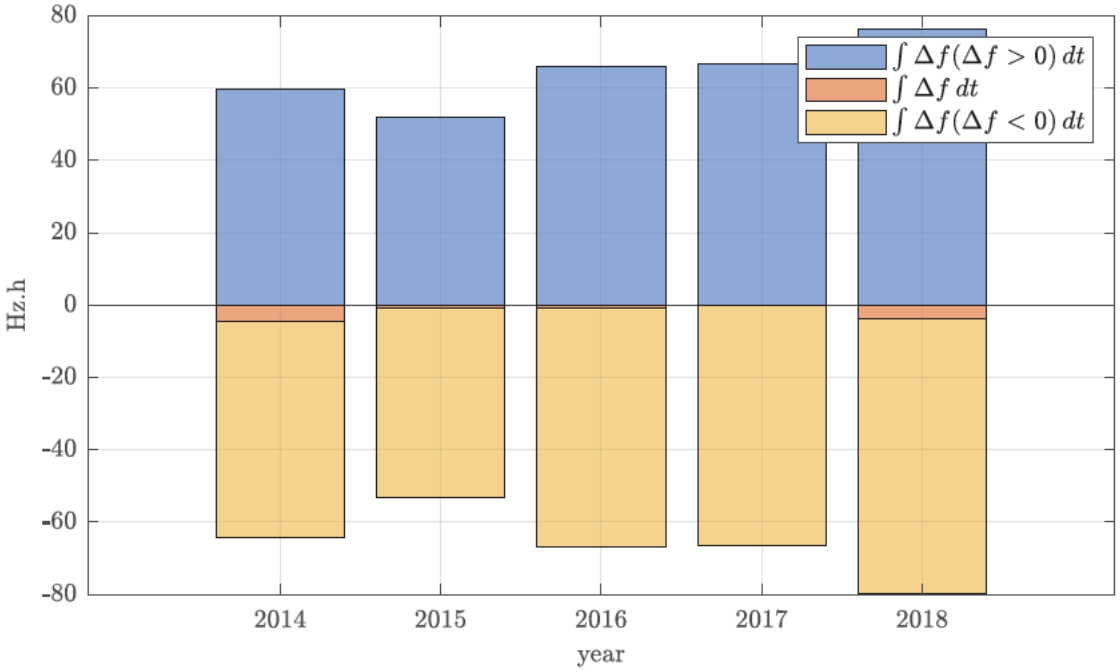

Figure 4.7: Cumulative frequency deviation for the years 2014 – 2018, with $\Delta f = f - f_n$.

results to:

$$SoE(t) \overset{U_B=const}{=} SoC(t) = SoC(T_1) + \frac{1}{E}\int_{T_1}^{t} P(\tilde{t})\, d\tilde{t}. \tag{4.3}$$

4.1.3.1 SoC-Management within Balance Groups

The SoC-management starts to charge or discharge the BESS to keep the SoC inside the SoC-band that equals the working area defined in Fig. 4.1. The energy that is necessary for the charging or discharging process can be compensated by another generation unit inside the balance group. Therefore, no market rules have to be respected. The SoC-management is allowed to start any time and is allowed to be active as long as necessary. An SoC-management that respects the allowable SoC-band defined in Fig. 4.1, which is related to the "30 min-criterion" (or "15 min-criterion"), can be described with the help of SoC-limits which act as activation trigger for the SoC-management. Because the SoC-management within balance groups allows the instant execution of charging or discharging actions, these SoC-limits are identical to the ones defined by the "30 min-criterion" (or "15 min-criterion"). After the SoC exceeds these SoC-limits, the charging or discharging actions are triggered and activated as long as a certain SoC-level is reached. This SoC-level is defined as target-SoC SoC_T. The power for these charging and discharging actions has to be chosen with a power of at least $\frac{X_{FCR}}{4}$. According to Chp. 4.1.1, with such a choice a constant standard frequency deviation of $\Delta f = \pm 50\,\text{mHz}$ can be compensated. A corresponding mathematical description for the implementation of such a SoC-management is given below. The SoC-band that results from the "30 min-criterion" (or "15 min-criterion") is described by

$$\mathbf{SoC_B} = \begin{pmatrix} SoC_{B,1} \\ SoC_{B,2} \end{pmatrix} = \begin{pmatrix} \frac{X_{FCR} \cdot T_{crit}}{E} \\ 1 - SoC_{B,1} \end{pmatrix}. \tag{4.4}$$

The activation of the SoC-management is described via $a_{SoC,1}$ and $a_{SoC2,2}$. $a_{SoC,1}$ describes if the SoC-level is inside the SoC-band SoC_B:

$$a_{SoC,1} = \begin{cases} 0, & SoC_{B,1} < SoC < SoC_{B,2}, \\ 1, & else \end{cases}. \tag{4.5}$$

$a_{SoC,2}$ describes the behavior of a flip-flop. After the SoC-level exceeds SoC_B, the SoC-management is started with a power of P_{SoC} until SoC_T is reached:

$$a_{SoC,2}(t) = \begin{cases} 1, & [a_{SoC,2}(t - \Delta t) = 1 \wedge SoC \neq SoC_T] \vee a_{SoC,1} = 1, \\ 0, & else \end{cases}. \tag{4.6}$$

The power P_{SoC} of the SoC-management within balance groups is defined by

$$P_{SoC} = a_{SoC,2} \cdot \frac{X_{FCR}}{4} \cdot \begin{cases} 1, & SoC < SoC_T, \\ -1, & SoC > SoC_T \end{cases}. \tag{4.7}$$

4.1.3.2 SoC-Management across Balance Groups

Because of market rules, a time delay between announcement and actual execution of schedules to fulfill SoC-management arises when doing the SoC-management across balance groups. According to Chp. 4.1.1.2, during this time delay a worst case frequency deviation of ±50 mHz can be assumed. To guarantee that after such a lead time the SoC is still inside the working area according to Fig. 4.1 the following SoC-levels are defined as trigger levels to announce a new schedule for SoC-management:

$$\mathbf{SoC_B} = \begin{pmatrix} SoC_{B,1} \\ SoC_{B,2} \end{pmatrix} = \begin{pmatrix} \frac{X_{FCR} \cdot \left(T_{crit} + \frac{50\,\text{mHz}}{200\,\text{mHz}} \cdot (T_{ann} + 0.25\,\text{h})\right)}{E} \\ 1 - SoC_{B,1} \end{pmatrix}. \tag{4.8}$$

The announcement of the SoC-management for a new schedule is described via $a_{SoC,1}$:

$$a_{SoC,1} = \begin{cases} 0, & SoC_{B,1} < SoC < SoC_{B,2}, \\ 1, & else \end{cases} \tag{4.9}$$

The trigger of an announcement is defined by

$$T_t = max\left(t | a_{SoC,1} = 1\right). \tag{4.10}$$

The time of the actual execution of a schedule after an announcement would be T_{st}, if market rules for the discretized execution scheme of schedules are neglected:

$$T_{st} = T_t + T_{ann}. \tag{4.11}$$

But as already mentioned, market rules allow changes of schedules only on a quarter-hourly basis. For this reason, time intervals are defined with $I_m = (a_m, b_m) := \{t | a_m \leq t < b_m, a_{m+1} \geq b_m, m \in \mathbb{N}\}$. The duration of a time interval is $\Delta I_m = b_m - a_m$. Market rules require the start of time intervals during a day to be $I_m(a_m) = \{00{:}00{:}00,\ 00{:}15{:}00,\ ...,\ 23{:}45{:}00\}$ o'clock with $\Delta I_m = 15\,\text{min}$. Therefore, the time of the actual execution of a schedule is $T_{st,d}$ and is the beginning of the next time interval $I_m(a_m)$ after T_{st}:

$$T_{st,d} = t | \{t \geq T_{st}, t = I_m(a_m), m \in \mathbb{N} : m < 4/\text{h} \cdot 24\,\text{h}\}. \tag{4.12}$$

The case may arise that during the lead time, the SoC returns into the SoC-band SoC_B. Since after announcing a schedule, it has to be executed accordingly, an activation function Π is defined to guarantee this:

$$\Pi = \begin{cases} 1, & \int_{t-T_{st,d}-\Delta I_m}^{t} a_{2,1}(\tilde{t})\, d\tilde{t} > 0, \\ 0, & else \end{cases}. \tag{4.13}$$

The power used for SoC-Management is limited to a certain amount X_{SoC}. Dependent on the energy reservoir and the SoC-target SoC_T which is sought, this power may not be sufficient to reach SoC_T in one time interval. Therefore, the duration of a schedule is defined with rep as the number of repetitions:

$$rep = \left\lceil \frac{|SoC(T_t) - SoC_T| \cdot E}{X_{SoC} \cdot \Delta I_m} \right\rceil. \tag{4.14}$$

If the required energy to reach SoC_T is smaller than $X_{SoC}\Delta I_m$, power will be reduced accordingly, otherwise X_{SoC} is used for rep repetitions of the schedule:

$$\chi = \begin{cases} X_{SoC}, & rep > 1, \\ \frac{|SoC(T_t) - SoC_T| \cdot E}{\Delta I_m}, & else \end{cases}. \tag{4.15}$$

The power P_{SoC} of the SoC-management across balance groups is defined by

$$P_{SoC} = \chi \sum_{k=0}^{rep-1} \Pi(t - k\Delta I_m) \begin{cases} 1, & SoC < SoC_T, \\ -1, & SoC > SoC_T \end{cases}. \tag{4.16}$$

4.1.3.3 Comparison of SoC-Management Implementations

To illustrate how the two implementations of SoC-management work, the following test case is assumed. A BESS is providing FCR with $X_{FCR} = 1\,\mathrm{MW}$. The dimensioning of the energy reservoir is assumed to fulfill the requirements according to Eq. (4.2), with $T_{crit} = 0.5\,\mathrm{h}$, $T_{ann} = 0.25\,\mathrm{h}$ and $T_{lead} = 0.5\,\mathrm{h}$. Therefore, the energy reservoir is assumed to be $E = 1.375\,\mathrm{MW\,h}$, which lies above the requirements. According to Eq. (4.4), the SoC-levels $\mathbf{SoC_B}$ to start SoC-management within balance groups are

$$\mathbf{SoC_B} = \begin{pmatrix} SoC_{B,1} \\ SoC_{B,2} \end{pmatrix} = \begin{pmatrix} 36.36\,\% \\ 63.64\,\% \end{pmatrix} \tag{4.17}$$

while according to Eq. (4.8) the SoC-levels to trigger an announcement of a new schedule of SoC-management across balance groups are

$$\mathbf{SoC_B} = \begin{pmatrix} SoC_{B,1} \\ SoC_{B,2} \end{pmatrix} = \begin{pmatrix} 45.45\,\% \\ 54.55\,\% \end{pmatrix}. \tag{4.18}$$

Fig. 4.8 shows the behavior of the two implementations of SoC-management, assuming a constant frequency of $f = 49.75\,\mathrm{Hz}$. The start SoC of the BESS is 50 % and decreases as a consequence of providing FCR with $P_{FCR} = -X_{FCR}\frac{\Delta f}{200\,\mathrm{mHz}} = -125\,\mathrm{kW}$ caused by the frequency deviation Δf.

Fig. 4.8(b,c) shows that SoC-management across balance groups announces a schedule at the time T_t when the SoC reaches $SoC_{B,1}$ and respects a lead time of T_{ann}. Because at the time T_{st}, the time is not an exact quarter-hour time stamp the schedule is executed at the next quarter-hour time stamp, at the time $T_{st,d}$. According to Eq. (4.14), the schedule lasts for 0.5 h. The same procedure starts one hour later in the shown example.

Fig. 4.8(d,e) shows that SoC-management inside a balance group starts immediately when the SoC reaches $SoC_{B,1}$ and is active as long as the SoC-target $SoC_T = 50\,\%$ is reached.

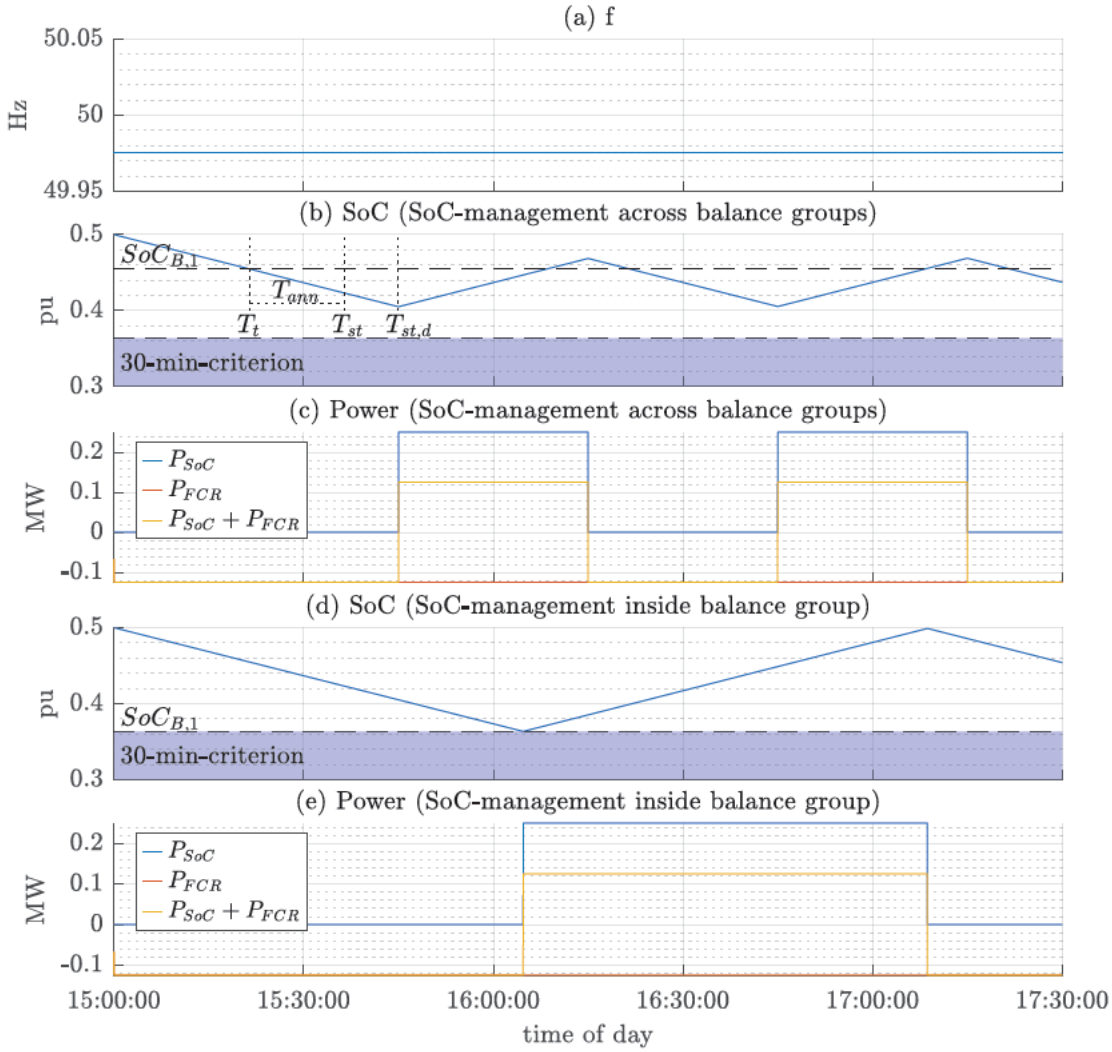

Figure 4.8: Example to illustrate the behavior of the two implementations of SoC-management intra and inter balance group.

4.1.4 Degrees of Freedom (DoF) during Provision of FCR

Usually, the SoC-management causes costs because charging outweighs discharging actions. Therefore, in Germany a set of DoF [2] during provision of FCR is defined. These DoF are designed not to act against the load-frequency control but to overfulfill their requirements described in Chp. 2.3.2. The DoF are involving the frequency deadband, the overfulfillment of the bid size and the variation of the full activation time. Fig. 4.9 shows the allowable ranges of the DoF "deadband" and the DoF "overfulfillment" and Fig. 4.10 shows the allowable range of the "steepness". The DoF deadband allows the provision of FCR within the frequency deadband, as long as the provision follows a continuous linear characteristic and doesn't counteract to the frequency deviation. A prerequisite for the use of this DoF is a sufficiently accurate frequency measurement. Otherwise, the possibility would arise that the FCR provision counteracts the frequency deviation what should be strictly avoided. The DoF overfulfillment allows to provide up to 20 % more FCR than according to the actual bid size.

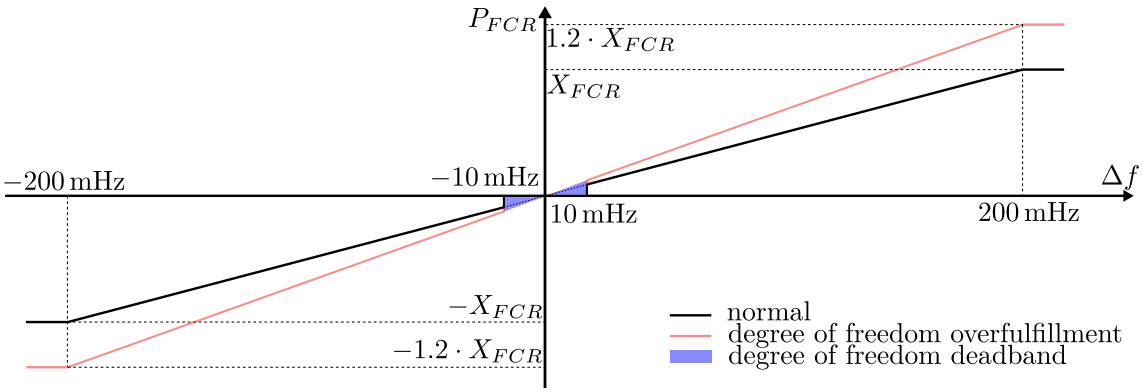

Figure 4.9: DoF "deadband" and "overfulfillment" (according to [2]) based on the load reference system.

The DoF steepness allows to vary the full activation time, dependent on the actual SoC, as long as the basic requirements on FCR are respected.

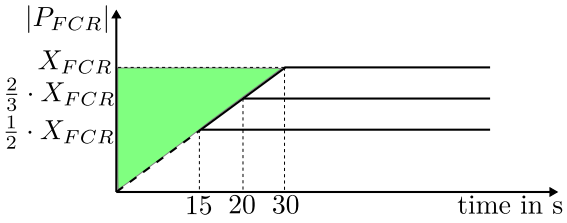

Figure 4.10: DoF "steepness" (according to [2]).

One operation strategy to use the DoF to reduce SoC-management would be to activate the DoF dependent on the SoC. By doing so, the range of overfulfillment, which is provided by the DoF, can be exploited to achieve a faster return of the SoC to the SoC-target SoC_T, solely through the provision of FCR and not by explicit activation of SoC-management. It can be seen as a function $P_{FCR}(f, SoC)$, while the normal provision of FCR is a function $P_{FCR}(f)$. A more detailed description of such an operation strategy is given in Chp. 4.1.5. Other operation strategies to use the DoF are discussed in [85] and include strategies like "maximize discharging", "minimize cycles" or "maximize charging".

4.1.5 Mathematical Description of FCR and DoF

The behavior of FCR, including the optional DoF, can be described mathematically by a set of parameters

$$\mathbf{X} = \{X_1, X_2, ..., X_8\} \tag{4.19}$$

and the frequency f as control variable for the resulting active power output according to Eq. (4.20). $P_{SR,FCR}$ is defined as the statically requested active power and equals the static operating point of FCR according to Fig. 4.9:

$$P_{SR,FCR} = \mathrm{f}(\mathbf{X}, f(t)). \tag{4.20}$$

The dynamic power output of can be described by Eq. (4.21), which is called the dynamically requested power and represents the behavior according to Fig. 4.10:

$$P_{DR,FCR} = \mathrm{f}(\mathbf{X}, P_{SR,FCR}, t). \tag{4.21}$$

The necessary parameters $\mathbf{X}$ to describe FCR are summarized in Tab. 4.1.

Table 4.1: Description of the parameters $\mathbf{X}$ of FCR.

parameter	description	parameter range
$X_1 = X_{FCR}$	prequalified FCR-power	$\{\mathrm{x} \in \mathbb{N} \vert \mathrm{SoC_{B,1}} < \mathrm{SoC_{B,2}}\}$ MW
X_2	frequency deviation deadband	10 mHz
X_3	full activation frequency deviation	200 mHz
X_4	normal full activation time (DoF inactive)	30 s
X_5	minimum full activation time (DoF active)	1 s
X_6	activation of DoF “deadband”	$\{0, 1\}$
X_7	activation of DoF “overfulfillment”	$\{0, 1\}$
X_8	activation of DoF “steepness”	$\{0, 1\}$

Assuming an operation strategy of the DoF as described in Chp. 4.1.4, the corresponding mathematical description can be given as follows. Based on the parameters in Tab. 4.1, the statically requested power of Eq. (4.20) can be defined by

$$P_{SR,FCR} = X_1 \cdot \frac{\Delta f}{X_3} \cdot p_{DoFof} \cdot \begin{cases} 1, & |\Delta f| > X_2, \\ a_{DoFdb}, & else \end{cases} \tag{4.22}$$

and the dynamically requested power of Eq. (4.21) can be defined by

$$P_{DR,FCR}(t) = P_{DR,FCR}(t - \Delta t) + \dot{P}_{DoFst} \cdot \begin{cases} \Delta t, & P_{DR,FCR}(t - \Delta t) \leq P_{SR,FCR}, \\ -\Delta t, & P_{DR,FCR}(t - \Delta t) > P_{SR,FCR}, \\ 0, & else \end{cases} \tag{4.23}$$

where p_{DoFof}, a_{DoFdb} and $\dot{P}_{DoFst}$ represent the influence of the DoF on the static and dynamic behavior of FCR as shown in Fig. 4.9 and Fig. 4.10 and Δt represents an infinitesimally small time range. As described in Chp. 4.1.4, the DoF are to be used in a way not to act against the load-frequency control. A corresponding operation strategy, also described in Chp. 4.1.4, lets become the DoF active only when it is beneficial for the stabilization of the grid frequency. Such a beneficial activation can be described by

$$a_{ben} = \begin{cases} 1, & (\Delta f > 0 \wedge SoC < SoC_T) \vee (\Delta f < 0 \wedge SoC > SoC_T), \\ 0, & else \end{cases} \tag{4.24}$$

which represents the operation strategy of the DoF.

With the help of a_{ben} and the parameters of Tab. 4.1, p_{DoFof}, a_{DoFdb} and $\dot{P}_{DoFst}$ can be described as follows. When activated by the parameter $X_6 = 1$, the DoF “deadband” becomes active, when it is beneficial for frequency stabilization, which is described via a_{ben}:

$$a_{DoFdb} = X_6 \cdot a_{ben}. \tag{4.25}$$

When activated by the parameter $X_7 = 1$, the DoF “overfulfillment” becomes active identically to the DoF “deadband”:

$$p_{DoFof} = X_7 \cdot (1 + 0.2 \cdot a_{ben}). \tag{4.26}$$

It is assumed that the amount of overfulfillment is fixed to a value of 120 % as shown in Fig. 4.9.

When activated by the parameter $X_8 = 1$, the DoF "steepness" utilizes a power gradient based on the normal full activation time X_4, when a dynamic overfulfillment is counterproductive for frequency stabilization and a minimum full activation time X_5, when a dynamic overfulfillment is beneficial for frequency stabilization:

$$\dot{P}_{DoFst} = X_8 \cdot \begin{cases} \frac{X_1}{X_5}, & a_{ben} = 1, \\ \frac{X_1}{X_4}, & else. \end{cases} \tag{4.27}$$

4.1.6 Reducing Losses during Provision of FCR

The efficiency of a system is defined by the ratio of the power delivered at the output and the power absorbed from the input. The losses in the conversion process consist of losses by switching or conduction of the semiconductors and ancillary systems such as drive, protection or signaling circuits. The total losses composition of a converter varies in function of its operating points. For low power levels, losses in the driving circuits of the switches may be more significant and also approximately constant. As power level increases, losses related to switching and conduction of semiconductors, become more significant [36].

During provision of FCR a BESS generates losses, which can be divided into standby losses (e.g. for the control system or the heating and cooling system) and conversion losses, which are dependent on the actual operating point. In the partial load range of the BESS and its converters, the efficiency is rather small and the conversion losses increase. Since BESS usually consist of several subunits, it is possible to only activate the number of subunits that are necessary to cover the actual operating point. This increases the efficiency (and reduces the conversion losses) of the individual subunits and reduces the standby losses of the remaining deactivated subunits. Fig. 4.11 shows the duration curves of the frequency deviation for the years 2014 – 2018 in order to illustrate the potential of loss reduction. The operating point that arises from the provision of FCR is depending on the frequency deviation. Assuming four subunits with equal nominal power, a low frequency deviation, therefore can be covered by a subset of the four subunits. Fig. 4.11 shows three levels of the frequency deviation at 50 mHz, 100 mHz and 150 mHz, which correspond to the potential levels of operating power for FCR of $\frac{1}{4}X_{FCR}$, $\frac{1}{2}X_{FCR}$ and $\frac{3}{4}X_{FCR}$ that can be covered by a subset of one, two or three of the four subunits. Fig. 4.11 illustrates for these three levels that they are exceeded only for a limited amount of the time during a year: 2.1 % for the level of 50 mHz, 0.03 % for the level of 100 mHz and 0.0003 % for the level of 150 mHz.

Overall the total efficiency of the BESS increases when only activating the number of subunits required to cover the actual operating point. For example, Fig. 4.11 shows that only 1.9 % of the time during the years 2014 – 2018 more than one subunit is required to cover the operating point that arises by the provision of FCR.

A similar approach may be used for virtual BESS consisting of many smaller BESS that are geographically distributed. By combining the smaller BESS to a virtual BESS makes it possible to provide FCR, which requires a minimum power capability of 1 MW and can only be achieved by such a combination. In [157] and [158] algorithms are presented that are capable to dispatch the contracted FCR power to the single BESS within the virtual BESS in a way that the overall efficiency of the virtual BESS increases. A central control instance dispatches the corresponding setpoints every 15 min via a communication link. The number of activated BESS within the virtual BESS is determined by frequency clustering. Frequency ranges are defined and correspond to an appropriate number of BESS to cover the corresponding FCR demand. The setpoints of the single BESS are determined based on their individual SoC. The higher the SoC of an individual BESS, the higher the corresponding setpoint of this BESS. Such an approach is generally described in the patent [192]. In the following descriptions, a similar approach is applied for a single BESS,

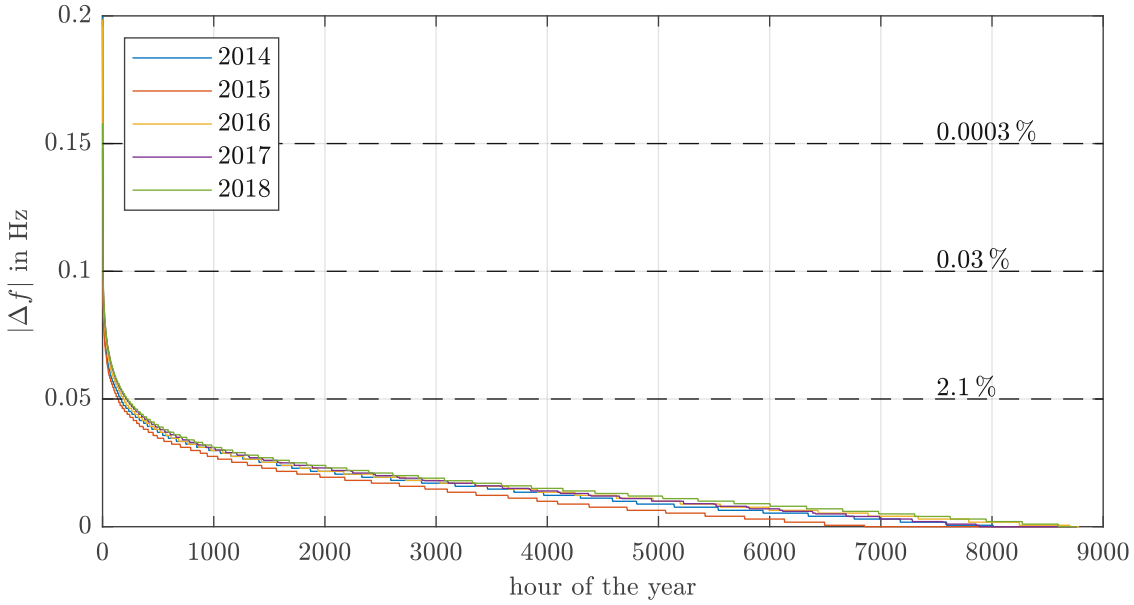

Figure 4.11: Duration curves of the frequency deviation for the years 2014 – 2018. Percentage calculations are based on mean values of the frequency deviations for all years.

consisting of several subunits that are geographically concentrated in a single BESS. A special requirement to be considered for a single BESS is the need to operate in real time. The reason lies in the necessary consideration of the SoC-management in an algorithm to minimize losses. Compared to a virtual BESS, where every BESS is able to fulfill its SoC-management separately, the SoC-management of a single BESS has to consider all subunits. For this reason, an algorithm to minimize losses has to consider a proper SoC-balancing between the subunits to guarantee the "30 min-criterion" for every subunit of a BESS.

The SoC-bands defined in Eq. (4.4) and Eq. (4.8) need to be extended in case of a consideration of losses. Assuming the system shown in Fig. 4.12 with a PCC at the 30 kV-busbar, the SoC-band in Eq. (4.4) has to be extended to:

$$\mathbf{SoC_B} = \begin{pmatrix} SoC_{B,1} \\ SoC_{B,2} \end{pmatrix} = \begin{pmatrix} \frac{(X_{FCR}+P^{dchg}_{loss,max})\cdot T_{crit}}{E} \\ 1 - \frac{(X_{FCR}-P^{chg}_{loss,max})\cdot T_{crit}}{E} \end{pmatrix}. \tag{4.28}$$

To guarantee a certain amount of FCR-power at the PCC, the necessary power at the DC-side of the battery has to be higher than at the PCC during the discharging process and lower during the charging process.

The SoC-band in Eq. (4.28) considers $P^{dchg}_{loss,max}$ as the maximum power losses while charging and $P^{chg}_{loss,max}$ as the maximum power loss while discharging.

Assuming a system consisting of n subunits capable of providing an individual nominal power of $\frac{S_n}{n}$, the power output of every subunit is defined as $P_{u,i}$. The sum of the power outputs of the units is the total power output P

$$P = \sum_{i=1}^{n} P_{u,i} \tag{4.29}$$

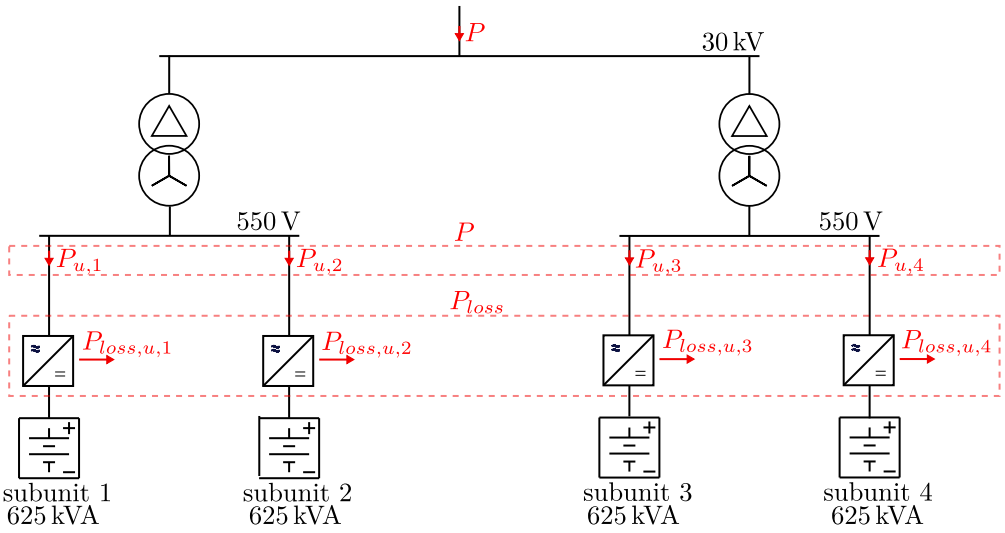

Figure 4.12: Single Line diagram [122].

and

$$\boldsymbol{P} = (P_{u,1}, P_{u,2}, ..., P_{u,n})^{\top} \tag{4.30}$$

is defined as vector of power outputs of the subunits. Every subunit has efficiency curves $\eta(P_{u,i} \cdot n/S_n)$, as exemplary shown in Fig. 4.13. At very low and very high values of the operating point, the efficiency of the subunit is lower. Therefore, a range between p_{low} and p_{high} in Fig. 4.13 can be determined as range of optimal efficiency. The values p_{low} and p_{high} are dependent on the efficiency curve of the subunits and have to fulfill the condition $p_{high} \geq 2 \cdot p_{low}$. The total losses of the system can be minimized by activating only the corresponding number of subunits required to cover the actual operating point P.

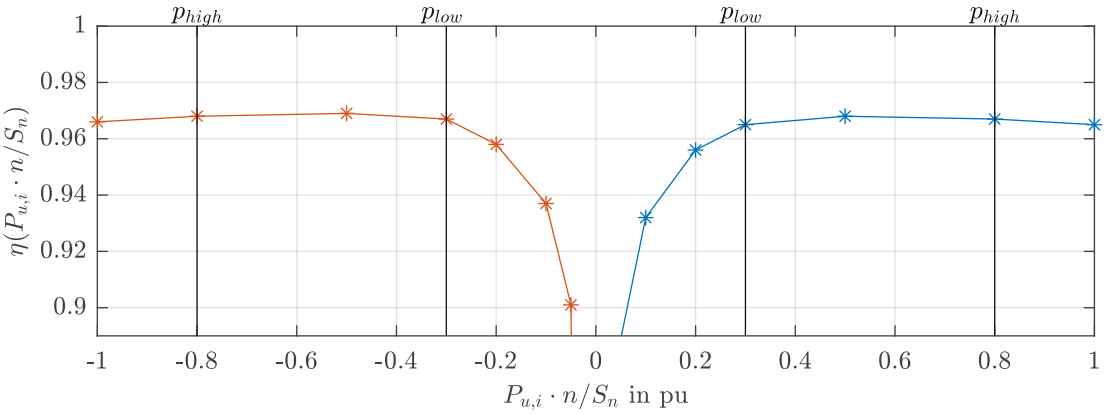

Figure 4.13: Efficiency curves of subunits for charging and discharging. The optimal efficiency is between a power output of (-0.8,-0.3)pu and (0.3,0.8)pu [122].

The Fig. 4.14 shows an example to illustrate a corresponding algorithm for minimizing losses in a way as described above.

Based on the efficiency curve shown in Fig. 4.13, a lower and a higher border of a maximum efficiency area are specified with $p_{high} = 0.8$ and $p_{low} = 0.3$. This example is based on the system

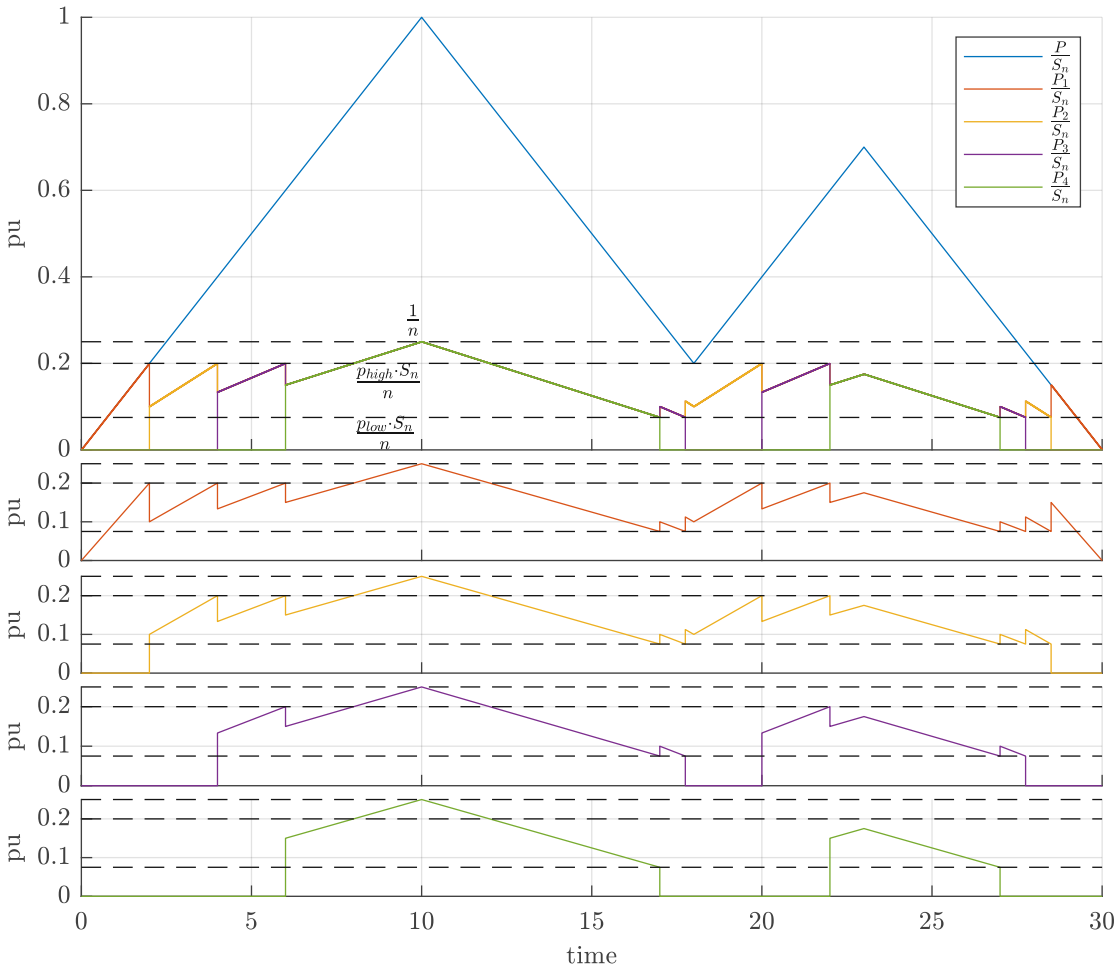

Figure 4.14: A simple application example of the algorithm to minimize losses [122].

shown in Fig. 4.12, therefore, $n = 4$. The reference power $\frac{P}{S_n}$ gradually increases from 0 pu to a value of 1 pu. Below a value of $P = 0.8\frac{S_n}{n}$ only one subunit covers the reference power $P_{u,1} = P$. In the following, this first inverter is also called the "leading subunit". Above this point, the second subunit is activated such that $P_{u,1} = P_{u,2} = \frac{P}{2}$ until the point $P = 2 \cdot 0.8\frac{S_n}{n}$ is reached. Above this point, the third subunit is activated such that $P_{u,1} = P_{u,2} = P_{u,3} = \frac{P}{3}$. At the next stage $P = 3 \cdot 0.8\frac{S_n}{n}$, the fourth subunit is activated such that $P_{u,1} = P_{u,2} = P_{u,3} = P_{u,4} = \frac{P}{4}$. Until the reference power decreases to an operating point $P = 4 \cdot 0.3\frac{S_n}{n}$, the system continues this state of operation. After going below this point, the fourth subunit is deactivated such that $P_{u,1} = P_{u,2} = P_{u,3} = \frac{P}{3}$. The sustained decrease leads to a further deactivation of the subunits analogous to the situation with increasing reference power.

In general, the algorithm can be described as follows. To determine the powers of subunits according to the algorithm described above, a vector

$$\mathbf{P'} = (P'_1, P'_2, ..., P'_n)^\top \tag{4.31}$$

is defined. Based on the sum power P, the elements of this vector $\mathbf{P'}$ are calculated with the help of m_{high} as the number of activated subunits for positive steepness of P

$$m_{high} = \min\left(\left\lceil \frac{n \cdot |P|}{p_{high} \cdot S_n} \right\rceil, n\right) \tag{4.32}$$

and m_{low} as the number of activated subunits for negative steepness of P

$$m_{low} = \min\left(\left\lfloor \frac{n \cdot |P|}{p_{low} \cdot S_n} \right\rfloor, n\right) \tag{4.33}$$

as follows:

$$P'_i = \begin{cases} \frac{P}{m_{high}}, & i \leq m_{high} \wedge P(t-\Delta t) > P(t), \\ \frac{P}{m_{low}}, & i \leq m_{low} \wedge P(t-\Delta t) < P(t), \\ 0, & else. \end{cases} \tag{4.34}$$

The losses $P_{loss,u,i}$ of each subunit are calculated by

$$P_{loss,u,i} = \left[1 - \eta\left(\frac{P_{u,i} \cdot n}{S_n}\right)\right] \cdot |P_{u,i}| + P_{stby} \cdot \left\lceil \frac{|P_{u,i}| \cdot n}{S_n} \right\rceil + P_{add,u,i} \tag{4.35}$$

where P_{stby} are the standby losses of each subunit and $P_{add,u,i}$ is defined as additional losses of the subunit. The total losses of all subunits can be calculated by

$$P_{loss} = \left| \left[1 - \eta\left(\frac{\mathbf{P} \cdot n}{S_n}\right)\right] \cdot \mathbf{P}^\top \right| + P_{stby} \cdot \left\lceil \left| \frac{\|\mathbf{P}\|_1 \cdot n}{S_n} \right| \right\rceil + P_{add} \tag{4.36}$$

where

$$P_{add} = \sum_{i=1}^{n} P_{add,u,i} \tag{4.37}$$

are the additional losses (e.g. transformer losses). As the load reference system is used, P_{loss} is positive at any time. Assuming the batteries of the subunits to have equal capacity of $\frac{E}{n}$, the SoC of each subunit based on Eq. (4.3) is calculated by

$$SoC_{u,i}(t) = SoC_{u,i}(T_1) + \frac{n}{E} \int_{T_1}^{t} \left[P_{u,i}(\tilde{t}) - P_{loss,u,i}(\tilde{t})\right] \, d\tilde{t}. \tag{4.38}$$

By using the vector $\mathbf{P'}$ to determine the power output of the subunits with $\mathbf{P} = \mathbf{P'}$, subunits with a low element number would be activated more often than subunits with a high element number. Besides that, the application of this algorithm leads to different SoC-levels in the subunits. Therefore, a sensible approach to keep the SoC-levels and the activation time of subunits approximately the same is an assignment of the elements of the vector $\mathbf{P'}$ to the subunits according to the actual SoC-levels of the subunits. At powers $P > 0$ the leading subunit should be the subunit with the lowest SoC. At powers $P < 0$ the leading subunit should be the subunit with the highest SoC. To do so, the SoC-levels of the subunits have to be sorted in ascending order (for $P > 0$), which is described by the function

$$aSoC : \mathbb{R}^n \to \mathbb{N}^n : \mathbf{SoC} \to \mathbf{aSoC} \tag{4.39}$$

and in descending order (for $P < 0$), which is described by the function

$$dSoC : \mathbb{R}^n \to \mathbb{N}^n : \mathbf{SoC} \to \mathbf{dSoC}. \tag{4.40}$$

The vector **SoC** is defined by

$$\mathbf{SoC} = (SoC_{u,1}, SoC_{u,2}, ..., SoC_{u,n})^\top \tag{4.41}$$

and describes the SoC-levels of the subunits. The result of the functions $aSoC$ and $dSoC$ can be described based on a example for this vector $\mathbf{SoC} = (0.3, 0.2, 0.1, 0.5)^\top$, assuming $n = 4$. This leads to results of the function $aSoC$, which is $aSoC(\mathbf{SoC}) = (aSoC_3, aSoC_2, aSoC_1, aSoC_4)^\top = (3, 2, 1, 4)^\top$, and the function $dSoC$, which is $dSoC(\mathbf{SoC}) = (dSoC_4, dSoC_1, dSoC_2, dSoC_3)^\top = (4, 1, 2, 3)^\top$. By using the sorted SoC-levels of the subunits in the vectors **aSoC** and **dSoC**, the assignment of the vector $\mathbf{P}'$ to the subunits can be described by Eq. (4.42):

$$P_{u,i} = \begin{cases} P'_{aSoC_i}, & P > 0, \\ P'_{dSoC_i}, & P < 0 \end{cases}, i = \{1, 2, ..., n\}. \tag{4.42}$$

The whole procedure described above is summarized in Fig. 4.15.

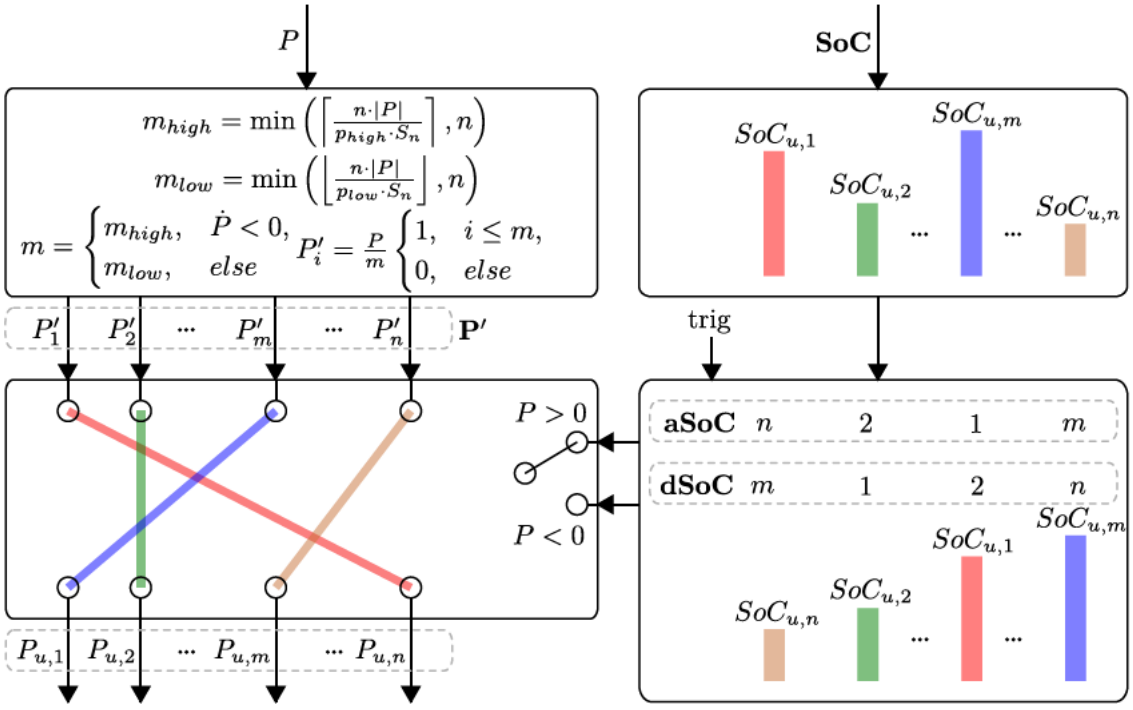

Figure 4.15: Procedure of minimizing losses.

Assuming the SoC-levels of all subunits to be equal, a value of P which can be provided by only one subunit would lead to rapidly changing assignment of the leading unit, because the result of the sorting of SoC-levels would change instantly. Therefore, the sorting of SoC-levels has to be done at discretized times. These discretized times are determined by the following conditions

- the absolute energy which was already exchanged,
- a change of the sign of P

and described by

$$trig = \begin{cases} 1, & mod\left(\int_{T_1}^{t} |P(\tilde{t})| d\tilde{t}, E_{chg}\right) = 0, \\ 1, & sgn\left[P(t)\right] \neq sgn\left[P(t-\Delta t)\right], \\ 0, & else \end{cases} \tag{4.43}$$

with E_{chg} as the maximum energy which is allowed to be delivered by one subunit at once[4]. If any of the conditions mentioned above is fulfilled and $trig = 1$, a new sorting of the SoC-levels is initiated in ascending

$$\mathbf{aSoC} = \begin{cases} aSoC\left[(\mathbf{SoC}(t)\right], & trig = 1, \\ aSoC(t-\Delta t), & else \end{cases} \tag{4.44}$$

and descending order

$$\mathbf{dSoC} = \begin{cases} dSoC\left[\mathbf{SoC}(t)\right], & trig = 1, \\ dSoC(t-\Delta t), & else. \end{cases} \tag{4.45}$$

Fig. 4.16 shows an example of P and **SoC** in response to a power reference signal P for a simulation in MATLAB/SIMULINK, in which the algorithm described above is implemented according to Eq. (4.42) for $n = 4$. Since $SoC(T_1) = 0.5$ and P gradually increases from zero, the subunits are activated subunit by subunit, beginning from the leading unit 3. At a time of approximately 4 s E_{chg} is reached. Therefore, the leading unit changes from subunit 3 to subunit 4. As the SoC-levels of subunit 1 and 4 are equal at that moment and $|P| > p_{high}\frac{S_n}{4}$, the subunit 1 is also activated at that moment, while subunits 2 and 3 are deactivated. At a time of approximately 23 s all four subunits are active and $|P|$ falls below $4 \cdot p_{low}\frac{S_n}{4}$. Therefore, the first subunit that is deactivated is subunit 3 which has the lowest SoC-level. Shortly after that P becomes zero and all subunits are deactivated. Because subunit 3 has the lowest SoC-level, it becomes the leading unit at a value of $P > 0$. At a time of approximately 53 s, E_{chg} is reached again. Therefore, the leading unit changes from subunit 1 to subunit 4.

4.1.7 Simulation

Simulations of a BESS providing FCR are carried out with a model created in MATLAB/SIMULINK. This model takes into account the properties of FCR, described in Chp. 2.3.2. The model includes a proper SoC-management, which offers the possibility to select between the two implementations of SoC-management according to Chp. 4.1.3. The DoF, described in Chp. 4.1.4, and the presented algorithm to reduce losses, described in Chp. 4.1.6, are also included in the model. In the following chapters, the general functionality of the model is described, followed by investigations on the influence of the DoF and the algorithm to reduce losses.

4.1.7.1 Simulation of the General Behavior

The historical frequency data of 10.01.2019 is used as input data of the model to show the general behavior of the model for activated and deactivated DoF. To simulate the general behavior of the model with deactivated DoF, the parameters of P_{FCR} according Eq. 4.23 are chosen with $\mathbf{X} = \{1\,\text{MW}, 10\,\text{mHz}, 200\,\text{mHz}, 30\,\text{s}, 0\,\text{s}, 0, 0, 0\}$. Fig. 4.17 shows simulation results of the model

[4]The maximum difference of SoC-levels between subunits is determined by E_{chg}, because such a situation is achieved by a continuous activation of only one subunit for a energy delivery of E_{chg}.

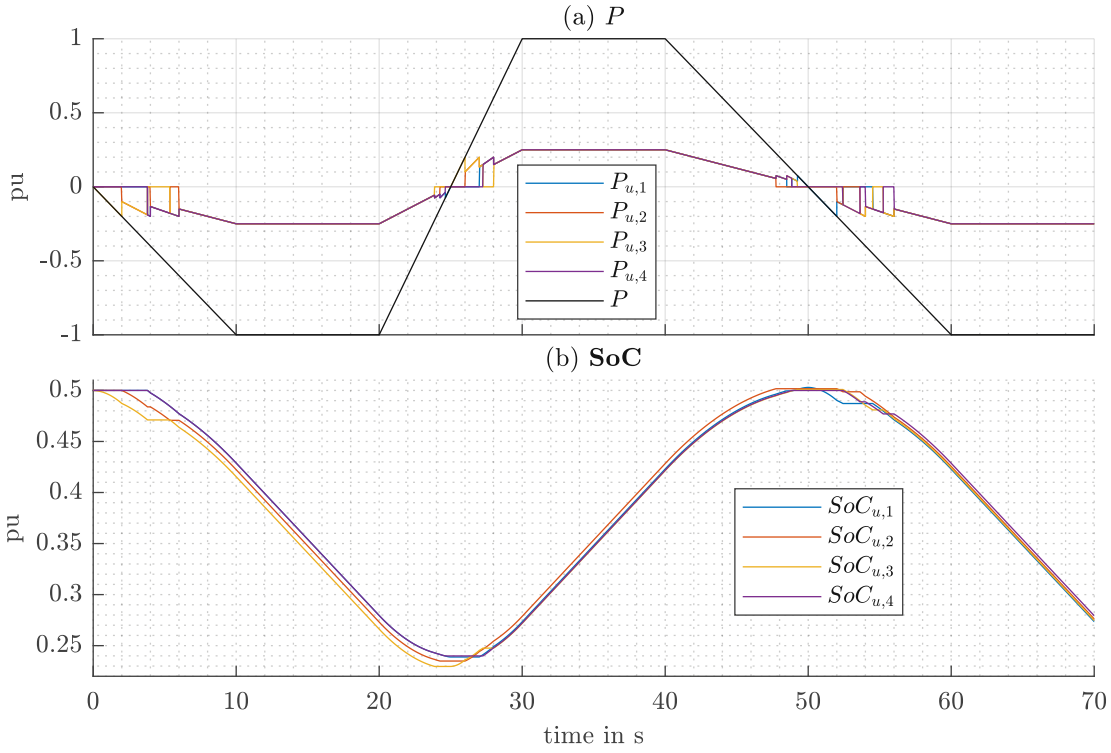

Figure 4.16: Example for the application of the algorithm for levelling SoC-levels of the subunits. For better illustration $E/S_n = 0.02\,\text{h}$ is used. For this example $S_n = 1\,\text{MW}$ and $E_{chg} = 100\,\text{Wh}$. (a) shows the power output of the subunits and the total power output. (b) shows the SoC-levels of the subunits [122].

as time series of the frequency, the power output and the SoC. Fig. 4.18 shows the droop curve $P_{FCR}(f)$ of the results. The two figures prove that the model can simulate the behavior of FCR as shown in Fig. 2.5 in Chp. 2.3.2 and the SoC-management (within balance groups) described in Chp. 4.1.3. Analogous to Fig. 4.8 the Fig. 4.17(c) also shows that the "30 min-criterion" is respected.

To simulate the general behavior of the model with activated DoF, the parameters of P_{FCR} according Eq. 4.23 are chosen with $\mathbf{X} = \{1\,\text{MW}, 10\,\text{mHz}, 200\,\text{mHz}, 30\,\text{s}, 1\,\text{s}, 1, 1, 1\}$. Fig. 4.19 shows the corresponding droop curve $P_{FCR}(f)$ of the results. As shown in Fig. 4.17(c), the SoC is lower than SoC_T for the entire simulation time, caused by a tendency to an under-frequency on 10.01.2019. Therefore, Fig. 4.19 shows the influence of the active DoF deadband, as well as the DoF overfulfillment for $f > 50\,\text{Hz}$. As both DoF are activated, they overlap within the deadband according to Eq. (4.22). For $f < 50\,\text{Hz}$ the DoF are inactive. This behavior helps to restore the SoC to the SoC-target.

4.1.7.2 Comparison of SoC-Management Implementations

In order to demonstrate the behavior of the two implementations of SoC-management, which are described in Chp. 4.1.3, historical frequency data of January 2019 is used in a simulation in MATLAB/SIMULINK for a BESS providing FCR and which uses either SoC-management within balance groups or SoC-management across balance groups. The simulation results allow a comparison between the two implementations of SoC-management. For this reason, Fig 4.21 and

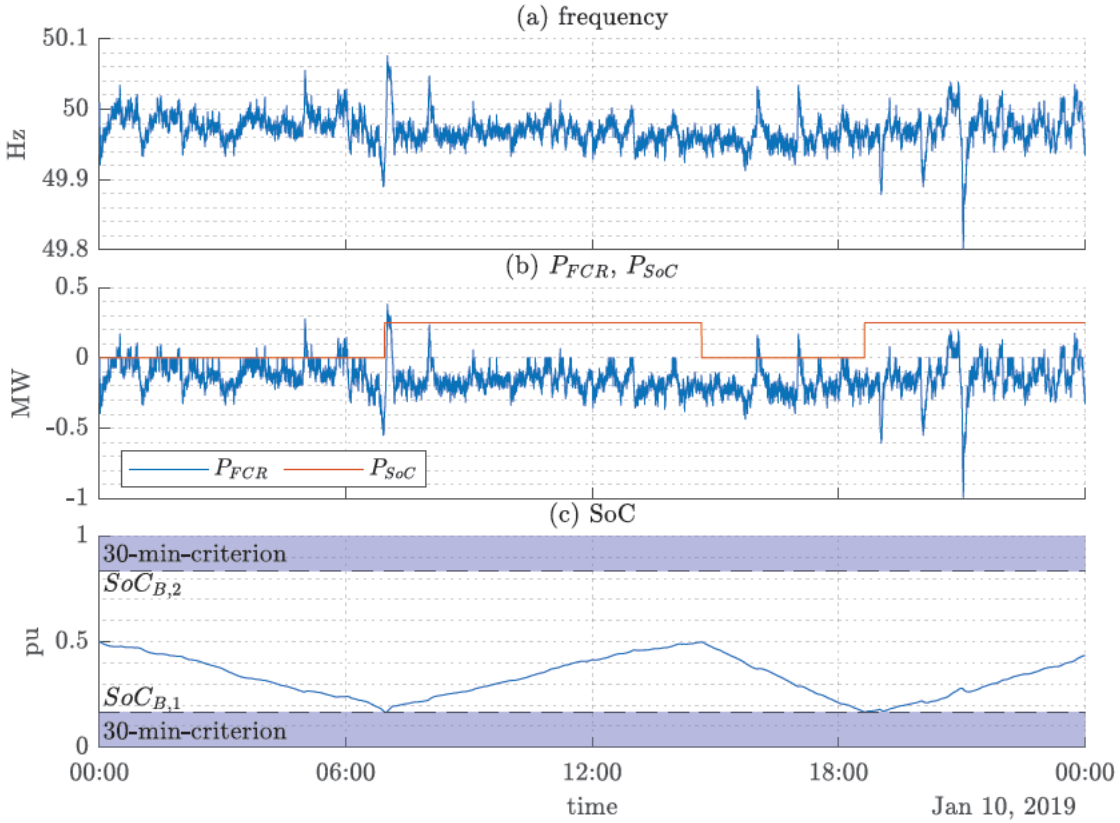

Figure 4.17: Simulation results on the basis of input data of historical frequency data of 10.01.2019; Time series of (a) frequency, (b) power and (c) SoC. The parameters of the simulation are $E = 3\,\text{MW h}$, $X_{FCR} = 1\,\text{MW}$, $X_{SoC} = 0.25\,\text{MW}$, $SoC_T = 0.5$.

Fig. 4.22 illustrate the activation of the corresponding SoC-management during the day for each day of January 2019. This month is used as input data for the simulation since two significant frequency events ocurred during this time [53] which are challenging for the SoC-management. On the 10.01.2019 at 10:00 o'clock a frequency drop to a value of about 49.8 Hz occurred, whereas on the 24.01.2019 a frequency rise to a value of about 50.2 Hz occurred.

The simulation results in Fig. 4.21, Fig. 4.21 and Fig. 4.20 are based on a BESS that provides FCR with a prequalified power of $X_{FCR} = 1\,\text{MW}$ and uses a power of $X_{SoC} = 0.25\,\text{MW}$ for SoC-management. The difference between Fig. 4.21, Fig. 4.21 and Fig. 4.20 is the energy content of the BESS, which is $E = 1.5\,\text{MWh}$ for Fig. 4.20, $E = 2\,\text{MWh}$ for Fig. 4.21 and $E = 3\,\text{MWh}$ for Fig. 4.22. Each figure consists of two subfigures (a) and (b), which represent the simulation results for the corresponding implementation of SoC-management.

Fig. 4.20(a) shows the simulation results for the SoC-management within balance groups andFig. 4.20(b) shows the simulation results for the SoC-management across balance groups. For one charging event on day 3 in Fig. 4.20(a) and Fig. 4.20(b) the corresponding exact time of activation and deactivation is illustrated. Fig. 4.20(b) shows that the activation and deactivation is done on a quarter-hourly basis as described in Chp. 4.1.3. Fig. 4.20(a), on the other hand, shows that the activation and deactivation is done at any time, regardless of the quarter-hourly basis. Due to the smaller working area for (b) according to Chp. 4.1.3.3, the number of activations is higher than in (a). Furthermore, the number of activations in (b) compared to (a) is increased due to the determination of the duration of SoC-management for (b) according to Eq. (4.16). While a

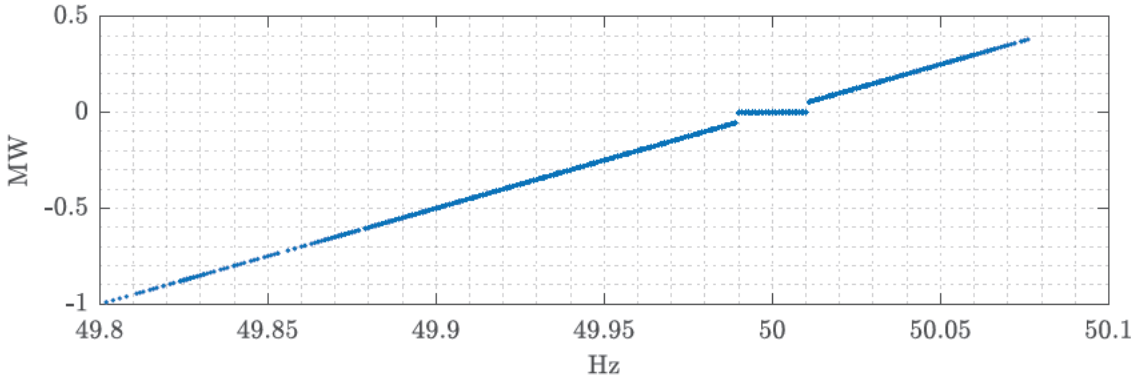

Figure 4.18: Simulation results of a BESS providing FCR with corresponding SoC-management, on the basis of input data of historical frequency data of 10.01.2019; Droop curve $P_{FCR}(f)$.

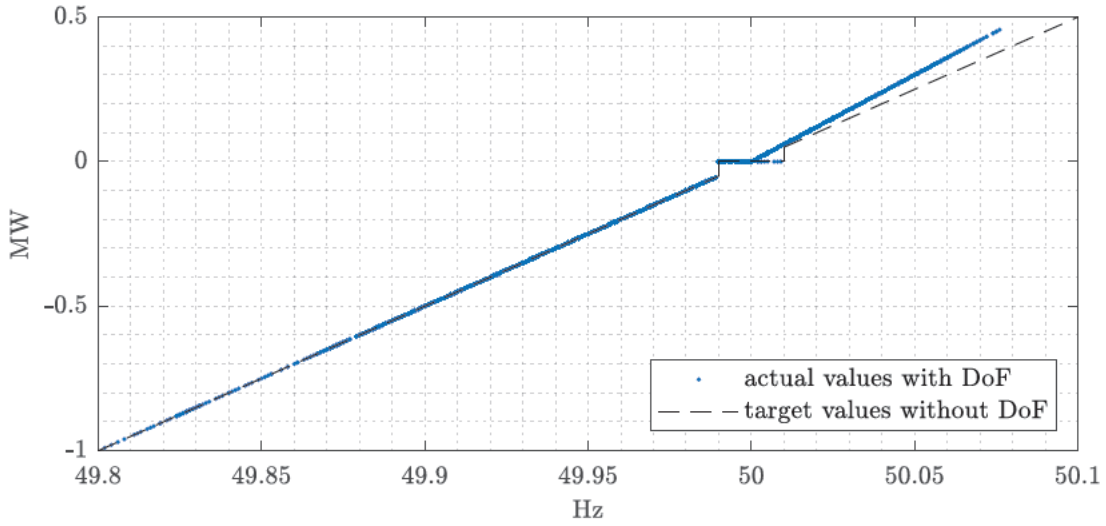

Figure 4.19: Simulation results on the basis of input data of historical frequency data of 10.01.2019; Droop curve $P_{FCR}(f)$ in case of activated DoF.

frequency deviation during an active SoC-management in (a) dynamically extends or shortens the duration of SoC-management, the duration of SoC-management in (b) is determined based on the actual system states at the moment of triggering when exceeding the border of the working area. Therefore, frequency deviations do not have an influence on the duration. The first effect of a more pronounced SoC-management in b) compared to a) due to a reduced working area becomes more visible with a smaller energy-to-power ratio, while the second effect, due to the determination of the duration, becomes becomes more visible with a higher energy-to-power ratio.

The expectations according to Fig. 4.7, which indicates that the required energy for charging is higher than the required energy for discharging by SoC-management due to the tendency of the grid frequency to be smaller than 50 Hz, can be confirmed for Fig. 4.20, Fig. 4.21 and Fig. 4.22. Especially on day 10, when a frequency drop to 49.8 Hz occurred, as already described above, the number of charging operations and the corresponding required energy for charging operations is very high in all cases.

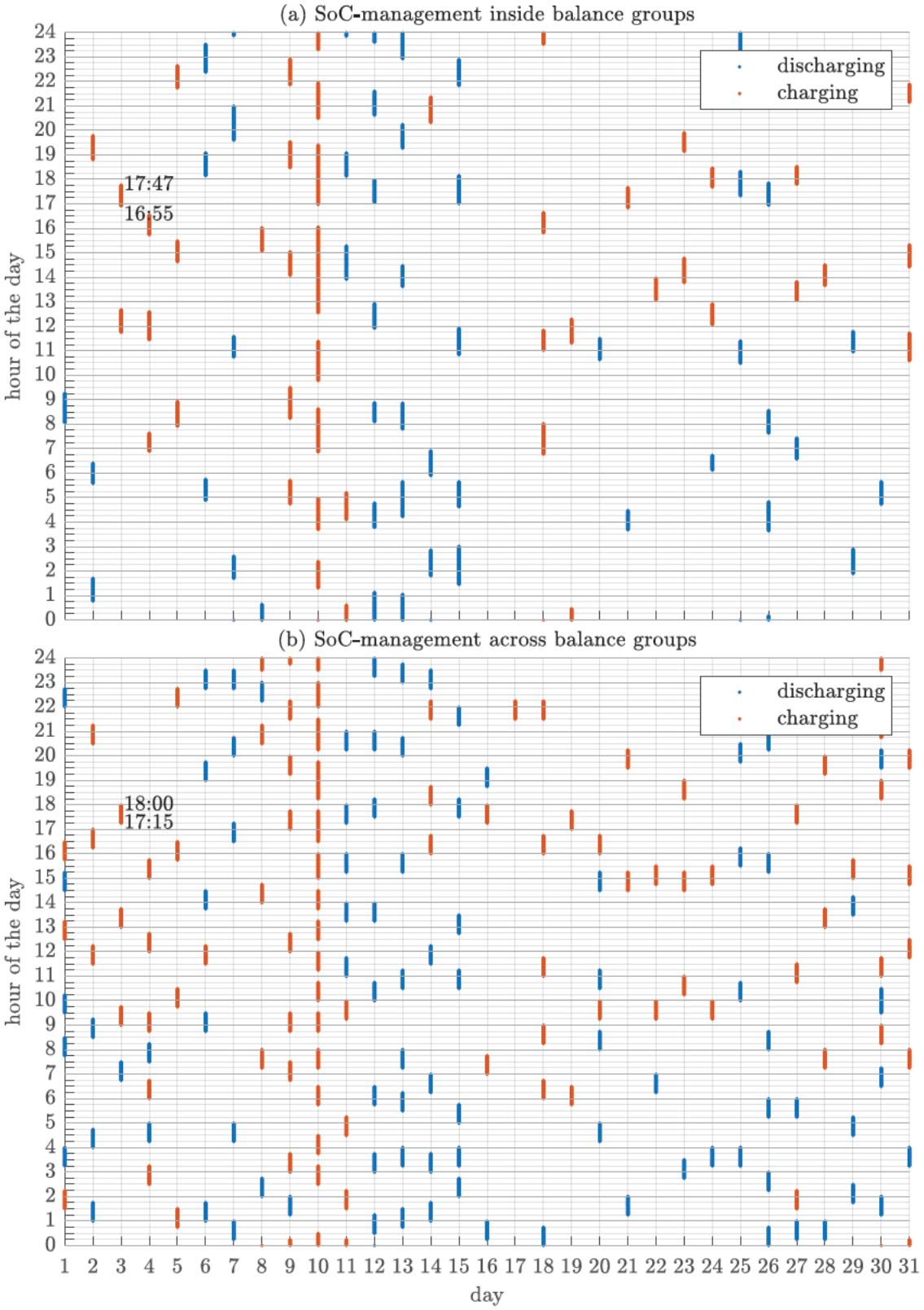

Figure 4.20: Comparison of the activation of SoC-management for a BESS providing FCR with $X_{FCR} = 1\,\text{MW}$, $X_{SoC} = 0.25\,\text{MW}$ and $E = 1.5\,\text{MWh}$, simulated for the historical frequency data of January 2019.

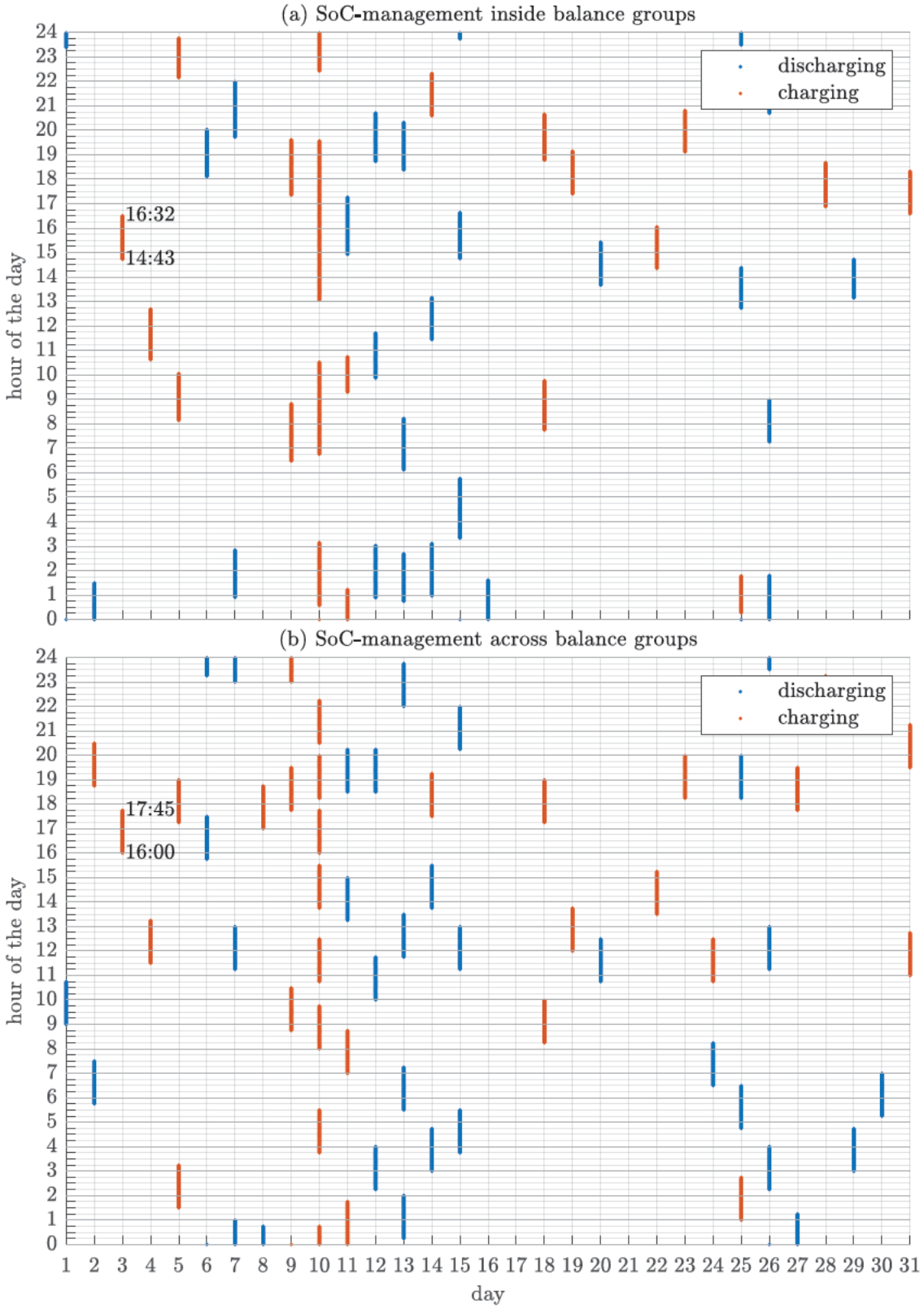

Figure 4.21: Comparison of the activation of SoC-management for a BESS providing FCR with $X_{FCR} = 1\,\text{MW}$, $X_{SoC} = 0.25\,\text{MW}$ and $E = 2\,\text{MWh}$, simulated for the historical frequency data of January 2019.

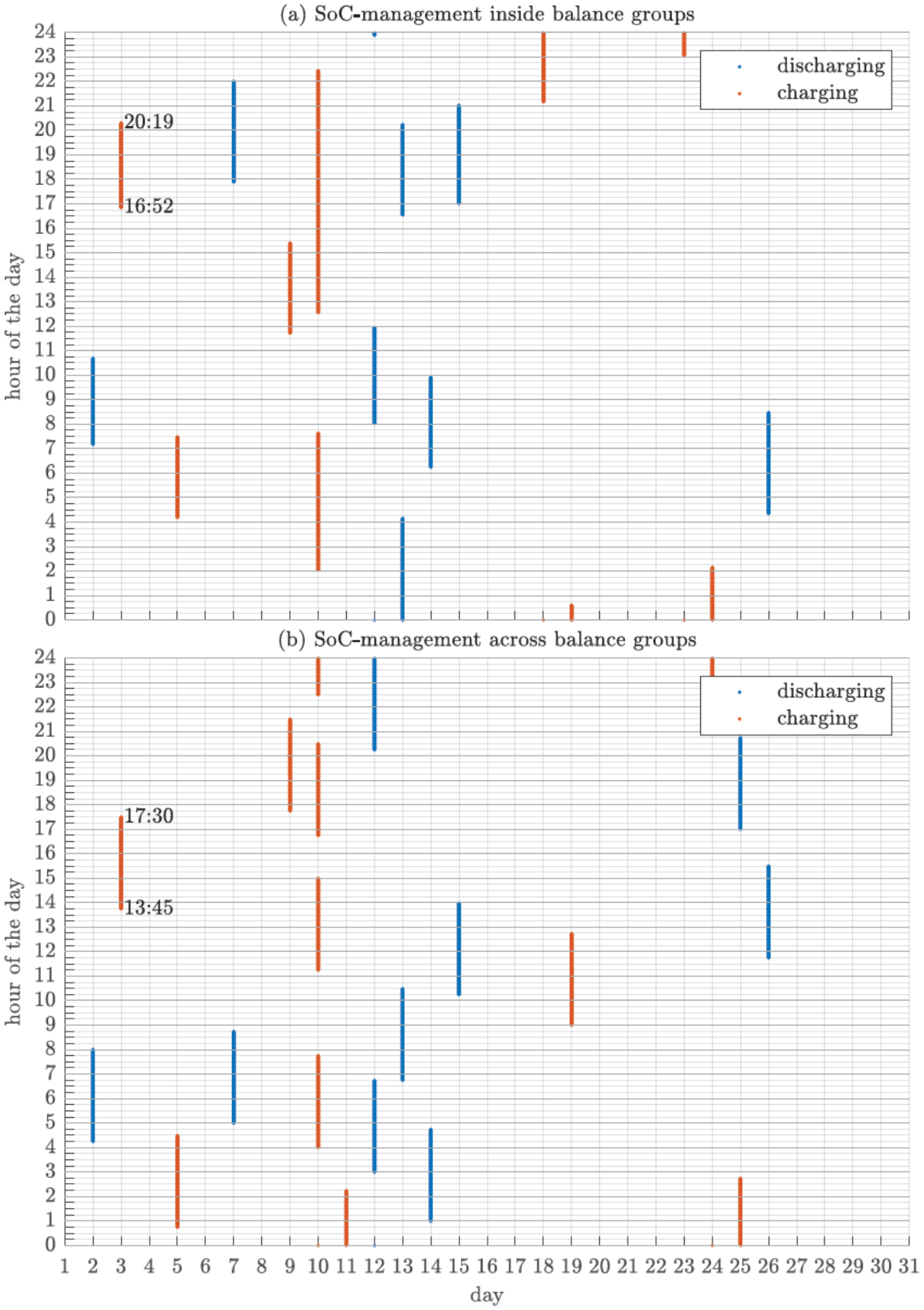

Figure 4.22: Comparison of the activation of SoC-management for a BESS providing FCR with $X_{FCR} = 1\,\text{MW}$, $X_{SoC} = 0.25\,\text{MW}$ and $E = 3\,\text{MWh}$, simulated for the historical frequency data of January 2019.

Compared to Fig. 4.20, Fig. 4.21 shows the longer duration of charging and discharging operations due to the larger working area as a consequence of a higher energy content. This effect becomes even more visible when comparing Fig. 4.21 and Fig. 4.22. The higher working area requires a higher energy that is necessary to restore the SoC to the target-SoC when reaching the SoC-borders of the working area. The larger working area in Fig. 4.22 leads to a lower number of charging and discharging operations compared to Fig. 4.21 and an even lower number compared to Fig. 4.20. For a large working area the possibility that positive and negative frequency deviations cancel each other out before reaching the SoC-borders of the working area is higher than for a small working area.

Fig. 4.23 compares the durations of charging and discharging operations for the two implementations of SoC-management and for the different energy contents of 1.5 MWh, 2 MWh and 3 MWh in the form of boxplots. The median of the duration for SoC-management within balance groups, which is shown in each case (a) in Fig. 4.23, has a value of 3.75 h for $E = 3\,\text{MWh}$, 2 h for $E = 2\,\text{MWh}$ and 1 h for $E = 1.5\,\text{MWh}$. Since the duration for SoC-management within balance groups is influenced by the frequency deviation that occurs during charging or discharging operations, especially severe frequency events lead to the outliers in each case (a) in Fig. 4.23. The median of the duration for SoC-management across balance groups, which is shown in each case (b) in Fig. 4.23, has a value of 3.8 h for $E = 3\,\text{MWh}$, 1.8 h for $E = 2\,\text{MWh}$ and 0.8 h for $E = 1.5\,\text{MWh}$. Since the duration for SoC-management across balance groups is basically a fixed value, the first two cases (b) in Fig. 4.23 only show median values in the corresponding boxplots. The outliers for the last case (b) in Fig. 4.23, which shows the results for an energy content of 1.5 MWh, on the other hand, shows outliers, which arise from situations of alert states on 10.01.2019. During an alert state, the SoC-management is not capable of compensating the power output caused by FCR, which may result in situations where the SoC after a charging or discharging operation is still outside the working area. The following charging or discharging operation based on SoC-management across balance groups therefore uses a higher duration according to Eq. (4.16) in order to reach the target-SoC. Such situations explain the outliers shown in the last case (b) in Fig. 4.23 for an energy content of 1.5 MWh. Due to the smaller working areas in case of smaller energy contents it is clear that the smaller the energy content the smaller the median values of the duration between charging and discharging operations, as shown in Fig. 4.23.

Instead of analyzing the durations of operations themselves, Fig. 4.24 compares the durations between charging and discharging operations for the two implementations of SoC-management and for the different energy contents of 1.5 MWh, 2 MWh and 3 MWh in the form of boxplots. The results show a tendency of the median values for the cases (a) to be higher than for the cases (b). Analogous to the descriptions for Fig. 4.23, Fig. 4.24 also shows a tendency of smaller median values for smaller energy contents.

Tab. 4.2 summarizes relevant values of the simulation results described above. Compared with the required energy for charging operations, which is higher than the required energy for discharging, the number of charging and discharging operations is approximately the same.

4.1.7.3 Simulation of Degrees of Freedom To Reduce SoC-Management

To investigate the influence of the DoF during provision of FCR on the necessary energy for SoC-management, the historical frequency data between 01.12.2018 to 29.08.2019 is used as input data of the model since during this period measurements were taken at the BESS described in Chp. 3.1. For all three DoF, a "potential energy" that could be generated by them can be calculated based on historical frequency data. A general view on this potential energy for the different DoF is given below.

To compare the effectiveness of the two DoF "overfulfillment" and "deadband", Fig. 4.25 shows the duration curve of the frequency deviation Δf. An active DoF generates a surplus of energy

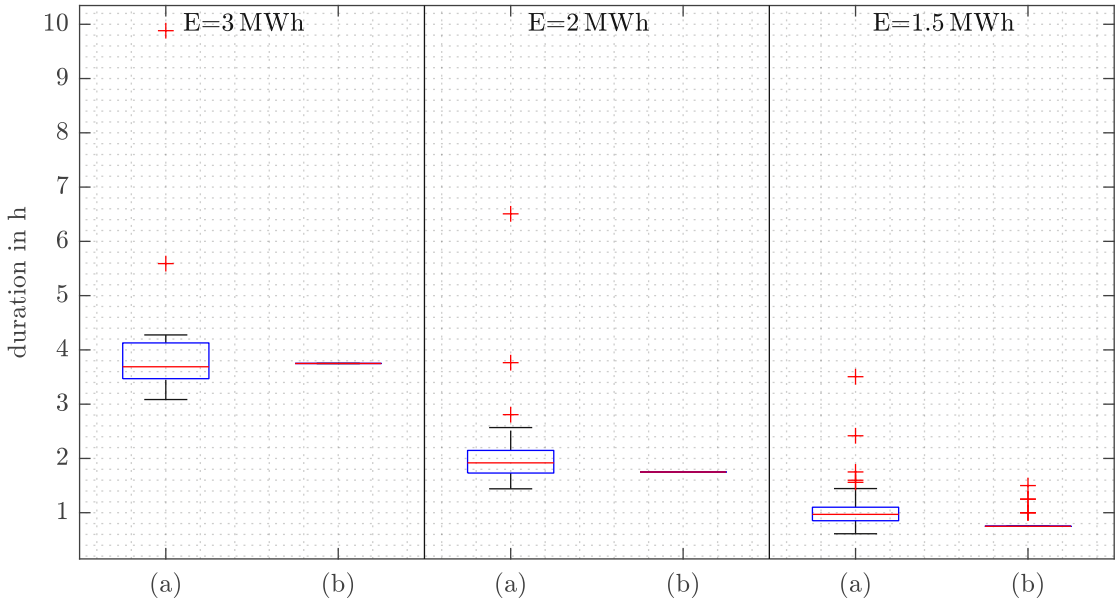

Figure 4.23: Comparison of the duration of charging and discharging operations of the SoC-management for a BESS providing FCR with $X_{FCR} = 1\,\text{MW}$, $X_{SoC} = 0.25\,\text{MW}$ and different values of the energy content E, simulated for the historical frequency data of January 2019. Each case (a) shows the durations when applying SoC-management within balance groups and each case (b) shows the durations when applying SoC-management across balance groups.

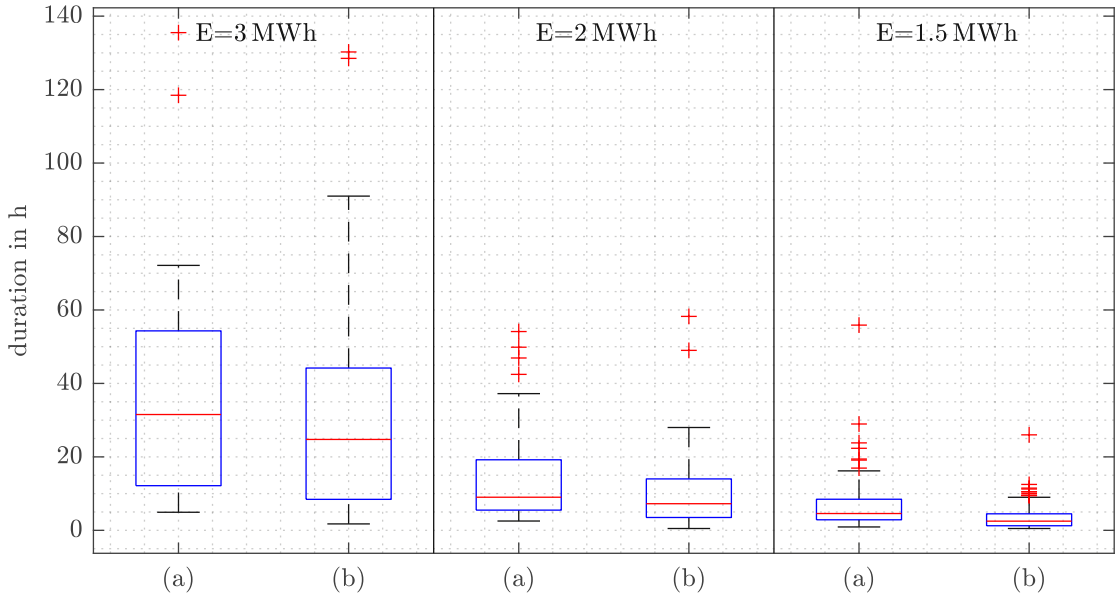

Figure 4.24: Comparison of the duration between charging and discharging operations of the SoC-management for a BESS providing FCR with $X_{FCR} = 1\,\text{MW}$, $X_{SoC} = 0.25\,\text{MW}$ and different values of the energy content E, simulated for the historical frequency data of January 2019. Each case (a) shows the durations when applying SoC-management within balance groups and each case (b) shows the durations when applying SoC-management across balance groups.

Table 4.2: Summary of relevant values of the comparison of implementations for SoC-management.

	E=1.5 MWh		E=2 MWh		E=3 MWh	
	(a)	(b)	(a)	(b)	(a)	(b)
number of charging operations	43	90	20	30	7	9
number of discharging operations	45	90	22	29	8	9
median of duration for charging and discharging operations in h	0.96	0.75	1.92	1.75	3.96	3.75
median of duration between charging and discharging operations in h	4.58	2.5	9.02	7.25	31.5	24.75
required energy for discharging operations in MWh	11.38	16.9	10.9	12.7	7.8	8.4
required energy for charging operations in MWh	11.74	17.4	11.2	13.1	8.4	8.4

consumption/generation, besides the energy consumption/generation by FCR without DoF. In Fig. 4.25 two areas are shown, which represent the potential energy that could be generated by the DoF deadband and overfulfillment. As the activation of the DoF is dependent on the actual SoC and its deviation from the target-SoC, only a fraction of this potential energy can be used to restore the SoC during operation. The potential energy of the DoF deadband is $E_{db} = e_{db}\frac{X_{FCR}}{200\,\mathrm{mHz}} \approx 63\,\mathrm{h} \cdot X_{FCR}$, the potential energy of the DoF overfulfillment is $E_{of} = e_{of}\frac{X_{FCR}}{200\,\mathrm{mHz}} \approx 89\,\mathrm{h} \cdot X_{FCR}$. Therefore, the potential effectiveness of the DoF overfulfillment is higher than the potential effectiveness of the DoF deadband. In case of an activation of both the DoF deadband and overfulfillment, the potential energy of the DoF overfulfillment increases by the value $E_{of,db} = e_{of,db}\frac{X_{FCR}}{200\,\mathrm{mHz}} \approx 13\,\mathrm{h} \cdot X_{FCR}$, which is also shown in Fig. 4.25.

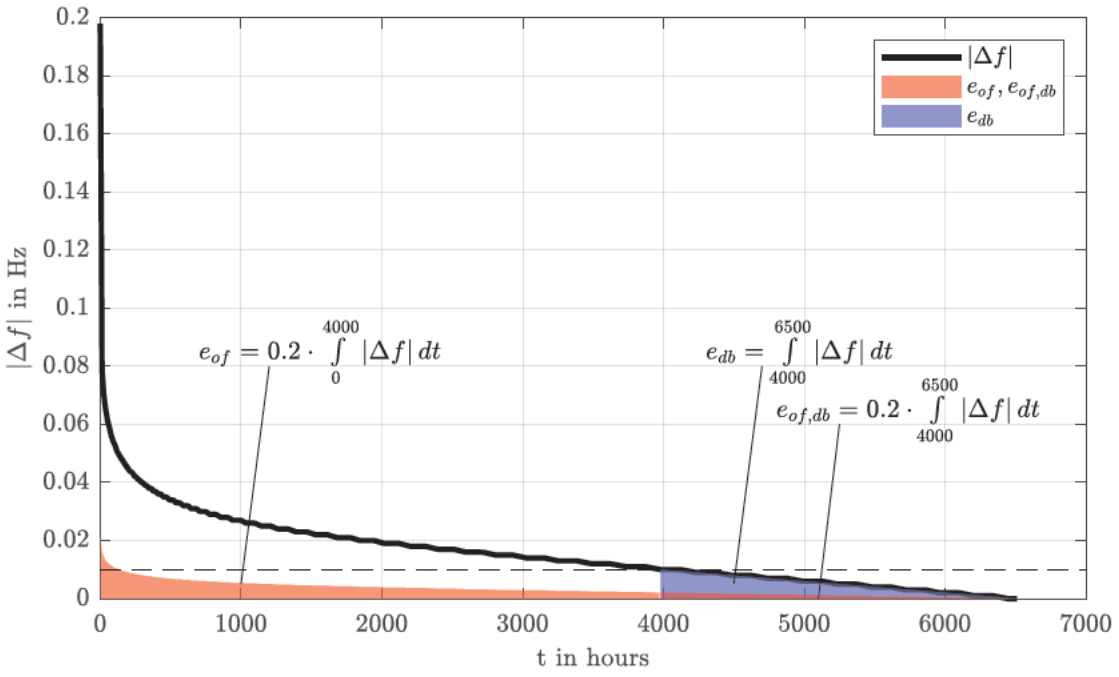

Figure 4.25: Duration curve of the frequency deviation between 01.12.2018 to 29.08.2019. The potential energy $E_{db} = e_{db}\frac{X_{FCR}}{200\,\mathrm{mHz}}$, which can be generated by the DoF deadband, is denoted by the blue area. The potential energy $E_{of} = e_{of}\frac{X_{FCR}}{200\,\mathrm{mHz}}$, which can be generated by the DoF overfulfillment, is denoted by the blue area.

The potential energy that could be generated by the third DoF, steepness, is dependent on the steepness of the frequency deviation and the maximum power steepness the system is capable of. But the most important factor for the potential energy of the DoF steepness is the progression of the frequency itself. The higher and more frequent the changes in frequency, the higher the effectiveness of the DoF steepness. The maximum potential energy can be generated in case of a progression of the frequency as shown in Fig. 4.26 and a frequency gradient of $\frac{df}{dt} = \infty$. Assuming the system to be capable of a power steepness of $\dot{P}_{\max} = \infty$, the maximum potential energy of the DoF steepness is $E_{st} = |\Delta f| \cdot \Delta t \frac{X_{FCR}}{200\,\mathrm{mHz}}$. As Fig. 4.25 shows, the frequency deviation stays at values $\Delta f \ll 200\,\mathrm{mHz}$ most of the time. But also the frequency gradient has limited values, which diminishes the potential energy even further.

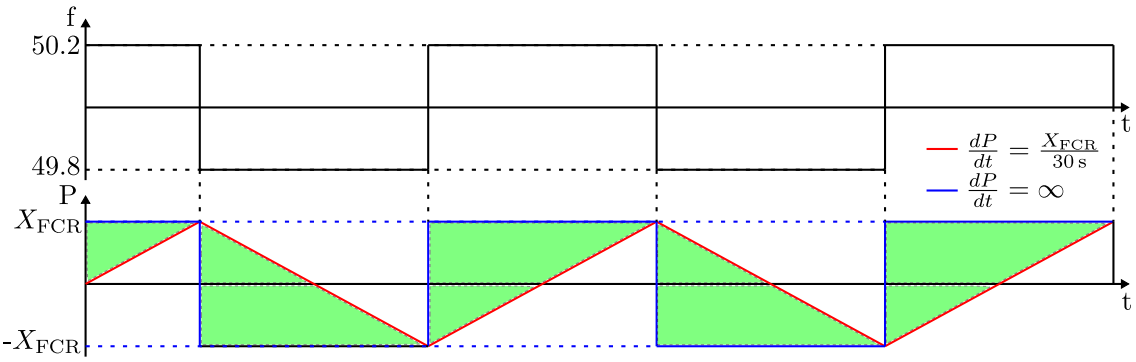

Figure 4.26: Potential energy of the DoF steepness in case of a frequency deviation that leads to a maximum effectiveness of the DoF.

Therefore, the potential energy of the DoF steepness is much smaller than shown in Fig. 4.26.

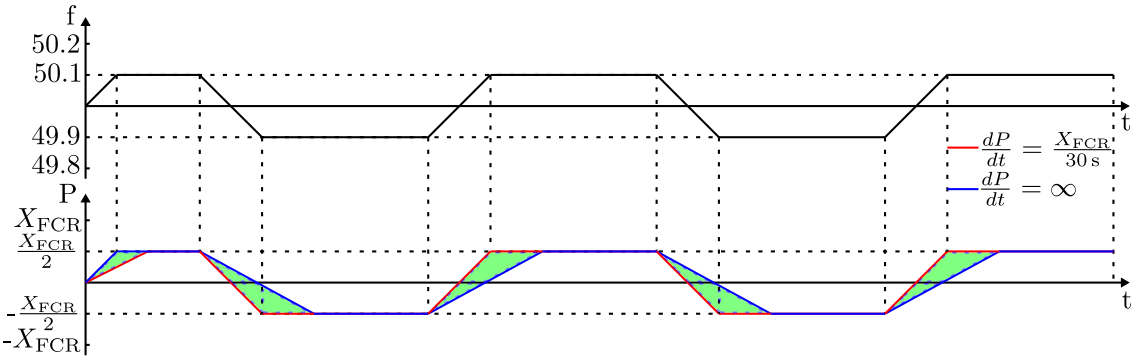

Figure 4.27: Potential energy of the DoF steepness in case of a frequency deviation that leads to a maximum effectiveness of the DoF but respects a limited frequency gradient and smaller values of the frequency deviation.

Fig. 4.27 shows the effects of a limited frequency deviation and a limited frequency gradient resulting in a much smaller area corresponding to the potential energy of the DoF steepness. In case of a frequency gradient $\frac{df}{dt} < \frac{200\,\mathrm{mHz}}{30\,\mathrm{s}} \approx 7\,\mathrm{mHz/s}$, the DoF steepness has no effect at all. For 99 % of the time the frequency gradient of the historical frequency data between 01.12.2018 to 29.08.2019 is smaller than 7 mHz/s. Therefore, the effectiveness of the DoF steepness is very limited.

Dependent on the operation strategy of the DoF, their potential energy described above can not be used entirely during the provision of FCR. Considering an operation strategy as described in

Chp. 4.1.4, the actual activation of the DoF depends on the actual SoC and its deviation from the target-SoC. The "usable energy" for such an operation strategy can be calculated based on a simulation which considers the SoC during the provision of FCR with activated DoF. Such a simulation is carried out using the historical frequency data between 01.12.2018 to 29.08.2019. As implementation of the SoC-management, the SoC-management within balance groups according Chp. 4.1.3.1 is selected. The simulation results can be compared to the potential energies e_{of} and e_{db} by considering only situations when the DoF are activated, as described in Eq. (4.26), Eq. (4.25) and Eq. (4.27).

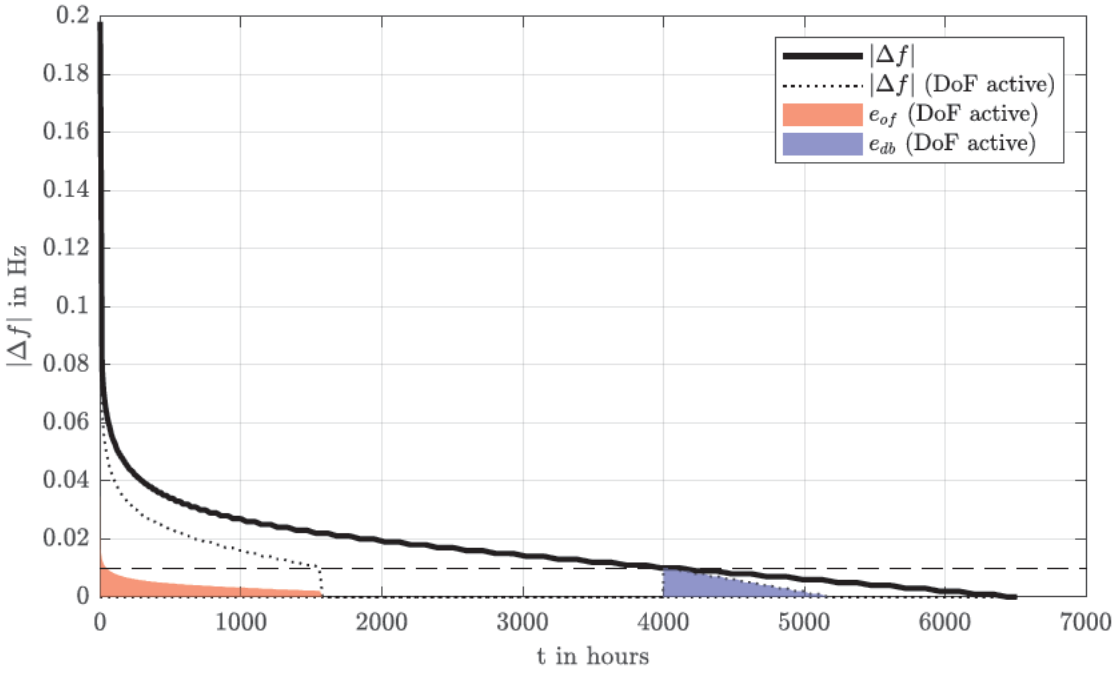

Figure 4.28: Duration curve of the frequency deviation between 01.12.2018 to 29.08.2019. Usable DoF-energy. The parameters of the simulation, the results of which are taken into account here, are $E = 3\,\mathrm{MW\,h}$, $\mathbf{X} = \{1\,\mathrm{MW}, 10\,\mathrm{mHz}, 200\,\mathrm{mHz}, 1, 1, 1, 30\,\mathrm{s}, 0\,\mathrm{s}\}$, $X_{SoC} = 0.25\,\mathrm{MW}$. As implementation of the SoC-management, the SoC-management within balance groups according Chp. 4.1.3.1 is selected.

Fig. 4.28 shows the same duration curve of the frequency deviation as shown in Fig. 4.25, but two additional duration curves are shown, representing the frequency deviation in case of the activated DoF deadband and overfulfillment. These duration curves are considering the actual SoC of the simulation results. The area under these duration curves represents the normalized usable energy e_{of} (considering the factor 20 % of Eq. (4.26)) and e_{db}. Comparing the normalized usable energies e_{of} and e_{db} between Fig. 4.25 and Fig. 4.28, the decrease of usable energy compared to potential energy can clearly be seen.

The normalized usable energies e_{of} and e_{db} of Fig. 4.28 are generated by the DoF overfulfillment and deadband during the simulation period 01.12.2018 to 29.08.2019. The corresponding values of E_{of} and E_{db} can be calculated with $E_{of} = e_{of} \cdot \frac{X_{FCR}}{200\,\mathrm{mHz}} = 33.9\,\mathrm{h} \cdot X_{FCR}$ and $E_{db} = e_{db} \cdot \frac{X_{FCR}}{200\,\mathrm{mHz}} = 30.4\,\mathrm{h} \cdot X_{FCR}$, following the same trend as the potential energies calculated above with $E_{of} > E_{db}$. But based on this trend no general assumption on the influence of the DoF on the necessary energy for SoC-management can be made. The energies E_{of} and E_{db} do affect the actual SoC during simulation, but the SoC is more strongly affected by the energy provided for FCR. Therefore, the effectiveness of a DoF is strongly dependent on when the corresponding energies E_{of} and E_{db} are

generated. For this reason, these energies are divided into two components. The first component represents the energy which is generated during active SoC-management and the second component represents the energy which is generated between actions of SoC-management, where only FCR is provided. The first component reduces the duration of SoC-management activations, while the second component delays exceeding the SoC-band SoC_B according to Eq. (4.4) and thus the moment in which SoC-management has to become active. This delay in SoC-management, therefore, also leads to a reduction in the number of SoC-management operations required. To be able to compare the two components of E_{of} and E_{db}, Tab. 4.3 shows the relevant simulation results for three different simulations. In the first simulation all DoF are deactivated, in the second simulation the DoF overfulfillment is activated and in the third simulation the DoF deadband is activated.

Table 4.3: Relevant values to describe the influence of the DoF on the SoC-management for different simulations. The first column describes the activation of the DoF during simulation in the following order {deadband,overfulfillment,steepness}. "0" means the DoF is deactivated, "1" means the DoF is activated.

simulation	**usable energy of DoF**	**energy for SoC-management**	**duration of activations**	**number of activations**	**effectiveness ε**
000	-	101 MWh	3.85 h	105	0
010	E_{of} = 33.8 MWh	88 MWh	3.83 h	92	$\varepsilon_{of} = 0.26$
100	E_{db} = 30.4 MWh	66 MWh	3.9 h	68	$\varepsilon_{db} = 0.31$

The second column shows the usable energy which is generated by the DoF during the whole simulation period. The third column shows the energy which is needed for SoC-management. Both energies are summed up as absolute values. Compared to the simulation with activated DoF overfulfillment, the usable energy of the DoF deadband is lower than the usable energy of the DoF overfulfillment. On the other hand, the comparison of the energy for SoC-management between the reference simulation, where all DoF are deactivated, the reduction is higher for the DoF deadband than for the DoF overfulfillment. The reason can be argued with the other values of Tab. 4.3. The fourth column shows the mean value of the duration of all SoC-management activities. As the duration of activities of SOC-management is rather short, the influence of the DoF is predictably small. The values in the fourth column confirm this fact. For the DoF overfulfillment the duration is slightly smaller, while for DoF deadband the duration is even a little bit larger than the duration of the reference simulation with deactivated DoF. The fifth column shows the number of activations of SoC-management. Compared to the reference simulation, the activated DoF deadband leads to a higher reduction of the number of activations from 105 to 68, than the DoF overfulfillment with a reduction of the number of activations from 105 to 92. Comparing these number with the first column, the question arises, why the DoF overfulfillment can not effectively use its higher usable energy to reduce SOC-management activities. The DoF deadband is more effective to delay exceeding the SoC-band SoC_B according Eq. (4.4), as defined above as "second component" of usable energy of the DoF. To describe this effectiveness the size ε is introduced, which is defined as the mean value of all components of the energy generated by DoF during a SoC-management activation divided by the energy provided by FCR during this SoC-management activation. For a mathematical description the definition of an interval I_m of Chp. 4.1.3.2 is used. Assuming the set $\mathbf{I} = \{I_1, I_2, ...I_m, ...\}, m \in \mathbb{N}$ to describe the beginning and the ending of periods between SoC-management activities, ΔI_m as the duration of the m-th activity and P_{DoF} as the power

generated only by an active DoF, the effectiveness is defined by the following equation:

$$\varepsilon = \frac{1}{|\mathbf{I}|} \sum_{m=1}^{|\mathbf{I}|} \frac{\int_{I_m(a_m)}^{I_m(b_m)} P_{DoF}(t)\, dt}{\int_{I_m(a_m)}^{I_m(b_m)} P_{FCR}(t)\, dt}. \tag{4.46}$$

The sixth column in Tab. 4.3 shows the value of the effectiveness ε for the simulation in which DoF overfulfillment or DoF deadband are activated. By definition ε is zero for the simulation with deactivated DoF. The table shows that $\varepsilon_{db} > \varepsilon_{of}$, indicating that the DoF deadband can use its generated energy E_{db} more effective than the DoF overfulfillment can use its generated energy E_{of}. As already described above, the Eq. (4.26) and Eq. (4.25) describe the frequency-dependent activation of the DoF overfulfillment and DoF deadband. These equations show that the DoF deadband is active when no "conventional" FCR (following a droop curve as shown in Fig. 2.5) is active, while the DoF overfulfillment is working in parallel with "conventional" FCR. As the FCR power is much higher than the power which takes effect by the DoF, the influence by the DoF overfulfillment on the SoC is much smaller than it is by "conventional" FCR. Also, the energy generated by the DoF overfulfillment is increasing with increasing frequency deviation. But the higher the frequency deviation the higher the provision of "conventional" FCR. This means, that in situations in which the DoF overfulfillment generates the most energy, it is more likely that SoC-management is activated. The DoF deadband, on the other hand, is active during times, when "conventional" FCR is inactive. Compared to the DoF overfulfillment it generates its energy in times in which is less likely that SoC-management is activated. The two values ε_{db} and ε_{of} reflect this argumentation.

In order to compare the influence of all combinations of DoF on SoC management, the corresponding simulations were carried out in the same setup as mentioned above. Based on the considerations mentioned above, the expectation on the effectiveness of the DoF is arranged as follows: DoF deadband, DoF overfulfillment and DoF steepness. Fig. 4.29 shows the necessary energy for SoC-management dependent on the activations of the DoF.

The DoF overfulfillment reduces the necessary energy for SoC-management by 13 %, while the DoF deadband reduces the necessary energy for SoC-management by 34 %. As expected, the DoF steepness has practically no effect, because of the limited frequency gradient. A combination of all DoF leads to a reduction of the energy for SoC-management by 43 %. The results meet the expectations mentioned above.

4.1.7.4 Simulation of Power Losses during Provision of FCR

To investigate the effectiveness of the algorithm to minimize losses, described in Chp. 4.1.6, different scenarios are simulated in MATLAB/SIMULINK. The simulation model is based on the system shown in Fig. 4.12 and a SoC-management within balance groups according to Chp. 4.1.3 is used. The used parameters are listed in the following. The parameters of FCR are selected with $\mathbf{X} = \{1\,\text{MW}, 10\,\text{mHz}, 200\,\text{mHz}, 30\,\text{s}, 1\,\text{s}, 1, 1, 1\}$. The maximum power output of the system is $S_n = 2.5\,\text{MVA}$. The total energy reservoir of the BESS is $E = 2.2\,\text{MWh}$, which is equally distributed between the four batteries of the subunits. The maximum power gradient is $\dot{P}_{\max} = 2.5\,\text{MW/s}$. The target-SoC is $SoC_T = 0.5$. For the algorithm to minimize losses $p_{high} = 0.8\,\text{pu}$ and $p_{low} = 0.3\,\text{pu}$ are used. The losses of the system are calculated according to Eq. (4.36) with P_{stby} that acts as shown in the measurement in Tab. 3.2, with a linear characteristic beginning with $P_{stby} = 2.5\,\text{kW@}P = 0$ up to $P_{stby} = 10\,\text{kW@}P = S_n$. To switch between the subunits, an energy $E_{chg} = 50\,\text{kWh}$ is chosen. According to Fig. 4.12 additional losses are caused

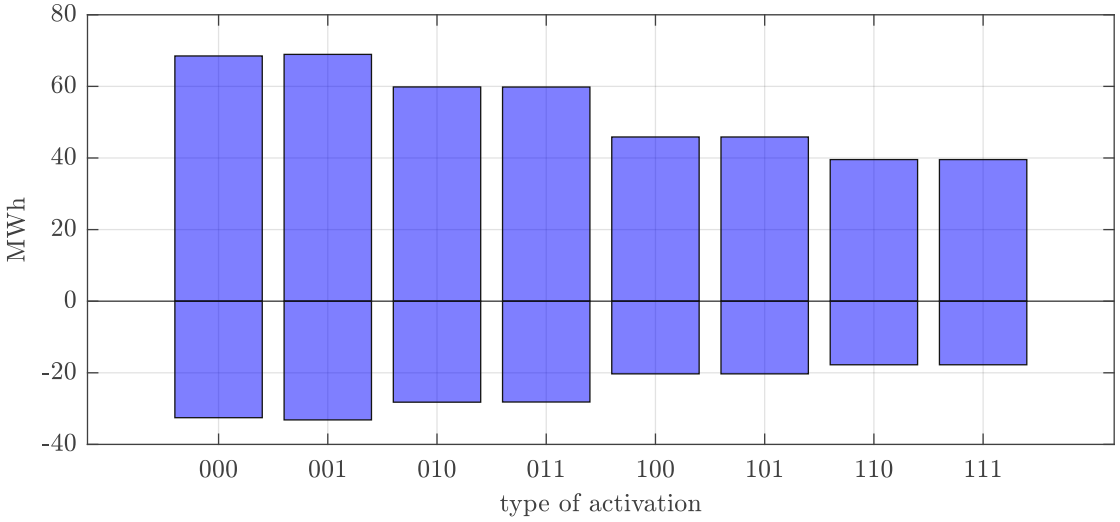

Figure 4.29: Comparison of necessary energy (charge and discharge) for SoC-Management $\int P_{SoC}\,dt$. The activation order of the DoF is {deadband,overfulfillment,steepness}. "0" means the DoF is deactivated, "1" means the DoF is activated. The parameters of the simulation are $E = 3\,\mathrm{MW\,h}$, $X_{FCR} = 1\,\mathrm{MW}$, $X_{SoC} = 0.25\,\mathrm{MW}$. Frequency measurement data of the period between 01.12.2018 to 29.08.2019 is used as input data.

by the transformers. Therefore, in the simulation the additional losses according to Eq. (4.35) are defined by

$$P_{add,u,1} = \frac{r_T}{S_n} \begin{cases} \frac{1}{2}\left(P_1 + P_2\right)^2, & |P_2| > 0, \\ P_1^2, & else \end{cases} \tag{4.47}$$

$$P_{add,u,2} = \frac{r_T}{S_n} \begin{cases} \frac{1}{2}\left(P_1 + P_2\right)^2, & |P_1| > 0, \\ P_2^2, & else \end{cases} \tag{4.48}$$

$$P_{add,u,3} = \frac{r_T}{S_n} \begin{cases} \frac{1}{2}\left(P_3 + P_4\right)^2, & |P_4| > 0, \\ P_3^2, & else \end{cases} \tag{4.49}$$

$$P_{add,u,4} = \frac{r_T}{S_n} \begin{cases} \frac{1}{2}\left(P_3 + P_4\right)^2, & |P_3| > 0, \\ P_4^2, & else \end{cases} \tag{4.50}$$

with $r_T = 0.023\,\mathrm{pu}$ as the normalized winding resistance of the transformers shown in Fig. 4.12. The maximum losses while charging/discharging, which define the permissible SoC-band $\mathbf{SoC_B}$ according to Eq. (4.28) are calculated as follows:

$$P_{loss,max}^{dchg} = X_1 \left[1 - \eta\left(-\frac{X_1}{S_n}\right)\right] + 4 \cdot P_{stby} + \frac{r_T \cdot S_n}{4} \tag{4.51}$$

$$P_{loss,max}^{chg} = X_1 \left[1 - \eta\left(\frac{X_1}{S_n}\right)\right] + 4 \cdot P_{stby} + \frac{r_T \cdot S_n}{4}. \tag{4.52}$$

Two simulations with an activated (power distribution among the subunits determined by the algorithm) and a deactivated (equal power distribution among the subunits) algorithm are done.

These two simulations are done with activated and deactivated DoF. This results in four different cases of simulations. The generated results of these simulations are compared regarding the occurring losses and the necessary energy for SoC-management. The operability of the algorithm in the simulation is shown via Fig. 4.30, which shows the time series of several parameters during the first day of the simulation over one month. Fig. 4.30(a) shows the progression of the frequency. Fig. 4.30(b) shows the resulting total power P, splitted up in the two components of FCR-power P_{FCR} and the power for SoC-management P_{SoC}. Fig. 4.30(c) shows the corresponding total power distribution between the subunits. And Fig. 4.30(d) shows the SoC of the subunits. Reaching the limit of the SoC-band SoC_B leads to an activation of the SoC-management, as shown in Fig. 4.30(b), which is active until the SoC-target SoC_T is reached. The SoC of the subunits also show the regular change of the "leading subunit" as defined by Eq. (4.43), which guarantees a defined maximum delta between the SoC of the subunits.

The comparison of the required energies of the four cases; case 1 ("00" DoF are deactivated, algorithm to minimize losses is deactivated), case 2 ("01" DoF deactivated, algorithm activated), case 3 ("10" DoF activated, algorithm deactivated) and case 4 ("11" DoF activated, algorithm deactivated) is shown in Fig. 4.31. The activated algorithm to minimize losses reduces the losses by 40 % with deactivated DoF and by 43 % with activated DoF as shown in Fig. 4.31(a). The losses in case 3 and case 4 are higher than in case 1 and case 2, because of a higher energy for FCR-provision due to the DoF. This is shown in Fig. 4.31(b). The energy for FCR-provision in the cases 3/4 is higher than in the cases 1/2. The increased energy for positive FCR-provision P^{+}_{FCR} can be covered by the losses itself. The increased energy for negative FCR-provision P^{-}_{FCR} is relatively small, but the corresponding losses increase the effect on the SoC, also because of the standby losses also arise in the partial load range of FCR. Therefore, the activation of DoF creates higher losses, but in summary these losses do not have an increasing impact on the energy for SoC-management, and still result in a reduction of this energy for SoC-management. Fig. 4.31(c) shows the energy for SoC-management. The necessary energy for SoC-management is reduced in the cases 3/4, compared to the cases 1/2 by 25 % and 33 %. The activation of the DoF as well as the algorithm to minimize losses leads to a reduction of the necessary energy for SoC-management of 48 %, as shown in Fig. 4.31(c) by comparing case 1/4.

4.1.8 Field Measurements

The DoF and the algorithm to minimize losses described above were implemented and tested on a BESS test site described in Chp. 3.1. Measurement results of the corresponding tests are presented and described below.

4.1.8.1 Provision of FCR

In Chp. 4.1.1.2 the "normal state" was introduced as a situation in which the system is within operational security limits. The normal state prevails in most of the time and the frequency deviations are mainly in a range of ±50 mHz. Therefore, the FCR-power of all FCR-regulating units is only partly activated. According to Chp. 4.1.2, the droop curve of FCR-regulating units is tested via synthetic frequency deviations during the prequalification process. To be able to measure the droop curve of FCR during operation of an FCR-regulating unit, significant frequency deviations can be used. Such significant frequency deviations occurred, for example, at the 10.01.2019 and at the 24.01.2019. At 10.01.2019 the frequency dropped to a value of about 49.2 Hz, whereas at 24.01.2019 the frequency rose to a value of about 50.2 Hz. Detailed information on the circumstances of these massive frequency events can be found in [53]. The combined measurements of the power output of a FCR-regulating unit at these two days allows the mapping of the entire droop curve as shown in Fig. 4.32. Fig. 4.32 the power measurements of the BESS described in Chp. 3.1 during these two frequency events and compares their values with the reference droop curve.

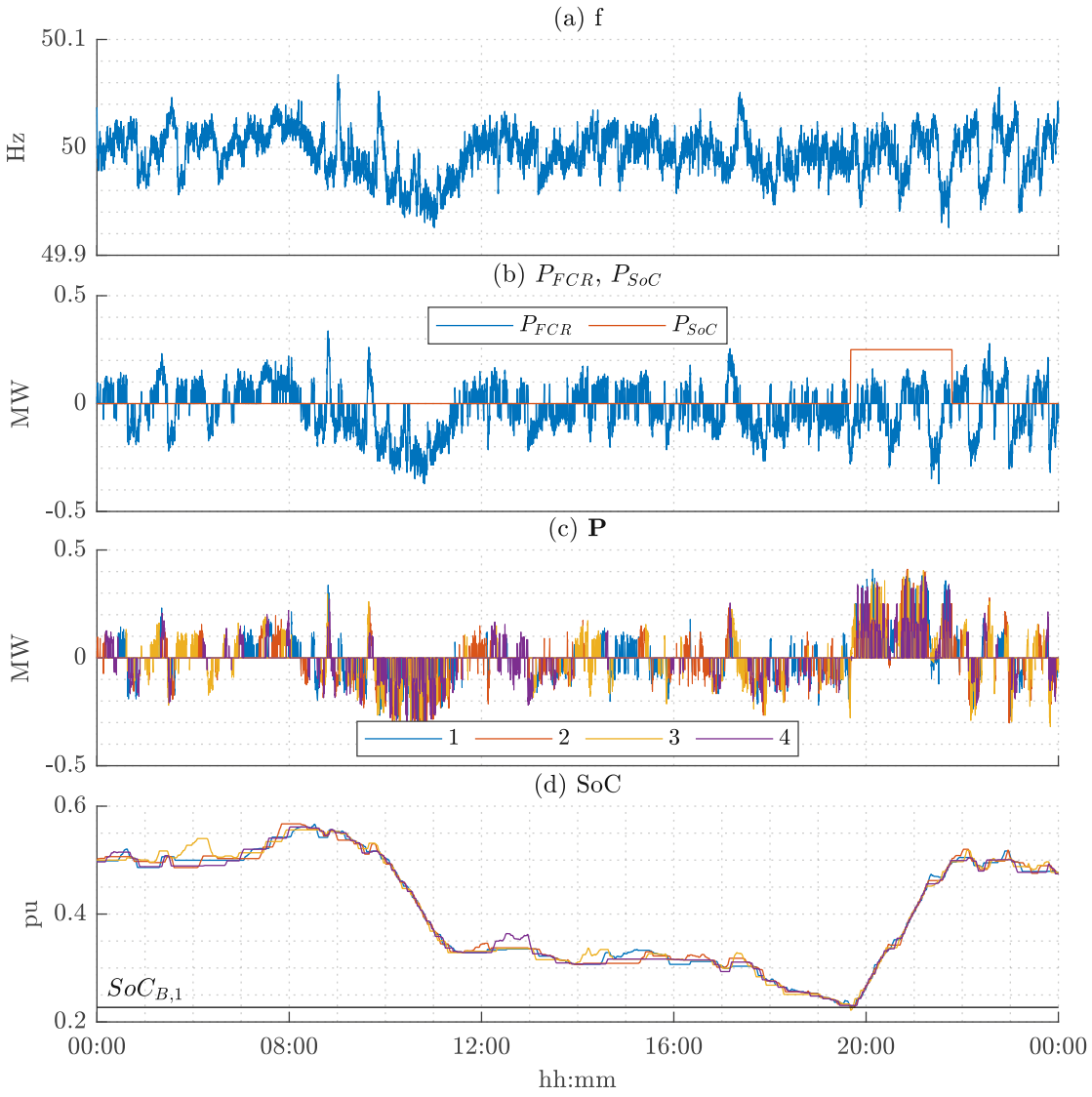

Figure 4.30: Simulation results of FCR provision with activated algorithm to minimize losses for one day. (a) shows the frequency, (b) shows the provided FCR-power output and the power output for SoC-management, (c) shows the power output of the subunits and (d) shows the SoC-levels of the subunits [122].

Besides the inactivity within the frequency deadband around 50 Hz, Fig. 4.32 also shows that the power output follows this reference droop curve very good. The measurement was taken at the PCC of the BESS, which is the 30 kV busbar according to Fig. 3.1. Therefore, the measured power values also prove a correct compensation of all losses and the power consumption by auxiliary systems by the control system of the BESS since the reference droop curve is related to the PCC of the BESS.

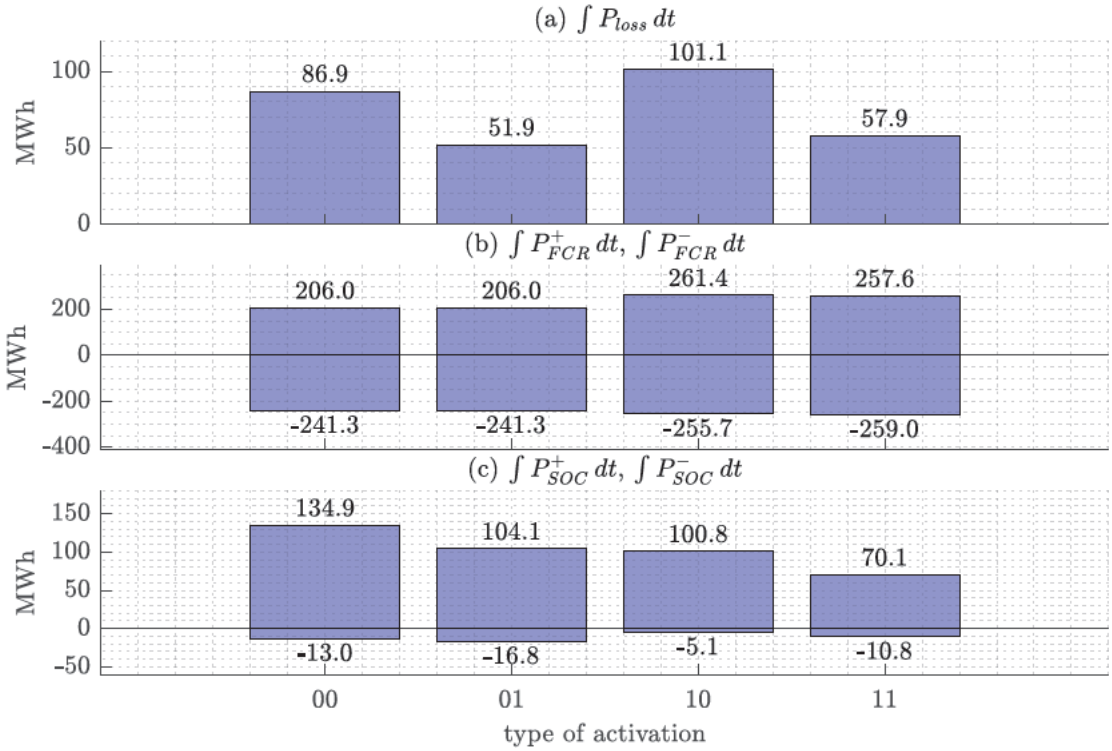

Figure 4.31: Comparison of resulting (a) losses, (b) energy for FCR and (c) energy for SoC-management, for the four possibilities of {active/inactive DoF, active/inactive algorithm to minimize losses}. "10" means the DoF are activated and the algorithm to minimize losses is deactivated. Frequency measurement data of the period between 01.12.2018 to 29.08.2019 is used as input data.

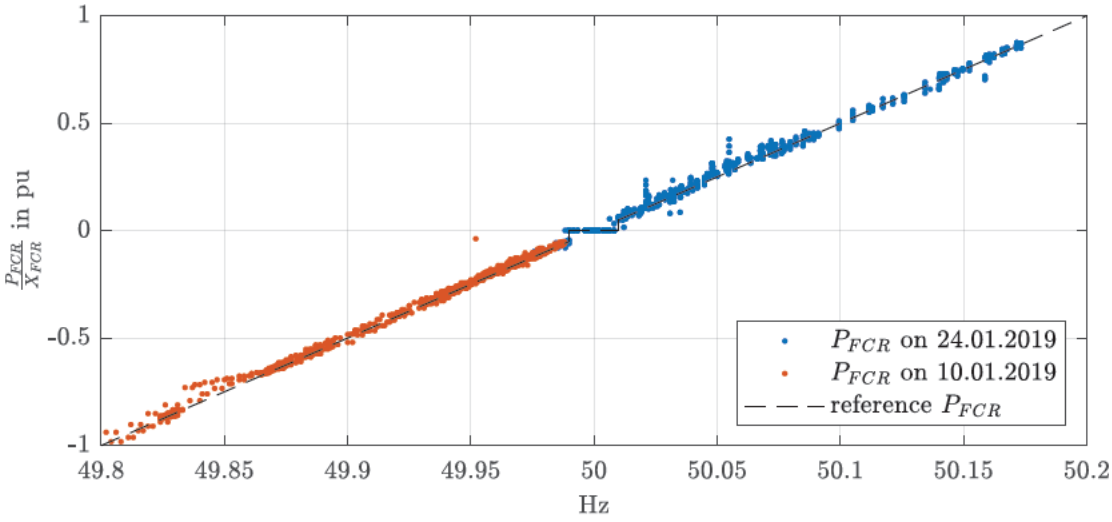

Figure 4.32: Measurement of the droop curve of FCR of two days at which significant frequency deviations occurred, measured at a test site described in Chp. 3.1.

4.1.8.2 SoC-Management

The frequency events mentioned in Chp. 4.1.8.1 are leading to alert states as described in Chp. 4.1.1.2 and shown in Fig. 4.2. Therefore, these frequency events are also valuable to verify the correct behavior of the SoC-management, since the occurrence of an alert state requires the mandatory activation of the SoC-management. Fig. 4.33 shows the behavior of the SoC-management during the first frequency event on January 10, 2019. Fig. 4.33(a) shows the measurement of the frequency over time and marks times when the criteria for an alert state are met. During the hour change at 19:00, 20:00 and 21:00, frequency drops of up to -200 mHz are visible. All three frequency drops meet the requirement for the occurrence of an alert state. The course of the frequency also shows a trend to be below 50 Hz, which indicates a permanent shortage of power in the power system. Fig. 4.33(b) shows the measurement of the total power output of the BESS over time and the corresponding reference output for FCR $P_{FCR,ref}$. The total power output consists of the shares for FCR P_{FCR} and the SoC-management P_{SoC}. The permanent under-frequency leads to an offset between the reference power for FCR and the total power output, since the SoC-management is active almost permanently in order to compensate for the continuous activation of FCR. Fig. 4.33(c) shows the actual SoC of the four battery groups of the BESS according to Fig. 3.1. The figure also marks the working area of the BESS, whose boundaries are indicated by "AS". As described in Chp. 4.1.6, the losses of the BESS have to be taken into account when calculating the boundaries of the working area. The mean efficiency of the BESS can be used to consider the losses. Furthermore, the energy content of the BESS is dependent on the usable SoC-window as described in Tab. 3.1. This usable SoC-window is parameterized as 6 % – 93 % during these field test. Considering the efficiency and the usable SoC-window, the working area can be calculated by

$$\mathbf{AS} = \begin{pmatrix} 0.06 + \frac{\frac{X_{FCR}}{\eta} \cdot T_{crit}}{E} \\ 0.93 - \frac{\eta \cdot X_{FCR} \cdot T_{crit}}{E} \end{pmatrix} = \begin{pmatrix} 0.06 + \frac{\frac{2\,\mathrm{MW}}{0.96} \cdot 0.5\,\mathrm{h}}{3.286\,\mathrm{MWh}} \\ 0.93 - \frac{0.96 \cdot 2\,\mathrm{MW} \cdot 0.5\,\mathrm{h}}{3.286\,\mathrm{MWh}} \end{pmatrix} = \begin{pmatrix} 0.38 \\ 0.63 \end{pmatrix}. \tag{4.53}$$

This leads to an SoC-band for the activation of the SoC-management that can be calculated by

$$\mathbf{SoC}_B = \begin{pmatrix} 0.06 + \frac{\frac{X_{FCR}}{\eta} \cdot (T_{crit} + \frac{T_{Lead}}{4})}{E} \\ 0.93 - \frac{\eta \cdot X_{FCR} \cdot (T_{crit} + \frac{T_{Lead}}{4})}{E} \end{pmatrix} = \begin{pmatrix} 0.06 + \frac{\frac{2\,\mathrm{MW}}{0.96} \cdot (0.5\,\mathrm{h} + \frac{0.25\,\mathrm{h}}{4})}{3.286\,\mathrm{MWh}} \\ 0.93 - \frac{0.96 \cdot 2\,\mathrm{MW} \cdot (0.5\,\mathrm{h} + \frac{0.25\,\mathrm{h}}{4})}{3.286\,\mathrm{MWh}} \end{pmatrix} = \begin{pmatrix} 0.42 \\ 0.60 \end{pmatrix}. \tag{4.54}$$

Fig. 4.33(c) proves that the SoC of each battery group stays within the working area, excluding the times when an alert state is present.

Fig. 4.34 shows the behavior of the SoC-management during the second frequency event on January 24, 2019. The figure shows the same information and has the same structure as Fig. 4.33.

Contrary to the first frequency event, the frequency shows three frequency rises at 06:00, 07:00 and 08:00, as shown in Fig. 4.34(a). The first of these three events reaches a frequency deviation of nearly 200 mHz and fulfills the criteria of an alert state. Fig. 4.34(b) shows the corresponding reaction of the BESS, whose total power consumption reaches a value of nearly 2 MW. Since the mean SoC of the BESS stays within the working area, the total power and the reference power for FCR are rather identical in Fig. 4.34(b). Fig. 4.34(c) shows that the SoC of each battery group stays within the working area.

4.1.8.3 Degrees of Freedom during Provision of FCR

The DoF described in Chp. 4.1.4 were implemented and tested at a BESS test site described in [121]. To test functionality, the SoC of the BESS was set to high/low values intentionally during two time periods. The corresponding measurements are shown in Fig. 4.35.

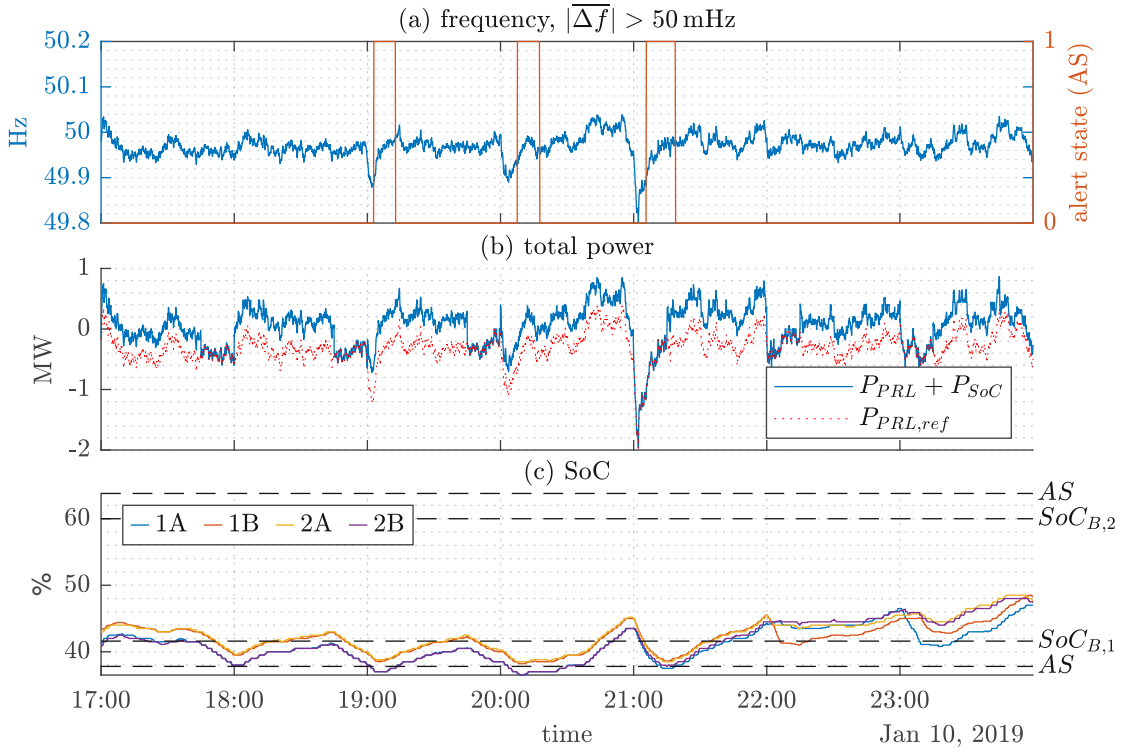

Figure 4.33: Behavior of the SoC-management on January 10, 2019.

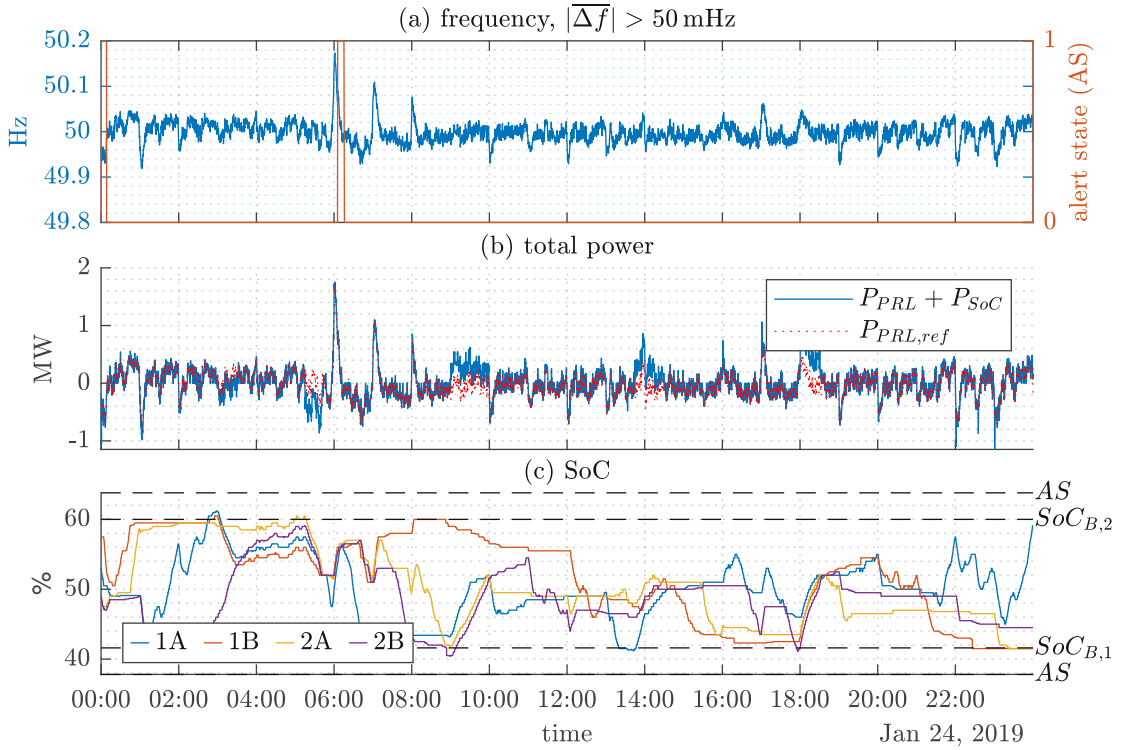

Figure 4.34: Behavior of the SoC-management on January 24, 2019.

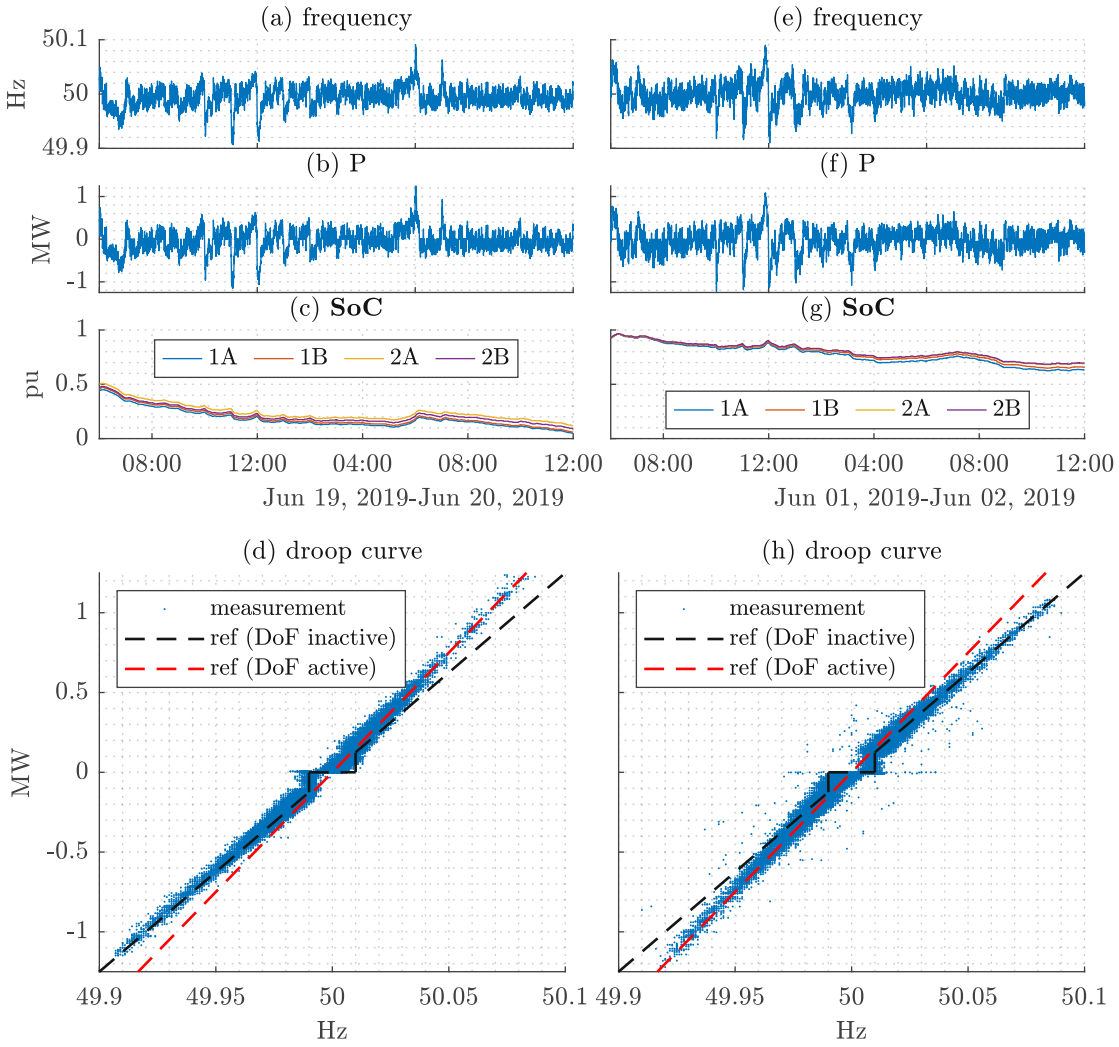

Figure 4.35: Test site measurement of a BESS (described in Chp. 3.1) providing FCR. For two time periods the frequency, the FCR-power, the SoC of all subunits and the droop curve are shown in (a),(b),(c),(d) and (e),(f),(g),(h). The subfigures (d) and (h) show the measurements and the reference droop curves in case of activated/deactivated DoF.

Fig. 4.35(d) shows the corresponding normalized droop curve $\frac{P_{FCR}}{X_1}(f)$ in case of a continuously low SoC ($SoC < SoC_T$). This circumstance guarantees a continuous activation of the DoF in times of $f > 50\,\text{Hz}$ and a deactivation of the DoF in times of $f < 50\,\text{Hz}$.

Fig. 4.35(h) shows the corresponding normalized droop curve $\frac{P_{FCR}}{X_1}(f)$ in case of a continuously high SoC ($SoC > SoC_T$). This circumstance guarantees a continuous activation of the DoF in times of $f < 50\,\text{Hz}$ and a deactivation of the DoF in times of $f > 50\,\text{Hz}$. The two droop curves prove the correct functionality of the DoF deadband according the Eq. (4.25) and the DoF overfulfillment according to Eq. (4.26) as described in Chp. 4.1.4.

4.2 Synthetic Inertia

The increasing amount of renewable energy sources in the electrical energy system leads to an increasing number of converter-based generators connected to the electrical power grid. Other than conventional power plants that are often connected to the grid via synchronous generators, converter-based generators do not provide mechanical inertia intrinsically. Therefore, ensuring frequency stability in the electrical power grid might become even more difficult in the future. With the concept of SI, the converter-based generators partially imitate the behavior of conventional generators. By implementing such a concept in converters, they are capable of contributing to frequency stability as well.

This chapter compares two strategies to realize SI by modeling converter-based generators in MATLAB/SIMULINK and simulating their behavior in a small Microgrid. The results prove that any kind of realization of SI helps to improve frequency stability. Each of the two investigated strategies may have their scope of application in a future electrical energy system. This chapter also presents and discusses measurements which are taken at the BESS test site described in Chp. 3.1, where SI has been implemented.

This chapter incorporates investigations and analyses published in paper [115].

4.2.1 Basic Considerations

Generators in conventional power plants provide mechanical inertial response due to their rotating masses. The entirety of all rotating masses results in a network inertia constant, which represents a characteristic value of how the electric power grid instantaneously reacts to power disturbances caused by imbalances between load and generation. The globally desired goal of reducing greenhouse gases by integrating Renewable Energy Sources (RES) into the power grid generally leads to a displacement of conventional power plants. In further consequence, the network inertia constant in the electric power system decreases, since a high amount of RES is mainly based on converter-based generators, which do not inherently provide an inertial response. A decreased network inertia constant may lead to critical stability challenges [128]. Results of a reduced inertia in the system are more frequent large frequency deviations which may affect system operation, security and reliability by overloading transmission lines, damaging equipment or triggering system defence plans and protection relays [19]. Such frequency stability issues due to reduced inertia already appear today, especially in smaller interconnected areas such as in the United Kingdom [67] or the Nordic synchronous area [44]. According to [147], the predicted decrease of system inertia in the regional group CE may not lead to an unacceptable frequency behavior in the near future. But particularly in the case of a system split after a disturbance, the resulting imbalance combined with low inertia could result in unstable system behavior. The purpose of the concept of SI is to mimic the behavior of the inertial response of synchronous generators. The aim of its implementation in converter-based generators is to maintain frequency stability in a future electric power system with a high amount of RES integrated in the grid. Several studies have already shown the usefulness of the concept of SI to improve resilience in the electric power system [17, 109]. A possible challenge for the introduction of synthetic inertia is the lack of harmonized requirements in international grid codes and financial incentives to equip converters with the capability to provide such a service. Possible ways to realize a market for providing synthetic inertia are discussed in [76, 142].

There are several strategies to realize synthetic inertia. The paper [173] presents an overview of current state-of-the-art strategies to realize synthetic inertia and compares them. Conventional converter control of grid-connected converters is mainly based on a “grid-following” approach, which means that the converter synchronizes with a stable voltage at its terminals. Some converters are capable of producing an output voltage on their own. A corresponding converter control is usually referred to as “grid-forming” control. The most straightforward approach to realize

synthetic inertia is based on a grid-following approach where the local frequency measurement is used in order to provide a power reference that behaves identical to the inertial response of conventional generators according to the swing equation. Such an approach has been studied in several works [127, 99, 171]. However, the necessary power output for such a grid-following approach to realize synthetic inertia is coupled with a delay of the frequency measurement that may lead to instabilities [107]. Therefore, recent activities concentrate on grid-forming control techniques, which do not necessariliy have such an inherent delay, but are capable of instantly providing a power response in case the frequency changes. The "virtual synchronous machine" is a popular concept that implements such an approach and goes beyond by trying to exactly imitate the behavior of a synchronous machine [15]. Converters implementing such a control approach are also called "synchronverters" [207]. A variety of reasearch activities investigated strategies to emulate synchronous machines in the converter control [206, 18, 30]. However, according to [128] this approach has its limitations and may also be a wasteful approach, considering that many strengths of a converter-based generator become unused, as for example its very fast control system emulates the comparably slow dynamics of a synchronous machine. An overview of possible grid-forming control strategies such as droop control, synchronverters, machine matching control or virtual oscillator control is given in [175].

Based on the control approach that is used, which is either a grid-following or a grid-forming control approach, the converter control has to be designed accordingly. Basic structures to realize the converter control including the grid synchronization, the voltage and current control, as well as the PWM generation are presented in [177]. Several studies investigated the behavior of grid-following and grid-forming approaches to realize synthetic inertia via simulations by using and expanding these basic control structures. An example of a simulation of the behavior of different grid-forming strategies to realize synthetic inertia is performed in [176]. By using an IEEE nine-bus test system, [176] proves that the presence of grid-forming converters improves the frequency stability metrics compared to a test system without their integration. The paper also reveals that under large load disturbances it is vital to implement a current limiting scheme. In [43] a qualitative analysis of the characteristics of grid-following and grid-forming control topologies to provide a transient response is carried out. A minimum measuring period of about 20 ms to detect the grid voltage and to generate a corresponding response in grid-following converters is stated as the major drawback of grid-following converters compared to grid-forming converters in [43], especially since grid-forming converters are theoretically capable of injecting power into the grid instantaneously after a grid event. However, a comparison of the effectiveness of the two approaches to realize synthetic inertia may still be an issue to be investigated in more detail, especially as most existing converters are based on a grid-following control structure, also due to its easier and cheaper implementation. Changing the control approach of existing converters to a grid-forming control approach is not an option, but upgrading a grid-following approach by a corresponding realization of synthetic inertia may be a feasible option. In addition, there are several open questions of how to realize a grid-forming control structure, e.g., an appropriate current limitation. Therefore, this paper investigates the differences between a grid-following and a grid-forming control approach in more detail in order to compare their effectiveness.

This chapter is structured as follows. Chp. 4.2.2 presents the basics on realizing synthetic inertia by describing the inertial response of conventional generators. Building on that, Chp. 4.2.3 describes the models in Chp. 4.2.3.2 and Chp. 4.2.3.3 that are used to investigate two strategies to realize synthetic inertia. Chp. 4.2.4.2.1 presents simulation results of a load-step in a Microgrid. Chp. 4.2.4.2.2 presents the results of a sensitivity analysis.

4.2.2 Strategies To Realize Synthetic Inertia

The majority of generators in power plants are synchronous machines. A change of their electrical load leads to a mechanical torque on the rotor of these synchronous machines. The rotor of these

synchronous machines has a certain mass, which manifests itself in the form of inertia in case of a load change. Based on the swing equation, the electromagnetic torque M and the mechanical torque M_m coming from a turbine are set in context by

$$M_m - M = J\dot{\omega} \tag{4.55}$$

where ω is the rotational speed, $\dot{w}$ is its derivative and J is the rotation inertia of the synchronous machine. The relationship between the power difference of mechanical power P_m and electrical power P during a load-step then becomes

$$P_m - P = \Delta P = J\dot{\omega}\omega \tag{4.56}$$

by multiplying the equation above by ω. By introducing the inertia constant $H = \frac{1}{2}\frac{J\omega_n^2}{S_n}$ and the starting time constant $T_A = 2H$, the equation can be rearranged to

$$T_A\dot{\omega}\omega = \frac{\Delta P}{S_n}\omega_n^2 = \Delta p\omega_n^2 \tag{4.57}$$

where S_n is the nominal apparent power and ω_n is the nominal rotation speed of the synchronous machine. The load-frequency control in a synchronous area in a first step is handled via the so-called "frequency containment reserves" (FCR). The droop control of FCR is realized in the speed governor of a synchronous machine, whose reference power output is proportional to the change of speed. In the equation above, according to [208] the FCR can be taken into account by adding a second term

$$T_A\dot{\omega}\omega = \Delta p\omega_n^2 + \frac{1}{\sigma}\Delta\omega\omega_n \tag{4.58}$$

where $\sigma = \frac{\frac{\Delta f}{f_n}}{\frac{\Delta P}{S_n}}$ is the droop, which is a proportional factor with $[\sigma] = \frac{\mathrm{Hz/Hz}}{\mathrm{W/W}}$. By assuming $\omega \approx \omega_n$ the equation can be rearranged to

$$T_A\dot{\omega} = \Delta p\omega_n + \frac{1}{\sigma}\Delta\omega. \tag{4.59}$$

Imitating a power output according to Eq. (4.57) in converter-based generators is termed as "synthetic inertia". This thesis considers two approaches to realize such a synthetic inertia:

- "Active synthetic inertia", realized by using a grid-forming control strategy that relies on determining the grid angle based on Eq. (4.59) and
- "Passive synthetic inertia", realized by calculating a reference power according to Eq. (4.58) that is used in the control of a grid-following converter.

The first approach is the best way to imitate the behavior of a synchronous machine but its drawback is the complex control structure that has to be implemented in a converter. The quality of the power output of the second approach, on the other hand, relies mainly on the quality of the frequency measurement device that is used, whose design is a trade-off between accuracy and speed. An actual implementation of the two approaches is described in Chp. 4.2.3.

4.2.3 Model Description

As already mentioned in Chp. 4.2.2, the realization of an "active synthetic inertia" is based on grid-forming converters. Grid-forming converters actively control their output voltage and therefore are capable of building an island grid. Active synthetic inertia in grid-forming converters can be realized by calculating a reference grid angle θ based on Eq. (4.59), which is used in the converter

control instead of using a fixed value $\omega_n t$. Chp. 4.2.3.2 describes the realization of active synthetic inertia in more detail. Chp. 4.2.2 also describes the basis for the realization of "passive synthetic inertia", which is the only way to realize synthetic inertia in grid-following converters. Passive synthetic inertia is based on a calculation of the reference power based on Eq. (4.59). The grid synchronization of grid-following converters measures the grid angle θ and the grid frequency f. The latter can be used in a feed-forward control to calculate a reference power according to Eq. (4.59). Chp. 4.2.3.3 describes the realization of passive synthetic inertia in more detail.

For both approaches of realizing synthetic inertia, a simplified model of a converter is used in this model. The model of the three-phase Voltage Source Converter (VSC) used in Fig. 4.36 represents a two-level converter consisting of a DC-link and an inverter, followed by an LC-filter. To simplify matters, the DC-link is represented by a constant voltage source. The inverter is modeled by a self-commutated three-phase bridge that is controlled by a PWM signal. The output filter consists of an LC-filter, with the resistance representing the parasitic resistance of the inductance.

4.2.3.1 Design Considerations for the Output Filter

Because of the fast switching inverter, an output filter is required to smooth the AC output currents. A series inductor fulfills this task. Its value is determined on the basis of the maximum AC current ripple ΔI_{rip} that is permissible at the converter output. According to [177] a corresponding calculation of this value for two-level PWM converters can be carried out by

$$L = \frac{U_{DCL}}{2 \cdot \Delta I_{rip} \cdot f_{sw}} \tag{4.60}$$

where f_{sw} is the switching frequency of the PWM generation and U_{DCL} is the DC-link voltage. The capacitors at the converter output are used to filter the switching frequency harmonics. Fig. 4.36 shows that the capacitor voltage is sensed for the converter control. In this way, the power factor at the terminals of the converter is reduced because part of the reactive power of the inductors is compensated for by the capacitors. The desired power factor at the converter output is the basis for calculating the value of the capacitors. According to [16] this calculation can be carried out by

$$C = 0.05 \cdot \frac{1}{\omega_n \frac{U_n^2}{S_n}} \tag{4.61}$$

with S_n as the nominal apparent power of the converter.

4.2.3.2 Model of a Grid-Forming Converter with Active Synthetic Inertia

In order to describe the realization of active synthetic inertia, Fig. 4.36 shows a simplified converter model of a grid-forming converter and its control.

The different components of the control structure are described in the following sections.

4.2.3.2.1 Power Calculation

At the output of the converter the instantaneous phase-to-neutral voltages $\mathbf{u}_{N,t}$ and the instantaneous phase currents $\mathbf{i}_t$ are measured. In the "power calculation" these values are used to calculate the power output by using $p = \mathbf{u}_{N,t}^{\top} \cdot \mathbf{i}_t$. This power is used in the "SI control" to calculate the reference angle θ as shown in Fig. 4.37.

The droop share is provided with a rate limiter in order to decouple it from the power output related to synthetic inertia.

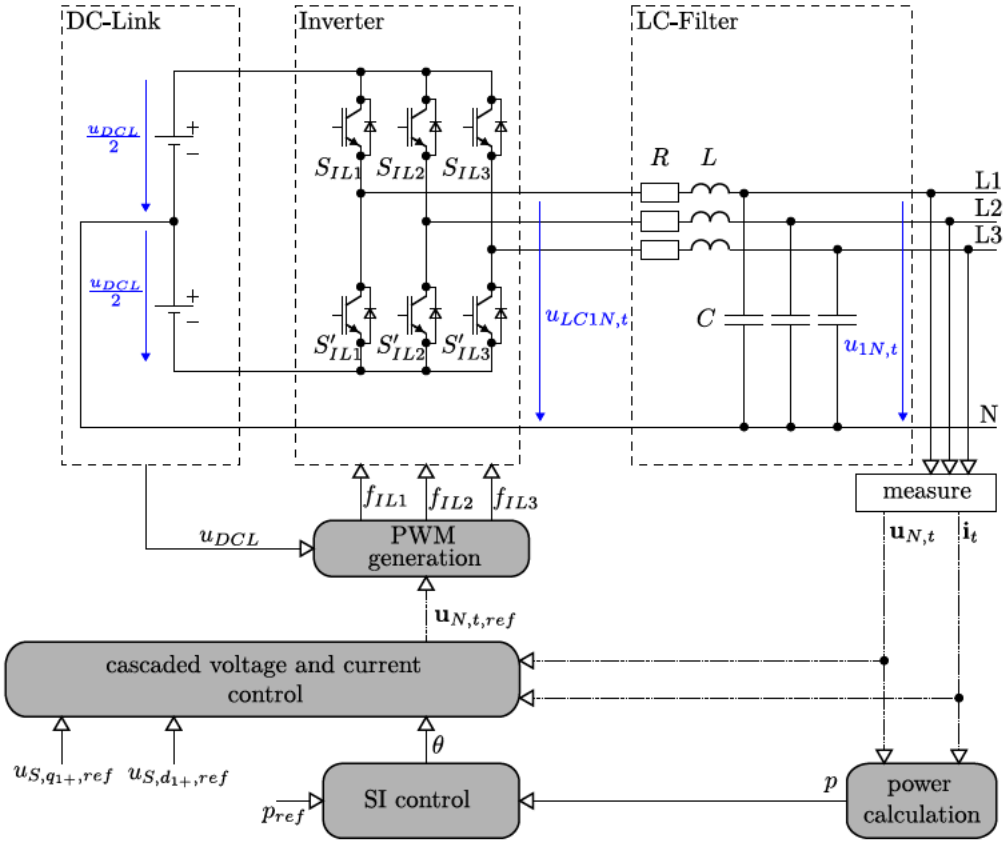

Figure 4.36: Model of a grid-forming converter and its control. The figure also shows relevant voltages which are marked in blue.

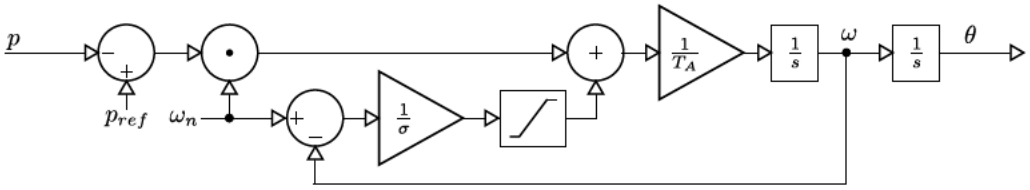

Figure 4.37: SI control of Fig. 4.36.

4.2.3.2.2 SI Control

Fig. 4.37 is based on Eq. (4.59), which is transformed into the Laplace domain:

$$T_A s\omega = \Delta p\omega_n + \frac{1}{\sigma}\Delta\omega \tag{4.62}$$

and integrated to determine the grid angle θ as follows

$$\theta = \frac{1}{s}\omega = \frac{1}{s^2}\frac{1}{T_A}\left[(p_{ref} - p)\omega_n + \frac{1}{\sigma}(\omega_n - \omega)\right]. \tag{4.63}$$

4.2.3.2.3 Cascaded Voltage and Current Control

The grid angle θ, combined with two reference voltages $u_{S,d_{1+},ref}$ and $u_{S,q_{1+},ref}$, which represent the direct/active and quadrature/reactive positive-sequence component of the voltage space vector $\underline{u}_{S,ref}$, are used as input of the "cascaded voltage and current control". This cascaded voltage and current control is shown in Fig. 4.38.

It consists of the voltage control (lower part in the figure) and the current control (upper part in the figure), which both use the SRF to control the direct/active- and quadrature/reactive- voltage and current component via PI-controllers. Park-transformations are used to calculate the voltage space vector $\underline{u}_{S,dq}$ and the current space vector $\underline{i}_{S,dq}$ based on the measured voltages $\mathbf{u}_{N,t}$ and the measured currents $\mathbf{i}_t$. To decouple the direct/active and quadrature/reactive components in the current control the decoupling terms $\frac{\omega}{\omega_n} l$ have to be taken into account. Across the LC-filter a voltage drop occurs that can be described by the difference between the voltage $\mathbf{u}_{LC,t}$ at the output of the inverter and the voltage $\mathbf{u}_{N,t}$ at the converter output. The voltage drop over the LC-filter can be calculated by using the normalized inductance l

$$l = \frac{\omega_n \cdot L}{\frac{U_n^2}{S_n}} \tag{4.64}$$

with the equation

$$\underline{u}_{LC,S,dq} = \underline{u}_{S,dq} + j\frac{\omega}{\omega_n} l \cdot \underline{i}_{S,dq} = u_{S,d} + i_{S,d}R - \frac{\omega}{\omega_n} l \cdot i_{S,q} + j \cdot (u_{S,q} + i_{S,q}R + \frac{\omega}{\omega_n} l \cdot i_{S,d}). \tag{4.65}$$

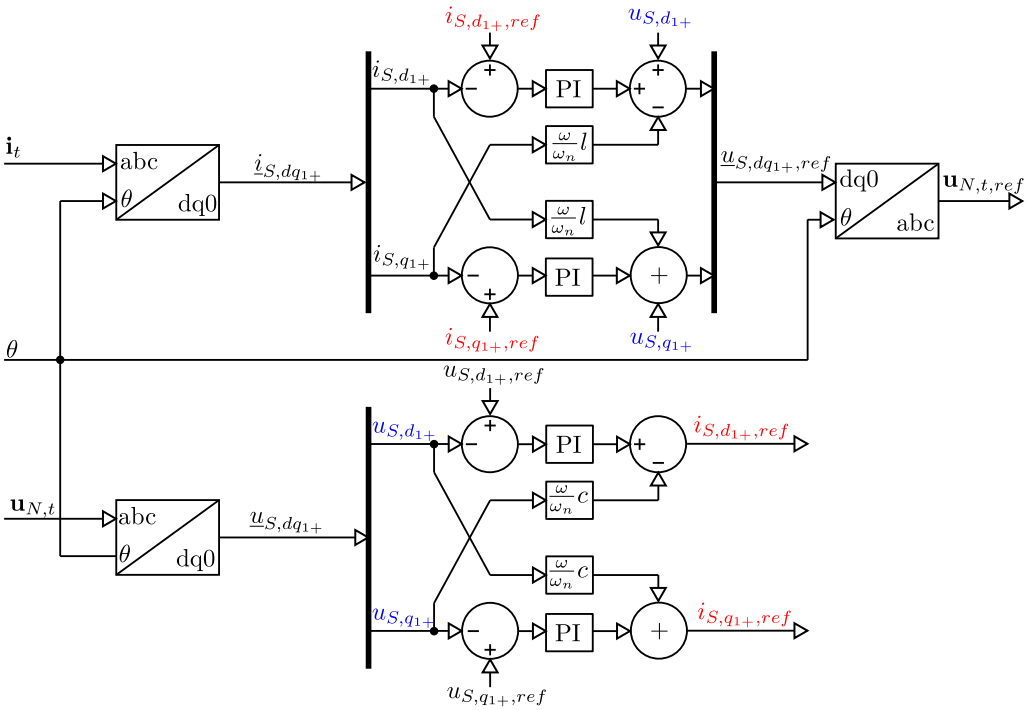

Figure 4.38: Cascaded voltage and current control of Fig. 4.36 (R of Eq. (4.65) is neglected). In order to improve clarity, the connection between $u_{S,d_{1+}}$ and $u_{S,q_{1+}}$ as well as the connection between $i_{S,d_{1+},ref}$ and $i_{S,q_{1+},ref}$ each from voltage control to current control are not shown directly but indicated in blue for the voltages and in red for the currents.

The same applies to the voltage control by using the decoupling terms $\frac{\omega}{\omega_n}c$ to take into account the currents through the capacitors in the LC-filter. The value of these currents can be calculated by using the normalized capacitance c

$$c = \frac{\omega_n C}{\frac{U_n^2}{S_n}} \tag{4.66}$$

with the equation

$$\underline{i}_{LC,S,dq} = \underline{u}_{S,dq} \cdot j\frac{\omega}{\omega_n}c = -u_{S,q}\frac{\omega}{\omega_n}c + ju_{S,d}\frac{\omega}{\omega_n}c. \tag{4.67}$$

The voltage control delivers a reference current space vector $\underline{i}_{S,dq_{1+},ref}$ which is used in the current control. The current control delivers an instantaneous reference voltage vector $\mathbf{u}_{N,t,ref}$ which is used as input of the "PWM generation".

4.2.3.2.4 Tuning Considerations

The tuning of the cascaded control structure relies on a decoupled consideration of the voltage and the current control which is achieved by tuning the current control much faster (about ten times) than the voltage control. The tuning then can be performed in a stepwise approach according to [80]. In a first step the current control is tuned. By using the decoupling network shown in Fig. 4.38 the active and reactive currents can be controlled separately via PI-controllers. According to [201] the tuning of these PI-controllers can be carried out as follows. The PI-controllers are represented by $R_I(s)$ in the Laplace domain:

$$R_I(s) = K_{I,P} + \frac{K_{I,I}}{s}. \tag{4.68}$$

By neglecting the dynamics of the PWM generation and the inverter, which are considered to act very fast due to high switching frequency, the plant only consists of the LC-filter. Therefore, the transfer function of the LC-filter $G_I(s)$ can be described by

$$G_I(s) = \frac{\frac{1}{R}}{1 + s\frac{L}{R}} \tag{4.69}$$

resulting in a loop gain $L_I(s)$ of

$$L_I(s) = R_I(s)G_I(s) = \frac{K_{I,P}}{sL} \cdot \frac{s + \frac{K_{I,I}}{K_{I,P}}}{s + \frac{R}{L}}. \tag{4.70}$$

By choosing $K_{I,P} = \frac{L}{\tau_i}$ and $K_{I,I} = \frac{R}{\tau_i}$ the closed-loop transfer function $\frac{L_I(s)}{1+L_I(s)}$ has a first-order behavior with a freely selectable time constant τ_i.

According to [80] the voltage controller can be tuned in a second step. The PI-controllers of the voltage control are represented by $R_U(s)$ in the Laplace domain:

$$R_U(s) = K_{U,P} + \frac{K_{U,I}}{s}. \tag{4.71}$$

From the point of view of the voltage control, the transfer function of the plant also includes the transfer function of the current control. Due to the tuning of the current control it can be taken into account by a simple first-order transfer function. The voltage output of the converter only

depends on the current through the capacitance of the LC-filter. As a consequence, the transfer function of the plant can be summarized as

$$G_U(s) = \frac{1}{1+\tau_i s}\frac{1}{sC}. \tag{4.72}$$

This results in a loop gain $L_U(s)$ of

$$L_U(s) = R_U(s)G_U(s) = \left(K_{U,P} + \frac{K_{U,I}}{s}\right)\frac{1}{1+\tau_i s}\frac{1}{sC} \tag{4.73}$$

whose parameters $K_{U,P}$ and $K_{U,I}$ can be tuned by using the symmetrical optimum according to [201] with

$$K_{U,P} = \frac{C}{\tau_i}\sqrt{\frac{1-\sin\Phi_R}{1+\sin\Phi_R}} \tag{4.74}$$

and

$$K_{U,I} = \frac{K_{U,P}}{\tau_i}\frac{1-\sin\Phi_R}{1+\sin\Phi_R} \tag{4.75}$$

where Φ_R is the desired phase margin.

4.2.3.2.5 PWM Generation

The PWM generation generates the PWM-signals f_{IL1}, f_{IL2} and f_{IL3} based on the instantaneous reference voltage vector $\mathbf{u}_{N,t,ref}$. These PWM-signals control the switches S_{IL1}, S_{IL2} and S_{IL3}. The complementary switches S'_{IL1}, S'_{IL2} and S'_{IL3} are controlled by the PWM-signals f'_{IL1}, f'_{IL2} and f'_{IL3}. In order to speed up the simulation, the model uses an average-model based VSC, which is available in MATLAB/SIMULINK [179]. As the reference voltage $\mathbf{u}_{N,t,ref}$ can be used directly as an input of the VSC model, an actual representation of the PWM generation is not necessary.

4.2.3.3 Model of a Grid-Following Converter with Passive Synthetic Inertia

In order to describe the realization of passive synthetic inertia, Fig. 4.39 shows a simplified converter model and its control of a grid-following converter.

For the PWM generation the same properties as for Chp. 4.2.3.2.5 apply.

4.2.3.3.1 Grid Synchronization and Sequence Analyzer

Compared to a grid-forming converter that generates its own angle θ in order to build a reference signal for the PWM generation, a grid-following converter relies on an angle θ that is determined from the voltages $\mathbf{u}_{N,t}$ measured at the terminals of the converter. The "grid synchronization" accomplishes this task. The most common structure for grid synchronization is based on the synchronous reference phase-locked loop (SRF-PLL) which is shown in Fig. 4.40.

Via a Park-transformation the voltage vector $\mathbf{u}_{N,t}$ is transformed into a voltage space vector in the dq-plane, whose reactive/quadrature component $u_{S,q}$ is controlled via PID-controller in order to synchronize the output θ of an integrator with the measured voltage vector $\mathbf{u}_{N,t}$. In the case of an unsymmetrical voltage vector $\mathbf{u}_{N,t}$ or in case it contains harmonics the reactive/quadrature component $u_{S,q}$ oscillates. In order to provide a frequency measurement by the SRF-PLL, therefore, a filtering method is necessary. Fig. 4.40 shows a low-pass filter to accomplish this task. The speed and accuracy of active synthetic inertia depends heavily on the tuning of this low-pass filter.

The "sequence analyzer" shown in Fig. 4.39 determines the normalized positive-sequence voltage u_{1+} which is used in the active and reactive power control to calculate a corresponding current reference.

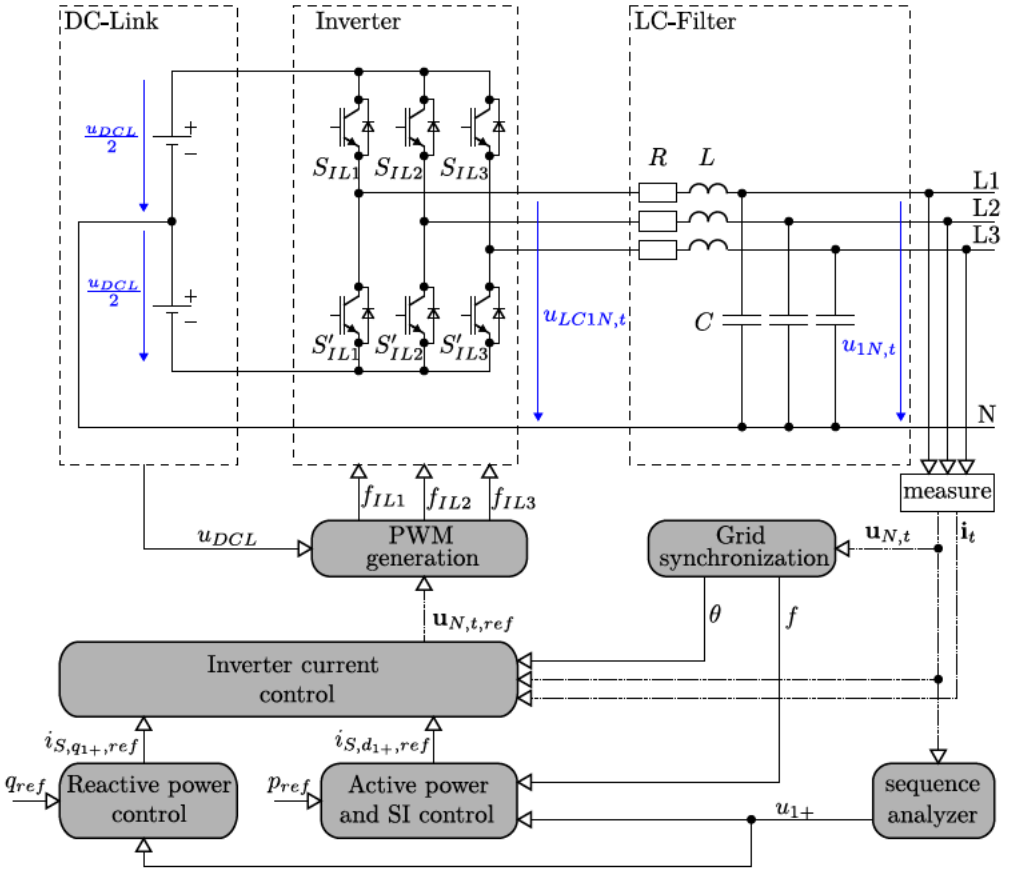

Figure 4.39: Model of a converter and its control, which is capable of providing passive synthetic inertia. The figure also shows relevant voltages which are marked in blue.

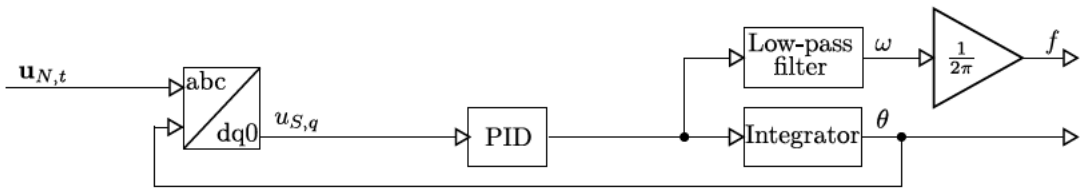

Figure 4.40: Grid synchronization of Fig. 4.39 realized as SRF-PLL.

4.2.3.3.2 Power and SI Control

The "active power and SI control" calculates an active current reference signal $i_{S,d_{1+},ref}$ in the positive-sequence system. Fig. 4.41 shows the structure of how this task can be accomplished.

The basic structure of the converter model has already been described in Chp. 4.2.3 and consists of a simplified DC-Link and an inverter, followed by an output filter. Based on Eq. (4.58) the passive synthetic inertia is implemented by using the measured frequency of the grid synchronization:

$$\Delta p = T_A \frac{df}{dt} \frac{f}{f_n^2} + \frac{1}{\sigma f_n} (f - f_n) \,. \tag{4.76}$$

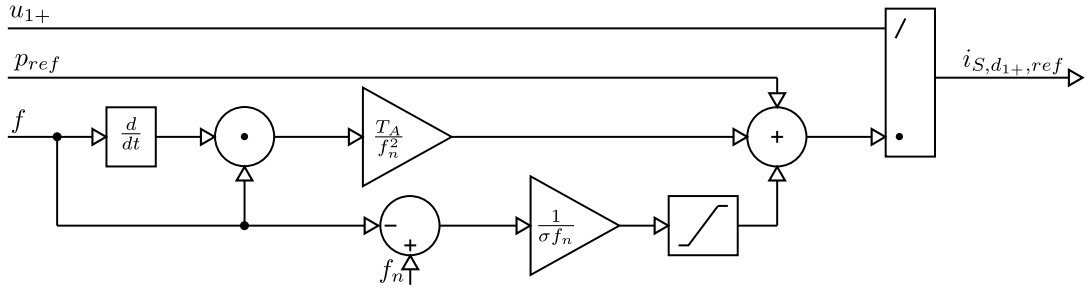

Figure 4.41: Active power and SI control of Fig. 4.39.

The derivative $\frac{df}{dt}$ in this equation which is also shown in Fig. 4.41 reacts very sensitive to changes of the frequency. Therefore, an appropriate filtering method has to be implemented. A possible way to do so is discussed in more detail in Chp. 4.2.4.1. As shown in Fig. 4.41 the droop share is provided with a rate limiter in order to decouple it from the power output related to synthetic inertia. Besides this power reference signal Δp, which is only different to zero when frequency gradients occur, the steady-state power reference signal p_{ref} is added. In order to take into account the voltage u_{1+}, this reference power is divided by u_{1+} in order to guarantee a corresponding current reference $i_{S,d_{1+},ref}$ in steady-state.

4.2.3.3.3 Reactive Power Control

The "reactive power control" provides a current reference signal $i_{S,q_{1+},ref}$ in the positive-sequence system by calculating

$$i_{S,q_{1+},ref} = \frac{q_{ref}}{u_{1+}}. \tag{4.77}$$

4.2.3.3.4 Inverter Current Control

The "inverter current control" uses the current reference signals $i_{S,d_{1+},ref}$ and $i_{S,q_{1+},ref}$, which are components of the current space vector in the dq-plane, the grid angle θ provided by the grid synchronization, the measured voltage vector $\mathbf{u}_{N,t}$ and the current vector $\mathbf{i}_t$ in order to determine a voltage reference vector $\mathbf{u}_{N,t,ref}$ for the PWM generation. The control structure of the current control is shown in Fig. 4.42 and basically has the same structure as the current control of the cascaded voltage and current control shown in Fig. 4.38, which is also based on a synchronous reference frame.

It uses the angle θ for Park-transformations of the voltage vector $\mathbf{u}_{N,t}$ and the current vector $\mathbf{i}_t$. The current components are controlled via PI-controllers each. By using the decoupling terms $\frac{\omega}{\omega_n} l$ each component can be controlled separately. Before generating the reference voltage vector $\mathbf{u}_{N,tref}$ by an inverse Park-transformation, the voltage components in the dq-plane are added to the output of the PI-controller.

4.2.3.3.5 Tuning Considerations

In order to tune the PI-controllers of Fig. 4.42 the same considerations as already mentioned for the current controller in Chp. 4.2.3.2.3 can be applied. This leads to a choice of parameters of the corresponding PI-controllers of $K_{I,P} = \frac{L}{\tau_i}$ and $K_{I,I} = \frac{R}{\tau_i}$.

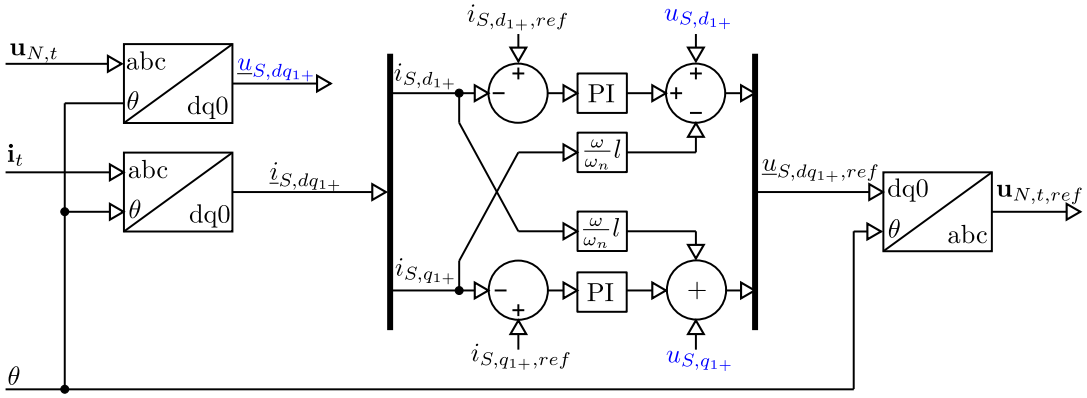

Figure 4.42: Inverter current control of Fig. 4.39. In order to improve clarity, the connection between $u_{S,d_{1+}}$ and $u_{S,q_{1+}}$ are not shown directly but indicated in blue.

4.2.4 Simulation

Basically, all converter-based technologies are capable of providing synthetic inertia by using one of the control strategies presented above. However, technologies based on renewable energy sources may have trouble providing the necessary power response at any given time. For example, there are wind turbines that are already commercially available today, which are capable of providing synthetic inertia [65, 129, 186]. One approach used in wind turbines to generate an inertial response is to temporarily increase the active power output based on the energy of the rotating masses. In response to a drop in grid frequency they temporarily increase their active power even beyond the available power from the wind by drawing energy from the rotating masses of the generator, the shaft and the blades. But at low wind speeds, the available energy in the rotating masses may be too low to provide a noteworthy amount of synthetic inertia, or the rotor may even stand still, which makes it impossible to provide inertial response. Assuming that synthetic inertia plays a key role regarding frequency stability in a future energy system, a certain percentage of technologies providing such a service may be required to deliver synthetic inertia at any time. Aside from technologies based on renewable energy sources, BESS can meet such a requirement. Furthermore, BESS are considered to be very well-suited to deliver such kind of highly dynamic system service and are also considered to replace conventional generators, which provide frequency reserves, to some extent in a future energy system [168]. Therefore, the following simulations consider battery converter systems for parametrization of the simulation models.

Chp. 4.2.4.1 describes the simulation set-up, Chp. 4.2.4.2 presents relevant simulation results and Chp. 4.2.4.3 discusses the results.

4.2.4.1 Simulation Set-Up

Fig. 4.43 shows a small Microgrid by which the behavior of the two converter models presented above is investigated. The Microgrid consists of a converter, a line, a load and a synchronous generator. Via Electromagnetic Transient (EMT) simulations in MATLAB/SIMULINK, the performance of the active and passive synthetic inertia approaches in reaction to load-steps is investigated and compared.

The parameters used in the simulation are summarized in Tab. 4.4. As already mentioned, the converter parameters are based on a converter that is used in a BESS which is described in more detail in [197]. For the synchronous generator, a MATLAB/SIMULINK-internal pre-set model is used [179]. As governor for the synchronous generator the MATLAB/SIMULINK-internal “SM Governor

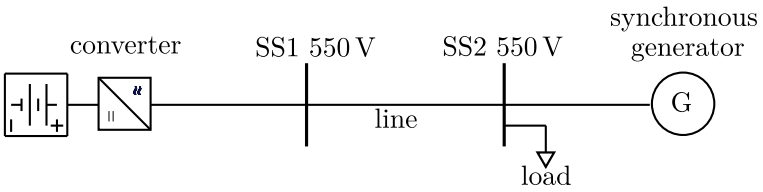

Figure 4.43: Microgrid used for the simulations.

with Droop" is used, where a time constant $\tau_{SM,G}$ and a droop σ are used that are listed in Tab. 4.4. As automatic voltage regulator of the synchronous generator the MATLAB/SIMULINK-internal model "ST1A Excitation system" with pre-set parameters is used. The constant impedance load is configured as a base load with 465 kW that is distributed between converter and generators with a reference power of the converter of 0.1 pu and a reference power of the generator of 0.4 pu.

First-order filter elements with a time constant of 1 s are used to implement the rate limiter in the control structures shown in Fig. 4.37 and Fig. 4.41. As already mentioned above, the realization of passive synthetic inertia requires several other filter elements. One of such filter elements is needed for the grid synchronization shown in Fig. 4.40. The frequency output of the SRF-PLL shown in Figure 4.40 requires an output filter in order to filter asymmetry of the input voltage $\mathbf{u}_{N,t}$ or harmonics in this input voltage. In the following simulations, this filter is realized as a second-order filter with a cut-off frequency of 10 Hz. Another filter element is necessary in the active power and SI control shown in Fig. 4.41. The use of a numerical derivative without filtering might be very sensitive to the dynamics of the entire model during simulation. But also in case of the implementation in a real converter system such a filtering method may be necessary. The frequency in real converter systems is usually measured in discrete time steps. The corresponding numerical calculation of the derivative might be sensitive to measurement errors. An appropriate filtering method can be applied to smooth the corresponding output of this calculation. For the following simulations, the filter element in Fig. 4.41 is modeled as a first-order filtered-derivative with a time constant of 50 ms.

4.2.4.2 Results

An active power load-step in the Microgrid is the simplest way to compare the behavior of the two presented control strategies of synthetic inertia. Therefore, Chp. 4.2.4.2.1 presents the simulation results of a single active power load-step in more detail. Building on that, a sensitivity analysis for different values of this active power load-step is performed. This sensitivity analysis also investigates the influence of the starting time constant T_A for both control strategies. Chp. 4.2.4.2.2 presents the results of this sensitivity analysis.

4.2.4.2.1 Simulation of a Single Load-Step for Both Models

In order to investigate the reaction to a load-step, the power of the load shown in Fig. 4.43 is increased by 500 kW, which leads to a maximum power output of the converter if the starting time constant of $T_A = 10$ s listed in Tab. 4.4 is taken into account.

The simulation results of such a load-step at 5 s are shown in Fig. 4.44. The figure compares the behavior of the active synthetic inertia ((a) and (b)) and the passive synthetic inertia ((c) and (d)). It shows the frequency of the generator f_{SM} and the converter f_C in (a) and (c), and the normalized power output of the generator p_{SM} and the converter p_C in (b) and (d). Fig. 4.44e shows a comparison of the power outputs p_C of active and passive synthetic inertia. For both variants identical parameters according to Tab. 4.4 are applied.

Table 4.4: Parameters used in the simulation.

Converter		Generator		Line	
Parameter	**Value**	**Parameter**	**Value**	**Parameter**	**Value**
U_n	550 V	U_n	550 V	R	0.01 Ω
S_n	650 kVA	S_n	1 MVA	L	0.1 mH
U_{DCL}	900 V				
L	260 µH				
R	1 mΩ				
C	342 µF				
τ_i	0.1 ms	$\tau_{SM,G}$	5 s		
$K_{I,P}$	2.6 pu				
$K_{I,I}$	10 pu				
Φ_R	60°				
$K_{U,P}$	0.916 pu				
$K_{U,I}$	658 pu				
σ	$\frac{1}{100}$ pu	σ	$\frac{1}{100}$ pu		
T_A	10 s	T_A	0.8 s		

The comparison of both simulation results shows a significantly improved frequency stability in case of active synthetic inertia leading to a frequency nadir (minimum frequency) of 49 Hz, compared to a frequency nadir of 48 Hz in case of passive synthetic inertia. A zoomed area of the relevant time range of the power output in Fig. 4.44 shows a noticeable delay of passive synthetic inertia compared to active synthetic inertia. This delay results from the filtering methods used in the SRF-PLL and the derivative of passive synthetic inertia. Both, the second-order low-pass filter, whose influence can be seen in the delayed frequency output shown in Fig. 4.44c, as well as the first-order filtered-derivative contribute to this delay and cause the power output of passive synthetic inertia not to reach the full power output of 1 pu as it is the case with active synthetic inertia. Comparing the time of occurrence of the frequency nadir in Fig. 4.44c with the peak power output of passive synthetic inertia in Fig. 4.44d shows that the peak power occurs after the frequency nadir. For active synthetic inertia, on the other hand, such a comparison in Fig. 4.44a,b shows that the first local frequency nadir occurs about at the same time as the peak power output of active synthetic inertia.

The frequency nadir is significantly influenced by the Rate of Change of Frequency (RoCoF) at the beginning of the load-step. The faster the reaction of synthetic inertia, the faster this RoCoF at the beginning of the load-step can be limited and the less pronounced the frequency nadir becomes. Therefore, the delayed reaction of passive synthetic inertia leads to a lower frequency nadir than in case of active synthetic inertia. Of course, it is theoretically possible to minimize the delays due to the PLL and the derivative computation, but at the cost of increasing the sensitivity of the system towards noise, faults and other fast transients.

4.2.4.2.2 Sensitivity Analysis

In order to investigate the behavior of active and passive synthetic inertia in dependence of the size of the load-step and the starting time constant of the converter, a sensitivity analysis is performed. The active power value of the load-step is varied with values of the set {50, 100, 200, 300, 400, 500} kW and the starting time constant is varied with values of the set {1, 2, 3, 4, 5, 6, 7, 8, 9} s for both models. Figure 4.45 shows the outcome of this sensitivity analysis. It displays the frequency nadir of the synchronous generator as a consequence of the corresponding load-step. A starting time constant of $T_A = 0$ s means that synthetic inertia is inactive and the synchronous generator is the only equipment in the Microgrid that dynamically stabilizes the frequency.

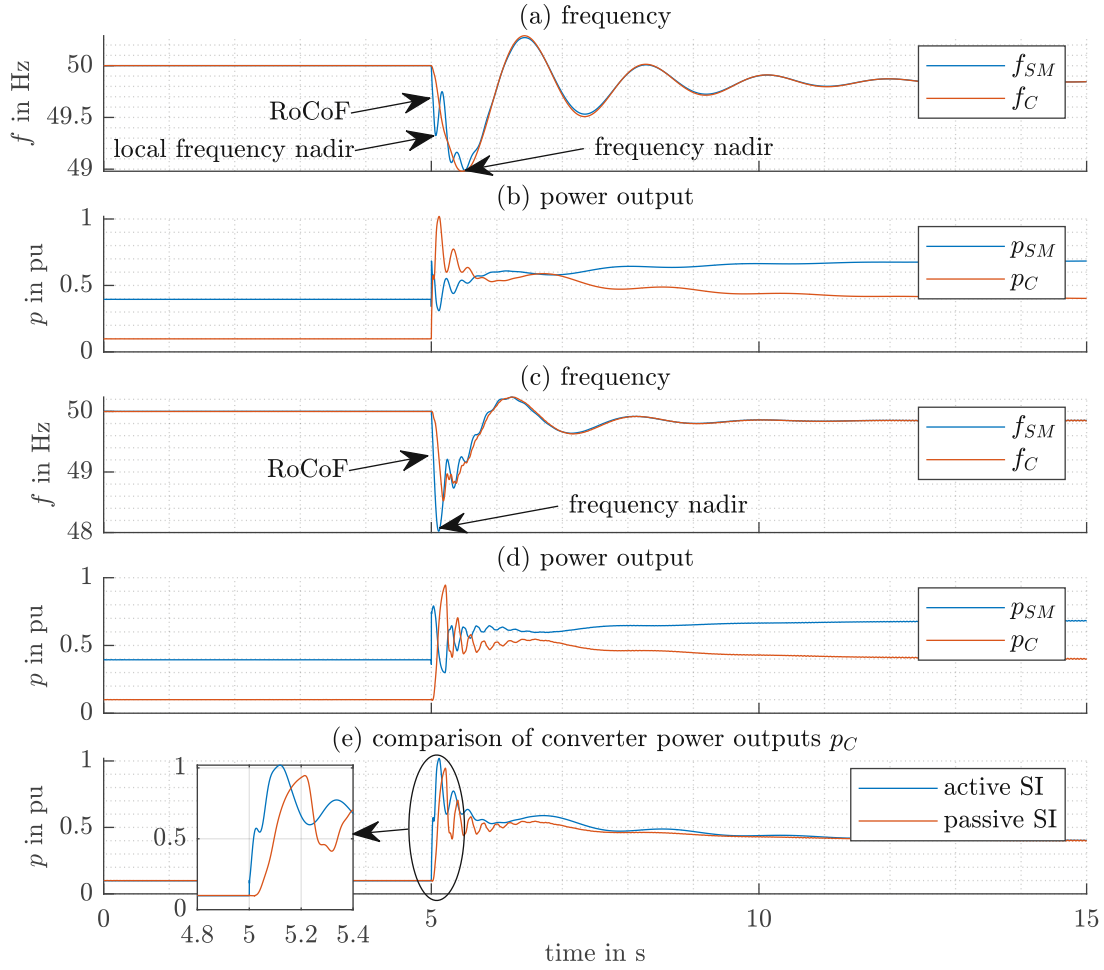

Figure 4.44: Simulation results of a load-step in the Microgrid shown in Fig. 4.43 in case active synthetic inertia is used in (**a**,**b**) and passive synthetic inertia is used in (**c**,**d**). (**a**,**c**) each show the frequency of the synchronous machine f_{SM} and the converter f_C, (**c**,**d**) each show the normalized power output of the synchronous machine p_{SM} and the converter p_C. (**e**) compares the converter power outputs for active and passive synthetic inertia where the relevant time range is zoomed out in an additional subfigure.

As already shown in Fig. 4.44 and described above, passive synthetic inertia is less effective in improving frequency stability as a consequence of the filtering techniques that are necessary to be implemented in the converter control. This can also be seen in Fig. 4.45, which shows that compared to $T_A = 0\,\mathrm{s}$, where only the synchronous generator stabilizes the Microgrid, already a small starting time constant of $T_A = 1\,\mathrm{s}$ massively helps to reduce the frequency drop in case of active synthetic inertia, whereas passive synthetic inertia has much less effect on the frequency nadir. During very small load-steps, the difference of the effectiveness between the two strategies is hardly visible, but becomes clearly visible with growing values of the load-step. Especially for small values of the starting time constant T_A, the effectiveness of active synthetic inertia is much higher compared to passive synthetic inertia. With increasing value of the starting time constant, a saturation effect becomes visible for both control strategies. This saturation effect can be argued with a limited power gradient of both control strategies. As already described in Chp. 4.2.4.2.1 for passive synthetic inertia, situations may occur when the RoCoF at the beginning of the load-step

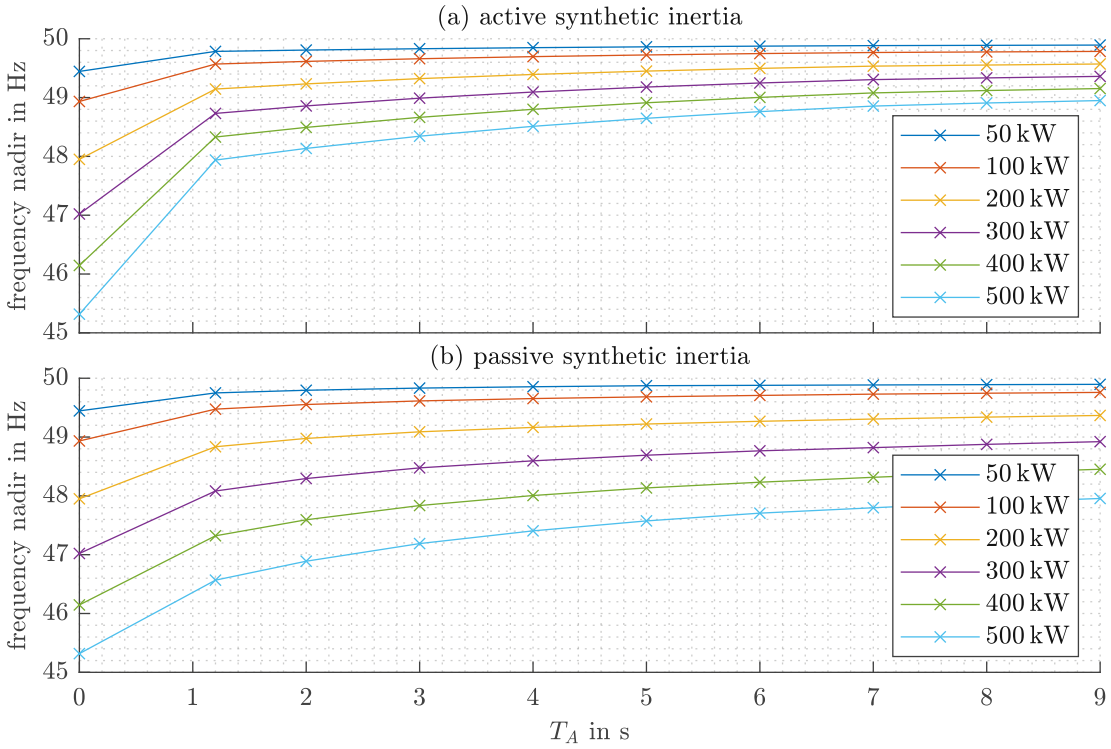

Figure 4.45: Comparison of frequency nadir for the sensitivity analysis of active and passive synthetic inertia with varying starting time constants T_A of the converter and different load-steps.

is so high that the time which is necessary to reach a certain amount of power output inherently leads to a certain frequency nadir, regardless of the value of the starting time constant. This is due to the limited maximum power gradient of the converter and its control. The impact of the two control strategies on the RoCoF can be seen more clearly in Fig. 4.46.

Fig. 4.46 shows the RoCoF over the frequency nadir for all results of the sensitivity analysis. The starting time constant of $T_A = 0\,\mathrm{s}$ indicates the inactivity of synthetic inertia and is the starting point for the lines which represent the increasing value of T_A, whose course continuously runs from the left to the right. While the RoCoF in case of using active synthetic inertia reaches its lowest value already at the lowest value of the starting time constant $T_A = 1\,\mathrm{s}$, the RoCoF in case of using passive synthetic inertia continuously decreases with an increasing value of the starting time constant.

4.2.4.3 Discussion

Figures 4.44 – 4.46 show that both strategies to realize synthetic inertia are capable of improving frequency stability during power deviations. The positive effect of synthetic inertia on frequency stability has already been proven in several other studies [56, 146]. The simulations above confirm these findings. In particular, the use of grid-forming converters and their positive effect on frequency stability has been shown already [175]. The simulations performed in this chapter allow to compare the effectiveness of the approaches of passive and active synthetic inertia. With increasing starting time constant, the effect of passive synthetic inertia increases, while the effect of active synthetic inertia is already saturated at small values of the starting time constant. Fig. 4.46 shows

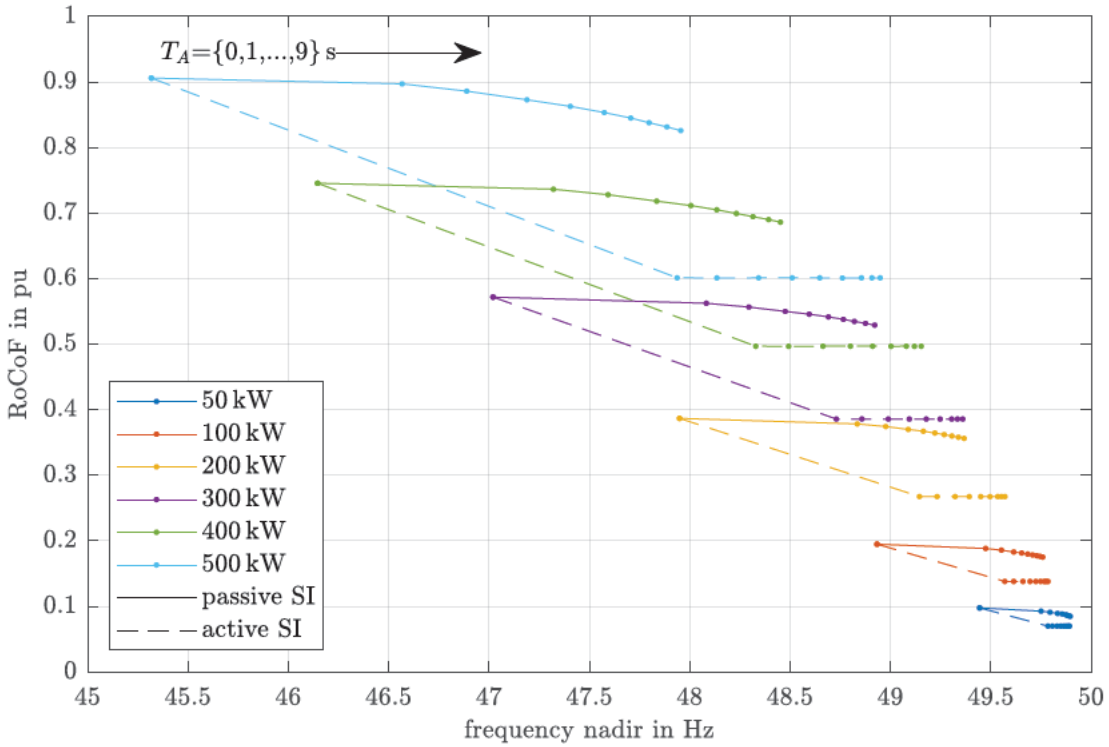

Figure 4.46: Comparison of the RoCoF over the frequency nadir for the sensitivity analysis of active and passive synthetic inertia with varying starting time constants T_A of the converter and different load-steps. The small points in the lines indicate the discrete values of the starting time constant which increases from left to right. The RoCoF is normalized to a value of 30 Hz/s. The high RoCoF values result from the relatively low inertia constant of the synchronous machine.

that the reason lies in the influence of synthetic inertia on the RoCoF. In case of active synthetic inertia, the minimum of the RoCoF is reached already at very small values of the starting time constant, whereas in case of passive synthetic inertia the RoCoF continuously decreases further with increasing value of the starting time constant. Therefore, the inevitable delay due to filtering methods in case of passive synthetic inertia can be compensated somewhat by choosing a higher starting time constant. A direct comparison of a grid-following and a grid-forming approach has also been carried out in [143]. The results in [143] show a larger variance of the frequency nadir in case of the grid-following approach, which can be confirmed by the simulation results generated in this paper. The finding of a higher necessary starting time constant in case of passive synthetic inertia in order to reach similar frequency metrics compared to active synthetic inertia resembles the statement in [143] of a necessary higher peak power injection of grid-following converters to reach similar frequency metrics compared to grid-forming converters.

In order to ensure a flawless operation of the loads connected to a grid, certain requirements regarding power quality have to be met. One of these requirements are frequency limits within which a grid has to be operated. According to relevant power quality standards [138], even in island operation the frequency has to be kept within certain limits. The lower value for this frequency limits during island operation is 49 Hz [138]. Keeping in mind this requirement, Fig. 4.45 shows that by using active synthetic inertia, load-steps of up to 500 kW are possible while still remaining in the allowable frequency range. By using passive synthetic inertia, on the other hand, Fig. 4.45 shows that only a maximum load-step of 300 kW would be possible.

4.2.5 Field Measurements

The BESS described in Chp. 3.1 is equipped with an implementation of "passive synthetic inertia" as described in Chp. 4.2.3.3. In order to investigate the behavior of passive synthetic inertia at a real BESS, two test environments are used:

- converter tests in the laboratory and
- BESS tests at the test site.

Since it is very difficult to influence the grid frequency at a real test site and the main functionality of passive synthetic inertia lies in the converter, the converter tests have the purpose to investigate the behavior of passive synthetic inertia under the influence of frequency test signals, which allow investigating the whole path from frequency measurement to power output of the converter. To be able to generate such signals, the converter tests are performed in the laboratory by using a corresponding voltage source, which is coupled to the converter. The BESS tests, on the other hand, have the purpose to investigate the behavior in a real world situation, where the whole BESS is involved in the process of providing passive synthetic inertia. To explain the difference between the two test environments in more detail, Fig. 4.47 presents an overview of relevant control parts for the realization of passive synthetic inertia and the test environment that results during the converter tests and the BESS tests. Fig. 4.47 shows that during the converter tests in the laboratory the DC-side of the converter is connected to a DC-voltage source that generates constant voltage, whereas during the BESS tests the converter is connected to the actual battery of the BESS. Fig. 4.47 also shows that during the converter tests the converter is connected to a AC-voltage source, which is used to generate a corresponding three-phase voltage system whose frequency varies based on the input of synthetic frequency signals. During the BESS tests, on the other hand, the converter is connected to the external MV-grid at the connection point of the BESS. In Fig. 4.47 the synthetic frequency signals that are used to investigate the behavior of passive synthetic inertia are used as input of the AC-voltage source during the converter tests and these signals are directly used as input of the "Active power and SI-control" during the BESS tests. The dynamics of the grid synchronization are therefore not taken into account in the BESS tests.

The converter control which is shown in Fig. 4.47 illustrates relevant parts for the realization of passive synthetic inertia, such as the grid synchronization and the active power and SI-control. The grid synchronization in Fig. 4.47 is based on Fig. 4.40, which shows a SRF-PLL, and illustrates the output LPF only. Both during the converter and the BESS tests for this LPF, a Butterworth filter 6th order with a cut-off frequency of 18 Hz is used. As described in [97], the accuracy of the frequency measurement is at least 1.25 mHz at a sampling rate of 100 ms. The minimum sampling rate that is supported is 20 ms, combined with an accuracy of 1.25 mHz. The Active power and SI-control in Fig. 4.47 is based on Fig. 4.41, but only illustrates the realization of the frequency derivative by using a LPF and a subsequent numerical derivative block. For the LPF a Butterworth filter 2nd order with a cut-off frequency of 0.5 Hz is used.

Fig. 4.48(b) shows a measurement result of the converter tests where synthetic frequency signals are used as input, which have different frequency gradients of $\{\pm 0.04\,\text{Hz/s}, \pm 0.125\,\text{Hz/s}, \pm 0.2\,\text{Hz/s}, \pm 0.33\,\text{Hz/s}\}$ and are shown in Fig. 4.48(a). Fig. 4.48(b) compares the ideal behavior of passive synthetic inertia in response to such synthetic frequency signals. An ideal behavior refers to an ideal frequency measurement without delay or inaccuracy and an ideal control of the converter. Besides this ideal behavior, Fig. 4.48(b) shows the measured power output of the converter and the simulated behavior. The simulated behavior only takes into account the "Grid synchronization" and the "Active power" and "SI-control" blocks of Fig. 4.47, neglecting the dynamics of the remaining converter control or the dynamics of the converter. It uses the measurement of measurements of the instantaneous voltage of the AC-voltage source of Fig. 4.47 as input signal.

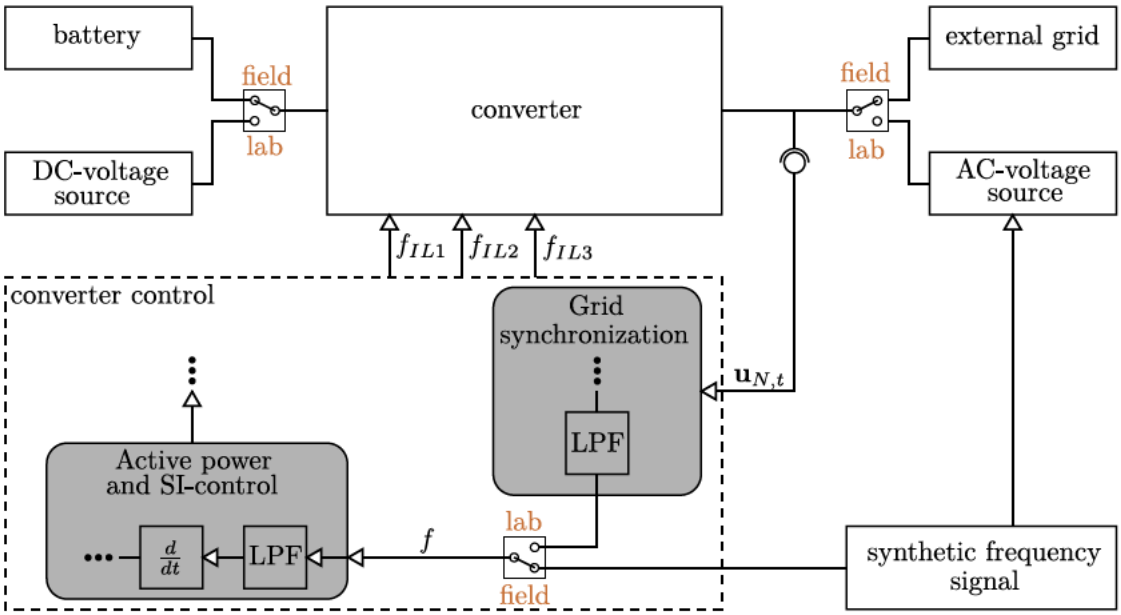

Figure 4.47: Relevant control parts for the realization of passive synthetic inertia according to Fig. 4.39 and the test environment that results during the converter tests (lab) and the BESS tests (field). "LPF" stands for Low Pass Filter.

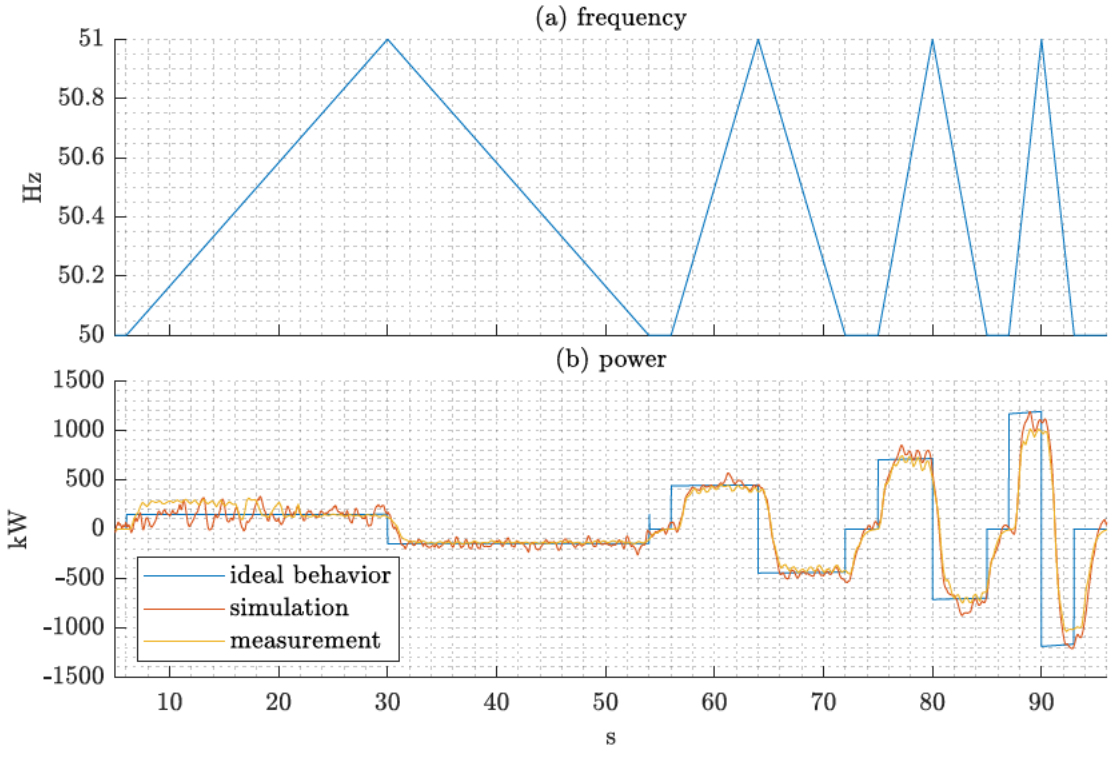

Figure 4.48: Comparison between ideal behavior, simulated behavior and measured behavior of passive synthetic inertia. The synthetic frequency signals result in frequency gradients of $\{\pm 0.04\,\text{Hz/s}, \pm 0.125\,\text{Hz/s}, \pm 0.2\,\text{Hz/s}, \pm 0.33\,\text{Hz/s}\}$.

The comparison of the ideal, the simulated and the measured behavior in Fig. 4.48(b) clearly shows the influence of the frequency measurement and the calculation of the setpoint for passive synthetic inertia in case of the simulated and measured behavior. With a frequency gradient of ±0.125 Hz/s, for example, a delay of approximately 2 s can be seen in order to achieve the ideal setpoint value of approximately ±500 kW. At a higher frequency gradient of ±0.33 Hz/s, Fig. 4.48(b) shows that the measured power output is no more capable of reaching the final setpoint of about ±1250 kW due to the short duration of the frequency gradient.

Fig. 4.49 shows measurement results of the BESS tests, where synthetic frequency signals with different frequency gradients are used to investigate the behavior of the BESS with activated passive synthetic inertia. As shown in Fig. 4.47, the "Grid synchronization" is bypassed in order to imitate the grid frequency by synthetic frequency signals. Due to this bypassing the dynamics of the frequency measurement in the "Grid synchronization" are not included in the measurements of Fig. 4.49. Fig. 4.49 shows the power output of the BESS in response to synthetic frequency signals. The dashed line indicates the beginning of the appearance of frequency gradients in the synthetic frequency signals. According to Eq. (4.57) the normalized power output of the BESS for passive synthetic inertia is based on

$$\Delta p = T_A \dot{f} \frac{f}{f_n} \tag{4.78}$$

where T_A is the starting time constant, which is parameterizable. For the BESS tests a value of $T_A = 10\,\mathrm{s}$ is used.

For all responses of the power output a delay between 200 ms to 500 ms is visible. Fig. 4.49 also shows overshoots of the power output before reaching a stable operating point. Especially for high frequency gradients the necessary power gradient is that high that the converter control is not capable of following the operating point without such an overshoot. In comparison to Fig. 4.49, Fig. 4.48 does not show such overshoots, firstly due to the lower frequency gradients and secondly due to the influence of the frequency measurement, which is bypassed in the BESS tests.

Besides the converter tests and the BESS tests discussed above, the investigation of the behavior of passive synthetic inertia during a live operation when connected to the external grid is discussed in the following. The difficulties when performing such an investigation is the unpredictability of the real grid frequency. Events with large frequency gradients rarely occur and frequency gradients occurring in the grid frequency during "normal operation" are usually well below ±50 mHz/s [200]. In the case of exceptional events such as system splits, however the frequency gradient is expected to take on values of up to ±1 Hz/s – 2 Hz/s in the regional group CE [148]. To illustrate the typical behavior of the frequency gradient during normal operation Fig. 4.50 shows corresponding measurement results of August 2019, which were measured with a frequency measurement device with an accuracy of ±1 mHz and a reporting rate of 1 s.

Fig. 4.50 shows that over 50 % of the measured frequency gradients lie below a value of ±1 mHz/s. All outliers lie within the boundaries of ±6 mHz/s. This observation coincides with the analyzes of ENTSO-E [148], which observe only a few events with frequency gradients larger than ±3 mHz/s. However, the value of the frequency gradient is also highly dependent on the reporting rate of the frequency measurement. Fig. 4.51 shows a illustrative example of the influence of the reporting rate on the resulting frequency gradient.

The higher the reporting rate the higher the observed frequency gradient. Since a higher reporting rate is also associated with a higher measurement error, a compromise must be found between a fast or accurate measurement. An adequate expectation for a frequency measurement device with a reporting rate of 0.5 s – 1 s according to ENTSO-E [150] is an accuracy of 1 mHz/s. For higher reporting rates, the phasor measurement standard IEEE 60255 [88] lists corresponding requirements for accuracy.

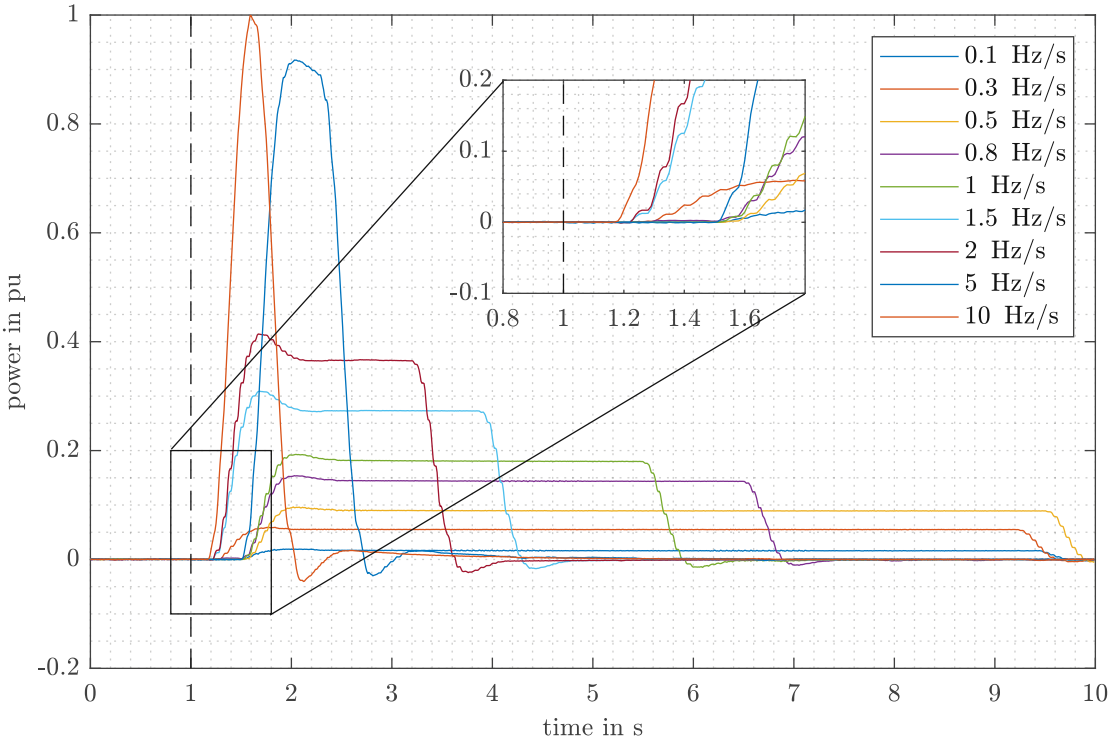

Figure 4.49: Measurement of the power output of the BESS in response to synthetic frequency signals with different frequency gradients. The dashed line indicates the beginning of the appearance of frequency gradients in the synthetic frequency signals.

According to Eq. (4.78) the power output of passive synthetic inertia is dependent on the value of the starting time constant T_A and the measured frequency gradient. For values of T_A below a value of 10 s, which corresponds to values of conventional generators, the power output during occurrence of frequency gradients, as shown in Fig. 4.50 is therefore very low. On the other hand, as shown in Fig. 4.48 and Fig. 4.49, the response of passive synthetic inertia is coupled with a delay, which means that a valid response of passive synthetic inertia can only be observed during longer lasting frequency gradients. Therefore, the investigation of the behavior of passive synthetic inertia during normal grid conditions is rather difficult.

In order to test the behavior of passive synthetic connected to the main grid during typical grid conditions, the function is parameterized with a starting time constant of $T_A = 80$ s, which is the maximum value that can be used and corresponds to a inertia of 200 MW s. The frequency measurement device A-Eberle PQ-Box 200 is used to measure the power, the frequency and the frequency gradient continuously with a reporting rate of 200 ms. Additionally, fault records are triggered when exceeding a frequency gradient of 10 mHz/s, which measure the same values with a reporting rate of 10 ms. Over a period of 1 h the measurement was taken on May 23rd 2018. Fig. 4.52 shows boxplots of the frequency gradient during the measurement.

As already described above, a higher reporting rate is coupled with larger frequency gradients. Such a behavior is visible in Fig. 4.52. However, the high reporting rate of 10 ms is coupled with a very low accuracy. Therefore, it is difficult to distinguish a measurement error from an actual high frequency gradient. To illustrate the time behavior of the frequency, the frequency gradient and the power, the highest absolute value of the frequency gradient of the 200 ms is used as indicator for a high frequency gradient that lasts for longer period. In Fig. 4.52 this maximum absolute value of the frequency gradient is marked for the 200 ms-measurement.

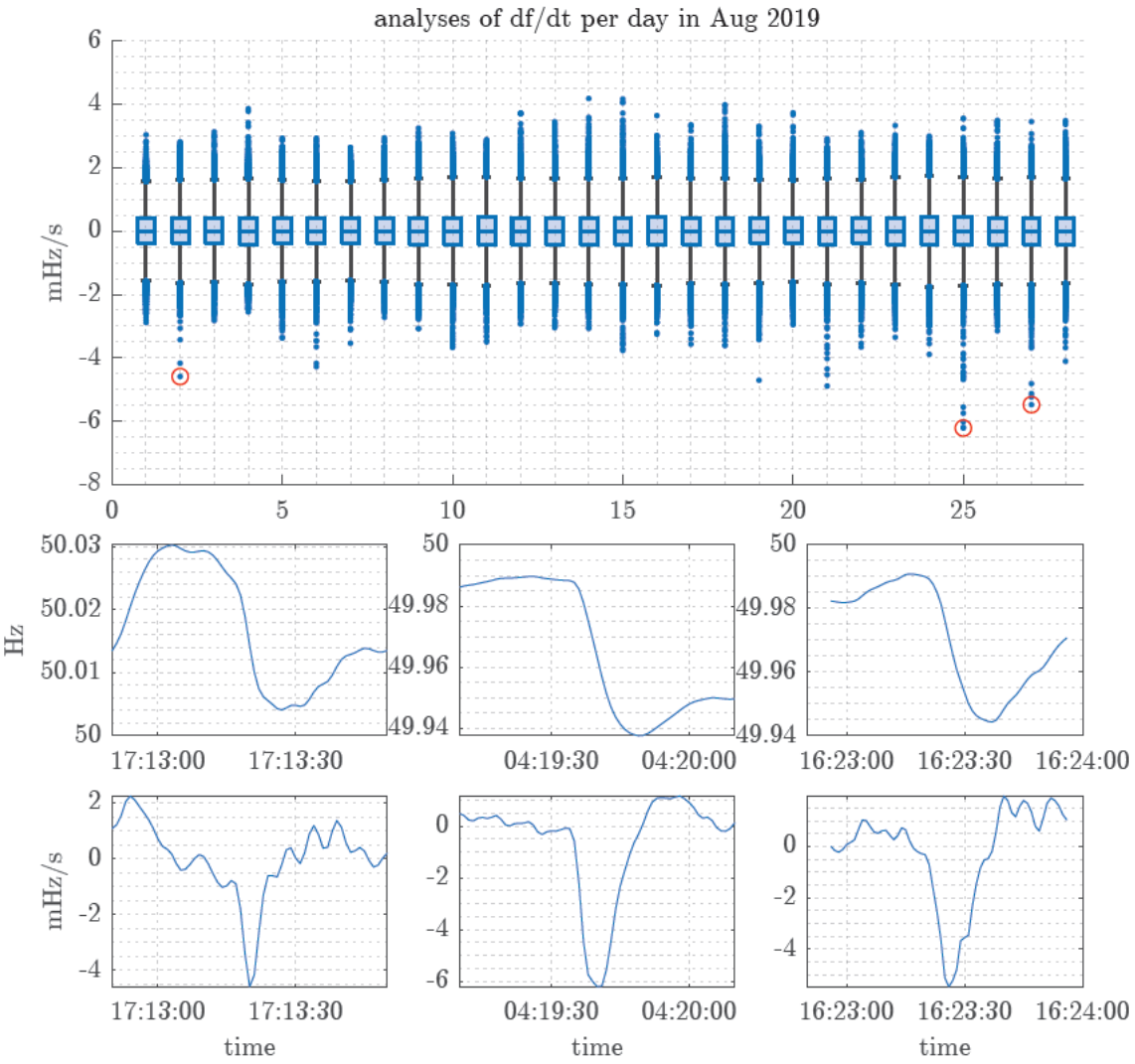

Figure 4.50: Analyses of the frequency gradient per day of August 2019. The upper part of the figure shows boxplots of the frequency gradient for each day. For the three largest outliers, which are marked in red in the boxplots, the lower part of the figure shows the corresponding time series of the frequency and the frequency gradient in the corresponding minute in which the event takes place. The outliers with red markings in the upper part of the figure relate to the corresponding time series in the lower part of the figure, so that the left outlier is associated with the left subfigure, the middle outlier with the middle subfigure and the right outlier is associated with the right subfigure.

According to Eq. (4.78) the parameterized starting time constant $T_A = 80\,\mathrm{s}$ guarantees measurable power outputs, also in response to such low frequency gradients as shown in Fig. 4.52. Fig. 4.53 shows the corresponding measurement time series of the power, the frequency and the frequency gradient for the event marked in Fig. 4.52.

By comparing the power in Fig. 4.53(a) with the frequency in Fig. 4.53(b) the differential character of Eq. (4.78) becomes visible. However, a frequency gradient of $-7\,\mathrm{mHz/s}$ results in a reference power output of $-0.01\,\mathrm{pu}$ according to Eq. (4.78). Since Fig. 4.53(a) shows a power output of $-0.1\,\mathrm{pu}$ when Fig. 4.53(c) shows a frequency gradient of $-7\,\mathrm{mHz/s}$ for the 200 ms-measurement, the

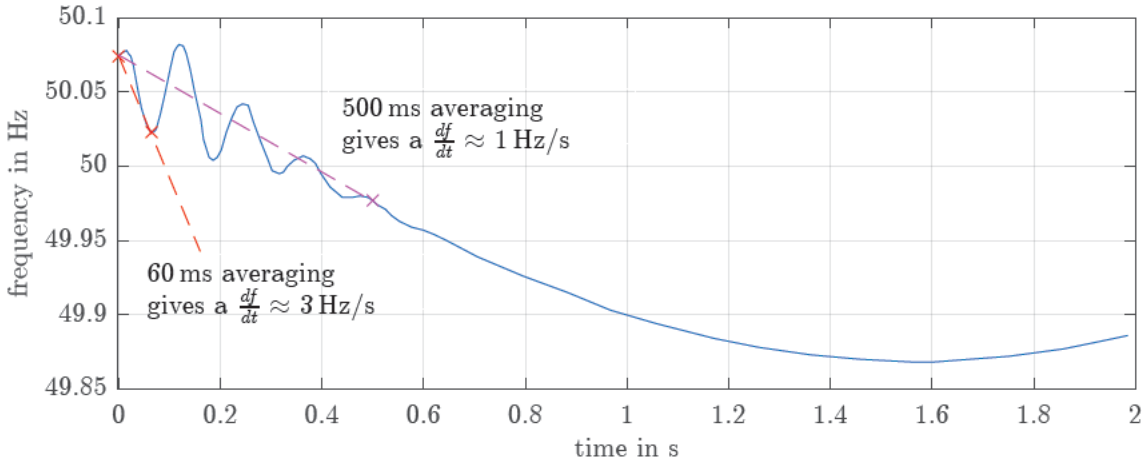

Figure 4.51: Illustrative example of the influence of the reporting rate on the measured frequency gradient [32].

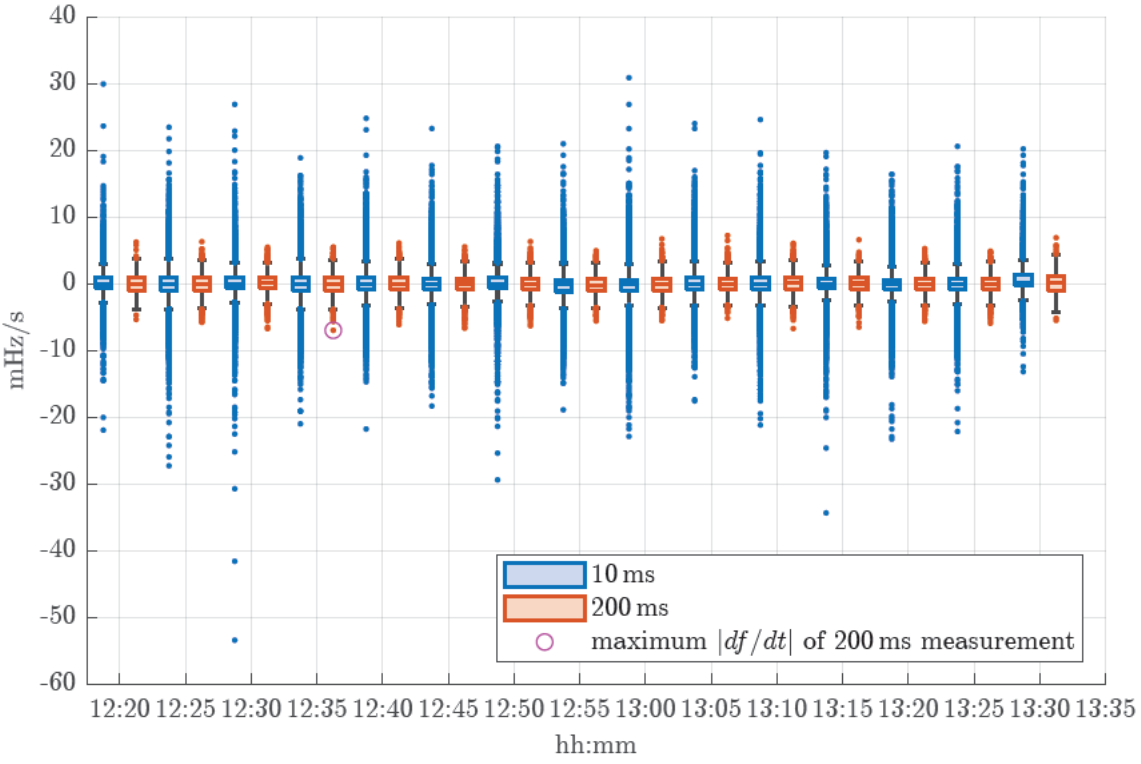

Figure 4.52: Boxplots of the frequency gradient on May 23rd 2018 for the reporting rates 10 ms and 200 ms during 5-minute-time-slots.

internal frequency measurement of the BESS seems to measure much higher frequency gradients, which lead to this higher power output. Such higher frequency gradients are shown in Fig. 4.53(c) for the 10 mHz/s. However, these values are highly inaccurate, since the measuring principle relies on calculating the frequency based on zero-crossing-detection and calculating the frequency gradient based on the difference of two consecutive frequency measurement points. As shown in Fig. 4.47 the BESS' internal grid synchronization unit, on the other hand, relies on calculating the frequency and the frequency gradient based on a PLL as shown in Fig. 4.40. The reporting

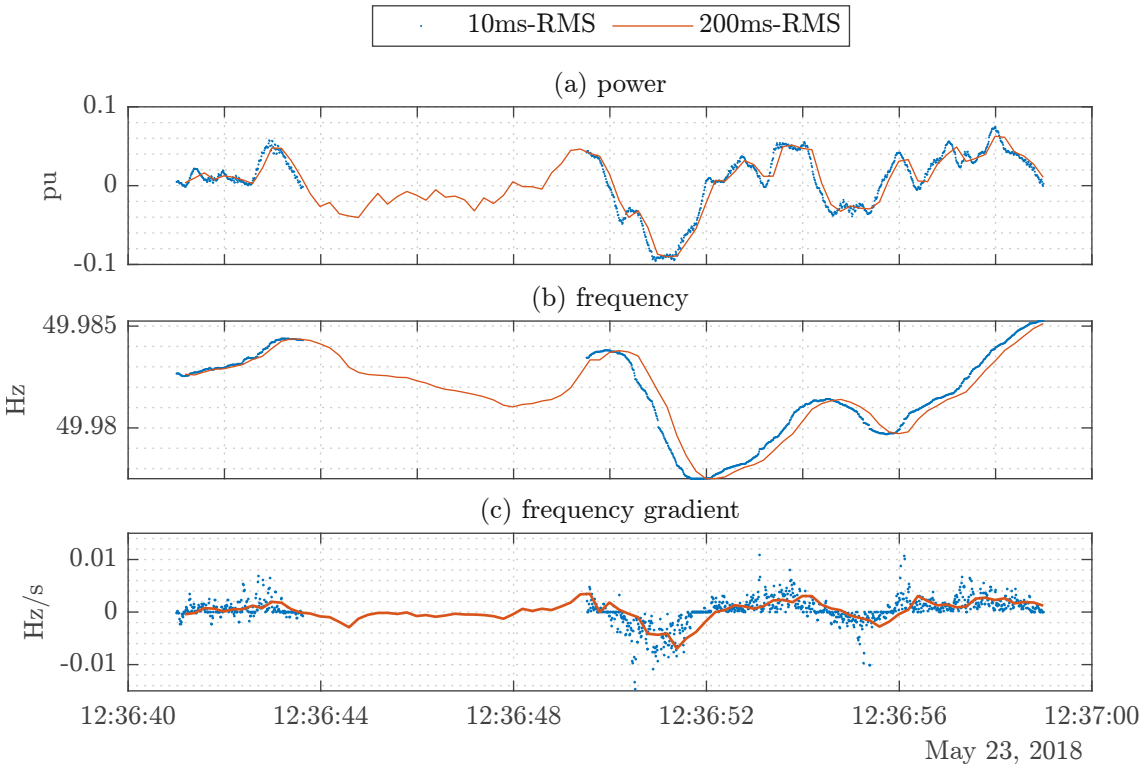

Figure 4.53: Measurement results of passive synthetic inertia at "normal" grid conditions during the event marked in Fig. 4.52. Passive synthetic inertia is parameterized with a starting time constant of $T_A = 80\,\mathrm{s}$ according to Eq. (4.78).

rate of the BESS' internal frequency gradient measurement is set to 20 ms, which leads to higher frequency gradients and, therefore, higher power output.

To illustrate the relationship of power and frequency gradient based on all data points of Fig. 4.52, Fig. 4.54 shows corresponding droop curves for the 10 ms and the 200 ms measurement. Fig. 4.54 also shows the reference droop curve according to Eq. (4.78) taking into account a starting time constant of $T_A = 80\,\mathrm{s}$.

Due to the amount of data points, Fig. 4.54(a) applies filter methods in order to show only relevant data points. These filter methods are based on a peak-filter, which considers the highly fluctuating frequency gradient that is also shown in Fig. 4.53 in such way that the data points are filtered for the highest values of consecutive frequency gradient values. By applying such a filter method, the measured data points in Fig. 4.54(a) show a trend that correlates with the reference droop curve. This correlation is illustrated by a linear fitted curve that behaves similarly to the reference curve. However, the high reporting rate 10 ms is coupled with a high inaccuracy, which is also reflected by the relatively low value of R^2 of the fitted curve.

Fig. 4.54(b) uses all data points of the 200 ms-measurement to illustrate the droop curve. Although the linear fitted curve shows a lower inaccuary, which is also reflected by the higher value of R^2, the comparison between the fitted curve and the reference curve shows a major difference. This difference has already been observed in Fig. 4.53 and is because of the internal frequency measurement unit of the BESS measuring higher frequency gradients due to a lower reporting rate.

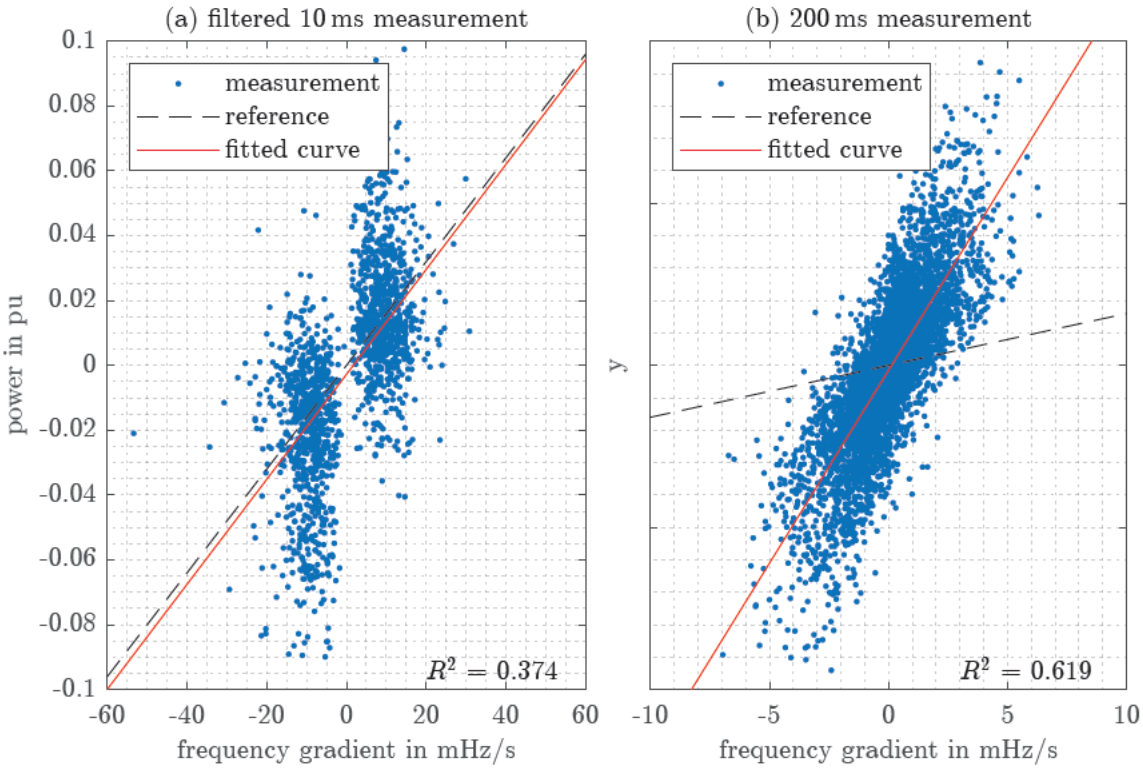

Figure 4.54: Illustration of droop curves based on the 10 ms and the 200 msmeasurement.

4.3 Dynamic Voltage Support

The ever-growing number of power converters connected to the grid has enforced TSO to require fault ride-through capability of these converters in order to provide grid support during abnormal events, such as grid faults. Depending on the type of fault, there are numerous ways for the realization of the converter current reference strategy. The most common grid faults are asymmetrical grid faults. Especially those asymmetrical grid faults, which lead to unbalanced voltage conditions at the PCC of the converter, are challenging for the converter control. The currents injected in the grid during such conditions lose their sinusoidal and balanced appearance. The interaction between such currents and the unbalanced voltage at the PCC may give rise to uncontrolled oscillations in the active and reactive power delivered to the grid. With a suitable implementation of the control of the converter, the injection of unbalanced currents may give rise to useful effects; for instance, balancing the grid voltage at the PCC in order to improve fault detection from power system protection devices [57].

Recent updates of grid codes (for example [183] in Germany, [41] in Austria) define requirements on the injection of reactive currents during grid faults in order to take into account these useful effects of voltage balancing. In this thesis, the injection of reactive currents according to grid codes is referred to as “dynamic voltage support”. During asymmetrical grid faults, this dynamic voltage support may lead to unbalanced currents through the converter, which results in different instantaneous values from phase to phase. Since an overcurrent in any of the phases of the power converter usually results in the disconnection of the converter from the grid, the converter control has to consider the maximum current capability of the converter in the converter current reference strategy.

There are several strategies to control the current injection of converters during grid faults. These strategies all have different objectives such as the quality of the injected current, reduction of DC-link voltage ripple, or constant instantaneous active or reactive power. They have already been investigated in many contributions [27, 28, 131, 26]. An overview of the possible strategies is given in [177, 94]. The most straightforward strategy is the "balanced positive-sequence control" which only provides positive-sequence current injection and still is used in many industrial applications [34]. But recent grid codes also require a current injection in the negative-sequence system during asymmetrical grid faults. The most used control structure for an unbalanced current control is the Flexible Positive- and Negative-Sequence Control (FPNSC). It represents the most generalized structure for converter control and uses two independent controller gains in order to accommodate different control objectives. The use of FPNSC has been widely studied [94, 151]. But the consideration of requirements according to national grid codes remains a very topical question. For example, Lopéz et al. [111] and Shin et al. [162] both investigate the injection of unbalanced current during grid faults, but only consider grid code requirements on positive-sequence current injection. As already described above, the unbalanced current injection results in different peak values in the phases. Therefore, a proper current limitation of the current reference values is needed. The two controller gains in FPNSC are used to control the ratio between positive-sequence and negative-sequence active and reactive power. How to determine these ratios for the positive-sequence as well as for the negative-sequence system according to grid codes and at the same time guarantee a proper current limitation is the challenge. There is a very limited amount of contributions investigating this topic. In [77] for example, a "dual-sequence current provision strategy" is proposed, but no current limitation strategy that defines the distribution of active and reactive power in case of current saturation is discussed. Based on FPNSC, [174] proposes a direct and explicit method to calculate power references during grid faults, where the two controller gains of FPNSC are calculated considering grid code requirements. Taul et al. [174] also proposes a current limitation strategy to ensure that the maximum current capability is maintained while at the same time respecting the grid code requirements. The current limitation strategy proposed by Taul et al. [174] uses a two-step approach, beginning with a limitation of the active current reference value in the positive-sequence system in case of a current saturation, which is followed by a limitation of the reactive current reference values in both sequence systems when the active current is already limited to zero. The second step of this approach results in equal reactive reference current values.

The requirements on and the corresponding standards for converters during grid faults will be discussed in Chp. 4.3.1. Chp. 4.3.1.3 presents an algorithm for a current limitation in order to apply the requirements of the relevant standards and to guarantee that the maximum current capability is respected. In Chp. 4.3.2 simulation models are presented, which are capable of simulating the behavior of converters during grid faults. In Chp. 4.3.2.2.3 one of these models is used to simulate the behavior of a converter, based on voltages which were measured in the real grid during forced short-circuits [196]. Detailed insights in these measurement results are presented in Chp. 4.3.3. This chapter incorporates investigations and analyses published in paper [118].

4.3.1 Requirements and Relevant Standards for the Behavior of Converters during Grid Faults

Requirements for Generators (RfG) are defined in a corresponding network code [59] at the European level. These requirements increase with the size of the generator, which can be classified into types A-D depending on the power capability. The RfG contains exhaustive (exhaustively regulated) and non-exhaustive (nationally regulated) requirements for power generation systems for connection to the electricity grids as well as process definitions and deadlines. Non-exhaustive requirements are defined in national regulations. In Austria these national regulations are defined in the TOR, which is also categorized in the types A-D. In the following, only types of type B are considered, which includes all generation systems with a power capability greater 250 kW. The

corresponding national regulations are defined in [41]. These national regulations include the description of the behavior of power-generating modules during grid faults. Relevant requirements can be divided into two parts:

- Low Voltage Ride Through (LVRT),
- grid support during grid faults,

which are discussed in the following two chapters.

4.3.1.1 Low Voltage Ride Through (LVRT)

It only makes sense to define the behavior of converters during grid faults in case they stay connected to the grid in the event of a fault. The LVRT-capability means the capability of electrical devices to be able to remain connected to the network and operate through periods of low voltage at the connection point caused by secured faults. This LVRT-capability is described by LVRT-curves, which define a time series of a minimum voltage at which the power-generating module has to stay connected to the grid. The grid voltage is a local value, therefore, the LVRT-curve is defined nationally. Both in the RfG and the national TOR, a division into synchronous and asynchronous power generation modules is made. Converter-based power generating units are non-synchronous modules and named "power park modules" in the RfG. The corresponding LVRT-curve for converter-based power generating units, which can be found in [41], is shown in Fig. 4.55.

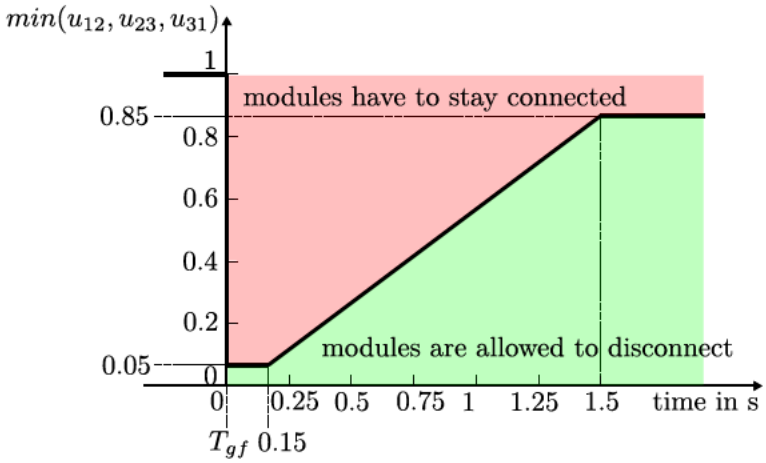

Figure 4.55: LVRT-curve for type B non-synchronous power-generating modules (power park modules) in Austria [41]. Relevant for the decision if a module is allowed to disconnect is the minimum phase-to-phase-voltage at PCC. The LVRT-curve is valid both for symmetrical as well as asymmetrical grid faults. The starting point of the LVRT-curve is defined as T_{gf}, which is described in Eq. (4.84).

4.3.1.2 Grid Support during Short-Circuits

As already mentioned above, a suitable implementation of the control of converters allows to provide dynamic voltage support by converters during short-circuits. This dynamic voltage support is referred to as "fast fault current" in the RfG. The basic idea is to inject reactive current up to the rated current during short-circuits. The corresponding national requirements are described in the TOR [41]. The injection of reactive current has to to be fulfilled according to Eq. (4.79) in

case of a symmetrical short-circuit and also according to Eq. (4.80) in case of an asymmetrical short-circuit:

$$\mathfrak{Im}(\Delta \underline{i}_{1+}) = k_{1+} \cdot \Delta u_{1+} \tag{4.79}$$

$$\mathfrak{Im}(\Delta \underline{i}_{1-}) = k_{1-} \cdot \Delta u_{1-}. \tag{4.80}$$

In accordance with Chp. 2.1.1, $\mathfrak{Im}(\Delta \underline{i}_{1+})$ means an additional reactive current in the positive-sequence system, $\mathfrak{Im}(\Delta \underline{i}_{1-})$ means an additional reactive current in the negative-sequence system, Δu_{1+} means the voltage drop in the positive-sequence system and Δu_{1-} means the voltage drop in the negative-sequence system. The additional injection of reactive power refers to the injection before and during a short-circuit. The parameters k_{1+} and k_{1-} can take values between $k_{1\pm} \in [2, 6]$ and can be defined by the distribution system operators. The most common choice for this parameters is $k_{1+} = k_{1-} = 2$. The national grid codes [41][183] also define the determination of the values Δu_{1+} and Δu_{1-} based on Eq. (A.63) and are defined by

$$\Delta u_{1+} = \overline{u}_{1\,\mathrm{min}} - u_{1+} \tag{4.81}$$

and

$$\Delta u_{1-} = \overline{u}_{1\,\mathrm{min}} - u_{1-} \tag{4.82}$$

with

$$\overline{u}_{1\,\mathrm{min}} = \frac{1}{1\,\mathrm{min}} \cdot \int_{t-1\,\mathrm{min}}^{t} \frac{\|\mathbf{U}(\tilde{t})\|_1}{3 \cdot U_n}\, d\tilde{t} \tag{4.83}$$

as the 1 min-average of the mean value of the phase-to-phase voltages $\mathbf{U}$[5]. A description of how to calculate the positive-sequence and negative-sequence voltage u_{1+} and u_{1-} is given in Chp. A.2.1. The determination of whether a short-circuit is present or not, is made based on the minimum phase-to-phase-voltage. During normal operation the voltages $\mathbf{u}$ are in the range of $[0.9, 1.1]$ pu, otherwise a fault is present. Therefore, T_{gf} is defined as

$$T_{gf} = \max\left(t | \{\min\{u_{12}(t), u_{23}(t), u_{31}(t)\} < 0.9\}\right) \tag{4.84}$$

which is also shown in Fig. 4.55.

4.3.1.3 Current Limitation

Assuming a converter to feed in power before a fault occurs, an additional injection of reactive current during the fault according to Eq. (4.79) and Eq. (4.80) may lead to a current output that would exceed the maximum current capability i_{max} of the converter. In order to prevent such a situation, a proper current limitation has to be applied in the converter control. As shown in Fig. 2.8, which presents a typical structure of a battery-converter and its control, the inverter current control is fed by setpoints of the current in park-coordinates ($i'_{S,d_{1+},ref}$, $i'_{S,q_{1+},ref}$, $i'_{S,d_{1-},ref}$, $i'_{S,q_{1-},ref}$). The apostrophe is used to indicate the unlimited current reference values. These reference values are divided into active and reactive components in the positive-sequence and negative-sequence system. The relation of these components to the actual phase currents i_{L1}, i_{L2} and i_{L3} is crucial to realize a current limitation. This relationship is derived using Fig. 4.56.

Any space vector can be divided into two space vectors, each for the positive-sequence and negative-sequence system. Fig. 4.56 shows these two space vectors $\underline{i}'_{S,dq_{1+}}$ and $\underline{i}'_{S,dq_{1-}}$ which are defined by

$$\underline{i}'_{S,dq_{1+}} = i'_{S,d_{1+}} + j i'_{S,q_{1+}} \tag{4.85}$$

[5] A short fault duration is assumed. Therefore, the influence of the voltages on $\overline{u}_{1\,\mathrm{min}}$ during the short-circuit can be neglected.

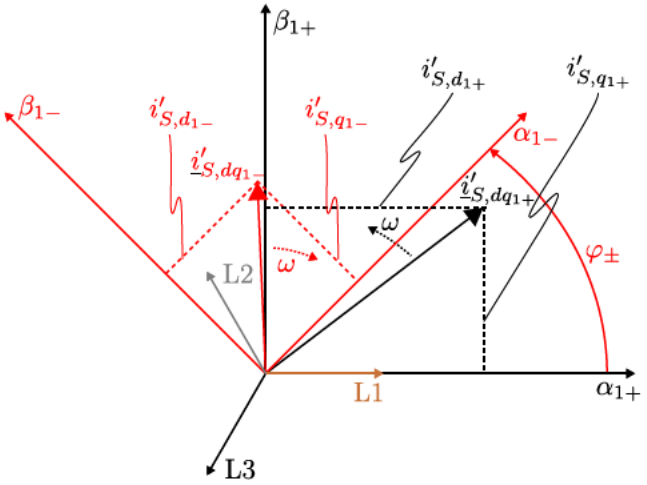

Figure 4.56: Vector diagram to derive the calculation for the current limitation (valid only for $\omega t = 0$).

and

$$\underline{i}'_{S,dq_{1-}} = i'_{S,d_{1-}} + j i'_{S,q_{1-}} \tag{4.86}$$

in a positive-sequence $\alpha\beta$-plane indexed with α_{1+} and β_{1+} and a negative-sequence $\alpha\beta$-plane indexed with α_{1-} and β_{1-}.

Assuming the positive-sequence $\alpha\beta$-plane to be aligned with the phase L1, the negative-sequence $\alpha\beta$-plane has to be shifted by an angle $\varphi_\pm$ in respect to L1, that represents the angle of the negative-sequence voltage $\underline{u}_{1-}$ in relation to the positive-sequence voltage $\underline{u}_{1+}$. The space vector $\underline{i}_{S,dq_{1+}}$ rotates with an angular frequency ω in the positive-sequence $\alpha\beta$-plane and the space vector $\underline{i}_{S,dq_{1-}}$ rotates with an angular frequency $-\omega$ in the negative-sequence $\alpha\beta$-plane. The total current space vector $\underline{i}'_S$ in the positive-sequence $\alpha\beta$-plane can be calculated by

$$\underline{i}'_S = \underline{i}'_{S,dq_{1+}} e^{j\omega t} + \underline{i}'_{S,dq_{1-}} e^{-j\omega t} e^{j\varphi_\pm}. \tag{4.87}$$

The "grid synchronization" often consists of a synchronous reference phase-locked loop (SRF-PLL) which delivers an angle θ that represents the angle of the positive-sequence voltage $\underline{u}_{1+}$ in respect to a reference angle, e.g. 0° or 90°. The angle of the voltage vector of Phase L1 may differ from this reference angle, but all vectors in Fig. 4.56 would only be shifted by this angle difference. Therefore, the following statements are still valid if using θ instead of ωt. The corresponding total current using θ is given by

$$\underline{i}'_S = \underline{i}'_{S,dq_{1+}} e^{j\theta} + \underline{i}'_{S,dq_{1-}} e^{-j\theta} e^{j\varphi_\pm}. \tag{4.88}$$

The currents in the phases can be calculated by the projection of the total current space vector on the corresponding vectors L1, L2, and L3 shown in Fig. 4.56. These projections are given by

$$i_{L1,t} = \mathfrak{Re}\left(\underline{i}'_{S,dq_{1+}} e^{j\theta} + \underline{i}'_{S,dq_{1-}} e^{-j\theta} e^{j\varphi_\pm}\right), \tag{4.89}$$

$$i_{L2,t} = \mathfrak{Re}\left(\underline{i}'_{S,dq_{1+}} e^{j\theta} e^{-j\frac{2\pi}{3}} + \underline{i}'_{S,dq_{1-}} e^{-j\theta} e^{j\varphi_\pm} e^{-j\frac{2\pi}{3}}\right), \tag{4.90}$$

$$i_{L3,t} = \mathfrak{Re}\left(\underline{i}'_{S,dq_{1+}} e^{j\theta} e^{-j\frac{4\pi}{3}} + \underline{i}'_{S,dq_{1-}} e^{-j\theta} e^{j\varphi_\pm} e^{-j\frac{4\pi}{3}}\right). \tag{4.91}$$

National regulations according to TOR require the reactive currents to be prioritized before active currents. Assuming that component $i'_{S,d_{1-}}$ is zero, which means that there is no active current injection in the negative-sequence system, the component $i'_{S,d_{1+}}$ has to be limited if a phase current exceeds i_{max}. If a phase current still exceeds i_{max} after a limitation of $i'_{Sd_{1+}}$ to zero, the remaining components also have to be limited. Limited components are named without an apostrophe. Therefore, the limited component of $i'_{S,d_{1+}}$ is $i_{S,d_{1+}}$. The procedure to calculate the limited component $i_{S,d_{1+}}$ in such a way that the maximum phase current is exactly i_{max} is derived as follows. It is assumed that the maximum current occurs in phase L1, but the derivation for the maximum current in another phase can be carried out analogously. At first, the angle θ at which the current in phase L1 is maximum is calculated by solving:

$$\frac{d}{d\theta}\left(\mathfrak{Re}\left((i_{S,d_{1+}}+ji'_{S,q_{1+}})e^{j\theta}+ji'_{S,q_{1-}}e^{-j\theta}e^{j\varphi_{\pm}}\right)\right)=0\rightarrow\theta(i_{S,d_{1+}}):=\theta_{max}(i_{S,d_{1+}}) \tag{4.92}$$

where the component $i_{S,d_{1+}}$ is the only variable. The equation can be solved analytically and the corresponding angle is named $\theta_{max}(i_{S,d_{1+}})$ and is dependent on $i_{S,d_{1+}}$. This angle is inserted in Eq. (4.89) taking into account the assumptions made above, resulting in

$$\mathfrak{Re}\left((i_{S,d_{1+}}+ji'_{S,q_{1+}})e^{j\theta_{max}(i_{S,d_{1+}})}+ji'_{S,q_{1-}}e^{-j\theta_{max}(i_{S,d_{1+}})}e^{j\varphi_{\pm}}\right)=i_{max}\rightarrow i_{S,d_{1+}} \tag{4.93}$$

which then can be solved to calculate a corresponding value of $i_{S,d_{1+}}$ to guarantee a maximum current i_{max} in the phase current $i_{L1,t}$. Eq. (4.93) cannot be solved analytically, but only numerically.

As already mentioned above, besides the limitation of $i'_{S,d_{1+}}$ it may also be necessary to limit the reactive current components $i'_{S,q_{1+}}$ and $i'_{S,q_{1-}}$, if despite a limitation of $i_{S,d_{1+}}=0$, the maximum current still exceeds i_{max}. The national regulations in Austria [41] do not specify the limitation in such a case. The German regulations [183], on the other hand, prescribe an even reduction of both reactive current components in such a case. In order to calculate the required reduction, the same approach as for the active current component can be followed. It is assumed that the maximum current occurs in phase L1. At first, the angle θ at which the current in phase L1 is maximum is calculated by solving:

$$\frac{d}{d\theta}\left(\mathfrak{Re}\left(j\cdot x\cdot i'_{S,q_{1+}}e^{j\theta}+j\cdot x\cdot i'_{S,q_{1-}}e^{-j\theta}e^{j\varphi_{\pm}}\right)\right)=0\rightarrow\theta(x):=\theta_{max}(x) \tag{4.94}$$

where x is the required reduction factor for the reactive current components. The equation can be solved analytically and the corresponding angle is named $\theta_{max}(x)$ which is dependent on x. This angle is inserted in Eq. (4.89) taking into account the assumptions made above:

$$\mathfrak{Re}\left(j\cdot x\cdot i'_{S,q_{1+}}e^{j\theta_{max}(x)}+j\cdot x\cdot i'_{S,q_{1-}}e^{-j\theta_{max}(x)}e^{j\varphi_{\pm}}\right)=i_{max}\rightarrow x. \tag{4.95}$$

This equation can be solved numerically only. Its result can be used to calculate the limited reactive current components $i_{S,q_{1+}}=x\cdot i'_{S,q_{1+}}$ and $i_{S,q_{1-}}=x\cdot i'_{S,q_{1-}}$.

In order to use the Eq. (4.93) and Eq. (4.95) in an algorithm for a current limitation, a corresponding procedure has to guarantee, that there is a solution for the equations. For example, the equations cannot be solved numerically if the values of the components of the maximum current occurs in another phase than in L1 or the maximum phase current is smaller than i_{max}. These situations have to be considered in a corresponding procedure. A possible way to do this, is described in Chp. 4.3.2.2.

4.3.1.4 Approximated Current Limitation

It is often not possible to solve Eq. (4.93), e.g. by limited computing capacity or due to a lack of tools for the numerical solution of equations. An easier procedure to calculate the limited current components can be carried out by using an approximation approach. This approach is described via Fig. 4.57, which shows the park-transformation of Fig. 4.56.

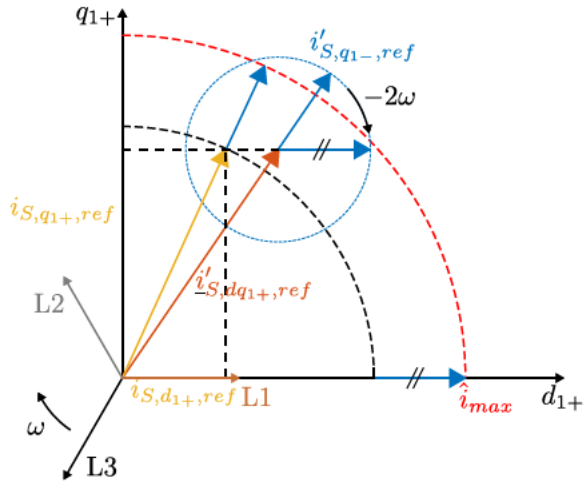

Figure 4.57: Derivation of the approximated current limitation.

In the positive-sequence dq-plane the current components $i'_{S,d_{1+},ref}$ and $i'_{S,q_{1+},ref}$ are constant, whereas the three-phase system L1-L2-L3 rotates with ωt. The current component $i'_{S,q_{1-},ref}$ also rotates, but with doubled angular frequenc $2\omega t$ due to the park-transformation, which multiplies Eq. (4.88) with $e^{-j\theta}$. The approximation approach assumes that the maximum current occurs when the vector $\underline{i}'_{S,dq_{1+},ref}$ is aligned with the current component $i'_{S,q_{1-},ref}$ and the corresponding sum-vector of these two vectors is also aligned with one of the phases L1-L2-L3. This assumption guarantees that the maximum current capability i_{max} is not exceeded, but only allows a conservative calculation of the maximum current component $i_{S,d_{1+},ref}$, since such a situation is rather unlikely. As already described above, national regulations [41][183] require the injection of reactive currents to be prioritized over active currents during short-circuits. Assuming the current component $i'_{S,d_{1-},ref} = 0$ to be zero, the maximum values of the other current components can be derived by simple geometric relationships based on Fig. 4.57. According to Eq. (4.79) and (4.80) the reactive current components are given by

$$i'_{S,q_{1+},ref}(t) = i'_{S,q_{1+},ref}(T_{gf}) + k_{1+} \cdot \Delta u_{1+}(t) \tag{4.96}$$

$$i'_{S,q_{1-},ref}(t) = i'_{S,q_{1-},ref}(T_{gf}) + k_{1-} \cdot \Delta u_{1-}(t). \tag{4.97}$$

They have to be limited in case their sum $|i_{S,q_{1+},ref}| + |i_{S,q_{1-},ref}| > i_{max}$ is larger than the maximum current capability i_{max}:

$$i_{S,q_{1+},ref} = \begin{cases} i'_{S,q_{1+},ref}, & |i_{S,q_{1+},ref}| + |i_{S,q_{1-},ref}| < i_{max}, \\ i'_{S,q_{1+},ref} \frac{i_{max}}{|i_{S,q_{1+},ref}| + |i_{S,q_{1-},ref}|}, & else \end{cases} \tag{4.98}$$

$$i_{S,q_{1-},ref} = \begin{cases} i'_{S,q_{1-},ref}, & |i_{S,q_{1+},ref}| + |i_{S,q_{1-},ref}| < i_{max}, \\ i'_{S,q_{1-},ref} \frac{i_{max}}{|i_{S,q_{1+},ref}| + |i_{S,q_{1-},ref}|}, & else \end{cases}. \tag{4.99}$$

The current component $i'_{S,d_{1+},ref}$ depends on the actual positive-sequence voltage $u_{1+}(t)$ and the current components $i'_{S,d_{1+},ref} = 0$ is assumed to be zero, which means that active power is only

injected in the positive-sequence system. The maximum value of $i'_{S,d_{1+},ref}$ to respect i_{max} can be calculated with

$$i_{S,d_{1+},max} = \sqrt{\left(i_{max} - i_{S,q_{1-},ref}\right)^2 - i^2_{S,q_{1+},ref}} \tag{4.100}$$

to

$$i_{S,d_{1+},ref} = \begin{cases} i_{S,d_{1+},max}, & |i_{S,q_{1+},ref}| + |i_{S,q_{1-},ref}| < i_{max} \wedge i'_{S,d_{1+},ref} > i_{S,d_{1+},max}, \\ i'_{S,d_{1+},ref}, & |i_{S,q_{1+},ref}| + |i_{S,q_{1-},ref}| < i_{max} \wedge i'_{S,d_{1+},ref} < i_{S,d_{1+},max}, \\ 0, & else \end{cases} \tag{4.101}$$

based on geometrical relationships in Fig. 4.57. To solve Eq. (4.101) is much easier than to solve Eq. (4.93).

The approximation approach described above is used in the RMS simulation model described in Chp. 4.3.2.1 to investigated the behavior of a converter during short-circuits in DIGSILENT/POWERFACTORY.

4.3.2 Simulation

Converter-based generators have so far been neglected in short-circuit calculations due to their small number and their relatively low short-circuit contribution. The latest revision of the standard for short-circuit calculations IEC 60909-0:2016 [87] requires consideration of inverter-based infeed if their contribution to the short-circuit current is at least 5 %. In the case of a contribution exceeding 5 %, the short-circuit contribution of inverter-based infeed is approximated by a current source in the positive-sequence system. The behavior in the negative-sequence system is not further defined and it is noted that this has to be determined as project-specific. Because of the increasing popularity of inverter-based infeed, studies that call for a detailed description of the short-circuit behavior of such equipment may be required. For this reason, simulation models to simulate the behavior of converters during a grid fault were created. These simulation models take into account the descriptions in Chp. 4.3.1. The two simulation models which were created are

- a RMS simulation model in DIGSILENT POWERFACTORY,
- and a EMT simulation model in MATLAB/SIMULINK,

which will be discussed in detail in the following chapters.

4.3.2.1 RMS Simulation Model and Its Application

The following chapters describe the RMS simulation model and its verification.

4.3.2.1.1 Description of the Model

Fig. 4.58 shows the corresponding model which was created in DIGSILENT POWERFACTORY with the built-in tools. The software does not provide any tools for numerical solving equations. Therefore, the approximation approach described in Chp. 4.3.1.4 is applied to calculate the corresponding current setpoints. A description of this model can also be found in [123]. Basically, the "positive-sequence PQ control" defines the setpoints $i'_{S,d_{1+},ref}$ and $i'_{S,q_{1+},ref}$ based on the measurement of the current power output via "PQ measurement". During normal operation, the setpoints of the active and reactive power are defined by the entries of the load-flow or external signals, which are controlled via PI-control based on the measurement of the current power output. During fault

condition, which is identified by the "voltage measurement", the "positive-sequence PQ control" switches its behavior to operate according to Eq. (4.79).

During normal operation the "negative-sequence PQ control" does not provide any setpoints (they are zero), whereas during fault condition it provides the setpoints $i'_{S,d_{1-},ref}$ and $i'_{S,q_{1-},ref}$ according to Eq. (4.80). The "Current Control" ensures the current output to be within the maximum current capabilities by applying Eq. (4.101), by using the approximated current limitation presented in Chp. 4.3.1.4. The resulting setpoints $i_{S,d_{1+},ref}$, $i_{S,q_{1+},ref}$, $i_{S,d_{1-},ref}$ and $i_{S,q_{1-},ref}$ are fed into a "Generator", which calculates its power output based on the input of a "PLL". In the simulation model this "Generator" does not possess any dynamics. The current output therefore is identical to the reference currents: $i_{S,d_{1+}} = i_{S,d_{1+},ref}$, $i_{S,q_{1+}} = i_{S,q_{1+},ref}$, $i_{S,d_{1-}} = i_{S,d_{1-},ref}$ and $i_{S,q_{1-}} = i_{S,q_{1-},ref}$.

Due to the approximated current limitation which is used in the current control, the reference current $i_{S,d_{1+},ref}$ tends to be smaller than the maximum possible value according to Chp. 4.3.1.3, especially in case of a current output near the maximum current i_{max}. The error which results from this approximation approach will be investigated in the next section.

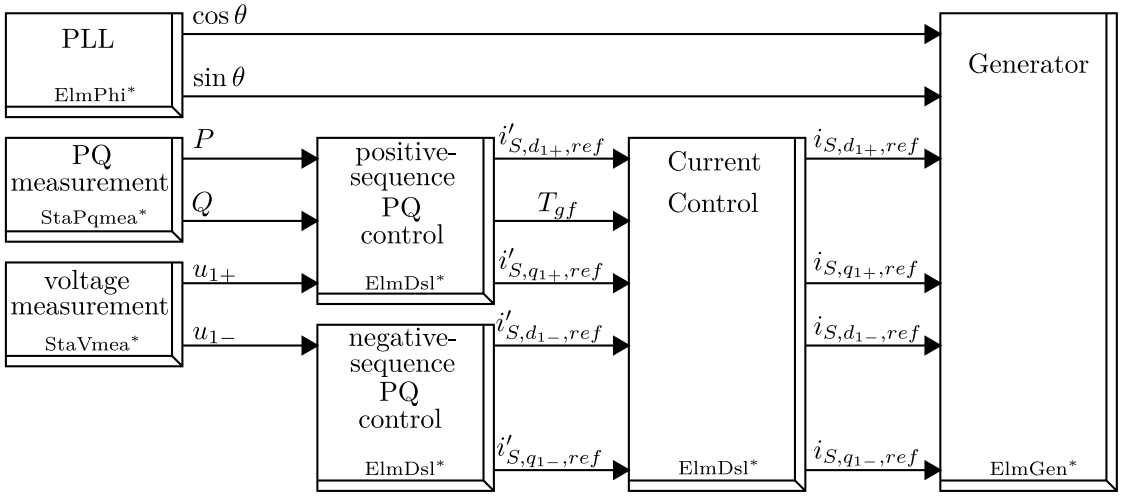

Figure 4.58: Block diagram of the RMS simulation model in DIgSILENT PowerFactory.

4.3.2.1.2 Verification of the Model

In Chp. 2.2 the calculation of short-circuits according to IEC 60909-0:2016 [87] was demonstrated based on an example-grid shown in Fig. 2.2. To investigate the behavior of the model described above, this grid is expanded by connecting the exemplary BESS field plant described in Chp. 3.1 at the bus "SS1 30 kV". The grid is also expanded by an additional feeder with the two busses "SS3 110 kV" and "SS4 110 kV" connected by the two lines "L4" and "L5". The resulting grid is shown in the single-line diagram in Fig. 4.59. By investigating different fault conditions at the buses "SS4 110 kV" and "SS2 30 kV", the behavior of the model presented above can be demonstrated.

For this reason, RMS simulations of the grid shown in Fig. 4.59 are fulfilled. The figure also shows the simulation results in case of a two-phase short-circuit at the bus "SS2 30 kV". In Chp. 2.2 such a short-circuit was already calculated according to IEC 60909-0:2016 and can be compared with the simulated results. As already shown in Fig. A.9, there is a difference between the initial short-circuit current and the steady-state short-circuit current. The calculation in Chp. 2.2 aimed to calculate the initial short-circuit current, whereas the Fig. 4.59 shows the steady-state short-circuit current. As the influence of the subtransient reactance x''_d is very small due to length of the

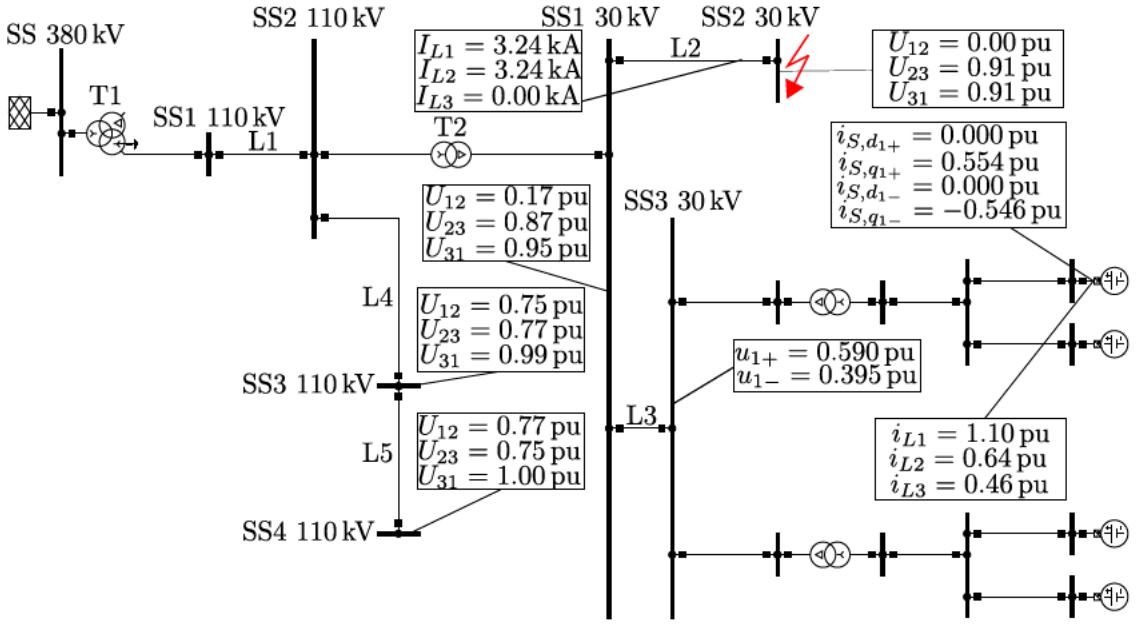

Figure 4.59: Single-line diagram of the investigated grid and results of a RMS simulation during a two-phase short-circuit at "SS2 30 kV" in DIgSILENT PowerFactory.

fault path, the difference between the initial-state and the steady-state short circuit current can mainly be argued by the safety factor $c_{max} = 1.1$ as well as the fault current contribution by the BESS.

The time behavior of the BESS and its current output during fault conditions is shown in Fig. 4.60 for different values of k_{1+} and k_{1-} for a two-phase short-circuit as well as for a three-phase short-circuit at "SS2 30 kV". The operating point of the active power of the BESS is $-0.75 \cdot S_n$. Therefore, the BESS feeds in active power into the grid in normal operation, before and after a fault condition. Fig. 4.60(a),(d) show the time behavior of the current output before, during and after a two-phase/three-phase short-circuit with $k_{1+} = k_{1-} = 0$. Due to the drop in the voltage u_{1+} the BESS increases its current output $i_{S,d_{1+},ref}$ to its maximum current capability of $i_{max} = 1.1\,\text{pu}$ as long as the fault lasts in order to meet the active power operating point as best as possible. The remaining components of the reference space vector are zero. A minor settling process of $i_{S,q_{1+},ref}$ is caused by the dynamics of the PLL and the PI-control in the "positive-sequence PQ control" shown in Fig. 4.58.

Fig. 4.60(b),(e) show the same situation with $k_{1+} = k_{1-} = 1$. According to the equations in Chp. 4.3.1.2 the BESS provides reactive current in the positive-sequence system $i_{S,q_{1+},ref}$ and in the negative-sequence system $i_{S,q_{1-},ref}$ proportional to the changes of u_{1+} and u_{1-}. For the three-phase short-circuit in Fig. 4.60(e) there is only a change in u_{1+}, whereas for the two-phase short-circuit in Fig. 4.60(b) there is a change in u_{1+} as well as in u_{1-}. The current output $i_{S,q_{1+},ref}$ and $i_{S,q_{1-},ref}$ in case of the two-phase short-circuit are directly related to the changes in the voltages, e.g. $i_{S,q_{1-},ref}(t = 4\,\text{s}) = u_{1-}(t = 4\,\text{s}) = 0.43\,\text{pu}$. In both short-circuit cases the active current in the positive-sequence system $i'_{S,d_{1+},ref}$ is limited according to Eq. (4.101) in consideration of the maximum current capability. This limitation is calculated in the "Current Control" shown in Fig. 4.58 resulting in the reference current $i_{S,d_{1+},ref}$.

Fig. 4.60(c),(f) show the same situation with $k_{1+} = k_{1-} = 2$. For the two-phase short-circuit as well as for the three-phase short-circuit the values $k_{1+}\Delta u_{1+}$ and $k_{1-}\Delta u_{1-}$ make it necessary to

limit the active current in the positive-sequence system $i'_{S,d_{1+},ref}$ to zero. In case of the two-phase short-circuit in Fig. 4.60(f) also the reactive currents $i'_{S,q_{1+},ref}$ and $i'_{S,q_{1-},ref}$ have to be limited according to Eq. (4.98) and (4.98).

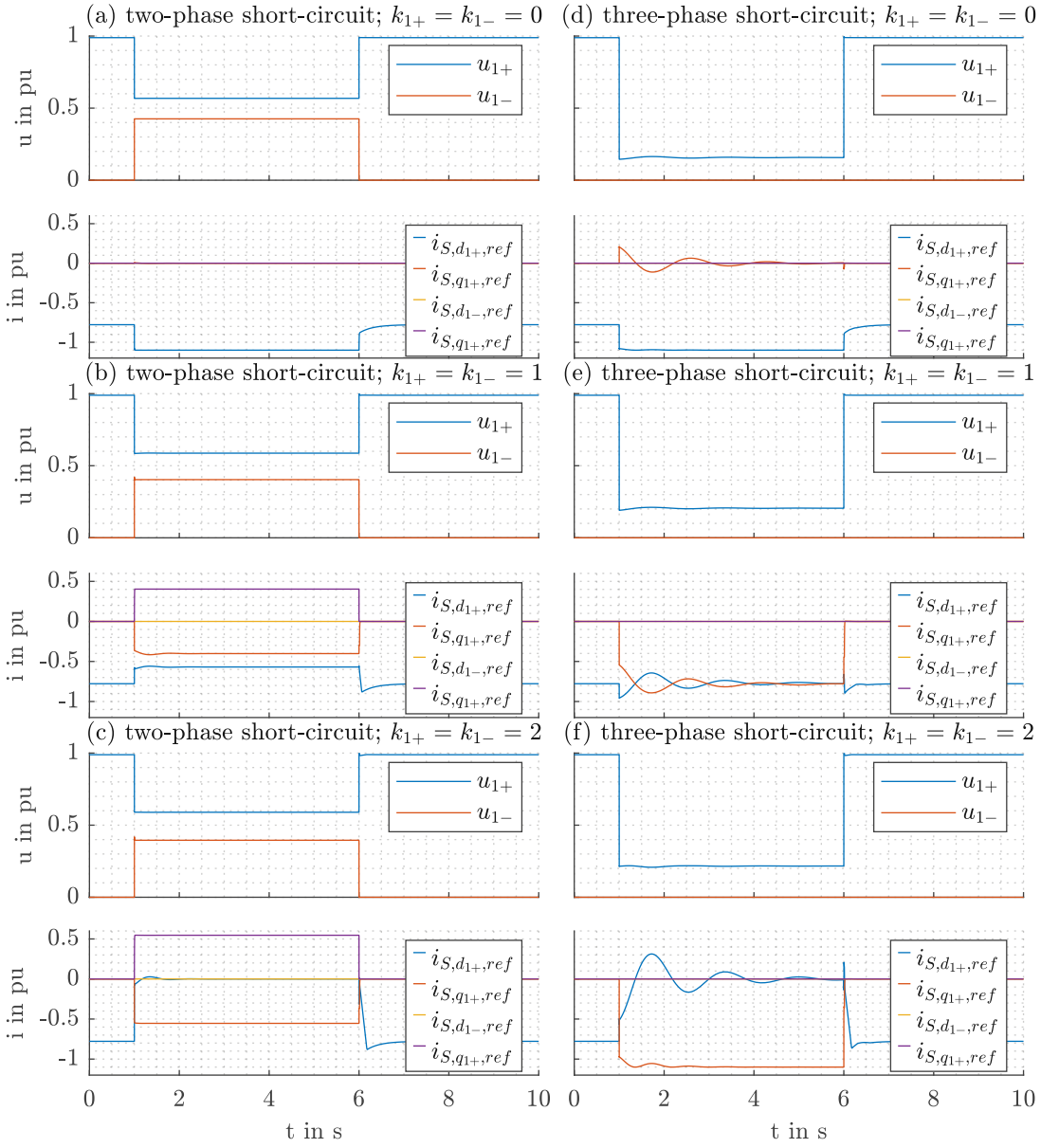

Figure 4.60: Time series of simulation results during two-phase and three-phase short-circuits at "SS2 30 kV".

The application of the approximation approach leads to an error of the calculated value of $i_{S,d_{1+},ref}$, as already described in Chp. 4.3.1.4. Referring to Fig. 4.60, this error is only striking in case (b) and (c). To investigate this error, Fig. 4.61 shows the corresponding phase currents $\mathbf{i}_t$ in the time range 3 s – 3.1 s of the current components shown in Fig. 4.60(b). With a maximum current capability of $i_{max} = 1.1$ pu the Fig. 4.61 shows an error of 15 %, since the maximum peak current in the phase L1 is 0.95 pu but should reach the maximum current.

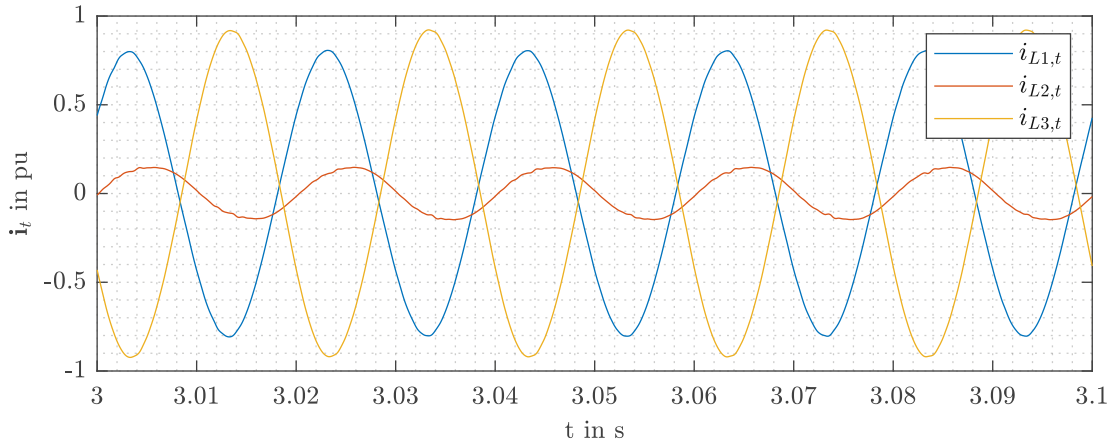

Figure 4.61: Actual phase currents during short-circuit of Fig. 4.60(b) (two-phase short-circuit with $k_{1+} = k_{1-} = 1$).

Fig. 4.62 shows the corresponding phase currents $\mathbf{i}_t$ in the time range 3 s-3.1 s of the current components shown in Fig. 4.60(c). Due to a $\varphi_{\pm} \approx -60°$, the maximum current is $i_{max} \approx 1.1$ pu, as also shown in Fig. 4.59. For the factor $k_{1+} = k_{1-}$ very often $k_{1+} = k_{1-} = 2$ is used. The error due to the approximation approach is dependent on the distance between fault location and the PCC of the inverter-based generator. The higher this distance the higher the error. But on the other hand, the smaller this distance the higher the reactive current injection and its influence on the voltage. Therefore, the error due to the approximation approach may be justifiable for the use in network calculation programs. Especially as conventional network calculation programs do not offer the possibility to map this level of detail of inverter-based generators in their conventional short-circuit calculation modules.

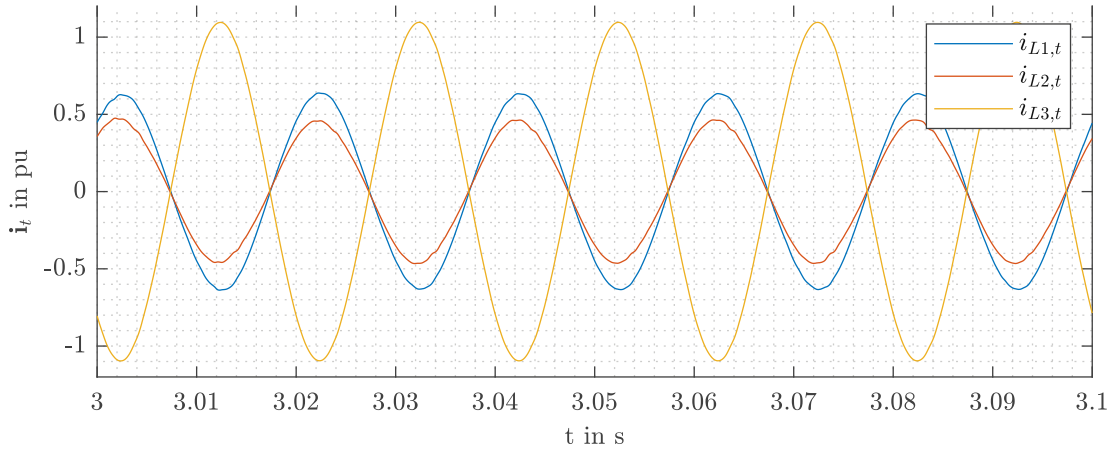

Figure 4.62: Actual phase currents during short-circuit of Fig. 4.60(c) (two-phase short-circuit with $k_{1+} = k_{1-} = 2$).

4.3.2.2 EMT Simulation Model

The following chapters describe the EMT simulation model, its implementation in MATLAB/SIMULINK, a proper realization of a current limitation algorithm and the verification of the model.

4.3.2.2.1 Description of the Model

This EMT simulation model was created to simulate the converter behavior during grid faults in finer time resolution than the model described in Chp. 4.3.2.1. As a start to describe this EMT simulation model in detail, a reference is made to Fig. 2.8 in Chp. 2.4. This figure presents the basic structure of a battery converter and its corresponding control routines based on a power closed-loop approach. Building on this, Fig. 4.63 shows the components and control structure used in the EMT simulation model. The two-level voltage source converter model consists of a DC-link and an inverter which is followed by an LC-filter. For simplification, the DC-link is represented by a constant voltage source. The inverter model is a self-commutated three-phase bridge, which is controlled by a PWM signal. The output filter consists of an LC-filter where the resistor represents the parasitic resistance of the inductance. The control structure follows a power-open-loop approach. Therefore, the current reference space vector $\underline{i}'_{S,dq,ref}$ is directly calculated based on $\frac{p_{ref}}{u_{1+}}$ and $\frac{q_{ref}}{u_{1+}}$, assuming the converter during normal operation (no grid fault) to only inject active and reactive power in the positive-sequence system. The inverter current control is based on a Double Synchronous Reference Frame (DSRF), where PI-controllers are used for the positive-sequence as well as for the negative-sequence system to determine an instantaneous reference voltage vector $\mathbf{u}_{N,t,ref}$. The necessary transformations of the measured instantaneous voltage vector $\mathbf{u}_{N,t}$ and the measured instantaneous current vector $\mathbf{i}_t$ into the dq-plane, to determine the corresponding space vectors $\underline{u}_{S,dq}$ and $\underline{i}_{S,dq}$ are based on the angle θ, which is provided by the grid synchronization. This grid synchronization is realized as an SRF-PLL. The switching control uses the instantaneous reference voltage vector $\mathbf{u}_{N,t,ref}$ to generate the PWM-signals f_{IL1}, f_{IL2} and f_{IL3} for the inverter, that control the switches S_{IL1}, S_{IL2} and S_{IL3}. The complementary PWM-signals f'_{IL1}, f'_{IL2} and f'_{IL3} are used to control the switches S'_{IL1}, S'_{IL2} and S'_{IL3}. The major difference between the EMT simulation model shown in Fig. 2.8 and the battery converter shown in Fig. 2.8, is the simplification of the battery, the buck-boost converter and the DC-link.

To describe the inverter current control in more detail, the requirements described in Chp. 4.3.1.2 are relevant. The injection of reactive currents according to Eq. (4.79) and (4.80) require an estimation of the positive-sequence voltage u_{1+} and the negative-sequence voltage u_{1-}. The "sequence analyzer" in Fig. 4.63 performs this estimation by calculating these voltages.

As already mentioned, the EMT simulation model is based on a power open-loop approach. The corresponding setpoints for active and reactive power are calculated inside the "active power control", respectively the "reactive power control". During normal operation (no grid fault) the reactive power control calculates the corresponding current setpoint $i'_{S,q_{1+},ref}$[6] according to the reference power q_{ref}:

$$i'_{S,q_{1+},ref} = \frac{q_{ref}}{u_{1+}}. \tag{4.102}$$

It is assumed that during normal operation reactive power is only injected in the positive-sequence system, therefore, the reference value $i'_{S,q_{1-},ref} = 0$ is zero. During a grid fault, the reference values are calculated based on Eq. (4.79) and (4.80):

$$i'_{S,q_{1+},ref}(t) = i'_{S,q_{1+},ref}(T_{gf}) + k_{1+} \cdot \Delta u_{1+}(t) \tag{4.103}$$

$$i'_{S,q_{1-},ref}(t) = k_{1-} \cdot \Delta u_{1-}(t). \tag{4.104}$$

The "active power control" calculates the current reference value $i'_{S,d_{1+},ref}$ as follows:

$$i'_{S,d_{1+},ref} = \frac{p_{ref}}{u_{1+}}. \tag{4.105}$$

The power control is followed by the inverter current control, which is shown in Fig. 4.64.

[6] According to Eq. (A.63), $u_{1+} = u_{1+,N}$.

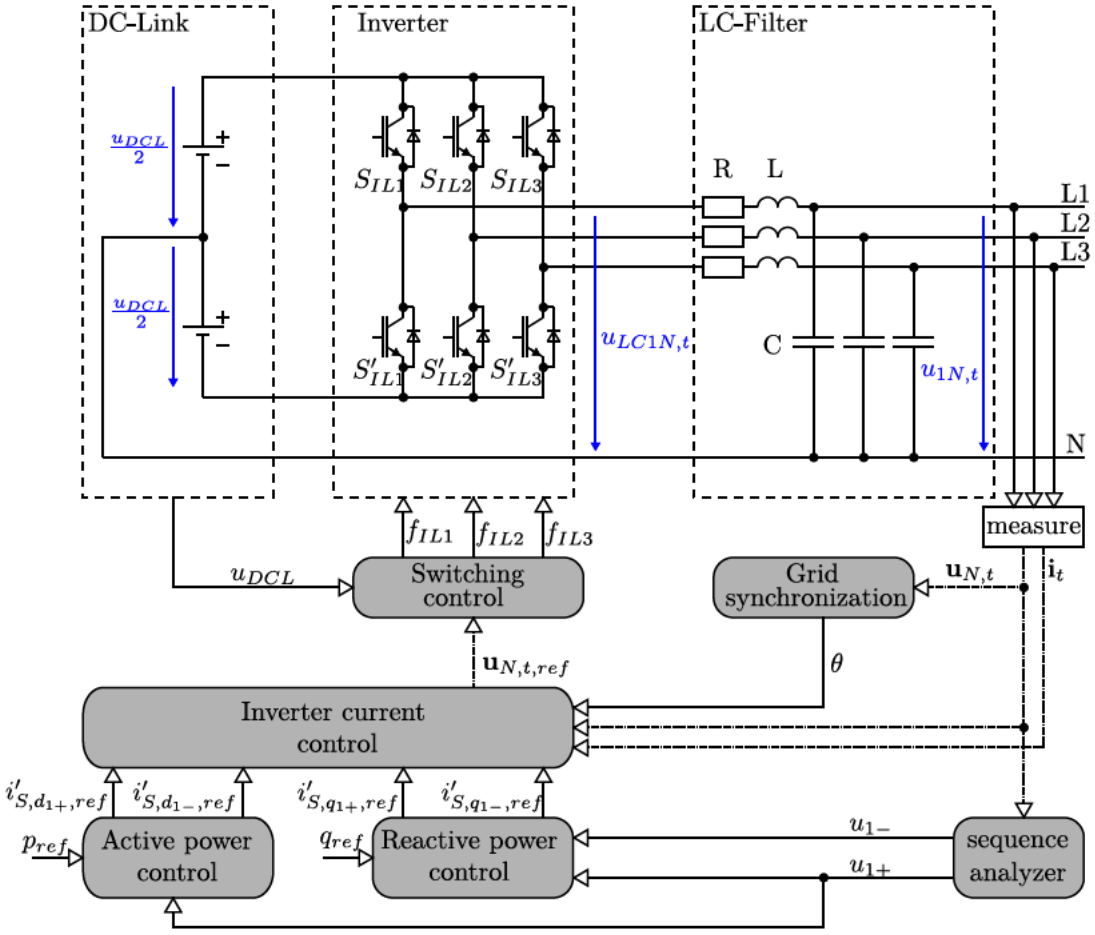

Figure 4.63: Converter and its control routines used in the EMT simulation model (based on Fig. 2.8).

The inverter current control block in Fig. 2.8 and Fig. 4.63 are identical. Therefore, this control structure is not only being used in Fig. 4.63, but can also be used in Fig. 2.8. It consists of two parts: the "current limitation" and the actual current controller. The current limitation implements the explanations described in Chp. 4.3.1.3. The pseudo-code in Alg. 4.1 shows the actual implementation of the current limitation.

The current limitation is followed by a "negative-sequence transformation". This block is necessary to take into account the angle $\varphi_{\pm}$ shown in Fig. 4.56. The PLL provides the angle θ, which represents the angle of the positive-sequence voltage space vectors $\underline{u}_{S,dq_{1+}}$. Since the components $i_{S,d_{1-}}$ and $i_{S,q_{1-}}$ are given with reference to the $\alpha\beta$-plane in the negative-sequence system, they have to be transformed in the $\alpha\beta$-plane in the positive-sequence system accordingly, as already shown in Eq. (4.87):

$$\underline{i}'_{S,dq_{1-}} e^{-j\omega t} e^{j\varphi_{\pm}} \tag{4.106}$$

where

$$\varphi_{\pm} = arg(u_{S,d_{1-}} + j u_{S,q_{1-}}). \tag{4.107}$$

This transformation is performed by the "negative-sequence transformation".

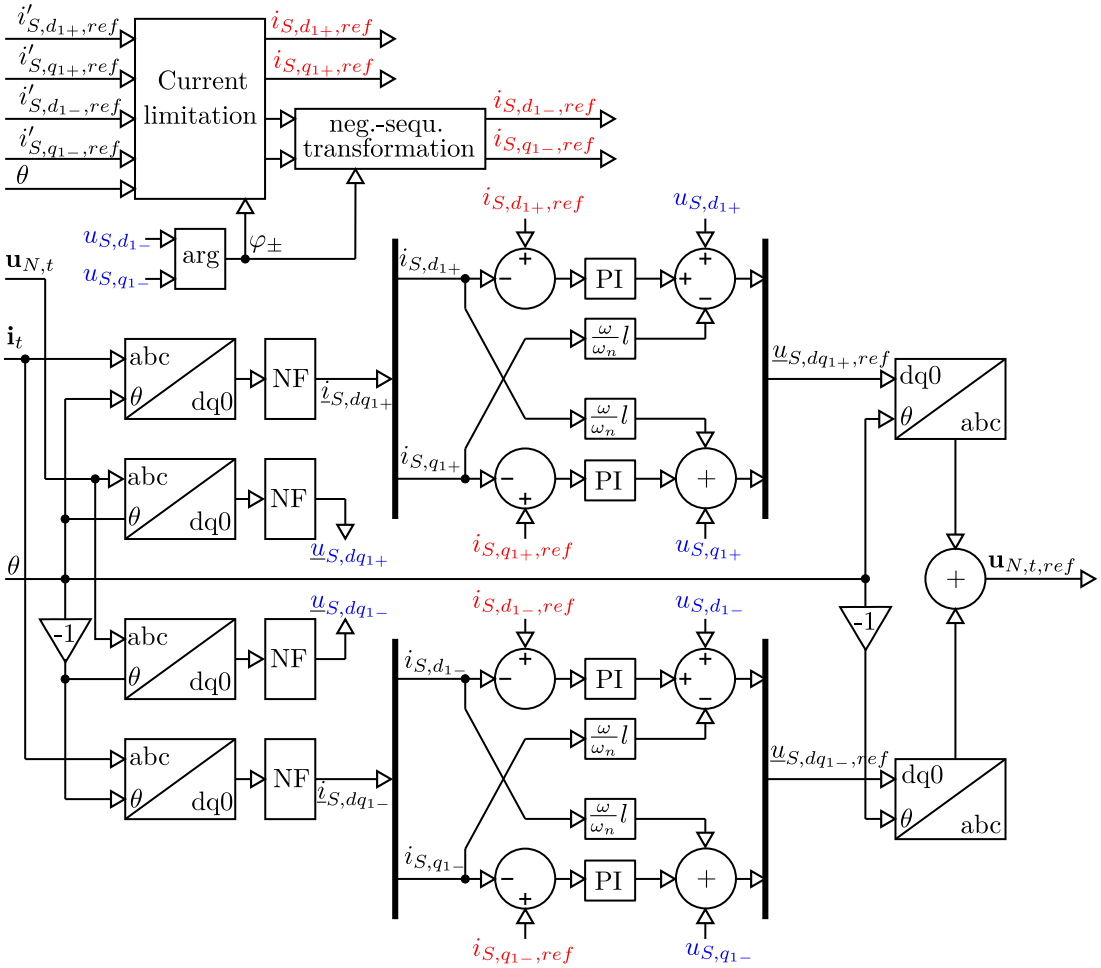

Figure 4.64: "Inverter current control"-block of Fig. 4.63 and Fig. 4.63, using a DSRF with Notch Filter (NF) based on [177] (R of Eq. (4.109) is neglected). The current limitation implements the explanations from Chp. 4.3.1.3.

The actual current controller is based on four PI-controllers for each component of the (limited) reference currents $i_{S,d_{1+},ref}$, $i_{S,q_{1+},ref}$, $i_{S,d_{1-},ref}$ and $i_{S,q_{1-},ref}$. To determine the corresponding current components that are currently injected at the output of the converter, these components have to be extracted from the measured phase currents $\mathbf{i}_t$. In order to do this, the park-transformation is followed by Notch-filters which are tuned to 2ω. As already shown in Fig. A.6, the occurrence of negative-sequence components leads to a second harmonic in the positive-sequence dq-components. This is also the case for the negative-sequence components when a positive-sequence occurs. By using park-transformations for the positive-sequence system $(+\theta)$ and for the negative-sequence system $(-\theta)$, where each component of the dq-output is followed by a Notch-filter tuned to 2ω, these second harmonic can be filtered. The differences of these measured components $\{i_{S,d_{1+}}, i_{S,q_{1+}}, i_{S,d_{1-}}, i_{S,q_{1-}}\}$ and $\{i_{S,d_{1+},ref}, i_{S,q_{1+},ref}, i_{S,d_{1-},ref}, i_{S,q_{1-},ref}\}$ are used as input of the corresponding PI-controllers. Between the voltage at the output of the inverter $\mathbf{u}_{LC,t}$ and the voltage output of the whole converter $\mathbf{u}_{N,t}$ a voltage drop over the LCL-filter occurs. This voltage drop has to be considered in the inverter current control. The voltage drop over the LCL-filter is taken

Algorithmus 4.1: Implementation of a current limitation according to Chp. 4.3.1.3.

Input: $i'_{S,d_{1+},ref}$, $i'_{S,q_{1+},ref}$, $i'_{S,d_{1-},ref}(=0)$, $i'_{S,q_{1-},ref}$, θ, $\varphi_{\pm}$
Data: i_{max}
Output: $i_{S,d_{1+},ref}$, $i_{S,q_{1+},ref}$, $i_{S,d_{1-},ref}(=0)$, $i_{S,q_{1-},ref}$
calculate the maximum phase current assuming $i'_{S,d_{1+},ref}=0$;
if *maximum phase current* $(i'_{S,d_{1+},ref}=0) > i_{max}$ **then**
  $i_{S,d_{1+},ref}=0$;
  determine which phase has maximum current: phase={1,2,3};
  solve symbolically:
  $\frac{d}{d\theta}\left(\mathfrak{Re}\left(jxi'_{S,q_{1+},ref}e^{j\theta}e^{-j(phase-1)\frac{2\pi}{3}}+jxi'_{S,q_{1-},ref}e^{-j\theta}e^{j\varphi_{\pm}}e^{-j(phase-1)\frac{2\pi}{3}}\right)\right)=0 \rightarrow$
  $\theta(x):=\theta_{max}(x)$;
  solve numerically:
  $\mathfrak{Re}\left(jxi'_{S,q_{1+}}e^{j\theta_{max}}e^{-j(phase-1)\frac{2\pi}{3}}+jxi'_{S,q_{1-},ref}e^{-j\theta_{max}}e^{j\varphi_{\pm}}e^{-j(phase-1)\frac{2\pi}{3}}\right)=$
  $i_{max}\rightarrow x$;
  $i_{S,q_{1+},ref}=x\cdot i'_{S,q_{1+},ref}$;
  $i_{S,q_{1-},ref}=x\cdot i'_{S,q_{1-},ref}$;
else
  $i_{S,q_{1+},ref}=i'_{S,q_{1+},ref}$;
  $i_{S,q_{1-},ref}=i'_{S,q_{1-},ref}$;
  determine which phase has maximum current: phase={1,2,3};
  solve symbolically:
  $\frac{d}{d\theta}\left(\mathfrak{Re}\left((i_{S,d_{1+},ref}+ji_{S,q_{1+},ref})e^{j\theta}e^{-j(phase-1)\frac{2\pi}{3}}+\right.\right.$
  $\left.\left.ji_{S,q_{1-},ref}e^{-j\theta}e^{j\varphi_{\pm}}e^{-j(phase-1)\frac{2\pi}{3}}\right)\right)=0\rightarrow\theta(i_{S,d_{1+},ref}):=\theta_{max}(i_{S,d_{1+},ref})$;
  solve numerically:
  $\mathfrak{Re}\Big((i_{S,d_{1+},ref}+ji_{S,q_{1+},ref})e^{j\theta_{max}}e^{-j(phase-1)\frac{2\pi}{3}}+$
  $ji_{S,q_{1-},ref}e^{-j\theta_{max}}e^{j\varphi_{\pm}}e^{-j(phase-1)\frac{2\pi}{3}}\Big)=i_{max}\rightarrow i_{S,d_{1+},ref}$

into account by using the normalized inductance l:

$$l=\frac{\omega_n\cdot L}{\frac{U_n^2}{S_n}} \tag{4.108}$$

with the equation

$$\underline{u}_{LC,S,dq}=\underline{u}_{S,dq}+j\frac{\omega}{\omega_n}l\cdot\underline{i}_{S,dq}=(u_{S,d}+i_{S,d}R-\frac{\omega}{\omega_n}l\cdot i_{S,q})+j(u_{S,q}+i_{S,q}R+\frac{\omega}{\omega_n}l\cdot i_{S,d}) \tag{4.109}$$

that is valid for both sequence systems. To extract the components of the voltage space vector $\underline{u}_{S,dq}$ out of the measured voltages $\mathbf{u}_{N,t}$, the same approach as for the currents is used, which consists of a park-transformation followed by Notch-filters, each for the positive-sequence and negative-sequence system.

4.3.2.2.2 Tuning of the Inverter Control

The tuning of the PI-controllers shown in Fig. 4.63 can be done according to [201]. The decoupling $\frac{\omega}{\omega_n}l$-terms in Fig. 4.64 guarantee the direct/active and quadrature/reactive components in the positive-sequence as well as in the negative-sequence system to be decoupled. Therefore, a change of reference values of a certain component only influences the corresponding output component.

For example, a change of $i_{S,d_{1+},ref}$ only has an influence on $i_{S,d_{1+}}$ and not on $i_{S,q_{1+}}$ or any other component. Each of the four components can therefore be considered as a single-input single-output system. In the Laplace domain, the PI-controllers are represented by

$$R_I(s) = K_P + \frac{K_I}{s} \tag{4.110}$$

and the process function can be approximated by neglecting the transfer function of the switching control and the inverter with

$$G_I(s) = \frac{\frac{1}{R}}{1 + s\frac{L}{R}} \tag{4.111}$$

resulting in a loop gain of

$$L_I(s) = R_I(s)G_I(s) = \frac{K_P}{sL} \cdot \frac{s + \frac{K_I}{K_P}}{s + \frac{R}{L}}. \tag{4.112}$$

By choosing $K_P = \frac{L}{\tau_i}$ and $K_I = \frac{R}{\tau_i}$ the closed-loop transfer function $\frac{L_I(s)}{1+L_I(s)}$ has a PT1-behavior with a freely selectable time constant τ_i. A corresponding choice of L, C and the gains K_P, K_I for each of the four current control loops shown in Fig. 4.64 is summarized in Tab. 4.5.

4.3.2.2.3 Verification of the Model

Chp. 4.3.3 presents measurements that were taken during forced short-circuits in the real grid. Parts of these measurements are used as input of the model presented above by using the measured voltage as the input of a controlled voltage source connected to the converter model shown in Fig. 4.63. The selected measurements are taken from the short-circuit event in the 30 kV-grid, shown in Fig. 4.67 indicated with "A".

The parameters of the converter model shown in Fig. 4.63 and the gains of the current controller shown in Fig. 4.64 are summarized in Tab. 4.5.

parameter	value
U_n	550 V
S_n	650 kVA
U_{DCL}	900 V
f_{sw}	8 kHz
L	280 µH
R	1 mΩ
C	342 µF
i_{max}	1.1 pu
τ_i	20 µs
K_P	14 pu
K_I	50 pu

Table 4.5: Parameters of the converter model and its control used in the simulation.

Two test cases are selected out of the available measurements, which are based on

- a two-phase short-circuit and
- a three-phase short-circuit

in the upstream 30 kV-grid. There is an impedance between the measuring point, which was the PCC of the battery converter, and the fault point, which leads to a residual voltage at the measurement point during a fault. This residual voltage determines the behavior of the battery converter according to Eq. (4.79) and (4.80). Based on the simulation model presented above, this behavior is simulated. For both test cases, the two factors k_{1+} and k_{1-} are chosen out of {1,2} for simulation. A maximum current capability of $i_{max} = 1.1\,\text{pu}$ is assumed.

Fig. 4.65 shows the corresponding simulation results for the two-phase short-circuit[7].

The measured voltage according to [196] is shown in Fig. 4.65(a). Fig. 4.65(b) and (c) show the simulation results for $k_{1+} = k_{1-} = 1$ and $k_{1+} = k_{1-} = 2$. The results consist of the phase current output $\mathbf{i}_t$, the reference current space vector $\underline{i}_S$ consisting of the current components $i_{S,d_{1+},ref}$, $i_{S,q_{1+},ref}$, $i_{S,q_{1-},ref}$ and the active power output p and the reactive power output q of the converter. At the beginning of the simulation it is assumed that the converter feeds in active power at an operating point of $p = -0.77\,\text{pu}$, $q = 0\,\text{pu}$. At $T_{gf} = 50\,\text{ms}$, the two-phase short-circuit in the upstream 30 kV-grid leads to a drop in the positive-sequence voltage u_{1+} and a rise in the negative-sequence voltage u_{1-}. According to Eq. (4.79) and (4.80) the converter starts to inject reactive current. The corresponding reference current components are shown in Fig. 4.65(b) and (c). Since the load-reference system is used, the drop in positive-sequence voltage leads to a negative reference current component $i_{S,q_{1+},ref}$, while the rise in negative-sequence voltage leads to a positive reference current component $i_{S,q_{1-},ref}$. In case of (c) the current components are higher than in (b), due to the higher values of k_{1+} and k_{1-}. According to Alg. 4.1, the active current component $i_{S,d_{1+},ref}$ has to be limited so that the maximum phase current i_{max} is respected. In (c) the reactive current components do have such high values that the active current component has to be limited to zero and also the reactive current components have to be limited. In (b) only the active current component is limited. In both cases the current output $\mathbf{i}_t$ in Fig. 4.65(b) and (c) shows that the maximum current capability of i_{max} is respected. Due to this limitation the active power p in (b) is reduced. Because reactive currents are injected both in the positive-sequence as well as in the negative-sequence system, and they have opposite sign, the reactive power q in (b) is only slightly higher than zero. In (c) the active power p is reduced to zero and the reactive power q is slightly higher than in (b).

Fig. 4.66 shows the corresponding simulation results for the three-phase short-circuit. The measured voltage according to [196] is shown in Fig. 4.66(a).

Fig. 4.66(b) and (c) show the simulation results for $k_{1+} = k_{1-} = 1$ and $k_{1+} = k_{1-} = 2$. The results consist of the phase current output $\mathbf{i}_t$, the reference current space vector $\underline{i}_S$ consisting of the current components $i_{S,d_{1+},ref}$, $i_{S,q_{1+},ref}$, $i_{S,q_{1-},ref}$ and the active power output p and the reactive power output q of the converter. At the beginning of the simulation it is assumed that the converter feeds in active power at an operating point of $p = -0.77\,\text{pu}$, $q = 0\,\text{pu}$. At $T_{gf} = 50\,\text{ms}$, the two-phase short-circuit in the upstream 30 kV-grid leads to a drop in the positive-sequence voltage u_{1+}. The negative-sequence voltage u_{1-} stays at zero. According to Eq. (4.79) the converter starts to inject reactive current. The corresponding reference current components are shown in Fig. 4.66(b) and (c). Since the load-reference system is used, the drop in positive-sequence voltage leads to a negative reference current component $i_{S,q_{1+},ref}$. The current component $i_{S,q_{1-},ref} = 0$ is zero, because there is no change of the negative-sequence voltage ($\Delta u_{1-} = 0$). According to Alg. 4.1, the active current component $i_{S,d_{1+},ref}$ has to be limited so that the maximum phase current i_{max} is respected. In (c) the reactive current component $i_{S,q_{1+},ref}$ does have such high values that the active current component has to be limited to zero and the reactive current component must also be limited. In (b) only the active current component has to be limited. In both cases the current output $\mathbf{i}_t$ in Fig. 4.65(b) and (c) shows that the maximum current capability of i_{max} is respected. Due to this current limitation, the active power p in (b) is reduced and limited to zero in (c). Due to the low voltage $\mathbf{u}_{N,t}$ during the fault, the reactive power only reaches low values of about 0.15 pu in (b) and about 0.2 pu in (c).

[7] Since there is no earth contact, the neutral point is identical to earth potential, therefore, $\mathbf{u}_{N,t} = \mathbf{u}_{E,t}$

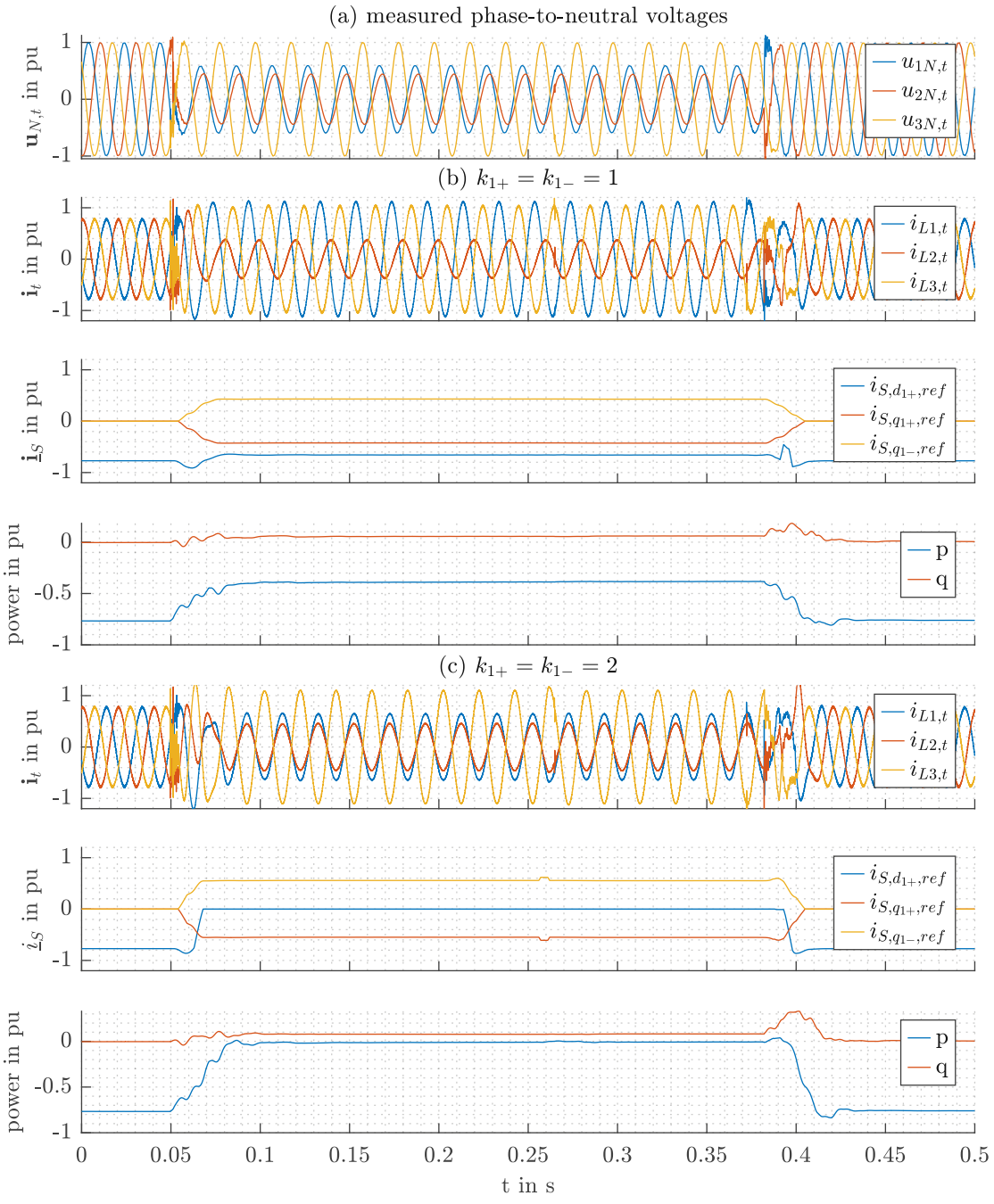

Figure 4.65: Simulation results of a two-phase short-circuit (the load reference system is used).

4.3.3 Field Measurements

In [196][123] the LVRT-behavior and the dynamic voltage support of a BESS, which is described in Chp. 3.1, during real faults in a feeder were investigated. Forced balanced (symmetrical) and unbalanced (asymmetrical) faults in the upstream 110 kV and the 30 kV grid were carried out and measured by suitable measurement equipment. The corresponding single-line diagram of the

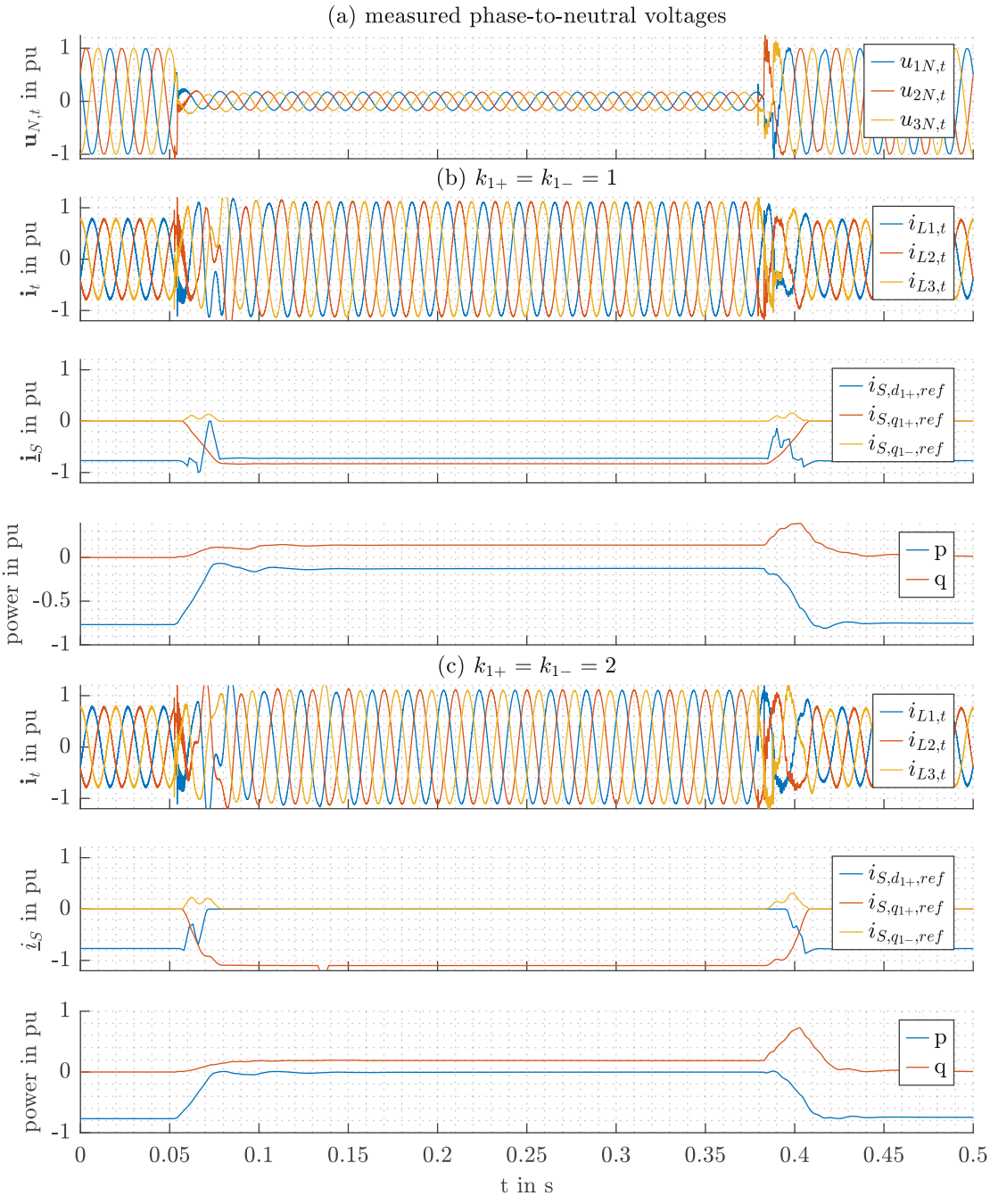

Figure 4.66: Simulation results of a three-phase short-circuit (the load reference system is used).

short-circuits carried out is shown in Fig. 4.67. The fault position in the upstream 30 kV-grid is indicated with "A" and the fault position in the upstream 110 kV-grid is indicated with "B". Selected measurements are presented and discussed in the following.

The requirements on the behavior of converter-based generators during faults described in Chp. 4.3.1 have been changed recently in many grid codes throughout Europe in order to satisfy the requirements given by the RfG [59]. Also the national grid codes in Austria [41] have been changed

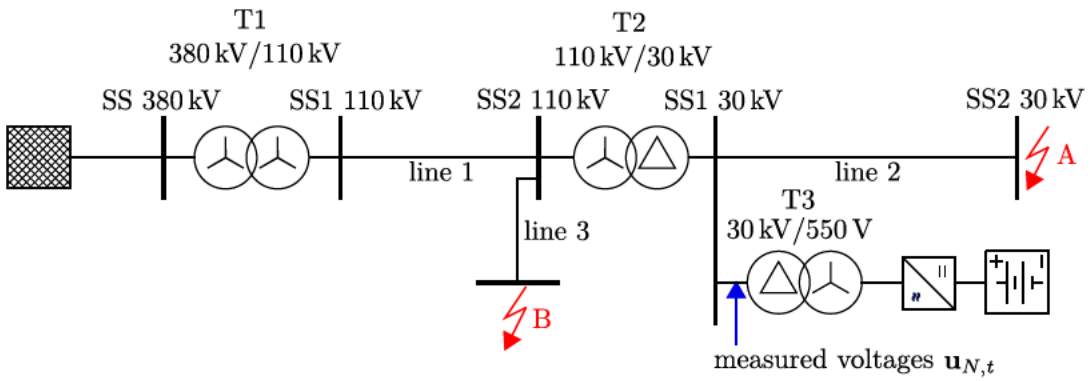

Figure 4.67: Single-line diagram of short-circuit voltage measurements performed in [196][123].

correspondingly. Although these updated grid codes are in force since 2019, many existing generators are still not capable to meet the requirements in the newest grid codes. Therefore, in the following it is also referred to the older grid code [38] in order to show both requirements. The measurements and tests done in [196, 123] were performed at a time when the newest grid code was announced and public available, but not in force. Therefore, only parts of its requirements are fulfilled. Nevertheless, the procedure of testing converter-based systems remains identical. The evaluations presented in the following will be referring to the requirements of both the old [38] and new [41] grid codes.

Based on the model presented in Chp. 4.3.2.1 the smallest phase-to-phase voltage at each busbar of Fig. 4.67 is calculated. The verification of the model is done by comparing the resulting short-circuit currents with the results of Chp. 2.2. Due to privacy policy, the parameters of all components shown in Fig. 2.2 are different from the actual parameters in the real grid. Nevertheless, the procedure to calculate short-circuit currents is identical. In order to check the LVRT-behavior according to Fig. 4.55 the voltages at the PCC of the BESS are relevant. The calculated voltages for the different short-circuit events are summarized in Fig. 4.68.

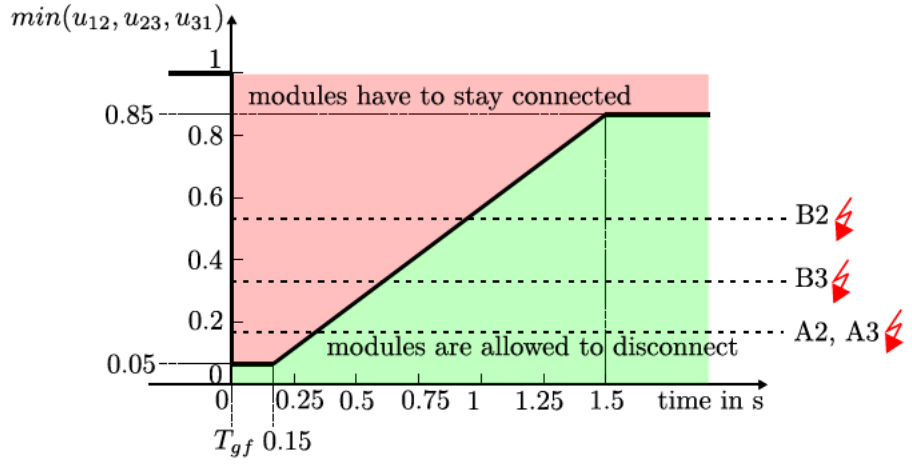

Figure 4.68: Calculated values of the voltages at the PCC drawn in the LVRT-curve of Fig. 4.55, based on the model described in Chp. 4.3.2.1. "A2" stands for a two-phase short-circuit at fault location A. "A3" stands for a three-phase short-circuit at fault location A. "B2" stands for a two-phase short-circuit at fault location B. "B3" stands for a three-phase short-circuit at fault location B.

The choice of the fault locations was done in a way to cover the largest possible area of the LVRT-curve shown in Fig. 4.55.

The measurements of the voltages $\mathbf{u}_{N,t}$ and the currents $\mathbf{i}_t$ at the PCC can be used to calculate the corresponding instantaneous symmetrical components and the corresponding park-components according to Chp. A.2.1. As the measurements at fault location A were already used in Chp. 4.3.2.2.3, these measurements are discussed in the following. This allows a comparison between the behavior which is actually required and the behavior which was measured.

Fig. 4.69 shows the measurements taken during a two-phase short-circuit at fault location A.

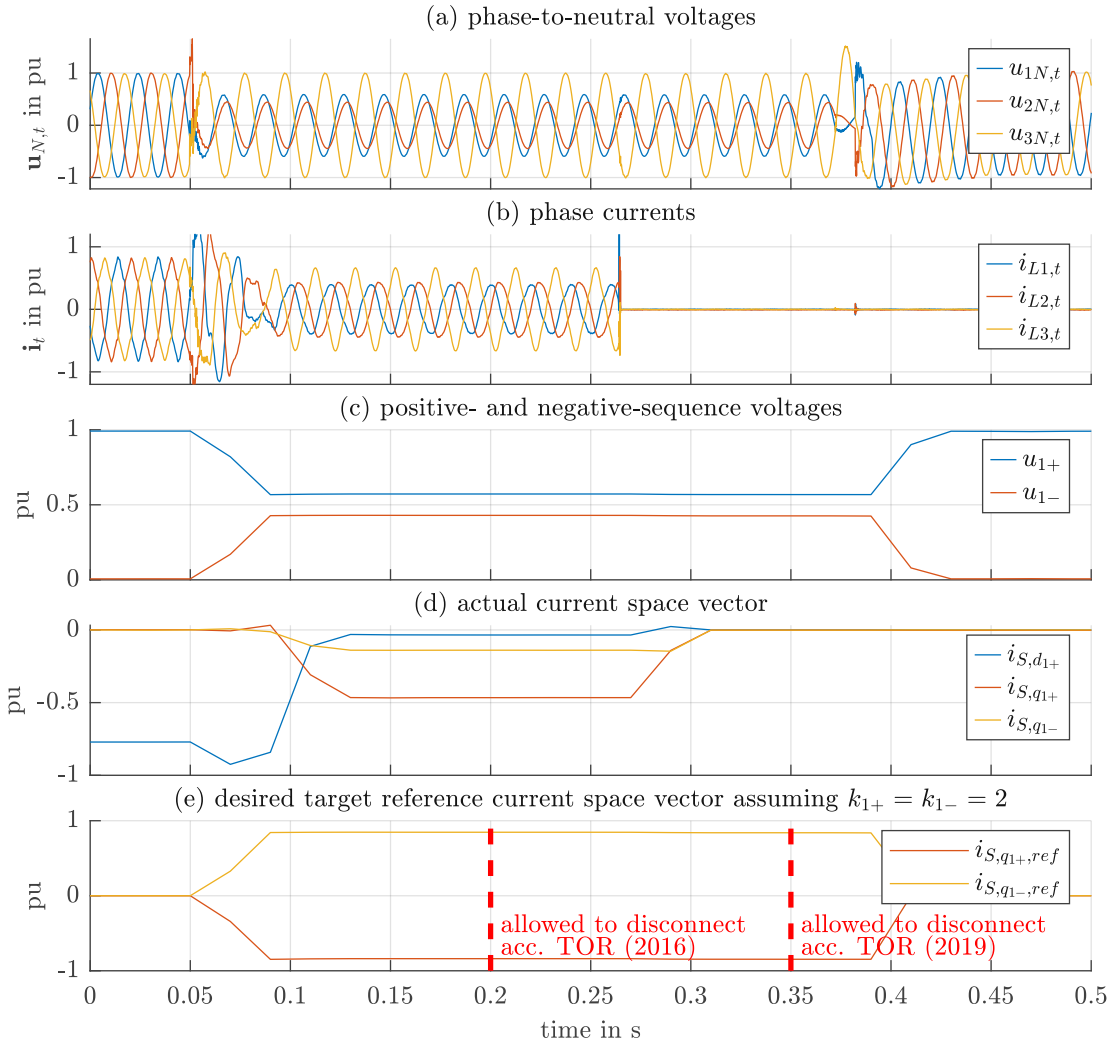

Figure 4.69: Measurements of a two-phase short-circuit at fault location A. (a) shows the measured voltages $\mathbf{u}_{N,t}$ at the PCC. (b) shows the measured currents $\mathbf{i}_t$ at the PCC. (c) shows the positive-sequence and negative-sequence voltage calculated according to Chp. A.2.1. (d) shows the park-components of the current calculated according to Chp. A.2.1. (e) shows the desired reference park-components according to the results of the simulation shown in Fig. 4.65. In (e) the two red dotted lines show the time when a disconnection according to the old grid code [38] and the new grid code [41] is allowed.

The corresponding simulation results investigated in Chp. 4.3.2.2.3 are shown in Fig. 4.65. The forced short-circuit is initiated at about 50 ms and is cleared manually at a about 380 ms. During the short-circuit the BESS starts to inject unbalanced currents after a short settling process. The desired current park-components to fulfill the new grid code are shown in (e) and are based on the simulations shown in Fig. 4.65. They are based on the voltage drop in the positive-sequence and negative-sequence system shown in (c). In (d) the actual current park-components are shown. Although a reactive current injection, both in the positive-sequence as well as in the negative-sequence system can be seen, the comparison with (e) shows that the negative-sequence components $i_{S,q1-}$ has a wrong sign. Because a reactive current in the negative-sequence system is injected, this leads to an even increasing negative-sequence voltage, although it should be reduced by drawing a corresponding reactive current in the negative-sequence system. The current component in the positive-sequence system has the right sign, but its magnitude is too low compared to the desired value shown in (e). Because the old grid code [38] does not make any requirement on the magnitude of the current injection these requirements are fulfilled. Also the old grid code does not require a current injection in the negative-sequence system.

As shown in (b) the BESS disconnects at about 270 ms. In comparison with the allowed durations shown in (e) it can be stated that the LVRT-requirements according to the old grid code [38] are fulfilled while the requirements according to the new grid code [41] are not.

In summary, the measurements shown in Fig. 4.69 show that all requirements according to the old grid code [38] are fulfilled, while not a single requirement of the new grid code [41] is met in detail, neither the requirements on LVRT nor on current injection.

Fig. 4.70 shows the measurements taken during a three-phase short-circuit at fault location A.

The corresponding simulation results investigated in Chp. 4.3.2.2.3 are shown in Fig. 4.66. The forced short-circuit is initiated at about 50 ms and is cleared manually at a about 380 ms. During the short-circuit the BESS starts to inject reactive currents after a short settling process. The desired current park-components to fulfill the new grid code are shown in (e) and are based on the simulations shown in Fig. 4.66. They are based on the voltage drop in the positive-sequence and negative-sequence system shown in (c). In (d) the actual current park-components are shown. Although a reactive current injection in the positive-sequence system can be seen, the comparison with (e) shows that the magnitude of $i_{S,q1+}$ is too small. Because the old grid code [38] does not make any requirement on the magnitude of the current injection its requirements are fulfilled.

As shown in (b) the BESS disconnects at about 270 ms. In comparison with the allowed durations shown in (e) it can be stated that the LVRT-requirements according to the old grid code [38] are fulfilled while the requirements according to the new grid code [41] are not.

In summary, the measurements shown in Fig. 4.70 show that all requirements according to the old grid code [38] are fulfilled, while not a single requirement of the new grid code [41] is met in detail, neither the requirements on LVRT nor on current injection.

4.4 Black-Starting and Operating a Microgrid

In order to mitigate global warming, the integration of renewable energy will increase dramatically in the coming years. Several studies calculate a share of 50 % of renewable energy in the power sector in 2030 [69, 91]. A high percentage of this share will be covered by variable renewable energy, namely solar photovoltaic and wind power systems. Due to the variable infeed-behavior of these technologies, severe power fluctuations of the total power infeed in the electric power grid are expected to become common. These power fluctuations lead to high differences between load and generation. The need for additional flexibilities in the power system to balance these differences is therefore indisputable. Storage technologies are one way to create additional flexibility. Long-term

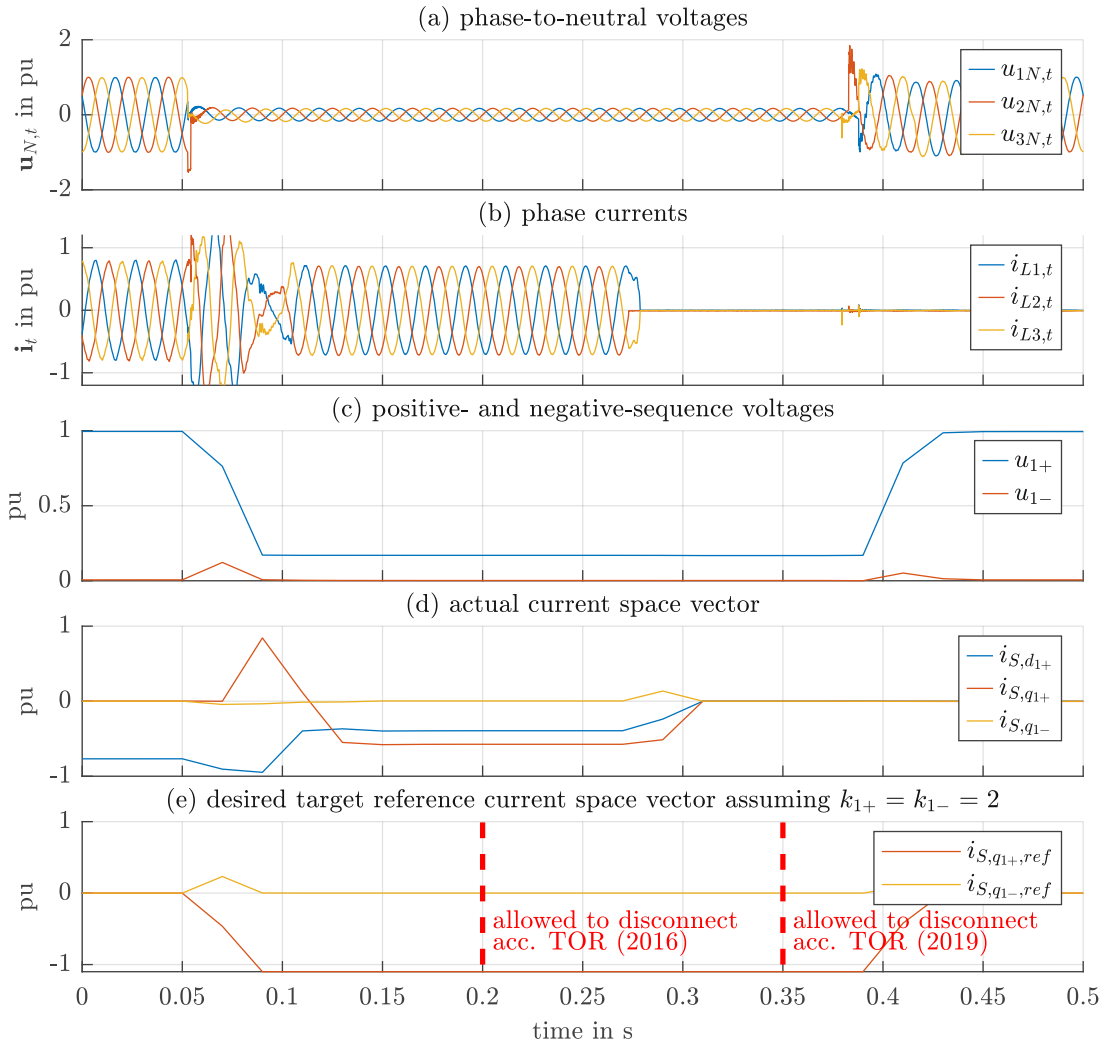

Figure 4.70: Measurements of a three-phase short-circuit at fault location A. (a) shows the measured voltages $\mathbf{u}_{N,t}$ at the PCC. (b) shows the measured currents $\mathbf{i}_t$ at the PCC. (c) shows the positive-sequence and negative-sequence voltage calculated according to Chp. A.2.1. (d) shows the park-components of the current calculated according to Chp. A.2.1. (e) shows the desired reference park-components according to the results of the simulation shown in Fig. 4.66. In (e) the two red dotted lines show the time when a disconnection according to the old grid code [38] and the new grid code [41] is allowed.

and short-term storage technologies are therefore expected to be increasingly integrated into the power system [168]. BESS are expected to cover a part of the short-term storage demand for durations between minutes, hours or days. Examples of how the flexibility of BESS will be used to handle power fluctuations, for example, are the application of “peak-shaving” to avoid overload of transmission lines or their contribution to frequency control by providing frequency reserves. There are more of such examples, but they all have one property in common, which is that no continuous activation will take place. For example, peak-shaving may only be necessary in times of high stress of the grid, otherwise the surplus power may be transmitted to places of higher demand. The corresponding flexibility in the latter situation would be transmission of power,

leading to the necessity of grid expansion, which is also listed as a requirement for flexibility in the future power system in several studies [69, 91]. Because BESS are considered not to perform peak-shaving, frequency control, or other services, continuously, the idea of "value-stacking" arises. Other services or applications, which are not directly related to handle power fluctuations in the future power system, are considered as a way to increase the profitability of a BESS, by providing them besides other services. Islanding can be considered as one of such applications. Due to the high amount of renewable energy in the future power system, the risk of blackouts increases. By building local Microgrids and perform an island operation during such blackouts, the reliability of supply can be increased.

The increasing amount of DER offers the possibility to build such a Microgrid (MG). According to Marney et al. [125] Microgrids comprise low voltage distribution systems with distributed energy sources, storage devices, and controllable loads, operated connected to the main power grid or islanded, in a controlled, coordinated way. According to Mahmoud et al. [112] there are several ways to to categorize MG, for example, by their application type (Utility MG, Commercial MG, Industrial MG, remote/off-grid MG), their system structure (single-stage/two-stage power-conversion systems), the type of control (centralized, decentralized or ditributed), etc. Based on the application type the MG are embedded into the low-voltage or medium-voltage level of the main grid, depending on the size of the integrated loads and DER. Remote MG are an exception, which are operating without any connection to the main grid. A Microgrid has two operation modes, which are termed as "grid-connected mode" and "island mode". The operation of a Microgrid separate from the main grid in island mode is based on suitable control algorithms. In the case of a blackout of the main grid, a Microgrid is able to switch from grid-connected mode to island mode, either via a black-start or by a smooth transition. Therefore, an appropriately designed Microgrid improves reliability and resiliency by providing a back-up system against grid faults [170]. There may also be an application for Microgrids to facilitate the restoration process after blackouts [152]. Besides such applications of Microgrids which are "embedded" into the main grid, the most straight-forward application of Microgrids is their application in remote areas, where it is not possible or economically not feasible to provide a sufficient power link to the main grid, as for example described in [204].

Many DER are connected to the grid via converters. To be able to operate an islanded Microgrid, at least one of these DER must have island capabilities in order to control the voltage and frequency in the Microgrid. Such converters are called "grid-forming" converters. The major difference between grid-forming converters and conventional "grid-following" converters is their ability to build the grid angle on their own, whereas grid-following converters rely on the determination of the grid angle based on the voltage measurement at their PCC. The supply of an islanded Microgrid by multiple grid-forming units requires the application of appropriate load sharing techniques. Conventionally, a voltage and frequency droop control is adopted in such cases, as for example described by Katiraei and Iravani [99] or by Barklund et al. [13]. However, conventional droop control neglects the influence of the coupling of the grid-forming units [140]. This results in large power circulating-currents and power fluctuations of the Microgrid [79]. Improved droop control strategies, as for example proposed by Peng et al. [140], are using virtual impedances in order to take into account the coupling of the grid-forming units. For the application of a Microgrid to build a backup supply during the blackout of the main grid, as described above, the use of several grid-forming units may be not very practical, at least for smaller Microgrids. Most of the DER, which will be integrated into the main grid in the future are based on variable renewable generation. Therefore, they are not fully capable of contributing to power balancing during a backup supply in an islanded Microgrid, because they are connected via grid-following converters and may only cover a share of the energy demand of the loads in an intermittent way. But as described above, the integration of decentralized BESS nearby to larger DER based on variable renewable energy is very likely in the future in order to handle the power fluctuations of these DER. By designing such BESS to be able to switch between a grid-following and a grid-forming mode, this opens the possibility to build Microgrids of certain sections of the main grid. The most practicable approach for such an

arrangement is a master-slave control approach. Such a master-slave approach is characterized by using only one grid-forming unit, which represents the "master" during island operation, while the other DER are acting as "slave" in a grid-following mode. This approach is usually also used when Microgrids are supplied with large diesel generators, for example as described in [72], but can also be used to achieve a sustainable supply of Microgrids based only based on renewable energy. Although master-slave control approaches for Microgrids have already been investigated in several studies [172, 184, 72, 25], the major drawbacks can be identified by the need for communication [172, 184, 25] and the lack of experimental investigations in real world grid sections, since all studies are limited to simulations. An example for real world measurements can be found in [72] where power quality measurements in an artificial test Microgrid were performed. But Garde et al. [72] conclude the lack of energy management for the BESS, which acts as master unit in their test Microgrid. The following chapters present a master-slave approach without the need for communication and the possibility to perform a simple energy management of the BESS.

As already mentioned above, BESS are considered to become a necessity to provide flexibility in the future power system as short-term storages. Due to decreasing prices of Li-Ion battery cells [31] this technology is considered to make up the majority of BESS which are used in the future. Against the background of value-stacking, islanding is considered as an additional service BESS can provide to increase their profitability, while at the same time increasing the reliability of supply in case of blackouts of the interconnected power grid by building local Microgrids. Assuming such Microgrids to comprise a high share of variable renewable energy, an easy approach for ensuring their functionality during island operation is desired in order to lower the requirements of the energy reserves of the BESS and to increase the maximum duration of island operation. This thesis presents a master-slave approach based on a variable frequency, which allows the power infeed of variable renewable energy during island operation of a Microgrid, without the need for additional communication. Furthermore, the black-start and island operation of a real Microgrid is investigated, within which this master-slave approach is applied. This real Microgrid comprises a BESS, wind turbines and loads, which are used to reflect the behavior of a residential grid section. The motivation for this chapter is to investigate the possibility of black-starting and operating a residential grid section during an assumed blackout of the interconnected power grid, the residential network is connected with. Whereas the BESS and the wind turbines are integrated in the corresponding grid section during normal operation, the connection of the nearby residential grid section, comprising several households, was not possible due to safety reasons. Therefore, several impedance-loads and motor-loads are used to reproduce significant load-steps of this residential grid section. Via field tests the black-starting and islanding capabilities of the Microgrid and the master-slave approach presented in this chapter are investigated. For preparation of these field tests, simulations in MATLAB/SIMULINK were performed, which allowed an evaluation of the expected results.

To present the corresponding results and findings, this chapter is structured as follows. Chp. 4.4.3 presents the simulation model used in the simulations and presents the simulation results of a black-start and during load-changes in island operation. Chp. 4.4.4 presents the measurement results which were taken during field tests in a real Microgrid.

This chapter focuses on Microgrids that use a BESS as master unit in a master-slave control strategy described above. Related to this type of Microgrids the following Chp. 4.4.1 discusses more details on the black-start of such Microgrids and Chp. 4.4.2 discusses more details on master-slave control approach which is investigated in this chapter.

This chapter incorporates investigations and analyses published in paper [119].

4.4.1 Black-Start

The black-start of a Microgrid defines the process of restoring it after a shutdown without any external voltage support. The operation of an islanded Microgrid is often preceded by a black-start, which may be necessary in case of a blackout of the main grid, when no smooth transition of the Microgrid from grid-connected into island mode takes place, or in case of a remote Microgrid, where a supply may only be given during specific time periods during the day. The black-start of a Microgrid is a challenging task which special attention must be paid to. The main issue with black-starting an island grid is a phenomenon which is termed as "cold load pickup". Especially a high penetration of thermostatically controlled devices leads to a high power demand during the black-start of a Microgrid [70]. During normal operation their activity is evenly distributed, whereas during a black-start all of these devices drain power at the same time, as the thermostatically controlled area got "cold" during the blackout. The same behavior occurs with many devices, as their random switching during normal operation may be lost during a black-start. In addition, their power consumption during start-up may be higher than during normal operation, for example because of certain start-up routines. Also most types of loads drain power depending on the temperature. If they possess a negative temperature coefficient, their resistance decreases with rising temperature. Therefore, during a start-up process of a load where the load temperatures are lowest they drain higher power than in their nominal operating point. The remaining equipment of a Microgrid, as for example transformers and cables, also have a higher power demand during start-up. The inrush currents of transformers and the initial charging process of the capacitances of cables are the main reasons for this higher power demand. The challenge of performing a black-start, therefore, is to handle the "cold load pickup" in terms of both active and reactive power.

The most important property to perform a black-start is the black-start ability of at least one grid-forming unit in the Microgrid. Assuming a BESS to be this grid-forming unit, such a black-start ability can only be achieved if all of its components and control systems can be activated and maintained without any external power supply. The most common solution to reach such a condition is the use of an additional Uninterruptable Power Supply (UPS) to supply these components of the BESS. The primary battery of the BESS itself can also be an option to serve as a power supply. But as some of the components are necessary to start-up and run the battery itself and the AC-output voltage of the BESS often differs from the voltage that is needed to supply all components and auxiliary systems (e.g. 400 V), the use of an additional UPS is also a common approach. One of the biggest consumer of all necessary components to maintain a BESS is its HVAC-system. Therefore, the UPS must be designed to handle such a power consumption or the BESS must be designed to start-up without an active HVAC system.

In general, black-start ability also requires the BESS to be operable automatically, remotely or by local staff. It has to be guaranteed that all breakers are functional without any external power supply in order to start-up the BESS and establish a connection to the Microgrid. A corresponding start-up routine has to guarantee a procedure to appropriately control these breakers in an intended sequence. A crucial point of such a start-up routine is an appropriate island detection. The island detection guarantees that a black-start and further connection to a Microgrid, by closing the relevant breaker at the PCC of the BESS, is only possible when the Microgrid is without voltage and not connected to the main grid. Otherwise, massive damage may be caused to the BESS and other components due to very high currents as a result of possible phase differences between the voltage of the BESS and the voltage of the main grid. Therefore, a synchronization unit is essential for a connection to the main grid. At the end of a start-up routine, the relevant breaker of the PCC is closed in order to energize the Microgrid. As already mentioned above, the BESS has to be capable of handling the cold load pickup that may arise during this process. A simple way to deal with the cold load pickup is to gradually increase the system voltage instead of performing a black-start with nominal voltage during this last step of connecting to the Microgrid. Especially the inrush currents of all transformers and the charging currents of the cable capacitances in the

island grid can be decreased by doing so. Although most of the electrical equipment and loads will not be damaged due to operation with under-voltage, there may be processes that rely on voltage magnitudes within certain limits. For loads that are part of such processes, a corresponding breaker logic has to guarantee that their connection is only established after a certain voltage limit has been reached. Also protection devices may have to be reconfigured to handle the gradual increase of the system voltage. Especially the protection devices of the BESS that are configured to trip as a consequence of under-voltage have to be reconfigured.

4.4.2 Island Operation

The black-start of a Microgrid is followed by the island operation. The challenge during island operation is to manage the active and reactive power demand that results from the load behavior, and the active and reactive infeed that results from DER in the Microgrid. Therefore, an islanded Microgrid that contains several DER requires suitable control mechanisms to ensure that the maximum power of the grid-forming unit is respected. The implementation of such control mechanisms offers the possibility of operating an islanded Microgrid, the peak load and peak infeed of which exceed the nominal power of its grid-forming unit. At least a part of the load can be supplied by DER while the grid-forming unit only has to deliver balancing power. The challenge of such an operation is the impact of a sudden imbalance between load and generation. The control mechanisms mentioned above have to ensure that such imbalances become controllable by the grid-forming unit.

The ability of grid-forming converters to generate the grid angle on their own offers the potential of dictating the frequency to actively influence the power output of other generating units and the power consumption of loads in an islanded Microgrid via pre-defined frequency characteristics.

The simplest approach for such control mechanisms is using load-shedding for a surplus of load and power reduction for a surplus of infeed, in case either of them exceeds the power limits of the grid-forming unit. The frequency in the Microgrid can be used as control signal for both operations without the need for additional communication. For load-shedding, additional breakers that trip at certain frequency limits and a stepwise load-shedding plan with prioritization of loads may be necessary. For power reduction of generation units, the Limited Frequency Sensitive Mode (LFSMO) can be used. According to latest grid codes [41], generation units have to reduce their power output in case of a frequency that exceeds a limit of 50.2 Hz in appliance with this Limited Frequency Sensitive Mode (LFSMO). This mechanism can be used in an islanded Microgrid to actively influence the power output of DER. This kind of frequency control approach can not only be used to limit power flows beyond the limits of the BESS, but can also be used to perform an energy management to manage the SoC. Such a frequency control approach is already being used in home storage systems [164]. A corresponding frequency characteristic to be used in a Microgrid described above is shown in Fig. 4.71.

The normalized power intake of the grid-forming BESS is defined by $p = \frac{P_{DER} - P_{LOAD}}{S_n}$ and equals the power imbalance between the power infeed of DER P_{DER} and the power consumption of loads P_{LOAD} in the Microgrid, which is normalized to the nominal apparent power S_n of the BESS. The values p_0 and SoC_0 can be used to parameterize the frequency characteristic. The grid-forming BESS controls its output frequency according to the resulting frequency characteristic. As a consequence of the LFSMO, the DER start to reduce their currently possible power output P'_{DER} above a frequency of 50.2 Hz in 50 Hz-systems to a reduced power output P_{DER}. According to Fig. 4.71, the frequency f of the BESS is a function of the normalized power intake p and the SoC SoC, defined by $f = \mathrm{f}(p, SoC)$. To deal with situations when $p > p_0$ and $SoC > SoC_0$, this function is defined by

$$f = \mathrm{f}(p, SoC) = \max[\mathrm{f}_p(p), \mathrm{f}_{SoC}(SoC)]. \tag{4.113}$$

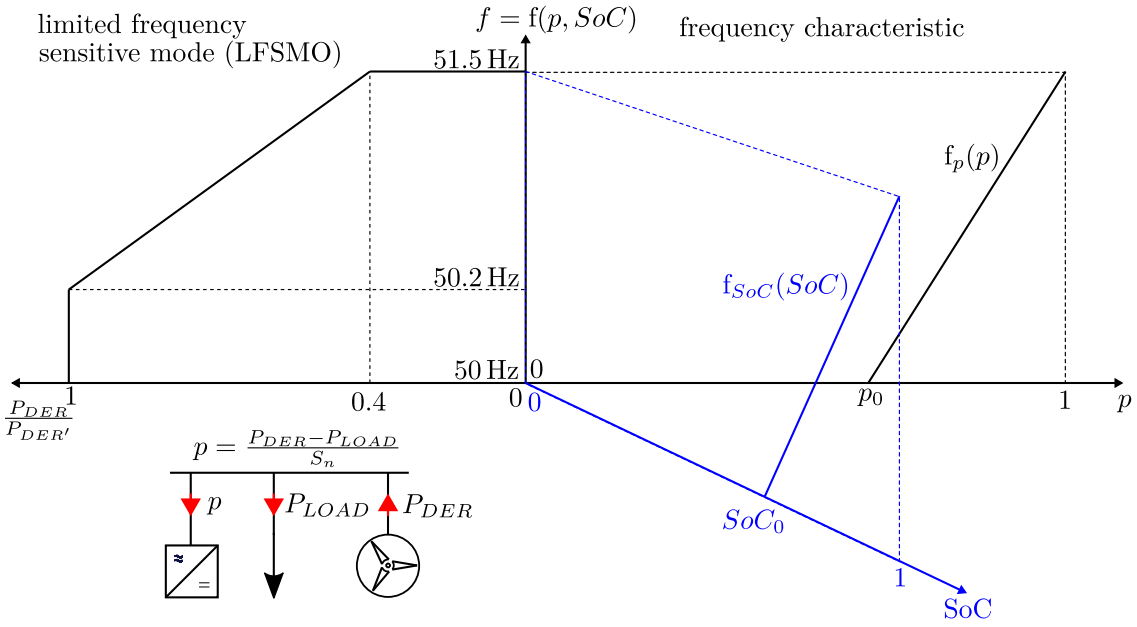

Figure 4.71: Characteristic to control the frequency of a grid-forming BESS in order to reduce the currently possible power output P'_{DER} of other generating units to a reduced power output P_{DER} in case of a high SoC or in case the imbalance between generation and load p reaches values near 100 % (rated power of the BESS).

The frequency curve may be expanded by an additional part to reduce the output frequency of the grid-forming BESS in order to trigger corresponding under-frequency relays that initiate load-shedding as mentioned above.

During island operation, the massively reduced short-circuit power leads to larger voltage excursions during imbalances of load and generation. However ,also during island operation the power quality still remains an important issue.

4.4.3 Simulation

For the preparation of the field tests, a converter model in MATLAB/SIMULINK was created in order to investigate the expected behavior during island operation. The estimation of voltage dips during load-steps and start-up of motors was a goal to choose permissible sizes for the load and the motors. Furthermore, it was aimed to investigate the influence of control parameters on these voltage dips in order to get information under which conditions instabilities and maximum voltage dips during the field tests can be expected.

4.4.3.1 Model Description

The ability of a BESS to black-start and maintain a Microgrid relies on an appropriate control design of its converter, which has already been named grid-forming converter above. As many BESS not only operate in island mode but also in grid-connected mode, the control design of theirs converter has to be able to switch between these two operation modes. Based on a simplified converter model, Fig. 4.72 shows an appropriate control design which is capable of operating in both “island mode” and “grid-connected mode”.

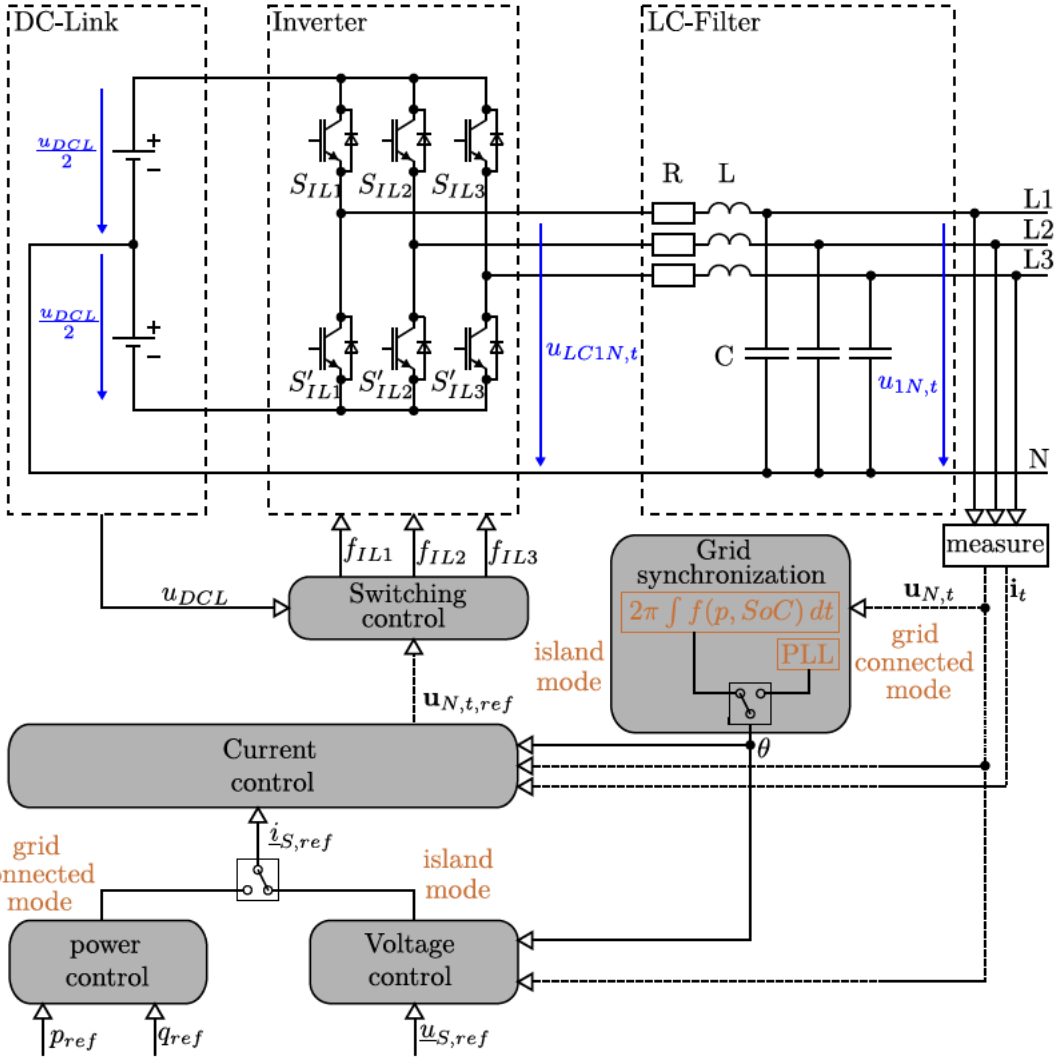

Figure 4.72: Converter model and its control to realize both island mode and grid-connected mode. The blue color indicates normalized voltages. The orange color indicates selectable control elements during grid-connected and island mode.

The simplified converter model of a three-phase VSC shown in Fig. 4.72 is a two-level converter, which consists of a DC-Link, an inverter and an LC-filter. For simplification, the DC-link is modeled as a constant voltage source. The inverter model consists of a self-commutated three-phase bridge, which is controlled by a pulse-width modulation signal. The resistance in the LC-filter at the output of the converter represents the parasitic resistance of the inductance.

The lower part of Fig. 4.72 shows the control structure of the converter model. It consists of a "grid synchronization", which builds the grid angle θ. This grid angle is used in the "current control" to generate a reference voltage $\mathbf{u}_{N,t,ref}$ based on a current reference space vector $\underline{i}_{S,ref}$. The control structure includes two switches by which the operation mode, either grid-connected or island mode, and therefore a corresponding converter control structure is selected. In grid-connected mode the current reference signal is generated by the "power control", which calculates $\underline{i}_{S,ref}$ based on active and reactive power reference signals p_{ref} and q_{ref}. The grid angle θ during grid-connected mode is delivered via a synchronous reference frame phase-locked loop (SRF-PLL). During island mode, the grid angle θ is delivered based on a parametrizable value of the angular

frequency ω with $\theta = \int \omega \, dt$. The current reference space vector during island mode is generated by the "voltage control", which uses a voltage reference space vector $\underline{u}_{S,ref}$ to calculate it. The current control is followed by the "switching control" which generates the switching signals f_{IL1}, f_{IL2} and f_{IL3} based on the voltage reference signal $\mathbf{u}_{N,t,ref}$ and the DC-link voltage u_{DCL} in order to control the switches S_{IL1}, S_{IL2} and S_{IL3} of the inverter. The complementary switching signals f'_{IL1}, f'_{IL2} and f'_{IL3} are used to control the switches S'_{IL1}, S'_{IL2} and S'_{IL3} of the inverter. More details about the control structure during grid-connected mode can be found in [118, 115]. For the simulations in the following chapters only the control structure during island mode is relevant.

In island mode, the voltage and current control build a cascaded control structure, which is presented in more detail in Fig. 4.73.

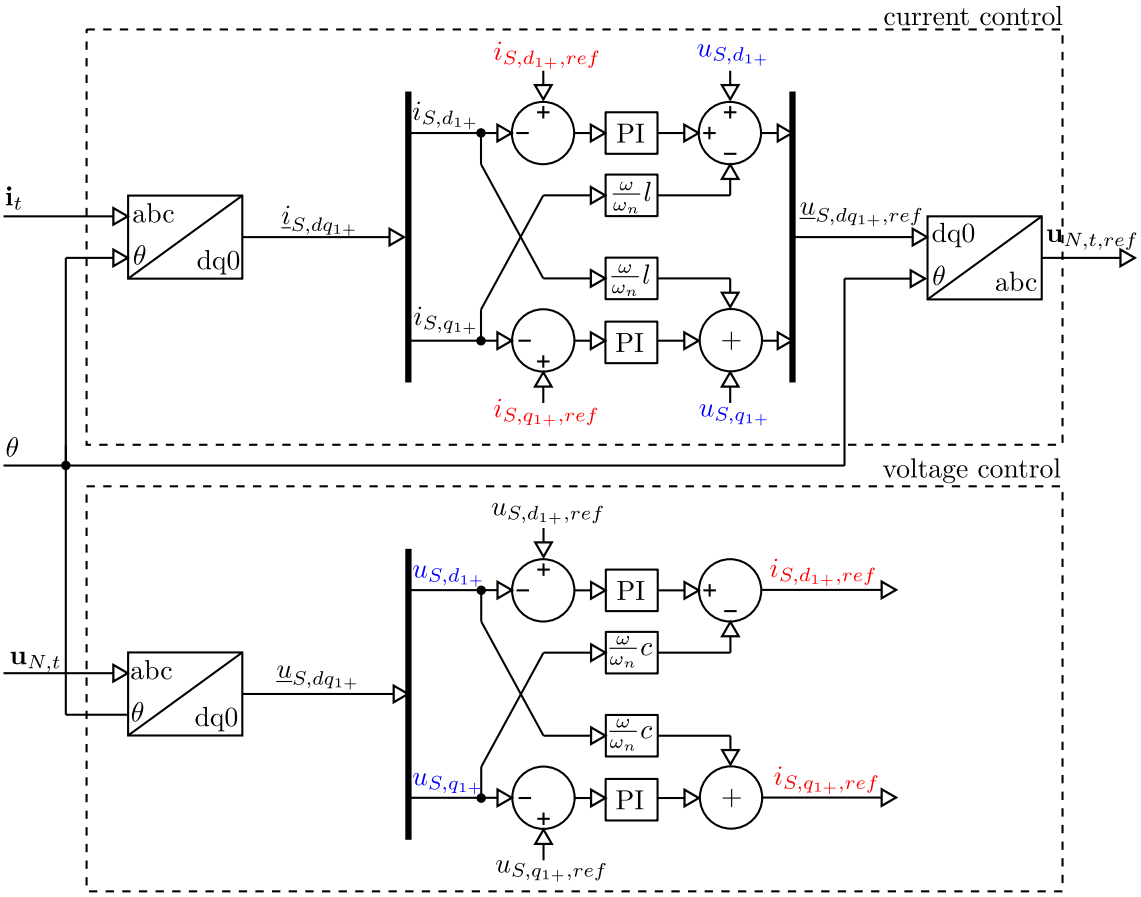

Figure 4.73: Cascaded voltage and current control of Fig. 4.72 in island mode.

Based on the grid angle θ, the measured voltage and current vectors $\mathbf{u}_{N,t}$ and $\mathbf{i}_t$ are used to calculate corresponding space vectors $\underline{u}_{S,dq_{1+}}$ and $\underline{i}_{S,dq_{1+}}$ via Park-transformation. In the voltage control, the voltage space vector $\underline{u}_{S,dq_{1+}}$ is used to control the corresponding d and q-components via PI-control based on a reference space vector $\underline{u}_{S,dq_{1+},ref}$. The coupling between the d and q-components due to the LC-filter is taken into account by corresponding decoupling terms $\frac{\omega}{\omega_n} c$, where c is the normalized capacitance of the LC-filter, which is defined by $c = \frac{\omega_n C S_n}{U_n^2}$, with S_n as the nominal apparent power and U_n as the nominal voltage of the converter. The resulting current reference space vector $\underline{i}_{S,dq_{1+},ref}$ of the voltage control is used as input of the current control, which uses the current space vector $\underline{i}_{S,dq_{1+}}$ to control the corresponding d and q-components via PI-control based on this current reference space vector. The coupling between the d and q-components due to the

LC-filter is taken into account by corresponding decoupling terms $\frac{\omega}{\omega_n} l$, where l is the normalized inductance of the LC-filter, which is defined by $l = \frac{\omega_n L S_n}{U_n^2}$.

The tuning of the PI-controllers of the voltage and current control can be conducted based on a stepwise approach according to Henninger [80], where the first step is the definition of a freely choosable time constant τ_i according to Yazdani and Iravani [201], which allows the current control to be represented by a first-order filter with the time constant τ_i. The voltage control can then be tuned by using the symmetrical optimum according to Yazdani and Iravani [201]. The resulting parameters $K_{U,P}$ and $K_{U,I}$ of the PI-controllers of the voltage control and the parameters $K_{I,P}$ and $K_{I,I}$ of the PI-controllers of the current control based on this tuning approach result in the following definitions:

$$K_{I,P} = \frac{L}{\tau_i}, \tag{4.114}$$

$$K_{I,I} = \frac{R}{\tau_i}, \tag{4.115}$$

$$K_{U,P} = \frac{C}{\tau_i} \sqrt{\frac{1 - \sin \Phi_R}{1 + \sin \Phi_R}} \tag{4.116}$$

and

$$K_{U,I} = \frac{K_{U,P}}{\tau_i} \frac{1 - \sin \Phi_R}{1 + \sin \Phi_R} \tag{4.117}$$

with Φ_R as the phase margin of the voltage control. A detailed description of the tuning of the PI-controllers of the voltage and current control and a corresponding derivation of the parameters is given in [115]. Assuming the parameters of the LC-filter to be given, the tuning of the voltage- and current control is only dependent on the time constant τ_i and the phase margin Φ_R.

Fig. 4.74 shows the single line diagram of the Microgrid which is investigated in the simulation. This Microgrid is based on a real Microgrid which was also investigated in [197]. In an extended version of this Microgrid also the field tests were performed, which are presented in Chp. 4.4.4. It consists of a BESS based on Li-Ion technology with a rated power of 2.6 MVA, which is connected via line 1 to a 30 kV-substation. Via line 2 and a transformer, an active load and an asynchronous machine are connected to the substation.

Since the Microgrid shown in Fig. 4.74 consists of four battery converters, which are connected in parallel, the converter model shown in Fig. 4.72 has to be adapted in order to consider this parallel connection. In case of a parallel connection of several converters an equivalent converter model can be used by adapting the values of the LC-filter at the output of the model accordingly. Every single converter during a parallel operation behaves identically compared to a single operation. The only difference is the higher apparent power and the changed impedance due to parallel connection. Assuming the LC-filter of a single converter to be L', R' and C', the resulting values of the LC-filter of the equivalent converter model can be calculated by

$$L = \frac{L'}{n} \tag{4.118}$$

$$R = \frac{R'}{n} \tag{4.119}$$

and

$$C = n \cdot C' \tag{4.120}$$

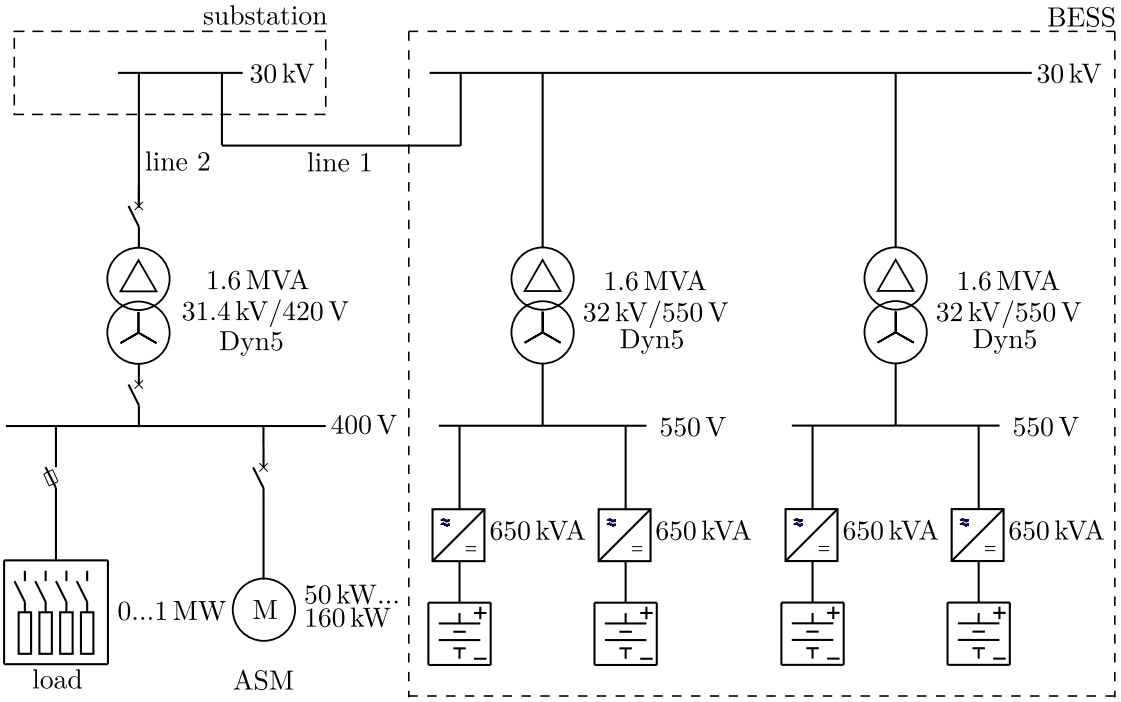

Figure 4.74: Single line diagram of the island grid investigated in the simulation.

with n as the number of parallel connected converters. As the cascaded voltage and current control shown in Fig. 4.73 uses normalized values of the voltage $\mathbf{u}_{N,t}$ and the current $\mathbf{i}_t$ as input, the parameters of the PI-controllers for the equivalent converter model remain identical compared to the single converter model. The higher apparent power of the equivalent converter model

$$S_n = n \cdot S'_n \tag{4.121}$$

only reflects in the normalization of the measured voltage $\mathbf{U}_{N,t}$ and current $\mathbf{I}_t$. Therefore, the control dynamics of the equivalent converter model is identical to the single converter model. Only the normalization and the LC-filter has to be adapted in the equivalent converter model compared to the single converter model.

The relevant parameters of the components of the Microgrid shown in Fig. 4.78 are summarized in Tab. 4.6.

4.4.3.2 Simulation of Load-Steps and Motor Start-Ups

As already mentioned in Chp. 4.4.2, an important property of a Microgrid is its robustness against load changes. Such load changes can be divided into active and reactive load changes. In the simulations as well as in the field tests, the significant active and reactive load changes of a residential grid section are reproduced by a load-bank and motor start-ups. During the island operation of a Microgrid its robustness against such load changes may be crucial to guarantee a stable grid operation with sufficient power quality. According to Bagert et al. [12], a value of 0.8 pu can be assumed as reasonable value for a minimum dynamic voltage drop in a Microgrid. The converter model described in Chp. 4.4.3.1 is therefore used to simulate the voltage drop during load-steps and the start-up of motors in order to identify the minimum dynamic voltage drop that can be expected during the field tests. Based on these simulations, the choice of the size of

Table 4.6: Parameters of the components in Fig. 4.74 used in the simulation.

characteristic	**value**
line 1	
R'_{l1}	$0.26\,\Omega/\mathrm{km}$
L'_{l1}	$0.43\,\mathrm{mH/km}$
length	$50\,\mathrm{m}$
line 2	
R'_{l2}	$0.7\,\Omega/\mathrm{km}$
L'_{l2}	$0.5\,\mathrm{mH/km}$
length	$40\,\mathrm{m}$
transformers (values used for all transformers)	
u_k	$0.06\,\mathrm{pu}$
P_K	$13\,\mathrm{kW}$, i.e. $0.0082\,\mathrm{pu}$
equivalent converter model	
n	4
L	$L = \frac{L'}{n} = \frac{260\,\mu\mathrm{H}}{4} = 65\,\mu\mathrm{H}$
R	$R = \frac{R'}{n} = \frac{1\,\mathrm{m}\Omega}{4} = 0.25\,\mathrm{m}\Omega$
C	$C = n \cdot C' = 4 \cdot 342\,\mu\mathrm{F} = 1368\,\mu\mathrm{F}$
Φ_R	$50°$

the loads and the motors for the field tests is made. As these voltage drops are depending on the control parameters of the converter, their influence is investigated in order to provide corresponding information for the field tests. This also applies to the motors, the successful start-up of which also depends on the control parameters.

The load bank shown in Fig. 4.74 represents an impedance load, which is used to simulate active power load-steps. Fig. 4.75 shows the results of the simulation of an active power load-step of 800 kW through the load bank.

Fig. 4.75(a) shows the active power, Fig. 4.75(b) the reactive power, Fig. 4.75(c) the voltage at the PCC of the BESS and Fig. 4.75(d) the voltage at the connection point of the asynchronous machine. The different curves show the results for different values of the converter control time constant τ_i, which defines the parameters for the PI-controllers of the voltage and current control shown in Fig. 4.73 according to Eq. (4.114)–(4.117). Other than in the main grid, where an active power load-step usually is coupled with a change in the frequency, the frequency in the islanded Microgrid is fixed at a value of $f = \frac{\omega_n}{2\pi}$ in case no frequency droop characteristic is included in the control structure shwon in Fig. 4.72. An active power load-step in the islanded Microgrid, therefore, only leads to a voltage drop, which is to be controlled by the converter control. With an increasing value of τ_i the voltage drop at the converter terminals increases as well. A higher time constant τ_i results in a longer settling process until the stable active power operating point of $800\,\mathrm{kW} \equiv 0.3\,\mathrm{pu}$ is reached. With a time constant of $\tau_i = 0.4\,\mathrm{ms}$ the voltage drop at the converter terminals leads to a value of $u = 0.4\,\mathrm{pu}$. Due to the influence of the transformers and lines in the Microgrid, the voltage drop at the 400 V-bus of the load bank has slower dynamics and leads to a less drastic voltage drop to a value of $u = 0.8\,\mathrm{pu}$.

Fig. 4.76 shows a sensitivity analysis of the minimum voltages, at the PCC of the converter and the 400 V-bus of the load bank, over the settling time, until a stable operating point of the active power is reached. For this consideration, the settling time is defined as the duration between the beginning of a load-step and the moment when the voltage gradient during the voltage restoration process becomes smaller than $0.3\,\mathrm{pu/s}$. The minimum voltages $min(u_C) \approx 0.4\,\mathrm{pu}$ and $min(u_{load}) \approx 0.8\,\mathrm{pu}$ of Fig. 4.75 with a time constant of $\tau_i = 0.4\,\mathrm{ms}$ are marked in Fig. 4.76. Especially for low values of the time constant τ_i the size of the voltage drop and the corresponding duration of the settling process back to a nominal value is very sensitive to changes of τ_i. Regarding power quality, the

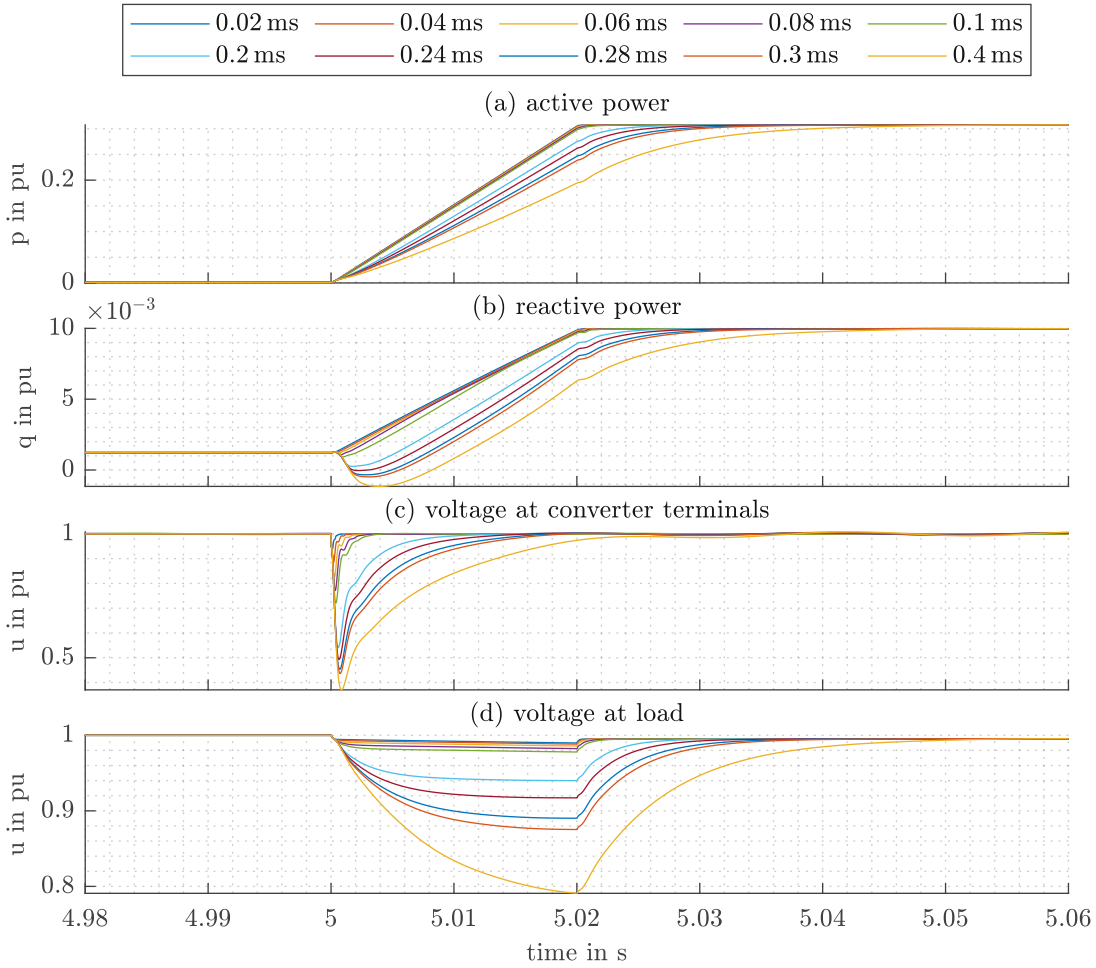

Figure 4.75: Results of the simulation of a load-step of 800 kW for different values of τ_i.

voltage at the load is relevant. The corresponding voltage behavior can be classified as a short voltage dip, which is not likely to affect the operation of connected devices in the Microgrid.

Based on the assumption that a voltage drop to 0.8 pu is considered as the minimum dynamic voltage drop according to Bagert et al. [12], a maximum load-step of 800 kW is selected to be used in the field test, taking into account that the control parameters of the real converter are parametrized faster than a corresponding $\tau_i = 0.4$ ms.

Besides the influence of an active power load-step, also the influence of a reactive power load-step is relevant during island operation. When starting an asynchronous machine, its starting current reaches values five to seven times higher than its nominal current. A motor start-up, therefore, can be used to simulate a massive reactive load-step in the Microgrid. Fig. 4.77 shows the results of the simulation of a start-up of a 160 kW asynchronous machine to investigate such a situation of a massive reactive power load-step.

The parameters of the asynchronous machine are defined by a preset-model available in MATLAB/SIMULINK. Fig. 4.77(a) shows the active power, Fig. 4.77(b) the reactive power, Fig. 4.77(c) the voltage at the PCC of the BESS, Fig. 4.77(d) the voltage at the 400 V-bus of the asynchronous machine and Fig. 4.77(e) shows the speed of the asynchronous machine. The different curves show the results for different values of the converter control time constant τ_i. With increasing value

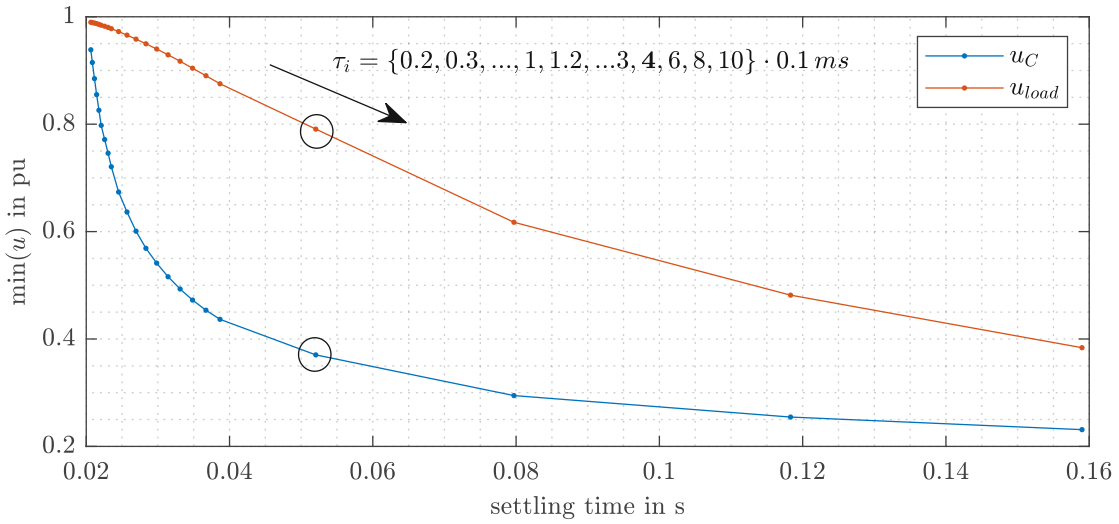

Figure 4.76: Sensitivity analysis of the influence of a 800 kW load-step on the voltage u_C at the PCC of the converter and the voltage u_{load} at the connection point of the load in dependence of the settling time until a stable operating point of the active power is reached. The results of $\tau_i = 0.4$ ms are circled.

of τ_i the voltage at the PCC of the converter starts to oscillate, resulting in oscillations of the active and reactive power. With values higher than $\tau_i = 0.09$ ms the asynchronous machine can no longer be started. The corresponding results for an unstable motor start-up with $\tau_i = 0.1$ ms are also shown in Fig. 4.77. Fig. 4.77(e) shows that the motor is not able to reach nominal speed any more. Therefore, the active and reactive power demands remain at rather high values. This results in an ongoing voltage drop at the 400 V-bus of the motor. A converter controller time constant of $\tau_i = 0.1$ ms poses the stability limit for the start-up of a asynchronous machine with an apparent power of 160 kW in the Microgrid. Only with lower values of $\tau_i < 0.1$ ms a motor start-up is possible. Such stability limits can be determined for different motor sizes. Tab. 4.7 summarizes these stability limits.

Table 4.7: Summary of stability limits for different motor types.

preset model motor type	**largest value of τ_i**
37 kW	0.4 ms
75 kW	0.2 ms
110 kW	0.1 ms
160 kW	0.09 ms

Tab. 4.7 lists the largest time constant τ_i with which a start-up of the corresponding motor is still possible. The different motor types represent the available preset-models in MATLAB/SIMULINK. Only a motor size of 200 kW was available for the field tests. But based on the results of Tab. 4.7, with a parameterization of control parameters on the real converter which are faster than a corresponding $\tau_i = 0.09$ ms, it can be assumed that a successful start-up during the field tests is possible.

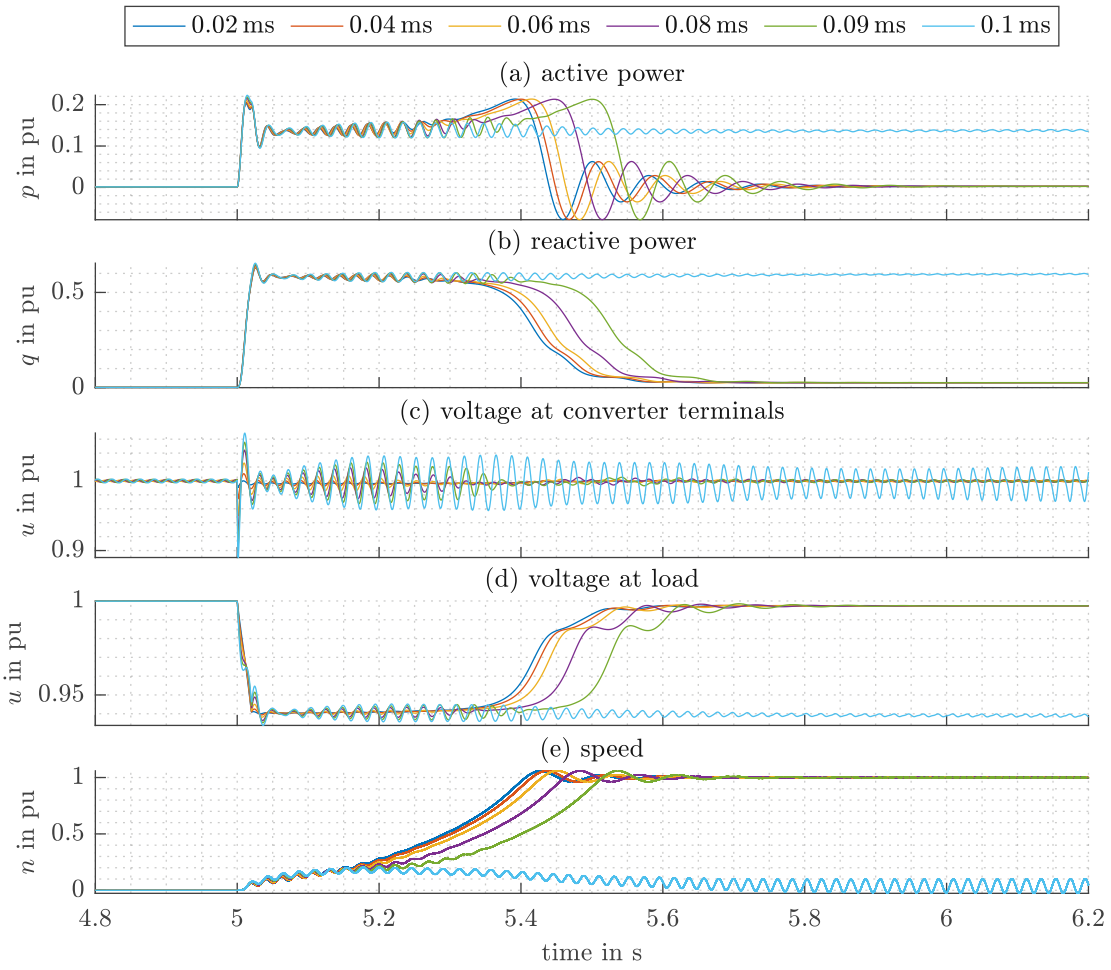

Figure 4.77: Results of the simulation of a motor start-up of a 160 kW asynchronous machine for different values of τ_i.

4.4.4 Field Measurements

During the field tests, a small residential grid section was disconnected from the main grid in order to build an islanded Microgrid. More details about the field test setup can also be found in [197, 116]. The corresponding single line diagram of this Microgrid is shown in Fig. 4.78 and consists of the BESS, which has already been described in Chp. 4.4.3.1, a local grid, which acts as "artificial" representation of a low voltage grid, and a wind park feeder.

The local grid consists of a freely adjustable active power load bank and an asynchronous machine, which acts as reactive power sink. This local grid is capable of imitating massive load changes of a low voltage grid. The wind park consists of several feeders, each of them serially connecting several wind turbines. Each of these wind turbines has an apparent power of 3 MVA, which is fully deployed at a wind speed of 13 m/s.

One of these feeders, which serially connects two wind turbines, is connected to the islanded Microgrid, the other feeders were disconnected during the field test. The single line diagram shown in Fig. 4.74, which was used for simulation, is identical to the single line diagram shown in

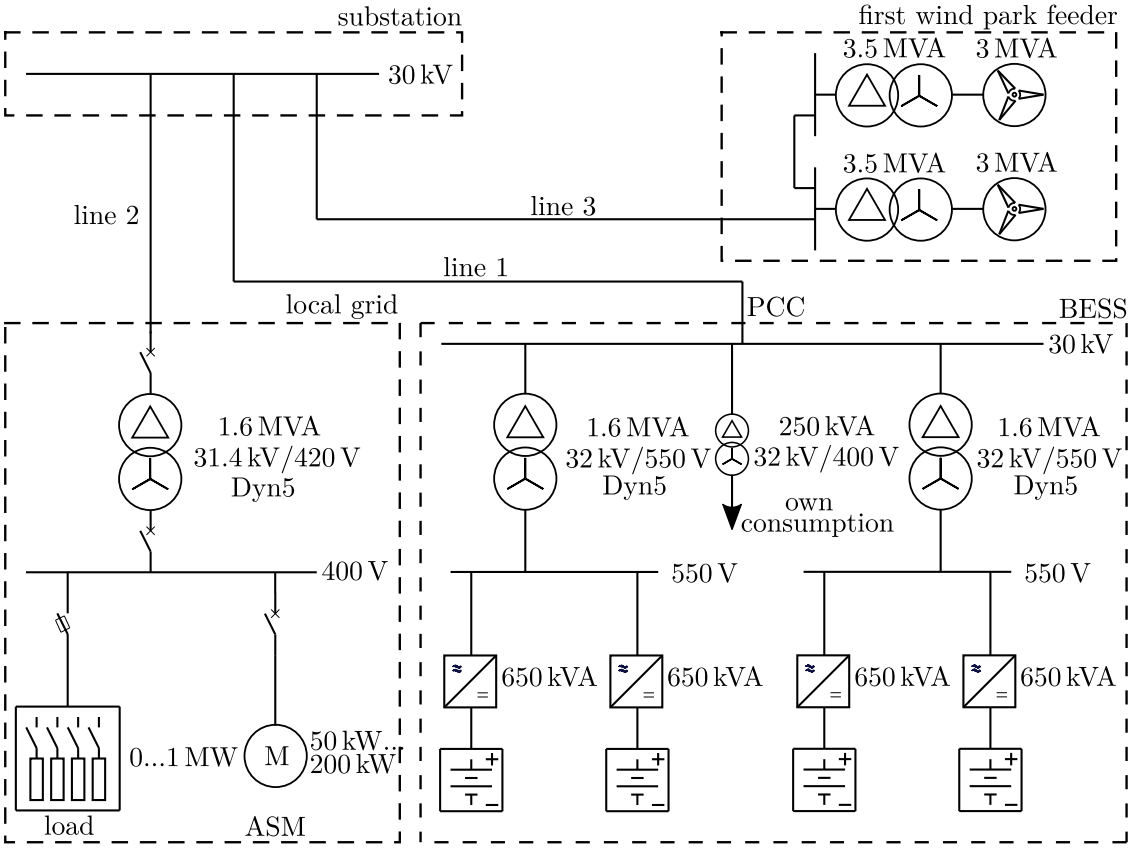

Figure 4.78: Single line diagram of the island grid investigated in the field tests.

Fig. 4.78 but does not include the wind park as it was not considered in the simulation model in Chp. 4.4.3.1. The goals of the field test include the investigation of

- the black-start of the Microgrid,
- the synchronization of the wind park to the Microgrid,
- the island operation with an active power infeed of the wind park, where an implementation of the frequency control characteristic described in Chp. 4.4.2 based on a master-slave control approach is active and
- the investigation of active and reactive load changes of the local grid.

The findings of the corresponding field tests are described in the following sections.

4.4.4.1 Black-Start of the Microgrid

As already mentioned, the cold load pickup during black-start of a Microgrid is a challenging issue. The corresponding high current demand of the cold load pickup may be misinterpreted as fault condition by the protective relays and therefore carries the risk of preventing a successful black-start as the protective relays may trip. An example for the behavior of the cold load pickup is shown in Fig. 4.79, which presents the current demand during connection of the auxiliary transformer of the Microgrid shown in Fig. 4.78.

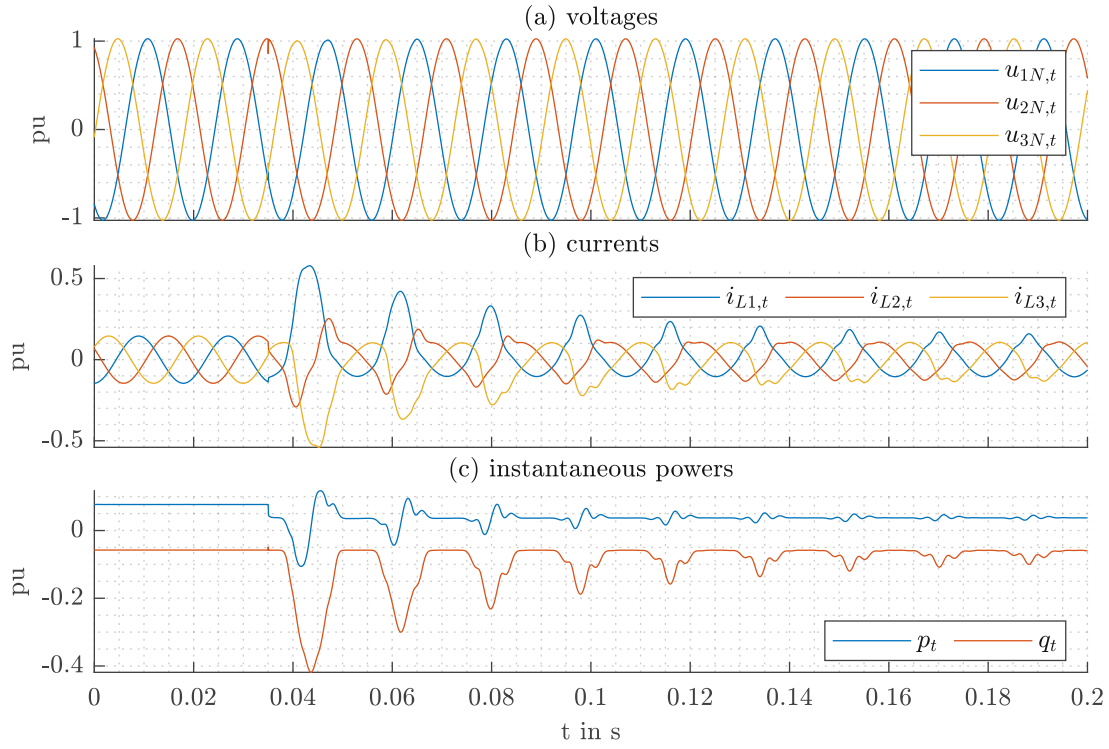

Figure 4.79: Measurement of the inrush current of the own auxiliary transformer of the Microgrid shown in Fig. 4.78.

Due to the nonlinear relationship of the flux and the magnetizing current of the transformer, the connection of the transformer leads to high current peaks during the first several cycles. Their magnitude is initially 6-10 times higher than the rated load current. The auxiliary transformer with a nominal power of 250 kVA has a rated load current of 4.6 A, which corresponds to a current demand of 0.1 pu for the BESS. The maximum expected inrush current corresponds to a current demand of 1 pu for the BESS. The magnitude of the inrush current shown in Fig. 4.79(b) is about 0.35 pu and therefore only 3.5 times higher than the rated current. The magnitude depends on the exact time of connection and the corresponding angle of the phase voltage. The maximum inrush current results from a time of connection when the magnitude of the phase voltage is in its minimum. Fig. 4.79(a) shows that the phase voltages $u_{2N,t}$ and $u_{3N,t}$ have a magnitude of about 50 % and therefore the resulting inrush current is lower than the maximum expected one.

Building on the findings of Fig. 4.79, it can be stated that a black-start of the Microgrid shown in Fig. 4.78, with connected transformers of the wind park and the local grid, would lead to a current demand much higher than the current capabilities of the BESS. But it is possible to gradually increase the output voltage of the BESS while all transformers are connected to the Microgrid. By doing so, inrush currents, which result from switching actions that connect feeders with corresponding transformers, can be prevented. A measurement of such a gradual increase of the supplying voltage is shown in Fig. 4.80.

Fig. 4.80 shows a gradual increase of the output voltage of the BESS within 10 s. Fig. 4.80(b) shows that the current demand during this black-start of the Microgrid is only about 5 % of the current capability of the BESS. About 15 s after the black-start a stable supply voltage of 1 pu is reached and all feeders of the Microgrid are supplied.

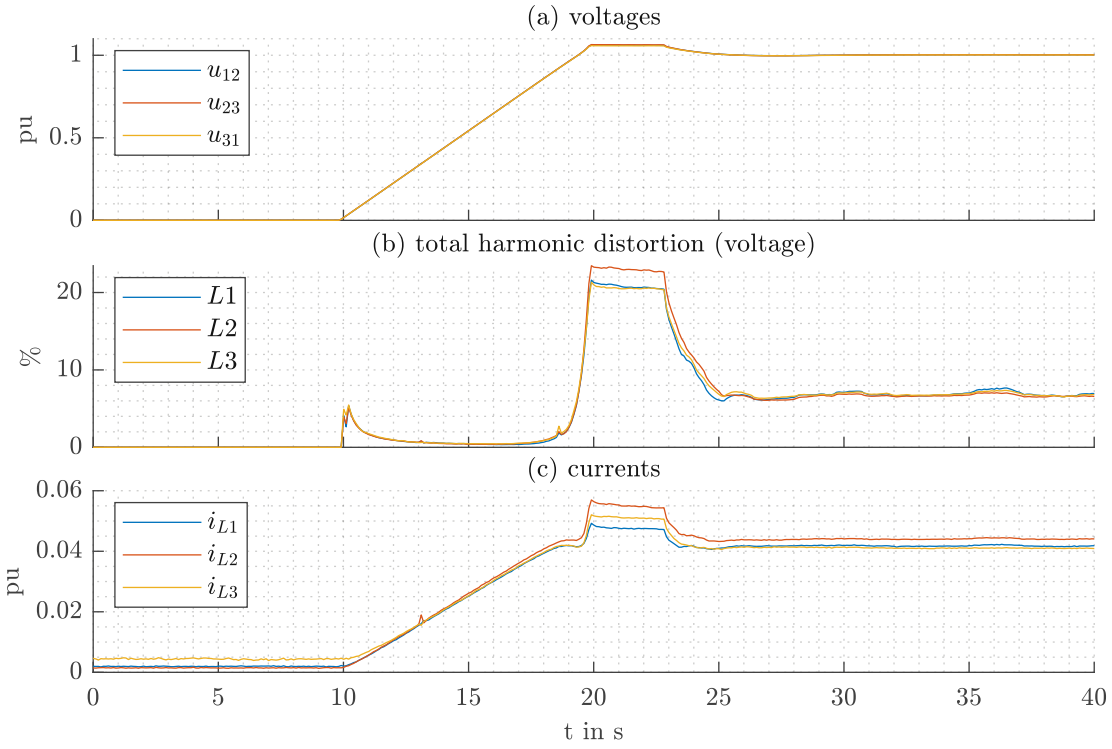

Figure 4.80: Measurement of voltages and current during a gradual increase of the voltage of the BESS in the Microgrid shown in Fig. 4.78 while all transformers are connected. The small peak in i_{L2} can be considered as measurement error. Between 20 s-25 s the voltage exceeds a value of 1 pu due to a high level of harmonics, indicated by the total harmonic distortion in (b), which leads to higher RMS values of the voltages.

4.4.4.2 Synchronization of the Wind Park to the Microgrid

After a black-start of the island grid the wind turbines are able to synchronize with the supply voltage in the Microgrid. A wind turbine follows a start-up routine when it is activated from a state where it is switched off. The first step in this routine is the supply of its auxiliary systems, which, for example, includes the motors of the pitch control of the rotor blades (pitch drive) and the motor which aligns the wind turbine in the wind direction (azimuth drive). In the second step, the mechanical brake of the rotor of the wind turbine is released. In this "idle mode" the rotor rotates dependent on the wind speed, but no power infeed takes place. The measurement of a constant wind speed or a corresponding angular frequency of the rotor over a time period of several minutes, which lies above a minimum threshold, heralds the third step of the start-up routine. In the third step, the actual synchronization takes place, where the converter of the wind turbine synchronizes with the supply voltage in the Microgrid and starts to feed in active power, dependent on the actual wind speed and the corresponding angular frequency of the rotor.

4.4.4.3 Island Operation with an Active Frequency Control Characteristic

The frequency control characteristic shown in Fig. 4.71 has been described as a simple possibility to integrate DER in the Microgrid based on a master-slave control approach. Such a frequency control characteristic was implemented in the BESS of the Microgrid by simply altering the value $\omega = 2\pi f(p, SoC)$ of the grid synchronization shown in Fig. 4.72 according to the curve in Fig.

4.71, which leads to a grid angle $\theta = 2\pi \int f(p, SoC)\, dt$. The behavior of such a control approach was measured during island operation after successfully synchronizing the wind park. The wind turbines in Microgrid support LFSMO with corresponding options for its parameterization. This parameterization was carried out according to the frequency curve shown in Fig. 4.71 via several parameterizable fulcrums. The reaction of an activated LFSMO on the wind turbines works as a percentual power reduction in relation to the reference operating point of the wind turbine. For example, assuming a wind speed of 10 m/s leads to a reference operating point of the wind turbine of 50 % of its nominal power. This reference operating point is executed directly as actual power output at 50 Hz and this reference operating point is executed as reduced power output point according to the frequency characteristic shown in Fig. 4.71 at higher frequencies.

A measurement result of an islanded Microgrid operation, during which the frequency control approach mentioned above is active and the wind turbines are synchronized and feeding in power, is shown in Fig. 4.81.

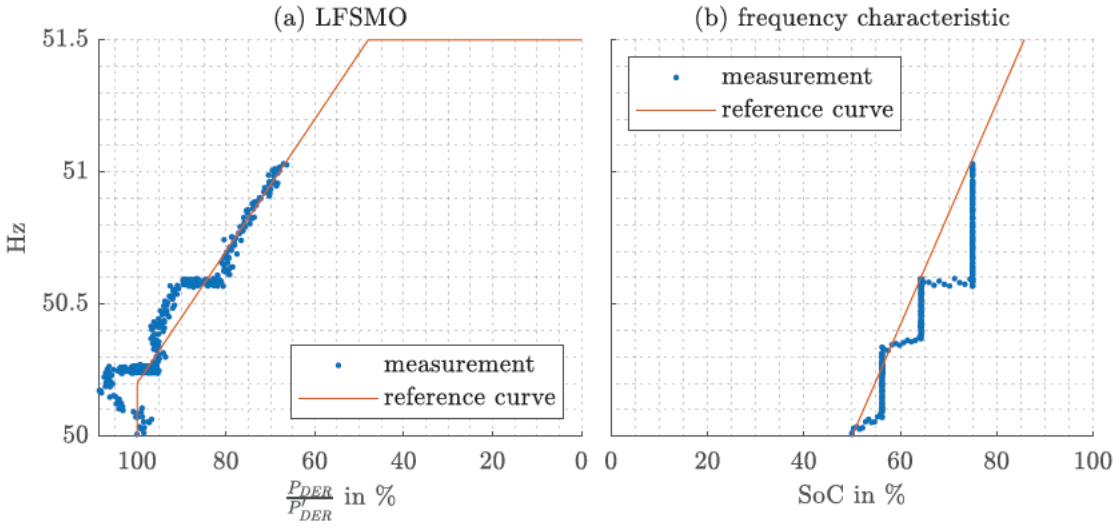

Figure 4.81: Measurement of the frequency control characteristic according to Fig. 4.71.

The field test started with a SoC of the BESS of 50 % and an active power infeed of the wind park. Fig. 4.81(b) shows the stepwise increase of the SoC of the BESS, which has been achieved by a manual narrowing of the usable SoC-window of the BESS. This manual change of the SoC was applied in order to shorten the time period of the field test. Due to the stepwise change of the SoC, the frequency needs some time to reach the corresponding reference value of the frequency control characteristic. The vertical lines represent these time periods. During these gradual changes of the frequency, the wind turbines reduce their currently possible power output P'_{DER} to a reduced power output P_{DER} according to the corresponding reference curve, which is shown in Fig. 4.81(a). During the time period of this gradual change of the frequency, the wind speed can be considered constant. In contrast, the time between manual changes of the usable SoC-window is quite long. Therefore, during these manual changes of the usable SoC-window the wind speed and the corresponding power infeed of the wind park changes. The horizontal lines of the power infeed in Fig. 4.81(a) are related to these changes of the wind speed and the corresponding operating point P'_{DER} of the wind park. Nevertheless, Fig. 4.81 proves a successfull application of the frequency control approach according to Fig. 4.71.

4.4.4.4 Load Changes during Island Operation

The local grid of the Microgrid shown in Fig. 4.78 is used to imitate significant load increases of a residential low voltage grid. The active power load bank consists of several resistors, which are connected to each other depending on which active power consumption is to be achieved. Fig. 4.82 shows the measurement results of two load-steps of 200 kW and 800 kW and their influence on the voltage at the PCC of the BESS. During these load changes, the wind turbines were deactivated. Since the frequency characteristic in Fig. 4.71 only influences the frequency when $p > 0 \wedge p > p_0$ or when $SoC > 0 \wedge SoC > SoC_0$ and a load-step leads to $p < 0$, the frequency during the load changes can therefore be considered to be constant $f = 50\,\text{Hz}$ when assuming a SoC of about $SoC = 50\,\%$.

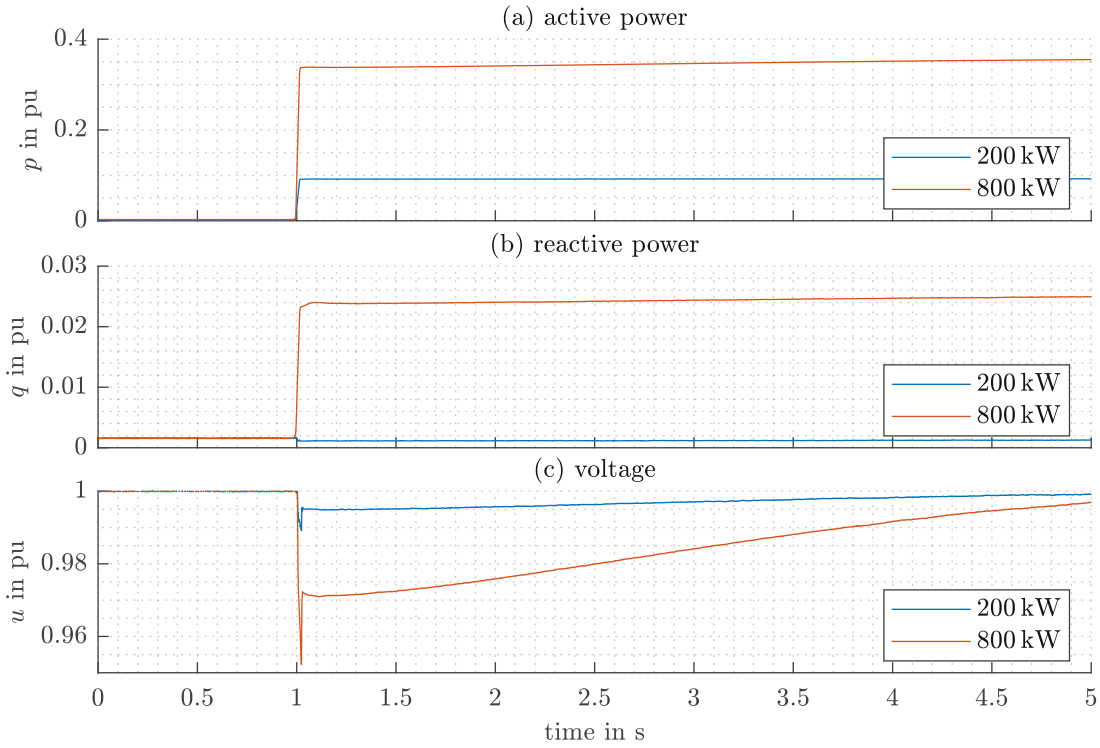

Figure 4.82: Measurements during an active power load-step of 200 kW and 800 kW. The voltage u is the mean value of all normalized line-to-line voltages.

The load-steps are coupled with a highly dynamic voltage drop, similar to the simulation results shown in Fig. 4.75. However, the stabilization of the voltage to the nominal value takes about 4 s for both load-steps, which is much longer than observed in the simulations. Compared to the model used in the simulations, the control algorithms in the real converter are more complex and additional output filters are installed, which both explain the differences between field test and simulation. The voltage in Fig. 4.75 does not fall below the value of of 0.8 pu, which is considered as the minimum dynamic voltage drop according to Bagert et al. [12].

The asynchronous machine of the local grid shown in Fig. 4.78 is used to imitate massive reactive load changes of a typical low voltage grid. Fig. 4.83 shows the measurement results of the start-up of two asynchronous machines with a nominal power of 50 kW and 200 kW and their influence on the voltage at the PCC of the BESS. The measurement results show a similar behavior compared to the simulation results shown in Fig. 4.77.

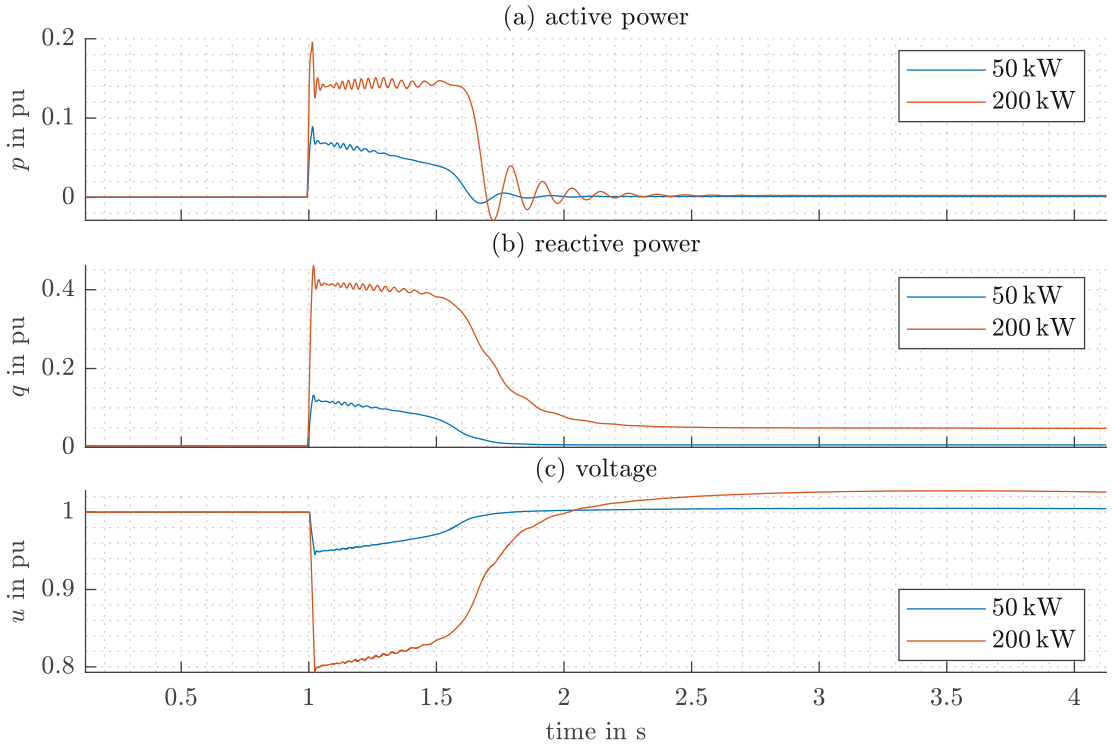

Figure 4.83: Measurements during the motor start-up with a nominal power of 50 kW and 200 kW.

As already described for the active power load changes, the differences between the measurement- and simulations results can be explained by the much more complex control structure of the real converter.

4.4.4.5 Power Quality

Besides the voltage drops during load changes, which affect the power quality in a Microgrid, the occurrence of harmonics is another issue that affects the power quality. As shown in Fig. 4.80, a high value of the Total Harmonic Distortion (THD) may occur during the black-start of a Microgrid, which reaches a value of up to 20 % in Fig. 4.80(b). Tab. 4.8 summarizes the THD for different operating points and situations during the field tests.

Table 4.8: Measured THD for different operating points and situations during the field tests.

operating point	**value of THD**	**situation**	**value of THD**
$p = 0.08\,\text{pu}$	2.5 %	running 50 kW-motor	0.6 %
$p = 0.16\,\text{pu}$	2 %	running 200 kW-motor	0.4 %
$p = 0.24\,\text{pu}$	1.5 %	synchronization of wind turbines	15 %
$p = 0.32\,\text{pu}$	1 %	$p = -0.2\,\text{pu}$ (moderate power infeed of wind turbines)	5 %

The measurement results in Tab. 4.8 show a decreasing trend of the THD for an increasing value of the active power operating point p of the BESS. This can be explained by the fact that the associated converter of the BESS has been optimized for operation at $p = 0.8\,\text{pu}$. Besides the

rather high THD of 20 % during the black-start of the Microgrid, as shown in Fig. 4.80, during the synchronization of wind turbines a simular high THD of 15 % occurs. During the power infeed of wind turbines the THD reaches a moderate level of 5 %.

4.4.4.6 Discussion

In summary, the field tests prove that the BESS shown in Fig. 4.78 is capable of performing a black-start of the Microgrid by using a gradual increase of the supply voltage during start-up. During island operation, the application of a frequency control characteristic based on a master-slave control approach allows the integration of DER with nominal powers higher than the BESS into the Microgrid, while also carrying out an appropriate energy management by guaranteeing the SoC of the BESS within allowable limits. The BESS is capable of controlling active and reactive load changes, which are considered to be representative for significant load changes in a residential grid section, with an acceptable level of power quality, indicated by voltage drops not to fall below a value of 0.8 pu and by the THD, which only reaches high values during the black-start of the Microgrid and the synchronization of wind turbines.

4.5 Arbitrage

In the following chapters, the basic considerations for carrying out arbitrage transactions with BESS are discussed and an exemplary simulation result of an implementation of such a service is presented.

4.5.1 Basic Considerations

In economics and finance, “arbitrage” is the practice of taking advantage of a price difference between markets. The temporal arbitrage generates profit opportunities in a single market by purchasing and selling a good with price difference at different times. Any kind of storage is predestined to use temporal arbitrage to increase profitability. For the sake of simplicity, “arbitrage” and “temporary arbitrage” are used synonymously in the following. On a large scale, PHSS are used to achieve high profits with arbitrage. The energy reservoir of BESS is very low compared to PHSS. Together with the high investment costs for BESS, the sole execution of arbitrage transactions is not an option to achieve profitability. To reach profitability, a combined execution of several functions or ancillary services is necessary, with arbitrage as one of them.

On the energy market there are usually several peaks of the energy prices during the day. To analyze the occurrence of these peaks, Fig. 4.84 shows heatmaps of the price on the intraday market of the years 2015 – 2018 during the day. It can be seen, that price peaks occur between 06:00 – 08:00 o’clock and 18:00 – 20:00 o’clock. These peaks express themselves in a kind of “heart shape” during the seasons.

4.5.2 Implementation of Arbitrage in Combination with FCR

For a BESS executing several functions and ancillary services, only a small part of the energy reservoir can be used for arbitrage. Assuming a BESS providing FCR, the “30 min-criterion” decreases the available energy reservoir usable for arbitrage. But dependent on the factor $\frac{E}{X_{PRL}}$ there are still energy reserves for arbitrage. Considering Fig. 4.84, two arbitrage transactions are possible on the intraday market. An implementation of a function to do arbitrage transactions can be realized by a variation of the target-SoC SoC_T between an upper and a lower SoC-level which are within an appropriate range of the working area. By doing so, the SoC-management doesn’t

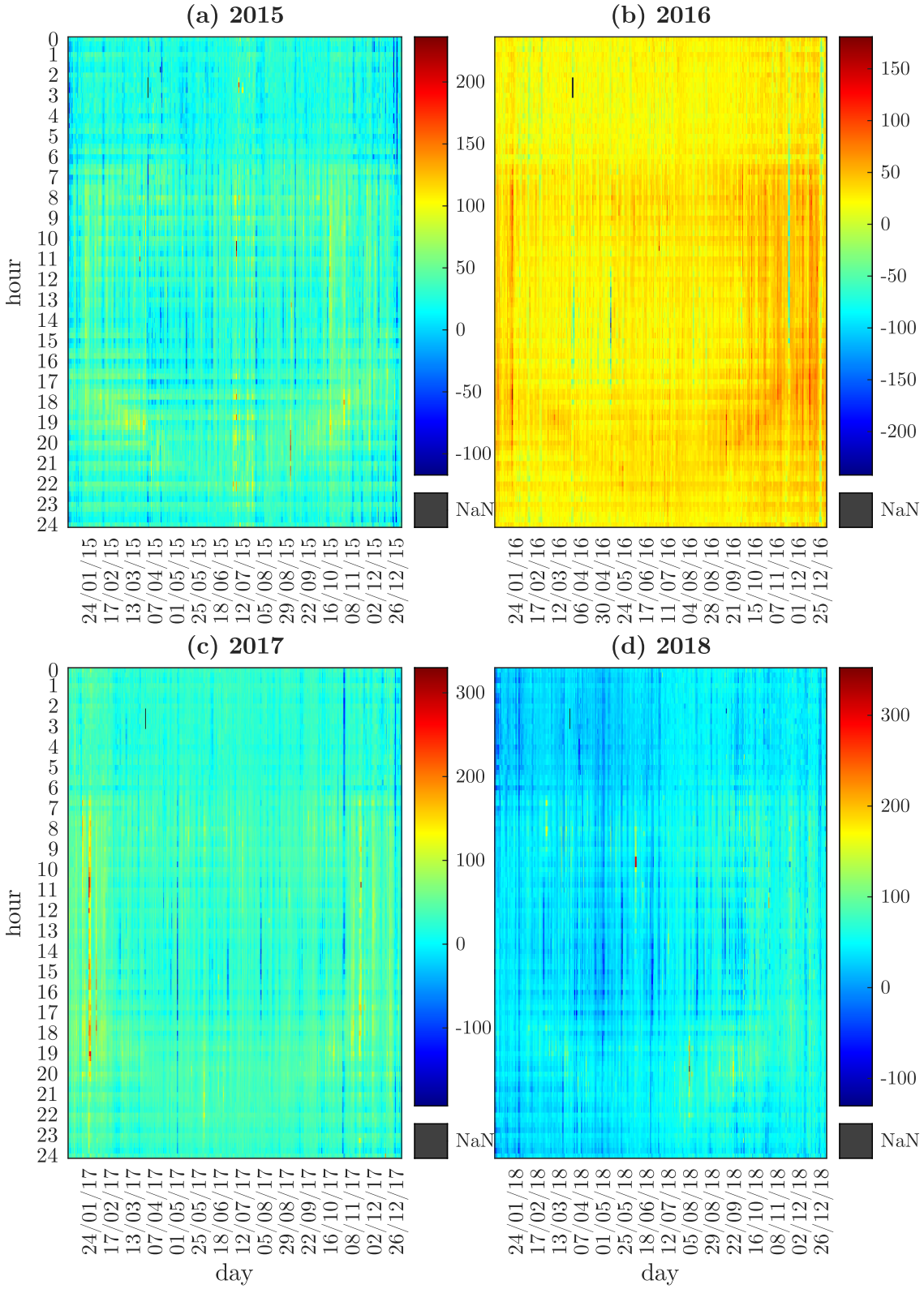

Figure 4.84: Intraday prices in Euro/MWh based on data of [55]. The data was generated with "R" based on an adapted version of `emarketcrawlR` [187].

work counterproductive to the arbitrage action. The activation of an arbitrage action is triggered by a change of the target-SoC SoC_T and described via $a_{ARB,1}$:

$$a_{ARB,1} = \begin{cases} 1, & SoC_T(t - \Delta t) \neq SoC_T(t), \\ 0, & else. \end{cases} \tag{4.122}$$

A rational range for the target-SoC can be found with consideration of an energy buffer in the working area. With consideration of such an energy buffer analogous as decribed in Chp. 4.1.3.2 for the SoC-management across balance groups, a range for the target-SoC of

$$SoC_T = \left(\frac{X_{FCR} \cdot (T_{crit} + \frac{1}{4} 0.5\,\mathrm{h})}{E}, 1 - \frac{X_{FCR} \cdot (T_{crit} + \frac{1}{4} 0.5\,\mathrm{h})}{E} \right). \tag{4.123}$$

can be defined. This range assumes a realization of the arbitrage actions inside a balance group. It does not consider market rules as defined in Chp. 4.1.3.2 for SoC-management across balance groups. The actual transgression of the target-SoC is dependent on the energy price. Considering one peak of the energy price in the forenoon and one in the afternoon, as described above and shown in Fig. 4.84, the target-SoC is switched between its lowest value and its highest value four times a day. A lowest and a highest value of the energy price are assumed for each the forenoon and the afternoon. The target-SoC is switched from its lowest value to its highest value if the energy price is lowest and from its highest value to its lowest value if the energy price is highest.

An implementation of a function to realize arbitrage is defined analogous to the SoC-management within balance groups as defined in Chp. 4.1.3.1. After $a_{ARB,1}$ has become active with $a_{ARB,1} = 1$, the arbitrage function is started with a power of P_{ARB} until SoC_T is reached:

$$a_{ARB,2}(t) = \begin{cases} 1, & [a_{ARB,2}(t - \Delta t) = 1 \wedge SoC \neq SoC_T] \vee a_{ARB,1} = 1, \\ 0, & else. \end{cases} \tag{4.124}$$

The power P_{ARB} is defined by

$$P_{ARB} = a_{ARB,2} \cdot X_{ARB} \cdot \begin{cases} 1, & SoC < SoC_T, \\ -1, & SoC > SoC_T, \\ 0, & else \end{cases} \tag{4.125}$$

with X_{ARB} as a parameter of the function.

Since the target-SoC switches between values according to Eq. (4.123), issues arise when this switch-over takes place while the function is active, which is indicated by $a_{ARB,2} = 1$. Assuming the target-SoC to be constant while the function is active, it is stopped when the target-SoC is reached. However, during a situation as mentioned above, when the switch-over happens at a moment when the actual SoC is higher than the new target-SoC while charging or when the actual SoC is lower than the new target-SoC while discharging, the target-SoC may never be reached. Therefore, an implementation of such a function of arbitrage has to take into account this issue by storing the actual target-SoC at the beginning of a charging or discharging operation.

4.5.3 Simulation

The arbitrage function as described in Chp. 4.5.2 was modelled in MATLAB/SIMULINK. This model will be used in Chp. 5.8 to investigate the value stacking of various services. This chapter has the goal to illustrate the behavior of arbitrage in the model. However, this chapter will not present detailed simulation results, since such investigations will be carried out and described in Chp. 5.8.

To show the functionality of the arbitrage function, Fig. 4.85 shows simulation results of a BESS providing FCR, executing SoC-management and arbitrage based on historical frequency data for FCR and energy prices of the intraday market of 02.07.2019 – 03.07.2019. An optimal knowledge of the prices is assumed to execute the maximum arbitrage transactions. Considering this knowledge of the prices, the time series of the target-SoC turns out as shown in Fig. 4.85. Fig. 4.85(a) shows the target-SoC, which is varied according to the minimum and maximum price signals during the day shown in Fig. 4.85(c). Fig. 4.85(a) also shows the actual SoC, which is influenced by the power outputs P_{FCR}, P_{SOC} and P_{ARB}. The last two powers are shown in Fig. 4.85(b), the influence of P_{FCR} is only visible in the actual SoC in Fig. 4.85(a) and is dependent on the actual frequency. The SoC in Fig. 4.85(a) shows that the energy that is temporally shifted by arbitrage is influenced by the FCR-output P_{FCR}. During operation with a frequency at its normal state (according to Chp. 4.1.1.2), as it is the case in Fig. 4.85, the influence of P_{FCR} is marginal and the energy of approximately $[max(SoC_T) - min(SoC_T)] \cdot E$ is used for the four arbitrage transactions shown in Fig. 4.85.

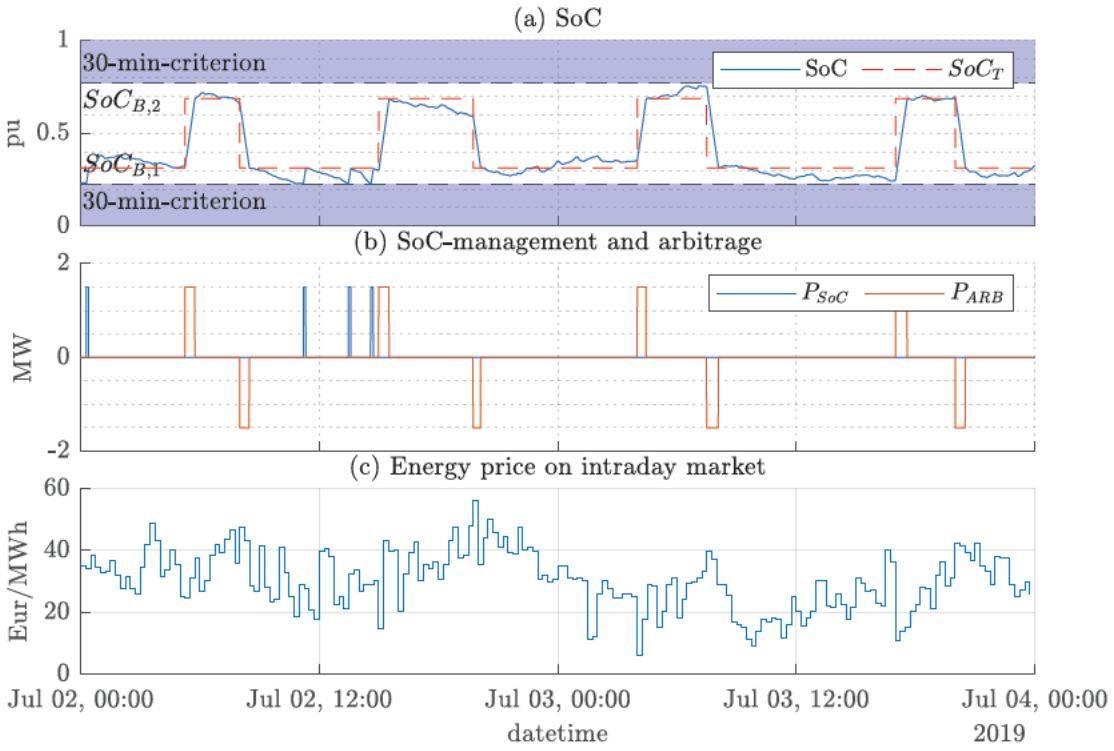

Figure 4.85: Simulation results on the basis of input data of historical frequency data of 02.07.2019 – 03.07.2019 with a BESS providing FCR, executing SoC-management and arbitrage; Time series of (a) SoC, (b) power output of SoC-management and arbitrage function and (c) the energy price on intraday market. The parameters of the simulation are $E = 2.2\,\text{MWh}$, $X_{FCR} = 1\,\text{MW}$, $X_{SoC} = 1.5\,\text{MW}$, $X_{ARB} = 1.5\,\text{MW}$.

By comparing the periods in Fig. 4.85(b) when arbitrage actions occur with the corresponding prices during these periods in Fig. 4.85(c), it becomes visible that per each arbitrage transaction per half day revenues are generated. The sum of revenues by all arbitrage transactions is diminished by the costs that arise for the SoC-management in order to hold the SoC within the working area.

5 Multi-Use Operation of BESS

This chapter deals with the third research question listed in Chp. 1.5. Besides an overview of existing work in literature, the general compatibilities of services are discussed and concepts to realize a multi-use operation are described. A mathematical framework is presented that allows the detailed description of services and their corresponding interaction during multi-use operation. Within this mathematical framework, a concept is presented coping with limitations such as energy and current capabilities of the BESS. Based on this concept, long-time simulations in MATLAB/SIMULINK are performed and discussed in order to investigate the influence of a combined provision of services on certain indicators such as profitability and aging.

This chapter is structured as follows. Chp. 5.1 summarizes basic considerations on multi-use operation of BESS. Chp. 5.2 discusses the general compatibility of services based on a literature research. Chp. 5.3 presents possible concepts to realize a real-time multi-use operation of BESS. Chp. 5.3 discusses how to implement these concepts in a battery converter. Chp. 5.5 presents a mathematical framework to describe a multi-use operation of a BESS applying the concept of dynamic prioritization of functions, including the description of a corresponding current limitation in Chp. 5.5.1. Chp. 5.5.2 summarizes the mathematical framework and the concept of dynamic prioritization in a block diagram. Chp. 5.5.3 describes typical services provided by BESS via functions inside the mathematical framework. Chp. 5.6 presents several applications to demonstrate the behavior of the concept of dynamic prioritization and possible advantages over other concepts for a real-time multi-use operation. Chp. 5.7 discusses the results of a long-time simulation of one selected application. Finally, Chp. 5.8 investigates all possible combinations of four services based on long-time simulation and compares the influence on certain indicators such as profitability and aging.

This chapter incorporates investigations and analyses published in paper [120].

5.1 Basic Considerations on Multi-Use Operation

One challenge of a multi-use operation has already been identified as the question of compatibility of services. Constraints coupled with this question can be location-related, time-related or related to the prioritization among services. Some services are only accessible at certain locations. For example, self-consumption optimization requires a location behind-the-meter, either on residential or community scale. Time-related constraints refer to the feasibility of providing concurrent services. For example, that a service that requires discharging does not conflict with a service that requires charging, or that providing one service now does not preclude another constraint service in the future (e.g. an acceptable range of SoC for future applications). Constraints regarding prioritization of services refer to the circumstance that certain services may have priority over other services. For example, the service of congestion management may provide power reserves during periods of peak infeed at a congestion point in order to store surplus power to prevent congestion or curtailment. Such a service demands power reserves regardless of wholesale market prices. Assuming congestion management to be valuable for system stability, it may have priority over services that are aiming on gaining revenues on the energy market, such as energy arbitrage or self-consumption optimization. During periods when a conflict of interest arises for such services, priorities are an option to handle their behavior.

Location-related constraints can be identified during an early stage of the realization of a BESS project. It is therefore assumed that services that can be provided at the point of integration of the BESS are easy to identify. Time-related constraints, on the other hand, are depending on the type of multi-use operation. Englberger et al. [45] identify three types, such as sequential, parallel and dynamic. With the naming "vertical", "horizontal" and "mixed vertical/horizontal" sharing of ressources the three types are also introduced by Lombardi et al. [110]. These three types are illustrated in Fig. 5.1.

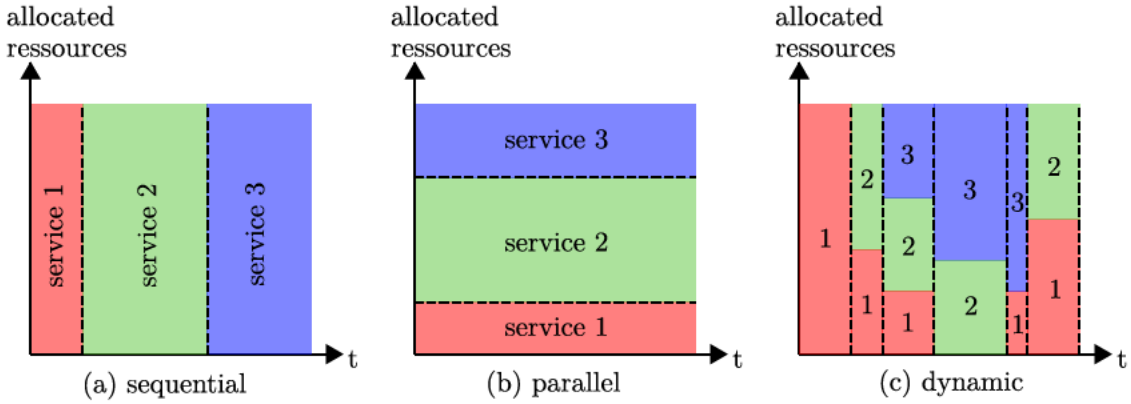

Figure 5.1: Types of multi-use operation according to [45] based on the example of three services.

A sequential multi-use operation is defined as an operation in which one service uses all resources of the BESS for a given time, after which another service takes over, etc. A parallel multi-use operation is defined as an operation in which the resources of the BESS are divided in a predefined proportion between different services that are active at the same time. Shares of each resource can be viewed as "virtual" BESS, which provides a corresponding service and when put together form the real BESS. A dynamic multi-use operation is similar to the parallel operation, but dynamically allocates the share of resources for different time slots. The constraints are growing with the type of multi-use operation, which are few with a sequential multi-use operation and increase when using a parallel or even a dynamic multi-use operation. These constraints result from the limited power- and energy resources of a BESS. Assuming a dynamic multi-use operation, a certain number of virtual BESS can be assigned to each time slot, each assigned to a certain service.

Building on that, two phases can be identified for a dynamic multi-use operation: operational planning and real-time operation. Operational planning tries to identify the number of services and their size of virtual BESS for each time slot of, for example, the following day, which in total lead to a goal of maximum revenues or other global optimization goals of the multi-use operation. In general, the operational planning is an optimization problem that relies on the prediction of the behavior of services. This optimization problem has to take into account the requirements of each service. An example for such a requirement regarding emergency supply is to ensure a certain energy reserve at the beginning and throughout a time slot when this service is provided. A similar example can be given for the service of peak shaving, where also a certain energy reserve has to be ensured at the beginning of the time slot where it is provided, but not for providing energy, as it is the case for emergency supply, but for consuming energy. A third example can be given for the service of arbitrage, where a certain amount of energy is stored in one time slot and released in another time slot. All these examples illustrate the interdependency between the time slots and some constraints of the optimization problem. But there are services whose behavior is very difficult to predict during operational planning. Such services include services for frequency control or voltage control, as well as services for congestion management. Only during rare events do these services require a high proportion of the resources of the BESS, but most of the time their demand of resources is rather low. Since these services are relevant for the system stability in the grid, it is

crucial that during these rare events, the BESS is capable of providing these services as specified. With regards to operational planning this would mean a consideration of corresponding virtual BESS for each service, which takes into account the worst case power and energy requirements that can be expected for their full activation in rare events. However, this approach leads to rather strict constraints during operational planning and diminishes flexibilities for other services.

5.2 Compatibility of Services

Based on the descriptions in Chp. 5.1 it is very difficult to evaluate a general compatibility of services for their simultaneous provision, since this compatibility depends on many project-specific influence factors such as dimensioning of the BESS, location of the BESS, etc. Furthermore, services may or may not be compatible depending on the type of multi-use operation. A sequential multi-use operation according to Fig. 5.1 may be possible for most combinations of services, as long as their location-related requirements are compatible. A dynamic multi-use operation, on the other hand, may have time-related constraints that may prevent the simultaneous provision of services, at least during specific system states. As already mentioned in Chp. 5.1, the report [63] presents a matrix that evaluates the compatibility of couples of services. However, this assessment is done on an abstract level and embraces many exclusions and special conditions. The difficult question, therefore, is not which services are generally compatible with each other, but how dynamic resource allocation can be implemented to ensure that each service meets its goals. As described in Chp. 5.1 this dynamic resource allocation can be planned in the scope of the operational planning phase. However, several characteristics can be identified in order to evaluate the general compatibility of services. These characteristics are listed and described below.

- Compatibility regarding location. Is the BESS integrated at a location where the provision of all services is possible and effective?
  - For example, the provision of services for frequency control may require an integration of the BESS in a grid section with rather high short-circuit power, since the minimum bid size for such services lies above several MW. The provision of static voltage support, however, may only be useful at locations with relatively low short-circuit power. A combination of both services, therefore, may be possible, but not effective. A more useful approach for such a combination may be in the form of a pool, where many small distributed units work as one virtual unit that ensures the minimum bid size for frequency control services at any time, instead of one centralized unit. Since the smaller units can also be integrated in grid sections with relatively low short-circuit power, such an approach may lead to a more effective combination of these two services.
  - Some services may require a very specific location in order to be provided at all. Providing black-start capability, for instance, requires an integration in essential grid sections within which larger generating units are located, and which may act as a starting point of a grid restoration. Other examples include the provision of behind-the-meter services such as self-consumption optimization, where - as the name says - a location behind the meter of the corresponding consumer is necessary.

- Compatibility regarding regulatory aspects. When combining behind-the-meter services and front-of-the-meter services, a distinct treatment of the services may be necessary in order to comply with regulatory requirements, as described in [46]. Since behind-the-meter services serve end-consumer purposes, whereas front-of-the-meter services predominantly improve grid stability and therefore fulfill central goals, unbundling laws may require the separation of value generation. According to Englberger et al. [46] this can be addressed by separating the physical BESS into distinct virtual partitions.

- Compatibility regarding operational functionality. The functionality of services may be harmed when combining with certain other services. For example, the provision of FCR requires a frequency-dependent power output. Other services that act on the same timescale as FCR may affect this frequency-dependent power output.

- Compatibility regarding absolute priority. BESS may be designed to provide certain must-run capabilities such as for congestion management. Congestion may occur only during rare events, which means that the BESS is inactive most of the time. However, exactly during these rare events the service may require the BESS to make its full resources available to avoid congestion and, therefore, this service has absolute priority. Since such rare events are difficult to predict, it may not be possible to combine with other services that require similar must-run capabilities. Other services with such a must-run behavior, for example, are FCR or black-start capability.

- Compatibility regarding permanent energy reservations. Some services permanently reserve a fixed amount of energy resources while for other services an allocation of energy resources can be done dynamically. Services whose sum of their permanent reservation of energy resources exceeds the resources of the BESS are incompatible. An example for such a combination of services may be the combination of FCR and black-start capability.

Regarding the more difficult question of how dynamic resource allocation can be implemented, a rough assessment of the compatibility of services can be made on the basis of a categorization of services into energy-intensive and power-intensive services. While a combination of several energy-intensive or power-intensive services may lead to strict constraints during operational planning, the combination of a mix may hold potential for a more effective combination. For example, based on the services illustrated in Fig. 3.7, the service peak shaving can be considered as energy-intensive, whereas the provision of instantaneous reserves can be considered as power-intensive. Peak shaving requires a certain amount of energy resources to reach its goals, while the activation of instantaneous reserves requires less energy- but possibly higher power resources. Due to the uncertainty of the degree of activation of services, as well as the uncertainty regarding the time of activation, the operational planning is rather difficult for most of the services. For other services, on the other hand, the requirements regarding resources are easier to plan. The requirements on energy resources for providing FCR, for example, can easily be planned, due to the strict legal requirements based on the "30-minute-criterion". Another example is the provision of black-starting capability. The required energy resources, or more precisely the discharge duration to perform a black-start of a grid section are easy to determine and have to be reserved at any time during provision of such a service in order to guarantee a successful black-start in case of a power outage. More examples of the categorization of services into energy-intensive and power-intensive services, for example, can be found in [83] and in [110] on the basis of E/P-diagrams.

Another approach for evaluating the compatibility of services regarding dynamic resource allocation is the evaluation according to the synergies of services. Services may behave differently but it may be possible to merge their objectives. Such synergies of services are described in [63] and several examples are described below.

- Self-consumption optimization and peak shaving. The best example for merging objectives of two services is the combination of self-consumption optimization and peak shaving. The goal of self-consumption optimization is to maximize the use of self-produced energy behind the meter of the corresponding consumer. However, this goal can also be achieved while serving the goal of peak shaving, which is to prevent the occurrence of large power peaks. Fig. 5.2 illustrates an abstract example of merging the corresponding objectives. Fig. 5.2 shows how surplus energy behind the meter can be stored so that the objectives of both services can be merged.

- Congestion management and peak shaving. Assuming the service of peak shaving to be implemented in distributed BESS, a coordination of its behavior may contribute to a central congestion management in the distribution or transmission grid.

- Energy arbitrage and firm capacity. Assuming the presence of a capacity market, synergies for trading energy and power can be found.

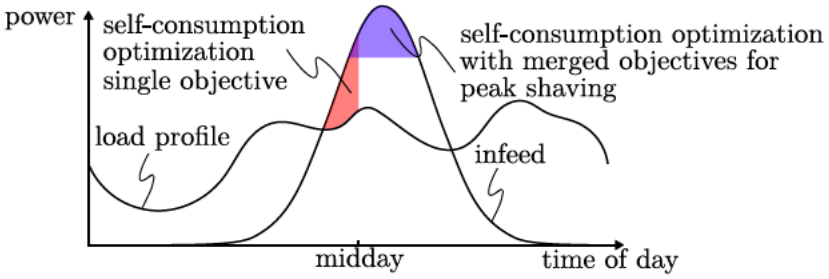

Figure 5.2: Example for merging objectives based on combining the services self-consumption optimization and peak shaving in the way of storing surplus energy.

Since a general assessment of the compatibility of services as described above is very difficult, some examples of existing research are discussed below in order to identify the most promising combinations of services. For this reason, Tab. 5.1 shows an overview of existing research work within which the combined provision of services is investigated. Each column A – Q provides information of the corresponding research work about which combinations of services are investigated and which BESS size is used for investigation. For each service two categories are used to indicate whether the services are provided without any restrictions, or with restrictions. The best way to describe such a situation is on behalf of column E in Tab. 5.1, which shows six types of pairs of services, each of which includes a service specified for restricted provision only. The corresponding reference [167] in column E uses an approach for multi-use operation where one of the services in each pair is defined as "primary service", whereas the second service in each pair is defined as "secondary service". While the primary service is provided according to its function principle, the secondary service uses the actual remaining resources of the BESS to follow its function principle. Therefore, the secondary service may be limited depending on the actual resource demand of the primary service, which has priority at any time. Arteaga et al. [9] in column I describe a similar approach of defining secondary services that only use the remaining resources. Additional examples for such a combination of primary and secondary services that are not listed in Tab. 5.1 are described by Fitzgerald et al. [66]. In Tab. 5.1 such kind of restriction is indicated as "restricted provision" by the symbol ◯. However, besides such a restriction of a service to only use the actual remaining resources, this symbol also indicates other forms of restrictions. In column H, for example, FCR is indicated as a service with restricted provision, because it is deactivated while peak shaving is being active. According to the corresponding reference [46] in column H, this restriction arises from the fact that peak shaving requires most of the energy resources of the BESS in order to work properly. Therefore, the symbol ◯ also indicates that the corresponding service may only be provided sequentially and not in parallel with other services.

A combination of FCR and peak shaving can also be found in column Q. Compared to column I the provision of FCR is not indicated as restricted in column Q. However, in the corresponding reference of column Q, Xi et al. [198] conclude that FCR can only be active in a minimal amount which is only possible because FCR is provided in a pool with other units.

The services FCR, peak shaving and energy arbitrage are the services which are most often combined. Tab. 5.1 also lists the corresponding size of the BESS that is used as basis for the investigations in the references. Tab. 5.1 reveals that services for conventional frequency control,

Table 5.1: Best practice examples for combined provision of services based on existing research work. FCR...Frequency Containment Reserve, aFRR...automatic Frequency Restoration Reserve, mFRR...manual Frequency Restoration Reserve
SI...Synthetic Inertia, EFR...Enhanced Frequency Reserve, FFR...Fast Frequency Reserve, FR...Fast Reserve, SVS...Static Voltage Support, DVS...Dynamic Voltage Support RPC...Reactive Power Compensation, BS...Black-start Capability, ISL...Islanding, PS...Peak Shaving, CF...Capacity Firming, SCO...Self-consumption Optimization, CM...Congestion Management, RAMP...Ramping, ARB...Energy Arbitrage, SPOT...Spot-Market Trading, CAP...Firm Capacity. ×...provision, ◯...restricted provision.

	reference																							
	A	B	C	D			E					F	G	H	I	J	K	L	M	N	O	P	Q	
	[45]	[132]	[23]	[8]			[167]					[181]	[203]	[46]	[9]	[110]	[22]	[161]	[194]	[100]	[101]	[29]	[198]	
E kWh	-	560	1.5k 2.5k	13.5	60		4.5		90			200	10	1340	20k	370	500	50	16k	30k	30k	500	11.2	
P kW	-	720	1k	7			-					250	-	1250	10k	400	1200	1k	4k	30k	30k	1k	7.2	
FCR	×	×		×	◯		◯		◯				×	◯	×		×	×		×	×	×	×	
aFRR						◯		◯		◯		×			◯				×		×			
mFRR							◯		◯		◯													
SI																								
EFR																								
FFR			×																					
FR																								
SVS				×																				
DVS																								
RPC	◯																							
BS																								
ISL																			×				×	
PS	×								×	×	×	×		×		×	×	×	×				×	
CF		×																						
SCO							×	×	×				×			×								
CM																								
RAMP																								
ARB	◯		×		×	×	×							◯	◯		×		×	×		×	×	
SPOT														×	×	×				×	×			
CAP																								

regardless of the size of the BESS, are the ones that are most frequently combined with other services. For smaller BESS sizes ($< 10\,\text{kWh}$) the provision of FCR is always assumed to be provided in a pool with other units in order to achieve the minimum bid size of 1 MW. This cancels out the constraints regarding energy reserves, since it is assumed that the corresponding actual power requirements of FCR can always be compensated by other units in the pool when the BESS is not capable of providing its power share. With this assumption, FCR becomes a power-intensive service and is compatible also with energy-intensive services, such as capacity firming, peak shaving or self-consumption optimization. For larger BESS sizes, however, the service FCR may also be categorized as energy-intensive, due to the required energy reserves as described in Chp. 4.1.1. The combination of FCR with other energy-intensive services is also shown for larger BESS sizes in Tab. 5.1, however, operational planning becomes more difficult and several columns indicate the restrictions that arise by such combinations. Nevertheless, the combination of FCR with peak shaving is listed most often in Tab. 5.1 for large BESS sizes. For small BESS sizes also a combination of FCR with self-consumption optimization is listed several times. Tab. 5.1 also lists energy arbitrage in combination with other services. Energy arbitrage is the most straight-forward service for storages to generate revenues, therefore, a desired combination with other services seems expectable. In particular, the actual operating point of this service can be varied very easily, since an adaptation of a planned working point only results in diminished revenues but does not influence its basic operation functionality.

Another interesting finding of Tab. 5.1 is the fact that combining FCR with other services does not lead to any issues regarding operational functionality. Especially peak shaving is a service frequently combined with FCR in Tab. 5.1. The fact that compatibility regarding operational functionality of FCR and peak shaving is given tells that peak shaving seems not to operate on the same time scale as FCR.

There are four approaches of combining services that can be extracted from all references in Tab. 5.1.

- Categorization in primary and secondary services. Whereas the primary services have absolute priority to pursue their goal at any time, the secondary services only use the remaining resources which are actually available and can therefore only pursue their goal to a limited extent. For the FCR service, however, such an approach can only be implemented if FCR is provided in a pool with other units. Otherwise, FCR has to be considered as "must-run" service that is incompatible as secondary service.
- Allocating resources according to operational planning. In contrast to a categorization into primary and secondary services, with this type basically every service can use the resources of the BESS equally. However, the actual allocation of resources is based on an operational planning phase and is therefore much more complicated than the first approach above. Since most of the references listed in Tab. 5.1 are investigating a multi-use operation based on optimization with perfect foresight, the realization of a real-time operation is therefore an open topic. With perfect foresight an optimal allocation of resources is relatively easy to identify. However, an implementation in real-time requires a prioritization algorithm in order to deal with the uncertainty of control values such as frequency, renewable power output, etc.
- Combined provision of services by merging objectives. For some combinations of services, allocating resources according to prioritization may not be an issue. By merging goals, two services can use identical resources just by merging the way the goal of each service is pursued, as shown in Fig. 5.2 for example.
- Sequential multi-use operation. A sequential multi-use operation as illustrated in Fig. 5.1 is not the main focus of this thesis. However, for specific constellations such a type of multi-use operation may be the best way to increase profitability. Especially for must-run services that are active during rare events only, but the time horizon occurs in recurring and predictable

time periods, a sequential stacking with other services is a promising solution to increase the utilization of a BESS. For example, a combination with another service like FCR can be a good way to use the resources of the BESS even in winter if a BESS only provides congestion management in a place with recurring congestion in summer, when the renewable supply is high.

Since the second approach listed above is the most frequently used in Tab. 5.1 and may be the most promising candidate for an economic-optimal multi-use operation, the following chapters deal with the question of how to realize a prioritization algorithm as mentioned above.

5.3 Concepts of Real-Time Multi-Use Operation

In Chp. 5.1 three types of multi-use operation are described as sequential, parallel and dynamic, which were originally identified by Englberger et al. [45]. For all of these three types, time-related constraints arise. As described in Chp. 1.4, there is existing literature on the consideration of these time-related constraints in optimization models, which allow the calculation of an optimal allocation of resources of the BESS for several services for each time slot in the optimization horizon regarding a specific optimization goal such as maximizing revenues. As described in Chp. 5.1, this phase is referred to as operational planning. The results of the operational planning can be used to parametrize corresponding schedules of services for each time slot in a real BESS accordingly. However, there are several services whose behavior is unpredictable during operational planning. This chapter discusses possible concepts to deal with such unpredictable behavior of services during real-time operation.

In this thesis the implementation of a service in a BESS is referred to as "function". A service is considered as an abstract definition, whereas a function is a detailed definition of its implementation in a system. The implementation of a service as a function may differ between systems. Therefore, functions describe in detail how a service is executed. Besides such functions that are executing services, there may be additional functions that are necessary to operate a BESS or to guarantee the continuous execution of services. For example, the management of the state of charge is one such function.

The first concept of real-time operation is based on a given allocation of virtual BESS for different services, which is the result of the operational planning for a specific time slot. The resources of a BESS can be split up into several virtual BESS. Such a division into virtual BESS has to be done for the power resources and the energy resources of the BESS, resulting in corresponding power bands and energy bands that represent the share of resources of each virtual BESS related to the total resources of the BESS. However, there is a difference between power bands and energy bands in the way they are influenced during real-time operation. While the power band of a virtual BESS defines the limits within which the operating point of an assigned function is allowed to operate, the energy band of a virtual BESS defines the reservation of energy resources of the BESS for a later usage by the corresponding function.

Fig. 5.3 illustrates the first concept of real-time multi-use operation based on the allocated energy bands for each function in a specific time slot. A BESS that executes four services simultaneously is assumed. Since the state of energy is a state variable, it has an influence in which way the energy band of the corresponding virtual BESS is allocated within the energy resources of the BESS. The energy bands can either be allocated symmetrically, positively or negatively. In the case of symmetrical allocation, the energy resources of the corresponding virtual BESS are allocated with half their value in the upper and lower region of the energy resources. In case of positive allocation the energy resources of the corresponding virtual BESS are allocated in the lower region of the energy resources. In case of negative allocation, the energy resources of the corresponding virtual BESS are allocated in the upper region of the energy resources. A symmetrical allocation ensures

that the BESS can store and provide energy at a later point in time, while a positive allocation only ensures the provision and a negative allocation only ensures the storage at a later point in time. As described in [122] an example of a service that requires symmetrical allocation is FCR. An example of a service that requires negative allocation is peak shaving. Peak shaving requires specific negative energy resources to be available in advance of its activation in order to be able to store energy while it is active. An example for positive allocation is the provision of firm capacity. Providing firm capacity requires specific positive energy resources to be available in advance of its activation in order to be able to provide energy while it is active. Furthermore, there are functions whose requirement for an energy band is zero. All voltage control services are of such type. Fig. 5.3 shows a symmetrical allocation for function 1, a positive allocation for function 2, a negative allocation for function 3 and no energy band for function 4 in order to illustrate the resulting energy band, the so-called "working area", within which the state of energy of the BESS is allowed to operate.

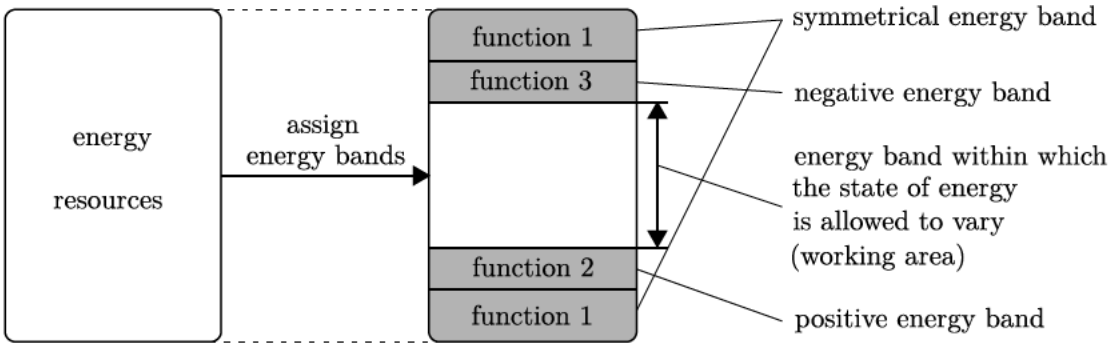

Figure 5.3: Concept of allocation of virtual BESS for each function on the example of assignment of energy bands for each function in a specific time slot. The grey color marks the reserved energy band of corresponding functions.

Fig. 5.4 illustrates the first concept of real-time multi-use operation based on the allocated power bands for each function in a specific time slot. A BESS that executes four services is assumed, where function 1 and function 3 are only partly exploiting their power band, whereas function 2 fully exploits its power band and function 4 does not have any power output. Conflicts of functions are avoided on the basis of such a concept. Since power resources are divided in advance to the actual real-time operation, the sum of the power output of all functions cannot exceed the power resources of the BESS.

However, as described in Chp. 5.1, most of the unpredictable services require large amounts of power resources only during rare events such as abnormal grid conditions. On the one hand, these power resources have to be reserved in corresponding virtual BESS at all times, on the other hand, this reduces the flexibility for other services. With regard to Fig. 5.4, such a situation may arise when function 1 and function 4 are assumed to be functions that execute such unpredictable services. Most of the time their request of power resources is small compared to the size of the allocated virtual BESS. The flexibility to allocate resources for function 2 and function 3 during operational planning is therefore limited, although a high share of the resources is unused most of the time.

The question arises as to whether there are services that are capable of using the same resources and whether there are situations when the concept of virtual BESS needs to be expanded. Sharing energy bands is not possible, but sharing power bands may be an option. For example, different services for frequency control may be considered as decoupled in time to some extent and may be candidates to use shared power bands. Furthermore, there are services whose provision quality is not affected by the short-term sharing of power bands. As will be shown in Chp. 5.6, static

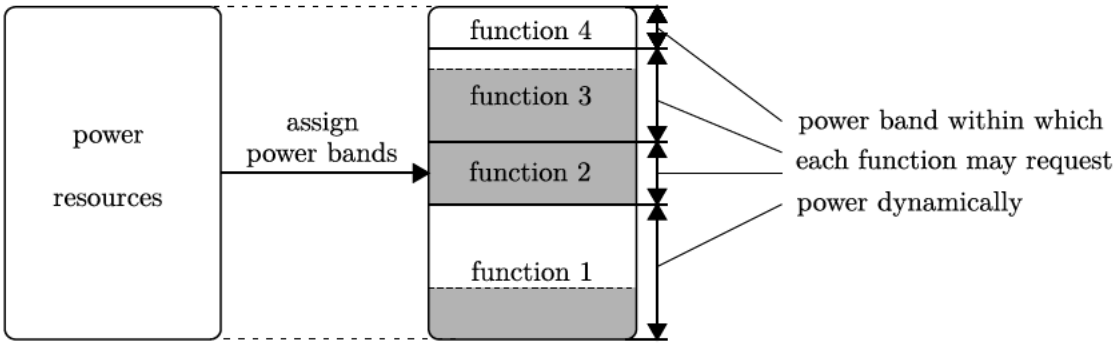

Figure 5.4: Concept of allocation of virtual BESS for each function on the example of static assignment of power bands for each function in a specific time slot. The grey color marks the currently occupied share of the power band of the corresponding function.

voltage support can be considered as such a service. Besides the argument of better utilization of resources, there are services whose resource demand cannot be identified in advance and which may require the concept of allocation of virtual BESS to be overruled in order to contribute to system stabilization. As will be shown in Chp. 5.6, dynamic voltage support can be considered as such a service. All of these thoughts are tried to be considered in the next concept, which is described below.

The concept of dynamic prioritization is also based on the allocation of virtual BESS and allocates energy bands identical as shown in Fig. 5.3. However, regarding power bands, an allocation is only done for functions for which such an allocation is possible. Based on priorities, the power resources of virtual BESS for functions with lower priority are made available for functions with higher priority when required. With such an approach it is possible to deal with the unpredictable behavior of services in such a way that during abnormal grid conditions they can exploit the corresponding resources, but at the same time do not waste resources through corresponding reservations during normal grid conditions.

Fig. 5.5 illustrates this concept of dynamic prioritization, again assuming a BESS providing four functions.

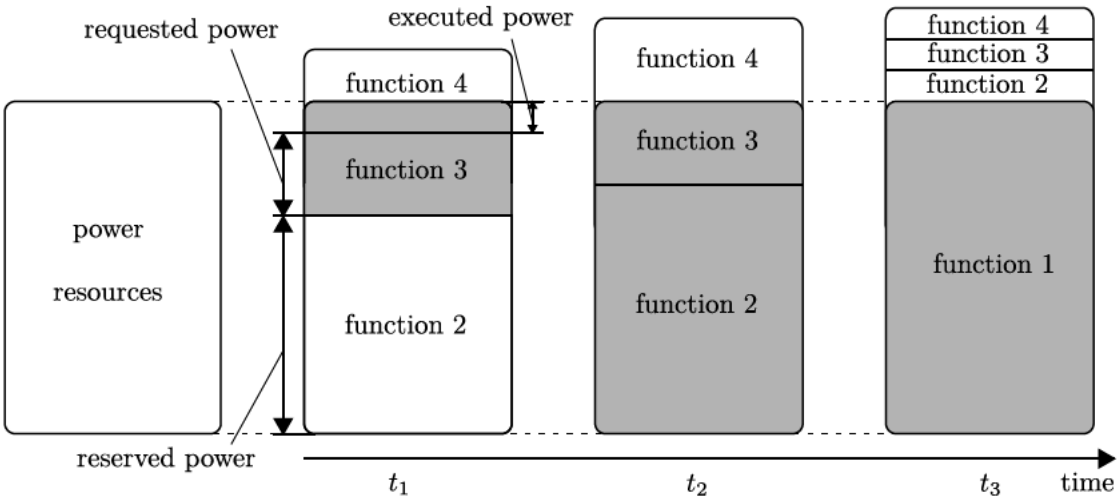

Figure 5.5: Concept of dynamic prioritization of functions.

Priorities are assigned beginning with function 1, which is assigned the highest priority, up to function 4, which is assigned the lowest priority. In this example, a virtual BESS with a corresponding power band is assigned only to function 2, which ensures the reservation of certain power resources of the BESS. In order to describe the behavior of functions in this concept, it is distinguished between

- reserved power: power resources according to the size of the virtual BESS assigned to the corresponding function,
- requested power: real-time power demand of the function and
- executed power: power output the system is able to execute for the corresponding function.

An activated function is allowed to reserve, request and execute power, whereas a deactivated function is not allowed to do so. A function is active only when its executed power differs from zero, otherwise the function is inactive.

Fig. 5.5 shows three different situations at the time t_1, t_2 and t_3, where the four functions are activated and have different requested powers for each situation. At the time t_1 function 1 and function 2 are inactive. But for function 2, power resources are reserved according to the size of the allocated virtual BESS. Function 3 and function 4 are active and are using the remaining power resources. However, since the requested powers of all functions exceed the power resources there is a conflict of functions, which is resolved based on the priorities. Since function 3 has a higher priority than function 4, the requested power of function 3 can be fully executed, whereas the requested power output of function 4 is limited, leading to an executed power that is lower than the requested power. At the time t_2, function 2 fully exploits its allocated power resources and even requests a higher amount than reserved according to its virtual BESS. Due to the priorities, the power requests of function 4 cannot be executed any more and the function becomes inactive. At the time t_4, it is assumed that an abnormal grid condition leads to a power request of function 1 that fully exploits the whole power resources of the system. Due to the highest priority of function 1, requested powers of all other functions cannot be executed any more and power reservations are overruled. Therefore, the functions 2 – 4 become inactive.

Compared to the concept of virtual BESS of Fig. 5.4, which prevents the occurrence of conflict of functions, the concept of dynamic prioritization of Fig. 5.5 handles conflicts based on the priorities assigned to each function.

At the times t_2 and t_3, the whole power resources of the BESS are exploited. Assuming an immediate transition between these two situations, the question arises, what influence the different assignments of power resources have, since the total power output of the system does not seem to change. The description of concepts in this chapter is based on a one-dimensional view. For example, it is not distinguished between active and reactive power. Assuming the function 2 and function 3 to request active power and function 1 to request reactive power in Fig. 5.5, the change of the total power output between the time t_2 and t_3 becomes visible. There are several other dimensions that have to be considered during the multi-use operation. Besides the active and reactive power, for example the influence of asymmetry and harmonics has to be taken into account. With consideration of such additional dimensions, a change of assignments at the time t_2 and t_3 in Fig. 5.5 therefore has an influence on the total power output of the system, since the waveform may change depending on the functions that are active. The sign of the power is an additional matter that is not considered in the exemplary descriptions above.

5.4 Considerations on Realization in Battery Converters

The descriptions of concepts in Chp. 5.3 are based on the assumption of a limited power capability of a BESS. To describe concepts, this assumption is helpful, because it allows a simplified descrip-

tion. However, in more detail, this limited power capability goes back on the maximum current a BESS is capable of handling, which is limited by its converter. This maximum instantaneous current $\hat{I}_{max}$, therefore, is the ultimate value, which has to be considered in the converter control. As already described at the end of Chp. 5.3, there are several dimensions that have to be taken into account when assigning power resources to different functions. Compared to the one-dimensional examples described in Chp. 5.3, this chapter considers such a multi-dimensional assignment of resources.

Fig. 5.6 shows a typical converter control structure based on a simplified converter representation.

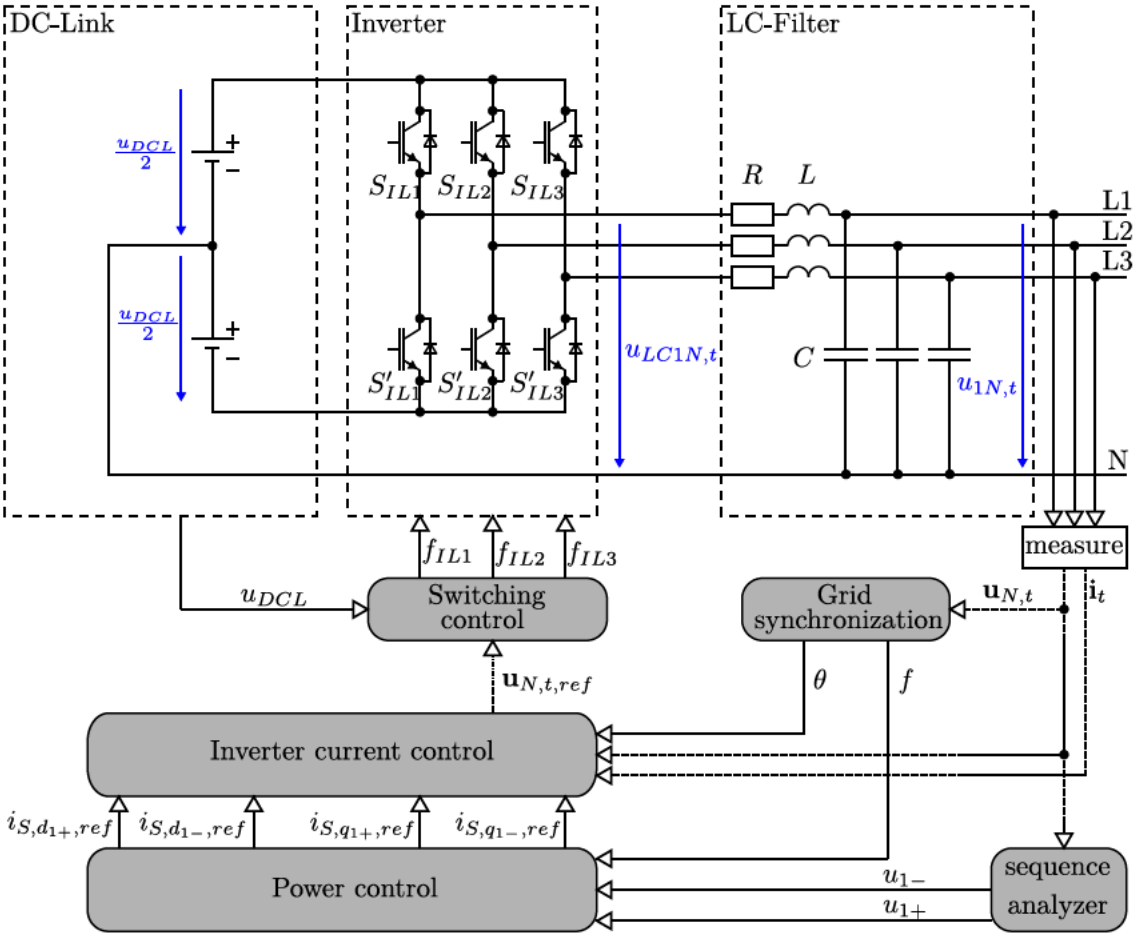

Figure 5.6: Simplified converter representation and its control.

This simplified converter consists of an LC-filter at the output, an inverter and a DC-Link, which is only represented by a voltage source. But this simplified converter representation is sufficient to describe the corresponding realization of a multi-use operation in the converter control. The "grid synchronization" of the converter control in Fig. 5.6 uses the measurement of the normalized instantaneous phase-to-neutral voltages $\mathbf{u}_{N,t}$ and the normalized phase currents $\mathbf{i}_t$ to calculate the grid angle θ, for example, by using a phase-locked-loop. Based on this grid angle θ also the frequency f can be calculated. The "power control" uses control variables, as for example the frequency f, or the normalized positive-sequence and negative-sequence voltage u_{1+} and u_{1-}, which are calculated by the "sequence analyzer" to calculate reference current values

$\mathbf{i}_{S,dq,ref} = (i_{S,d_{1+},ref}, i_{S,q_{1+},ref}, i_{S,d_{1-},ref}, i_{S,q_{1-},ref})^\top$, which are composed of direct and quadrature components, indicated by d and q, in the positive-sequence and negative-sequence system, indicated by "1+" and "1−". This reference current values are used in the "inverter current control" to calculate a normalized reference voltage $\mathbf{u}_{N,t,ref}$, which is used in the "switching control" to generate switching signals f_{IL1}, f_{IL2} and f_{IL3} for the inverter to control the switches S_{IL1}, S_{IL2} and S_{IL3} of the inverter. Complementary switching signals f'_{IL1}, f'_{IL2} and f'_{IL3} are used to control the switches S'_{IL1}, S'_{IL2} and S'_{IL3} of the inverter. The "inverter current control" can be realized by corresponding PI-controllers, each for the direct and quadrature components of each the positive- and negative-sequence system, which results in four PI-control loops. A corresponding implementation of such an "inverter current control", for example, is described in [118].

The requested power output of functions, which were introduced in Chp. 5.3, can be realized in the "power control" in Fig. 5.6. Several control variables, for example the frequency f, or the positive-sequence and negative-sequence voltage u_{1+} and u_{1-}, are used to calculate the corresponding requested power outputs of functions. These requested powers are superimposed and are the basis to calculate the reference current space vector $\underline{i}_{S,dq,ref}$, which is used in the "inverter current control" in Fig. 5.6. The resulting current space vector may exceed the maximum current $\hat{I}_{max}$ of the converter. Therefore, an extended version of the concept described in Fig. 5.5 may be applied in order to ensure the condition

$$\underline{i}_{S,dq,ref}(t) \leq i_{max} = \frac{\hat{I}_{max}}{\sqrt{2} I_n} \forall t \tag{5.1}$$

at any time. A detailed description of a realization of the concept of Fig. 5.5 in the "power control" of Fig. 5.6 is given in Chp. 5.5. Based on a mathematical framework, which allows the definition of functions, the description of their behavior regarding requested powers and the formulation of a dynamic prioritization of functions based on priorities, a systematic description of a real-time multi-use operation of BESS is possible.

5.5 Mathematical Framework To Describe a Multi-Use Operation

The multi-use operation is based on a set of functions

$$\mathbf{F} = \{F_1, F_2, ...F_k, ..., F_{N_F}\} \tag{5.2}$$

where each function F_k, with $k \in \mathbb{N} : k \leq N_F$ describes the behavior of the corresponding service the BESS provides. The number of functions is $|\mathbf{F}| = N_F$. A function is either activated or deactivated. This activation of functions is described by the set $\mathbf{A}$

$$\mathbf{A} = \{A_1, A_2, ..., A_k, ...A_{N_F}\} \in \mathbf{B}^{N_F} \tag{5.3}$$

with $\mathbf{B} = \{0, 1\}$, and where $A_k = 0$ means the function F_k is deactivated, and where $A_k = 1$ means the function F_k is activated. There may be functions that must not be activated at the same time because they are incompatible. These forbidden activations are summarized in the set

$$\mathcal{U} \subset \mathbf{B}^{N_F}. \tag{5.4}$$

According to Chp. 5.3, it is distinguished between the reserved, the requested, and the executed power. Each function F_k describes the behavior of its requested power, based on a set of parameters

$$\mathbf{X}_k = \{X_{k,1}, X_{k,2}, ..., X_{k,N_{X_k}}\} \in \mathbb{R}^{N_{X_k}} \tag{5.5}$$

where N_{X_k} is the number of parameters of the function F_k and a set of control variables

$$\mathbf{C}_k = \{C_{k,1}, C_{k,2}, ..., C_{k,N_{C_k}}\} \in \mathbb{R}^{N_{C_k}} \tag{5.6}$$

where N_{C_k} is the number of control variables of the function F_k. Based on these parameters $\mathbf{X}_k$ and control variables $\mathbf{C}_k$, the behavior of the requested power of each function F_k can be described. The requested power is divided into two parts, a statically requested part and a dynamically requested part. The statically requested power represents the static operating point, whereas the dynamically requested power represents the dynamic behavior of the power output that follows this operating point. The statically requested power of a function F_k is defined by

$$\underline{S}_{SR_k} = A_k \cdot \mathrm{f}[\mathbf{X}_k, \mathbf{C}_k(t)] \tag{5.7}$$

and the dynamically requested power of the function F_k results from the dynamic behavior, defined in the parameters of the function, and the statically requested power

$$\underline{S}_{DR_k} = \mathrm{f}(\underline{S}_{SR_k}, \mathbf{X}_k, t). \tag{5.8}$$

Both the statically as well as the dynamically requested part are apparent powers, which consist of an active and a reactive power, which are P_{SR_k} and Q_{SR_k} for the statically requested power and P_{DR_k} and Q_{DR_k} for the dynamically requested power.

Many functions only request either active or reactive power. The two sets $\mathcal{A}$ and $\mathcal{R}$ are therefore defined by

$$\mathcal{A} = \{F_k \in \mathbf{F} | Q_{DR_k} = 0 \forall t\} \tag{5.9}$$
$$\mathcal{R} = \{F_k \in \mathbf{F} | P_{DR_k} = 0 \forall t\} \tag{5.10}$$

and include the corresponding functions that only request active or reactive power. All functions included in the set $\mathcal{A}$ are called "active power functions" and all functions included in the set $\mathcal{R}$ are called "reactive power functions".

Fig. 5.6 shows that the output of the "power control" are four Park-components, which are summarized in the vector

$$\mathbf{i}_{S,dq,ref} = (i_{S,d_{1+},ref}, i_{S,q_{1+},ref}, i_{S,d_{1-},ref}, i_{S,q_{1-},ref})^\top. \tag{5.11}$$

The contribution of each function F_k to $\mathbf{i}_{S,dq,ref}$ has to be calculated based on the dynamically requested power $\underline{S}_{DR_k}$ on the basis of the corresponding current request:

$$\mathbf{i}'_{S,dq_k} = \mathrm{f}(\underline{S}_{DR_k}, \mathbf{C}_k) = (i'_{S,d_{1+,k}}, i'_{S,q_{1+,k}}, i'_{S,d_{1-,k}}, i'_{S,q_{1-,k}})^\top. \tag{5.12}$$

Besides the requested power, Chp. 5.3 lists the reservation of power resources in order to ensure that functions are capable of executing certain power increments at any time. Such a power reservation of a function F_k results in a corresponding reservation of current reserves in the "power control" of Fig. 5.5, which is defined by

$$\mathbf{i}''_{S,dq_k} = A_k \cdot \mathrm{f}(\mathbf{X}_k, \mathbf{C}_k) = (i''_{S,d_{1+,k}}, i''_{S,q_{1+,k}}, i''_{S,d_{1-,k}}, i''_{S,q_{1-,k}})^\top \tag{5.13}$$

$$sgn(\mathbf{i}''_{S,dq_k}) = \begin{cases} +, & \text{positive reservation,} \\ -, & \text{negative reservation,} \\ \pm, & \text{symmetrical reservation} \end{cases} \tag{5.14}$$

and reserves either positive, negative, or symmetrical power resources. For example, FCR requires a symmetrical reservation of power resources, whereas for aFRR it is possible to tender positive and negative products separately.

In Chp. 5.3 a conflict of functions was indirectly defined as a situation where a function requests power, but is prohibited to execute it. With regard to the corresponding current request $\mathbf{i}'_{S,dq_k}$, such a situation is characterized by a limitation of $\mathbf{i}'_{S,dq_k}$. Therefore, the different current contributions of functions sum up to

$$\mathbf{i}_{S,dq,ref} = \sum_{k=1}^{N_F} \mathbf{i}_{S,dq,ref_k} = (i_{S,d_{1+},ref}, i_{S,q_{1+},ref}, i_{S,d_{1-},ref}, i_{S,q_{1-},ref})^\top \tag{5.15}$$

where the executable current request of each function F_k is $\mathbf{i}_{S,dq,ref_k}$. This executable current request is defined by

$$\mathbf{i}_{S,dq,ref_k} = \mathrm{f}(\mathbf{i}'_{S,dq_k}, \mathbf{o}_{S,dq_k}). \tag{5.16}$$

and depends on the requested current $\mathbf{i}'_{S,dq_k}$ and the already "occupied current reserves" $\mathbf{o}_{S,dq_k}$ of functions with a higher priority than the function F_k, which will be defined in Eq. (5.23).

In case of a conflict of functions, at least one current request $\mathbf{i}'_{S,dq_k}$ of a function F_k has to be limited, which leads to

$$\|\mathbf{i}_{S,dq,ref_k}\|_1 < \|\mathbf{i}'_{S,dq_k}\|_1. \tag{5.17}$$

To manage such a conflict of functions a set of priorities is defined by

$$\mathbf{V} = \{V_1, V_2, ..., V_k, ..., V_{N_F}\}. \tag{5.18}$$

Each function is assigned a priority according to

$$V : \mathbf{F} \rightleftarrows \{v \in \mathbb{N} | v \leq N_F\}. \tag{5.19}$$

A function F_k has highest priority when $V(F_k) = V_k = 1$ and it has lowest priority when $V(F_k) = V_k = N_F$. When a conflict of function occurs, the current requests $\mathbf{i}'_{S,dq_k}$ of functions are limited, beginning from the function F_k with lowest priority $V_k = N_F$, up to the function F_k with highest priority $V_k = 1$, until the condition according to Eq. (5.1) is fulfilled. In order to identify the functions which have to be limited, a set $\mathbf{H}_k$ is defined for each function F_k, which consists of all function indices with higher priorities than F_k. These sets $\mathbf{H}_k$ are defined by

$$\mathbf{H}_k = \{h \in \mathbb{N} | \exists V_h \wedge (V_h < V_k)\}. \tag{5.20}$$

In order to calculate the limited currents for each function F_k in case of a conflict of functions, a matrix $\tilde{\mathbf{o}}_{S,dq_k} \in \mathbb{R}^{4\times m}$ is defined by

$$\tilde{\mathbf{o}}_{S,dq_k} = \mathbf{i}'_{S,dq_k} + \sum_{n=1}^{|\mathbf{H}_k|} \begin{cases} \mathbf{i}'_{S,dq_{\mathbf{H}_k(n)}}, & \|\mathbf{i}'_{S,dq_{\mathbf{H}_k(n)}}\|_1 > \|\mathbf{i}''_{S,dq_{\mathbf{H}_k(n)}}\|_1, \\ \left(i''_{S,d_{1+},\mathbf{H}_k(n)}, 0, i''_{S,d_{1-},\mathbf{H}_k(n)}, 0\right)^\top, & \|\mathbf{i}'_{S,dq_{\mathbf{H}_k(n)}}\|_1 \leq \|\mathbf{i}''_{S,dq_{\mathbf{H}_k(n)}}\|_1 \wedge F_k \in \mathcal{A}, \\ \left(0, i''_{S,q_{1+},\mathbf{H}_k(n)}, 0, i''_{S,q_{1-},\mathbf{H}_k(n)}, 0\right)^\top, & \|\mathbf{i}'_{S,dq_{\mathbf{H}_k(n)}}\|_1 \leq \|\mathbf{i}''_{S,dq_{\mathbf{H}_k(n)}}\|_1 \wedge F_k \in \mathcal{R} \end{cases} \tag{5.21}$$

which describes the already "occupied" current resources considered from the point of view of function F_k and where the value of m is depending on the number of current requests, which exceed the current reservation of the corresponding function. In case there are no current reservations, this leads to $m = 1$. In case of at least one function with higher priority reserving current resources symmetrically and assuming all current requests are zero, this leads to $m = 2$, since every symmetrical current reservation has to be taken into account with positive and negative sign. In order to realize a behavior as shown in Fig. 5.5, the occupied current resources for each

function F_k are depending on the current requests $\mathbf{i}'_{S,dq_{\mathbf{H}_k(n)}}$ and current reservations $\mathbf{i}''_{S,dq_{\mathbf{H}_k(n)}}$ of all functions with higher priority than F_k. Since each function may have positive, negative, or symmetrical current reservations and may be an active or reactive power function, this leads to a rather complex structure of Eq. (5.21). The first part of the case distinction in Eq. (5.21) takes into account a situation when a current request exceeds current reservations, but also comes into force when a function has no current reservation. For example, a current request $\mathbf{i}'_{S,dq_1} = (0.5, 0, 0, 0)^\top$ with a corresponding current reservation $\mathbf{i}''_{S,dq_1} = (\pm 1, 0, 0, 0)^\top$ and a current request $\mathbf{i}'_{S,dq_2} = (-2.5, 0, 0, 0,)^\top$ has to result in executable currents of $\mathbf{i}_{S,dq,ref_1} = (0.5, 0, 0, 0)^\top$ and $\mathbf{i}_{S,dq,ref_2} = (-1, 0, 0, 0)^\top$ when $V_1 < V_2$ and $i_{max} = 2$. However, current reservations only have to be taken into account for the corresponding type of function. For example, for an active power function F_k, only current reservations of other active power functions with higher priority have to be taken into account, whereas current reservations of reactive power functions do not have to be taken into account. Such a behavior is described by the second and third part of the case distinction in Eq. (5.21).

Each column vector in $\tilde{\mathbf{o}}_{S,dq_k}$ can be assigned a maximum phase current that would occur in one of the three phases, in case the corresponding vector would be executed. The set of these maximum currents where each entry is the maximum phase current of the corresponding column vector out of $\tilde{\mathbf{o}}_{S,dq_k}$ is defined by

$$\mathbf{i}_{o_k} = \mathrm{f}(\tilde{\mathbf{o}}_{S,dq_k}, \varphi_\pm) \tag{5.22}$$

where $\varphi_\pm$ is the angle between the positive-sequence and negative-sequence system. In this set of maximum phase currents $\mathbf{i}_{o_k}$, a maximum $\max(\mathbf{i}_{o_k})$ can be found, which is assigned to the corresponding vector. This corresponding vector that leads to this maximum phase current is defined by

$$\mathbf{o}_{S,dq_k} \in \tilde{\mathbf{o}}_{S,dq_k} | \mathrm{f}(\mathbf{o}_{S,dq_k}, \varphi_\pm) = \max(\mathbf{i}_{o_k}). \tag{5.23}$$

The maximum phase current $\max(\mathbf{i}_{o_k})$ and its corresponding vector $\mathbf{o}_{S,dq_k}$ can be used to calculate the executable currents of each function F_k by

$$\mathbf{i}_{S,dq,ref_k} = \begin{cases} \mathbf{i}'_{S,dq_k}, & \max(\mathbf{i}_{o_k}) \leq i_{max}, \\ \mathrm{f}\left(\mathbf{i}'_{S,dq_k}, \mathbf{o}_{S,dq_k}\right), & else \end{cases} \tag{5.24}$$

where the lower part of the Eq. corresponds to Eq. (5.16) and leads to a current limitation of the current request of function F_k. A detailed description of the calculation of this current limitation $\mathrm{f}\left(\mathbf{i}'_{S,dq_k}, \mathbf{o}_{S,dq_k}\right)$ of Eq. (5.24) is described in Chp. 5.5.1.

5.5.1 Calculation of Limited Currents

Any current space vector $\underline{i}_S$ in the $\alpha\beta$-plane is a function of its Park-components, the grid angle θ and the angle $\varphi_\pm$ between positive-sequence and negative-sequence system:

$$\underline{i}_S = \mathrm{f}(\mathbf{i}_{S,dq}, \theta, \varphi_\pm). \tag{5.25}$$

Assuming there is no zero-sequence system, the relationship between a current space vector in the $\alpha\beta$-plane and a current space vector in the dq-plane is given by the Park-transformation

$$\underline{i}_{S,dq} = \underline{i}_S e^{-j\theta}. \tag{5.26}$$

In more detail, a current space vector can be expressed by

$$\underline{i}_S = \left(\underline{i}_{S,dq_{1+}} \cdot e^{j\theta} + \underline{i}_{S,dq_{1-}} \cdot e^{-j\theta} \cdot e^{j\varphi_\pm}\right) \tag{5.27}$$

where a division of the space vector $\underline{i}_S$ in a positive-sequence part $\underline{i}_{S,dq_{1+}}$ and a negative-sequence part $\underline{i}_{S,dq_{1+}}$ is considered. Each of these two parts can be further divided into a direct and a quadrature part by using

$$\underline{i}_{S,dq_{1+}} = i_{S,d_{1+}} + j \cdot i_{S,q_{1+}} \tag{5.28}$$

$$\underline{i}_{S,dq_{1-}} = i_{S,d_{1-}} + j \cdot i_{S,q_{1-}}. \tag{5.29}$$

All four Park-components can be summarized in a vector $\mathbf{i}_{S,dq} = (i_{S,d_{1+}}, i_{S,q_{1+}}, i_{S,d_{1-}}, i_{S,q_{1-}})^\top$. The instantaneous phase currents $\mathbf{i}_t = (i_{L1,t}, i_{L2,t}, i_{L3,t})^\top$ can be calculated by projecting the space vector $\underline{i}_S$ on the corresponding phase:

$$\mathbf{i}_t = \mathfrak{Re}\left[\left(i_{S,d_{1+}} + j \cdot i_{S,q_{1+}}\right) e^{j\theta} e^{-j(0,1,2)^\top \frac{2\pi}{3}} + \left(i_{S,d_{1-}} + j \cdot i_{S,q_{1-}}\right) e^{-j\theta} e^{j\varphi_\pm} e^{-j(0,1,2)^\top \frac{2\pi}{3}}\right]. \tag{5.30}$$

To calculate the maximum phase current, the corresponding grid angle θ_{max}, which is calculated by

$$\theta_{max} = \theta \Big| \frac{\mathrm{d}\mathbf{i}_t}{\mathrm{d}\theta} = 0 \tag{5.31}$$

can be used as follows

$$\max\left[\mathbf{i}_t(\mathbf{i}_{S,dq}, \theta = \theta_{max}, \varphi_\pm)\right]. \tag{5.32}$$

Eq. (5.32) can be used to calculate the individual maximum phase currents in Eq. (5.22):

$$\mathbf{i}_{o_k} = \mathrm{f}(\tilde{\mathbf{o}}_{S,dq_k}, \varphi_\pm) = \max\left[\mathbf{i}_t(\tilde{\mathbf{o}}_{S,dq_k}, \theta = \theta_{max}, \varphi_\pm)\right] \tag{5.33}$$

which leads to the maximum phase current

$$\max(\mathbf{i}_{o_k}) = \mathrm{f}(\mathbf{o}_{S,dq_k}, \varphi_\pm) = \max\left[\mathbf{i}_t(\mathbf{o}_{S,dq_k}, \theta = \theta_{max}, \varphi_\pm)\right] \tag{5.34}$$

in Eq. (5.23).

When a current limitation according to the lower part in Eq. (5.24) is necessary, a procedure has to be defined that determines which of the four components of the corresponding current request $\mathbf{i}'_{\mathbf{S},\mathbf{dq_k}}$ of a function F_k have to be limited and to what value they have to be limited. In Eq. (5.24) this procedure is represented by the term $\mathrm{f}\left(\mathbf{i}'_{S,dq_k}, \mathbf{o}_{S,dq_k}\right)$. In order to describe this term in more detail, all functions that need to be limited have to be identified first. The case distinction in Eq. (5.24) implicitly reveals all functions that have to be limited. According to Eq. (5.24), all functions F_k with the function index k out of the following set

$$\mathbf{L} = \left\{k \in \mathbb{N} \middle| k \leq N_F \wedge \max(\mathbf{i}_{o_k}) > i_{max}\right\} \tag{5.35}$$

have to be limited. In this set $\mathbf{L}$, the function with highest priority can execute a limited amount of its current request, whereas the current request of all other functions have to be limited to zero. This function F_k is defined by

$$F_L = F_k | V_k \leq V_h \forall k, h \in \mathbf{L}. \tag{5.36}$$

For this function F_L, the limited currents have to be calculated explicitly, whereas for all other functions $\{F_k | k \in \mathbf{L} \wedge F_k \neq F_L\}$, the corresponding executable currents $\mathbf{i}_{S,dq,ref_k}$ according to Eq. (5.24) are zero:

$$\mathbf{i}_{S,dq,ref_k} = \mathrm{f}\left(\mathbf{i}'_{S,dq_k}, \mathbf{o}_{S,dq_k}\right) = 0, \forall k \in \mathbf{L} \wedge F_k \neq F_L. \tag{5.37}$$

For the calculation of $\mathbf{i}_{S,dq,ref_L}$ of the function F_L, a stepwise approach as described in [118] can be applied under the use of $\mathbf{o}_{S,dq_L}$, where $\left(\mathbf{o}_{S,dq_L} - \mathbf{i}'_{S,dq_L}\right)$ consists of fixed values of executable currents of functions with higher priority than the function F_L and $\mathbf{i}'_{S,dq_L}$ is to be calculated by the current limitation algorithm described in [118]. In a first step, a prioritization of the direct or quadrature components of the function F_L has to be defined. For the sake of simplicity, this prioritization is assumed for the quadrature components, identical as in [118]. Furthermore, it is assumed that the $i'_{S,d_{1-,L}}$-component is zero. Taking into account these assumptions, the three remaining components $i'_{S,d_{1+,L}}$, $i'_{S,q_{1+,L}}$ and $i'_{S,q_{1-,L}}$ can be calculated according to the Algorithm described in [118].

5.5.2 Block Diagram of the Concept of Dynamic Prioritization

To illustrate the procedure of dynamic prioritization of functions, Fig. 5.7 shows a corresponding block diagram, which represents the "power control" of Fig. 5.6 and summarizes the mathematical descriptions in Chp. 5.5 and Chp. 5.5.1.

The input of the block diagram in Fig. 5.7 consists of control variables $\mathbf{C}_k$ for each function F_k as introduced in Eq. (5.6). Such control variables were already shown in Fig. 5.6, for example, the frequency f, the positive-sequence and the negative-sequence voltage u_{1+} and u_{1-}, which are also listed in Fig. 5.7. Control variables $\mathbf{C}_k$ of a function F_k are not limited to these examples, but can include various other variables.

As shown in Fig. 5.7, for each function F_k its control variables $\mathbf{C}_k$ and a set of parameters $\mathbf{X}_k$, as defined in Eq. (5.5), are used to define its static behavior $\mathrm{f}(\mathbf{X}_k, \mathbf{C}_k)$, which results in a statically requested power $\underline{S}_{SR_k}$. This statically requested power also depends on the activation A_k of the corresponding function. Only an activated function F_k is able to request power.

As shown in Fig. 5.7, besides the static behavior, for each function a dynamic behavior is defined based on the parameters $\mathbf{X}_k$ of the function. The corresponding dynamically requested power $\underline{S}_{DR_k}$ therefore depends on the time t, and its static operating point is defined by the corresponding statically requested power $\underline{S}_{SR_k}$.

The corresponding current request $\mathbf{i}'_{S,dq_k}$ of each function is depending on the dynamically requested power and the control variables $\mathbf{C}_k$, more precisely, the voltage, which is part of the control variables.

Besides the current requests $\mathbf{i}'_{S,dq_k}$, also the current reservations $\mathbf{i}''_{S,dq_k}$ are shown in Fig. 5.7. Based on the definition in Eq. (5.13), these current reservations go back on static power reservations, which are only dependent on the parameters $\mathbf{X}_k$ of the function. In order to calculate the corresponding current reservation based on these static power reservations, the control variables $\mathbf{C}_k$ are used, more precisely, the voltage, which is part of the control variables. Current reservations are only different to zero when the corresponding function is activated by $A_k = 1$.

In Fig. 5.7, the current requests $\mathbf{i}'_{S,dq_k}$ and the current reservations $\mathbf{i}''_{S,dq_k}$ are used as input of a "current limitation"-block, which represents the descriptions of Chp. 5.5.1. Based on the priorities $\mathbf{V}$ of the functions, for each function the occupied current resources of the functions with higher priorities are calculated by $\tilde{\mathbf{o}}_{S,dq_k}$, which is a matrix where each vector corresponds to a combination of current requests and current reserves of functions with higher priorities. For each

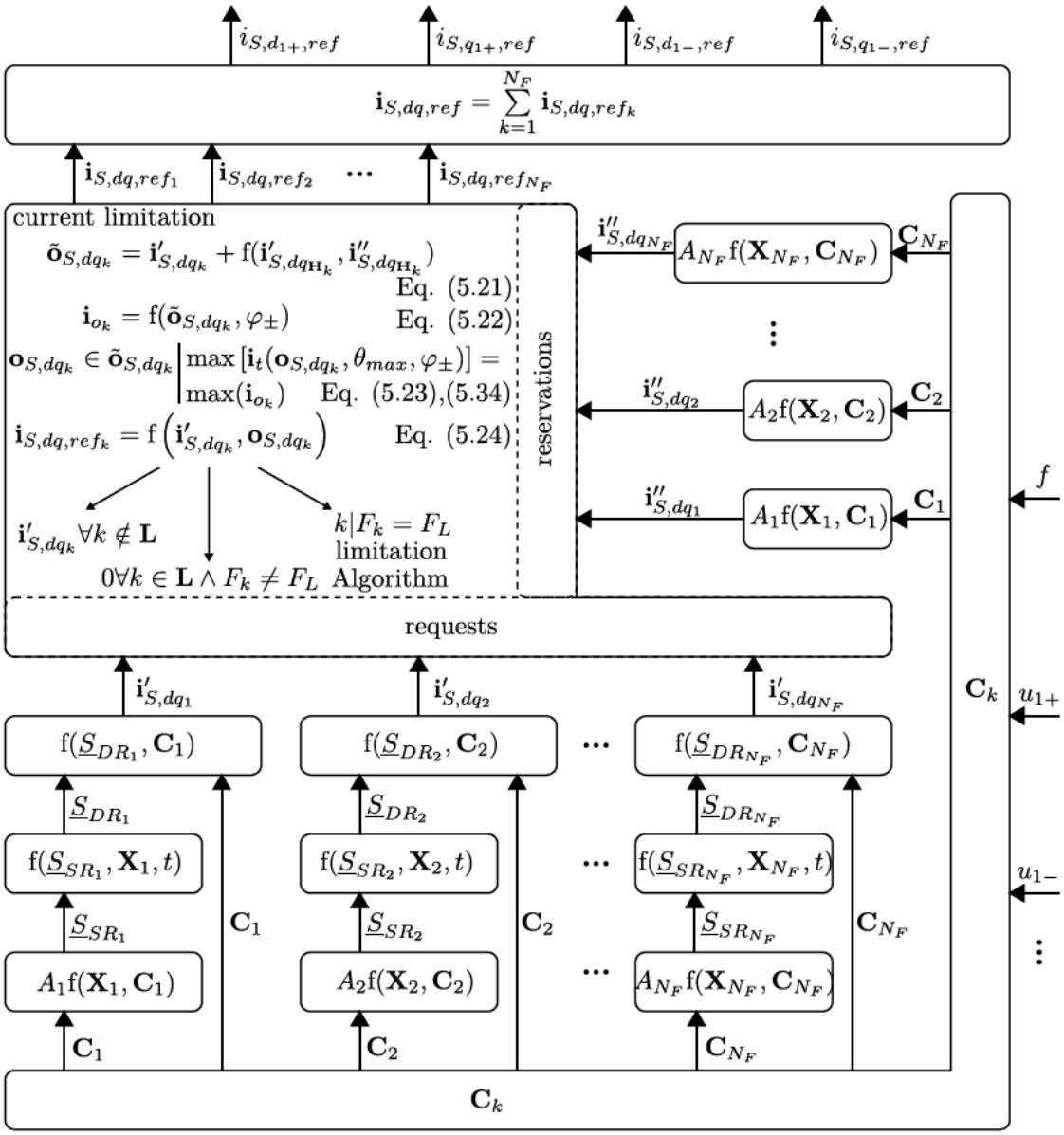

Figure 5.7: Block diagram to describe the procedure of dynamic prioritization of functions. The block diagram corresponds to the "power control" in Fig. 5.6.

of these vectors, a maximum phase current can be calculated. These values of maximum phase currents for each vector in the set $\tilde{\mathbf{o}}_{S,dq_k}$ are summarized in $\mathbf{i}_{o_k}$. There is one vector $\mathbf{o}_{S,dq_k} \in \tilde{\mathbf{o}}_{S,dq_k}$ whose maximum phase current leads to a maximum in $\mathbf{i}_{o_k}$. For all functions whose corresponding value $\max(\mathbf{i}_{o_k}) > i_{max}$, the current requests have to be limited. They are part of a set of limited functions whose function index k is part of the set $k \in \mathbf{L}$. For all functions which are not part of $\mathbf{L}$. the current requests $\mathbf{i}'_{S,dq_k}$ are identical to their executable currents $\mathbf{i}_{S,dq,ref_k}$. There is one function - the function F_L - which has the highest priority among all limited functions. The executable current $\mathbf{i}_{S,dq,ref_L}$ of the function F_L has to be calculated based on a current limitation algorithm described in Chp. 5.5.1. The executable currents of all other functions that are part of $\mathbf{L}$ have to be limited to zero.

As shown in Fig. 5.7, the reference currents $\mathbf{i}_{S,dq,ref}$ are composed of the executable currents $\mathbf{i}_{S,dq,ref_k}$ of all functions F_k. The four components of the reference currents $\mathbf{i}_{S,dq,ref}$ are the output of the block diagram in Fig. 5.7 and are used as input of the "inverter current control" in Fig. 5.6.

5.5.3 Description of Selected Functions

Based on the services described in Chp. 3.3, selected functions are presented in this chapter, which are described within the mathematical framework of Chp. 5.5. Tab. 5.2 gives an overview of these functions. Each of the functions is assigned a function index according to Eq. (5.2).

Table 5.2: Overview of selected functions.

function	function description
F_1	Frequency containment reserve (FCR)
F_2	Management of the state of charge (SoC-management)
F_3	Fast Reserve (FR)
F_4	Synthetic inertia (SI)
F_5	Static voltage support
F_6	Dynamic voltage support
F_7	Island operation
F_8	Arbitrage

5.5.3.1 F_1 Frequency Containment Reserve (FCR)

FCR has already been mentioned in Chp. 3.3 as the first stage of the conventional load-frequency control. Following a difference between load and generation in the electric power grid, a frequency deviation in relation to the nominal frequency f_n occurs. All technical entities (TE) which are providing FCR are taking part in stabilizing the grid frequency according to a droop control. According to the system operation guideline (SOGL) [60], which defines the regulatory requirements for FCR in Continental Europe, a full activation of FCR takes place in the case of a frequency deviation of 200 mHz. A full activation equals a power output of the TE, which is identical to the corresponding tendered FCR-power. The full activation time (FAT) after which such a full activation has to be reached is 30 s following the occurrence of a frequency deviation. These requirements are illustrated in Fig. 5.8, where the frequency deviation is calculated by

$$\Delta f = f - f_n. \tag{5.38}$$

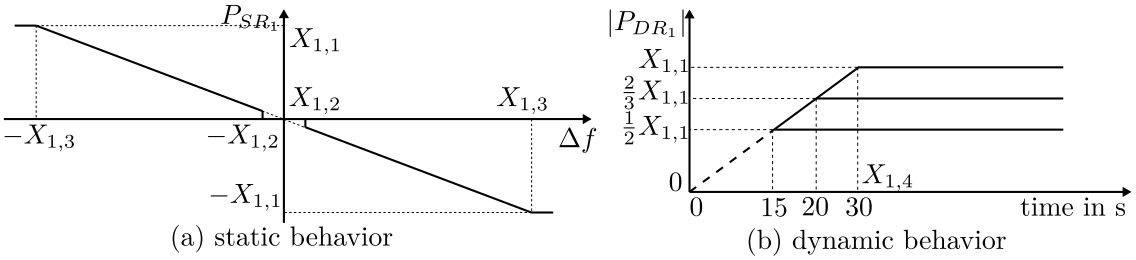

Figure 5.8: Static and dynamic behavior of FCR.

In accordance with Chp. 5.5, the corresponding statically and dynamically requested powers of the function F_1 can be defined by

$$\underline{S}_{SR,1} = P_{SR_1} = A_1 \cdot X_{1,1} \cdot \frac{\Delta f}{X_{1,3}} \cdot \begin{cases} 0, & |\Delta f| < X_{1,2}, \\ 1, & else \end{cases} \tag{5.39}$$

and

$$\underline{S}_{DR_1}(t) = P_{DR_1}(t) = P_{DR_1}(t - \Delta t) + \frac{X_{1,1}}{X_{1,4}} \cdot \begin{cases} \Delta t, & P_{DR_1}(t - \Delta t) < \underline{S}_{SR,1}, \\ -\Delta t, & P_{DR_1}(t - \Delta t) > \underline{S}_{SR,1}, \\ 0, & else \end{cases}. \tag{5.40}$$

The parameter $X_{1,2}$ defines a frequency deadband, which represents an insensitivity area that takes into account possible frequency measurement errors and which is usually defined with 10 mHz. All parameters $\mathbf{X}_1$ of the function F_1 are summarized in Tab. 5.3.

Table 5.3: Parameters $\mathbf{X}_1$ of function F_1.

parameter	parameters description
$X_{1,1}$	tendered FCR-power
$X_{1,2}$	frequency deadband (usually 10 mHz)
$X_{1,3}$	full activation frequency (200 mHz according to SOGL [60])
$X_{1,4}$	Full activation time (30 s according to SOGL [60])

Although most of the parameters in $\mathbf{X}_1$ are prescribed by SOGL [60], there are cases where some of them may be altered. For example, it may be an option to dynamically adapt the parameters dependent on the SoC in order to contribute to SoC-management, as described in [122].

According to Fig. 5.7, the corresponding current request of function F_1 has to be calculated based on the dynamically requested power. Taking into account the descriptions in Chp. 2.1.5.2, the current request can be calculated by

$$\mathbf{i}'_{S,dq_1} = \left(\frac{\underline{S}_{DR_1}}{S_n} \frac{1}{u_{1+}}, 0, 0, 0 \right)^\top. \tag{5.41}$$

The control variables of function F_1 can therefore be summarized to $\mathbf{C}_1 = \{f, u_{1+}\}$. Assuming $A_1 = 1$ and nominal frequency $f = f_n$, a power increment with a value of $X_{1,1}$ should be possible all the time. Therefore, a corresponding current reservation according to Fig. 5.7 has to be done. This current reservation can be calculated by

$$\mathbf{i}''_{S,dq_1} = \pm A_1 \cdot \left(\frac{X_{1,1}}{S_n} \frac{1}{u_{1+}}, 0, 0, 0 \right)^\top \tag{5.42}$$

in accordance with Eq. (5.13).

5.5.3.2 F_2 SoC-Management

Due to the limited energy reservoir of a BESS, a suitable SoC-management is essential. The SoC-management does not implement a corresponding service, but ensures that other services can be offered continuously. The basic concept for handling energy resources has already been described in Chp. 5.3. This function implements the behavior described in Fig. 5.3, which shows an energy band within which the state of energy is allowed during real-time operation. The state of energy is directly related to the state of charge. However, during real-time operation usually the state of

charge is used. The energy bands of Fig. 5.3 can be transformed into corresponding SoC-bands. The consideration of each SoC-band leads to an area within which the actual SoC is allowed to operate, which is termed as "working area" of the SoC. This function therefore ensures that the actual SoC is kept within this working area. When the actual SoC of the BESS reaches the corresponding limits of such SoC-bands, a charging or discharging action is initiated.

According to Fig. 5.3 a symmetrical energy band, and therefore SoC-band has to be considered for FCR.

Fig. 5.9 shows a possible implementation of such a behavior in function F_2.

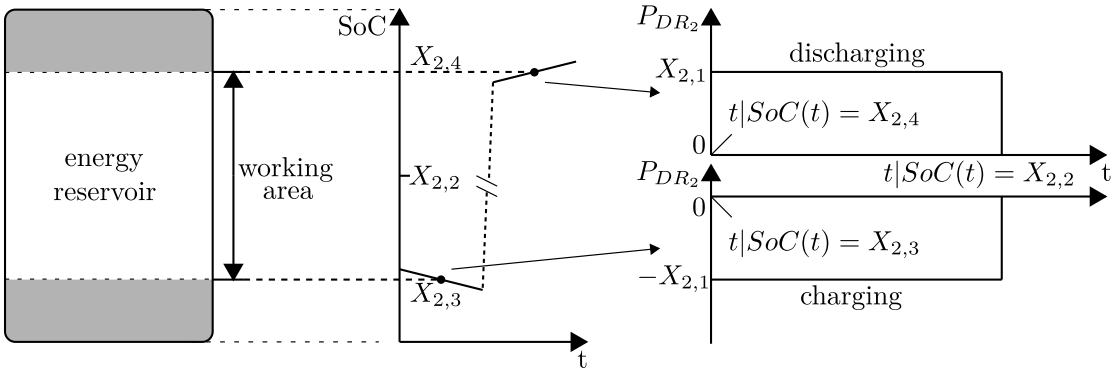

Figure 5.9: Behavior of SoC-management.

In accordance with Chp. 5.5 the corresponding statically and dynamically requested powers of the function F_2 can be defined by

$$\underline{S}_{SR,2} = P_{SR_2} = A_2 \cdot X_{2,1} \cdot \begin{cases} -1, & SoC \leq X_{2,3}, \\ 1, & SoC \geq X_{2,4}, \\ 0, & else \end{cases} \tag{5.43}$$

and

$$\underline{S}_{DR_2}(t) = P_{DR_2}(t) = P_{DR_2}(t - \Delta t) \cdot \begin{cases} 1, & SoC \neq X_{2,2}, \\ 0, & else \end{cases} + \underline{S}_{SR_2} \cdot \begin{cases} 1, & P_{DR_2}(t - \Delta t) = 0, \\ 0, & else. \end{cases} \tag{5.44}$$

All parameters $\mathbf{X}_2$ of the function F_2 are summarized in Tab. 5.4.

Table 5.4: Parameters $\mathbf{X}_2$ of function F_2.

parameter	parameters description
$X_{2,1}$	power for SoC-management
$X_{2,2}$	target-SoC
$X_{2,3}$	lower limit of SoC-band
$X_{2,4}$	upper limit of SoC-band

According to Fig. 5.7 the corresponding current request of function F_2 has to be calculated based on the dynamically requested power. Taking into account the descriptions in Chp. 2.1.5.2, the current request can be calculated by

$$\mathbf{i}'_{S,dq_2} = \left(\frac{\underline{S}_{DR_2}}{S_n} \frac{1}{u_{1+}}, 0, 0, 0 \right)^\top . \tag{5.45}$$

The control variables of function F_2, therefore, can be summarized to $\mathbf{C}_2 = \{SoC, u_{1+}\}$. Although SoC-management is essential for continuous operation of the BESS, a corresponding power reservation for function F_2 may not be necessary when assuming a suitable operation management, which handles the priorities of functions, their activations and parametrization of their parameters. Therefore, the current reservation of function F_2 is defined by

$$\mathbf{i}''_{S,dq_2} = (0,0,0,0)^\top . \tag{5.46}$$

5.5.3.3 F_3 Fast Reserve (FR)

As already described in Chp. 3.3, "Fast Reserve" (FR) is one possibility to offer a service which acts as faster control reserve. FR basically has a similar behavior as FCR, but its full activation time is much shorter, compared to the full activation time of FCR. Futhermore, its duration of activation is limited, whereas the duration of activation of FCR generally is not limited. The static and dynamic behavior of FR is illustrated in Fig. 5.10.

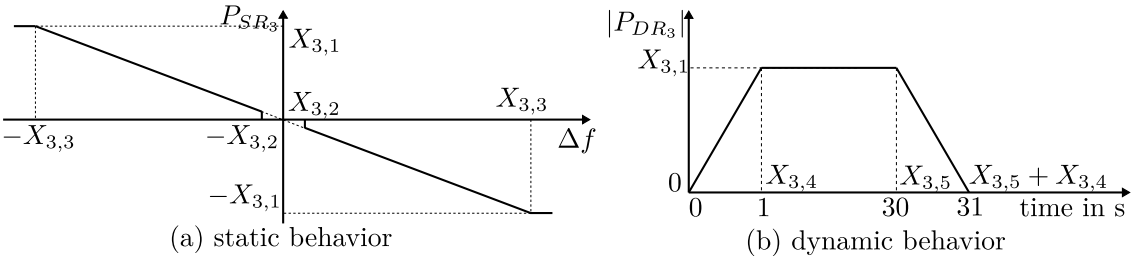

Figure 5.10: Static and dynamic behavior of FR.

As shown in Fig. 5.10(a), the static behavior looks identical to the static behavior of FCR, which is shown in Fig. 5.8(a). But as already mentioned, the dynamic behavior which is shown in Fig. 5.10(b) of FR looks different compared to the dynamic behavior of FCR which is shown in Fig. 5.8(b). The full activation of FR has to be reached within 1 s (respectively the value parametrized in $X_{3,4}$) after a frequency deviation of 200 mHz (respectively the value parametrized in $X_{3,3}$). But compared to FCR, the dynamic behavior of FR includes a "release time" $X_{3,5}$ after which the power output returns to zero, independent from the actual frequency deviation.

In accordance with Chp. 5.5 the corresponding statically and dynamically requested powers of the function F_3 can be defined by

$$\underline{S}_{SR,3} = P_{SR_3} = A_3 \cdot X_{3,1} \cdot \frac{\Delta f}{X_{3,3}} \cdot \begin{cases} 0, & |\Delta f| < X_{3,2}, \\ 1, & else \end{cases} \tag{5.47}$$

which looks similar to $\underline{S}_{SR_1}$ and

$$\underline{S}_{DR_3}(t) = P_{DR_3}(t) = P_{DR_3}(t-\Delta t) + \frac{X_{3,1}}{X_{3,4}} \cdot \begin{cases} \Delta t, & \left[P_{DR_3}(t-\Delta t) < \underline{S}_{SR,3} \wedge a_3 = 1\right] \vee \\ & \left[a_3 = 0 \wedge P_{DR_3} < 0)\right], \\ -\Delta t, & \left[P_{DR_3}(t-\Delta t) > \underline{S}_{SR,3} \wedge a_3 = 1\right] \vee \\ & \left[a_3 = 0 \wedge P_{DR_3} > 0)\right], \\ 0, & else \end{cases} \tag{5.48}$$

where a_3 is related to the release time $X_{3,5}$ according to Fig. 5.10. The issue with the implementation of such a release time is the dealing with part activations. For example, assuming a frequency deviation which oscillates between $X_{3,2} < \Delta f < X_{3,3}$, the power gradient and the power output

of the function changes continuously. The determination of the release time for such a situation is a more complex issue than illustrated in Fig. 5.10. It is even more difficult when the frequency deviation oscillates in a small range around the frequency deadband $X_{3,2}$. The "timer" for the release time has to be defined rather clearly to deal with such part activations. The start of such a timer is defined by the moment when the frequency deviation reaches the frequency deadband and when the function F_3 is not already active ($a_3 = 0$):

$$T_3 = \max \left[t \middle| |\Delta f(t)| \geq X_{3,2} \wedge |\Delta f(t - \Delta t)| < X_{3,2} \wedge a_3 = 0 \right]. \tag{5.49}$$

By defining a time mean value of the frequency deviation

$$\overline{\Delta f} = \frac{1}{t - T_3} \int_{T_3}^{t} \Delta f(\tau)\, d\tau \tag{5.50}$$

the "timer" for the release time can be defined by

$$a_3 = \begin{cases} 1, & |\overline{\Delta f}| \geq X_{3,2} \wedge (t - T_3) \leq X_{3,5}, \\ 0, & else \end{cases} \tag{5.51}$$

which is used in Eq. (5.48) to consider the release time. The time mean value $\overline{\Delta f}$ ensures that in case of an oscillation around the frequency deadband, the function F_3 becomes also inactive after a release time $X_{3,5}$. Since a_3 immediately switches from 1 to 0 when the release time $X_{3,5}$ is reached, Eq. (5.48) takes into account the terms $[a_3 = 0 \wedge P_{DR_3} < 0)]$ and $[a_3 = 0 \wedge P_{DR_3} > 0)]$ in order to describe the gradual decrease of P_{DR_3} back to zero, as shown in Fig. 5.10. All parameters $\mathbf{X}_3$ of the function F_3 are summarized in Tab. 5.5.

Table 5.5: Parameters $\mathbf{X}_3$ of function F_3.

parameter	**parameters description**
$X_{3,1}$	tendered EFR-power
$X_{3,2}$	frequency deadband (e.g. 50 mHz)
$X_{3,3}$	full activation frequency (e.g. 200 mHz)
$X_{3,4}$	Full activation time (1 s according to TERNA [178])
$X_{3,5}$	Release time (e.g. 30 s)

According to Fig. 5.7, the corresponding current request of function F_3 has to be calculated based on the dynamically requested power. Taking into account the descriptions in Chp. 2.1.5.2, the current request can be calculated by

$$\mathbf{i}'_{S,dq_3} = \left(\frac{S_{DR_3}}{S_n} \frac{1}{u_{1+}}, 0, 0, 0 \right)^{\top}. \tag{5.52}$$

The control variables of function F_3, therefore, can be summarized to $\mathbf{C}_3 = \{f, u_{1+}\}$. Chp. 5.6 describes how FCR and FR can be offered in combination by a single BESS. In such a combined operation a current reservation of function F_1 (FCR) can also be used by the function F_3 (FR), since F_3 acts much faster than F_1 and can be considered to be decoupled in time. A current reservation, therefore, is only useful when F_1 is deactivated or the tendered FR-power $X_{3,1} > X_{1,1}$ is higher than the tendered FCR-power. The current reservation of function F_3, therefore, can be defined by

$$\mathbf{i}''_{S,dq_3} = \pm A_3 \cdot \left(\frac{1}{u_{1+}} \frac{1}{S_n} \cdot \begin{cases} 0, & A_1 = 1 \wedge X_{3,1} \leq X_{1,1}, \\ (X_{3,1} - X_{1,1}), & A_1 = 1 \wedge X_{3,1} > X_{1,1}, \\ X_{3,1}, & else \end{cases}, 0, 0, 0 \right)^{\top}. \tag{5.53}$$

5.5.3.4 F_4 Synthetic Inertia (SI)

Synthetic inertia was introduced in Chp. 3.3 as imitation of the behavior of mechanical inertia in converter-based systems. A detailed description of possible implementations of synthetic inertia is given in [115]. The statically requested power of synthetic inertia is defined by

$$\underline{S}_{SR_4} = P_{SR,4} = A_4 \cdot X_{4,1}X_{4,2}\frac{df}{dt}\frac{f}{f_n^2} \cdot \begin{cases} 1, & \left|\dot{f}\right| > X_{4,3} \wedge \left[sgn(\dot{f}) = sgn(\Delta f)\right], \\ 0, & else \end{cases} \tag{5.54}$$

where the parameter $X_{4,1}$ represents the starting time constant and the parameter $X_{4,2}$ represents the apparent power of a corresponding mechanical inertia, whose behavior is imitated by the function F_4. The parameter $X_{4,3}$ defines a frequency gradient deadband. The term $\left[sgn(\dot{f}) = sgn(\Delta f)\right]$ leads to a zone-selective activation of the function, which ensures the function to request power only when it is contributory to the frequency restoration process. More details of the advantages of such a zone-selective activation are discussed in [73]. As synthetic inertia should be available instantaneously, the dynamically requested power is identical to the statically requested power:

$$\underline{S}_{DR_4} = P_{DR,4} = \underline{S}_{SR_4}. \tag{5.55}$$

All parameters $\mathbf{X}_4$ of the function F_4 are summarized in Tab. 5.6.

Table 5.6: Parameters $\mathbf{X}_4$ of function F_4.

parameter	parameters description
$X_{4,1}$	starting time constant of a corresponding generator whose mechanical inertia is to be imitated
$X_{4,2}$	apparent power of a corresponding generator whose mechanical inertia is to be imitated
$X_{4,3}$	frequency gradient deadband

According to Fig. 5.7 the corresponding current request of function F_4 has to be calculated based on the dynamically requested power. Taking into account the descriptions in Chp. 2.1.5.2, the current request can be calculated by

$$\mathbf{i}'_{S,dq_4} = \left(\frac{\underline{S}_{DR_4}}{S_n}\frac{1}{u_{1+}}, 0, 0, 0\right)^\top. \tag{5.56}$$

The control variables of function F_4, therefore, can be summarized to $\mathbf{C}_4 = \{f, \dot{f}, u_{1+}\}$.

Similar to function F_1, a certain power increment requested by function F_4 should be possible at any time in order to ensure a certain response to occurring frequency gradients. Otherwise the function F_4 would not be able to provide inertial response when other active power functions already occupy resources. In order to define a reasonable value for the current reservation, the maximum value of $\underline{S}_{SR_4}$ has to be considered. According to Eq. (5.54), this maximum value is depending on the maximum value of the frequency gradient $\dot{f}$ and the frequency f. The maximum frequency gradient in Continental Europe today is likely to be less than 1 Hz/s [149], including situations of system split. The maximum frequency can be considered with 51.5 Hz, as the protection relays of generators usually are parametrized to disconnect at frequencies above this value. Taking into account these values, the current reservation for function F_4 can be defined by

$$\mathbf{i}''_{S,dq_4} = \pm A_4 \cdot \left[\left(X_{4,1}X_{4,2}\frac{\dot{f}_{max} \cdot f_{max}}{f_n^2}\frac{1}{S_n}\frac{1}{u_{1+}}\right), 0, 0, 0\right]^\top = A_4 \cdot \left[\left(X_{4,1}X_{4,2} \cdot \frac{0.02}{\mathrm{s}}\frac{1}{S_n}\frac{1}{u_{1+}}\right), 0, 0, 0\right]^\top \tag{5.57}$$

in accordance with Eq. (5.13).

Assuming the parameters $X_{4,1}$ to be $X_{4,1} = 10\,\mathrm{s}$, which corresponds to the starting time constant of a typical gas turbine, and $X_{4,2} = S_n$, which leads to an imitation of the mechanical inertia of a gas turbine with an apparent power of S_n, and $u_{1+} = 1\,\mathrm{pu}$, this would lead to a current reservation of 20 %.

5.5.3.5 F_5 Static Voltage Support

Many grid codes, for example [41] in Austria and [183] in Germany, require inverter-based generators to provide static voltage support. This is achieved by certain reactive power consumption or reactive power infeed, depending on the actual voltage in the grid. The reactive power influences the local grid voltage and can therefore be actively controlled in order to support the voltage maintenance in the grid. There are several options to define the behavior of such a static voltage support:

- according to a voltage droop control [Q(U)-control],
- according to a power factor depending on the actual active power output [$\cos\varphi(P)$-control] ,
- according to a fixed power factor [$\cos\varphi$-control], or
- according to a parametrizeable value of reactive power (Q-control).

The last option, Q-control, is considered and described by function F_5. A description of the other options within the mathematical framework of Chp. 5.5 is easily possible. In accordance with Chp. 5.5 the statically requested powers of the function F_5 can be defined by

$$\underline{S}_{SR,5} = jQ_{SR_5} = A_5 \cdot jX_{5,1}. \tag{5.58}$$

There are no special requirements on the dynamic behavior of static voltage support. Therefore, the dynamically requested power equals the statically requested power:

$$\underline{S}_{DR,5} = jQ_{DR_5} = \underline{S}_{SR,5}. \tag{5.59}$$

Taking into account the descriptions in Chp. 2.1.5.3, the current request can be calculated by

$$\mathbf{i}'_{S,dq_5} = \left(0, \frac{\underline{S}_{DR_5}}{S_n}\frac{1}{u_{1+}}, 0, 0\right)^\top \tag{5.60}$$

where the parameter $X_{5,1}$ is a parametrizable value of the reactive power. The control variables of function F_5 can therefore be summarized to $\mathbf{C}_5 = \{u_{1+}\}$. As static voltage support does not require a certain power increment, but rather requires the voltage to be influenced over longer periods, there is no need for current reservation. The corresponding current reservation of function F_5 can therefore be defined by

$$\mathbf{i}''_{S,dq_5} = (0,0,0,0)^\top. \tag{5.61}$$

5.5.3.6 F_6 Dynamic Voltage Support

Besides the static voltage support, many grid codes also require inverter-based generators to provide dynamic voltage support. Similar to static voltage support, dynamic voltage support is achieved by reactive power injection or consumption. While static voltage support is used for contributing to voltage maintenance during normal grid conditions, dynamic voltage support becomes active only during grid faults, for example, short-circuits, to dynamically stabilize the voltage during such conditions. The prescriptions in grid codes, for example in [41] and [183], require a certain reactive current increment in response to the voltage drop during short-circuits. Due to these prescriptions, the direct definition of the current request of a function F_6, which describes the dynamic voltage support, is easier than defining it via the dynamically requested power, as it was the case with foregoing functions. The Park-components of this current request of function F_6 can be defined by

$$i'_{S,q_{1+},6} = A_6 \cdot \begin{cases} X_{6,2} \cdot \Delta u_{1+}, & |\Delta u_{1+}| > X_{6,1}, \\ 0, & else \end{cases} \tag{5.62}$$

$$i'_{S,q_{1-},6} = A_6 \cdot \begin{cases} X_{6,3} \cdot \Delta u_{1-}, & |\Delta u_{1-}| > X_{6,1}, \\ 0, & else \end{cases} \tag{5.63}$$

where the voltage deviation in the positive-sequence system Δu_{1+} and the voltage deviation in the negative-sequence system Δu_{1-} are defined by

$$\Delta u_{1+} = u_{1+} - \overline{u}_{1min} \tag{5.64}$$

$$\Delta u_{1-} = u_{1-} - \overline{u}_{1min} \tag{5.65}$$

which represent the voltage deviations of the actual voltages in relation to the time mean value $\overline{u}_{1min}$ of the voltage before the occurrence of a short-circuit:

$$\overline{u}_{1min} = \frac{1}{1\,\mathrm{min}} \int_{t-1min}^{t} \frac{\|\mathbf{u}\|_1}{3}\, d\tau \tag{5.66}$$

where $\mathbf{u}$ is the RMS value of $\mathbf{u}_{N,t}$. This leads to a current request of the function F_6 of

$$\mathbf{i}'_{S,dq_6} = \left(0, i'_{S,q_{1+},6}, 0, i'_{S,q_{1-},6}\right)^\top. \tag{5.67}$$

All parameters $\mathbf{X}_6$ of the function F_6 are summarized in Tab. 5.7.

Table 5.7: Parameters $\mathbf{X}_6$ of function F_6.

parameter	parameters description
$X_{6,1}$	voltage deadband (usually $10\,\% \cdot U_n$)
$X_{6,2}$	linear factor of reactive current injection in the positive-sequence system (usually this value is 2)
$X_{6,3}$	linear factor of reactive current injection in the negative-sequence system (usually this value is 2)

The current request $\underline{i}'_{S,dq_6}$ of the function F_6 can be calculated based on Eq. (5.27) with the corresponding Park-components defined above. The relation to the statically and dynamically requested power can be calculated according to Chp. 2.1.5.1 by

$$\underline{S}_{SR_6} = jQ_{SR_6} = \underline{S}_{DR_6} = jQ_{DR_6} = jS_n \left(u_{1+} i'_{S,q_{1+},6} + u_{1-} i'_{S,q_{1-},6}\right). \tag{5.68}$$

The control variables of function F_6 can therefore be summarized to $\mathbf{C}_6 = \{u_{1+}, u_{1-}, \mathbf{u}\}$.

Although the function F_6 requires a certain power increment in response to a voltage drop, Chp. 5.6 shows that such a power increment can be achieved by assigning this function the highest priority. Therefore, the current reservation of function F_6 is defined by

$$\mathbf{i}''_{S,dq_6} = (0,0,0,0)^\top . \tag{5.69}$$

5.5.3.7 F_7 Island Operation

All foregoing functions rely on a converter control structure as shown in Fig. 5.6, which is referred to as "grid-following" control approach. A grid-following control approach is based on a measurement of the grid angle θ by the "grid synchronization" as shown in Fig. 5.6. Therefore, such an approach is only feasible in case there are other generating units in the grid as well. In case of a Microgrid, on the other hand, where a BESS is the only generating unit, a so called "grid-forming" control approach has to be applied instead of a grid-following approach. With a grid-forming control approach, the grid angle θ is generated by the converter itself instead of measuring it based on the grid voltage. Therefore, an island operation requires the implementation of such a grid-forming control approach. This makes the function F_7, which describes the island operation, the only function out of the list in Tab. 5.2, which requires the control structure of Fig. 5.6 to be changed. A description of how to achieve such a change of the control approach from grid-following to grid-forming, for example, is illustrated in [115]. Due to this necessary change of the control approach, the combined activation of any function in Tab. 5.2 together with function F_7 automatically becomes a member of the set $\boldsymbol{\mathcal{U}} = \{\mathbf{A} \in \mathbf{B}^{N_F} | A_7 = 1\}$, as defined in Eq. (5.4), and must not be activated simultaneously. Instead of the "power control", which is shown in Fig. 5.6, a grid-forming control approach has to apply a voltage control. This voltage control directly controls the Park-components of the voltage $u_{S,d}$ and $u_{S,q}$ based on PI-controllers.

As the voltage control of a grid-forming control approach delivers current requests which are further processed by the inverter current control, the current request $\underline{i}_{S,dq_7}$ of the function F_7 can be defined directly by

$$i'_{S,dq_7} = A_7 \cdot \mathrm{f}(\mathbf{u}_{N,t}, \theta) \tag{5.70}$$

which is assumed to be controlled only in the positive-sequence system by the voltage control.

The relation to the statically and dynamically requested power can be calculated according to Chp. 2.1.5.4 by

$$\underline{S}_{SR_7} = \underline{S}_{DR_7} = S_n \left(u_{1+} i'_{S,d_{1+},7} + j u_{1+} i'_{S,q_{1+},7} \right) . \tag{5.71}$$

The control variables of function F_7 can therefore be summarized to $\mathbf{C}_7 = \{\mathbf{u}_{N,t}, \theta\}$.

During island control the full current capability has to be available for function F_7. But as activations $\mathbf{A}$ with other functions activated combined with F_7 are a member of the set $\mathbf{U}$ a current reservation for the function F_7 is not necessary. Therefore, the current reservation for the function F_7 is defined by

$$\mathbf{i}''_{S,dq_7} = (0,0,0,0)^\top . \tag{5.72}$$

5.5.3.8 F_8 Arbitrage

An implementation of energy arbitrage has already been described in Chp. 4.5. In accordance with Chp. 4.5 the corresponding statically and dynamically requested powers of the function F_8 can be defined by

$$\underline{S}_{SR,8} = P_{SR_8} = A_8 \cdot X_{8,1} \cdot X_{8,2} \tag{5.73}$$

and

$$\begin{aligned} \underline{S}_{DR_8}(t) = P_{DR_8}(t) = P_{DR_8}(t-\Delta t) \cdot \begin{cases} 1, & (SoC \neq X_{8,3} \wedge X_{8,2} = 1) \vee \\ & (SoC \neq X_{8,4} \wedge X_{8,2} = -1), + \\ 0, & else \end{cases} \\ + \underline{S}_{SR_8} \cdot \begin{cases} 1, & X_{8,2}(t) \neq X_{8,2}(t-\Delta t), \\ 0, & else. \end{cases} \end{aligned} \tag{5.74}$$

All parameters $\mathbf{X}_8$ of the function F_8 are summarized in Tab. 5.8.

Table 5.8: Parameters $\mathbf{X}_8$ of function F_8.

parameter	parameters description
$X_{8,1}$	power for SoC-management
$X_{8,2}$	buy/sell-input $\{-1,+1\} \equiv$\{buy,sell\}
$X_{8,3}$	lower limit of SoC-band
$X_{8,4}$	upper limit of SoC-band

According to Fig. 5.7 the corresponding current request of function F_8 has to be calculated based on the dynamically requested power. Taking into account the descriptions in Chp. 2.1.5.2, the current request can be calculated by

$$\mathbf{i}'_{S,dq_8} = \left(\frac{\underline{S}_{DR_8}}{S_n} \frac{1}{u_{1+}}, 0, 0, 0 \right)^\top . \tag{5.75}$$

The control variables of function F_8, therefore, can be summarized to $\mathbf{C}_8 = \{SoC, u_{1+}\}$. Although SoC-management is essential for continuous operation of the BESS, a corresponding power reservation for function F_8 may not be necessary when assuming a suitable operation management, which handles the priorities of functions, their activations and parametrization of their parameters. Therefore, the current reservation of function F_8 is defined by

$$\mathbf{i}''_{S,dq_8} = (0,0,0,0)^\top . \tag{5.76}$$

5.6 Selected Applications To Demonstrate the Use of Dynamic Prioritization

The mathematical framework presented in Chp. 5.5 introduces the set of activations $\mathbf{A}$, the set of priorities $\mathbf{V}$ and the sets of parameters $\mathbf{X}_k$ for each function F_k. Compared to the sets of control variables $\mathbf{C}_k$ of each function F_k, which are also introduced in Chp. 5.5, $\mathbf{A}$, $\mathbf{V}$ and $\mathbf{X}_k$ have to be parametrized in advance to a real-time operation, whereas the control variables $\mathbf{C}_k$ are measured during real-time operation.

With regard to Chp. 5.1, the operational planning phase results in the parametrization of $\mathbf{A}$, $\mathbf{V}$ and $\mathbf{X}_k$ for each time slot of the planning horizon. As described in Chp. 5.1, this determination takes place a predefined time before the real-time operation, e.g. one day ahead.

Chp. 5.3 and Chp. 1.4 mention the difficulties of unpredictable services to be considered in the operational planning phase. Considering the services whose execution is described via functions listed in Tab. 5.2, these difficulties can be discussed in more detail. As examples for such unpredictable services, Chp. 1.4 mentions services for frequency control. Three functions for frequency control are considered in Tab. 5.2. However, while the executed powers for all of these functions are unpredictable during the operational planning phase, for the functions F_1 FCR and F_3 FR at least a corresponding reservation of resources can be considered in the form of virtual BESS. For the service F_4 SI, on the other hand, its definition in Chp. 5.5.3.4 allows the request of the full power resources of the BESS, ignoring the borders of allocated virtual BESS. In the rare event of the occurrence of very high frequency gradients, such a situation may happen. Therefore, two categories of unpredictability of functions can be identified, which are

(a) unpredictability regarding execution inside a virtual BESS and

(b) unpredictability regarding the request of resources.

Such an unpredictability type can be assigned to all functions from Tab. 5.2. The results for such an assignment are summarized in Tab. 5.9.

Table 5.9: Unpredictability of selected functions.

function	**unpredictability**	**function description**
F_1	(a)	Frequency containment reserve (FCR)
F_2	(a)	Management of the state of charge (SoC-management)
F_3	(a)	Fast Reserve (FR)
F_4	(b)	Synthetic inertia (SI)
F_5	-	Static voltage support
F_6	(b)	Dynamic voltage support
F_7	(b)	Island operation
F_8	(a)	Arbitrage

Besides the function SI, Tab. 5.9 lists Dynamic Voltage Support and Island Operation to be from unpredictability type (b). Both functions may request the full power resources of the BESS in case of a short-circuit (Dynamic Voltage Support), or in case of a blackout of the power system (Island Operation). Due to the definition of the function Static Voltage Support in Chp. 5.5.3.5 this function can be considered as perfectly predictable, since it requests a predefined amount of resources at any time. With regard to Fig. 3.7, there are several other services which can be considered as perfectly predictable, such as energy arbitrage or providing firm capacity.

Since functions of unpredictability type (b) can not be considered during the operational planning phase by allocating virtual BESS, an appropriate concept of how to react during real-time operation in case of rare events during abnormal grid conditions, where corresponding functions may exploit the full power resources, is necessary. The concept of dynamic prioritization presented in Chp. 5.5 is capable of handling such events. One goal in this chapter is therefore to demonstrate the behavior of the concept of dynamic prioritization during such events based on the functions described in Chp. 5.5.3, Chp. 5.6.1 and Chp. 5.6.2.

Chp. 5.3 describes functions of unpredictability type (a) to diminish flexibilities for other functions. The allocation of virtual BESS for such functions during the operational planning phase leads to the reservation of relatively large amounts of resources, which are fully utilized only in the case of infrequent events during real-time operation. The concept of dynamic prioritization presented in Chp. 5.5 allows a better utilization of the reserved resources from functions of unpredictability

type (a). A second goal in this chapter is therefore to demonstrate how the concept of dynamic prioritization can be used to achieve such a better utilization of resources during normal grid conditions based on the functions described in Chp. 5.5.3. Chp. 5.6.3 describes a corresponding application.

The operational planning phase may result in different priorities $\mathbf{V}$ of functions between time slots. However, based on the functions which are listed in Tab. 5.2, a meaningful static assignment of priorities can be argued, which is used in order to describe the applications in this chapter. The highest priority is assigned to function F_7, island operation, with $V_7 = 1$. Although it has already been stated in Chp. 5.5.3.7 that a combined activation of another function together with F_7 is not allowed ($\mathcal{U} = \{\mathbf{A} \in \mathbf{B}^{N_F} | A_7 = 1\}$), according to Eq. (5.18) a priority has to be assigned to all functions, because $|\mathbf{V}| = N_F$. The next higher priority is assigned to function F_6, dynamic voltage support, with $V_6 = 2$. When the function becomes active, it contributes to solve a local- and dynamic voltage problem. Since a long duration of such a voltage problem may lead to the trip of protection relays in the feeder the BESS is connected to, the prevention of such a situation has high priority. Since fault conditions in the grid typically only last for short time periods until the fault is cleared (e.g. several seconds), the possible limitation of other functions by F_6 may not be considerable, for example regarding revenues. In addition, the function only provides reactive power, and therefore does not influence the SoC. The next higher priority is assigned to function F_2, SoC-Management, with $V_2 = 3$. Since the function ensures an appropriate energy reservoir at any time, which is necessary for a continuous provision of services, its priority is relatively high. Although functions as F_3, FR, and F_4, SI, are little energy intensive and are only active during short durations, a possible current reservation by these functions may lead to a longer lasting limitation of the function F_2, SoC-Management, when they are assigned higher priority than F_2 has. In order to prioritize current requests of F_2 over current reservations of other functions, the priority of F_2 is higher than the priorities of the remaining functions. The next higher priorities are assigned to the functions F_4, VI, F_3, FR and F_1, FCR, with $V_4 = 4$, $V_3 = 5$ and $V_1 = 6$. Since all of these three functions are contributing to the global stabilization of the frequency in the grid, which is one of the most relevant services in the electric power system, their priorities are relatively high. The function F_6 has higher priority $V_6 < \{V_4, V_3, V_1\}$, because the clearance of a local dynamic voltage problem is considered to be more important than the global frequency stabilization. The assignment of priorities between the three functions is discussed in more detail in Chp. 5.6.2. The lowest priority are assigned to function F_8, arbitrage, with $V_8 = 7$ and to function F_5, static voltage support, with $V_5 = 8$. Since the contribution to static voltage support can be considered as long-term goal, a possible limitation by other functions may not be a problem as long as the function can be temporarily active between times of short-time limitations. The limitation of the function arbitrage only has an influence on the achievable revenues, but does not affect the general functionality of this function.

For all applications it is assumed that a BESS with an apparent power of $S_n = 2.5\,\text{MVA}$ is offering the corresponding services of the functions of Tab. 5.2 with an assignment of priorities as described above: $\mathbf{V} = \{6, 3, 5, 4, 8, 2, 1, 7\}$. Furthermore, a nominal frequency of $f_n = 50\,\text{Hz}$ and a maximum current capability of $i_{max} = 1.1\,\text{pu@}u_{1+} < 0.9\,\text{pu}$ and $i_{max} = 1\,\text{pu@}u_{1+} > 0.9\,\text{pu}$ are assumed.

5.6.1 Application 1: Occurrence of Grid Faults

A short-circuit event can be viewed as an abnormal grid condition that cannot be predicted in the scope of the operational planning phase. During short-circuit events in the grid, the function F_6, Dynamic Voltage Support, becomes active in order to dynamically stabilize the grid voltage. At the moment of occurrence of the short-circuit, other functions of the BESS may be active already. Due to the high priority of the function F_6, its current request is prioritized over the current requests of other functions. Fig. 5.11(a) shows the normalized phase-to-phase voltages $\mathbf{u}$ during a two-phase short-circuit nearby the point of common coupling of the BESS, which were measured in the scope

of [196]. The two-phase short-circuit leads to a drop in the positive-sequence voltage u_{1+} and a rise in the negative-sequence voltage u_{1-}. According to Chp. 5.5.3.6 this leads to current requests $\mathbf{i}'_{S,dq_6} = (0, X_{6,2}\Delta u_{1+} > 0, 0, X_{6,3}\Delta u_{1-} < 0)^\top$ of the function F_6. Assuming the functions F_2 and F_6 to be the only activated functions $\mathbf{A} = \{0,1,0,0,0,1,0,0\}$ and also assuming the function F_2, SoC-Management, to be active before, during and after the short-circuit, this leads to a conflict of functions. It is assumed that $SoC > X_{2,4}$ and $X_{2,1} = 1\,\text{MW}$, which corresponds to $S_n \cdot 0.4\,\text{pu}$. Fig. 5.11(b) shows the corresponding current requests of the functions F_2 and F_6. Because of the drop of u_{1+} during the short-circuit, the current request of F_2 rises according to Eq. (5.45). Fig. 5.11(c) shows the corresponding executable currents. The current requests of the function F_6 are $i'_{S,q_{1+},6} = 0.91\,\text{pu}$ and $i'_{S,q_{1-},6} = -0.91\,\text{pu}$, which lead to a conflict of functions in combination with the current request of the function F_2, which is $i'_{S,d_{1+},2} = 0.7\,\text{pu}$. Due to the higher priority of F_6 in relation to F_2, with $V_6 < V_2$, the executable current of F_2 during the short-circuit is $i_{S,d_{1+},ref_2} = 0\,\text{pu}$. According to Chp. 5.5.1 also the current requests of F_6 have to be limited to respect the maximum current capability. Fig. 5.11(d) shows the corresponding phase currents, which result from the executable currents.

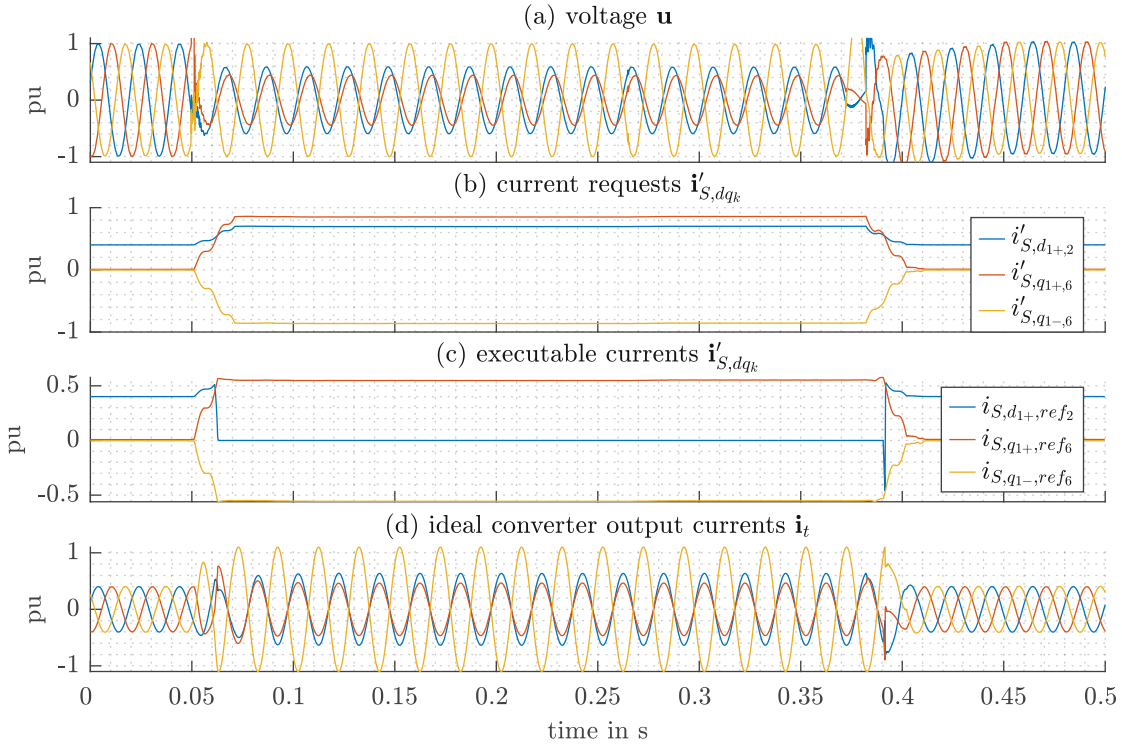

Figure 5.11: Dynamic prioritization during short-circuit event.

Fig. 5.12 shows the corresponding vector diagrams in the $\alpha\beta$-plane before and during the short-circuit event. Fig. 5.12(b) shows that the execution of the requested current space vector $\underline{i}'_S$ would exceed the current capability of i_{max}. The current limitation leads to a corresponding executable current space vector $\underline{i}_{S,ref}$. Fig. 5.11(c) and Fig. 5.12(b) both show that the maximum current capability of $i_{max} = 1.1\,\text{pu}$ is respected by this executable current space vector $\underline{i}_{S,ref}$.

With regard to Fig. 5.4 and Fig. 5.5, a comparison of the corresponding concepts of static power band assignment and dynamic prioritization can be made. Assuming a situation as described above and applying the concept of static power band assignment according to Fig. 5.4, this would make it necessary to predefine power bands for the function F_2 and F_6. This would lead to a different behavior in Fig. 5.11(c) and (d), where the output of function F_2 would remain constant and the

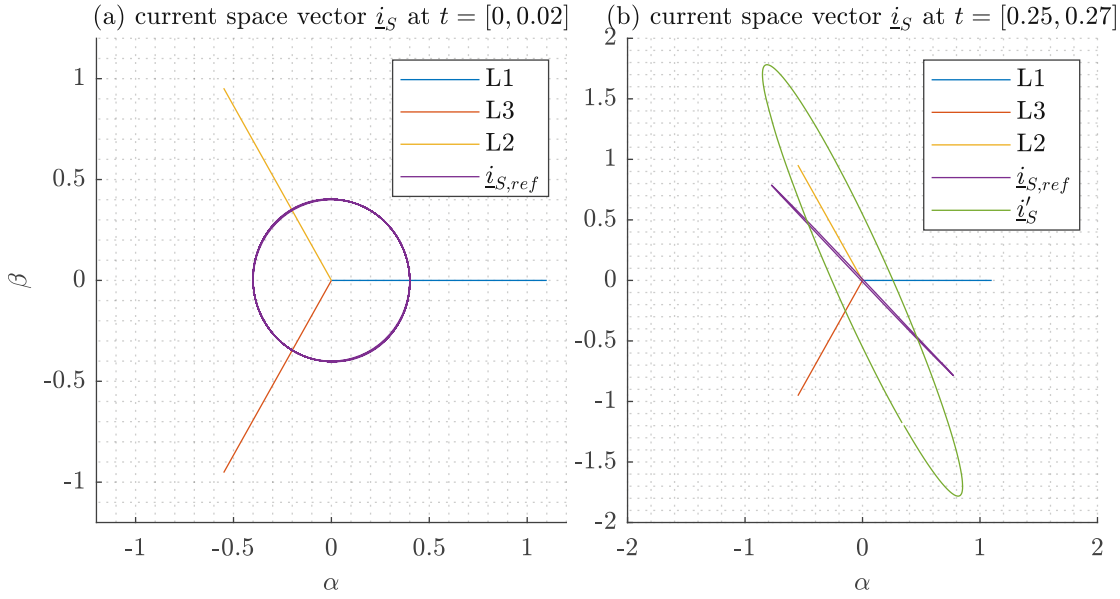

Figure 5.12: Vector diagrams of the space vectors in the $\alpha\beta$-plane before (a) and during (b) the short-circuit event. In (a) and (b) the vectors L1,L2 and L3 all have a length of i_{max}. (b) shows that during the short-circuit event the projection of $\underline{i}_{S,ref}$ on L3 equals the maximum current capability i_{max}.

reactive current contributions of F_6 would be lower. The result would be a less effective influence on the dynamic voltage stabilization during the short-circuit. Applying the concept of dynamic prioritization, on the other hand, allows the function F_6 to fully exploit the current capability of the BESS, without the necessity to share the power capability between F_2 and F_6.

5.6.2 Application 2: Simultaneous Provision of Frequency Reserves

With Synthetic Inertia (SI), Fast Reserve (FR) and Frequency Containment Reserve (FCR), three frequency control services have already been discussed. These services act in different time horizons. Whereas SI acts fastest in response to a frequency deviation, it is followed by FR and FCR, the latter acting slowest among the three services. Although the three services interact during activation, they can approximately be viewed as decoupled in time. Such a view opens up the possibility of providing all services based on the same power reserves without having to allocate reservations for each service. The tendering of the same amount of power reserves for different kind of frequency control services may be forbidden due to legal requirements. However, new services as FR are still under discussion, therefore, such a possibility of concurrent provision is assumed in the following.

All three services become active during frequency deviations. A so-called "reference incident" [182] is assumed to lead to the worst-case frequency deviation curve in Continental Europe. It assumes the failure of two major power plants with a corresponding power of 3 GW, leading to a frequency deviation curve as shown in Fig. 5.13(a). This reference incident is considered to discuss the simultaneous provision of the three frequency control reserves mentioned above, while applying dynamic prioritization of functions. It is assumed that the functions F_1, FCR, F_3, FR, and F_4, SI, are the only activated functions with $\mathbf{A} = \{1, 0, 1, 1, 0, 0, 0, 0\}$ and are parametrized as follows. For the function F_1, FCR, the tendered FCR-power is $X_{1,1} = 2\,\text{MW}$, which corresponds to $S_n \cdot 0.8\,\text{pu}$. For the function F_3, FR, the tendered EFR-power is $X_{3,1} = 2\,\text{MW}$, which corresponds to $S_n \cdot 0.8\,\text{pu}$.

For the function F_4, SI, the parameters are $X_{4,1} = 10\,\text{s}$ and $X_{4,2} = S_n \cdot 25$ and a static current reservation of $\mathbf{i}''_{S,dq_4} = (0.02, 0, 0, 0)^\top$ is parametrized. The positive-sequence voltage is assumed to be constant $u_{1+} = 1\,\text{pu}$.

Fig. 5.13(b) shows the corresponding current requests of the functions in response to a reference incident. In order to respect the current reservation of F_4, SI, and the maximum current capability of $i_{max} = 1\,\text{pu}$, the executable currents are calculated according to Fig. 5.7 and are shown in Fig. 5.13(c). The resulting reference currents are shown in Fig. 5.13(d).

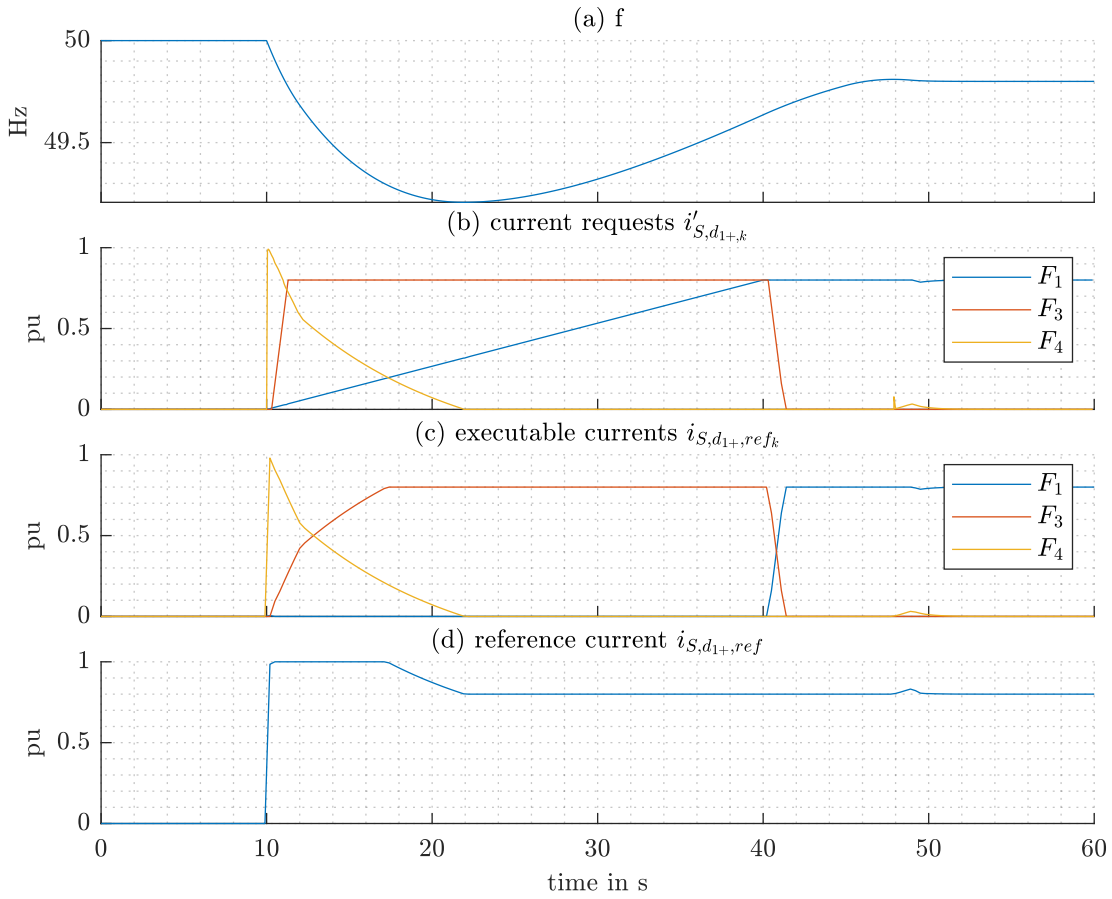

Figure 5.13: Dynamic prioritization during reference incident.

With regard to Fig. 5.4 and Fig. 5.5, a comparison of the corresponding concepts of static power band assignment and dynamic prioritization can be made. Assuming the static power band assignment is applied, any function has to be assigned a power band. Assuming the situation as described above, the power capability S_n has to be divided between the functions, for example, $\frac{S_n}{3}$ for each function. In this case, the individual functions can only be offered with this power of $\frac{S_n}{3}$. Applying dynamic prioritization, on the other hand, theoretically allows each of the functions to offer the whole power capability of S_n. In the special case of Fig. 5.13 the corresponding offerable power of F_1 and F_3 is reduced by the reservation of F_4. As shown in Fig. 5.13(c) the executable currents of F_1 and F_3, which are identical to the corresponding normalized power outputs because $u_{1+} = 1\,\text{pu}$, no longer meet their individual requirements according to the corresponding regulations regarding full activation time. However, the total power output in Fig. 5.13(d) does meet these individual requirements.

The frequency nadir is a relevant parameter during the grid stabilization after a massive power imbalance in the power system. Fig. 5.13(a) shows the frequency nadir for the reference incident. The value of this frequency nadir depends on the inertia in the power system and the reaction time (or full activation time) of frequency reserves [169]. The higher the inertia in the power system and the shorter the reaction time of frequency reserves, the less pronounced is the frequency nadir. The trend towards a decreasing number of conventional power plants goes hand in hand with a lower inertia in the power system. As already described in Chp. 3.3, there are several services for providing faster reserves that are suitable to compensate for the decreasing inertia in the power grid, including synthetic inertia and fast reserve. However, as shown in Fig. 5.13(b) the duration during which they are provided is limited to a very short period. Since the conventional load frequency control is based on temporally overlapping frequency reserves, of which FCR is the first stage, the mere provision of faster reserves does not contribute to the actual stabilization of the grid frequency, but only to intercepting the frequency nadir. At the moment, the regulatory requirements on faster reserves are still under debate. However, it can be stated that BESS are required to provide both faster reserves and conventional reserves in the future.

Since conventional reserves are very energy intensive regarding the required reservation of energy resources, a BESS loses flexibility when providing such services. On the other hand, the sole provision of conventional frequency reserves lacks the fast reaction time of faster reserves. The application in Fig. 5.13 shows a way for concurrent provision of frequency reserves by BESS, which allows a very flexible stacking of the services. Regardless of which combination of the services in Fig. 5.13 is activated, the total power output respects the regulatory requirements of every single service. Each combination of activations leads to a corresponding "new" frequency reserve product. Referring to Fig. 5.13 such combinations would be FCR, FCR+SI, FCR+FR, SI+FR or FCR+SI+FR. Such flexible stacking of frequency reserves allows a high flexibility during operational planning, while at the same time ensuring the highest contribution to frequency stability and probably the highest revenues for operators of BESS.

5.6.3 Application 3: Utilization of the Remaining Power Reserves of FCR through Static Voltage Support during Active SoC-Management

Chp. 5.5.3.2 mentions the requirements on SoC-Management during provision of FCR, which are based on the SOGL [50]. These requirements include a minimum power for the SoC-Management to be available at any time during provision of FCR in order to ensure that a compensation of the worst-case of a so-called "normal state" of the frequency is possible. This worst-case assumes a continuous frequency deviation of 50 mHz, which corresponds to a continuous provision of a quarter of the tendered FCR-power. In order to hold the SoC in such a situation, the SoC-management is required to compensate this power. This situation is used as an application to demonstrate the behavior of dynamic prioritization. It is assumed that the functions F_1, F_2 and F_5 are activated $\mathbf{A} = \{1, 1, 0, 0, 1, 0, 0, 0\}$ and are parametrized with the following parameters. The tendered FCR-power of the function F_1, FCR, is $X_{1,1} = 2\,\text{MW}$, which corresponds to $S_n \cdot 0.8\,\text{pu}$. According to the descriptions above this requires the power for SoC-Management to be parametrized with $X_{2,1} = \frac{X_{1,1}}{4} = 0.5\,\text{MW}$, which corresponds to $S_n \cdot 0.2\,\text{pu}$. Besides the functions F_1, FCR, and F_2, SoC-Management, the function F_5, Static Voltage Support, is assumed to provide reactive power compensation with a value of $X_{5,1} = -2.5\,\text{MVar}$, which corresponds to the nominal power S_n.

It is assumed that a continuous frequency deviation of $\Delta f = -50\,\text{mHz}$ and a constant positive-sequence voltage of $u_{1+} = 1\,\text{pu}$ are present. The function F_2, SoC-Management, is assumed to be inactive at the time $t = t_0$ and assumed to be active at the time $t = t_1$. Fig. 5.14 shows the corresponding vector diagrams of the current requests, the current reservations and the executable currents for the times t_0 and t_1. Due to the frequency deviation of $\Delta f = -50\,\text{mHz}$ a quarter of the tendered FCR-power is requested and executed $i'_{S,d_{1+},1} = i_{S,d_{1+},ref_1} = 0.2\,\text{pu}$, whereas the corresponding current reservation of the function F_1, FCR, is $i''_{S,d_{1+},1} = 0.8\,\text{pu}$. At the time t_0 in

Fig. 5.14(a) the SoC-Management is inactive, which allows the function F_5, Static Voltage Support, to execute a current request according to Eq. 5.21. Since the function F_5 is a reactive power function, the third part of the case distinction in Eq. 5.21 comes into force. Since function F_1 is the only function with higher priority and a current request different from zero, the occupied current becomes $\mathbf{o}_{S,dq_5} = (0.2\,\text{pu}, -1\,\text{pu}, 0, 0)^\top$. The current limitation algorithm of Chp. 5.5.1 for such a simple situation leads to an executable current of $i_{S,q_{1+},ref_5} = -\sqrt{i_{max}^2 - o_{S,d_{1+,5}}^2} = -0.98\,\text{pu}$, which is almost the requested current of $i'_{S,q_{1+,5}} = 1\,\text{pu}$.

At the time t_1 in Fig. 5.14(b) the function F_2, SoC-Management, becomes active. Due to higher priority of F_2 over F_5 ($V_2 < V_5$), the current request of F_2 is executed with $i'_{S,d_{1+,2}} = i_{S,d_{1+},ref_2} = -0.2\,\text{pu}$. Since function F_1 and F_2 both are active power functions the second part of the case distinction according to Eq. 5.21 comes into force. The occupied current therefore becomes $\tilde{\mathbf{o}}_{S,dq_2} = (-0.2\,\text{pu} \pm 0.8\,\text{pu}, 0, 0, 0)^\top$, but does not exceed the maximum current i_{max}. Therefore, the full amount of the requested current can be executed. For the occupied current of function F_5, on the other hand, the third part of the case distinction according to Eq. 5.21 comes into force and leads to $\mathbf{o}_{S,dq_5} = (-0.2\,\text{pu} + 0.2\,\text{pu}, -1\,\text{pu}, 0, 0)^\top$. Since the requested currents of the functions F_1 and F_2 sum up to zero, the full amount of the requested current can be executed with $i_{S,q_{1+},ref_5} = i'_{S,q_{1+,5}} = -1\,\text{pu}$.

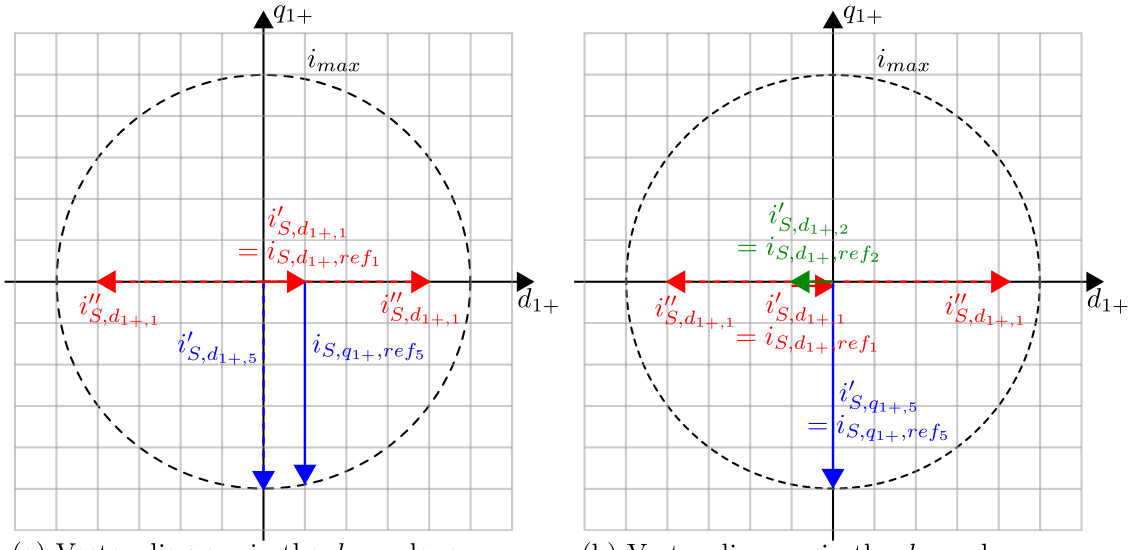

(a) Vector diagram in the dq_{1+}-plane at $t = t_0$

(b) Vector diagram in the dq_{1+}-plane at $t = t_1$

Figure 5.14: Dynamic prioritization during active functions F_1, FCR, F_2, SoC-Management, F_5, Static Voltage Support.

With regard to Fig. 5.4 and Fig. 5.5, a comparison between the corresponding concepts of static power band assignment and dynamic prioritization can be made. Assuming a static power band assignment to be applied for a situation as described above, this would make it necessary to predefine power bands for each function. In Fig. 5.14(a) this would prohibit function F_5 to execute its power, because the power capability is fully exploited by the reservations of function F_1 and F_2, including the case where no requests are present. As shown for dynamic prioritization in Fig. 5.14(a), on the other hand, the function F_5 is able to execute requests. Therefore, dynamic prioritization allows offering the services F_1 and F_5, besides an activated SoC-Management F_2, while a static power band assignment would only allow offering function F_1, besides an activated SoC-Management F_2. Therefore, applying dynamic prioritization may hold the potential of increased revenues, for example, when reactive power compensation in the scope of function F_5, Static Voltage Support, is being marketed. In the situation described above with the concept of static power band assignment

it would be possible to offer $X_{1,1} = 2\,\text{MW}$ of FCR via the function F_1, whereas with the concept of dynamic prioritization it would be possible to additionally offer $X_{5,1} = -2.5\,\text{MVar}$ of reactive power compensation via the function F_2. The dynamic prioritization therefore makes better use of the power resources of the BESS.

Since the limitation of the function F_5 in Fig. 5.14 is depending on the requested currents of the remaining functions, situations may arise when F_5 is limited to zero. In order to investigate the occurrence of limitations for such a case in more detail, Chp. 5.7 presents simulation results of a long-time simulation based on measurement data.

5.7 Long-Time Simulation of Application 3

Chp. 5.6 describes two types of unpredictability of functions. Three applications are discussed, which demonstrate the behavior of dynamic prioritization in order to handle the two types of unpredictability. As described in the beginning of Chp. 5.6, the first two applications demonstrate the behavior of dynamic prioritization to cope with functions of unpredictability type (b), when they are utilizing large amount of power resources during worst-case scenarios. The third application, on the other hand, demonstrates the potential of dynamic prioritization in order to better utilize the power reserves of functions of unpredictability type (a). Compared to the first two applications, whose goal is to show how to cope with functions of unpredictability type (b), which is only possible via worst-case scenarios, the potential of dynamic prioritization demonstrated in the third application can be investigated in more detail via long-time simulation.

This Chp. therefore presents and discusses the results of such a long-time simulation in order to assess the feasibility of the application in Chp. 5.6.3. The values of $\mathbf{A}$, $\mathbf{V}$ and $\mathbf{X}_k$ are identical to the description in Chp. 5.6.3. In addition to these values, the function F_2 SoC-management is parametrized with $\mathbf{X_2} = \{0.5\,\text{MW}, 0.5\,\text{pu}, 0.33\,\text{pu}, 0.67\,\text{pu}\}$, the value of $X_{5,1}$ is varied and the energy content of the battery is assumed to be $E = 3\,\text{MWh}$. As input for the control variables of function F_1, historical measurement data of the frequency f from January 2019 is used. The data is chosen due to several large frequency events that happened within this month [53]. A model created in MATLAB/SIMULINK allows the simulation of the behavior of the BESS, where the executed power of FCR based on the frequency influences the behavior of the functions F_2 SoC-management and F_5 static voltage support, based on the concept of dynamic prioritization. The step size for this simulation is one second.

Fig. 5.15 shows the results of this simulation depending on different, but only negative values of $X_{5,1}$. Fig. 5.15(a) presents box plots that show the extent of the limitation on the left y-axis for each moment in which a limitation of the function F_5 occurs. Fig. 5.15(a) also shows the percentage of time where limitations occur. The corresponding values can be read on the right y-axis. Fig. 5.15(b) shows the uninterrupted duration of each limitation in the form of box plots. The results show function F_5 is able to provide a value of $X_{5,1} = -0.65\,\text{pu} \cdot S_n$ at any time. This value corresponds to a maximum limitation of function F_5 due to the function F_1 following a frequency deviation of nearly $\Delta f = 200\,\text{mHz}$. For higher values of $X_{5,1}$, the percentage of limitations decreases. However, only for values of $X_{5,1}$ higher than $-0.95\,\text{pu} \cdot S_n$ the percentage of limitations is lower than 92 %. As indicated by the box plots, the majority of the extent of limitations remains at values higher than 90 %, even for values of $X_{5,1} < -0.99\,\text{pu}$. In Fig. 5.15(b) the results show that the uninterrupted duration of each limitation is kept below 10 min for values of up to $X_{5,1} = -0.9\,\text{pu} \cdot S_n$. Regardless of the value of $X_{5,1}$, the majority of durations lies below a value of 4 min.

The limitation of the function F_5 Static Voltage support has two consequences. The description in Chp. 5.6.3 defines the use of the function as reactive power compensation, to compensate for reactive power loads. A reactive power compensation reduces the payment of tariffs for reactive

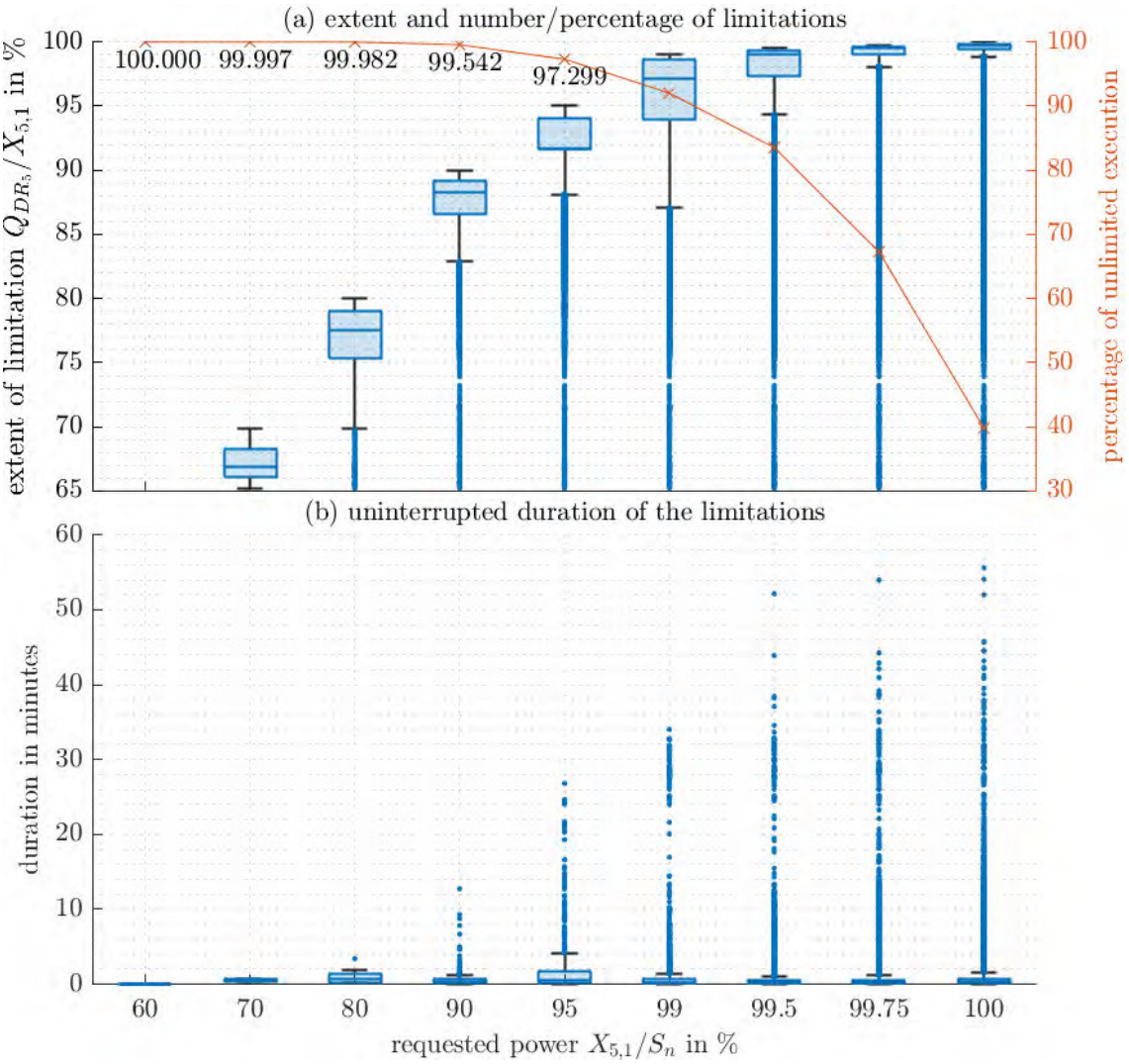

Figure 5.15: Simulation results of the limitation of the function F_5 static voltage support during long-time simulation in MATLAB/SIMULINK.

energy, which business customers have to pay. A limitation therefore leads to a decrease of this payment. However, limitations of short duration can be neglected. The second consequence of a limitation is the influence on the local voltage. A limitation of the reactive power compensation leads to increasing voltage values. However, limitations of short duration do not have that much impact on power quality. The power quality regarding voltage values usually refers to mean values over a predefined duration. According to the standard EN 50160 [138], this predefined duration is ten minutes. The limitation of the function F_5 influences the local voltage values. Taking into account the requirements regarding power quality, the results in Fig. 5.15 show that up to a value of $X_{5,1} = -0.9\,\text{pu} \cdot S_n$ the influence of the limitation of the function F_5 on the power quality can be neglected.

The results prove the potential of dynamic prioritization of better utilizing the power resources. Compared to a static power band assignment, where the function F_5 would not be able to utilize resources at any time, the concept of dynamic prioritization allows an utilization of power resources up to a value of $0.9\,\text{pu} \cdot S_n$ without compromising the power quality. Considering an appropriate behavior during operational planning holds the potential to increase the profitability of a BESS.

Based on the services summarized in Fig. 3.7 it is an interesting future research question which other services are suitable for taking advantage of the potential of dynamic prioritization as it has been shown for the application above.

5.8 Comparison of Indicators from Value Stacking Various Services via Long-Time Simulation

This chapter compares indicators of a multi-use operation for different combinations of services. One such indicator are the revenues that are achievable by value stacking of several services. According to Chp. 1.4, the achievable revenues by value stacking of services are crucial to reach profitability of BESS today. However, some of the functions listed in Tab. 5.2 implement services for which no corresponding markets are currently available or which are legally prescribed without being remunerated. Although for some of these services markets may exist in the near future or they may be coupled with a certain remuneration at some time, the following investigations are limited to services for which such markets or remunerations already exist today. The corresponding functions of these services according to Tab. 5.2 are listed below:

- F_1 FCR,
- F_2 SoC-management,
- F_5 static voltage support/reactive power provision and
- F_8 arbitrage.

5.8.1 Scenarios of Stacking Services and Input Data

Similar to Chp. 5.7 long-time simulations in MATLAB/SIMULINK are carried out in order to take into account all technical and legal aspects of each function as described in Chp. 4. Different scenarios of the value stacking of various services and the variation of the BESS size are taken into account. The scenarios are based on all possible combinations of services according to the list above. These six scenarios **S1** – **S6** are summarized in Tab. 5.10.

Table 5.10: Overview of scenarios for stacking services.

activation ↓/scenario →	**S1**	**S2**	**S3**	**S4**	**S5**	**S6**
A_1 Frequency containment reserve	0	0	1	1	1	1
A_2 SoC-management	1	1	1	1	1	1
A_3 Fast Reserve	0	0	0	0	0	0
A_4 Synthetic inertia	0	0	0	0	0	0
A_5 Static voltage support	0	1	0	0	1	1
A_6 Dynamic voltage support	0	0	0	0	0	0
A_7 Island operation	0	0	0	0	0	0
A_8 Arbitrage	1	1	0	1	0	1

For all of the scenarios shown in Tab. 5.10, the standard parameters according to the descriptions in Chp. 5.5.3 are used. The parameters relevant for the different scenarios are summarized as follows

- $E = [1.5\,\text{MWh} - 2.6\,\text{MWh}]$
- $S_n = [2.5\,\text{MVA} - 3.6\,\text{MVA}]$
- $X_{1,1} = \{0\,\text{MW}, 1\,\text{MW}\}$
- $X_{2,1} = S_n - X_{1,1}$
- $X_{5,1} = S_n$

- $X_{8,1} = S_n - X_{1,1}$.

The SoC-levels $X_{2,3}$ and $X_{2,4}$ for activating the function F_2, SoC-management, are parameterized according to Eq. (4.4) with $T_{crit} = 0.5\,\text{h}$. These SoC-levels are depending on the tendered FCR-power $X_{1,1}$ and the energy content E and result in the working area for other functions. According to Fig. 4.1, this FCR-related energy-to-power ratio $E/X_{1,1}$ limits the available working area, within which other functions than FCR are allowed to influence the SoC. Since this working area is defined by the tendered FCR-power $X_{1,1}$ only, another relevant energy-to-power ratio is the total energy-to-power ratio E/S_n, which corresponds to the energy-to-power ratio of the whole BESS. In order to investigate the effect of an increased working area for other functions, the FCR-related energy-to-power ratio is varied in the range between $[1.5\,\text{h} - 2.6\,\text{h}]$. The total energy-to-power ratio, on the other hand, is varied in the range of $[0.6\,\text{h} - 0.72\,\text{h}]$ and, therefore, stays almost constant. This ensures the duration of charging and discharging actions in the scope of arbitrage transactions to be relatively small. Due to the fluctuations of prices on the intraday market, long durations would make the arbitrage transactions less profitable.

The most relevant indicator that are examined by simulations is the achievable revenues. Since the achievable revenues are heavily depending on the input data of the market prices, this input data is summarized as follows. Analogous to Chp. 5.7, the data of January 2019 is used as input data. A trend of the FCR-prices has already been presented in Fig. 1.4. The corresponding market data of January 2019 is used from [10]. A trend of the intraday market prices on the energy market has been presented in Fig. 4.84. The corresponding market data of January 2019 is used from [55]. This market data is relevant for the functions F_2, SoC-management and F_8, arbitrage. As described in Chp. 4.5.3 and illustrated in Fig. 4.85, the buy/sell-input for arbitrage is generated based on the minima and maxima of the market price in order to ensure the highest revenues possible. This requires perfect foresight of the market price for the simulation. As illustrated in Fig. 4.85, buy- and sell transactions are performed once in the forenoon and once in the afternoon, resulting in two arbitrage transactions per day. These arbitrage transactions are initiated by switching the parameter $X_{8,2}$ accordingly, as described in Chp. 5.5.3.8. Each arbitrage transaction leads to a charging or discharging process that varies the actual SoC inside the working area, more precisely between the values of the parameters $X_{8,3}$ and $X_{8,4}$. In [24] the range of the remuneration for reactive power provision is given with 0.08 Euro/MVArh – 2.27 Euro/MVArh. For the following investigations a value of 1 Euro/MVArh is used.

Another indicator that is relevant to investigate the profitability of value stacking of services is the influence of such a multi-use operation on the aging of the batteries. Since a stacked provision of services is coupled with a higher number of charging and discharging activities, this results in a higher number of equivalent full cycles of the batteries. According to Chp. 2.5.1.7 the number of such equivalent full cycles is directly linked to the cyclic aging of the batteries. According to Eq. (2.130), the capacity fading due to cyclic aging decreases the SoH of the batteries and, therefore, leads to a reduced working area. The reduced working area, for example, reduces the achievable revenues by arbitrage actions or, in the worst case, may lead to a situation where the legal requirements for providing FCR cannot be met anymore. An economic investigation of a stacked provision of services, therefore, always has to consider the effects on cyclic aging.

5.8.2 Results and Discussion

The simulation results of the scenarios defined in Tab. 5.10 are presented in Fig. 5.16. The subfigures show the achievable revenues in (a), the number of full cycles in (b) and the statistics regarding limitation of reactive power provision in (c). The ranges for parameters as defined in Chp. 5.8.1 are shown on the x-axis. For each parameter value, each subfigure shows the simulation results for the scenarios S1 – S6. Fig. 5.16(a) shows the achievable revenues based on the market prices described in Chp. 5.8.1. For each scenario, the corresponding bar consists of the achievable

revenues of the corresponding service, which sum up to the total achievable revenues. The different contributions of revenues by services are also listed in the tables Tab. 5.11 – Tab. 5.14.

Table 5.11: Revenues by SoC-management in Euro according to Fig. 5.16(a).

$\frac{E}{X_{1,1}} \downarrow$ / scenario →	S1	S2	S3	S4	S5	S6
1.5 h	0	-64	-374	-147	-650	-308
1.6 h	0	-50	-364	-140	-656	-240
1.7 h	0	-39	-380	-114	-618	-215
1.8 h	0	-30	-378	-96	-650	-199
1.9 h	0	-14	-336	-88	-677	-198
2.0 h	0	-8	-360	-111	-646	-192
2.1 h	0	0	-362	-109	-640	-188
2.2 h	0	0	-371	-106	-642	-184
2.3 h	0	0	-344	-113	-666	-182
2.4 h	0	0	-358	-124	-587	-191
2.5 h	0	0	-374	-123	-627	-188
2.6 h	0	0	-317	-123	-651	-192

Table 5.12: Revenues by arbitrage in Euro according to Fig. 5.16(a).

$\frac{E}{X_{1,1}} \downarrow$ / scenario →	S1	S2	S3	S4	S5	S6
1.5 h	758	593	0	-21	0	-141
1.6 h	801	599	0	127	0	-55
1.7 h	874	666	0	288	0	77
1.8 h	915	713	0	404	0	205
1.9 h	957	784	0	508	0	311
2.0 h	1013	837	0	635	0	430
2.1 h	915	891	0	720	0	518
2.2 h	964	953	0	805	0	621
2.3 h	1013	1014	0	895	0	699
2.4 h	1025	1076	0	970	0	778
2.5 h	1004	1138	0	1035	0	898
2.6 h	1050	1200	0	1107	0	976

As shown in Fig. 5.16(a), the scenarios in Tab. 5.10 are sorted in a way that the total achievable revenues are increasing from scenario S1 with the lowest achievable revenues to scenario S6 with the highest achievable revenues. Hence, a trend is becoming apparent to increase the achievable revenues through an increasing number of stacked services. Any kind of combinations of services leads to such a positive effect on the achievable revenues compared to the value that can be achieved by the sole provision of a service. All scenarios according to Tab. 5.10 comprise an active SoC-management, which leads to negative revenues (costs) as shown in Fig. 5.16(a), since losses are to be compensated for and FCR tends to provide power instead of consuming it due to the trend of the frequency to stay below 50 Hz. While the share of revenues by providing FCR stays identical for all scenarios and parameter sweeps due to a constant value of the tendered FCR-power, the influence on the revenues by performing arbitrage transactions and providing reactive power increases with an increasing FCR-related energy-to-power ratio $E/X_{1,1}$. For example, the revenues by solely performing arbitrage transactions are shown for scenario S1 in Fig. 5.16(a) by the first bar per group. The revenues for arbitrage transactions of scenario S1 cannot be utilized in scenario S4 or S6 for a FCR-related energy-to-power ratio of $E/X_{1,1} = 1.5\,\text{h}$ due to the limited working area. For an increasing energy-to-power ratio, however, these revenues increase. The difference of revenues for arbitrage between the scenarios S1 and S4 or S6 decreases for higher FCR-related energy-to-power ratios. This becomes also visible by comparing the results of scenario S3 and S4 or by

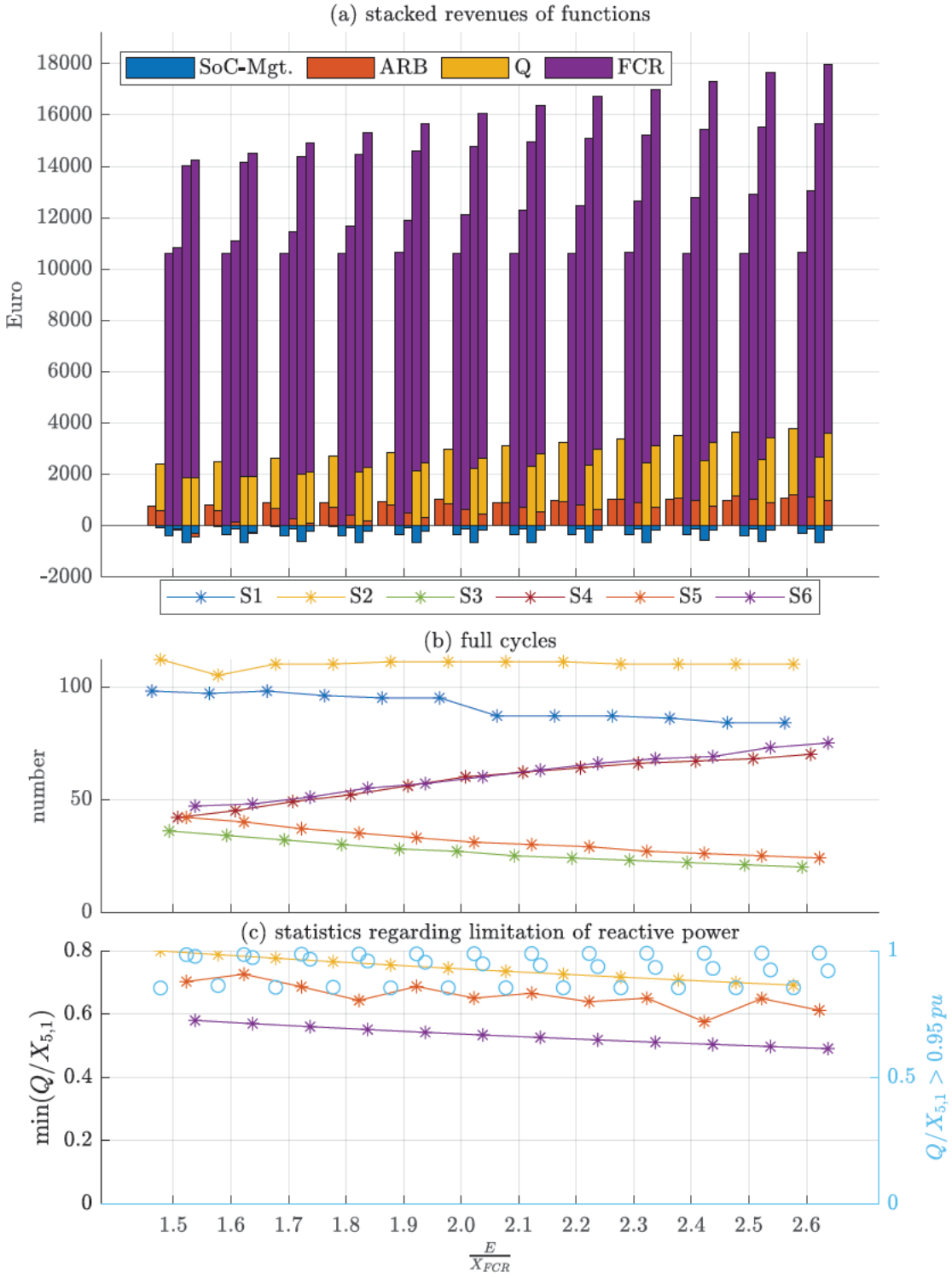

Figure 5.16: Simulation results of the long-time simulation of the stacked provision of services for six scenarios defined in Tab. 5.10 based on input data of January 2019. (a) shows the achievable revenues divided between the services. (b) shows the resulting equivalent full cycles for each scenario. (c) shows the minimum value of reactive power provision by maximum limitation through functions with higher priority and the probability of reactive power provision to be able to take on values above 95 % of $X_{5,1}$.

Table 5.13: Revenues by reactive power provision in Euro according to Fig. 5.16(a).

$\frac{E}{X_{1,1}} \downarrow$ / scenario →	S1	S2	S3	S4	S5	S6
1.5 h	0	1805	0	0	1854	1851
1.6 h	0	1878	0	0	1928	1922
1.7 h	0	1944	0	0	2002	1993
1.8 h	0	2013	0	0	2076	2063
1.9 h	0	2081	0	0	2151	2133
2.0 h	0	2150	0	0	2225	2202
2.1 h	0	2217	0	0	2299	2271
2.2 h	0	2286	0	0	2374	2340
2.3 h	0	2354	0	0	2448	2409
2.4 h	0	2422	0	0	2522	2478
2.5 h	0	2490	0	0	2597	2543
2.6 h	0	2558	0	0	2671	2613

Table 5.14: Revenues by FCR in Euro according to Fig. 5.16(a).

$\frac{E}{X_{1,1}} \downarrow$ / scenario →	S1	S2	S3	S4	S5	S6
1.5 h	0	0	10977	10977	10977	10977
1.6 h	0	0	”	”	”	”
1.7 h	0	0	”	”	”	”
1.8 h	0	0	”	”	”	”
1.9 h	0	0	”	”	”	”
2.0 h	0	0	”	”	”	”
2.1 h	0	0	”	”	”	”
2.2 h	0	0	”	”	”	”
2.3 h	0	0	”	”	”	”
2.4 h	0	0	”	”	”	”
2.5 h	0	0	”	”	”	”
2.6 h	0	0	”	”	”	”

comparing the results of scenario S5 and S6 for low FCR-related energy-to-power ratios and high FCR-related energy-to-power ratios in Fig. 5.16(a). Whereas the difference between achievable revenues between these pairs of scenarios is relatively small for low FCR-related energy-to-power ratios, the difference increases to a notable amount for high FCR-related energy-to-power ratios. The additional stacking of reactive power provision also has a beneficial effect on the achievable revenues in all scenarios. Since the service is able to fully utilize the power resources most of the time, as shown in Fig. 5.16(c), the achievable revenues are nearly identical for the different scenarios. Fig. 5.16(c) shows the minimum of the operating point $min(Q/X_{5,1})$ that is utilizable for this service and the probability to stay above a value of 95 % with the actual operating point. The higher the number of stacked services, the lower the minimum operating point, which is visible by comparing scenario S2 with scenario S5 or S6 in Fig. 5.16(c). However, the probability to utilize a high amount of the desired operating point is also high for scenario S5 or S6. Since according to Chp. 5.8.1 the usable power resources increase with increasing FCR-related energy-to-power ratios, also the achievable revenues for providing reactive power slightly increase. The beneficial effect of the additional provision of reactive power becomes visible by comparing the results of scenario S1 and S2, the results of scenario S3 and S5, or the results of scenario S4 and S6. In all these cases Fig. 5.16(a) shows a notable increase of the achievable revenues.

Fig. 5.16(b) shows the full cycles of the energy content of the BESS which arise in the different scenarios at the end of one month of simulation. A trend towards increasing full cycles becomes apparent for scenarios S4 and S6 when there is a significant working area available for arbitrage,

which is the case with a higher FCR-related energy-to-power ratio. The higher achievable revenues of scenarios S4 and S6 in Fig. 5.16(a) are therefore at the expense of more pronounced aging of the batteries. The numbers of full cycles of scenarios S3 and S5 decrease with increasing FCR-related energy-to-power ratio. This is due to the fact that the energy for providing FCR remains constant and there is only a relatively small influence on the energy which is necessary for SoC-management. Furthermore, the reactive power provision also has a relatively small influence on the number of full cycles, which results from the additional energy for SoC-management by increased losses due to reactive power. An increasing FCR-related energy-to-power ratio and the almost constant energy for the provision of services, therefore, results in a decreasing number of full cycles as it is visible in Fig. 5.16(b). The numbers of full cycles of scenarios S1 and S2 are the highest among all scenarios for all FCR-related energy-to-power ratios. This is due to the fact that there is no FCR provision, which leads to a working area that covers the entire SoC-range between 0 % – 100 %. Any arbitrage transaction is therefore able to utilize the entire SoC-range, which leads to a higher number of full cycles. Whereas the number of full cycles of scenario S2 remains relatively constant, the number of full cycles of scenario S1 slightly decreases with increasing FCR-related energy-to-power ratio. This tendency can be argued by the additional energy that is necessary to compensate for the losses of providing reactive power in scenario S2, which leads to additional energy that is necessary for SoC-management. With an increasing FCR-related energy-to-power ratio this additional energy holds the number of full cycles in scenario S2 at a constant level, while the number of full cycles in scenario S1 slightly decreases.

As described in Chp. 2.5.1.6, the number of full cycles, however, does not linearly correlate with the cyclic aging of batteries. In order to investigate the influence of the different scenarios on the cyclic aging, the term $f_{Woehler(DoD)}$ according to Eq. (2.128) is used. This term takes into account the fact that continuous charging or discharging operations which are using the whole SoC-range do have a more pronounced effect on cyclic aging than so-called "micro-cycles". Fig. 5.17 illustrates this effect based on a Woehler-curve, which shows the "cycles to failure" over the corresponding DoD for these cycles. The cycles to failure describe the possible number of cycles a battery can be used for until a certain SoH is reached. A value of $SoH = 80\,\%$ is very common. For example, according to Fig. 5.17, continuous charging and discharging operations within the whole SoC-range of a battery are coupled with the highest DoD of 100 % per cycle, for which a number of cycles of 4000 can be assumed until a SoH is reached. This number of 4000 cycles is termed as cycles to failure.

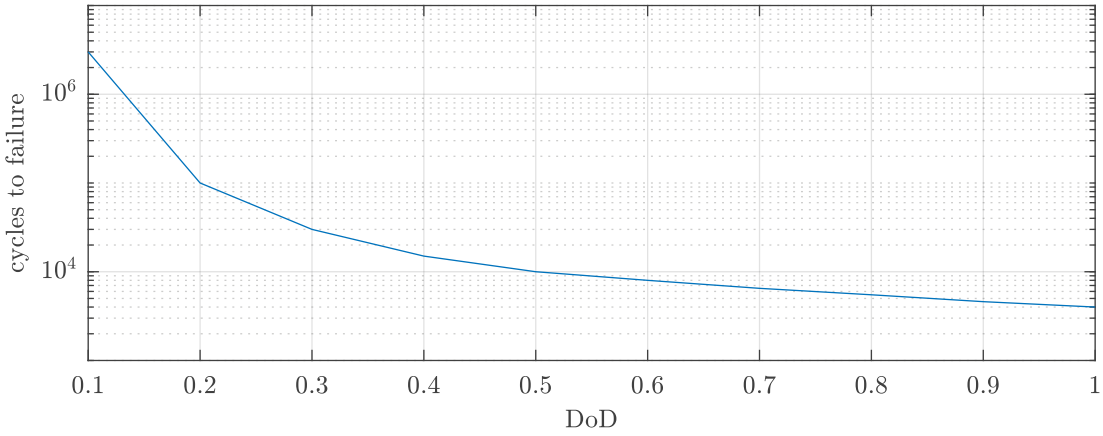

Figure 5.17: Woehler curve according to Eq. (2.128) that is used for determining the influence on cyclic aging.

According to Dufo-López et al. [35], the so-called "rainflow"-algorithm can be used to extract the number of cycles per different DoD-ranges from a SoC-time series. This algorithm turns the

time series into a sequence of reversals, which represent the local Minima and Maxima where the deviation of the SoC changes the sign. Each such reversal can be counted and assigned to a corresponding DoD. For the simulation result of Fig. 5.16, such an outcome of the rainflow-algorithm is presented in Fig. 5.18 for the six scenarios of Tab. 5.10 in (a)-(f).

For scenarios S1 and S2, the influence of arbitrage becomes visible in the high number of cycles at a DoD= 1 in Fig. 5.18(a-b), since every arbitrage transaction tries to fully use the SoC-range. The micro-cycles at a DoD= 0.1 are linked to the losses between arbitrage transactions. Since the starting-SoC of the simulation is 50 %, one half-cycle is also shown at a DoD= 0.5 in Fig. 5.18(a-b). Fig. 5.18(c,e) show the results for scenarios S3 and S5. Compared to scenario S1 and S2, scenarios S3 and S5 show the influence of providing FCR only, which is coupled with a very high number of micro-cycles at a DoD= 0.1. The cycles for higher DoD are linked to the SoC-management. Fig. 5.18(d,f) show the results for scenarios S4 and S6. Since besides FCR also arbitrage is provided, its influence on the number of cycles at mid-range DoD becomes visible for increasing FCR-related energy-to-power ratios. Since the working area for arbitrage increases with increasing FCR-related energy-to-power ratio, every arbitrage transaction is able to utilize a higher SoC-range.

The actual influence of the cycles shown in Fig. 5.18 on the lifetime of the batteries can be calculated with the help of the equation

$$\text{cyclic lifetime} = \frac{1}{\sum_{i=1}^{10} \frac{\text{number of cycles}_i}{\text{cycles to failure}_i}} \tag{5.77}$$

according to Zeh et al. [203]. By dividing the Woehler-curve into ten equal-sized DoD-segments, the number of cycles of Fig. 5.18 can be set in relation to the corresponding cycles to failure of the Woehler-curve, both indexed as "i" in the equation above. This results in a measure for the cyclic lifetime of batteries. The results of such a calculation are presented in Fig. 5.19 for each of the scenarios of Tab. 5.10.

Fig. 5.19 allows a comparison of the influence of the six scenarios on the cyclic lifetime of the batteries. Since the scenarios S1 and S2 in Fig. 5.18(a-b) show the highest number of cycles at a high DoD, it is clear that the corresponding cyclic lifetime in Fig. 5.19 is the smallest around 6 a. For scenarios S3 and S5, on the other hand, the number of cycles in Fig. 5.18(c,e) are accumulated at low values of DoD, since FCR mostly leads to micro-cycles. The resulting cycle lifetime in 5.19, therefore, shows the highest values among all scenarios around 14 a. The remaining scenarios S4 and S6 show a pronounced development of the number of cycles with increasing FCR-related energy-to-power ratio in Fig. 5.18(d,f). This trend becomes visible as decreasing cyclic lifetime in Fig. 5.19. With the smallest FCR-related energy-to-power ratio the cyclic lifetime lies around the values of scenarios S3 and S5, while with increasing FCR-related energy-to-power ratio the values for the cyclic lifetime of scenarios S4 and S6 approach those of scenarios S1 and S2. In summary, a compromise has to be found between higher achievable revenues by stacking a higher number of services and the impact on the aging of the batteries in order to reach the point of optimal profitability.

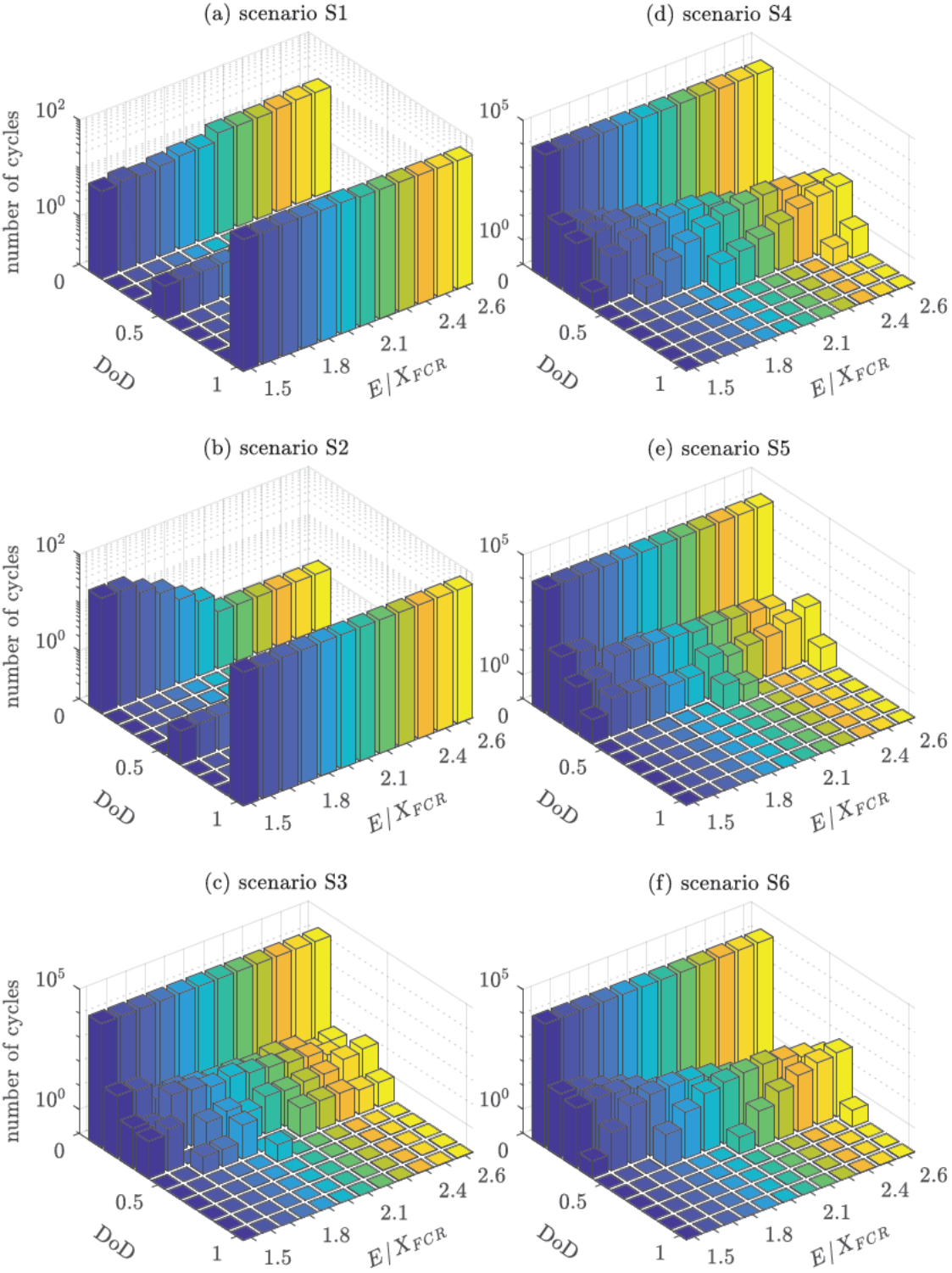

Figure 5.18: Simulation results of the long-time simulation of the stacked provision of services for six scenarios defined in Tab. 5.10 based on input data of January 2019. The results illustrate the number of cycles depending on the corresponding DoD for each scenario. Values on the x-axis are to be interpreted as discrete values, analogous to Fig. 5.16.

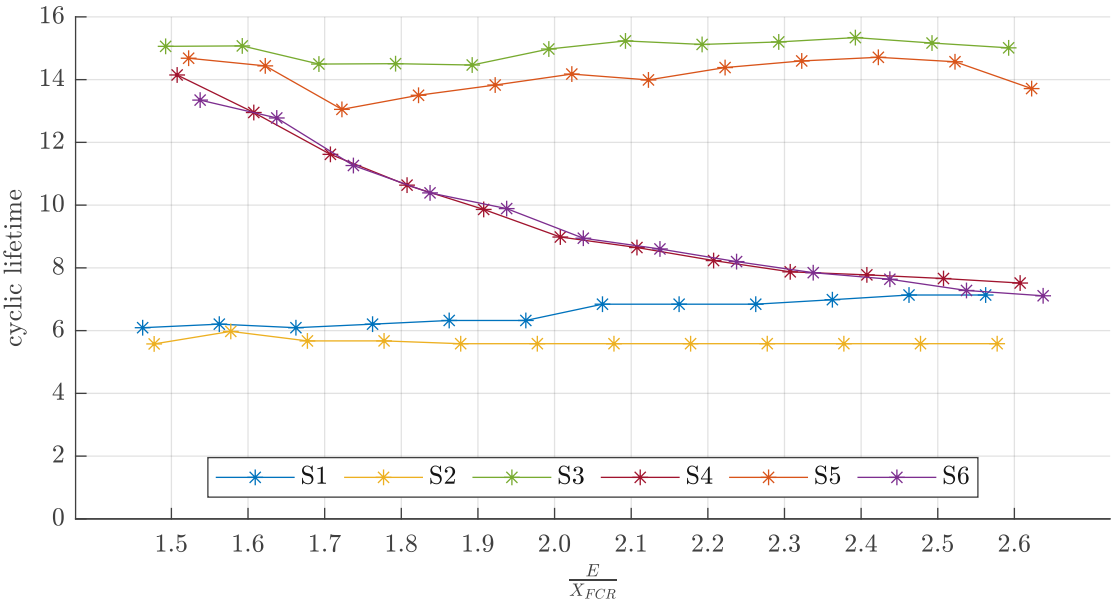

Figure 5.19: Simulation results regarding cyclic lifetime of the long-time simulation of the stacked provision of services for six scenarios defined in Tab. 5.10 based on input data of January 2019.

6 Conclusion and Outlook

This thesis deals with the multi-use operation of stationary BESS, which is based on stacking of various services in order to increase the profitability of BESS. The focus lies on BESS based on Li-Ion battery cells, which are assumed to represent the fastest growing market among storage technologies. Although there has been a downward trend in the price of Li-ion cells over the past decade, which is expected to continue in subsequent years due to the growing market for electric cars, the profitability of BESS projects today is difficult to achieve when providing a single service. Nevertheless, BESS are assumed to be an indispensable source of flexibility in a future power system with massive integration of fluctuating renewable energy. Therefore, several organizations such as IRENA recommend the introduction of incentives and the softening of regulatory barriers to increase profitability of BESS. Analogous to the integration of renewable energy, the integration of BESS in the power system, however, is a gradual process during which BESS struggle with achieving profitability. During such a transition phase, the concept of multi-use operation has the potential to facilitate the implementation of BESS projects by increasing potential revenues and ensuring better use of BESS resources.

This thesis engages the topic of multi-use operation in three parts, each assigned to a corresponding research question. The possibility to stack various services depends on the actual characteristics of the BESS. The first part of this thesis, therefore, covers the question of how to characterize BESS and measure corresponding values. This part also covers the question of which services a BESS is able to provide at all. The second part investigates five of these services in more detail. These investigations are based on simulations and measurement results on a real BESS system. The third part covers the question of how to actually realize a multi-use operation. In the following three chapters the results and conclusions of these three parts are summarized.

6.1 Characterization of BESS

The first research question in Chp. 1.5 was formulated as follows.

1. What are characteristic values of BESS related to the provision of services, especially regarding modeling of BESS, and what are the requirements regarding measuring these values?

In order to encounter this question, a real BESS was used to identify and measure characteristic values. The construction and integration of this BESS was scientifically accompanied and gave valuable insights in the composition and combination of components of the BESS. The most relevant components of a BESS are the battery cells, which are combined in a modular way. They represent the smallest units in BESS, which are interconnected inside battery modules, which in turn are connected inside battery strings. The sum of the number of serially connected battery cells inside a battery string multiplied with the nominal voltage of each cell results in the nominal DC-output voltage of the BESS, which is 725 V for the investigated BESS.

The actual DC-output voltage is analogous to the voltage of each cell, which depends on the actual SoC, the actual power output, the temperature, etc. Since each cell has very strict lower and upper voltage levels, the exceeding of which results in chemical destruction of a battery cell, also the lower and upper voltage levels of the whole BESS are defining the borders within which a save operation of the BESS is possible. Therefore, the voltage curve is an important characteristic of a BESS.

Chp. 3.2.1 presented the measurement of such a voltage curve of a BESS for different operating points over the available SoC-range. This measurement illustrated the usable SoC-window which corresponds to a share of the whole capacity of the BESS and arises from the fact that high power output leads to a voltage rise while charging and to a voltage drop while discharging. In order to ensure the BESS voltage to stay within safe levels, a maximum power output is only possible within this SoC-window. In comparison with electric cars, where the CCCV charging method is used to fully charge the battery to a SoC of 100 %, a service provision by BESS is only possible within a reduced "safe" SoC-window when a certain power output is required at any time. The measurements resulted in a safe SoC-window, which corresponds to about 90 % of the capacity at a SoH of 100 % (beginning of life (BOL)). In order to compensate for the battery degradation by cyclic and calendar aging, it was also found that this SoC-window is deliberately reduced to a higher extent than necessary by the safe area in order to guarantee a constant capacity over the project lifetime.

Another important characteristic of a BESS is assigned to the converter, or power conversion system, and is the efficiency with which the conversion from DC to AC or from AC to DC takes place. Besides the measurements of the converter efficiency curve from laboratory measurements, an option of online measurement of the converter efficiency during operation at the test-site was presented.

The available energy content, the usable capacity and the efficiency are values that highly depend on the location of integration or the age of the BESS and, therefore, are very project-specific. Therefore, Chp. 3.2.5 presented a test procedure that allows an online estimation of valuable characteristics of a BESS. By repeating this test procedure, the change of these properties, for example with regard to degradation, can be updated over the life of the project. By undergoing several full cycles of the BESS with different operating points, this test procedure allows an online estimation of:

- the voltage curve,
- the safe SoC-window,
- the converter efficiency,
- the power consumption by auxiliary systems,
- the actual BESS capacity,
- the the actual energy content of the BESS,
- the losses during charging and discharging and
- the round-trip energy efficiency and coulombic efficiency.

All these characteristics were identified as essential for modeling BESS in simulation tools.

6.2 Investigation of Selected Services

The second research question in Chp. 1.5 was formulated as follows.

2. Which existing or possible future services BESS are capable of providing, what are BESS particularly suitable for and how can these services be implemented as functions in BESS which comply with legal and technical requirements and constraints? Since BESS are particularly suitable for the provision of frequency control reserves, a sub-objective of this research question is to optimize the operation of the provision of such frequency control reserves, including the reduction of losses and operating costs.

In order to investigate selected services in more detail, Chp. 3 summarized all services for which BESS are suitable. A categorization was presented to assign each service to the goal it has to achieve. Based on the services listed in Chp. 3, five services were selected to be examined in more detail. Services such as frequency containment reserve or arbitrage were selected due to their

most common use in BESS. Furthermore, the service synthetic inertia was selected due to its likely importance to the future power system. The last two services include dynamic voltage support and black-starting and islanding services, which were selected as services that are often assigned to services a BESS is capable to provide, however, rarely applied in real operation. Therefore, they were selected in order to gather experience also for such rarely applied services. For each service, a similar structure was used. Basic considerations were discussed, followed by a presentation of simulations and field measurements.

Since the provision of FCR is the most common service BESS are being used for today, the most extensive investigations among all services were carried out. One focus was given to the legal requirements, which are related to a minimum energy reservoir that has to be reserved explicitly for FCR and leads to a reduced working area for other services. Based on the BESS test-site, measurement results for a prequalification procedure were presented and discussed. Since the continuous provision of FCR requires an appropriate SoC-management, a focus was therefore placed on possible implementations for such a SoC-management. In order to gather experience for the operation of a BESS, the behavior of the SoC-management was investigated by simulation for different BESS sizes. The procurement of charging energy for SoC-management diminishes the achievable revenues of the BESS. Therefore, so-called "degrees of freedom" during the provision of FCR were investigated, which were proved to reduce the necessary SoC-management by up to 43 % in simulations. They were implemented in the BESS test-site and their functionality was measured appropriately. The provision of FCR largely takes place in the partial operating range. Due to the low efficiency in the partial operating range of the BESS, an algorithm was developed that increases the actual efficiency by using only the required number of modular units of the BESS which can cover the actual operating point. The corresponding simulations proved a reduction in losses by up to 39 %.

The second service, energy arbitrage, was only investigated by simulation to demonstrate its basic functionality during combined provision with FCR. Among all services that were investigated it is the only exception that was not investigated by further simulations or field tests. However, the presentation of its functionality in simulation was necessary for the simulation of the multi-use operation in Chp. 5.

There is currently no uniform definition of synthetic inertia in terms of its properties and its implementation. The behavior of synthetic inertia is highly dependent on its implementation in the converter of the BESS. Two approaches were identified as passive and active method to realize synthetic inertia, which are based on the design principle of the converter as grid-following or grid-forming converter. By EMT simulation based on a simplified converter model, the behavior of both implementations was compared. Compared to the passive method, the active method shows better behavior in terms of dynamics, since compared to the passive method, no frequency measurement is required, which is the limiting factor for the passive method. However, the necessity of retrofitting synthetic inertia in existing systems may require a passive implementation. Therefore, fields of application were identified for both approaches. Since the design principle of the converter at the BESS test-site is based on a grid-following design, a passive approach was implemented. The investigation during field-tests focused on the question of how to prove its functionality with regard to a prequalification process. Since the influence of the frequency is a major factor of the passive method, a measurement based on the actual grid frequency is necessary. However, the usual frequency gradients of the grid frequency are very limited. Therefore, a measurement to prove the functionality of a passive method of synthetic inertia is very difficult, also due to the high requirements of a reference frequency measurement regarding accuracy and sample time. By configuring a maximum sensitivity of the service, a basic correlation of the measured frequency gradient and the power output could be measured, which could be a way of basically proving the general functionality of the service during a possible prequalification process.

Dynamic voltage support and LVRT-capability have been introduced as legal requirements for converter based systems in the recent past. Therefore, they were implemented in the BESS test-site

according to the legal requirements. On behalf of EMT simulations based on a simplified converter model, the behavior of dynamic voltage support was simulated during symmetrical and asymmetrical short-circuit events in MATLAB/SIMULINK. A special focus was given to the implementation of a current limitation algorithm which requires the consideration of positive-sequence and negative-sequence current shares with appropriate prioritization. Furthermore, a simplified RMS simulation model of the service and the grid section was created in DIGSILENT POWERFACTORY, which allowed a comparison with the measurement results of short-circuit tests conducted at the test-site. While the basic functionality of LVRT and dynamic voltage support could be proven, especially the behavior of the negative-sequence system showed differences to the latest legal requirements.

Black-starting and subsequently operating a Microgrid is often listed as a major benefit that BESS can offer. While this advantage is often discussed, the actual realization, however, is often limited to remote island grids. Therefore, the functionality of black-starting and operating a grid section was tested at the BESS test-site in order to gain experience with such an operation with foresight to possible future applications during power outages of the interconnected power grid. The test procedure was designed with the help of simulations based on a simplified converter model. A black-start of a medium voltage grid section was demonstrated based on ramping behavior of the supply voltage in order to prevent inrush currents from activating any over-current relays or other security measures. Several wind turbines were synchronized to the black-started Microgrid in order to investigate the possibility of using renewable energy during island operation of a grid section. A frequency control curve was proposed to control the power output of these wind turbines to prevent the BESS from being overloaded regarding power capabilities and maximum energy content. Since this frequency control curve does not require communication, it is a very simple way of operating renewable energy in an islanded Microgrid. Furthermore, the behavior of the BESS regarding load-steps was investigated during island operation. Based on active power load-steps and motor start-ups, the measurement results prove the capability of the BESS to withstand major active and reactive power load changes.

6.3 Multi-Use Operation of BESS

The third research question in Chp. 1.5 was formulated as follows.

3. How do different services interact with each other during simultaneous provision and how to ensure appropriate behavior of a BESS when conflicts of services due to limitations arise? How does this kind of value stacking influence the profitability of BESS?

The multi-use operation of BESS has already been investigated by several research works. However, the focus of existing research lies on solving an optimization of the operational planning in order to allocate resources to services. The question on how to deal with uncertainties of input variables during real-time operation was identified as an open question in Chp. 5. To encounter this question, the concept of dynamic prioritization was presented in the form of a mathematical framework that allows a systematic description of services and their combined provision, interaction and limitation. The concept of dynamic prioritization describes a method for organizing resources of the BESS based on priorities of services in order to handle unforeseen events when several services are requesting resources that go beyond the capabilities of the BESS and at the same time meet the legal requirements of all services adhered to as well as possible. Applications are described that demonstrate the use of this concept for events such as short-circuits or major frequency events when offering several services for frequency control, including synthetic inertia, fast reserve and FCR. It was also found that this concept may be beneficial during normal operation in order to better utilize the BESS resources.

Based on a simulation in MATLAB/SIMULINK, the influence of stacking services on the achievable revenues was investigated. The results prove the beneficial impact of stacking services. Based

on the example of combining the services FCR, energy arbitrage, reactive power provision and SoC-management, it was found that any combination leads to an increase of achievable revenues compared to the sole provision of each service. However, it was also found that stacking of services may have a serious impact on the battery lifetime due to cyclic aging. Especially arbitrage transactions are substantially reducing the lifetime of batteries up to 50 %. Therefore, a compromise has to be found between higher achievable revenues by stacking a higher number of services and the impact on the aging of the batteries in order to reach the point of optimal profitability.

6.4 Outlook

The ongoing integration of renewable energy with their highly fluctuating power infeed paired with the decreasing number of flexible conventional power plants based on fossil fuels will definitely create a need for other flexibilities in the future. The change in the mobility sector away from fossil-based vehicles to electric-based vehicles will lead to declining prices of battery cells and highly innovative new technologies in the field of battery systems in the coming years. Since identical battery cells can be used in stationary BESS, they can be assumed to play a role in a future power system to be one of the sources of such flexibilities. However, the integration and operation of BESS is not only depending on the financial feasibility of corresponding projects, but also on barriers existing today. It can be assumed that the dismantling of such barriers may lead to a further increase in the number of BESS projects in the coming years. For example, with the recent clarification in the "Electricity Market Directive" to specify conditions for system operators to operate BESS on their own, one such barrier has recently been eliminated. The disappearance of such barriers may open up new possibilities of BESS that may lead to further growth in the future.

One field of application for BESS in the future is assumed to be the provision of FCR. The actual energy demand during provision of FCR is relatively small most of the time. The "must-run" character of this service, however, requires the dimensioning of the BESS regarding energy resources to be relatively high. Although due to these requirements the profitability of BESS to provide FCR is not given today, declining prices of battery cells or higher remuneration of services due to lack of conventional power plants may lead to profitability in the near future. Therefore, further research activity regarding the optimization of BESS to provide FCR is recommended. Especially the optimization of losses in stationary BESS or concepts for providing FCR in large pools of smaller BESS are fields that may be promising for further research.

The decreasing number of conventional power plants is projected to lead to a reduced system inertia, which is paired with a higher susceptibility for fluctuation of the grid frequency. To avoid instabilities in the power grid, there seems to be no alternative but to replace real inertia with synthetic inertia. However, as shown in this thesis, the imitation of real inertia by synthetic inertia has a number of drawbacks when implementing it based on conventional converter design based on grid-following converters. The concept of grid-forming converters in order to implement synthetic inertia has evolved to a hotly debated topic in literature to overcome the drawbacks of a grid-following implementation. It can be expected that the field of grid-forming converters requires further research to address open questions such as current limitation. Nevertheless, grid-following concepts for implementing synthetic inertia may be useful for retrofitting existing systems.

The effects of reduced inertia and the influence of massive integration of renewable energy seem to become apparent already. According to ENTSO-E, the maximum value of frequency gradients has risen over the last few years. Massive frequency events like those observed in January 2020 and January 2021 could be more likely in the future. Although the root causes for these events were not directly coupled with reduced system inertia or renewable energy, such events show the danger of power outages also in the currently very reliable European power system. The consideration of BESS in grid restoration plans may therefore be an option to compensate for the lack

of conventional power plants with black-start capability in order to restore grid sections. Combined with renewable energy, a BESS holds the potential to contribute to restoring decentralized grid sections. Research activities on this topic can be useful in order to be able to adapt existing network restoration plans in advance to the decreasing number of conventional power plants with black start capabilities.

The driving force behind research activity related to multi-use operation of BESS today is to increase profitability. It can be assumed that this trend will continue in the next few years when barriers for BESS to participate in markets will be removed. This thesis addressed several research questions regarding the multi-use operation of BESS and tries to fill the gap between research activities related to simulation and planning and an actual implementation of a multi-use operation. However, the implementation of a multi-use operation is highly dependent on project-specific characteristics. With an increasing number of real BESS projects that are actually operated in multi-use operation, many new research questions can therefore be expected in the next few years. This also makes this topic interesting for future research. With this in mind, the topic of multi-use operation of BESS remains an interesting and challenging research topic for the future.

A Appendix: Additional Fundamentals of Power Systems and Batteries

The electric power grid transmits the energy generated in generators to the consumers. Historically, the transfer takes place in one direction only. Today, a trend to a generation also on the consumer side can be observed. This is due to the effort to integrate an enormous amount of DER into the grid to subsequently reduce greenhouse gas emissions as already described in Chp. 1. Fig. A.1 shows an example of the structure of the electric power grid. Primary energy resources (run-of-river, steam, gas, etc.) drive turbines, which in turn drive generators (traditionally synchronous generators). The generators produce a three-phase voltage system $\underline{\mathbf{U}}$. An electrical resistance connected to the generator would lead to a three-phase current system $\underline{\mathbf{I}}$, leading to an active power that is consumed by the resistor.

Since the consumer side is usually located at a certain distance from the power plant, the power is transmitted via a line. The line has a certain impedance, which leads to losses in the line. The impedance increases with the cable length and depends on the voltage level of the three-phase system. At a large distance between generation and load, the losses would be very high. To overcome such a situation, $\underline{\mathbf{U}}$ is transformed to higher voltage levels. This is done via transformers.

Traditionally, the electric power grid is divided into seven Network Layer (NL), which represent different voltage levels and the transformation between them. Dependent on the amount of power that is to be transmitted or consumed, the correspondent NL is used to keep losses at a rational level. The actual generation takes place outside of the NL system. Due to the design, maximum voltages of up to 27 kV can be provided by the generator. The conversion to the voltage level used in the power grid takes place via generator transformers. Large power plants use generator transformers that are among the largest technically used transformers due to their high power output and their weight of more than 500 t. The actual NL system starts at the secondary side of the generator transformer. In large power plants a transformation from 27 kV to the voltage level in the first NL is performed. The first NL, the "ultra-high voltage grid", is used to transmit the highest amount of power. In Europe the voltage levels of the first NL are usually 380 kV and 220 kV. Smaller power plants are connected to lower NL, either to the "high-voltage grid" or the "medium-voltage grid". On the consumer side the connection of the loads also depends on the amount of power that is consumed by the loads. Loads with high power consumption are connected to the medium-voltage grid, but most of the consumers, including households, are connected to the "low-voltage grid".

In order to ensure a successful supply of the consumers by the generators, certain characteristics of the network are required. Parts relevant to this work will be discussed below.

A.1 Fundamentals of Three-Phase Systems

In the following chapters definitions for three-phase systems are given.

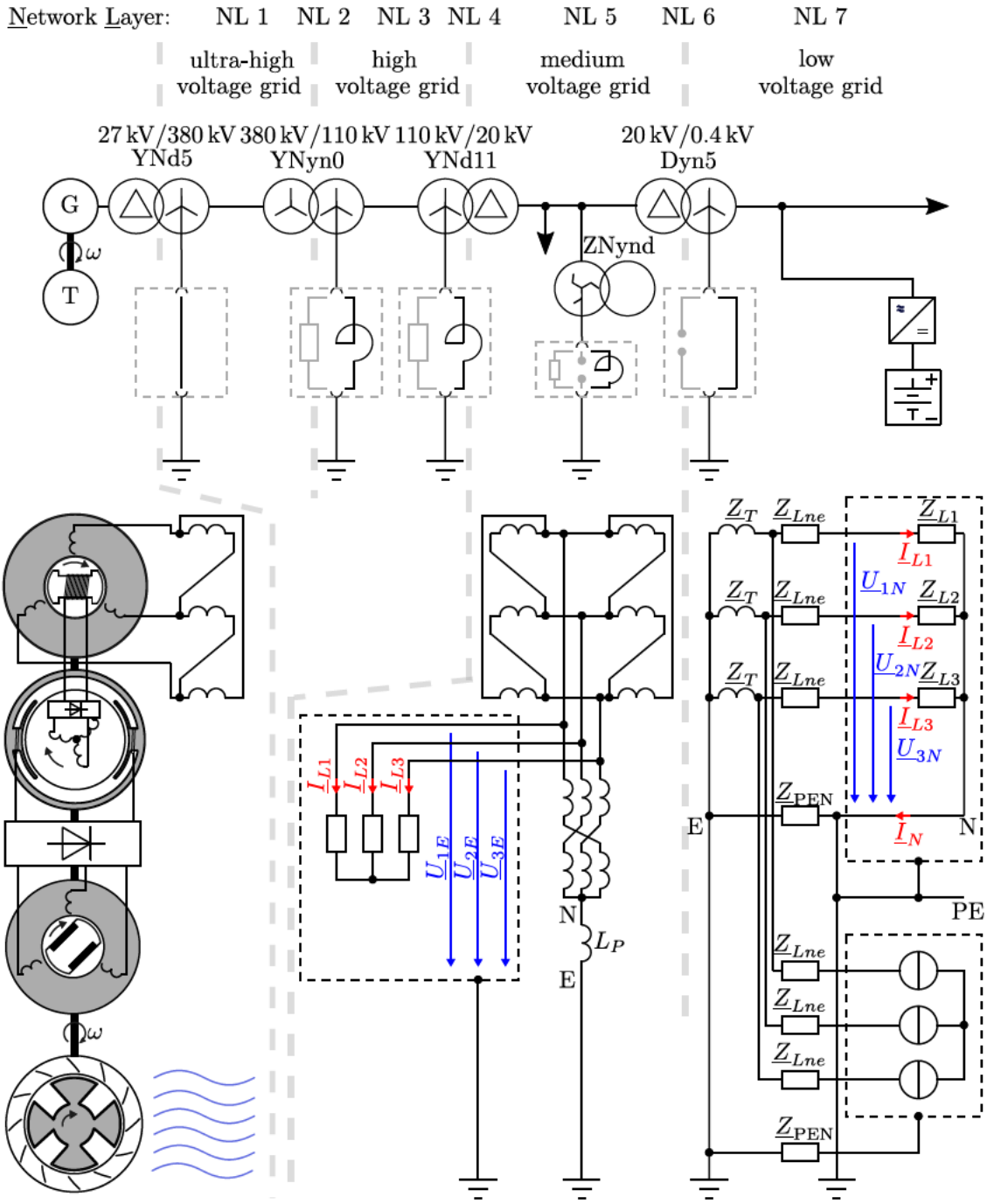

Figure A.1: Structure of the electric power grid.

A.1.1 Basic Definitions

The following chapters summarize the definitions of RMS-values, RMS-vectors, vectors of instantaneous values and waveforms.

A.1.1.1 RMS-Values

The cycle time of a harmonic function U_t is defined as $T = \frac{1}{f}$, where f is the frequency of the function. The angular frequency is defined as $\omega = 2\pi f$. Based on these definitions, the RMS-value U of a harmonic function

$$U_t = \hat{U} \cdot \sin(\omega t + \varphi_U) \tag{A.1}$$

is calculated by

$$\begin{aligned} U &= \sqrt{\frac{1}{T}\int_t^{t+T} U_t(\tilde{t})^2 \, d\tilde{t}} \overset{\varphi_U=0}{=} \sqrt{\frac{1}{T}\int_t^{t+T} \left(\hat{U} \cdot \sin \omega\tilde{t}\right)^2 \, d\tilde{t}} = \\ &= \hat{U} \cdot \sqrt{\frac{1}{T} \cdot \left[\frac{\tilde{t}}{2} - \frac{1}{4\omega}\sin(2\omega\tilde{t}) + const\right]_{\tilde{t}=0}^{\tilde{t}=T}} = \hat{U} \cdot \sqrt{\frac{1}{T} \cdot \frac{T}{2}} = \frac{\hat{U}}{\sqrt{2}}. \end{aligned} \tag{A.2}$$

A.1.1.2 RMS-Vectors

The complex AC calculation is a method of electrical engineering for the description and calculation of the behavior of linear time-invariant systems with sinusoidal alternating voltage and sinusoidal alternating current. For this purpose a RMS-vector $\underline{U}$ of a harmonic function U_t is defined by

$$\underline{U} = \frac{\hat{U}}{\sqrt{2}} \cdot e^{j(\omega t + \varphi_U)} = U \cdot e^{j(\omega t + \varphi_U)}. \tag{A.3}$$

A.1.1.3 Vector of Instantaneous Values

The vector of instantaneous values of the RMS-vector $\underline{U}$ is defined by $\hat{\underline{U}}$:

$$\hat{\underline{U}} = \hat{U} \cdot e^{j(\omega t + \varphi_U)}. \tag{A.4}$$

A.1.1.4 Waveform

The waveform of the harmonic function U_t can be calculated by building the imaginary part of the RMS-vector $\underline{U}$:

$$\begin{aligned} U_t &= \mathfrak{Im}\left(\hat{U} \cdot e^{j(\omega t + \varphi_U)}\right) = \frac{1}{2j} \cdot \left(\hat{\underline{U}} - \hat{\underline{U}}^*\right) \\ &= \frac{1}{2j} \cdot \left(\hat{U} \cdot e^{j(\omega t + \varphi_U)} - \hat{U} \cdot e^{-j(\omega t + \varphi_U)}\right) = \hat{U} \cdot \sin(\omega t + \varphi_U) = \\ &= \sqrt{2} \cdot U \cdot \sin(\omega t + \varphi_U). \end{aligned} \tag{A.5}$$

A.1.1.5 Addition of RMS-Vectors

There are three types of voltage vectors in three-phase systems; phase-to-phase voltages, phase-to-earth voltages and phase-to-neutral voltages. Definitions for these voltages are given in the next chapter. The phase-to-earth voltages can be calculated based on the vector addition of the corresponding phase-to-neutral voltages. Assuming a symmetric three-phase system and that there is no displacement voltage present, the vector addition is calculated by

$$\underline{U}_{12} = \underline{U}_{1N} - \underline{U}_{2N} = \underline{U}_{2E} - \underline{U}_{3E} = \frac{U_n}{\sqrt{3}} \cdot (1 - \underline{a}^2) = U_n \cdot e^{j30^\circ} \tag{A.6}$$

using the rotation operator $\underline{a} = e^{\frac{2\pi}{3}}$.

A.1.2 Voltage Definitions

The following chapters describe describe relevant voltage definitions.

A.1.2.1 Generator

The generator shown in Fig. A.1 is an externally excited synchronous generator, mostly used in large power plants to produce the power output. The excitement of such machines is usually realized by an External Pole Synchronous Machine (EPSM) and a Permanent-Magnet Synchronous Machine (PMSM), both mounted on the same shaft. The rotating rectifier in the EPSM provides the DC voltage for the rotor of the generator, while the PMSM provides the DC voltage for the excitation of the EPSM. On the common shaft, the turbine is also attached. It obtains the required torque from the primary energy source. In Fig. A.1 a Kaplan-turbine is shown, which converts the kinetic energy of the primary energy resource, which is run-of-river, to rotational energy. The torque to the turbine is controlled by guide vanes. As soon as the turbine starts to rotate, the excitation system supplies a DC voltage for the rotor of the generators. This leads to a constant magnetic field transverse to the axis of rotation of the rotor. Because the rotor is mounted on the same shaft as the turbine, it rotates at the same frequency as the turbine. The stator of the generator has three windings offset by 120°. Based on the law of induction, the rotating magnetic field induces voltages in these windings of the stator. The resulting voltages form the complex three-phase system $\underline{\mathbf{U}}_N$ with a nominal voltage U_n. The complex three-phase system is symmetric if the rotor is spinning steadily with an angular frequency ω and the excitation voltage is constant. Eq. (A.7) describes a symmetric, harmonic, complex three-phase system, where $\underline{a} = e^{(j\frac{2\pi}{3})}$ is the "phasor rotation operator" and $\underline{U}_{1N}$, $\underline{U}_{2N}$ and $\underline{U}_{3N}$ are the complex phase-to-neutral voltages:

$$\underline{\mathbf{U}}_N = \begin{pmatrix} \underline{U}_{1N} \\ \underline{U}_{2N} \\ \underline{U}_{3N} \end{pmatrix} = \begin{pmatrix} U_{1N} \cdot e^{j(\omega t + \varphi_{U1})} \\ U_{2N} \cdot e^{j(\omega t + \frac{4\pi}{3} + \varphi_{U2})} \\ U_{3N} \cdot e^{j(\omega t + \frac{2\pi}{3} + \varphi_{U3})} \end{pmatrix} \overset{symm}{=} \begin{pmatrix} \frac{U_n}{\sqrt{3}} \cdot e^{(j\omega t)} \\ \frac{U_n}{\sqrt{3}} \cdot e^{j(\omega t + \frac{4\pi}{3})} \\ \frac{U_n}{\sqrt{3}} \cdot e^{j(\omega t + \frac{2\pi}{3})} \end{pmatrix} = \begin{pmatrix} \underline{U}_{1N} \\ \underline{U}_{1N} \cdot \underline{a}^2 \\ \underline{U}_{1N} \cdot \underline{a} \end{pmatrix}. \tag{A.7}$$

The three-phase system can also be described by Eq. (A.8) with the complex phase-to-phase voltages $\underline{U}_{12}$, $\underline{U}_{23}$ and $\underline{U}_{31}$:

$$\underline{\mathbf{U}} = \begin{pmatrix} \underline{U}_{12} \\ \underline{U}_{23} \\ \underline{U}_{31} \end{pmatrix} = \begin{pmatrix} \underline{U}_{1N} - \underline{U}_{2N} \\ \underline{U}_{2N} - \underline{U}_{3N} \\ \underline{U}_{3N} - \underline{U}_{1N} \end{pmatrix} \overset{symm}{=} \frac{U_n}{\sqrt{3}} \cdot \begin{pmatrix} 1 - \underline{a}^2 \\ 1 - \underline{a} \\ \underline{a} - 1 \end{pmatrix} = U_n \cdot \begin{pmatrix} e^{j30°} \\ e^{-j30°} \\ e^{j150°} \end{pmatrix}. \tag{A.8}$$

The three-phase voltage system $\underline{\mathbf{U}}_N$ is conventionally indicated as a matrix of complex RMS-vectors. The three-phase system $\underline{\hat{\mathbf{U}}}_N$, on the other hand, is indicated as a matrix of complex vectors of instantaneous values:

$$\underline{\hat{\mathbf{U}}}_N = \begin{pmatrix} \underline{\hat{U}}_{1N} \\ \underline{\hat{U}}_{2N} \\ \underline{\hat{U}}_{3N} \end{pmatrix} = \begin{pmatrix} \hat{U}_{1N} \cdot e^{j(\omega t + \varphi_{U1})} \\ \hat{U}_{2N} \cdot e^{j(\omega t + \frac{4\pi}{3} + \varphi_{U2})} \\ \hat{U}_{3N} \cdot e^{j(\omega t + \frac{2\pi}{3} + \varphi_{U3})} \end{pmatrix} \overset{symm}{=} \begin{pmatrix} \sqrt{2} \cdot \frac{U_n}{\sqrt{3}} \cdot e^{(j\omega t)} \\ \sqrt{2} \cdot \frac{U_n}{\sqrt{3}} \cdot e^{j(\omega t + \frac{4\pi}{3})} \\ \sqrt{2} \cdot \frac{U_n}{\sqrt{3}} \cdot e^{j(\omega t + \frac{2\pi}{3})} \end{pmatrix} = \begin{pmatrix} \hat{U}_{1N} \\ \hat{U}_{1N} \cdot \underline{a}^2 \\ \hat{U}_{1N} \cdot \underline{a} \end{pmatrix}. \tag{A.9}$$

To describe the waveform of the phase-to-neutral voltages $\mathbf{U}_{N,t}$, the projection of the complex vectors to the imaginary axis are used as follows:

$$\mathbf{U}_{N,t} = \mathfrak{Im} \begin{pmatrix} \underline{\hat{U}}_{1N} \\ \underline{\hat{U}}_{2N} \\ \underline{\hat{U}}_{3N} \end{pmatrix} = \begin{pmatrix} U_{1N,t} \\ U_{2N,t} \\ U_{3N,t} \end{pmatrix} = \begin{pmatrix} \hat{U}_{1N} \cdot \sin(\omega t) \\ \hat{U}_{2N} \cdot \sin(\omega t + \frac{4\pi}{3}) \\ \hat{U}_{3N} \cdot \sin(\omega t + \frac{2\pi}{3}) \end{pmatrix} = \begin{pmatrix} \sqrt{2} \cdot U_n \cdot \sin(\omega t) \\ \sqrt{2} \cdot U_n \cdot \sin(\omega t + \frac{4\pi}{3}) \\ \sqrt{2} \cdot U_n \cdot \sin(\omega t + \frac{2\pi}{3}) \end{pmatrix}. \tag{A.10}$$

Fig. A.2 shows the different voltages in the generator, the circuit diagram, the vector diagram and a plot of the waveforms, with the conventions used in this thesis.

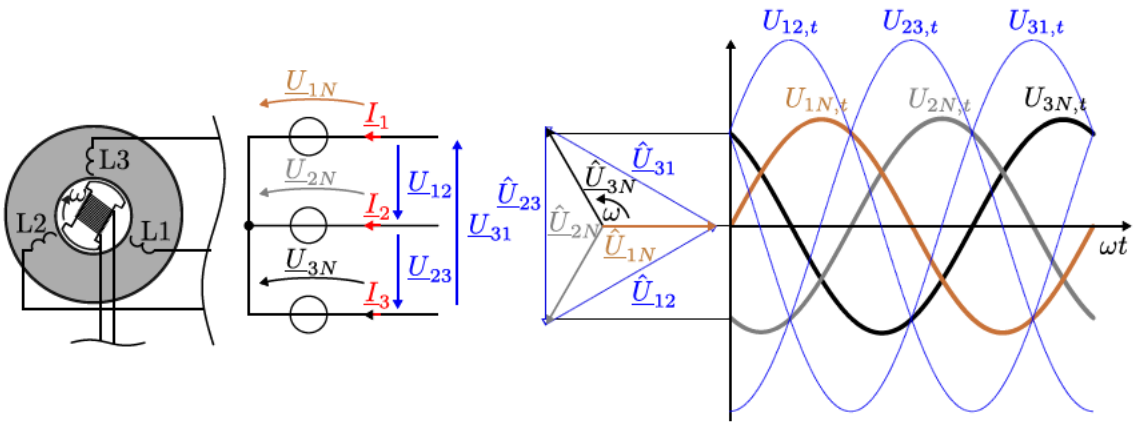

Figure A.2: Basic definitions of a three phase system in (a) the generator windings, (b) the circuit diagram, (c) the vector diagram and (d) in the waveforms.

A.1.2.2 MV-Loads

In Fig. A.1 a load is connected to NL 5. Because there is no neutral point at the MV-load, there are only phase-to-earth voltages available. The three phase-to-earth voltages $\underline{U}_{1E}$, $\underline{U}_{2E}$ and $\underline{U}_{3E}$ build a three-phase voltage system $\underline{\mathbf{U}}_E$. When there is no displacement voltage $\underline{U}_{NE} = 0$, then the three-phase system $\underline{\mathbf{U}}_E$ is symmetric and can be described by

$$\underline{\mathbf{U}}_E = \begin{pmatrix} \underline{U}_{1E} \\ \underline{U}_{2E} \\ \underline{U}_{3E} \end{pmatrix} = \begin{pmatrix} U_{1E} \cdot e^{(j\omega t + \varphi_{U_{1E}})} \\ U_{2E} \cdot e^{(j\omega t + \frac{4\pi}{3} + \varphi_{U_{2E}})} \\ U_{3E} \cdot e^{(j\omega t + \frac{2\pi}{3} + \varphi_{U_{3E}})} \end{pmatrix} \overset{\text{symm}}{\underset{\underline{U}_{NE}=0}{=}} \frac{U_n}{\sqrt{3}} \begin{pmatrix} e^{(j\omega t)} \\ e^{(j\omega t + \frac{4\pi}{3})} \\ e^{(j\omega t + \frac{2\pi}{3})} \end{pmatrix} = \begin{pmatrix} \underline{U}_{1E} \\ \underline{U}_{1E} \cdot \underline{a}^2 \\ \underline{U}_{1E} \cdot \underline{a} \end{pmatrix}. \tag{A.11}$$

The relation between the three-phase systems $\underline{\mathbf{U}}_N$ and $\underline{\mathbf{U}}_E$ at the MV-load is defined by

$$\underline{\mathbf{U}}_E = \underline{\mathbf{U}}_N + \underline{U}_{NE}. \tag{A.12}$$

The three-phase system $\underline{\mathbf{U}}$ in Eq. (A.8) can also be defined by the phase-to-earth voltages:

$$\underline{\mathbf{U}} = \begin{pmatrix} \underline{U}_{12} \\ \underline{U}_{23} \\ \underline{U}_{31} \end{pmatrix} = \begin{pmatrix} \underline{U}_{1E} - \underline{U}_{2E} \\ \underline{U}_{2E} - \underline{U}_{3E} \\ \underline{U}_{3E} - \underline{U}_{1E} \end{pmatrix} \overset{\text{symm}}{\underset{\underline{U}_{NE}=0}{=}} \frac{U_n}{\sqrt{3}} \cdot \begin{pmatrix} 1 - \underline{a}^2 \\ 1 - \underline{a} \\ \underline{a} - 1 \end{pmatrix} = U_n \cdot \begin{pmatrix} e^{j30°} \\ e^{-j30°} \\ e^{j150°} \end{pmatrix}. \tag{A.13}$$

The three-phase system $\underline{\mathbf{U}}_E$ is conventionally indicated as a matrix of complex RMS-vectors. The three-phase system $\hat{\underline{\mathbf{U}}}_E$ is indicated as a matrix of complex vectors of instantaneous values:

$$\hat{\underline{\mathbf{U}}}_E = \begin{pmatrix} \hat{\underline{U}}_{1E} \\ \hat{\underline{U}}_{2E} \\ \hat{\underline{U}}_{3E} \end{pmatrix} = \begin{pmatrix} \hat{U}_{1E} \cdot e^{j(\omega t + \varphi_{U_{1E}})} \\ \hat{U}_{2E} \cdot e^{j(\omega t + \frac{4\pi}{3} + \varphi_{U_{2E}})} \\ \hat{U}_{3E} \cdot e^{j(\omega t + \frac{2\pi}{3} + \varphi_{U_{3E}})} \end{pmatrix} \overset{\text{symm}}{\underset{\underline{U}_{NE}=0}{=}} \begin{pmatrix} \hat{U}_{1E} \\ \hat{U}_{1E} \cdot \underline{a}^2 \\ \hat{U}_{1E} \cdot \underline{a} \end{pmatrix} = \begin{pmatrix} \sqrt{2} \cdot U_n \cdot e^{(j\omega t)} \\ \sqrt{2} \cdot U_n \cdot e^{j(\omega t + \frac{4\pi}{3})} \\ \sqrt{2} \cdot U_n \cdot e^{j(\omega t + \frac{2\pi}{3})} \end{pmatrix}. \tag{A.14}$$

To describe the waveform of the phase-to-earth voltages $\mathbf{U}_{E,t}$, the projection of the complex vectors to the imaginary axis are used as follows:

$$\mathbf{U}_{E,t} = \Im\mathrm{m} \begin{pmatrix} \hat{\underline{U}}_{1E} \\ \hat{\underline{U}}_{2E} \\ \hat{\underline{U}}_{3E} \end{pmatrix} = \begin{pmatrix} U_{1E,t} \\ U_{2E,t} \\ U_{3E,t} \end{pmatrix} \overset{\text{symm}}{\underset{\underline{U}_{NE}=0}{=}} \begin{pmatrix} \hat{U}_{1E} \cdot \sin(\omega t) \\ \hat{U}_{2E} \cdot \sin(\omega t + \frac{4\pi}{3}) \\ \hat{U}_{3E} \cdot \sin(\omega t + \frac{2\pi}{3}) \end{pmatrix} = \begin{pmatrix} \sqrt{2} U_n \cdot \sin(\omega t) \\ \sqrt{2} U_n \cdot \sin(\omega t + \frac{4\pi}{3}) \\ \sqrt{2} U_n \cdot \sin(\omega t + \frac{2\pi}{3}) \end{pmatrix}. \tag{A.15}$$

Fig. A.3 shows the different voltages at the MV-load and in the vector diagram, with the conventions used in this thesis.

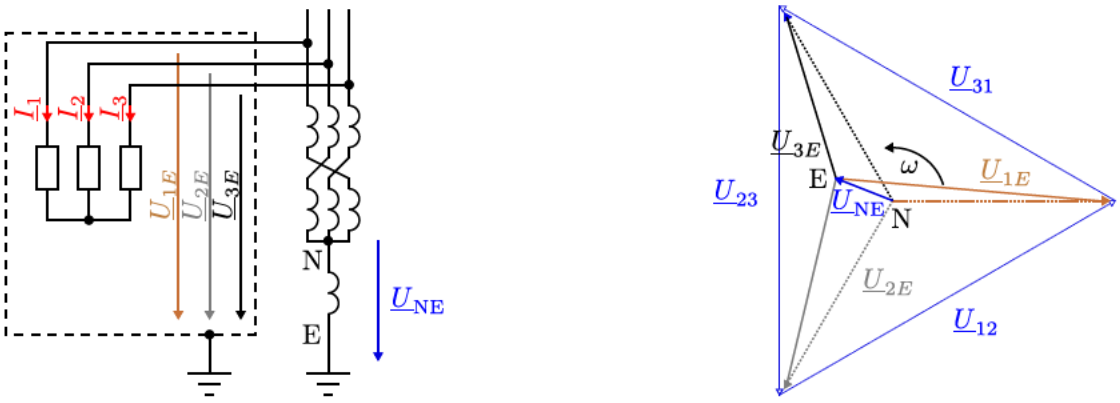

Figure A.3: Basic definitions of a three phase system.

A.1.2.3 LV-Loads

In Fig. A.1 a load is connected to NL 7, the low-voltage grid. The LV-grid is usually designed as a 4-wire-network. In this case the network system is called "TN-C" and the LV-grid is operated unbalanced intentionally. To ensure safety, the exposed conductive parts of the loads are earthed by connecting them to the neutral conductor. This protective measure is called "protective earthing". An earth-to-ground connection of the exposed conductive parts of electrical equipment helps protect from electric shock by keeping the exposed conductive surface of connected devices close to earth potential, when a failure of electrical insulation occurs. In the case of a "TN-C-S" network system, an additional protective conductor (PE) is used. The common neutral- and protective conductor (PEN) is thereby separated into a neutral conductor (N) and a protective conductor (PE). In this case, it is a 5-wire system. In households this separation is done at the PCC. When a fault occurs, current flows from the power system to earth. If a TN-C network system is used, any disruption of the neutral conductor would raise the voltage level of the exposed conductive parts of the loads to the nominal phase-to-neutral voltage. By using the TN-C-S network system such a case is prevented because the current can flow through the PE-conductor to the PEN-conductor.

An unbalanced operation of the LV network leads to a current in the PEN conductor, which in turn leads to a displacement voltage $\underline{U}_{NE}$. The formal definitions of $\underline{\mathbf{U}}_N$, $\underline{\mathbf{U}}_E$, $\underline{\mathbf{U}}$, $\hat{\underline{\mathbf{U}}}_N$, $\hat{\underline{\mathbf{U}}}_E$, $\hat{\underline{\mathbf{U}}}_{N,t}$ and $\hat{\underline{\mathbf{U}}}_{E,t}$ from above are also valid for the voltages in the LV grid as shown in Fig. A.4.

A.1.3 Current Definitions

The currents in a three-phase system $\underline{\mathbf{U}}_N$ are defined on the basis of the same definitions as used in Chp. A.1.2. In case of a symmetric three-phase system and a symmetric load, the current RMS-vectors $\underline{\mathbf{I}}$ are rotated by the angle φ_I with respect to the vector $\left(1, \underline{a}^2, \underline{a}\right)^\top$, which leads to

$$\underline{\mathbf{I}} = \begin{pmatrix} \underline{I}_{L1} \\ \underline{I}_{L2} \\ \underline{I}_{L3} \end{pmatrix} = \begin{pmatrix} I_{L1} \cdot e^{(j\omega t + \varphi_{I1})} \\ I_{L2} \cdot e^{(j\omega t + \frac{4\pi}{3} + \varphi_{I2})} \\ I_{L3} \cdot e^{(j\omega t + \frac{2\pi}{3} + \varphi_{I3})} \end{pmatrix} \overset{symm}{=} I_{L1} \cdot \begin{pmatrix} e^{(j\omega t + \varphi_I)} \\ e^{(j\omega t + \frac{4\pi}{3} + \varphi_I)} \\ e^{(j\omega t + \frac{2\pi}{3} + \varphi_I)} \end{pmatrix} = \underline{I}_{L1} \cdot \begin{pmatrix} 1 \\ \underline{a}^2 \\ \underline{a} \end{pmatrix} \tag{A.16}$$

and is shown in Fig. A.5.

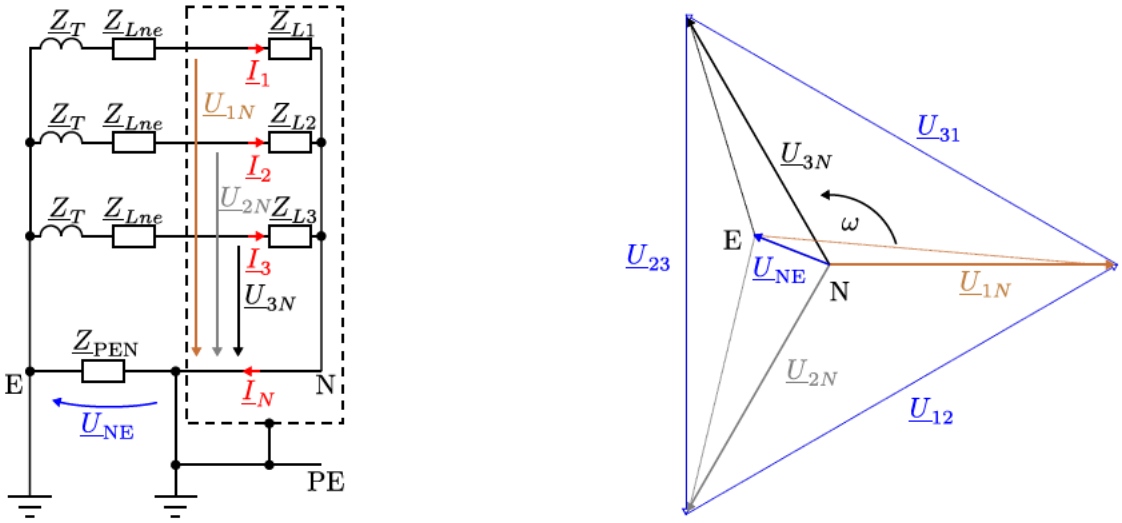

Figure A.4: Basic definitions of a three phase system.

The currents of vectors of instantaneous values are defined by $\hat{\underline{\mathbf{I}}}$:

$$\hat{\underline{\mathbf{I}}} = \begin{pmatrix} \hat{\underline{I}}_{L1} \\ \hat{\underline{I}}_{L2} \\ \hat{\underline{I}}_{L3} \end{pmatrix} = \begin{pmatrix} \hat{I}_{L1} \cdot e^{j(\omega t + \varphi_{I1})} \\ \hat{I}_{L2} \cdot e^{j(\omega t + \frac{4\pi}{3} + \varphi_{I2})} \\ \hat{I}_{L3} \cdot e^{j(\omega t + \frac{2\pi}{3} + \varphi_{I3})} \end{pmatrix} \overset{symm}{=} \hat{I}_1 \cdot \begin{pmatrix} e^{(j\omega t + \varphi_I)} \\ e^{(j\omega t + \frac{4\pi}{3} + \varphi_I)} \\ e^{(j\omega t + \frac{2\pi}{3} + \varphi_I)} \end{pmatrix} = \sqrt{2} \cdot I_1 \cdot \begin{pmatrix} 1 \\ \underline{a}^2 \\ \underline{a} \end{pmatrix}. \tag{A.17}$$

The waveform of currents are defined by $\mathbf{I}_t$:

$$\mathbf{I}_t = \Im\mathrm{m} \begin{pmatrix} \hat{\underline{I}}_{L1} \\ \hat{\underline{I}}_{L2} \\ \hat{\underline{I}}_{L3} \end{pmatrix} = \begin{pmatrix} I_{L1,t} \\ I_{L2,t} \\ I_{L3,t} \end{pmatrix} \overset{symm}{=} \begin{pmatrix} \hat{I}_{L1} \cdot \sin(\omega t + \varphi_I) \\ \hat{I}_{L2} \cdot \sin(\omega t + \frac{4\pi}{3} + \varphi_I) \\ \hat{I}_{L3} \cdot \sin(\omega t + \frac{2\pi}{3} + \varphi_I) \end{pmatrix} = \sqrt{2} I_{L1} \cdot \begin{pmatrix} \sin(\omega t + \varphi_I) \\ \sin(\omega t + \frac{4\pi}{3} + \varphi_I) \\ \sin(\omega t + \frac{2\pi}{3} + \varphi_I) \end{pmatrix}. \tag{A.18}$$

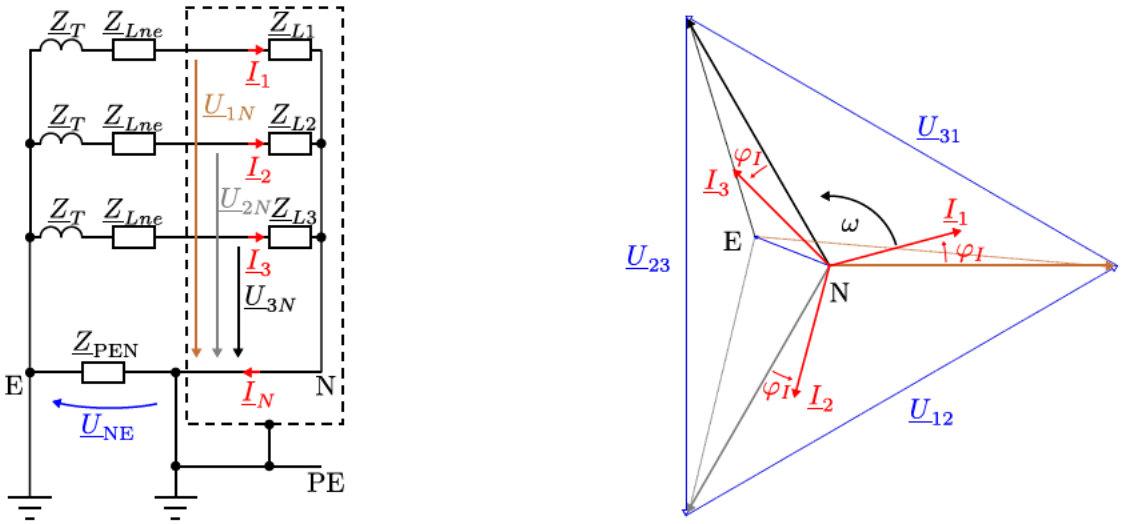

Figure A.5: Basic definitions of a three phase system.

A.1.4 Power Definitions

The following chapters describe relevant power definitions.

A.1.4.1 Basic Power Definitions

The complex apparent power in a three-phase system is defined by $\underline{S}$ and calculated as follows:

$$\begin{aligned}\underline{S} &= \underline{\mathbf{U}}_N^{\top} \cdot \underline{\mathbf{I}}^{*} = \underline{U}_{1N} \cdot \underline{I}_{L1}^{*} + \underline{U}_{2N} \cdot \underline{I}_{L2}^{*} + \underline{U}_{3N} \cdot \underline{I}_{L3}^{*} = \\ &= U_{1N} I_1 \cdot e^{j(\varphi_{U_{1N}} - \varphi_{I_{L1}})} + U_{2N} I_2 \cdot e^{j(\varphi_{U_{2N}} - \varphi_{I_{L2}})} + U_{3N} I_3 \cdot e^{j(\varphi_{U_{3N}} - \varphi_{I_{L3}})} =. \\ &\overset{symm}{=} 3U_{1N} I_1 \cdot e^{j(\varphi_{U_{1N}} - \varphi_{I_{L1}})} = \sqrt{3} U_{12} I_1 \cdot e^{j(\varphi_{U_{1N}} - \varphi_{I_{L1}})}\end{aligned} \tag{A.19}$$

The absolute value of $\underline{S}$ is defined by

$$S = |\underline{S}| \overset{symm}{=} \sqrt{3} U_{12} I_{L1}. \tag{A.20}$$

The apparent power in each phase is summarized in $\underline{\mathbf{S}}$:

$$\underline{\mathbf{S}} = \begin{pmatrix} \underline{S}_{L1} \\ \underline{S}_{L2} \\ \underline{S}_{L3} \end{pmatrix} = \begin{pmatrix} \underline{U}_{1N} \cdot \underline{I}_{L1}^{*} \\ \underline{U}_{2N} \cdot \underline{I}_{L2}^{*} \\ \underline{U}_{3N} \cdot \underline{I}_{L3}^{*} \end{pmatrix}. \tag{A.21}$$

The active power in a three-phase system is defined by P, which is the real part of $\underline{S}$ and calculated as follows:

$$\begin{aligned}P = \mathfrak{Re}\left(\underline{S}\right) &= U_{1N} I_{L1} \cos\left(\varphi_{U_{1N}} - \varphi_{I_{L1}}\right) + U_{2N} I_2 \cos\left(\varphi_{U_{2N}} - \varphi_{I_{L2}}\right) + U_{3N} I_{L3} \cos\left(\varphi_{U_{3N}} - \varphi_{I_{L3}}\right) = \\ &\overset{symm}{=} 3U_{1N} I_{L1} \cdot \cos\left(\varphi_I\right) = \sqrt{3} U_{12} I_{L1} \cdot \cos\left(\varphi_I\right)\end{aligned}. \tag{A.22}$$

The active power in each phase is summarized in $\mathbf{P}$, with $P = \|\mathbf{P}\|_1$:

$$\mathbf{P} = \begin{pmatrix} P_{L1} \\ P_{L2} \\ P_{L3} \end{pmatrix} = \begin{pmatrix} U_{1N} I_{L1} \cos\left(\varphi_{U_{1N}} - \varphi_{I_{L1}}\right) \\ U_{2N} I_{L2} \cos\left(\varphi_{U_{2N}} - \varphi_{I_{L2}}\right) \\ U_{3N} I_{L3} \cos\left(\varphi_{U_{3N}} - \varphi_{I_{L3}}\right) \end{pmatrix}. \tag{A.23}$$

The reactive power in a three-phase system is defined by Q, which is the imaginary part of $\underline{S}$ and calculated as follows:

$$\begin{aligned}Q = \mathfrak{Im}\left(\underline{S}\right) &= U_{1N} I_1 \sin\left(\varphi_{U_{1N}} - \varphi_{I_{L1}}\right) + U_{2N} I_2 \sin\left(\varphi_{U_{2N}} - \varphi_{I_{L2}}\right) + U_{3N} I_3 \sin\left(\varphi_{U_{3N}} - \varphi_{I_{L3}}\right) = \\ &\overset{symm}{=} 3U_{1N} I_{L1} \cdot \sin\left(\varphi_I\right) = \sqrt{3} U_{12} I_{L1} \cdot \sin\left(\varphi_I\right)\end{aligned}. \tag{A.24}$$

The reactive power in each phase is summarized in $\mathbf{Q}$, with $Q = \|\mathbf{Q}\|_1$:

$$\mathbf{Q} = \begin{pmatrix} Q_{L1} \\ Q_{L2} \\ Q_{L3} \end{pmatrix} = \begin{pmatrix} U_{1N} I_{L1} \sin\left(\varphi_{U_{1N}} - \varphi_{I_{L1}}\right) \\ U_{2N} I_2 \sin\left(\varphi_{U_{2N}} - \varphi_{I_{L2}}\right) \\ U_{3N} I_{L3} \sin\left(\varphi_{U_{3N}} - \varphi_{I_{L3}}\right) \end{pmatrix}. \tag{A.25}$$

A.1.4.2 Reference System

Based on the direction in which the currents in Fig. A.1 are drawn, a reference system is implicitly applied, which is referred to as "load reference system". In the load reference system the active power $P > 0$ if the load consumes power. When active power is fed into the grid, as it is shown in Fig. A.2, the active power $P < 0$.

A.1.4.3 Instantaneous Power

The instantaneous value of the active power is defined by P_t and is calculated by

$$\begin{aligned}
P_t &= \mathbf{U}_{N,t}^{\top} \cdot \mathbf{I}_t = U_{1N,t} \cdot I_{L1,t} + U_{2N,t} \cdot I_{L2,t} + U_{3N,t} \cdot I_{L3,t} = \\
&= \hat{U}_{1N}\hat{I}_{L1} \cdot \frac{1}{2}\left(\cos\left(\varphi_{U_{1N}} - \varphi_{I_{L1}}\right) + \cos\left(2\omega t + \varphi_{U_{1N}} + \varphi_{I_{L1}}\right)\right) + \\
&+ \hat{U}_{2N}\hat{I}_{L2} \cdot \frac{1}{2}\left(\cos\left(\varphi_{U_{2N}} - \varphi_{I_{L2}}\right) + \cos\left(2\omega t + \varphi_{U_{2N}} + \frac{4\pi}{3} + \varphi_{I_{L2}} + \frac{4\pi}{3}\right)\right) + \\
&+ \hat{U}_{3N}\hat{I}_{L3} \cdot \frac{1}{2}\left(\cos\left(\varphi_{U_{3N}} - \varphi_{I_{L3}}\right) + \cos\left(2\omega t + \varphi_{U_{3N}} + \frac{2\pi}{3} + \varphi_{I_{L3}} + \frac{2\pi}{3}\right)\right) \overset{symm}{=} \\
&\overset{symm}{=} \frac{1}{2}\hat{U}_{1N}\hat{I}_{L1} \cdot \left(3\cos\left(\varphi_I\right) + \cos\left(2\omega t + \varphi_I\right) + \cos\left(2\omega t + \frac{2\pi}{3} + \varphi_I\right) + \right. \\
&\left. + \cos\left(2\omega t + \frac{4\pi}{3} + \varphi_I\right)\right) = \\
&= 3U_{1N}I_{L1}\cos\left(\varphi_I\right) = P
\end{aligned} \tag{A.26}$$

where the three $\cos(2\omega t)$-terms sum up to zero in case of symmetrical three-phase systems. The major advantage of symmetric, harmonic three-phase systems, therefore, is the constant instantaneous active power $P_t = P$, while the instantaneous active power of each phase is time-dependent proportional to $\cos(2\omega t)$. The general relation between P_t and P is

$$P = \frac{1}{T}\int_t^{t+T} P_t(\tilde{t})\, d\tilde{t}. \tag{A.27}$$

According to Peng et al. [139] the instantaneous value of the reactive power is defined by Q_t, which is calculated by

$$\begin{aligned}
Q_t = \|\mathbf{Q}_t\|_2 &= \left\| \begin{pmatrix} Q_{L1,t} \\ Q_{L2,t} \\ Q_{L3,t} \end{pmatrix} \right\|_2 = \|\mathbf{U}_{N,t} \times \mathbf{I}_t\|_2 = \left\| \begin{pmatrix} 0 & -U_{3N,t} & U_{2N,t} \\ U_{3N,t} & 0 & -U_{1N,t} \\ -U_{2N,t} & U_{1N,t} & 0 \end{pmatrix} \cdot \begin{pmatrix} I_{L1,t} \\ I_{L2,t} \\ I_{L3,t} \end{pmatrix} \right\|_2 = \\
&= \sqrt{\left(U_{2N,t}I_{L3,t} - U_{3N,t}I_{L2,t}\right)^2 + \left(U_{3N,t}I_{L1,t} - U_{1N,t}I_{L3,t}\right)^2 + \left(U_{1N,t}I_{L2,t} - U_{2N,t}I_{L1,t}\right)^2}
\end{aligned} \tag{A.28}$$

The relation between Q_t and Q is

$$Q = \frac{1}{T}\int_t^{t+T} Q_t(\tilde{t})\, d\tilde{t}. \tag{A.29}$$

A.1.5 Per-Unit Definitions

Normalized values are described in lowercase letters. Normalized values are calculated by dividing them by their nominal value.

A.1.5.1 Voltages

All normalized RMS-voltages are calculated by dividing them by the nominal voltage U_n, which is defined as a phase-to-phase RMS-voltage (e.g. 400 V). The normalized three-phase voltage system $\underline{\mathbf{u}}_N$, therefore, is calculated by

$$\underline{\mathbf{u}}_N = \begin{pmatrix} \underline{u}_{1N} \\ \underline{u}_{2N} \\ \underline{u}_{3N} \end{pmatrix} = \frac{\underline{\mathbf{U}}_N}{\frac{U_n}{\sqrt{3}}} = \frac{\sqrt{3}}{U_n} \cdot \begin{pmatrix} \underline{U}_{1N} \\ \underline{U}_{2N} \\ \underline{U}_{3N} \end{pmatrix} \tag{A.30}$$

and the normalized three-phase voltage system $\underline{\mathbf{u}}_E$ is calculated by

$$\underline{\mathbf{u}}_E = \begin{pmatrix} \underline{u}_{1E} \\ \underline{u}_{2E} \\ \underline{u}_{3E} \end{pmatrix} = \frac{\underline{\mathbf{U}}_E}{\frac{U_E}{\sqrt{3}}} = \frac{\sqrt{3}}{U_E} \cdot \begin{pmatrix} \underline{U}_{1E} \\ \underline{U}_{2E} \\ \underline{U}_{3E} \end{pmatrix} \tag{A.31}$$

which both are identical to the three-phase voltage system $\underline{\mathbf{u}}$:

$$\underline{\mathbf{u}} = \underline{\mathbf{u}}_\mathbf{N} = \underline{\mathbf{u}}_\mathbf{E} = \begin{pmatrix} \underline{u}_{12} \\ \underline{u}_{23} \\ \underline{u}_{31} \end{pmatrix} = \frac{\underline{\mathbf{U}}}{U_n} = \frac{1}{U_n} \cdot \begin{pmatrix} \underline{U}_{12} \\ \underline{U}_{23} \\ \underline{U}_{31} \end{pmatrix}. \tag{A.32}$$

All normalized waveforms of voltages are calculated by dividing them by the voltage $\sqrt{2}U_n$. For example, the normalized three-phase voltage system $\mathbf{u}_{\mathbf{N},\mathbf{t}}$ is calculated by

$$\mathbf{u}_{\mathbf{N},\mathbf{t}} = \begin{pmatrix} u_{1N,t} \\ u_{2N,t} \\ u_{3N,t} \end{pmatrix} = \frac{\sqrt{3}}{\sqrt{2}U_n} \cdot \mathbf{U}_{\mathbf{N},\mathbf{t}} = \frac{\sqrt{3}}{\sqrt{2}U_n} \cdot \begin{pmatrix} U_{1N,t} \\ U_{2N,t} \\ U_{3N,t} \end{pmatrix}. \tag{A.33}$$

A.1.5.2 Currents

All RMS-currents are calculated by dividing them by the nominal current I_n, which is a RMS-value. The normalized RMS-current vectors $\underline{\mathbf{i}}$ are calculated by

$$\underline{\mathbf{i}} = \begin{pmatrix} i_{L1} \\ i_{L2} \\ i_{L3} \end{pmatrix} = \frac{\underline{\mathbf{i}}}{I_n} = \frac{1}{I_n} \cdot \begin{pmatrix} I_{L1} \\ I_{L2} \\ I_{L3} \end{pmatrix} \tag{A.34}$$

while the normalized waveforms of currents are calculated by dividing them by the current $\sqrt{2}I_n$:

$$\mathbf{i}_\mathbf{t} = \begin{pmatrix} i_{L1,t} \\ i_{L2,t} \\ i_{L3,t} \end{pmatrix} = \frac{\mathbf{I}_\mathbf{t}}{\sqrt{2}I_n} = \frac{1}{\sqrt{2}I_n} \cdot \begin{pmatrix} I_{L1,t} \\ I_{L2,t} \\ I_{L3,t} \end{pmatrix}. \tag{A.35}$$

A.1.5.3 Powers

The nominal value of power is defined by S_n, which is calculated based on the nominal voltage U_n and the nominal current I_n by

$$S_n = \sqrt{3}U_n I_n. \tag{A.36}$$

The normalized powers $\underline{s}$, s, q, p_t and q_t are calculated by dividing the corresponding unit-based powers by the nominal power. The normalized value of the active power, for example, is calculated by

$$p = \frac{P}{S_n}. \tag{A.37}$$

A.2 Transformations

The following chapters summarize relevant definitions of instantaneous symmetrical components and Park-components.

A.2.1 Instantaneous Symmetrical Components

To calculate the instantaneous values of the symmetrical components, the following definitions based on [64] can be used. The RMS-values of the symmetrical components are summarized by

$$\mathbf{U_{1\pm0,N}} = \begin{pmatrix} U_{10,N} \\ U_{1+,N} \\ U_{1-,N} \end{pmatrix} \tag{A.38}$$

where the zero-sequence voltage $U_{10,N}$ is defined by

$$U_{10,N} = \sqrt{\left(U_{10,N,\cos}^2 + U_{10,N,\sin}^2\right)}, \tag{A.39}$$

the positive-sequence voltage $U_{1+,N}$ is defined by

$$U_{1+,N} = \sqrt{\frac{1}{2}\left(U_{1+,N,\cos}^2 + U_{1+,N,\sin}^2\right)}, \tag{A.40}$$

and the negative-sequence voltage $U_{1-,N}$ is defined by

$$U_{1-,N} = \sqrt{\frac{1}{2}\left(U_{1-,N,\cos}^2 + U_{1-,N,\sin}^2\right)}. \tag{A.41}$$

The variables $U_{1\pm0,N,\cos}$, which are defined by

$$U_{10,N,\cos} = \frac{1}{3\cdot\sqrt{2}}\left(U_{1N,cos} + U_{2N,cos} + U_{3N,cos}\right) \tag{A.42}$$

$$U_{1+,N,\cos} = \frac{1}{6}\Big(2U_{1N,cos} - U_{2N,cos} - U_{3N,cos} - \sqrt{3}(U_{3N,sin} - U_{3N,sin})\Big) \tag{A.43}$$

$$U_{1-,N,\cos} = \frac{1}{6}\Big(2U_{1N,cos} - U_{2N,cos} - U_{3N,cos} - \sqrt{3}(U_{2N,sin} - U_{3N,sin})\Big) \tag{A.44}$$

and $U_{1\pm0,N,\sin}$, which are defined by

$$U_{10,N,\sin} = -\frac{1}{3\cdot\sqrt{2}}\left(U_{1N,sin} + U_{2N,sin} + U_{3N,sin}\right) \tag{A.45}$$

$$U_{1+,N,\sin} = \frac{1}{6}\Big(2U_{1N,sin} - U_{2N,sin} - U_{3N,sin} - \sqrt{3}(U_{2N,cos} - U_{3N,cos})\Big) \tag{A.46}$$

$$U_{1-,N,\sin} = \frac{1}{6}\Big(2U_{1N,sin} - U_{2N,sin} - U_{3N,sin} - \sqrt{3}(U_{3N,cos} - U_{2N,cos})\Big) \tag{A.47}$$

are used in these equations. There, in turn the variables $U_{iN,cos}$ and $U_{iN,sin}$ are used. which are defined by

$$U_{iN,cos} = \frac{2}{T}\int_{t-T}^{t} U_{iN,t}\cos\left(2\pi f_n\tilde{t}\right)\ d\tilde{t}, i \in \{1,2,3\} \tag{A.48}$$

$$U_{iN,sin} = \frac{2}{T}\int_{t-T}^{t} U_{iN,t}\sin\left(2\pi f_n\tilde{t}\right)\ d\tilde{t}, i \in \{1,2,3\}. \tag{A.49}$$

The symmetrical components based on phase-to-phase voltages are defined by:

$$\mathbf{U_{1\pm0}} = \begin{pmatrix} U_{10} \\ U_{1+} \\ U_{1-} \end{pmatrix} = \sqrt{3} \cdot \begin{pmatrix} U_{10,N} \\ U_{1+,N} \\ U_{1-,N} \end{pmatrix}. \tag{A.50}$$

The same calculation can be done to calculate the symmetrical components of the currents by using the correspondent phase currents in the equations. For the currents the index "N" is not used, because in contrast to the voltage, where phase-to-neutral and phase-to-earth voltages occur, the current only is defined as phase-current.

The active and reactive power in the positive-sequence system are defined by

$$P_{10} = 3 \cdot (U_{10,N,cos} I_{10,cos} + U_{10,N,sin} I_{10,sin}) \tag{A.51}$$
$$Q_{10} = 3 \cdot (U_{10,N,cos} I_{10,sin} - U_{10,N,sin} I_{10,cos}). \tag{A.52}$$

The active and reactive power in the positive-sequence system are defined by

$$P_{1+} = \frac{3}{2} (U_{1+,N,cos} I_{1+,cos} + U_{1+,N,sin} I_{1+,sin}) \tag{A.53}$$
$$Q_{1+} = \frac{3}{2} (U_{1+,N,cos} I_{1+,sin} - U_{1+,N,sin} I_{1+,cos}). \tag{A.54}$$

The active and reactive power in the negative-sequence system are defined by

$$P_{1-} = \frac{3}{2} (U_{1-,N,cos} I_{1-,cos} + U_{1-,N,sin} I_{1-,sin}) \tag{A.55}$$
$$Q_{1-} = \frac{3}{2} (U_{1-,N,cos} I_{1-,sin} - U_{1-,N,sin} I_{1-,cos}). \tag{A.56}$$

The zero-sequence active current I_{P10} is calculated by

$$I_{P10} = \frac{P_{10}}{\sqrt{3} U_{10}}, \tag{A.57}$$

the zero-sequence reactive current I_{Q10} is calculated by

$$I_{Q10} = \frac{Q_{10}}{\sqrt{3} U_{10}}, \tag{A.58}$$

the positive-sequence active current I_{P1+} is calculated by

$$I_{P1+} = \frac{P_{1+}}{\sqrt{3} U_{1+}}, \tag{A.59}$$

the positive-sequence reactive current I_{Q1+} is calculated by

$$I_{Q1+} = \frac{Q_{1+}}{\sqrt{3} U_{1+}}, \tag{A.60}$$

the negative-sequence active current I_{P1-} is calculated by

$$I_{P1-} = \frac{P_{1-}}{\sqrt{3} U_{1-}}, \tag{A.61}$$

and the positive-sequence reactive current I_{Q1-} is calculated by

$$I_{Q1-} = \frac{Q_{1-}}{\sqrt{3}U_{1-}}. \tag{A.62}$$

The normalized values are calculated in accordance with Chp. A.1.5. For example, the normalized voltages in the positive-sequence, negative-sequence and zero-sequence system $\mathbf{u_{1\pm0}}$ are calculated by

$$\mathbf{u_{1\pm0}} = \begin{pmatrix} u_{10} \\ u_{1+} \\ u_{1-} \end{pmatrix} = \frac{\mathbf{U_{1\pm0}}}{U_n} = \frac{1}{U_n} \cdot \begin{pmatrix} U_{10} \\ U_{1+} \\ U_{1-} \end{pmatrix} = \mathbf{u_{1\pm0,N}} = \begin{pmatrix} u_{10,N} \\ u_{1+,N} \\ u_{1-,N} \end{pmatrix} = \frac{\sqrt{3}}{U_n} \cdot \begin{pmatrix} U_{10,N} \\ U_{1+,N} \\ U_{1-,N} \end{pmatrix}. \tag{A.63}$$

The same method can be applied to the current;

$$\mathbf{i_{1\pm0}} = \begin{pmatrix} i_{10} \\ i_{1+} \\ i_{1-} \end{pmatrix} = \frac{\mathbf{I_{1\pm0}}}{I_n} = \frac{1}{I_n} \cdot \begin{pmatrix} I_{10} \\ I_{1+} \\ I_{1-} \end{pmatrix}. \tag{A.64}$$

A.2.2 Current Park-Components

The current components described in Chp. A.2.1 can be used to calculate the corresponding normalized Park-components as exemplary shown in the following.

The active/direct Park-component in the positive-sequence system can be calculated by

$$i_{S,d_{1+}} = \frac{I_{P1+}}{\sqrt{2}I_n}. \tag{A.65}$$

The reactive/quadrature Park-component in the positive-sequence system can be calculated by

$$i_{S,q_{1+}} = \frac{I_{Q1+}}{\sqrt{2}I_n}. \tag{A.66}$$

The active/direct Park-component in the negative-sequence system can be calculated by

$$i_{S,d_{1-}} = \frac{I_{P1-}}{\sqrt{2}I_n}. \tag{A.67}$$

The reactive/quadrature Park-component in the negative-sequence system can be calculated by

$$i_{S,q_{1-}} = \frac{I_{Q1-}}{\sqrt{2}I_n}. \tag{A.68}$$

A.2.3 Comparison of Transformations for Test Cases

The major advantage of the Park-transformation is the fact that $w_{S,d}$ and $w_{S,q}$ are constants in case of harmonic, symmetrical three-phase systems. This makes things much easier for controlling rotating machines and for controlling converters. The three-phase voltage systems in reality can only be approximated by a symmetrical three-phase system. The influence of deviations from symmetrical three-phase systems, such as unsymmetry and harmonics, are examined in the following test cases.

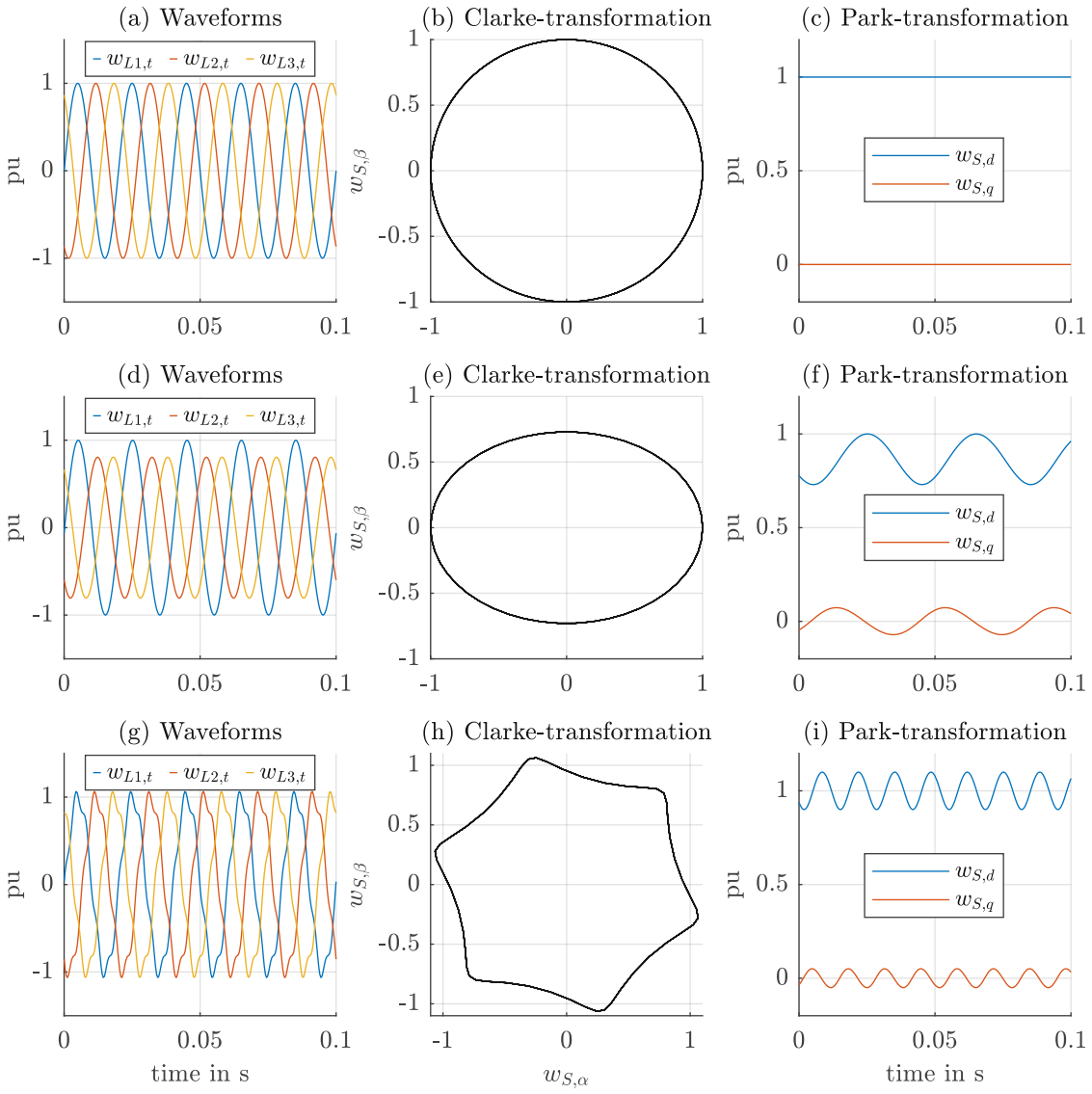

Figure A.6: Comparison of waveforms, the Clarke-transformation and the Park-transformation for three test cases. (a),(b) and (c) are showing the reference case of a harmonic, symmetrical three-phase system. (c),(d) and (f) are showing the test case of an unsymmetrical three-phase system. (g),(h) and (i) are showing the test case of a harmonic-distorted three-phase system.

As reference test case, a harmonic, symmetrical three-phase system is investigated. The corresponding waveforms, the Clarke-transformation, and the Park-transformation are shown in Fig. A.6(a), Fig. A.6(b) and Fig. A.6(c).

Since the space-vector in the $\alpha\beta 0$-coordinate-system is a perfect circle, the Park-transformation has constant values. In case of an unsymmetrical three-phase system, as shown in Fig. A.6(d), the space-vector in the $\alpha\beta 0$-coordinate-system becomes an ellipses, as shown in Fig. A.6(e). The Park-transformation, therefore, contains time-varying shares, as shown in Fig. A.6(f). In the third test case the three-phase system is subject to harmonics. A situation of an interaction of the fundamental frequency positive-sequence component with a fifth harmonic negative-sequence

component is investigated. The corresponding waveforms are shown in Fig. A.6(g). The space-vector in the $\alpha\beta 0$-coordinate-system in Fig. A.6(h) shows a clear deviation from a circular shape. The Park-transformation, therefore, contains time-varying shares, as shown in Fig. A.6(i).

A.3 Electrical Equipment

In the following chapter relevant fundamentals of synchronous generators, converters and transformers are discussed. Details regarding loads are investigated in [124].

A.3.1 Synchronous Generators

The following chapters summarize relevant fundamentals of synchronous generators.

A.3.1.1 Functional Principle in Stationary Operation

Most of the conventional power plants use synchronous machines to feed the power into the grid. The basic structure of a electrical excited synchronous machine has already been shown in Fig. 2.1. It consists of a stator and a rotor. The stator produces a rotating magnetic field, described by the flux density space vector $\underline{B}_S$, in the air gap between stator and rotor. In an electrical excited synchronous machine, a coil on the rotor produces a constant magnetic field, described by the flux density space vector $\underline{B}_R$, transversal to the rotor axis. A rotating rotor also leads to a rotating magnetic field.

In Fig. 2.1 the windings are represented as concentrated windings in each phase. The actual realization of the coil in phase L1 is shown in Fig. A.7. At $\omega t = \frac{\pi}{2}$ Fig. A.7 also represents an equivalent coil of the space vector $\underline{B}_S(\omega t = \frac{\pi}{2})$. The space vector of the flux density is built by a current in the equivalent coil with an amplitude I_S. Fig. 2.1 shows the resulting force based on the Lorentz force law. This simple example shows the basic relation between the static magnetic rotor field, the rotating field of the stator and the resulting force that sets the rotor in motion. If an external force reacts on the rotor, the force changes direction, so that also the current changes direction. In this case, the synchronous machine changes from motor to generator mode.

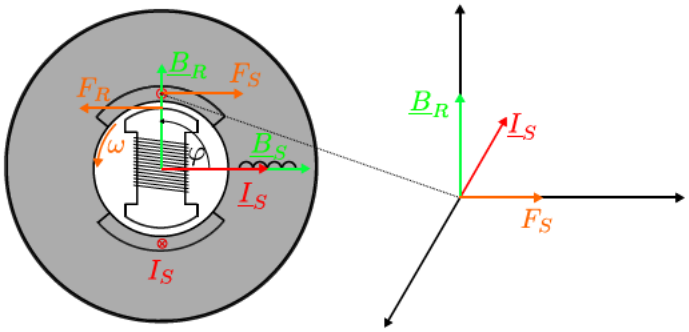

Figure A.7: Force in the rotating field.

The torque in Fig. A.7 can be calculated by Eq. (A.69) based on the current space vector $\underline{I}_S$ and the space vector of the rotor flux density:

$$M_{E,t} = -const \cdot B_R \cdot I_S \cdot \sin\varphi. \tag{A.69}$$

In order to obtain a generally valid equation for the torque, a more detailed model of the synchronous machine is necessary. A detailed model according to [103] is shown in Fig. A.8. The superposition of the magnetic field of the rotor and the magnetic field of the stator results in a space vector $\underline{\Phi}_h$ in Fig. A.8. A voltage U_R at the rotor winding causes a current I_R in the rotor winding that leads to a constant magnetic field. A rotating rotor induces a voltage space vector U_S in the stator, which is identical to the induced rotor voltage U_P, if the current $I_S = 0$. In case of a load connected to the generator, the resulting current I_S leads to a voltage drop over the stator resistance R_S, the reactance X_h and the leakage reactance X_σ. The reactance X_d is called synchronous reactance, which is $X_d = X_h + X_\sigma$.

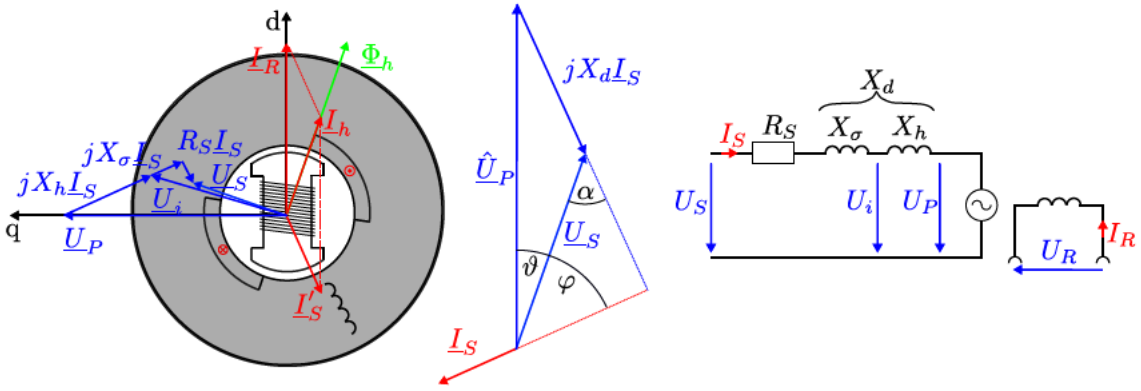

Figure A.8: Synchronous machine (compare [159]).

Neglecting the stator resistance R_S, the result is a vector diagram as shown in Fig. A.8. In this case, the power output of the generator in Fig. A.8 is calculated by:

$$P_{E,t} = -\frac{3}{2} \cdot U_S \cdot I_S \cdot \cos\varphi \overset{symm}{=} -3 \cdot \frac{\hat{U}_{1N}}{\sqrt{2}} \cdot \frac{\hat{I}_{L1}}{\sqrt{2}} \cdot \cos\varphi = -3 \cdot U_{1N} \cdot I_{L1} \cdot \cos\varphi. \tag{A.70}$$

Since $\alpha + \varphi = 90°$, this equation can be rewritten as

$$P_{E,t} = -\frac{3}{2} \cdot U_S \cdot \sin\alpha \cdot I_S \tag{A.71}$$

and with $X_d I_S \sin\alpha = U_P \sin\vartheta$ the equation results in

$$P_{E,t} = -\frac{3}{2} \cdot \frac{U_S U_P}{X_d} \sin\vartheta. \tag{A.72}$$

Based on Eq. (A.69) and according to Schröder [160], the power can also be calculated as

$$P_{E,t} = \omega \cdot M_{E,t} = -\omega \cdot \frac{3}{2} \cdot \psi_h \cdot I_S \cdot \sin\varphi = \omega \cdot \frac{3}{2} \Im\mathfrak{m}(\underline{\psi}_h \cdot \underline{I}_S^*) \tag{A.73}$$

with ψ_h as the interlinking flux, which is approximately the interlinking flux of the rotor $N\Phi_R$.

As shown in Fig. A.1 the rotor of the generator is driven by a turbine, which exerts a torque $M_{M,t}$. Based on the swing equation, the electromagnetic torque $M_{E,t}$ and the mechanical torque coming from the turbine $M_{M,t}$ are set in context by

$$M_{M,t} - M_{E,t} = J\frac{d\omega}{dt}. \tag{A.74}$$

Multiplying both sides of this equation by ω, this results in the equation

$$P_{M,t} - P_{E,t} = J\omega\frac{d\omega}{dt} \tag{A.75}$$

where, $P_{M,t}$ and $P_{E,t}$ are the mechanical and the electrical power. By introducing the inertia constant $H = \frac{J\omega_n^2}{2S_n}$, with ω_n as the nominal angular frequency, the equation can be rewritten as

$$P_{M,t} - P_{E,t} = \frac{2 \cdot H \cdot S_n}{\omega_n^2}\omega\frac{d\omega}{dt} = T_A\frac{S_n}{\omega_n^2}\omega\frac{d\omega}{dt} \tag{A.76}$$

with T_A as the starting time constant of the generator.

A.3.1.2 Short-Circuit Behavior

According to Binder [21] the components of the normalized current space vector in the $dq0$ coordinate system of a solid-pole synchronous generator in case of a three-phase short-circuit at the connection terminals can be expressed as follows:

$$i_{S,d} = -u_{S0} \cdot \left[\frac{1}{x_d} + \left(\frac{1}{x'_d} - \frac{1}{x_d}\right) \cdot e^{-\frac{\tau}{\tau'_d}} + \left(\frac{1}{x''_d} - \frac{1}{x'_d}\right) \cdot e^{-\frac{\tau}{\tau''_d}} - \frac{1}{x''_d}e^{-\frac{\tau}{\tau_a}} \cdot \cos\tau\right], \tag{A.77}$$

$$i_{S,q} = -u_{S0} \cdot \frac{1}{x''_q} \cdot e^{-\frac{\tau}{\tau_a}} \cdot \sin\tau. \tag{A.78}$$

The term u_{S0} defines the stator voltage of a synchronous machine, which is considered to be at idle before the short-circuit occurs. The remaining values, which are used in this equation are the normalized reactance x_d, the normalized transient reactance x'_d, the normalized subtransient reactance x''_d, the stator time constant τ_a, the transient time constant τ'_d and the subtransient time constant τ''_d. For τ applies $\tau = \omega t$. Therefore, the time constants can also be expressed as $\tau_a = \omega T_a$, $\tau'_d = \omega T'_d$ and $\tau''_d = \omega T''_d$. The corresponding phase current in L1 can be calculated by $i_{L1,t} = \mathfrak{Re}(\underline{i}_{S,dq})$, with γ_0 as the voltage angle of the moment when the short-circuit occurs. This results in

$$\begin{aligned} i_{L1,t} = -u_{S0}&\left[\frac{1}{x_d} + \left(\frac{1}{x'_d} - \frac{1}{x_d}\right) \cdot e^{-\frac{\tau}{\tau'_d}} + \left(\frac{1}{x''_d} - \frac{1}{x'_d}\right) \cdot e^{-\frac{\tau}{\tau''_d}}\right]\cos(\tau + \gamma_0) + \\ &+ u_{S0}\left[\frac{1}{x''_d} \cdot \cos\gamma_0\right] \cdot e^{-\frac{\tau}{\tau_a}}. \end{aligned} \tag{A.79}$$

The nominal current I_n of the generator is $I_n = \frac{U_{1N}}{X_d}$. Since $i_{L1,t} = \frac{I_{L1,t}}{\sqrt{2}I_n}$, the Fig. A.9 shows that about 1 s after the short-circuit the nominal current is reached with $i_{L1,t} = 1\,\text{pu}$. This time duration after the short-circuit, the current is called steady-state short-circuit current i_k. At the beginning of the short-circuit, the current is much higher than the nominal current. At $\tau = 0$ the Eq. (A.79) simplifies to

$$i_{L1,t}(\tau = 0) \overset{\gamma_0=0}{=} i''_k = -u_{S0} \cdot \frac{2}{x''_d} \tag{A.80}$$

which is called the initial short-circuit current i''_k. Usually, the RMS-values of the initial-state and steady-state short-circuit currents are used as $I''_k = i''_k \cdot I_n$ and $I_k = i_k \cdot I_n$. The maximum possible instantaneous value of the prospective short-circuit current is the peak short-circuit current i_p. Dependent on γ_0, a DC component occurs.

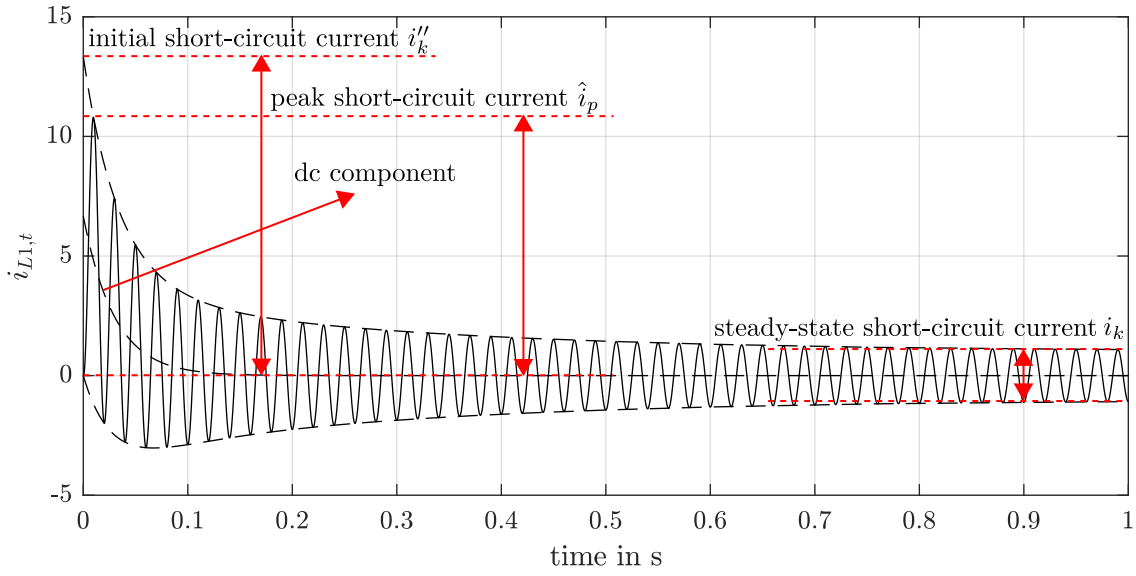

Figure A.9: Waveform of the current in L1 $i_{L1,t}$ when a near-to-generator three-phase short-circuit in a solid-rotor synchronous generator occurs at the zero crossing of the voltage ($\gamma_0 = 0$) with $u_{S0} = 1$. The used machine parameters are: $x_d = 1$, $x_d' = 0.3$, $x_d'' = 0.15$, $T_a = 0.03\,\mathrm{s}$, $T_d' = 0.3\,\mathrm{s}$ and $T_d'' = 0.05\,\mathrm{s}$.

A.3.2 Transformers

In the early days of the electricity industry, energy production and consumption were closely linked spatially. Bridging far distances was not possible with the DC-systems of that time due to excessive current heat losses on the lines. These can only be kept within economic limits by choosing much higher voltages with correspondingly lower currents for the energy transport than are possible in the power plant and on the consumer-side. The task of converting the electrical energy to arbitrary voltage values can be easily solved in AC-system via the law of induction. Therefore, the power grid developed in the way shown in Figure A.1. Several transformers adapt to the different voltage levels in the NLs. Depending on the maximum power that a power plant feeds in, or a consumer consumes, the highest NL is selected as PCC for low power values, or the lowest NL is used for very high power values.

Fig. A.10 shows the structure of a one-phase transformer and the magnetic fields in operation and a corresponding equivalent circuit.

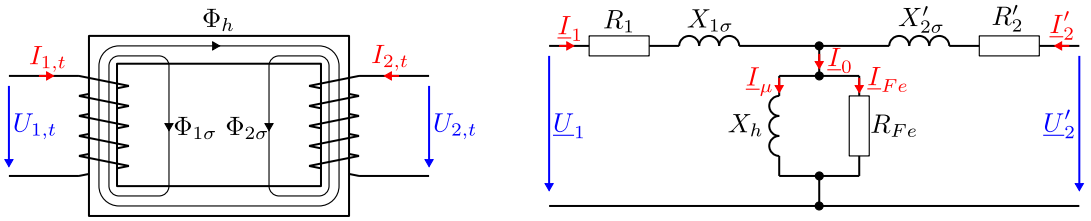

Figure A.10: Structure and magnetic fields in a one-phase transformer and a corresponding equivalent circuit.

In the basic structure of a transformer according to Fig. A.10 two windings with the numbers of turns N_1 and N_2 are magnetically coupled on a common iron core. If both windings carry current,

a magnetic field is created which can be devided into two parts. The first part is the magnetic main field Φ_h which closes in the iron core. The second part consists of the magnetic leakage field $\Phi_{1\sigma}$ of the first winding and the magnetic leakage field $\Phi_{2\sigma}$ of the second winding. The resulting equivalent circuit consists of the leakage reactance $X_{1\sigma}$ of the first winding, the leakage reactance $X'_{2\sigma}$, which is the reactance of the secondary side seen from the primary, the main reactance X_h, the copper resistance R_1, the copper resistance R'_2 and the resistance R_{Fe}, which represents the losses in the iron core. The magnetizing current $\underline{I}_\mu$ is much larger than the iron current $\underline{I}_{Fe}$. Based on the law of induction $U = N\frac{d\Phi}{dt} = L\frac{dI_t}{dt}$, $U'_{2,t} = \frac{N_1}{N_2}U_{2,t}$ and $I'_{2,t} = \frac{N_2}{N_1}I_{2,t}$, the voltage equations on both sides are

$$U_{1,t} = R_1 I_{1,t} + L_{1\sigma}\frac{dI_{1,t}}{dt} + L_{1h}\frac{dI_{1,t}}{dt} + L_{12}\left(\frac{N_1}{N_2}\right)\frac{dI'_{2,t}}{dt} \tag{A.81}$$

$$\frac{N_1}{N_2}U'_{2,t} = R_2\left(\frac{N_1}{N_2}\right)^2 I'_{2,t} + L_{2\sigma}\left(\frac{N_1}{N_2}\right)^2\frac{dI'_{2,t}}{dt} + L_{2h}\left(\frac{N_1}{N_2}\right)^2\frac{dI'_{2,t}}{dt} + L_{12}\frac{dI_{1,t}}{dt} \tag{A.82}$$

which can be simplified as follows when RMS-values and the definition $L_{1h} = L_{12}\frac{N_1}{N_2} = L_{2h}\left(\frac{N_1}{N_2}\right)^2 = L_h$ are used:

$$\underline{U}_1 = R_1\underline{I}_1 + jX_{1\sigma}\underline{I}_1 + jX_h\left(\underline{I}_1 + \underline{I}'_2\right), \tag{A.83}$$

$$\underline{U}_2 = R_2\underline{I}'_2 + jX'_{2\sigma}\underline{I}'_2 + jX_h\left(\underline{I}_1 + \underline{I}'_2\right). \tag{A.84}$$

In case of a transformer which is connected to the grid on the primary side and which is secondary unloaded, the steady-state current will only be reached after a transient electromagnetic process. Based on Eq. (A.81) an unloaded transformer leads to a voltage equation

$$U_{1,t} = R_1 I_{1,t} + (L_{1\sigma} + L_{1h})\cdot\frac{dI_{1,t}}{dt} = R_1 I_{1,t} + N_1\frac{\Phi_{1,t}}{dt}. \tag{A.85}$$

Therefore, a voltage waveform

$$U_{1,t} = \sqrt{2}U_1\sin(\omega t + \alpha) \tag{A.86}$$

leads to a magnetic field $\Phi_{1,t}$

$$\Phi_{1,t} = -\Phi_1\cos(\omega t + \alpha) + \Phi_1\cos\alpha + \Phi_{rem} - \frac{R_1}{N_1}\int I_{1,t}\,dt \tag{A.87}$$

with $\Phi_{1,t}(t=0) = \Phi_{rem}$, which becomes a maximum $\hat{\Phi}_1 = 2\Phi_1 + \Phi_{rem}$ when $\alpha = 0$. When a transformer is connected to the grid on the primary side at the moment of $U_{1,t} = 0$, the magnetic field is at its maximum. At these high values of the magnetic field, the magnetizing curve of the iron core is saturated, which means that the linear part of the magnetizing curve is reached and results in very high magnetizing currents. These transient currents are called “inrush current” of the transformer. An example for such an inrush current is shown in Fig. A.11. This example illustrates that in the worst case the inrush currents can reach values five times higher than the nominal current.

Three-phase transformers are constructed similarly to single-phase transformers. In contrast to single-phase transformers the primary and secondary side consist of three separate windings. The naming convention for the windings on the primary side is 1U1 and 1U2 for the primary winding on the first leg, 1V1 and 1V2 for the primary winding on the second leg, 1W1 and 1W2 for the primary winding on the third leg, while always the connection points 1U1, 1V1 and 1W1 are used for connection to the grid on the primary side. The naming convention for the windings on the secondary side is 2U1 and 2U2 for the secondary winding on the first leg, 2V1 and 2V2 for the secondary winding on the second leg, 2W1 and 2W2 for the secondary winding on the third leg,

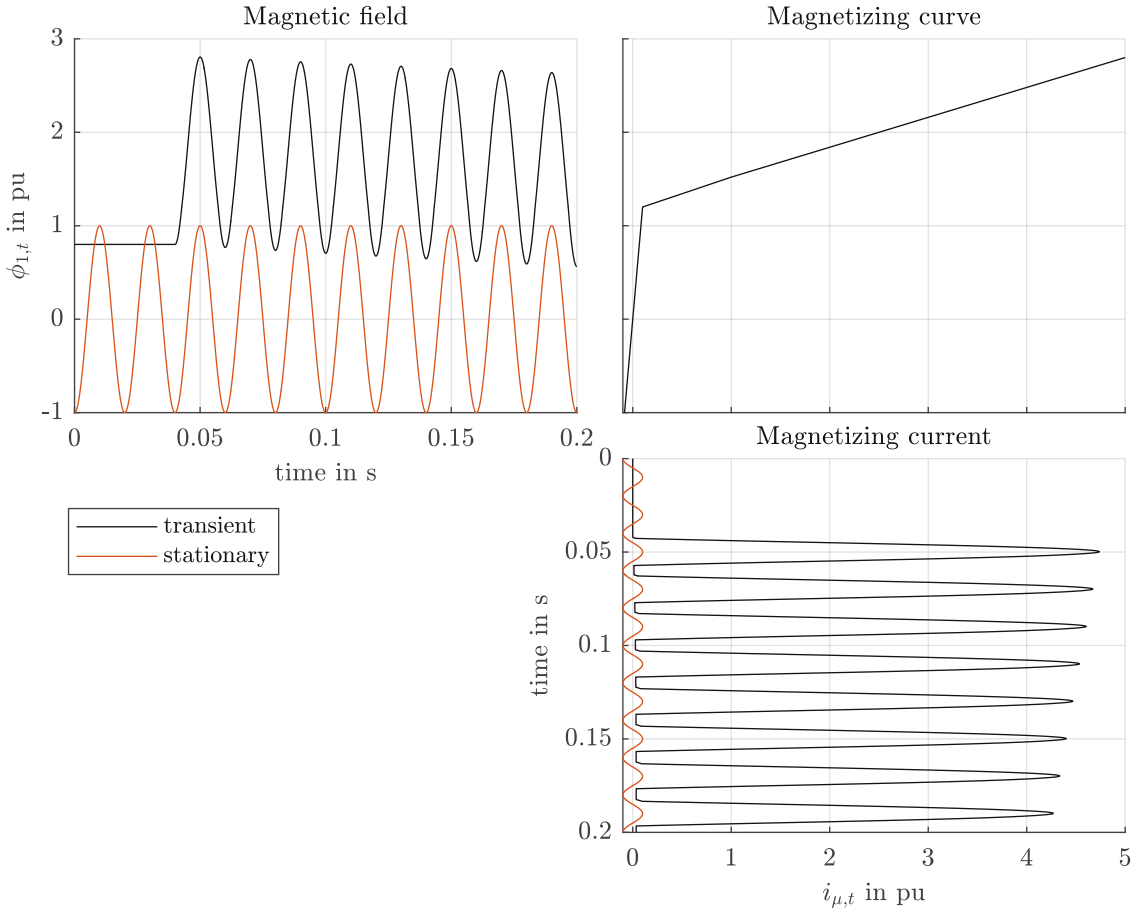

Figure A.11: Inrush current in the phase L1 of a three-phase-transformer, which was simulated with the built-in example `power_transfosat` in MATLAB/SIMULINK.

while always the connection points 2U1, 2V1 and 2W1 are used for connection to the grid on the secondary side. The connection points 1U2, 1V2 and 1W2 on the primary side and the connection points 2U2, 2V2 and 2W2 are connected either in delta or in wye. Depending on the choice of the interconnection, a vector group results. The naming convention for vector groups is defined with "Y" or "D" for a wye or delta connection on the primary side and "y" or "d" for a wye or delta connection on the secondary side. The number at the end defines the phase shift. Depending on whether the neutral conductor is accessible or not, this is indicated with "N" on the primary side and with "n" on the secondary side. An example for a vector group is "YNyn0". The structure of three-phase transformers and two examples of vector groups are shown in Fig. A.12.

Since the beginnings (1U1,1V1,1W1,2U1,2V1,2W1) of the windings are usually used to connect to the grid, the connection points are indicated with 1U,1V,1W,2U,2V,2W in circuit diagrams.

As already shown in Fig. A.1, the choice of the vector group is dependent on the NL and the required load capacity of the star point. In case of unsymmetrical current, Yy transformers are only loadable with about 10 % of their nominal current in case of unsymmetrical currents, whereas Dy and Yd transformers are fully loadable with unsymmetrical currents. The reason is that unbalanced currents in Yy transformers lead to magnetic fluxes in the iron core, which can only be closed by air and, therefore lead to high currents. In a delta-winding, however, circular current can occcur.

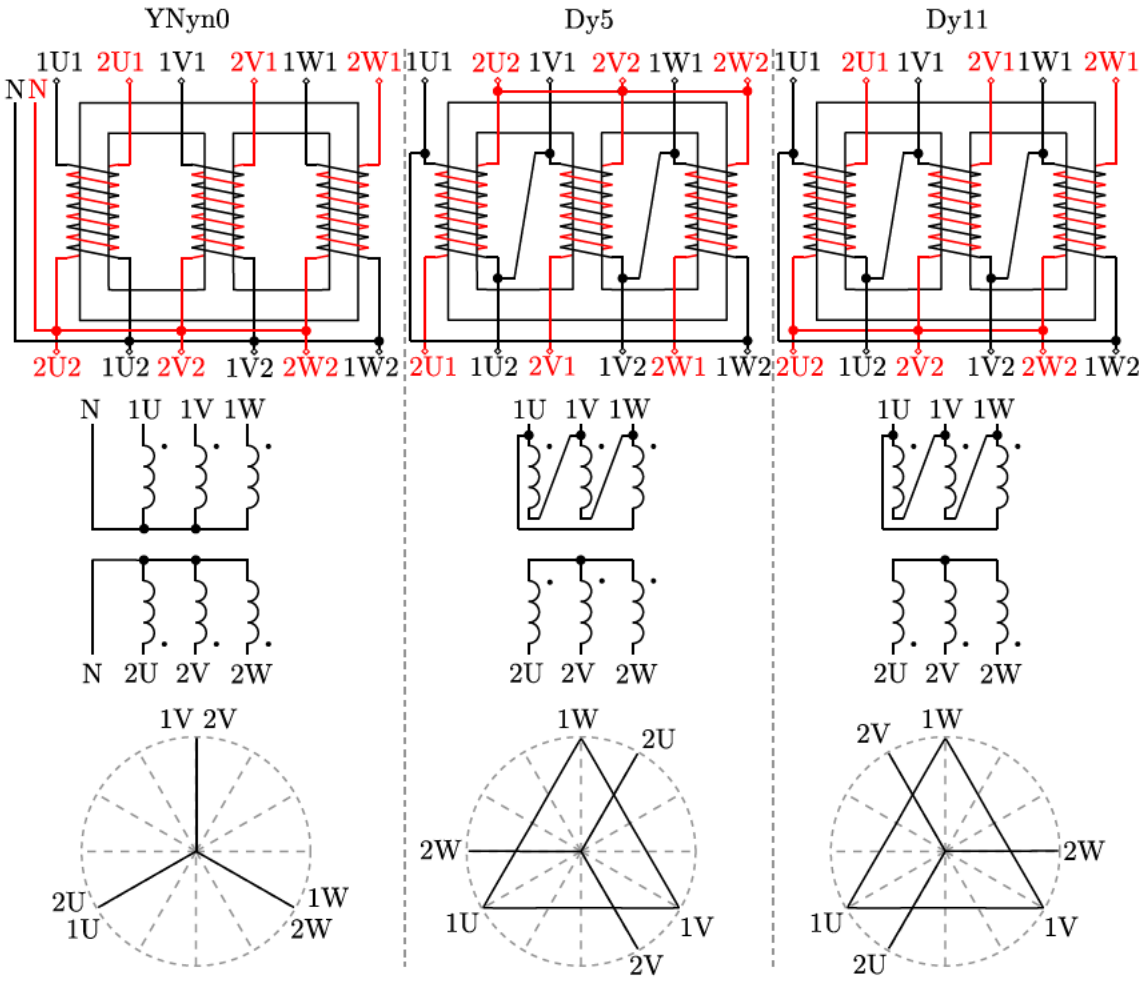

Figure A.12: Structure of three-phase transformers and examples for three vector groups including circuit and vector diagrams.

The vector group YNd5 is usually used for generator transformers, YNyn0 transformers are usually used as large coupling transformers on NL 2, YNd11 transformers are usually used on NL 4 and for distribution transformers the vector group Dyn5 is often used.

A.4 Batteries

The following chapters summarize relevant fundamentals of batteries, particularly Li-ion batteries, describe cell chemistries and explain relevant fundamentals of modeling battery cells.

A.4.1 Fundamentals of Batteries

The electrolytic solution pressure refers to the tendency of substances to go into solution. It characterizes the tendency of an element to form ions and to be dissolved. Thus, the solution pressure of solid metal in contact with water causes metal ions to dissolve in water. The metal becomes negatively charged, the solution positively. This formation consisting of an electrode (metal) and an

electrolyte (water) is called "half-cell". A half-cell contains a metal in two oxidation states. Inside an isolated half-cell there is an oxidation-reduction (redox) reaction that is in chemical equilibrium. The "full-cell" or "galvanic cell" consists of two half-cells, usually connected by a semi-permeable membrane or by a salt bridge that prevents the ions of one electrode from plating out at the other electrode.

A simplified explanation of the electrode processes in a full-cell can be given as follows. In the first half-cell metal A is dipped in the solution, whereupon it partly dissolves. Electrons remain at the electrode until a characteristic electron density is built up. In the second half-cell with a metal B, which is more noble than metal A, the same process takes place, but the amount of dissolution and, therefore the resulting electron density is lower. By connecting the two half-cells via electrical conductor, an electron flow starts from the negative electrode with the higher electron density to the positive electrode. The half-cell A tries to keep the electron density constant. As a consequence, additional amounts of metal A dissolve at the negative electrode forming A^+ in solution and electrons e^-, which are located at the surface of metal A:

$$A \rightarrow A^+ + e^-. \tag{A.88}$$

At the positive electrode the current results in an increasing electron density. The half-cell B compensates this process by the consumption of electrons for the deposition of B^+-ions:

$$B^+ + e^- \rightarrow B. \tag{A.89}$$

The flow of electrons and thus the current stops when metal A is completely dissolved or all B^+-ions are precipitated. As a consequence, it is necessary to add a soluble salt to the positive electrode compartment to maintain the current for a longer period. This salt consists of B^+-ions and corresponding negative ions. The two electrode compartments are divided by an appropriate separator to avoid the migration and the deposition of B^+-ions at the negative electrode A. A charge balancing process is necessary in order to close the electric circuit. Otherwise, with every electron leaving half-cell A and joining half-cell B, the charge of half-cell A would become more and more positive while the charge of half-cell B would become more and more negative. Since this separator blocks the exchange of positive ions, only the negative ions are responsible for this charge balancing process. This means that for each electron flowing from the negative to the positive electrode in the outer circuit, a negative ion in the electrolyte diffuses to the negative electrode compartment in order to close the electric circuit. Generally, the limiting factor for the electronic current flow is the transport of these ions. Therefore, the electrolyte solution should have a low resistance.

A very simple example for an explicit full-cell is the "Daniell cell", consisting of a zinc (Zn) half-cell containing a solution of $ZnSO_4$ (zinc sulfate) and a copper (Cu) half-cell containing a solution of $CuSO_4$ (copper sulfate). The two half-cells can be connected via a salt-bridge or clay layer as separator. The Daniell cell is shown in Fig. A.13. It can be described by the convention $Zn|ZnSO_4\|CuSO_4|Cu$ where | represents a phase boundary and ‖ a separator. In the zinc half-cell Zn dissolves in the electrolyte $ZnSO_4/H_2O$

$$Zn(s) \rightarrow Zn^{2+}(aq) + 2e^- \tag{A.90}$$

with "s" indicating solid state and "aq" indicating aqueous solution of the salt, due to the electrolytic solution pressure. In the chemical equilibrium of the half-cell the negative charge of polyatomic SO_4^{2-} (sulfate) ions balance out the positive charge of the Zn^{2+} ions. In the copper half-cell Cu dissolves in the electrolyte $CuSO_4/H_2O$

$$Cu(s) \rightarrow Cu^{2+}(aq) + 2e^- \tag{A.91}$$

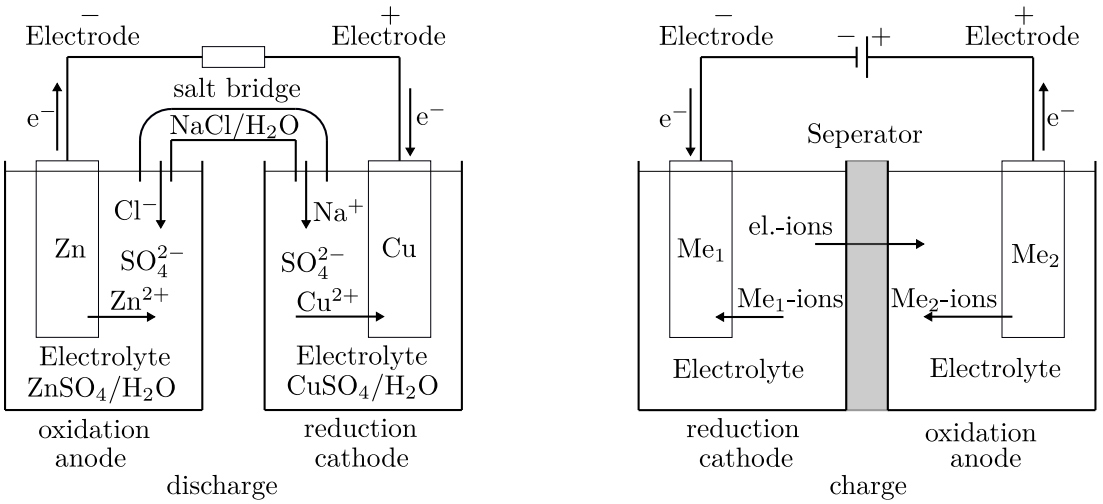

Figure A.13: (left) Chemical reaction during discharging process in a Daniell cell (non rechargeable primary cell). (right) General chemical reaction during charging process of a secondary cell.

also due to the electrolytic solution pressure. In the chemical equilibrium of the half-cell the negative charge of polyatomic SO_4^{2-} (sulfate) ions balance out the positive charge of the Cu^{2+} ions.

When a metallic electrode is placed in a solution, a redistribution of electrical charges tends to take place. Positive ions of the metal enter the solution, leaving the electrode negatively charged while the solution acquires a positive charge. If the solution already contains ions of the metal, there is a tendency for ions to be deposited on the electrode, giving it a positive charge. The electrode eventually reaches an equilibrium potential with respect to the solution, the magnitude and sign of the potential depending on the concentration of metallic ions in the solution and the nature of the metal. Zinc has such a strong tendency to form ions that the metal forms ions in all solutions of its salts, so it is always negatively charged relative to the solution. The standard electrode potential describes the potential of any half-cell in respect to a standard hydrogen electrode, which is defined upon by convention to have a potential of 0 V. It will be described in more detail in the next Chp. A.4.1.1. The standard electrode potential of zinc is $\varphi_{Zn} = -0.76\,\mathrm{V}$. On the other hand, with copper, the ions have such a strong tendency to give up their charge that the metal becomes positively charged, even when placed in the most dilute solution of copper salt. The standard electrode potential is $\varphi_{Cu} = 0.34\,\mathrm{V}$. Due to the lower potential of the zinc half-cell it becomes the minus pole of the Daniell cell and the copper half-cell becomes the plus pole of the Daniell cell.

When the Daniell cell is connected to an external load, electrons flow from the zinc half-cell to the copper half-cell. Therefore, an "oxidation" takes place as its oxidation number increases with increasing number of positive zinc-ions. The half-cell where the oxidation takes place is called "anode". In the copper half-cell on the other hand a "reduction" takes place as the oxidation number decreases with increasing number of negatively charged electrons. The half-cell where the reduction takes place is called "cathode". The electric circuit is completed in the electrolyte by the flow of anions (negative ions) and cations (positive ions) to the anode and cathode, respectively. In case of the Daniell cell in Fig. A.13 the combination of the two half-cells leads to a standard cell voltage of

$$E^0 = \varphi_{Cu} - \varphi_{Zn} = 0.34\,\mathrm{V} - (-0.76\,\mathrm{V}) = 1.1\,\mathrm{V} \tag{A.92}$$

based on the reaction

$$\begin{aligned} Zn(s) &\rightarrow Zn^{2+}(aq) + 2e^- && \text{at zinc electrode} \\ Zn^{2+} + CuSO_4 &\rightarrow ZnSO_4 + Cu^{2+} && \text{in electrolyte} \\ Cu^{2+}(aq) + 2e^- &\rightarrow Cu(s) && \text{at copper electrode} \end{aligned} \tag{A.93}$$

as shown in Fig. A.13. In case of using a salt bridge to separate the two half-cells the charge balancing process is performed by the ions of the salt-bridge. In case of using a clay layer separator the charge balancing process is performed by the negatively charged sulfate ions which leave the copper half-cell to join the zinc half-cell during the discharging process.

The electrochemical reaction of a galvanic cell can be reversed by connecting a voltage source to the galvanic cell. This technique that forces the opposite electrochemical reaction of a galvanic cell during discharging is called "electrolysis" and results in charging the galvanic cell. Some of the electrochemical reactions in galvanic cells are reversible and others are not. Galvanic cells whose electrochemical reactions are reversible and that are capable of performing several charging and discharging cycles are called "secondary cells". Galvanic cells whose electrochemical reactions are irreversible are called "primary cells". The Daniell cell is a primary cell which means that it is not rechargeable. Therefore, the right side of Fig. A.13 does not show the charging process of a Daniell cell but a general description of the charging process of a secondary cell. By connecting a voltage source to a secondary cell it forces the electrons of the positive half-cell to leave it and join the negative half-cell. This electron flow forces all electrochemical reactions during discharging process to be reversed. The anode is defined as the half-cell where the oxidation takes place. During the charging process, the positive half-cell is the anode while the negative half-cell is the cathode. Therefore, the anode and cathode switch place during charging and discharging. But there is a naming convention which defines the anode to be the half-cell during the discharging process. Therefore, in case of the Daniell cell the zinc half-cell is called the anode.

A.4.1.1 Standard Electrode Potential and Cell Voltage

The standard potential of a cell is determined by the type of active materials contained in the cell. It derives from the difference of the standard electrode potentials of its half-cells. The standard electrode potential is defined as the equilibrium value of an electrode potential when all the constituents taking part in the electrode reaction are in the standard state. Tab. A.1 summarizes electrode potentials of different metals. The standard electrode potential cannot be obtained empirically. It results from a pair of electrodes. Thus, only one empirical value is available in a pair of electrodes and it is not possible to determine the value for each electrode in the pair using the empirically obtained galvanic cell potential. Therefore, a reference electrode, the Standard Hydrogen Electrode (SHE), is used, for which the potential is defined to 0 V. Tab. A.1 shows the standard electrode potentials in respect to a SHE.

Table A.1: Standard electrode potential [168].

Half-reaction	**Standard electrode potential φ**
$Li^+(aq) + e^- \rightarrow Li(s)$	−3.04 V
$K^+(aq) + e^- \rightarrow K(s)$	−2.92 V
$Ca^{2+}(aq) + 2e^- \rightarrow Ca(s)$	−2.76 V
$Na^+(aq) + e^- \rightarrow Na(s)$	−2.71 V
$Zn^{2+}(aq) + 2e^- \rightarrow Zn(s)$	−0.76 V
$Cu^{2+}(aq) + 2e^- \rightarrow Cu(s)$	0.34 V
$F_2(g) + 2e^- \rightarrow 2F^-(g)(aq)$	2.87 V

The values for the table entries are reduction potentials and, therefore, represent the tendency to form ions. A very low potential represents a high electrolytic solution pressure and, therefore,

a high tendency to form ions and go into solution. Lithium at the top of the list has the most negative number, indicating that its tendency to give up its electrons and form ions is the highest of all elements. The strongest oxidizing agent is fluorine with the largest positive number of the standard electrode potential and, therefore, with the highest tendency to pick up electrons.

As already explained by using the example of the Daniell cell, the cell potential E^0 of a galvanic cell results from the difference of the standard electrode potentials of its half-cells. But in case of charging or discharging of the cell this cell voltage varies. The cell voltage is not only dependent on the standard electrode potential of its half-cells but also on other factors, including the actual ion concentration in every half-cell, the temperature, etc. The Nernst equation can be used to calculate the cell voltage U_B considering these aspects:

$$\begin{aligned} U_B &= \left[\varphi_{cathode} + \frac{RT}{zF}\ln\left(\frac{c_{Ox,cathode}}{c_{Red,cathode}}\right)\right] - \left[\varphi_{anode} + \frac{RT}{zF}\ln\left(\frac{c_{Ox,anode}}{c_{Red,anode}}\right)\right] = \\ &= E^0 - \frac{RT}{zF}\ln\left(\frac{c_{Ox,anode}}{c_{Red,anode}}\frac{c_{Ox,cathode}}{c_{Red,cathode}}\right) \end{aligned} \tag{A.94}$$

where E^0 is the standard cell voltage, R is the general gas constant, T is the temperature in °K, $F = e \cdot N_A$ is the Faraday constant, z is the charge exchanged per formula based on the reaction

$$Red \underset{\text{reduction}}{\overset{\text{oxidation}}{\leftrightarrows}} Ox^{z+} + ze^- \tag{A.95}$$

and $c_{Ox,anode}$, $c_{Red,anode}$, $c_{Ox,cathode}$ and $c_{Red,cathode}$ are the concentrations of the components in the corresponding half-cells. The discharging of a cell leads to an increasing factor $\frac{c_{Ox,anode}}{c_{Red,anode}}$ and also an increasing factor $\frac{c_{Ox,cathode}}{c_{Red,cathode}}$ in Eq. (A.95). Taking the Daniell cell as an example, the concentration $c_{Ox,anode}$ of zinc-ions increases during discharging while the concentration of metallic zinc $c_{Red,anode}$ decreases in the anode. In the cathode on the other hand the concentration $c_{Red,cathode}$ of metallic copper increases while the concentration $c_{Ox,cathode}$ of copper-ions decreases. The increasing value of these two factors in Eq. (A.95) leads to a continuously decreasing cell voltage U_B during discharging. During charging on the other hand the cell voltage U_B continuously increases. It has to be mentioned that Eq. A.95 is only valid in a deenergized state, or in case of very low currents.

Charging and discharging of a galvanic cell causes the concentrations of the embedded electrode material to change continually. According to Eq. (A.95) this leads to varying cell voltage. Therefore, the electrode's state of charge can be directly determined from the cell voltage. The cell voltage according to Eq. (A.95) refers to the OCV. Examples for OCV-curves in dependence of the state of charge are shown in Fig. A.14 for different cell chemistries. Fig. A.14 shows the behavior already described in Eq. (A.95) leading to a higher cell voltage at a higher state of charge and a lower cell voltage at a lower state of charge.

When current is applied, the cell's clamping voltage varies from its OCV due to "cell polarization". The chemical reactions inside the cell are composed of many partial processes. These include transport processes as diffusion or migration, adsorption and crystallization. These processes require that the energy thresholds inhibiting the reaction are exceeded first. From an electrical point of view these obstructions function like a resistance, changing the potential of the electrodes or the cell voltage. Such deviations from the equilibrium cell voltage are termed cell polarization. The physical effects that produce polarization have various time dependencies. Therefore, any resistance in an equivalent electrical circuit diagram is a variable resistance that is dependent on many parameters. The Butler-Volmer equation can be used to formulate the anodic and cathodic partial reactions that result from the processes mentioned above. It describes how the electrical current on an electrode depends on the electrode potential. In simple terms, the cell voltage rises with rising current during charging of the cell and the cell voltage decreases with rising current during discharging of the cell. Therefore, the OCV curve in Fig. A.14 shifts to higher values during

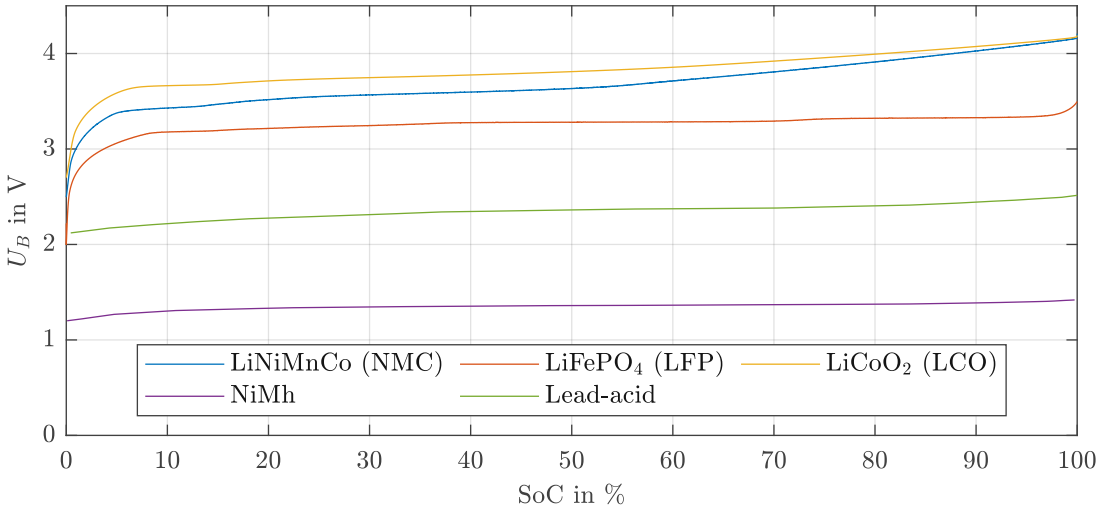

Figure A.14: OCV of battery cells with different cell chemistries (based on data of [199][205][193][108]).

charging with increasing current and it shifts to lower values during discharging with increasing current. The influence of the current on the cell voltage curve will be described in more detail in Chp. 2.5.1 and will be investigated for Li-ion batteries in Chp. 2.5.2.

A.4.1.2 Cell Shapes

A cell can be built in many shapes and configurations. The most relevant shapes for secondary cells can be divided into

- cylindrical cell design and
- prismatic cell design (further divided into hard-case and pouch design).

The long experience in the production of the cylindrical design is a considerable advantage of cylindrical cells. Their container is dense and can withstand some inner pressure (which can arise from side reactions) without deformation. A disadvantage is the low packaging density and the lower heat transport from inner cell parts to the outside. However, the relation between the surface and the volume is more efficient, which makes cooling concepts easier. On the other hand prismatic cells have higher packaging density, but cooling concepts are more complex. In terms of safety, the housing stability of the cylindrical and the prismatic hard-case cell is considerably higher than the pouch cell housing, which requires additional housing stability as part of a battery system. But in comparison to the pouch cell, the housings for the cylindrical and prismatic hard-case cell are heavier. This leads to a reduced energy density.

A.4.2 Cell Chemstries

The most popular cell chemistries for secondary battery cells are:

- lead-acid,
- Ni-Cd,
- Ni-Mh,

- Li-ion,
- Na/NiCl ("ZEBRA") and
- Na-S.

The most common type of secondary battery is the lead-acid battery. The lead-acid battery is the oldest type of rechargeable battery that can be found as starter battery in the automotive area. It is relatively low-cost and reliable, but it has the lowest energy density of the major types of secondary batteries. This makes it popular for applications in which weight and space are not a major concern. Until the breakthrough of Li-ion batteries, Ni-Cd and Ni-Mh batteries were used for portable devices, e.g. cordless power tools. Major drawback of these cell chemistries is the "memory effect", which describes the effect of gradually losing the maximum usable energy content if a battery is repeatedly being recharged after being only partially discharged. Ni-Cd and Ni-Mh batteries today are mostly replaced by Li-ion batteries. Li-ion batteries are the fastest growing battery market today, mainly because commercially available Li-ion battery cells have the highest energy density of any cell chemistry. All cell chemistries mentioned so far can be classified as "classical batteries", whereas the Na/NiCl and the Na-S batteries belong to the "high-temperature/thermal batteries" and in particular to the "molten-salt batteries". They are batteries that contain solid electrolytes and are inactive when stored at ambient temperature. The electrolytes only melt at high temperatures, which activates the battery. They are mainly used for stationary applications.

A.4.3 Lithium Ion Batteries

In chemistry "intercalation" means the insertion of molecules or ions between layers in an atomic structure. Lithium-ion (Li-ion) batteries are comprised of cells that employ lithium intercalation compounds as the positive and negative materials. The intercalation process of Li-ions does not significantly change the structure of the electrode material. As a Li-ion battery is cycled, lithium ions exchange between the positive and negative electrodes. The positive electrode material is typically a metal oxide with a layered structure, such as lithium cobalt oxide ($LiCoO_2$), on a current collector of aluminum foil. The negative electrode material is typically a graphitic carbon, in particular Li_xC_6 ($0 < x < 1$), also a layered material, on a copper current collector. In case of Lithium-Titanate-Oxide (LTO)-cells these graphitic carbon electrodes are replaced by lithium-titanate nanocrystals. LTO cells are not sensitive to thermal run-away but do have a very low cell voltage. As Li-ion batteries mainly differ in the positive material that is used, the characterization of cell types is done based on the corresponding material. Most commonly used positive materials are

- $LiCoO_2$ Lithium-Ion-Cobalt-Oxide (LCO),
- $LiNiCoAlO_2$ Lithium-Nickel-Cobalt-Aluminium-Oxide (NCA),
- $LiNiCoMnO_2$ Lithium-Nickel-Manganese-Cobalt-Oxide (NMC),
- $LiMn_2O_4$ Lithium-Ion-Manganese-Oxide (LMO) and
- $LiFePO_4$ Lithium-Iron-Phosphate (LFP).

LCO is the first and the commercially most successful form of cathode material. This material is still used in the majority of commercial Li-ion batteries. NCA has found relatively widespread commercial use, for example, in Panasonic batteries for Tesla EVs. NCA has high usable discharge capacity and long storage calendar life compared to conventional Co-based oxide cathodes. LMO can also be promising because Mn is much cheaper and less toxic compared to Co or Ni. LFP is known for its thermal stability and high power capability. The major weaknesses of the LFP include its relatively low cell voltage and its flat voltage curve over a wide SoC-range, which makes the determination of the SoC more complex, but on the other hand also allows more efficient converter

operation. LCO cathodes are mostly used in battery cells for portable devices, e.g. mobile phones, tablets, etc. NCA cathodes are mostly used in battery cells for electric vehicles. NMC cathodes are mostly used for battery cells in E-bikes, medical devices or electric vehicles. LMO cathodes are mostly used in battery cells for power tools or medical devices. And LFP cathodes are mostly used in portable and stationary high-load applications.

When a Li-ion cell is charged, the positive material is oxidized and the negative material is reduced. In this process, lithium ions are de-intercalated from the positive material and intercalated into the negative material, as illustrated in Fig. A.15 based on the example of a LCO cell with an electrolyte that consists of a solution of lithium salt ($LiPF_6$) in a mixed organic solvent embedded in a separator felt [166]. The reactions in the half-cells and the overall reaction can be described as follows:

$$\begin{aligned} LiCoO_2 &\underset{\text{charge}}{\overset{\text{discharge}}{\leftrightarrows}} CoO_2 + Li^+ + e^- && \text{positive half-cell,} \\ C_6 + Li^+ + xe^- &\underset{\text{charge}}{\overset{\text{discharge}}{\leftrightarrows}} LiC_6 && \text{negative half-cell,} \\ xLiCoO_2 + xC_6 &\underset{\text{charge}}{\overset{\text{discharge}}{\leftrightarrows}} xLiC_6 + xCoO_2 && \text{overall.} \end{aligned} \tag{A.96}$$

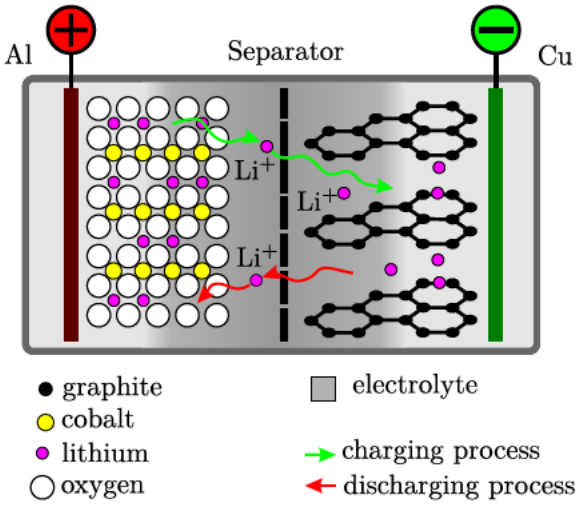

Figure A.15: Cell Chemistry of a $LiC_6|LiPF_6\|LiPF_6|LiCoO_2$ cell.

A.4.3.1 Electrolyte

Three types of electrolytes are used in Li-ion batteries:

- liquid (lithium salts in organic solvents),
- gel/polymer and
- ceramic electrolytes (generally: solid-state materials that are ionically conductive).

The characterization of Li-ion batteries is also possible based on the electrolyte used in the battery. Independently from the electrolyte used in the battery, all batteries relying on lithium intercalation are termed Li-ion batteries. Therefore, lithium-polymer (LiPo) batteries more correctly have to be termed lithium-ion polymer batteries.

A.4.3.2 Separator

The main function of the separator is keeping the two electrodes apart to prevent short-circuits while also allowing transport of ions. Thin porous films, currently mostly made of polyethylene or polypropylene, are used as separators [108]. The electrolyte is only passable by lithium ions and not passable by electrons. Therefore, the electrolyte naturally separates the electrodes. But when the cell temperature rises due to abnormal conditions, a liquid electrolyte would dry up, which would lead to a short-circuit between the electrodes. Therefore, separators are used for safety reasons.

A.4.3.3 Solid Electrolyte Interface (SEI)

During the first few charge/discharge cycles of Li-ion batteries, electrolytes (e.g. $LiPF_6$) are reduced on the anode surface. This generates an insoluble passivating film on the anode surface known as the solid electrolyte interphase (SEI). The SEI is a critical component of Li-ion batteries because it prevents further parasitic electrolyte decomposition and stabilizes battery operation and capacity [189]. The electrolyte decomposition can be described based on the example of a fully charged battery. At this state, lithium ions and the same amount of electrons are trapped between the graphite layers. The electrolyte would be degraded if the electrons came into contact with it. However, the electrons never come into contact with the electrolyte due to the SEI. The SEI is created by solvent molecules in the electrolyte, which cover the lithium ions during trespassing the electrolyte at the first charging cycles and which then react with the graphite to build a SEI layer. This SEI layer prevents any direct contact between the electrons and the electrolyte, thus saving the electrolyte from degradation.

A.4.3.4 Battery Degradation

As already described in Chp. 2.5.1, cycling and calendaric aging leads to a decrease of usable capacity of batteries. In case of Li-ion batteries the most relevant influence on capacity degradation is based on the growth of the SEI. Over time more and more Li-ions get lost to build up a thicker and denser SEI, even at deenergised state, which leads to calendaric aging. This process is accelerated at high temperatures and leads to the fact that less available Li-ions can be cyclized. The reduction of available Li-ions inevitably causes a battery degradation.

Besides the continuous growth of SEI there are several other mechanisms that lead to battery degradation. Especially at high SoC Li-ions tend to build metallic lithium, which is called “Li-plating”. This also leads to less available Li-ions which can be cycled. But this also increases the risk of dendrite building of metallic lithium, which in the worst case can build a conductive bridge between anode and cathode that finally leads to short-circuit and damage of the cell. Very low temperatures are also beneficial for Li-plating.

High currents are causing a high mechanical stress in the cells which may lead to particle cracking of the graphitic anode and an island formation of these areas. Any island builds a new SEI and leads to even higher consumption of Li-ions for SEI creation with the associated reduction of available Li-ions.

A very low SoC is also coupled with battery degradation as the current collectors tend to dissolve at low cell voltages. This leads to a higher electrical resistance which reduces the available energy content of the cell.

Battery degradation of Li-ion batteries, therefore, may be slowed down if guaranteeing moderate SoC-levels during operation (e.g. in the range of 20 %-80 %), ensuring appropriate cell temperatures or minimizing the number of peak loading.

A.4.3.5 Cell Types

Beside the characterization of a cell type based on the electrode and electrolyte chemistry, a more general characterization can be done by the value of power and energy density. As already described in Chp. 2.5.1.11, when designing cells there is a tradeoff between energy and power density, because methods to enlarge energy density often decrease power density [106]. Therefore, commercial Li-ion cells are either optimized for high energy density ("high energy cells") or high power density ("high performance cells"). In [106] relevant design parameters are summarized to optimize Li-ion cells either for high power or energy density. Some of these design parameters are summarized in Tab A.2.

Table A.2: Design parameters used to optimize Li-ion cells regarding energy density or power density.

component	high energy cell	high performance cell
electrode	low coating porosity	high coating porosity
current collector	thinner	thicker
connection tags	thin tags, single tag	thick tags, multiple tags

Typical performance characteristics of high energy cells and high performance cells are given in Tab. A.3.

Table A.3: Typical performance characteristics of high energy cells and high performance cells based on LCO cell chemistry [168].

characteristic	high performance cell	high energy cell
$\frac{I_{B,max}}{C_r}$@charging (constant)	3C	2C
$\frac{I_{B,max}}{C_r}$@charging (pulse)	5C	3C
$\frac{I_{B,max}}{C_r}$@discharging (pulse)	12C	5C
$\frac{I_{B,max}}{C_r}$@discharging (pulse)	15C	8C

A.4.4 Modeling of Battery Cells

There are different types of battery models that capture battery behavior in sufficient detail. There are several characteristics to be considered in battery models. Most of them were introduced in Chp. 2.5.1, including the voltage curve, the cell polarization and calendar aging (capacity fading), as the most relevant characteristics. The most accurate battery models consider all these characteristics, and also consider various parameters they are dependent on, as, for example, the c-rate, the temperature or the SoC. Generally, battery models according to [144] can be divided into physical, empirical and abstract models.

Physical models are also named electrochemical models in other contributions [96] and provide a detailed description of all physical processes occurring inside the battery. These models rely on several differential equations which describe these physical processes and which provide the cell potential values as a function of time when solved. The calculation time to solve these differential equations is rather high, so that physical models are not suitable for modeling battery cells in real time, but physical models are the most accurate ones.

Empirical models are also called stochastical models in other contributions [96] and rely on equations describing the battery cell's behavior with parameters fitted to match experimental data.

Abstract models attempt to provide an equivalent representation of the battery cell instead of modeling the exact physical behavior. The most popular representatives of abstract models are

Equivalent Electric Circuit (EEC) models, which consist of linear passive elements, voltage sources, and lookup tables for their parameters. Fig. A.16 shows three examples for EEC models. Fig. A.16(a) shows the most simple model including a constant voltage source and a constant internal resistance. As shown in Fig. A.14, around a SoC of 50 % the voltage curve is rather flat. Therefore, this simple model shown in Fig. A.16(a) is only valid in this region of the SoC. Otherwise the voltage curve has to be considered in the voltage source, for example via lookup table. This is the case in A.16(b), where both the voltage source and the internal resistance are dependent on SoC and temperature. To get an even more accurate model, the electrochemical effects of polarization or diffusion are modeled via an element called "Warburg impedance" [190], consisting of a resistance in parallel with a capacitance. Fig. A.16(c) shows a corresponding model including two Warburg impedances, each representing an electrochemical effect. The first element represents polarization and the second element represents diffusion.

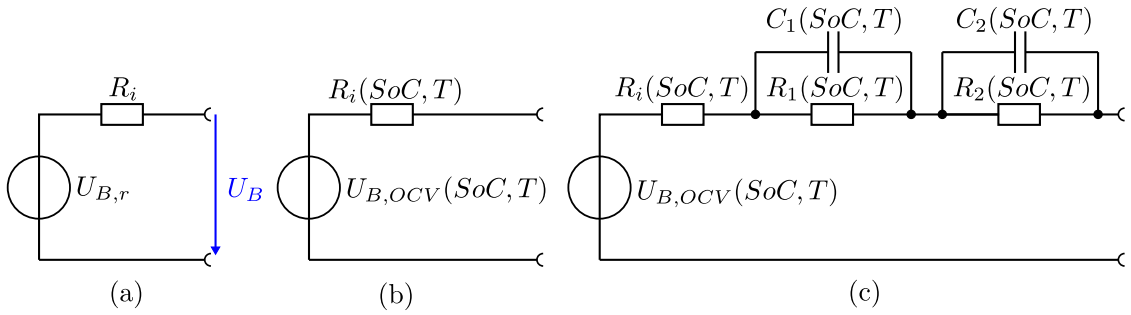

Figure A.16: Different types of EEC battery models. (a) simple model, (b) simple model considering lookup tables for the voltage curve and the internal resistance and (c) complex model considering electrochemical effects as for example activation/concentration polarization and diffusion.

The values for the lookup tables of abstract models, for example the lookup tables for the elements in Fig. A.16(b) and (c), are determined by laboratory measurements of the battery cells to be modeled. These measurements consist of pulse charging and discharging measurements at various states of charge and current rates. They comprise a series of discharge and charge pulses across the full SoC range. The procedure of a pulse measurement starts with a fully charged battery cell that is discharged with predefined values of pulses of the capacity (e.g. 1 % of C_r) with predefined rest periods between the pulses (e.g. one hour). With very high and very low value of the SoC the predefined values of the pulses and rest periods are chosen to be smaller. A more detailed description of the procedure can be found in [6]. Fig. A.17 shows an exemplary measurement of such a pulse measurement.

MATLAB/SIMULINK offers a possibility to derive values for the parameters of an EEC model according to Fig. A.16(c) by using the script `Example_DischargePulseEstimation`.

A.5 Short-Circuits in Three-Phase Systems

The following chapters describe relevant fundamentals of the calculation of short-circuits and neutral point treatment.

A.5.1 Basic Considerations

Short-circuits occur due to bridging or breakdown of the insulation between three conductors, between two conductors or between windings (phase windings) of the three-phase system and can

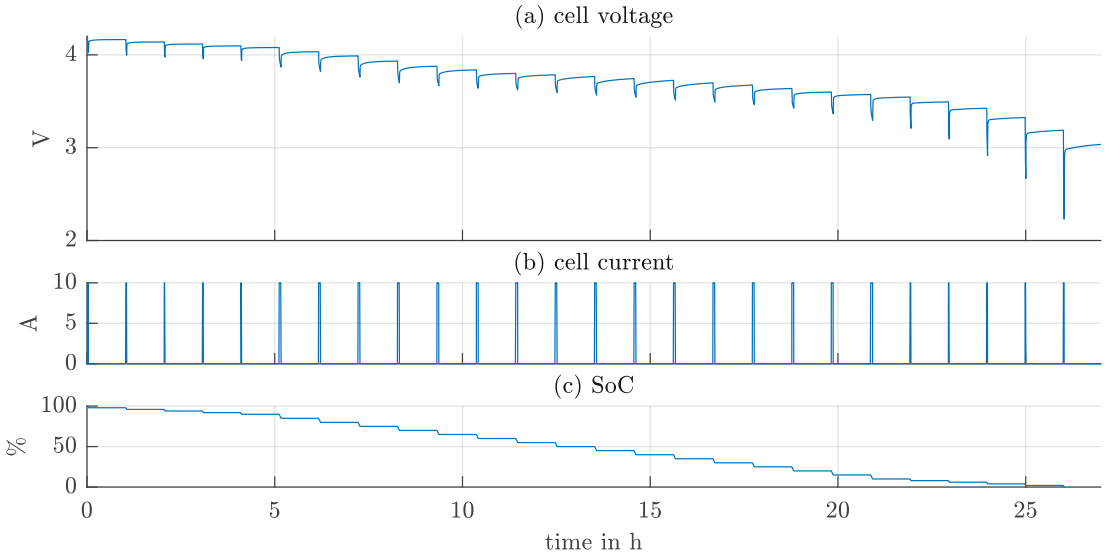

Figure A.17: Pulse measurement of a battery cell based on MATLAB/SIMULINK example `Example_DischargePulseEstimation`.

happen with or without earth contact. Earth short-circuits occur due to bridging or breakdown of the insulation between a conductor and ground, earthed conductors or earthed system components in three-phase networks with low-impedance earthing of the neutral point. In case of an isolated neutral system or earth fault compensation by a resonant earthed neutral system, a line-to-earth fault (earth short-circuit) is called earth fault. The different sorts of short-circuits are summarized in Fig. A.18.

Based on the following fault conditions, which summarize the voltage and current conditions in the fault location, every single type of short-circuit can be represented in symmetrical components:

- three-phase short-circuit:

$$\underline{U}_{1E} = \underline{U}_{2E} = \underline{U}_{3E} \rightarrow \underline{U}_{1+,E} = \underline{U}_{1-,E} \tag{A.97}$$

- three-phase earth short-circuit:

$$\underline{U}_{1E} = \underline{U}_{2E} = \underline{U}_{3E} = 0 \rightarrow \underline{U}_{1+,E} = \underline{U}_{1-,E} = \underline{U}_{10,E} \tag{A.98}$$

- two-phase short-circuit:

$$\begin{aligned} \underline{U}_{2E} = \underline{U}_{3E} &\rightarrow \underline{U}_{1+,E} = \underline{U}_{1-,E} \\ \underline{I}_{L1} = 0 &\rightarrow \underline{I}_{10} = 0 \\ \underline{I}_{L2} = \underline{I}_{L3} &\rightarrow \underline{I}_{1+} = -\underline{I}_{1-} \end{aligned} \tag{A.99}$$

- two-phase earth short-circuit:

$$\begin{aligned} \underline{U}_{2E} = \underline{U}_{3E} = 0 &\rightarrow \underline{U}_{10,E} = \underline{U}_{1+,E} = \underline{U}_{1-,E} \\ \underline{I}_{L1} = 0 &\rightarrow \underline{I}_{10} + \underline{I}_{1+} + \underline{I}_{1-} = 0 \end{aligned} \tag{A.100}$$

- earth short-circuit and earth fault:

$$\begin{aligned} \underline{U}_{1E} = 0 &\rightarrow \underline{U}_{10,E} + \underline{U}_{1+,E} + \underline{U}_{1-,E} = 0 \\ \underline{I}_{L1} = \underline{I}_{L2} = 0 &\rightarrow \underline{I}_{10} = \underline{I}_{1+} = \underline{I}_{1-} = 0 \end{aligned} \tag{A.101}$$

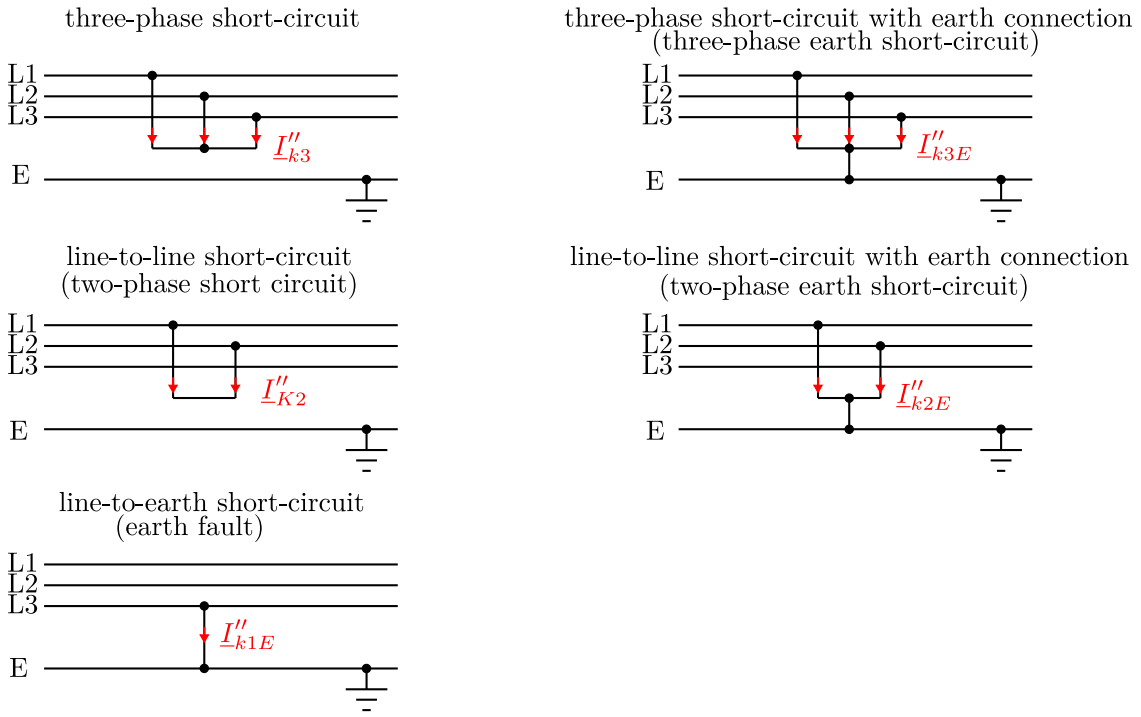

Figure A.18: Characterization of short-circuits and their currents (in MV-grids).

A.5.2 Neutral Point Treatment

The neutral point treatment is an important aspect of power system design because the performance of the system regarding short-circuits, stability, protection, etc., is greatly affected by the condition of the neutral point. Especially as line-to-earth faults (earth faults) and single-phase short-circuits (earth short-circuits) are the most frequently occurring faults, the neutral earthing will be discussed below. The methods commonly used for neutral earthing are

- isolated neutral system
- solid earthed neutral system
- resistance earthed neutral system
- Petersen-coil earthed neutral system (or resonant earthed)

Industrial grids or wind farms are primarily operated as isolated grids. In the event of an earth fault, the resulting short-circuit current only develops due to the earth capacitances of the lines in the grid. Because these are rather small, the corresponding impedances are very high and the short-circuit current is also rather small. Therefore, the isolated grid can continue to operate in case of an earth fault. Typically, the fault location is done by protection devices based on a sufficient distance between maximum operating current and minimum short-circuit current. Due to the low ground fault current in isolated networks, fault location is difficult. Therefore, the isolated neutral point is used exclusively in networks of small spatial extent. Because of the high effective neutral point impedance of the earth capacitances, the voltage drop across is very large. This leads to a displacement voltage of the neutral point which can rise to a maximum of $\sqrt{3}$ of the rated phase voltages. This increases the risk that another earth fault will occur at another point in the grid. The previous earth fault then expands into a double earth fault.

Solid earthed neutral systems are primarily used in the ultra-high voltage grid. The reason lies in the stressing of the insulation in case of earth short-circuits as a result of high displacement voltages of the neutral point when the effective impedances of the short-circuit are high. Solid earthing is also used in low-voltage grids. In low-voltage grids the neutral earthing is identical to the network form (IT,TT,TN-S,TN-C,TN-C-S), which describes the earthing on the transformer star point on NL 6 and the earthing on the load side.

Resistance earthed neutral systems are primarily used in the high-voltage grid. For common values of zero impedances of resistance earthed grids an earth short-circuit is not significantly smaller than the three-phase short-circuit current. The major advantage compared to isolated grids, as well as resonant grounded grids is the smaller displacement voltage in case of an earth short-circuit. This minimizes the risk for double earth faults.

In large grids, the earth capacitance becomes very large. Therefore, the resulting earth fault current in case of an earth fault grows to undesirably high values. This earth fault current can be decreased by earthing at least one star point in the grid with a Petersen coil. As a result of a resonance between earth capacitances and Petersen coil, the effective fault impedance becomes very large, which minimizes the earth fault current. The displacement voltage during an earth fault is identical to isolated grids. Therefore, resonant earthing is used if the share of overhead lines in the grid is rather high. In grids with a high share of cables resonant earthing is rarely used, because cables are much more vulnerable to double earth faults.

Fig. A.1 shows the neutral earthing systems that are commonly used in the different NLs. In case of several used methods for neutral earthing, the predominantly used one is colored black while the alternative methods are colored gray. In the NL 3 and 5 the method for neutral earthing is dependent on the share of overhead lines. In case of a high share resonant earthing is used, while in case of a high share of cables a solid grounding is used. Due to historical reasons in the NL 5 there are no star points of the transformers available, because of the usage of delta-wye transformers in the NL 4 and 6. Therefore, three-phase earthing transformers are used to provide a star point in case of a resonant earthing. Fig. A.1 shows such an earthing transformer with a vector group ZNynd.

List of Figures

List of Tables

Bibliography

[1] 50Hertz, "Historical frequency data," Website, Available online: https://www.50hertz.com/de/Transparenz/Kennzahlen/Regelenergie/ArchivNetzfrequenz; accessed on 04. November 2019. 12

[2] 50Hertz, Amprion, Tennet, and Transnet BW, "Eckpunkte und Freiheitsgrade bei Erbringung von Primärregelleistung," Policy, 2014, Available online: https://www.regelleistung.net/ext/download/eckpunktePRL; accessed on 19. March 2019. 92, 93, 282

[3] 50Hertz, Amprion, Tennet, and TransnetBW, "Präqualifikationsverfahren für Reservenanbieter," Policy, May 29, 2020, Available online: https://www.regelleistung.net/ext/download/PQ_Bedingungen_FCR_aFRR_mFRR; accessed on 19. March 2019. 37, 83, 84, 85

[4] 50Hertz and Amprion and Tennet and Transnet BW, "Capacity settlement price for FCR," Website, Available online: https://www.regelleistung.net/apps/datacenter/tenders/?productTypes=PRL&from=2019-09-01&to=2019-09-22&tid=PRL_20190901_D1; accessed on 04. November 2019. 8

[5] 50Hertz and Amprion and Tennet and Transnet BW and APG and and elia and ENERGINET and Rte and swissgrid, "TSOs' proposal for the establishment of common and harmonised rules and processes for the exchange and procurement of Balancing Capacity for Frequency Containment Reserves (FCR) in accordance with Article 33 of Commission Regulation (EU) 2017/2195 establishing a guideline on electricity balancing," Policy Draft, 2018, Available online: https://www.regelleistung.net/ext/download/FCR_Proposal_Art33; accessed on 27. June 2019. 38

[6] R. Ahmed, J. Gazzarri, S. Onori, S. Habibi, R. Jackey, K. Rzemien, J. Tjong, and J. LeSage, "Model-based parameter identification of healthy and aged li-ion batteries for electric vehicle applications," *SAE International Journal of Alternative Powertrains*, vol. 4, no. 2, pp. 233–247, 2015. 277

[7] C. Alacs, J. Marchgraber, Y. Guo, W. Gawlik, A. Anta, J. Kathan, B. Weiss, K. Oberhauser, M. Lenz, A. Stimmer, and M. Leonhardt, "Mögliche Umsetzung von schnellen Regelreserven im kontinentaleuropäischen Verbundystem," in *Proc. of the 16th Symposium Energieinnovation (EnInnov 2020)*, Graz, Austria, Feb. 12 – 14, 2020, pp. 1–2.

[8] H. Almasalma and G. Deconinck, "Simultaneous provision of voltage and frequency control by pv-battery systems," *IEEE Access*, vol. 8, pp. 152 820–152 836, 2020. 76, 198

[9] J. Arteaga and H. Zareipour, "A price-maker/price-taker model for the operation of battery storage systems in electricity markets," *IEEE Transactions on Smart Grid*, vol. 10, no. 6, pp. 6912–6920, 2019. 14, 16, 197, 198

[10] Austrian Power Grid (APG), "Capacity settlement price for FCR," Website, Available online: https://www.apg.at/de/markt/netzregelung/statistik; accessed on 04. November 2019. 8, 232

[11] Austrian Power Grid (APG), "Erläuterungen Regelreserven," Policy, Oct. 09, 2015, Available online: https://www.apg.at/-/media/3F8C9277B7684F1FBFC1CFF6D933E1AF.pdf; accessed on 19. March 2019. 36, 85

[12] M. Bagert, *Elektrischer Eigenbedarf : Elektrotechnik in Kraftwerken und Industrie, Zusammenwirken von Kraftwerken und Netzen, Beispiele ausgeführter Anlagen*, 3rd ed. Berlin, Germany: VDE Verlag, 2012. 177, 179, 186

[13] E. Barklund, N. Pogaku, M. Prodanovic, C. Hernandez-Aramburo, and T. C. Green, "Energy management in autonomous microgrid using stability-constrained droop control of inverters," *IEEE Transactions on Power Electronics*, vol. 23, no. 5, pp. 2346–2352, 2008. 169

[14] BDEW, "Entso-e consultation on the deterministic frequency deviation report," Position Paper, Jan. 31, 2020, Available online: https://www.bdew.de/media/documents/Stn_20200131_frequency-deviation-report.pdf; accessed on 19. March 2020. 79

[15] H.-P. Beck and R. Hesse, "Virtual synchronous machine," in *Proc. of the 9th International Conference on Electrical Power Quality and Utilisation (EPQU 2007)*, Barcelona, Spain, Oct. 9 – 11, 2007, pp. 1–6. 123

[16] R. N. Beres, X. Wang, M. Liserre, F. Blaabjerg, and C. L. Bak, "A review of passive power filters for three-phase grid-connected voltage-source converters," *IEEE Journal of Emerging and Selected Topics in Power Electronics*, vol. 4, no. 1, pp. 54–69, 2015. 47, 125

[17] H. Bevrani, B. François, and T. Ise, *Microgrid dynamics and control*. Hoboken, USA: John Wiley & Sons, 2017. 122

[18] H. Bevrani, T. Ise, and Y. Miura, "Virtual synchronous generators: A survey and new perspectives," *International Journal of Electrical Power & Energy Systems*, vol. 54, pp. 244–254, 2014. 123

[19] H. Bevrani and J. Raisch, "On virtual inertia application in power grid frequency control," *Energy Procedia*, vol. 141, pp. 681–688, 2017. 122

[20] A. Binder, *Elektrische Maschinen und Antriebe*. Berlin, Germany: Springer-Verlag Berlin Heidelberg, 2012, p. 1018. 24

[21] A. Binder, *Elektrische Maschinen und Antriebe*. Berlin, Germany: Springer-Verlag Berlin Heidelberg, 2012, pp. 1180–1193. 263

[22] F. Braeuer, J. Rominger, R. McKenna, and W. Fichtner, "Battery storage systems: An economic model-based analysis of parallel revenue streams and general implications for industry," *Applied Energy*, vol. 239, pp. 1424–1440, 2019. 198

[23] P. V. Brogan, R. Best, J. Morrow, R. Duncan, and M. Kubik, "Stacking battery energy storage revenues with enhanced service provision," *IET Smart Grid*, vol. 3, no. 4, pp. 520–529, 2019. 198

[24] Bundesnetzagentur, "Diskussionspapier Blindleistungsbereitstellung für den Netzbetrieb," Discussion Paper, Bundesnetzagentur, Bonn, Germany, 2018, Available online: https://www.bundesnetzagentur.de/SharedDocs/Downloads/DE/Sachgebiete/Energie/Unternehmen_Institutionen/NetzentwicklungUndSmartGrid/SmartGrid/Blindleistungspapier.pdf?__blob=publicationFile&v=1 (accessed on 27.06.2020). 232

[25] T. Caldognetto and P. Tenti, "Microgrids operation based on master–slave cooperative control," *IEEE Journal of Emerging and Selected Topics in Power Electronics*, vol. 2, no. 4, pp. 1081–1088, 2014. 170

[26] A. Camacho, M. Castilla, J. Miret, A. Borrell, and L. G. de Vicuña, "Active and reactive power strategies with peak current limitation for distributed generation inverters during unbalanced grid faults," *IEEE Transactions on Industrial Electronics*, vol. 62, no. 3, pp. 1515–1525, 2014. 146

[27] M. Castilla, J. Miret, J. L. Sosa, J. Matas, and L. G. de Vicuña, "Grid-fault control scheme for three-phase photovoltaic inverters with adjustable power quality characteristics," *IEEE Transactions on Power Electronics*, vol. 25, no. 12, pp. 2930–2940, 2010. 146

[28] S. K. Chaudhary, R. Teodorescu, P. Rodriguez, P. C. Kjaer, and A. M. Gole, "Negative sequence current control in wind power plants with vsc-hvdc connection," *IEEE Transactions on Sustainable Energy*, vol. 3, no. 3, pp. 535–544, 2012. 146

[29] B. Cheng and W. B. Powell, "Co-optimizing battery storage for the frequency regulation and energy arbitrage using multi-scale dynamic programming," *IEEE Transactions on Smart Grid*, vol. 9, no. 3, pp. 1997–2005, 2016. 198

[30] S. D'Arco and J. A. Suul, "Virtual synchronous machines—classification of implementations and analysis of equivalence to droop controllers for microgrids," in *Proc. of the IEEE Grenoble Conference PowerTech (POWERTECH 2013)*, Grenoble, France, Jun. 16 – 20, 2013, pp. 1–7. 123

[31] A. M. Divakaran, D. Hamilton, K. N. Manjunatha, and M. Minakshi, "Design, development and thermal analysis of reusable li-ion battery module for future mobile and stationary applications," *Energies*, vol. 13, no. 6, p. 1477, 2020. 170

[32] DNV GL Energy Advisory, "RoCoF Alternative Solutions Technology Assessment," EirGrid, London, UK, Tech. Rep., Jun. 2015, Available online: https://www.eirgridgroup.com/site-files/library/EirGrid/RoCoF-Alternative-Solutions-Technology-Assessment-Phase-1-DNV-GL-Report_.pdf (accessed on 23.06.2020). 143, 283

[33] E. Drury, P. Denholm, and R. Sioshansi, "The value of compressed air energy storage in energy and reserve markets," *Energy*, vol. 36, no. 8, pp. 4959 – 4973, 2011, pRES 2010. 7

[34] X. Du, Y. Wu, S. Gu, H.-M. Tai, P. Sun, and Y. Ji, "Power oscillation analysis and control of three-phase grid-connected voltage source converters under unbalanced grid faults," *IET Power Electronics*, vol. 9, no. 11, pp. 2162–2173, 2016. 146

[35] R. Dufo-López, J. M. Lujano-Rojas, and J. L. Bernal-Agustín, "Comparison of different lead–acid battery lifetime prediction models for use in simulation of stand-alone photovoltaic systems," *Applied Energy*, vol. 115, pp. 242–253, 2014. 236

[36] F. H. Dupont, J. Z. Bertomeu, C. Rech, and J. R. Pinheiro, "Mathematical efficiency modeling of static power converters," in *Proc. of the IEEE 13th Brazilian Power Electronics Conference and 1st Southern Power Electronics Conference (COBEP/SPEC 2015)*, Fortaleza, Brazil, Nov. 29 –Dec. 2 2015, pp. 1–6. 95

[37] E-Control, "Technische und organisatorische Regeln für Betreiber und Benutzer von Netzen: Teil E: Technische Maßnahmen zur Vermeidung von Großstörungen und Begrenzung ihrer Auswirkungen," Policy, 2015, Available online: https://www.e-control.at/recht/marktregeln/tor; accessed on 19. March 2019. 40

[38] E-Control, "Technische und organisatorische Regeln für Betreiber und Benutzer von Netzen: Teil D: Besondere technische Regeln. Hauptabschnitt D4: Parallelbetrieb von Erzeugungsanlagen mit Verteilernetzen," Policy, 2016, Available online: https://www.e-control.at/recht/marktregeln/tor; accessed on 19. March 2019. 165, 166, 167, 168

[39] E-Control, "Betriebsstatistik 2018," Website, 2018, Available online: https://www.e-control.at/betriebsstatistik2018 (accessed on 08.09.2020). 3

[40] E-Control, "Sonstige Marktregeln Strom. Kaptiel 3. Version 5.6," Policy, 2018, Available online: https://www.e-control.at/recht/marktregeln/sonstige-marktregeln-strom; accessed on 19. March 2019. 87

[41] E-Control, "Technische und organisatorische Regeln für Betreiber und Benutzer von Netzen: TOR Erzeuger: Anschluss und Parallelbetrieb von Stromerzeugungsanlagen des Typs B," Policy, 2019, Available online: https://www.e-control.at/recht/marktregeln/tor; accessed on 19. March 2019. 76, 145, 147, 148, 150, 151, 164, 165, 166, 167, 168, 172, 218, 219, 283

[42] Electric Power Research Institute (EPRI), "Storage value estimation tool (storagevet)," Website, 2020, Available online: https://www.storagevet.com/ (accessed on 05.08.2020). 14, 16

[43] H. Emanuel, J. Brombach, R. Rosso, and K. Pierros, "Requirements for control strategies of grid-connected converters in the future power system," *IET Renewable Power Generation*, vol. 14, no. 8, pp. 1288–1295, 2020. 123

[44] Energienet, Fingrid, Statnett, and Svenska Kräftnät, "Fast Frequency Reserve – Solution to the Nordic inertia challenge," ENTSO-E, Brussels, Belgium, Tech. Rep., Dec. 13, 2019, Available online: epressi.com/media/userfiles/107305/1576157646/fast-frequency-reserve-solution-to-the-nordic-inertia-challenge-1.pdf (accessed on 23.06.2020). 76, 122

[45] S. Englberger, H. Hesse, N. Hanselmann, and A. Jossen, "Simses multi-use: A simulation tool for multiple storage system applications," in *Proc. of the IEEE 16th International Conference on the European Energy Market (EEM 2019)*, Ljubljana, Slovakia, Sep. 18 – 20, 2019, pp. 1–5. 15, 194, 198, 200, 284

[46] S. Englberger, A. Jossen, and H. Hesse, "Unlocking the potential of battery storage with the dynamic stacking of multiple applications," *Cell Reports Physical Science*, vol. 1, no. 11, p. 100238, 2020. 15, 195, 197, 198

[47] ENTSO-E, "Appendix 1: Load-Frequency Control and Performance," Policy, 2004, Available online: https://www.entsoe.eu/fileadmin/user_upload/_library/publications/entsoe/Operation_Handbook/Policy_1_final.pdf; accessed on 19. March 2019. 41

[48] ENTSO-E, "UCTE Operation Handbook - Policy 1: Load-Frequency Control," Policy, 2009, Available online: https://www.entsoe.eu/fileadmin/user_upload/_library/publications/entsoe/Operation_Handbook/Policy_1_final.pdf; accessed on 27. June 2019. 41

[49] ENTSO-E, "Supporting document for the network code on load-frequency control and reserves," Policy, 2013, Available online: https://www.acer.europa.eu/Official_documents/Acts_of_the_Agency/Annexes/ENTSO-E%E2%80%99s%20supporting%20document%20to%20the%20submitted%20Network%20Code%20on%20Load-Frequency%20Control%20and%20Reserves.pdf; accessed on 27. June 2019. 38

[50] ENTSO-E, "All CE TSOs' proposal for additional properties of FCR in accordance with Article 154(2) of the Commission Regulation (EU) 2017/1485 of 2 August 2017 establishing a guideline on electricity transmission system operations," Policy, 2018, Available online: https://consultations.entsoe.eu/system-operations/synchronous-area-operational-agreement-policy-1-lo/supporting_documents/Article%20A2_Additional%20properties%20of%20FCR%20002.pdf; accessed on 27. June 2019. 36, 81, 227

[51] ENTSO-E, "Explanatory document to all TSOs' proposal for the implementation framework for a European platform for the exchange of balancing energy from frequency restoration reserves with automatic activation in accordance with Article 21 of Commission Regulation (EU) 2017/2195 establishing a guideline on electricity balancing," Policy, 2018, Available online: https://docstore.entsoe.eu/Documents/nc-tasks/EBGL/EBGL_A21_181218_ALL%20TSOs%20proposal_aFRRIF_explanatory_document_for%20submission.pdf?Web=0; accessed on 27. June 2019. 42

[52] ENTSO-E, "Ten year network development plan (tyndp)," Main Report, 2018, Available online: https://tyndp.entsoe.eu/tyndp2018/ (accessed on 05.08.2020). 9, 10

[53] ENTSO-E, "Continental Europe; Significant Frequency Deviations - January 2019," Belgium, Brussels, Tech. Rep., Jan. 2019, Available online: https://eepublicdownloads.entsoe.eu/clean-documents/news/2019/190522_SOC_TOP_11.6_Task%20Force%20Significant%20Frequency%20Deviations_External%20Report.pdf; accessed on 27. June 2019. 103, 116, 229

[54] ENTSO-E, "Report on deterministic frequency deviations," Belgium, Brussels, Tech. Rep., Nov. 04, 2019, Available online: https://consultations.entsoe.eu/system-development/deterministic_frequency_deviations_report/user_uploads/report_deterministic_frequency_deviations_final-draft-for-consultation.pdf; accessed on 27. November 2019. 9

[55] EPEXSpot, "Intraday-market prices," Website, Available online: https://www.epexspot.com/en/market-data/intradaycontinuous/intraday-table/-/AT; accessed on 04. November 2019. 189, 232, 284

[56] R. Eriksson, N. Modig, and K. Elkington, "Synthetic inertia versus fast frequency response: a definition," *IET Renewable Power Generation*, vol. 12, no. 5, pp. 507–514, 2017. 136

[57] I. Erlich, T. Neumann, F. Shewarega, P. Schegner, and J. Meyer, "Wind turbine negative sequence current control and its effect on power system protection," in *Proc. of the IEEE Power & Energy Society General Meeting (PES GM 2013)*, Vancouver, British Columbia, Canada, Jul. 21 – 25, 2013, pp. 1–5. 145

[58] European Commission, "Short assessment of renewable energy sources (SHARES) 2015," Website, 2015, Available online: https://ec.europa.eu/eurostat/web/energy/data/shares (accessed on 08.09.2020). 2

[59] European Commission, "Commission regulation (EU) 2016/631; establishing a network code on requirements for grid connection of generators; (RfG)," Policy, Brussels, Belgium, 2016, Available online: https://eur-lex.europa.eu/eli/reg/2016/631/oj; accessed on 19. March 2019. 146, 164

[60] European Commission, "Commission regulation (EU) 2017/1485; establishing a guideline on electricity transmission system operation; System Operator guideline (SO GL)," Policy, Brussels, Belgium, 2017, Available online: https://eur-lex.europa.eu/eli/reg/2017/1485/oj; accessed on 19. March 2019. 36, 38, 82, 212, 213

[61] European Commission, "Photovoltaic geographical information system (pvgis)," Website, 2018, Available online: https://re.jrc.ec.europa.eu/pvg_tools/en/tools.html#MR (accessed on 08.09.2020). 3

[62] European Commission, "Directive 2019/944 of the european parliament and of the council on common rules for the internal market for electricity ("Electricity Market Directive")," Policy, Brussels, Belgium, 2019, Available online: https://eur-lex.europa.eu/eli/dir/2019/944/oj; (accessed on 05.08.2020). 7

[63] J. Eyer and G. Corey, "Energy storage for the electricity grid: Benefits and market potential assessment guide," *Sandia National Laboratories*, vol. 20, no. 10, p. 5, 2010. 15, 74, 79, 195, 196

[64] *FGW TR3: Technische Richtlinien für Erzeugungseinheiten und -anlagen; Teil 3 (TR3); Bestimmung der elektrischen Eigenschaften von Erzeugungseinheiten und -anlagen am Mittel-, Hoch- und Höchstspannungsnetz*, FGW Std., Rev. 24, 2017. 257

[65] M. Fischer, S. Engelken, N. Mihov, and A. Mendonca, "Operational experiences with inertial response provided by type 4 wind turbines," *IET Renewable Power Generation*, vol. 10, no. 1, pp. 17–24, 2016. 132

[66] G. Fitzgerald, J. Mandel, J. Morris, and H. Touati, "The economics of battery energy storage: How multi-use, customer-sited batteries deliver the most services and value to customers and the grid," Rocky Mountain Institute, Colorado, USA, Tech. Rep., Sep. 2015. 63, 79, 197

[67] K. Forkasiewicz, M. Coldwell, A. Cross, and D. Strickland, "Meeting frequency response requirements with uncertain system inertia—a uk perspective," in *Proc. of the IEEE International Conference on Renewable Energy Research and Applications (ICRERA 2016)*, Ljubljana, Slovakia, Nov. 20 – 23, 2016, pp. 538–543. 122

[68] C. L. Fortescue, "Method of symmetrical co-ordinates applied to the solution of polyphase networks," *Transactions of the American Institute of Electrical Engineers*, vol. 37, no. 2, pp. 1027–1140, 1918. 21

[69] Fraunhofer IWES, "The european power system in 2030: Flexibility challenges and integration benefits. an analysis with a focus on the pentalateral energy forum region," Analysis on behalf of Agora Energiewende, Berlin, Germany, Jun. 2015. 3, 75, 167, 169

[70] F. Friend, "Cold load pickup issues," in *Proc. of the IEEE 62nd Annual Conference for Protective Relay Engineers*, College Station, Texas, Mar. 30 –Apr. 2 2009, pp. 176–187. 171

[71] J. Garche, C. K. Dyer, P. T. Moseley, Z. Ogumi, D. A. Rand, and B. Scrosati, *Encyclopedia of Electrochemical Power Sources*. Amsterdam, The Netherlands: Elsevier, 2013. 56

[72] R. Garde, S. Casado, M. Santamaria, and M. Aguado, "Power quality and stability analysis during islanded mode operation in a microgrid based on master-slave configuration," in *Proc. of the IEEE Saudi Arabia Smart Grid (SASG 2015)*, Jeddah, Saudi Arabia, Dec. 7 – 9, 2015, pp. 1–8. 170

[73] W. Gawlik, C. Alacs, J. Marchgraber, Y. Guo, A. Anta, J. Kathan, B. Weiss, K. Oberhauser, M. Lenz, M. Froschauer *et al.*, "Improving synthetic inertia provision by power electronic interfaced power sources to support future system stability," *Elektrotech. Inftech.*, vol. 137, no. 8, pp. 460–469, 2020. 217

[74] W. Gawlik, A. Kerdegarbakhsh, M. Pesek, and C. Alacs, "Development of requirements for faster control reserves for the european power system," *Elektrotech. Inftech.*, vol. 135, no. 8, pp. 507–513, 2018. 76

[75] W. Gawlik, C. Alács, J. Marchgraber, Y. Guo, A. Anta, J. Kathan, B. Weiss, K. Oberhauser, M. Lenz, M. Forschauer, A. Stimmer, and M. Leonhard, "Improving synthetic inertia provision by power electronic interfaced power sources to support future system stability," in *Proc. of the CIGRE Session 2020*, Paris, France, Aug. 23 –Sep. 4 2020, pp. 1–10.

[76] W. Gawlik, A. Lechner, and R. Schürhuber, "Inertia Certificates – Bedeutung und Wert von Momentanreserve für den Verbundnetzbetrieb," in *Proc. of the 10th Internationale Energiewirtschaftstagung (IEWT 2017)*, Vienna, Austria, Feb. 15 – 17, 2017, pp. 1–8. 76, 122

[77] Ö. Göksu, R. Teodorescu, C. L. Bak, F. Iov, and P. C. Kjær, "Impact of wind power plant reactive current injection during asymmetrical grid faults," *IET Renewable Power Generation*, vol. 7, no. 5, pp. 484–492, 2013. 146

[78] N. Hadjsaid and J.-C. Sabonnadière, *Power Systems and Restructuring*. London, UK and Hoboken, USA: ISTE Ltd. and John Wiley & Sons, 2009. 21

[79] H. Han, Y. Liu, Y. Sun, M. Su, and J. M. Guerrero, "An improved droop control strategy for reactive power sharing in islanded microgrid," *IEEE Transactions on Power Electronics*, vol. 30, no. 6, pp. 3133–3141, 2014. 169

[80] S. Henninger, "Netzdienliche Integration regenerativer Energiequellen über stromrichtergekoppelte Einspeisenetze mit integrierten Energiespeichern," Ph.D. dissertation, FAU Erlangen, Erlangen, Germany, 2019. 128, 176

[81] S. Henninger, M. Schroeder, and J. Jaeger, "Combining frequency containment reserves and renewable power leveling in energy storage systems," in *Proc. of the 10th International Renewable Energy Storage Conference (IRES 2016)*, vol. 99, Düsseldorf, Germany, Mar. 15 – 17, 2016, pp. 147–156. 88

[82] J. Hernández, I. Gyuk, and C. Christensen, "Doe global energy storage database—a platform for large scale data analytics and system performance metrics," in *Proc. of the IEEE International Conference on Power System Technology (POWERCON 2016)*, Wollongong, Australia, Sep. 28 –Oct. 1 2016, pp. 1–6. 4, 5

[83] H. C. Hesse, M. Schimpe, D. Kucevic, and A. Jossen, "Lithium-ion battery storage for the grid—a review of stationary battery storage system design tailored for applications in modern power grids," *Energies*, vol. 10, no. 12, p. 2107, 2017. 13, 53, 60, 70, 74, 77, 196

[84] C. Heubner, A. Nickol, J. Seeba, S. Reuber, N. Junker, M. Wolter, M. Schneider, and A. Michaelis, "Understanding thickness and porosity effects on the electrochemical performance of lini0. 6co0. 2mn0. 2o2-based cathodes for high energy li-ion batteries," *Journal of Power Sources*, vol. 419, pp. 119–126, 2019. 55

[85] R. Hollinger, L. M. Diazgranados, C. Wittwer, and B. Engel, "Optimal provision of primary frequency control with battery systems by exploiting all degrees of freedom within regulation," in *Proc. of the International Renewable Energy Storage Conference (IRES 2016)*, vol. 99, Düsseldorf, Germany, Mar. 15 – 17, 2016, pp. 204–214. 93

[86] *IEC 61427-2: Secondary cells and batteries for renewable energy storage – General requirements and methods of test. Part 2: on-grid aplications*, IEC Std., Rev. 1, 2014. 73

[87] *IEC 60909-0:2016: Short-circuit currents in three-phase a.c. systems - Part 0: Calculation of currents*, IEC International Std., Rev. 2, 2016. 29, 30, 33, 152, 153

[88] *IEC/IEEE 60255-118-1:2018: IEEE/IEC International Standard - Measuring relays and protection equipment - Part 118-1: Synchrophasor for power systems - Measurements*, IEEE Std., 2018, Available online: https://doi.org/10.1109/IEEESTD.2018.8577045 (accessed on 23.06.2020). 140

[89] International Energy Agency (IEA), "Tracking report energy storage," Website, 2020, Available online: https://www.iea.org/reports/energy-storage; (accessed on 05.08.2020). 5, 7

[90] IRENA, "Electricity storage and renewables: Costs and markets to 2030," International Renewable Energy Agency (IRENA), European Commission (EC), Abu Dhabi, United Arab Emirates, Tech. Rep., 2017, Available online: https://www.irena.org/publications/2017/Oct/Electricity-storage-and-renewables-costs-and-markets (accessed on 05.08.2020). 4, 5, 6, 7

[91] IRENA, "Renewable energy prospects for the European Union," International Renewable Energy Agency (IRENA), European Commission (EC), Abu Dhabi, United Arab Emirates, Tech. Rep., Feb. 2018. 1, 2, 3, 167, 169

[92] IRENA, "Innovation landscape brief: Utility-scale batteries," International Renewable Energy Agency (IRENA), European Commission (EC), Abu Dhabi, United Arab Emirates, Tech. Rep., Sep. 2019, Available online: https://www.irena.org/-/media/Files/IRENA/Agency/Publication/2019/Sep/IRENA_Utility-scale-batteries_2019.pdf (accessed on 05.08.2020). 4, 5, 6, 13, 74, 77, 78

[93] IRENA, "Electricity storage valuation framework: Assessing system value and ensuring project viability," International Renewable Energy Agency (IRENA), European Commission (EC), Abu Dhabi, United Arab Emirates, Tech. Rep., Mar. 2020, Available online: https://www.irena.org/-/media/Files/IRENA/Agency/Publication/2020/Mar/IRENA_storage_valuation_2020.pdf; (accessed on 05.08.2020). 6, 7, 10, 14, 74, 78, 79

[94] J. Jia, G. Yang, and A. H. Nielsen, "Investigation of grid-connected voltage source converter performance under unbalanced faults," in *Proc. of the IEEE PES Asia-Pacific Power and Energy Engineering Conference (APPEEC 2016)*, Suzhou, China, Apr. 15 – 17, 2016, pp. 609–613. 146

[95] K. Johansen and R. Warzywoda, "Cost-benefit analysis," Presentation, ENTSO-E, Brussels, Belgium, Tech. Rep., May 23, 2018, Available online: https://docstore.entsoe.eu/Documents/Events/2019/Input%20data.pdf; accessed on 04. November 2019. 8, 9, 63

[96] M. R. Jongerden and B. R. Haverkort, "Which battery model to use?" *IET software*, vol. 3, no. 6, pp. 445–457, 2009. 276

[97] P. Jonke, A. Anta, and C. Seitl, "Validation of advanced grid functions of battery storage systems through a controller hardware-in-the-loop setup," *Elektrotech. Inftech.*, vol. 136, no. 1, pp. 12–20, 2019. 138

[98] I. Kasikci, *Short circuits in power systems*. Wenheim, Germany: Wiley-VCH, 2003. 30, 33

[99] F. Katiraei and M. R. Iravani, "Power management strategies for a microgrid with multiple distributed generation units," *IEEE Transactions on Power Systems*, vol. 21, no. 4, pp. 1821–1831, 2006. 123, 169

[100] M. Kazemi and H. Zareipour, "Long-term scheduling of battery storage systems in energy and regulation markets considering battery's lifespan," *IEEE Transactions on Smart Grid*, vol. 9, no. 6, pp. 6840–6849, 2017. 198

[101] M. Kazemi, H. Zareipour, N. Amjady, W. D. Rosehart, and M. Ehsan, "Operation scheduling of battery storage systems in joint energy and ancillary services markets," *IEEE Transactions on Sustainable Energy*, vol. 8, no. 4, pp. 1726–1735, 2017. 198

[102] P. Keil, S. F. Schuster, J. Wilhelm, J. Travi, A. Hauser, R. C. Karl, and A. Jossen, "Calendar aging of lithium-ion batteries i. impact of the graphite anode on capacity fade," *Journal of The Electrochemical Society*, vol. 163, no. 9, pp. A1872–A1880, 2016. 53

[103] H. Kleinrath, *Stromrichtergespeiste Drehfeldmaschinen*. Vienna, Austria: Springer-Verlag, 1980. 262

[104] D. Kucevic, B. Tepe, S. Englberger, A. Parlikar, M. Mühlbauer, O. Bohlen, A. Jossen, and H. Hesse, "Standard battery energy storage system profiles: Analysis of various applications for stationary energy storage systems using a holistic simulation framework," *Journal of Energy Storage*, vol. 28, p. 101077, 2020. 15

[105] P. P. Kundu and K. Dutta, *Progress and recent trends in microbial fuel cells*. Amsterdam, The Netherlands: Elsevier, 2018, ch. Biochemistry and Electrochemistry at the Electrodes of Microbial Fuel Cells. 54

[106] M. J. Lain, J. Brandon, and E. Kendrick, "Design strategies for high power vs. high energy lithium ion cells," *Batteries*, vol. 5, no. 4, p. 64, 2019. 55, 276

[107] Y. Lin, B. Johnson, V. Gevorgian, V. Purba, and S. Dhople, "Stability assessment of a system comprising a single machine and inverter with scalable ratings," in *Proc. of the North American Power Symposium (NAPS 2017)*, Morgantown, West Virginia, USA, Sep. 17 – 19, 2017, pp. 1–6. 123

[108] D. Linden and T. Reddy, *Handbook of Batteries*, 3rd ed. New York, USA: McGraw-Hill, 2002. 50, 56, 272, 275

[109] J. Liu, Y. Miura, H. Bevrani, and T. Ise, "Enhanced virtual synchronous generator control for parallel inverters in microgrids," *IEEE Transactions on Smart Grid*, vol. 8, no. 5, pp. 2268–2277, 2016. 122

[110] P. Lombardi and F. Schwabe, "Sharing economy as a new business model for energy storage systems," *Applied energy*, vol. 188, pp. 485–496, 2017. 194, 196, 198

[111] M. A. G. López, J. L. G. de Vicuña, J. Miret, M. Castilla, and R. Guzmán, "Control strategy for grid-connected three-phase inverters during voltage sags to meet grid codes and to maximize power delivery capability," *IEEE Transactions on Power Electronics*, vol. 33, no. 11, pp. 9360–9374, 2018. 146

[112] M. S. Mahmoud, *Microgrid: advanced control methods and renewable energy system integration*. Oxford, UK: Butterworth–Heinemann, 2016. 169

[113] J. Marchgraber, C. Alacs, G. Lettner, W. Gawlik, P. Jonke, M. Wurm, R. Lechner, R. Igelspacher, G. Wailzer, and W. Vitovec, "Erkenntnisse aus dem Forschungsprojekt BatterieSTABIL," in *Proc. of the 16th Symposium Energieinnovation (EnInnov 2020)*, Graz, Austria, Feb. 12 – 14, 2020, pp. 1–13.

[114] J. Marchgraber, C. Alacs, W. Gawlik, J. Kathan, M. Wurm, G. Wailzer, and W. Vitovec, "Netzdienstleistungen und Netzstabilisierung - Erste Erkenntnisse aus dem Forschungsprojekt BatterieSTABIL," in *Proc. of the 15th Symposium Energieinnovation (EnInnov 2018)*, Graz, Austria, Feb. 14 – 16, 2018, pp. 1–13. 65, 66, 281, 287

[115] J. Marchgraber, C. Alács, Y. Guo, W. Gawlik, A. Anta, A. Stimmer, M. Lenz, M. Froschauer, and M. Leonhardt, "Comparison of control strategies to realize synthetic inertia in converters," *Energies*, vol. 13, no. 13, p. 3491, 2020. 76, 122, 175, 176, 217, 220

[116] J. Marchgraber, C. Alács, S. Nemec-Begluk, W. Gawlik, P. Jonke, M. Wurm, G. Wailzer, and W. Vitovec, "Schwarzstart und Inselbetrieb eines Netzabschnitts mit Windenergieeinspeisung mithilfe eines Batteriespeichers," in *Proc. of the 11th Internationale Energiewirtschaftstagung (IEWT 2019)*, Vienna, Austria, Feb. 13 – 15, 2019, pp. 1–17. 181

[117] J. Marchgraber, D. Fasthuber, , M. Litzlbauer, and W. Gawlik, "Entwicklung von Regel-und Betriebsführungsstrategien für Microgrids im Zuge des SORGLOS-Projekts," in *Proc. of the D-A-CH Energieinformatik 2014*, Zürich, Switzerland, Nov. 13 – 14, 2014, pp. 1–7.

[118] J. Marchgraber and W. Gawlik, "Dynamic Voltage Support of Converters during Grid Faults in Accordance with National Grid Code Requirements," *Energies*, vol. 13, no. 10, p. 2484, 2020. 146, 175, 205, 210

[119] J. Marchgraber and W. Gawlik, "Investigation of Black-Starting and Islanding Capabilities of a Battery Energy Storage System Supplying a Microgrid Consisting of Wind Turbines, Impedance- and Motor-Loads," *Energies*, vol. 13, no. 19, p. 5170, 2020. 170

[120] J. Marchgraber and W. Gawlik, "Dynamic prioritization of functions during real-time multi-use operation of battery energy storage systems," *Energies*, vol. 14, no. 3, p. 655, 2021. 193

[121] J. Marchgraber, W. Gawlik, and C. Alács, "Modellierung und Simulation von Batteriespeichern bei der Erbringung von Primärregelleistung," *Elektrotech. Inftech.*, vol. 136, no. 1, pp. 3–11, 2019. 81, 119

[122] J. Marchgraber, W. Gawlik, and G. Wailzer, "Reducing SoC-management and losses of battery energy storage systems during provision of frequency containment reserve," *Journal of Energy Storage*, vol. 27, p. 101107, 2020. 81, 97, 98, 102, 117, 201, 213, 282

[123] J. Marchgraber, W. Gawlik, and M. Wurm, "Modellierung der dynamischen Netzstützung von über Umrichter angebundenen Erzeugungsanlagen und Speichern," *Elektrotechn. Inftech.*, vol. 136, no. 1, pp. 31–38, Feb 2019. 152, 163, 165, 284

[124] J. Marchgraber, E. Xypolytou, I. Lupandina, W. Gawlik, and M. Stifter, "Measurement-based determination of static load models in a low voltage grid," in *Proc. of the IEEE PES Innovative Smart Grid Technologies Conference Europe (ISGT-Europe 2016)*, Ljubljana, Slovenia, Oct. 9 – 16, 2016, pp. 1–6. 261

[125] C. Marnay, S. Chatzivasileiadis, C. Abbey, R. Iravani, G. Joos, P. Lombardi, P. Mancarella, and J. von Appen, "Microgrid evolution roadmap," in *Proc. of the International Symposium on Smart Electric Distribution Systems and Technologies (EDST 2015)*, Vienna, Austria, Sep. 8 – 11, 2015, pp. 139–144. 77, 169

[126] G. J. May, A. Davidson, and B. Monahov, "Lead batteries for utility energy storage: A review," *Journal of Energy Storage*, vol. 15, pp. 145–157, 2018. 56

[127] A. Mehrizi-Sani and R. Iravani, "Potential-function based control of a microgrid in islanded and grid-connected modes," *IEEE Transactions on Power Systems*, vol. 25, no. 4, pp. 1883–1891, 2010. 123

[128] F. Milano, F. Dörfler, G. Hug, D. J. Hill, and G. Verbič, "Foundations and challenges of low-inertia systems," in *Proc. of the IEEE Power Systems Computation Conference (PSCC 2018)*, Dublin, Ireland, Jun. 11 – 15, 2018, pp. 1–25. 122, 123

[129] N. Miller, K. Clark, and R. Walling, "Windinertia: controlled inertial response from ge wind turbine generators," in *Proc. of the 45th annual Minnesota power systems conference (MIPSYCON 2009)*, Minneapolis, Minnesota, USA, Nov. 3 – 5, 2009, pp. 1–14. 132

[130] K. Mongird, V. V. Viswanathan, P. J. Balducci, M. J. E. Alam, V. Fotedar, V. S. Koritarov, and B. Hadjerioua, "Energy storage technology and cost characterization report," Pacific Northwest National Laboratory (PNNL) operated by U.S. Department of Energy (DOE), Richland, Washington, USA, Tech. Rep. PNNL-28866, Jul. 2019. 8, 62, 287

[131] S. Mortazavian, M. M. Shabestary, and Y. A.-R. I. Mohamed, "Analysis and dynamic performance improvement of grid-connected voltage–source converters under unbalanced network conditions," *IEEE Transactions on Power Electronics*, vol. 32, no. 10, pp. 8134–8149, 2016. 146

[132] E. Namor, F. Sossan, R. Cherkaoui, and M. Paolone, "Control of battery storage systems for the simultaneous provision of multiple services," *IEEE Transactions on Smart Grid*, 2018. 15, 198

[133] National-Grid, "Enhanced frequency response: Invitation to tender for pre-qualified parties," Policy, 2018, Available online: https://www.nationalgrideso.com/sites/eso/files/documents/Enhanced%20Frequency%20Response%20ITT%20v2_2%20clean.pdf (accessed on 05.08.2020). 76

[134] T. Nikolakakis and V. Fthenakis, "Compressed air energy storage models for energy arbitrage and ancillary services: Comparison using mixed integer programming optimization with market data from the irish power system," *Energy Technology*, vol. 6, no. 7, pp. 1290–1301, 2018. 7

[135] N. Nitta, F. Wu, J. T. Lee, and G. Yushin, "Li-ion battery materials: present and future," *Materials today*, vol. 18, no. 5, pp. 252–264, 2015. 56

[136] Österreichs Energie, "Die Strategie von Oesterreichs Energie bis zum Jahr 2030," Brochure, 2015, Available online: https://oesterreichsenergie.at/files/Stromstrategie/Stromstrategie_Broschuere_kl.pdf (accessed on 08.09.2020). 2

[137] B. R. Oswald, *Berechnung von Drehstromnetzen*. Wiesbaden, Germany: Springer Vieweg, 2017, ch. Symmetrische Komponenten und Raumzeiger, p. 9. 22

[138] *OVE EN 50160:2011*, OVE Std., 2016, Available online: https://shop.austrian-standards.at/action/de/public/details/383226/OEVE_OENORM_EN_50160_2011_03_01 (accessed on 23.06.2020). 137, 230

[139] F. Z. Peng and J.-S. Lai, "Generalized instantaneous reactive power theory for three-phase power systems," *IEEE Transactions on Instrumentation and Measurement*, vol. 45, no. 1, pp. 293–297, 1996. 255

[140] Z. Peng, J. Wang, D. Bi, Y. Wen, Y. Dai, X. Yin, and Z. J. Shen, "Droop control strategy incorporating coupling compensation and virtual impedance for microgrid application," *IEEE Transactions on Energy Conversion*, vol. 34, no. 1, pp. 277–291, 2019. 169

[141] S. Ponnaluri, G. O. Linhofer, J. K. Steinke, and P. K. Steimer, "Comparison of single and two stage topologies for interface of bess or fuel cell system using the abb standard power electronics building blocks," in *Proc. of the IEEE European Conference on Power Electronics and Applications (EPE 2005)*, Dresden, Germany, Sep. 11 – 14, 2005, pp. 9–pp. 60

[142] B. K. Poolla, S. Bolognani, L. Na, and F. Dörfler, "A market mechanism for virtual inertia," *IEEE Transactions on Smart Grid*, vol. 11, no. 4, pp. 3570–3579, 2020. 122

[143] B. K. Poolla, D. Groß, and F. Dörfler, "Placement and implementation of grid-forming and grid-following virtual inertia and fast frequency response," *IEEE Transactions on Power Systems*, vol. 34, no. 4, pp. 3035–3046, 2019. 137

[144] R. Rao, S. Vrudhula, and D. N. Rakhmatov, "Battery modeling for energy aware system design," *Computer*, vol. 36, no. 12, pp. 77–87, 2003. 276

[145] regelleistung.net, "Results overview of capacity market," Website, 2020, Available online: https://www.regelleistung.net/apps/datacenter/tendering-files/?productTypes=FCR&markets=CAPACITY&fileTypes=RESULTS&dateRange=2014-01,2020-07 (accessed on 05.08.2020). 8

[146] M. Rezkalla, A. Zecchino, S. Martinenas, A. M. Prostejovsky, and M. Marinelli, "Comparison between synthetic inertia and fast frequency containment control based on single phase evs in a microgrid," *Applied Energy*, vol. 210, pp. 764–775, 2018. 136

[147] RG-CE System Protection and Dynamics Sub Group, "Frequency stability evaluation criteria for the synchronous zone of Continental Europe," ENTSO-E, Brussels, Belgium, Tech. Rep., Mar. 2016, Available online: https://eepublicdownloads.blob.core.windows.net/public-cdn-container/clean-documents/SOC%20documents/RGCE_SPD_frequency_stability_criteria_v10.pdf (accessed on 23.06.2020). 122

[148] RG-CE System Protection and Dynamics Sub Group, "Frequency Stability Evaluation Criteria for the Synchronous Zone of Continental Europe," ENTSO-E, Belgium, Brussels, Tech. Rep., Mar. 2016, Available online: https://eepublicdownloads.entsoe.eu/clean-documents/SOC%20documents/RGCE_SPD_frequency_stability_criteria_v10.pdf (accessed on 23.06.2020). 140

[149] RG-CE System Protection and Dynamics Sub Group, "Frequency Stability Evaluation Criteria for the Synchronous Zone of Continental Europe," ENTSO-E, Belgium, Brussels, Tech. Rep., Mar. 2016, Available online: https://eepublicdownloads.entsoe.eu/clean-documents/SOC%20documents/RGCE_SPD_frequency_stability_criteria_v10.pdf (accessed on 27.06.2019). 217

[150] RG-CE System Protection and Dynamics Sub Group, "Frequency Measurement Requirements and Usage," ENTSO-E, Belgium, Brussels, Tech. Rep., Jan. 2018, Available online: https://eepublicdownloads.entsoe.eu/clean-documents/SOC%20documents/Regional_Groups_Continental_Europe/2018/TF_Freq_Meas_v7.pdf (accessed on 23.06.2020). 140

[151] P. Rodriguez, A. V. Timbus, R. Teodorescu, M. Liserre, and F. Blaabjerg, "Flexible active power control of distributed power generation systems during grid faults," *IEEE Transactions on Industrial Electronics*, vol. 54, no. 5, pp. 2583–2592, 2007. 146

[152] C. Roggatz, M. Power, and N. Singh, "Power system restoration: Meeting the challenge to resiliency from distributed generation," *IEEE Power and Energy Magazine*, vol. 18, no. 4, pp. 31–40, 2020. 169

[153] M. B. Salles, J. Huang, M. J. Aziz, and W. W. Hogan, "Potential arbitrage revenue of energy storage systems in pjm," *Energies*, vol. 10, no. 8, p. 1100, 2017. 7

[154] S. Saxena, C. Hendricks, and M. Pecht, "Cycle life testing and modeling of graphite/licoo2 cells under different state of charge ranges," *Journal of Power Sources*, vol. 327, pp. 394–400, 2016, Supplementary data available online: https://calce.umd.edu/data#PL; accessed on 04. November 2020. 53, 281

[155] M. Schimpe, M. Naumann, N. Truong, H. C. Hesse, S. Santhanagopalan, A. Saxon, and A. Jossen, "Energy efficiency evaluation of a stationary lithium-ion battery container storage system via electro-thermal modeling and detailed component analysis," *Applied energy*, vol. 210, pp. 211–229, 2018. 69

[156] M. Schimpe, M. E. von Kuepach, M. Naumann, H. C. Hesse, K. Smith, and A. Jossen, "Comprehensive modeling of temperature-dependent degradation mechanisms in lithium iron phosphate batteries," *Journal of The Electrochemical Society*, vol. 165, no. 2, pp. A181–A193, 2018. 53

[157] J. Schlund and R. German, "A control algorithm for a heterogeneous virtual battery storage providing FCR power," in *Proc. of the IEEE International Conference on Smart Grid and Smart Cities (ICSGSC 2017)*, Singapore, Jun. 23 – 6, 2017, pp. 61–66. 95

[158] J. Schlund, D. Steber, P. Bazan, and R. German, "Increasing the efficiency of a virtual battery storage providing frequency containment reserve power by applying a clustering algorithm," in *Proc. of the IEEE Innovative Smart Grid Technologies-Asia (ISGT-Asia 2017)*, Auckland, New Zealand, Dec. 4 – 7, 2017, pp. 1–8. 95

[159] D. Schröder, *Elektrische Antriebe-Grundlagen: Mit durchgerechneten Übungs-und Prüfungsaufgaben*. Springer-Verlag, 2007, p. 372. 262, 285

[160] D. Schröder, *Elektrische Antriebe-Grundlagen: Mit durchgerechneten Übungs-und Prüfungsaufgaben*. Springer-Verlag, 2007, p. 312. 262

[161] Y. Shi, B. Xu, D. Wang, and B. Zhang, "Using battery storage for peak shaving and frequency regulation: Joint optimization for superlinear gains," *IEEE Transactions on Power Systems*, vol. 33, no. 3, pp. 2882–2894, 2017. 198

[162] D. Shin, K.-J. Lee, J.-P. Lee, D.-W. Yoo, and H.-J. Kim, "Implementation of fault ride-through techniques of grid-connected inverter for distributed energy resources with adaptive low-pass notch pll," *IEEE Transactions on Power Electronics*, vol. 30, no. 5, pp. 2859–2871, 2014. 146

[163] R. Sioshansi, P. Denholm, T. Jenkin, and J. Weiss, "Estimating the value of electricity storage in pjm: Arbitrage and some welfare effects," *Energy Economics*, vol. 31, no. 2, pp. 269 – 277, 2009. 7

[164] SMA, "Design of off-grid systems with sunny island 4.4m/6.0h/8.0h devices," Website, 2020, Available online: https://files.sma.de/downloads/Designing-OffGridSystem-PL-en-24.pdf (accessed on 23.06.2020). 172

[165] J. Specovius, *Grundkurs Leistungselektronik: Bauelemente, Schaltungen und Systeme*. Wiesbaden, Germany: Springer Vieweg, 2018. 47

[166] A.-I. Stan, M. Świerczyński, D.-I. Stroe, R. Teodorescu, and S. J. Andreasen, "Lithium ion battery chemistries from renewable energy storage to automotive and back-up power applications—an overview," in *Proc. of the IEEE International Conference on Optimization of Electrical and Electronic Equipment (OPTIM 2014)*, Brasov, Romania, May 22 – 24, 2014, pp. 713–720. 56, 274

[167] A. Stephan, B. Battke, M. D. Beuse, J. H. Clausdeinken, and T. S. Schmidt, "Limiting the public cost of stationary battery deployment by combining applications," *Nature Energy*, vol. 1, no. 7, pp. 1–9, 2016. 15, 197, 198

[168] M. Sterner and I. Stadler, *Handbook of Energy Storage: Demand, Technologies, Integration*. Berlin, Germany: Springer-Verlag Berlin Heidelberg, 2019. 3, 4, 9, 52, 74, 77, 132, 168, 270, 276, 287

[169] A. Stimmer, M. Lenz, M. Forschauer, M. Leonhardt, W. Gawlik, C. Alacs, C. Corinaldesi, G. Lettner, Y. Guo, J. Marchgraber, A. Anta, and K. Oberhauser, "Options for the implementation of fast control reserves in the continental european power system," in *Proc. of the 4th Grid Service Markets Symposium*, Luzern, Switzerland, Oct. 19 – 20, 2020, pp. 54–65. 227

[170] N. M. Tabatabaei, E. Kabalci, and N. Bizon, *Microgrid architectures, control and protection methods*, 1st ed. Basel, Switzerland: Springer International Publishing, 2020. 169

[171] A. Tabesh and R. Iravani, "Multivariable dynamic model and robust control of a voltage-source converter for power system applications," *IEEE Transactions on Power Delivery*, vol. 24, no. 1, pp. 462–471, 2008. 123

[172] G. G. Talapur, H. M. Suryawanshi, A. B. Shitole, and P. Nachankar, "Combined droop and master-slave method for load sharing in stand-alone ac microgrid," in *Proc. of the 44th Annual Conference of the IEEE Industrial Electronics Society (IECON 2018)*, Washington, D.C. , USA, Oct. 21 – 23, 2018, pp. 1705–1710. 170

[173] U. Tamrakar, D. Shrestha, M. Maharjan, B. P. Bhattarai, T. M. Hansen, and R. Tonkoski, "Virtual inertia: Current trends and future directions," *Applied Sciences*, vol. 7, no. 7, p. 654, 2017. 122

[174] M. G. Taul, X. Wang, P. Davari, and F. Blaabjerg, "Current reference generation based on next generation grid code requirements of grid-tied converters during asymmetrical faults," *IEEE Journal of Emerging and Selected Topics in Power Electronics*, 2019. 146

[175] A. Tayyebi, F. Dörfler, F. Kupzog, Z. Miletic, and W. Hribernik, "Grid-forming converters–inevitability, control strategies and challenges in future grids application," in *Proc. of the CIRED 2018 Ljubljana Workshop on Microgrids and Local Energy Communities (CIRED 2018)*, Ljubljana, Slovenia, Jun. 7 – 8, 2018, paper 0236, pp. 1–5. 123, 136

[176] A. Tayyebi, D. Groß, A. Anta, F. Kupzog, and F. Dörfler, "Frequency stability of synchronous machines and grid-forming power converters," *IEEE Journal of Emerging and Selected Topics in Power Electronics*, vol. 8, no. 2, pp. 1004–1018, 2020. 123

[177] R. Teodorescu, M. Liserre, and P. Rodriguez, *Grid converters for photovoltaic and wind power systems*. Hoboken, USA: John Wiley & Sons, 2011. 44, 46, 47, 123, 125, 146, 159

[178] TERNA, "Fast reserve," Presentation, Jul. 2020, Available online: https://download.terna.it/terna/Fast%20Reserve%20-%20Information%20pack_8d82fe02cbed7ad.pdf; (accessed on 05.08.2020). 76, 216

[179] The MathWorks, Inc., "Documentation; simulation and model-based design," Manual, 2020, Available online: https://www.mathworks.com/products/simulink.html (accessed on 23.06.2020). 129, 132

[180] T. Thien, H. Axelsen, M. Merten, S. Zurmühlen, J. Münderlein, M. Leuthold, and D. U. Sauer, "Planning of grid-scale battery energy storage systems: Lessons learned from a 5MW hybrid battery storage project in germany," in *Proc. of the 19th Battcon International Stationary Battery Conference (Battcon 2015)*, Orlando, Florida, USA, May 12 – 14, 2015, pp. 1–18. 58

[181] C. N. Truong, M. Schimpe, U. Bürger, H. C. Hesse, and A. Jossen, "Multi-use of stationary battery storage systems with blockchain based markets," *Energy Procedia*, vol. 155, pp. 3–16, 2018. 16, 198

[182] UCTE, "Load-frequency control and performance; Appendix A1," Policy, 2004, Available online: https://www.entsoe.eu/fileadmin/user_upload/_library/publications/entsoe/Operation_Handbook/Policy_1_Appendix%20_final.pdf; accessed on 19. March 2019. 39, 225

[183] *VDE-AR-N 4110: Technische Regeln für den Anschluss von Kundenanlagen an das Mittelspannungsnetz und deren Betrieb (TAR Mittelspannung)*, VDE Std., 2018. 145, 148, 150, 151, 218, 219

[184] V. Verma and G. G. Talpur, "Decentralized master-slave operation of microgrid using current controlled distributed generation sources," in *Proc. of the IEEE International Conference on Power Electronics, Drives and Energy Systems (PEDES 2012)*, Bengaluru, India, Dec. 16 – 19, 2012, pp. 1–6. 170

[185] H.-P. Vetö and J. Marchgraber, "Betrachtung von Kurzschlüssen in dieselgeneratorversorgten Inselnetzen–Vergleich transienter Rechnung mit Rechnung gemäß IEC 60909-0: 2016," *Elektrotech. Inftech.*, vol. 133, no. 8, pp. 407–415, 2016. 34

[186] S. Wachtel and A. Beekmann, "Contribution of wind energy converters with inertia emulation to frequency control and frequency stability in power systems," in *Proc. of the 8th International Workshop on Large-Scale Integration of Wind Power into Power Systems as well as on Transmission Networks for Offshore Wind Farms*, Bremen, Germany, Oct. 14 – 15, 2009, pp. 460–465. 132

[187] T. Wagner, "emarketcrawlR," Software, Available online: https://github.com/wagnertimo/emarketcrawlR; accessed on 04. November 2019. 189, 284

[188] K. Wang, "Study on low temperature performance of li ion battery," *Open Access Library Journal*, vol. 4, no. 11, pp. 1–12, 2017. 61

[189] L. Wang, A. Menakath, F. Han, Y. Wang, P. Y. Zavalij, K. J. Gaskell, O. Borodin, D. Iuga, S. P. Brown, C. Wang *et al.*, "Identifying the components of the solid–electrolyte interphase in li-ion batteries," *Nature chemistry*, vol. 11, no. 9, pp. 789–796, 2019. 275

[190] E. Warburg, "Über das verhalten sogenannter unpolarisirbarer Elektroden gegen Wechselstrom," *Annalen der Physik*, vol. 303, no. 3, pp. 493–499, 1899. 277

[191] M. Weidinger, "Untersuchung von niederfrequenten oszillationen im kontinentaleuropäischen verbundsystem mit hilfe eines mehrmassenschwinger modells," Master's thesis, TU Wien, Vienna, Austria, 2021. 79

[192] J. Wienböker, M. Möller, and R. Gersch, "System und Verfahren zur Erbringung einer Regelleistung für ein Stromnetz," Patent, 2016, European Patent EP3136532A1, US patent US15/241,366. Available online: https://patents.google.com/patent/EP3136532A1; accessed on 19. March 2019. 95

[193] N. Williard, W. He, M. Osterman, and M. Pecht, "Comparative analysis of features for determining state of health in lithium-ion batteries," *Int. J. Progn. Health Manag*, vol. 4, pp. 1–7, 2013, Available online: https://calce.umd.edu/data#CS2; accessed on 04. November 2020. 51, 55, 272, 281

[194] D. Wu, C. Jin, P. Balducci, and M. Kintner-Meyer, "An energy storage assessment: Using optimal control strategies to capture multiple services," in *Proc. of the IEEE Power & Energy Society General Meeting (PES GM 2015)*, Denver, Colorado, USA, Jul. 26 – 30, 2015, pp. 1–5. 198

[195] F.-B. Wu, J.-L. Ye, and B. Yang, *Grid-scale energy storage systems and applications*. London, UK: Academic Press, 2019. 58

[196] M. Wurm, "110-und 30-kV-Netzkurzschlussversuche mit einem 2,2-MWh-Batteriespeicher," *Elektrotech. Inftech.*, vol. 136, no. 1, pp. 21–30, 2019. 146, 162, 163, 165, 224, 284

[197] M. Wurm, P. Jonke, J. Marchgraber, W. Gawlik, and W. Vitovec, "Ortsnetz- Inselbetriebsversuch mit einem 2,5-MVA/2,2-MWh-Batteriespeicher: Messergebnisse und Vergleich mit einem Controller Hardware-in-the-loop Setup," *Elektrotech. Inftech.*, vol. 136, no. 8, pp. 368–376, 2019. 132, 176, 181

[198] X. Xi, R. Sioshansi, and V. Marano, "A stochastic dynamic programming model for co-optimization of distributed energy storage," *Energy Systems*, vol. 5, no. 3, pp. 475–505, 2014. 197, 198

[199] Y. Xing, W. He, M. Pecht, and K. L. Tsui, "State of charge estimation of lithium-ion batteries using the open-circuit voltage at various ambient temperatures," *Applied Energy*, vol. 113, pp. 106–115, 2014, Supplementary data available online: https://calce.umd.edu/data#A123; accessed on 04. November 2020. 272

[200] E. Xypolytou, W. Gawlik, T. Zseby, and J. Fabini, "Impact of asynchronous renewable generation infeed on grid frequency: Analysis based on synchrophasor measurements," *Sustainability*, vol. 10, no. 5, p. 1605, 2018. 140

[201] A. Yazdani and R. Iravani, *Voltage-sourced converters in power systems: modeling, control, and applications*. Hoboken, USA: John Wiley & Sons, 2010. 128, 129, 160, 176

[202] B. Zakeri and S. Syri, "Value of energy storage in the nordic power market-benefits from price arbitrage and ancillary services," in *Proc. of the 13th International Conference on the European Energy Market (EEM 2016)*, Porto, Portugal, Jun. 6 – 9, 2016, pp. 1–5. 7

[203] A. Zeh, M. Mueller, H. C. Hesse, A. Jossen, and R. Witzmann, "Operating a multitasking stationary battery storage system for providing secondary control reserve on low-voltage level," in *Proc. of the International ETG Congress 2015*, Bonn, Germany, Nov. 17 – 18, 2015, pp. 1–8. 198, 237

[204] B. Zhao, X. Zhang, P. Li, K. Wang, M. Xue, and C. Wang, "Optimal sizing, operating strategy and operational experience of a stand-alone microgrid on dongfushan island," *Applied Energy*, vol. 113, pp. 1656–1666, 2014. 169

[205] F. Zheng, Y. Xing, J. Jiang, B. Sun, J. Kim, and M. Pecht, "Influence of different open circuit voltage tests on state of charge online estimation for lithium-ion batteries," *Applied energy*, vol. 183, pp. 513–525, 2016, Supplementary data available online: https://calce.umd.edu/data#INR; accessed on 04. November 2020. 272

[206] Q.-C. Zhong and T. Hornik, *Control of power inverters in renewable energy and smart grid integration*. Chichester, West Sussex, UK: John Wiley & Sons, 2012, vol. 97. 123

[207] Q.-C. Zhong, P.-L. Nguyen, Z. Ma, and W. Sheng, "Self-synchronized synchronverters: Inverters without a dedicated synchronization unit," *IEEE Transactions on Power Electronics*, vol. 29, no. 2, pp. 617–630, 2013. 123

[208] Q.-C. Zhong and G. Weiss, "Synchronverters: Inverters that mimic synchronous generators," *IEEE Transactions on Industrial Electronics*, vol. 58, no. 4, pp. 1259–1267, 2010. 124